SCHOLARLY PUBLICATIONS

A CURRENT AWARENESS BULLETIN
OF RESEARCH OUTPUT

@DTU

(41st Edition)

MAY 2016

BY: CENTRAL LIBRARY

DELHI TECHNOLOGICAL UNIVERSITY
(FORMERLY *DELHI COLLEGE OF ENGINEERING)*
GOVT. OF N.C.T. OF DELHI
SHAHBAD DAULATPUR, MAIN BAWANA ROAD
DELHI 110042

PREFACE

This is the **Forty one** Issue of Current Awareness Bulletin started by Delhi Technological University, Central Library. The aim of the bulletin is to compile, preserve and disseminate information published by the faculty, students and alumni for mutual benefits. The bulletin also aims to propagate the intellectual contribution of Delhi Technological University (DTU) as a whole to the academia.

The bulletin contains information resources available in the internet in the form of articles, reports, presentations published in international journals, websites, etc. by the faculty and students of DTU. The publications of faculty and student which are not covered in this bulletin may be because of the reason that the full text either was not accessible or could not be searched by the search engine used by the library for this purpose.

The learned faculty and students are requested to provide their uncovered publications to the library either through email or in CD, etc to make the bulletin more comprehensive.

This issue contains the information published during **May 2016**. The arrangement of the contents is alphabetical. The full text of the article which is either subscribed by the university or available in the web is provided in this bulletin.

Central Library

CONTENTS

9. Compatibility issues of cement with water reducing admixture in concrete, ***3.A.K. Shrivastava*** and ***3.Munendra Kumar***, Civil Engineering, DTU

10. Degradation of Lindane by Sludge Enriched on Mixed Commercial Formulations of Organophosphate and Pyrethroid Pesticides, ***3.Satish Kumar***, ***3.Rajkumar Bidlan*** and ***3.Jai Gopal Sharma***, Biotechnology, DTU

11. Design and analysis of polarization independent all-optical logic gates in silicon-on-insulator photonic crystal, ***3.Preeti Rani***, ***3.Yogita Kalra***, and ***3.R.K. Sinha***, Applied Physics, DTU

12. Design and Analysis of Trench-assisted Leaky Channel Waveguide for High Power Applications, ***3.Himanshu Pandey***, ***3.Than Singh Saini*** and ***3.Ajeet Kumar***, Applied Physics, DTU

13. Design and Performance Analysis of Solar Parabolic Trough for Cooking Application**,** ***3.ShubhamGupta***, ***3.R.S.Mishra***, Mechanical Engineering, DTU

14. Designing an In-Silico Mimetic for Thrombopoietin Using Combinatorial Library, ***3.Vimal Kishor Singh***, ***3.Ishita Goyal***, ***3.Abhishek Saini*** , Neeraj Kumar, Manisha Kalsan, and Ramesh Chandra, Biotechnology, DTU

15. Effective relative permittivity and characteristic impedance of graphene loaded microstrip line by scalar S-parameters, Kamlesh Patel ,Neha, and ***3.Pawan K. Tyagi***, Applied Physics, DTU

16. Effects of Various Road Conditions on Dynamic Behaviour of Heavy Road Vehicle, ***6.Ashish Gupta*** and ***3.Vikas Rastogi***, Mechanical Engineering Department, DTU

17. Energy planning problems with interval-valued 2-tuple linguistic information, ***3.Anjali Singh***, ***3.Anjana Gupta*** and Aparna Mehra, Applied Mathematics, DTU

18. Experimental Investigation of Vibration Analysis of Multi-Crack Rotor Shaft, Anuj Kumar Jain, ***3.Vikas Rastogi***, and Atul Kumar Agrawal, Mechanical Engineering, DTU

19. Finite Element Modeling and Analysis of Powder Stream in Low Pressure Cold Spray Process, Tarun Goyal, ***3.Ravinderjit Singh Walia***, Prince Sharma and Tejinder Singh Sidhu, DTU

20. Genralized Positive Linear Operators Based On Ped And ***Iped Naokant Deo*** And ***Minakshi Dhamija***, Applied Mathematics, DTU

21. Interfacial Charge Analysis of Heterogeneous Gate Dielectric Gate All Around - Tunnel FET for Improve Device Reliability, ***3.Jaya Madan*** and ***3.Rishu Chaujar***, Engineering Physics, DTU

22. Low band gap polymeric solar cells using solution-processable copper iodide as hole transporting layer, ***3.Neeraj Chaudhary***, ***3.J.P. Kesari*** , ***3.Rajiv Chaudhary*** and Asit Patra, Mechanical Engineering, DTU

23. Performance of the vanadium redox-flow battery (VRB)for Si-PWA/PVA nanocomposite membrane, ***3.Jay Pandey*** and Bhagya R. Tankal, Polymer Science and Chemical Technology, DTU

24. Polyaniline modified flexible conducting paper for cancer detection, Saurabh Kumar, Anindita Sen, Suveen Kumar, Shine Augustine and Birendra K. Yadav, ***3.Sandeep Mishra*** and Bansi D. Malhotra, Applied Physics, DTU

25. Power system restructuring models in the Indian context, ***3.Madan Mohan Tripathi***, Anil Kumar Pandey and Dinesh Chandra, DTU

26. Recent developments in affective recommender systems, ***3.Rahul Katarya*** and ***3.Om Prakash Verma***, Computer Science & Engineering, DTU

27. Rectangular-core large-mode-area photonic crystal fiber for high power applications: design and analysis, ***3.Reena***, ***3.Than Singh Saini***, Ajeet Kumar, ***3.Yogita Kalra*** and ***3.Ravindra Kumar Sinha***, Applied Physics, DTU

28. Refractive index dispersion of swift heavy ion irradiated BFO thin films using Surface Plasmon Resonance technique, Ayushi Paliwal, ***3.Savita Sharma***, Monika Tomar, Fouran Singh and Vinay Gupta, Applied Physics, DTU

29. Removal of Zn (II) from Aqueous Solution Using Agro -based Adsorbents, Achla Kaushal and ***3.S.K.Singh***, Environmental Technology, DTU

30. Slow Light Generation in Single-Mode Rectangular Core Photonic Crystal Fiber, ***3.Sandeep Yadav, 3.Than Singh Saini*** and Ajeet Kumar, Applied Physics, DTU

31. Wear Characteristics of Al5083 Surface Hybrid Nano-composites by Friction Stir Processing, ***3.N.Yuvaraj***, S.Aravindan and ***3.Vipin***, Mechanical Engineering, DTU

1. Chancellor

2. Pro Vice Chancellor — ***2.1. Ex Pro Vice Chancellor***

3. Faculty — ***3.1. Ex Faculty***

4. Teaching-cum-Research Fellow

5. Alumni

6. Research Scholar — ***6.1. Ex Research Scholar***

7. PG Scholar — ***7.1. Ex PG Scholar***

8. Undergraduate Student — ***8.1. Ex Undergraduate Student***

A Comparative study of Wind Power Forecasting Techniques – A Review Article

Conference Paper · March 2016

2 authors, including:

Madanmohan Tripathi
Delhi Technological University
34 PUBLICATIONS **60** CITATIONS

Proceedings of the 10th INDIACom; INDIACom-2016; IEEE Conference ID: 37465
2016 3rd International Conference on "Computing for Sustainable Global Development", 16th - 18th March, 2016
Bharati Vidyapeeth's Institute of Computer Applications and Management (BVICAM), New Delhi (INDIA)

A Comparative study of Wind Power Forecasting Techniques – A Review Article

Jyothi Varanasi
Ph.D Research Scholar
Department of Electrical Engineering
Delhi Technological University
New Delhi, India
jyothi26varanasi@yahoo.com

M.M. Tripathi
Associate Professor
Department of Electrical Engineering
Delhi Technological University
New Delhi, India
mmtripathi@dce.ac.in

Abstract*— Globally, the power demand is increasing very rapidly. To meet this demand, the traditional expansion of conventional and fossil fuels leads to global warming. Also the long-term availability of the coal and other conventional energy sources is limited, which is one more reason for choosing renewable sources to generate electrical power. But, the major renewable energy sources especially wind energy is highly uncertain in its nature. In fact the high variability of wind power generation is affecting the power system operation. The integration of the renewable energy systems to grid is also an issue in terms of operation and control. The wind power forecasting has a major role in determining the size of operating reserves to balance the generation with load. To reduce the operating costs and to improve the reliability of the grid integrated to wind power systems, accurate wind power forecasting tools are necessary. This paper discusses the classification, various forecasting techniques and methods, performance evaluation factors etc. in forecasting of wind speed and wind power generation. This survey significantly shows the better performance by hybrid artificial intelligence models in terms of accuracy.

Keywords*— Wind power forecasting, statistical approach, physical approach, confidence interval, mean absolute percentage error, learning statistical method.

I. INTRODUCTION

About 75 to 80 percent of thermal pollution is generated by power plants which is primarily responsible for global warming. As the conventional energy sources are vanishing, renewable energy sources are the promising alternative to the conventional sources. Currently the world is moving towards clean energy with low carbon emissions. Smart grid technology development also encourages more wind power and solar power integration to the grid. The energy demand, by 2032 is estimated to be as high as 900 GW in India, out of which the renewable energy potential that can be exploited till 2032 is around 183 GW [1]. Wind power is growing rapidly all over the world especially in European countries, America and China .India also has sufficient potential for wind energy.

Globally 51473 MW of new wind generating capacity was added in 2014 according to the global wind market statistics given by the Global Wind Energy Council (GWEC). The Global Cumulative installed wind capacity by 2014 is 369597 MW [2]. Globally installed wind power capacity is increasing at a rate of 28% [3].It is also estimated that wind power contribution will be increased to 12% of the Global power generation by 2020. Worldwide, India has 5th largest wind installed capacity. The figure 1 shows 67 percent contribution of wind energy in India.

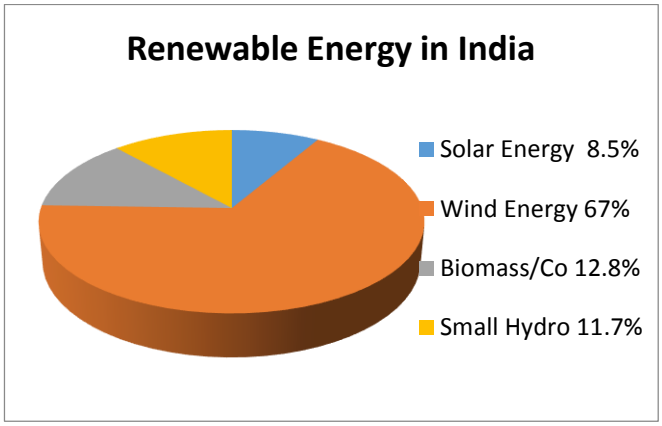

Fig.1: Current status of renewable energy in India

The variant nature of wind poses a few challenges to the power sector. Being uncertain and intermittent, the wind power integration leads to the unbalance between generation and load in the power grid. Wind power forecasting (WPF) is identified as an important task in the proper operation of power systems with large wind power penetrations. Wind speed and power forecasting plays a prominent role for maintaining balance of generation and load. Accurate wind power forecasting can provide a proper technical support for wind power trading in electricity market to achieve the significant economic benefit. To decide the operating reserves, the wind power forecasts are very much essential. Wind power

forecasts are also required in selecting the site & location of new wind farms. Accurate prediction of renewable energy is very much required, where the power system operators would be fined with the penalty cost for imbalance between predicted and actual generation. Since wind power is a non-linear function of wind speed, air density and turbulent kinetic energy and turbine characteristics [4], a lot of research is carried in the area of forecasting techniques of wind speed & wind power.

Wind power & speed forecasts are able to produce information about the wind speed & power in next few minutes, hours and days. Accordingly categorized into short term, medium term and long term as per the power system operational requirements. Short term forecasting is important for turbine control and also to balance with the load. Medium term forecasting is essential for managing power system and energy trading, whereas long term forecasting is focused for maintenance of wind farms. To plan the installation of new wind turbines and farms the technical assistance is obtained from long term wind speed and power forecasting. WPF is also a part of energy management system (EMS) implemented for Micro grid operation & control. EMS provides significant information for scheduling generating units and provides signals towards Demand side management [5], [6].Researchers developed many forecasting techniques with the increase of accuracy. This paper describes physical forecasting approach, statistical forecasting approach and the combination of both.

Rest of the paper is organized as follows. Section II discusses the classification of wind power forecasting. Section III presents wind power forecasting methods. Confidence level and interval are discussed in section IV and conclusion is presented in section V.

II. CLASSIFICATION OF WIND POWER FORECASTING

The wind energy forecasting methods basically can be categorized into 4 types based on the time horizon of forecasting as given below [7].

Very short term: It ranges from few seconds to30 minutes and used in wind turbine control, electricity market clearing etc.
Short term: It ranges from 30 minutes to 72 hrs and useful in economic load dispatch, load increment or decrement Decisions.
Medium term: It ranges from 72 hrs to one week ahead and used for maintenance related decisions/unit commitment.
Long term: It ranges from one week to one year ahead and applied in design of the wind farms.

Another classification of wind power forecasting according to used methods can be made as following.

A. Physical Approach

The physical approach needs the detailed physical description to model the on-site conditions by using Numerical weather prediction (NWP) data [8]. The economic benefit for Electricity Market using short term forecasting based on Physical method when there is high levels of wind power penetration into the grid is discussed [9]. The physical approach does not require training input from historical data. The other main forecasting method is statistical approach. It uses previous historical data to build statistical model.

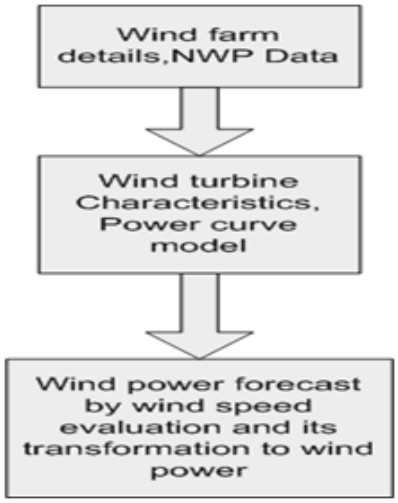

Fig. 2: The physical approach to wind speed & power forecast

B. Statistical Approach

The statistical methods are appropriate for short term, medium term, long term forecasting. But, in case of very short term and short term horizon, NWP data plays a vital role to achieve accuracy, Physical approaches are also essential. But most of the researchers aimed at short term forecasting using statistical methods [10].

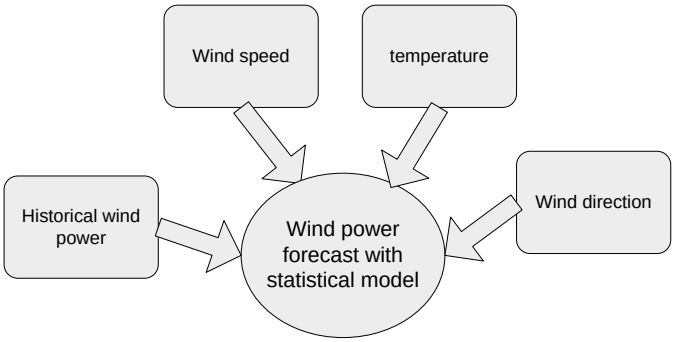

Fig.3: The Statistical approach to wind speed & power forecast

As per forecasting data, WPF can also be classified into wind speed forecasting (indirect method) and wind power forecasting (direct method) [11].

Some other additional forecasts as per the requirements are (i) Regional forecasting, (ii) Spatial correlation forecasting and (iii) Probabilistic forecasting.

(i) Regional forecasting

With more wind power penetration into grid because of fluctuating nature of wind, the grid stability may be the major issue to researchers. In fact regional or grid forecasting provides enough information to improve reliability of the grid.

In mainly two ways the grid connected wind power can be predicted. Forecasting wind power individually for each farm and then grid power can be estimated by adding all wind form power forecasts is one approach. On the other hand in Ref [12] the author proposed determination of weight coefficient of each farm by using correlation matrix of output power and forecast accuracy coefficient.

The weight coefficient is computed as below in Eq.1

$$Q_i = \frac{Cap_i(1-RMSE_i)}{\sum_{i=1}^{F}[Cap_i(1-RMSE_i)]} \quad (1)$$

In the above equation Q_i represents weight coefficient of i-th wind farm, Cap_i represents the installed capacity of i-th wind farm and $RMSE_i$ is RMSE of the i-th wind farm, where F indicates the total number of representative wind farms.

Grid power forecasting could be assessed by the following equation (2)

$$P_G = \frac{\sum_{i=1}^{F} P_i Q_i}{\sum_{i=1}^{F} Cap_i Q_i} Cap_T \quad (2)$$

Where

P_G represents the forecasted grid scale power,

$P_i$is the power forecast of i-th wind farm and Cap_T is indicating the maximum of running wind power capacity in the grid.

In fact the grid scale wind power forecast is found better in the performance with RMSE of 12.91% and MAE of 9.9% as mentioned in Ref. [12].

(ii) Spatial correlation forecasting

Spatial correlation forecasting is typically applied to forecast the wind speed and power at a wind farm where enough information is not available. The most commonly used approach is Measure Correlate Predict method. This model mainly used to predict the uncertainty of the total wind energy potential prior to the development of wind farms [13].

(iii) Probabilistic Forecasting

Unlike, conventional WPF the probabilistic forecasts could provide quantitative information on the uncertainty of wind power generation. With the help of Probability Density Function (PDF) the uncertainty could be evaluated [14]-[15].The propose methods are Kernel density estimation (KDE) and Quintile Regression [16].

III. WIND POWER FORECASTING METHODS

Some of the conventional Statistical methods are Simplistic Persistence model, Autoregressive model, Moving average model, ARMA, ARIMA etc. Some of the learning statistical methods are artificial neural network, Particle swarm optimization, Enhanced PSO, Modified Hybrid Neural Network and Genetic Algorithm etc.

Some of the researchers used combinational approach with ANN and PSO or ANN is combined with Fuzzy logic. ANNs are simple and flexible tools for forecasting. Large input, output samples are required along with proper number of hidden layers. Three layered feed forward ANNs are used for forecasting.

WPF with ANNs mainly requires NWP data like wind speed, wind direction, temperature etc. and historical wind power data. The optimal structure of Neural Network can be selected by some optimization process. There has been a clear comparison of various Neural Networks with the input parameters used in Ref. [17] for very short term forecasting and short term forecasting of wind power. ANN approach has been used for short term wind power forecasting in Portugal and forecasted data is computed by historical data with MAPE of 9.51% for winter [18]. Figure 4 shows basic steps of ANN approach.

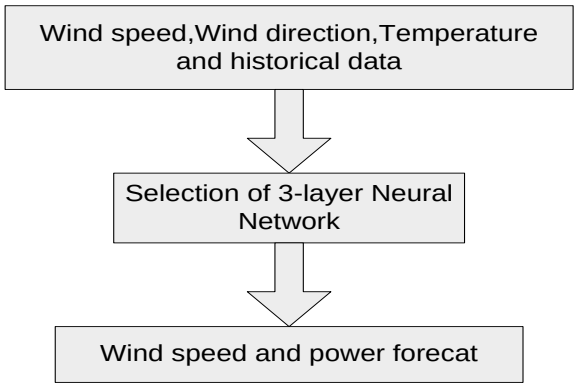

Fig.4: ANN based Approach

Both ANN and Markov chain are applied to short term forecast [19]. All Markov chain models are based on transitional probability matrices of various time steps. It is a random process that undergoes transitions from one state to another on a state space. Markov chains have wide applications as statistical methods of real world processes. This paper shows improved results in comparison to ANN application alone with MAPE for ANN-Markov approach is 4.025 and 4.055 for ANN approach.

Multi- layer perception Artificial neural network has been used to forecast wind power at Mia liao wind farm, Taiwan by using 5 years collected data from 2002 to 2007.Improved simplified swarm optimization (iSSO) is also proposed showing best performance out of GA ,PSO ,BP. In Ref [20] input variables for MLP are selected by using Autocorrelation function (ACF) and partial auto correlation function (PACF).Out of 53 variables two variables i.e last wind power and previous last wind speed are observed as most relevant variables under the confidence level 95%. It is also observed that MSE is greatly affected by number of training years. In WPF suitable parameter selection and data decomposition are observed to be crucial steps [21]. Figure 5 shows ANN approach using PSO technique.

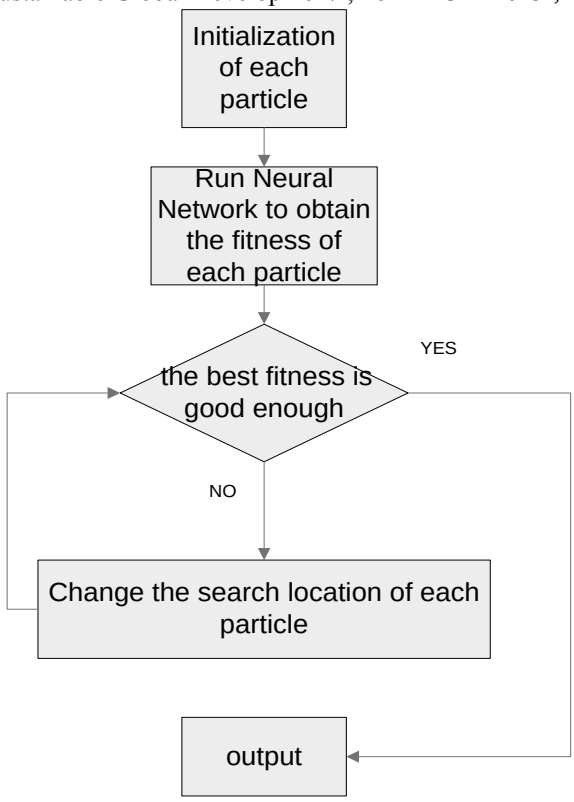

Fig.5: Flow chart for PSO based ANN

Persistence model is very much familiar and less costly. But, this method needs improvement for wind power forecasting technology. This method uses previous hour wind speed or wind power to forecast next hour wind power [22].One another notable conventional forecasting method is auto regressive time series models ARMA, ARIMA. ARMA model is mainly used to forecast wind speed and its direction. The general form is shown in equation 3.

$$X_t = C + \varepsilon_t + \Sigma_{i=1}^{p} \varphi_i X_{t-i} + \Sigma_{j=1}^{q} \theta_j \varepsilon_{t-j} \quad (3)$$

Where C is the constant term of the ARMA model, φ_i is the i-th Auto regressive coefficient, θ_j is the j-th moving average coefficient, ε_t is the error term at time period t, and represents the value of wind speed observed or forecasted at time period t.

There has been a comparison of four statistical methods component model, Traditional linked ARMA, vector auto regression and restricted VAR for short term wind speed and direction forecasting in Ref.[23].To forecast wind speed, Traditional linked ARMA has shown better performance and VAR based methods are performing better in forecasting wind direction .Among all the proposed models, the performance is evaluated in terms of Mean Absolute Error(MAE). ARMA model is well suited for WPF because of good correlation in

wind power generations. For very short term forecasting of wind energy, ARMA models are widely used [24],[25].

In [26], the author proposed a new forecast engine composed of Modified Hybrid Neural Network (MHNN) and Enhanced Particle Swarm Optimization (EPSO).HNN is efficient in price forecasting for Electricity Market with good accuracy. Due to complexity of wind power in case of wind power forecasting the combinational approach (HNN& EPSO) is proved to be effective. RMSE is evaluated as 6.71 for HNN alone and RMSE for the combination is 4.18.

In [27], indexed semi-Markov chains forecasting (ISMC) has been proposed and compared with Persistence and Auto Regressive models for RMSE values. To reproduce the statistical behavior of wind speed, ISMC is best suitable model .Since, the model doesn't need any assumption for wind speed distribution, ISMC model is considered for wind speed forecast in a specific site.

Ref [28] successfully presented the data mining Approach to predict future values of wind power over short time horizons. Data mining is an analytical process designed to explore large amount of data to find the systematic relation between the variables. It has been already proved to be successful approach in marketing sector and manufacturing industry.

IV. CONFIDENCE LEVEL AND INTERVAL

WPF mainly aims at the demand side management, maintenance of operating reserves and Generating units scheduling. Absolutely, the accurate prediction leads to the proper estimation of storage capacity and provides correct information to energy trading. In this context, to check the uncertainty in WPF, estimation of confidence interval for the errors is required. Evaluation of confidence interval promises the accuracy in the forecast. As error distribution of WPF is not the normal distribution due to non-linearity in the power curve, confidence intervals can be estimated using regression models and fuzzy interference [29]. Confidence interval is a range of values so defined that there is specific probability for the parameter value to fall in the range. The confidence interval is also used to express the degree of uncertainty .Confidence level is the probability that the value of the parameter falls within a specified range of values. A proper comparison has been carried among three methods for WPF i.e ANN, Wavelet Decomposition (WD) and Least squares support vector machine (LS-SVM) in terms of Error Range Probabilities in Ref.[30]. The author has evaluated confidence levels with the estimation of confidence intervals. The hybrid model with ANN&WD has performed better with 82.84% probability in the confidence interval of -10% to 10% for Mean Absolute Error (MAE).

An analysis on uncertainties associated with wind speed forecasts has been carried using a Hybrid model established by Cuckoo Search Optimization based (CSO) Back Propagation Neural Network(BPNN) for different wind speed intervals [31].

V. EVALUATION FACTORS

Some evaluation factors of wind forecasting tools used by researchers are discussed below. Most commonly used evaluation factors are expressed in equations 4, 5, 6 & 7. In these equations A_i is the actual value and F_i is the forecast value.

$$MAPE = \frac{1}{N}\sum_{i=1}^{N}\left|\frac{A_i - F_i}{A_i}\right| \quad (4)$$

MAPE stands for Mean Absolute Percentage Error. It is a measure of accuracy for a forecasting method.

$$MAE = \frac{1}{N}\sum_{i=1}^{N}|A_i - F_i| \quad (5)$$

MAE stands for Mean Absolute Error.

$$MSE = \frac{1}{N}\sum_{i=1}^{N}(A_i - F_i)^2 \quad (6)$$

MSE stands for Mean Squared Error.

$$RMSE = \sqrt{\frac{1}{N}\sum_{i=1}^{N}(A_i - F_i)^2} \quad (7)$$

RMSE stands for Root Mean Square Error. It is frequently used to measure the difference between actual and predicted values in forecasting. A lower value of RMSE indicates higher accuracy of the forecast

VI. CONCLUSION

So far the researchers developed many wind power forecasting models according to the power sector requirements and the situations. On the whole it is observed that accuracy is being improved with new models. Selection of the variables also plays a vital role in any forecasting along with the suitability of the approach. ACF and PACF are primarily used in the selection of input variables. Mostly, the combinational methods like ANN & Markov, HNN & EPSO have shown better results in terms of accuracy of forecasting . To check the uncertainty of WPF, Probabilistic forecasting needs greater importance. Statistical methods require large amount of historical data. Physical methods are suitable to forecast wind power for the development of wind farms. In short term forecasting, it is essential to evaluate confidence level of the

error. Further, the accuracy of the predicted data can be improved by evaluating confidence interval of the evaluation parameters.

References

[1] Er. Alekhya Datta, Dr. Parimita Mohanty, Er. Mukesh Gujar "Accelerated Deployment of Smart Grid Technologies in India – Present Scenario, Challenges and Way Forward " , TERI – The Energy and Resources Institute Darbari Seth Block, India Habitat Centre (IHC) Complex Lodhi Road, New Delhi – 110 003, India

[2] http://www.gwec.net/publications/global-wind-energy-outlook/

[3] Lei DONG, Shuang GAO, Xiaozhong LIAO, Yang GAO," Short-Term Wind Power Forecasting with Combined Prediction Based on Chaotic Analysis", PRZEGLĄD ELEKTROTECHNICZNY (Electrical Review), ISSN 0033-2097, R. 88 NR 5b/2012

[4] F.O. Thordarson, H. Madsen, H. A. Nielsen, and P. Pinson, "Conditional weighted combination of wind power forecasts," Wind Energy, Vol. 13, no. 8, pp. 751–763, Nov. 2010.

[5] Rodrigo Palma-Behnke, Carlos Benavides, Fernando Lanas, Bernardo Severino, Lorenzo Reyes, Jacqueline Llanos, and Doris Sáez, "A Microgrid Energy Management System Based on the Rolling Horizon Strategy " , IEEE Transactions On Smart Grid, Vol. 4, No. 2, June 2013

[6] Kai Strunz, Ehsan Abbasi, and Duc Nguyen Huu, "DC Microgrid for Wind and Solar Power Integration" , IEEE Journal Of Emerging And Selected Topics In Power Electronics, Vol. 2, No. 1, March 2014

[7] Jaesung Jung, Robert P. Broadwater, "Current status and future advances for wind speed and power forecasting" , Renewable and Sustainable Energy Reviews, Volume 31, 2014, Pages 762-777

[8] Aoife M. Foley, Paul G. Leahy , Antonino Marvuglia , Eamon J. McKeogh "Current methods and advances in forecasting of wind power generation" , Renewable Energy, Volume 37, Issue 1, January 2012, Pages 1-8

[9] R.J. Barthelmie, F. Murray, S.C. Pryor, " The economic benefit of short-term forecasting for wind energy in the UK electricity market" Energy Policy 36 (2008) 1687–1696.

[10] Xiaochen Wang , Peng Guoc, Xiaobin Huang "A Review of Wind Power Forecasting Models" ICSGCE 2011: 27–30 September 2011, Chengdu, China.

[11] Xin Zhao*, Shuangxin Wang, Tao Li, "Review of Evaluation Criteria and Main Methods of Wind Power Forecasting" ICSGCE 2011: 27–30 September 2011, Chengdu, China

[12] Chen Ying , Ding Yuyu, Ding Jie, Chan Zhibao, Sun Rongfu, Zhou Hai ,"A Statistical Approach of Wind Power Forecasting for Grid Scale" volume 2,2012 Pages 121–126, AASRI Conference on Power and Energy Systems

[13] Thogersen ML, Motta M, Sorensen T, Nielsen P. "Measure-correlate-predict methods: case studies and software implementation". In: Proceedings of the 2007 EWEA conference; 2007.

[14] Ricardo J. Bessa , Vladimiro Miranda , Audun Botterud , Jianhui Wang, and Emil M. Constantinescu, " Time adaptive conditional kernel density estimation for wind power forecasting " , IEEE Transactions On Sustainable Energy, Vol. 3, No. 4, October 2012, Pages 660-669.

[15] Peng Kou ,Deliang Liang , Feng Gao , Lin Gao " Probabilistic wind power forecasting with online model selection and warped gaussian process " Energy Conversion and Management 84 (2014) 649–663

[16] Yao Zhang, Jianxue Wang , Xifan Wang " Review on probabilistic forecasting of wind power generation" ,Renewable and Sustainable Energy Reviews 32(2014)255–270

[17] Ignacio J. Ramirez-Rosado , L. Alfredo Fernandez-Jimenez , Cla´udio Monteiro , Joa˜o Sousa, Ricardo Bessa , "Comparison of two new short-term wind-power forecasting systems" Renewable Energy 34 (2009) 1848–1854

[18] J. P. S. Catalão, H. M. I. Pousinho, and V. M. F. Mendes, "An Artificial Neural Network Approach for Short-Term Wind Power Forecasting in Portugal" Intelligent System Applications to Power Systems, 2009. ISAP '09. 15th International Conference

[19] S. A. Pourmousavi Kani, and G. H. Riahy, "A New ANN-Based Methodology for Very Short-Term Wind Speed Prediction Using Markov Chain Approach" , 2008 IEEE Electrical Power & Energy Conference.

[20] Wei-Chang Yeh, Yuan-Ming Yeh , Po-Chun Chang , Yun-Chin Ke , Vera Chung "Forecasting wind power in the Mai Liao Wind Farm based on the multi-layer perceptron artificial neural network model with improved simplified swarm optimization" Electrical Power and Energy Systems 55 (2014) 741–748.

[21] Wenyu Zhang, Jie Wu, Jianzhou Wang, Weigang Zhao , Lin Shen, " Performance analysis of four modified approaches for wind speed forecasting", Applied Energy 99 (2012) 324–333

[22] M. Milligan, M. Schwartz, Y. Wan," Statistical Wind Power Forecasting Models: Results for U.S. Wind Farms", WINDPOWER 2003 Austin, Texas May 18-21, 2003

[23] Ergin Erdem, Jing Shi ," ARMA based approaches for forecasting the tuple of wind speed and direction" Applied Energy 88 (2011) 1405–1414

[24] Moein Parastegari, Rahmat-Allah Hooshmand, Amin Khodabakhshian, Amir-Hossein Zare, " Joint operation of wind farm, photovoltaic, pump-storage and energy storage devices in energy and reserve markets", Electrical Power and Energy Systems 64 (2015) 275–284

[25] Cadenas E, Rivera W. "Wind speed forecasting in three different regions of Mexico, using a hybrid ARIMA-ANN model", Renewable Energy 2010;35:2732-8.

[26] Nima Amjady, Farshid Keynia, and Hamidreza Zareipour, "Wind Power Prediction by a New Forecast Engine Composed of Modified Hybrid Neural Network and Enhanced Particle Swarm Optimization" IEEE Transactions On Sustainable Energy, Vol. 2, No. 3, July 2011

[27] Guglielmo D'Amico, Filippo Petroni , Flavio Prattico "Wind speed and energy forecasting at different time scales A nonparametric approach" Physica A 406 (2014) 59–66

[28] Andrew Kusiak, Haiyang Zheng, and Zhe Song, "Short-Term Prediction of Wind Farm Power: A Data Mining Approach" IEEE Transactions on energy conversion, vol. 24, no. 1, march 2009

[29] Tatsuya Iizaka, TofU Jintsugawa, Hideyuki Kondo,Y ousuke Nakanishi, and Yoshikazu Fukuyama, Hiroyuki Mori, "A Wind Power Forecasting Method with Confidence Interval" Circuits and Systems (MWSCAS), 2011 IEEE 54th International Midwest Symposium

[30] Maria Grazia De Giorgi , Stefano Campilongo, Antonio Ficarella and Paolo Maria Congedo,v ,"Comparison Between Wind Power Prediction Models Based on Wavelet Decomposition with Least-Squares Support Vector Machine (LS-SVM) and Artificial Neural Network (ANN)", Energies 2014, 7, 5251-5272

[31] Shanshan Qin , Feng Liu , Jianzhou Wang, Yiliao Song, "Interval forecasts of a novelty hybrid model for wind speeds ", Energy Reports 1 (2015) 8–16.

International Journal of Computer Graphics
Vol. 7, No.1 (2016), pp.17-30
http://dx.doi.org/10.14257/ijcg.2016.7.1.02

Accelerating Genetic Algorithm Using General Purpose GPU and CUDA

Rashmi Sharan Sinha[1], Satvir Singh[2], Sarabjeet Singh[3] and Vijay Kumar Banga[4]

[1,2]Department of Electronics & Communication Engineering,
SBS State Technical Campus, Ferozepur–152004, (Punjab) India
[3]Department of Computer Science & Engineering,
SBS State Technical Campus, Ferozepur–152004, (Punjab) India
[4]Department of Electronics & Communication Engineering,
Amritsar College of Engg. & Tech., Amritsar–143001, (Punjab) India
[1]sinharashmisinha@hotmail.com, [2]drsatvir.in@gmail.com
[3]sarabjeet_singh13@yahoo.co, [4]v_banga@rediffmail.com

Abstract

Genetic Algorithm (GA) is one of most popular swarm based evolutionary search algorithm that simulates natural phenomenon of genetic evolution for searching solution to arbitrary engineering problems. Although GAs are very effective in solving many practical problems, their execution time can become a limiting factor for evolving solution to most of real life problems as it involve large number of parameters that are to be determined. Fortunately, the most time-consuming operators like fitness evaluations, selection, crossover and mutation operations that involves multiple data independent computations. Such computations can be made parallel on GPU cores using Compute Unified Design Architecture (CUDA) platform. In this paper, various operations of GA such as fitness evaluation, selection, crossover and mutation, etc. are implemented in parallel on GPU cores and then performance is compared with its serial implementation. The algorithm performances in serial and in parallel implementations are examined on a testbed of well-known benchmark optimization functions. The performances are analyzed with varying parameters viz. (i) population sizes, (ii) dimensional sizes, and (iii) problems of differing complexities. Results shows that the overall computational time can substantially be decreased by parallel implementation on GPU cores. The proposed implementations resulted in 1.18 to 4.15 times faster than the corresponding serial implementation on CPU.

Keywords: *Genetic Algorithm (GA), General Purpose Computing on Graphics Processing Unit (GPGPU), Compute Unified Device Architecture(CUDA)*

1. Introduction

Genetic Algorithm (GA) is a swarm based global search algorithm inspired natural mechanism of genetical improvements in biological species [1], described by Darwinian Theory of *Survival of Fittest*. It was developed by John Holland in 1970 at University of Michigan [2]. It simulates the process for evolving solutions to arbitrary problems [3].

GA is algorithm involves multiple solutions represented by a string of variables, analogous to the chromosomes in Genetics. With a initially randomly generated population, every swarm member is a required to be evolved. Evolution is based on the fitness pairs of parent solutions that are selected randomly and reproduce next generation of solutions, stochastically. Each child chromosome has features of both the parent as an output of crossover. Another is limited alteration in feature values of the generation represents effect of mutation.

ISSN: 2093-9663 IJCG

GA essentially strives to attain the global maximum (or minimum) of cost depending upon the nature of the problem. Over the period of advancements, GA is widely used and extensively researched as optimization and search tools in several fields such as, medical, engineering, and finance etc. The basic facts for their success are simple structure, broad relevance with problem [4]. Goldberg and Harik brought the term compact Genetic Algorithm (cGA) which represents the solution as a probability distribution over the wide space set of solutions, Huanlai and Rong well utilized the concept in minimization problem of resources of network codes [5]. Gas produces high-quality solutions through its high adaptation property with the environment changes [6]. Prakash and Deshmukh investigated the use of meta-heuristics for combinatorial decision-making problem in flexible manufacturing system with GA [7]. Prominent GA applications include pattern recognition [8], classification problems [9], protein folding [10] and neural network design [11] *etc*. GAs are also suitable for multi-objective optimal design problems [12], in solving multiple objectives.

Even though, GAs has powerful characteristic in determining many practical problems. However their execution time act as bottleneck in few real life problems. GA involve large number of trial vectors that needed to be evaluated. However, the major portion of time consuming function of fitness evaluations can be made parallel to perform independently due to data independency and, therefore, can be evaluated using parallel computational mechanisms.

With the advent of General Purpose GPU (GPGPUs), researchers have been evolving Evolutionary Computations [13-16] for parallel implementation. Similar advancements in the field of genetic programming are quickly adopted by GA researchers.

After this brief background, the remaining paper is organized as follows: Section II, describes GA Operators along with pseudo codes for implementation in parallel. Section III, introduces architecture detail of GPGPU and C-CUDA followed by Section IV of its implementation. Section V, summarizes performance evaluation of experimental result. Conclusion of this paper with future aspect is presented in Section VI.

2. GA Operators

GA provides number of solutions however best solution among them is one with least processing time [17]. The three primary operators involved in GA are: (1) Selection, (2) Crossover, (3) Mutation and (4) Elite Solutions operators described as follows.

2.1. Selection

There are three most popular different types of Selection Strategies viz., Tournament Selection, Ranked-Based Roulette Wheel, and Roulette Wheel Selection [18]. These strategies are used to search potential parent chromosomes based on the fitness level of individuals from the randomly generated population. The selection operator is expected to produce solutions with higher fitness in succeeding generations. On contrarily, selection operator anticipated to produce relative probability of being selected according to their fitness in the swarm. This leads the algorithm to find global best solution rather than converging to its nearest local best solution.

2.1.1. Tournament Selection: The mechanism of tournament selection is based upon random selection of solutions from current population. The selected solutions form a pool of solutions, which produces optimal solution among them for succeeding generation. The selection is done on the highest fitness among the pool of solution.

2.1.2. Rank-based Roulette Wheel Selection: The strategy of Rank-based Roulette Wheel Selection where fitness of each solution is given a rank relative to swarm, deals with the rank of solution rather than fitness value. The chance of selection of chromosome

is distributed rationally to the rank of individual solution. Rank-based Roulette Wheel Selection avoid premature conversions significantly.

2.1.3. Roulette Wheel: In this method, the selection of parent solutions for the next generation child solutions depend upon the probabilities of fitness values relative to portion of spinning a roulette wheel. The chromosomes are chosen for next generation on the basis of their values of fitness, i.e., a chromosome's selection is directly proportional to section of roulette wheel corresponding to the fitness level of the same. Let f_1, f_2, f_3,.....f_n be fitness values of chromosomes 1, 2, 3, . . . n. Then the probability of selection P_i for chromosomes *i* is defined as (1),

$$Pi = \frac{fi}{\sum_{j=1}^{n} fi}$$

Advantage of proportional roulette wheel selection is that it selects all of the solutions of swarm with the probability relational to fitness values. Hence it maintains diversity of solution.

2.1.4. Parallel implementation of Selection: In Roulette wheel selection function there is a global call of kernel for execution of GA on GPU. The thread number per block *threadIdx* is equal to the respective dimension of population. The selection is done in parallel generating uniformly distributed random numbers between zero to max (cumulative sum) and thereby checking which of the fitness lies immediate greater than that of generated number. Then the corresponding fitness of the trial solution gets selected as parent chromosome for next generation as depicted in Algorithm 1.

Algorithm 1: Pseudocode for Roulette Wheel Selection

```
Global call of kernel for Roulette Wheel Selection function
  No. of threads i is equal to  threadIdx
  Random number r ← (0, cumulative fitness)
   While size of population < pop_size do
    Generate random number r equal to pop_size
    Calculate fitness (pi), cumulative sum of fitness (CSum)
    Spin the wheel pop_size times with random force
        If CSum < r then
            Select the first chromosome, otherwise,
            Select the j^th chromosome
        End if
  End While
   Return solution with the fitness value proportion to
   the size of selected chromosome on roulette wheel
 End
```

2.2. Crossover

The process of producing child chromosomes from parent chromosomes is termed as crossover. It is a significant operator which mimics biological crossover and reproduction of the nature. This operator in GA is broadly classified into three different techniques viz., single point, double point, and uniform distribution crossover.

2.2.1. Single Point Crossover: In single point crossover, the selected parent solution chromosome string get swapped from a randomly selected crossover point. The resulting chromosome after swapping form children population for next generation.

2.2.2. Double Point Crossover: Double point crossover is similar to that of single point crossover however; the crossover points are two rather than one.

2.2.3. Uniform Distribution Crossover: In Uniform Distribution Crossover technique, chromosomes of parent solution are mixed uniformly with a fixed ratio termed as mixing ratio. The process of mixing parent chromosomes produces child chromosomes mixed at gene level as compared with single and double point crossover where mixing is done at segment level. Therefore uniform crossover is more suitable for larger search space. Hence in this paper uniform distribution crossover is used.

2.2.4. Parallel Implementation Uniform Crossover: In uniform crossover, there is a global call of kernel for execution of the function on GPU. Uniformly distributed random number is generated at the interval 0 to 1 while probability of crossover is defined at 0.9. The mixing ratio of 0.8 is applied at gene level to produce child chromosome. The pseudocode for its parallel implementation is shown in Algorithm 2.

Algorithm 1: Pseudocode for Uniform Crossover

```
Global call of kernel for uniform crossover function
  No. of threads i is equal to  threadIdx
  N is population size pop_size
  L is chromosome length of string chromoLength
  Crossover Probability is defined as probCross
  Mixing Ratio is defined as mixRatio
  r ← random no. between 0 to 1
if r ≥ probCross then
   if r ≥ mixRatio then
      crossPoint(i)← random (0, L-1)
      crossPoint(i+1)← crossPoint(i+1)
Else
      crossPoint(i) ← no change
      crossPoint(i+1) ← no change
    End if
  End if
End
```

2.3. Mutation

Mutation operator is applied to preserve genetic variance (diversity) in succeeding generation of population in GA. Mutation operator creates a new solution for each possible trial solution. To avoid optimal search stagnation, the difference between two chromosome is increased by a factor termed as mutation factor. In this experiment, the factor is kept relative to the number of iteration between 0.01 to 1.

2.3.1. Parallel Implementation Mutation:

Pseudocode represents the process carried out for mutation in GA on GPU Algorithm 3. There is a global call of kernel for execution of the function on GPU. Each solution of

the population get mutated by a single thread operations. Scheduling a block with a sufficient number thread is needed to mutate the whole population.

Algorithm 1: Pseudocode for Mutation

Global call of kernel for mutation function
No. of threads *i* is equal to *threadIdx*
Mutation factor is defined as *m_fact*
Obtain population after crossover *new_Pop*
Random no. *r* is generated between 0 to 1
for *i* =0 to *n*
if r < *m_fact*
new_Pop = 1- *new_Pop*
Else
new_Pop = *new_Pop*
End if
End

2.4. Elite Solutions

After the crossover and mutation operation, elite solution is applied. In this solution elite string is compared with parent chromosomes and current child chromosomes of entire solution. Elite solution is updated, if any solution in the child population is superior to the solution in elite string. When elite string stop showing any further improvement, it reflects the convergence of the swarm.

3. Basic GPGPU and C-CUDA

3.1. General Purpose GPU

The architectures of General Purpose Graphics Processing Unit (GPGPU) is highly parallel, data processing unit endorsed with multiple number of streaming processors. GPGPU interfaced with Compute Unified Device Architecture (CUDA). It was developed by nVIDIA Corporation in 2006 along with Geforce80 and programming model on CUDA platform [17]. It supports execution of arithmetic operations at higher rate, substantial hardware is computationally powerful then CPUs.

Libraries such as *curand kernel.h, cuda.h* and *curand.h etc.*, along with C language libraries provide high freedom of accessibility to interface user with General Purpose GPU. Researches and experiments in last few years prove its significance in several fields. On contrary it also have low cost and higher power-to-watt ratio as compared to CPUs [19]. In recent years, such features attracted lots of researcher and developers to harness GPUs for various general purpose computations (GPGPU).

Oiso Matumura achieved a speedup rate of 6x in evaluation of Steady State GA with population size of 256, taken benchmarking test functions to compared to the CPU implementation [19]. Jiri and Jaros proposed the application of GA by achieving speedup of 35-781 for determining the Knapsack Problem with a multi-GPU while population size was kept 128 to 2048 individuals per island [20]. Arora, Tulshyan and Deb employed GPGPU to apply a real and binary coded GA and talked about several data structures application on GPU, and archived a speedup of 40-400 for a population size of 128-16384 as compared to its sequential execution [21].

GA proves suitable in determining several realistic problems [22]. Therefore in this experiment, simultaneous kernel process taken out on GA using GPU. The performance

evaluation of single objective GA on set of benchmark test function using nVIDIA GeForce GT 740M GPU is used specifically. It gives speedup of 1.18-4.15 times as compared to CPU execution time.

3.2. Compute Unified Device Architecture (CUDA)

The program based on GPGPU can be easily developed using CUDA architecture. The execution of CUDA program composes of two parts: *host* section and *device* section. The *host* section is executed on CPU while the *device* section is executed on GPU respectively. However the execution of *device* section on GPU managed by kernel. The kernel handles synchronization of executing threads. It is invoked by *device* call for GPU.

The threads in GPU architecture can be grouped into *blocks* and *grids* as depicted in Figure 1. In GPU *grid* is with group of thread *blocks*, and a thread *block* comprises definite number of threads per *block*. Differentiating between unique threads, thread *block* and *grid* may be done by using a set of identifiers *threadIdx*, *blockIdx* and *gridIdx* variables respectively. Thread per *block* can exchange information to synchronize with each other. Per-*block* shared memory can be used for communication between each thread within a thread *block*, however there no direct interaction or synchronization possible between the threads of different *blocks* [19].

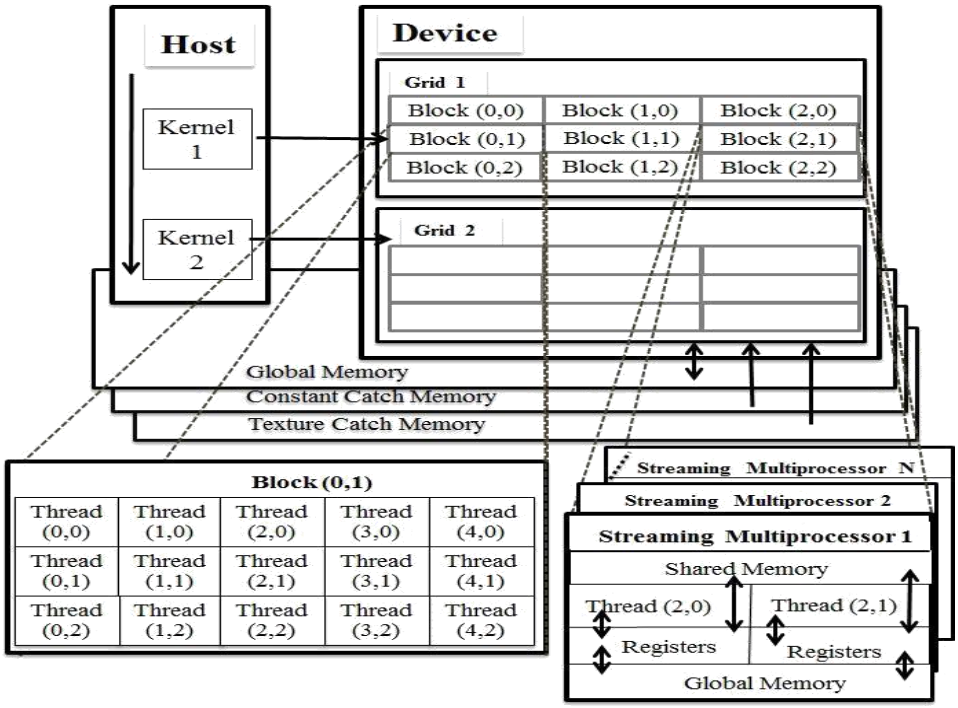

Figure 1. CUDA Architecture

The entire shared memory in CUDA architecture is divided into four types viz., texture memory, constant memory, perthread private local memory and global memory for data shared by all threads. Between these memories, texture memory and constant memory can be accumulated as fast read only caches; while registers and shared memories are the overall fastest memories.

For constant memory, the optimal access strategy adopts reading of same memory location by all threads. The threads can read neighboring thread addresses using texture catch with a high reading efficiency. CUDA functions for allocation and deallocation of memory *cudaMalloc* and *cudaFree*, respectively are used. CUDA function *cudaMemcpy* is used to copy data from host to device.

There are multiple Streaming Processors to handle GPU computations. It is considered as fundamental processor of *device* architecture. While Streaming Multiprocessors had to run on group of streaming processors. The number of thread *block* in streaming processors is scheduled by GPU *device* when kernel function is called.

When threads executing in a group of 32 streaming multiprocessors it is called *wrap* under the Single Instruction, Multiple Thread (SIMT) scheme, i.e., in nVIDIA GeForce GT 740M have 16KB of shared memory per streaming multiprocessor with 16384 64-bit registers. Shared memory and registers limits the thread *block* per streaming multiprocessors while executing threads. Hence streaming multiprocessors is limited up to 8 *blocks*.

4. Implementing GA Using C-CUDA

Implementation of GA includes parallel flow of algorithm to find global optimal solution using C-CUDA. The major implementation of algorithm consists generation of initial population using GPU, randomly generated numbers to find global best solution, selection of parent solution, implementation of genetic operators and elite solution and finally coping child population back to parent population. The overview of GA execution is depicted in Figure 2. The implementation of C-CUDA kernels on GA is based on under mentioned principle:

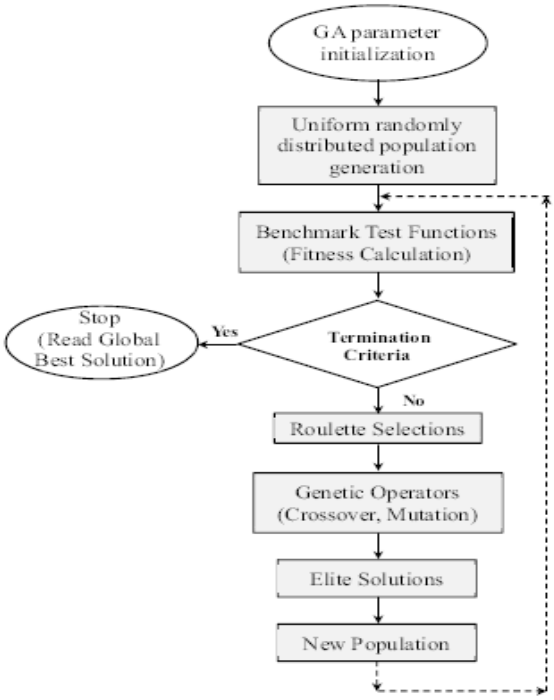

Figure 2. Implementation GA Flowchart (Shaded Modules Represents GPU Computation, Non-shaded Modules Represents Computation on CPU)

4.1. All GA solution is calculated using thread block at each generation. The maximum size of GA population at each generation is limited to the total number of threads which is currently $(2^{16}\text{-}1)^2$.

4.2. Every trial solution uses threads to compute possible outcome. GPU's computation capability is 512 threads per block for 1 x 1024. Hence it is directly proportional to the hardware capability.

4.3. GPU access all the trial solution in one step i.e., with each kernel call C-CUDA launches number of threads per block equivalent to the population size of the generation.

These characteristics turn out to be best feature for massive implementation of such algorithms. It easily provides speedup in overall computation time of GA. C-CUDA kernels generates population in one step then computes their respective fitness values. The genetic operator is applied to each solution where number of thread kept equal to its population size. The new generation of succeeding population follow same strategy to find solution. Hence due to these benefits of GPU takes less time as compared to its sequential execution on CPU.

5. Performance Evaluation

5.1. Experimental Setup

The experiments were conducted on two different PCs (PC1 and PC2) and with same nVidia cards (Refer Table I for System Specifications) for separate performance evaluations. PC1 is tested with active background applications. PC2 is kept ideal until complete performance evaluation carried out. The total number of streaming processors and streaming multiprocessors are 16 hence 256 streaming processors in each PC. Entire GA code of C-CUDA is written in Visual Studio C++ (2012 release mode) and complied on nvcc compiler. The result of above experiment is evaluated using two different iteration size of 10,000 and 100,000. The dimension size of experiment is kept fixed. The acceleration of GA on GPU is seen efficient with large number dimension size and maximum iteration. The result Table III and Table IV in next section shows a significant speedup.

Table I. Computational Systems Specification

Platform		PC1	PC2
CPU	Processor	Intel Core i5 4200(U)+ 2.6 GHz	Intel Core(TM) i5 333TU+ 1.8 GHz
	Catch	3072KB	3072KB
	Memory	16GB DDR3L	32 GB DDR3/L
	Interface	PCI-E 2.0	PCI-E 3.0
GPU	Graphic Card	nVIDIA GeForce GT 740M	nVIDIA GeForce GT 740M
	Version	9.18.13.2057	9.18.13.2702
	CUDA Version	5.5	5.5

5.2. Benchmark Test Functions

Benchmark Test Functions for our experiment with distinct minima (f_{min}) is given in Table II, which are numbered from f1(x) up to f7(x) and correspond to the functions in [23]. Here, range is the lower and upper limits of the universal discourse for every function.

Table II. Benchmark Functions with Different Local Minima [23]

Test Functions	Range of x_i	f_{min}
$f_1(x)=\sum_{i=1}^{n} x_i^2$	± 5.12	0
$f_2(x)=\sum_{i=1}^{n} x_i^4$	± 100	0
$f_3(x)=\frac{1}{4000}\sum_{i=1}^{n} x_i^2-\prod_{i=1}^{n}\cos(x/\sqrt{i})+1$	± 2048	0
$f_4(x)=\sum_{i=1}^{n}\lvert x_i^5-3x_i^4+4x_i^3+2x_i^2-10x_i-4\rvert$	± 10	0
$f_5(x)=\sum_{i=1}^{n}\lvert x_i\sin(x_i)+0.1x_i\rvert$	± 10	0
$f_6(x)=-\exp\left(-0.5\sum_{i=1}^{n} x_i^2\right)$	± 1	1
$f_7(x)=\sum_{i=0}^{n-1}[100(x_i-x_{i+1}^2)^2+(1-x_i)^2]$	± 2048	0

5.3. Result and Discussion

The ratio of total time consumed on CPU for serial implementation of code to the time consumed by GPU C-CUDA in parallel implementation gives speedup for the same experiment on different platforms.

5.3.1. Case Study 1: In this experiment, the dimension size of the population generation is kept first 32 and then 64. Each dimension size iterated for maximum number of iteration, which was set to 10,000. The performance shown in result table is average value of 20 trials. The speedup of GPU over CPU for all seven benchmark test functions are shown in Table III and indicated in Figure 3 & Figure 4.

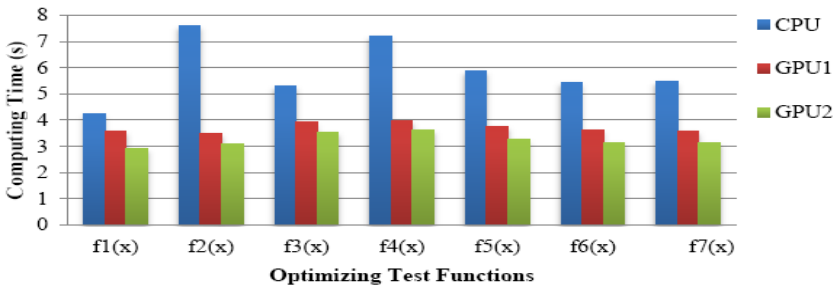

Figure 3. Computing Time for 10,000 Iterations with 32 Dimension Size

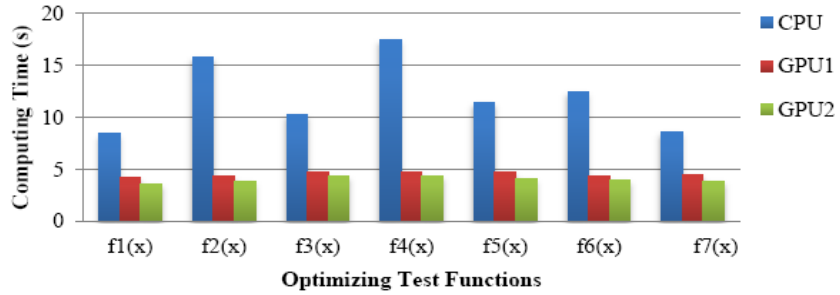

Figure 4. Computing Time 10,000 Iteration with 64 Dimension Size

The best computational performance achieved among GPU1 and GPU2 for dimension size of 32, is 2.17 times for f2(x) on GPU1, while on GPU2 with the dimension size of 64,

f2(x) shows a speedup of 4.15 times higher than its CPU execution time. The Table III depicts the best result for 10,000 iterations along with quality.

Table IV. C-CUDA Vs. C Performances for 100,000 Iterations

n	Function	CPU		GPU_1			GPU_2		
		Time (sec)	Std. Div.	Time (sec)	Std. Div.	Speed Up	Time (sec)	Std. Div.	Speed Up
32	$f_1(x)$	4.24	11.59	3.58	0.1300	1.18	2.92	0.0006	1.45
	$f_2(x)$	7.60	2.43	3.50	0.0003	2.17	3.07	0.0005	1.47
	$f_3(x)$	5.31	0.82	3.91	0.0057	1.35	3.54	0.0006	1.50
	$f_4(x)$	7.20	9.74	3.97	0.0004	1.81	3.61	0.0007	1.99
	$f_5(x)$	5.86	0.91	3.75	0.0212	1.56	3.27	0.0004	1.79
	$f_6(x)$	5.43	17.43	3.62	0.0006	1.50	3.15	0.0080	1.72
	$f_7(x)$	5.48	16.26	3.60	7.9E-05	1.52	3.13	0.0015	1.75
64	$f_1(x)$	8.42	11.73	4.28	0.0007	1.96	3.65	0.0004	2.30
	$f_2(x)$	15.84	14.77	4.30	0.0018	3.68	3.81	0.0090	4.15
	$f_3(x)$	10.30	6.61	4.78	0.0002	1.55	4.41	0.0003	2.33
	$f_4(x)$	17.47	10.20	4.75	0.0180	3.68	4.39	0.0007	3.97
	$f_5(x)$	11.43	10.81	4.68	0.0271	2.44	4.08	0.0004	2.80
	$f_6(x)$	12.49	4.04	4.33	0.0280	2.88	3.96	0.0013	3.15
	$f_7(x)$	8.58	4.41	4.50	0.0006	1.91	3.85	0.0010	2.23

5.3.2. Case Study 2: In this experiment the dimension size is kept same as Case Study 1, however the iterations size increased to 100,000. The respective speedup for all seven benchmark test functions is shown in Table IV and indicated in Figure 5 and Figure 6.

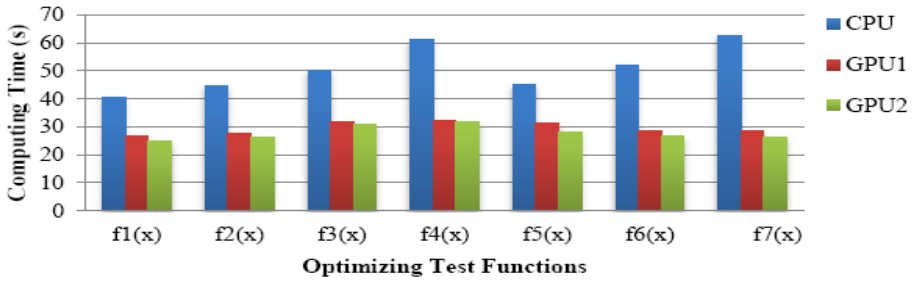

Figure 5. Computing Time for 100,000 Iterations with 32 Dimension Size

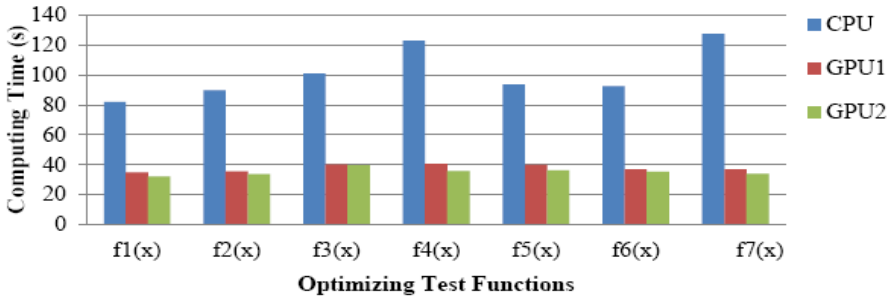

Figure 6. Computing Time for 100,000 Iterations with 64 Dimension Size

The highest speedup achieved in this case for dimension size 32 among GPU1 and GPU2 is 2.39 for test function f7(x). On the other hand, dimension size 64 has best speedup of 2.78 times for f7(x). The GPU average execution time is 33.70 seconds while 127.52 seconds in CPU.

Table IV. C-CUDA Vs. C Performances for 100,000 Iterations

n	Function	CPU		GPU_1			GPU_2		
		Time (sec)	Std. Div.	Time (sec)	Std. Div.	Speed Up	Time (sec)	Std. Div.	Speed Up
32	$f_1(x)$	40.61	0.11	26.92	0.0150	1.51	24.73	0.0016	1.62
	$f_2(x)$	44.81	0.48	27.55	0.0286	1.63	26.05	0.0019	1.72
	$f_3(x)$	50.06	0.30	31.90	0.0133	1.57	30.96	0.1046	1.62
	$f_4(x)$	61.31	0.23	32.22	0.0006	1.90	31.57	0.0009	1.94
	$f_5(x)$	45.24	2.07	31.14	0.0087	1.45	28.10	0.0019	1.61
	$f_6(x)$	52.16	0.44	28.61	0.0580	1.82	26.76	0.0026	1.95
	$f_7(x)$	62.69	0.09	28.76	0.0105	2.18	26.27	0.0031	2.39
64	$f_1(x)$	81.86	0.62	34.84	0.1179	2.35	32.06	0.0012	2.55
	$f_2(x)$	89.77	0.31	35.42	0.0779	2.53	33.43	0.0017	2.68
	$f_3(x)$	101.13	0.75	40.01	0.0510	2.53	39.51	0.0007	2.56
	$f_4(x)$	122.97	0.13	40.53	0.0047	3.03	35.61	0.0030	3.45
	$f_5(x)$	93.61	2.07	39.63	0.0142	2.36	36.25	0.0198	2.58
	$f_6(x)$	92.36	0.44	36.83	0.0090	2.51	35.30	0.6523	2.61
	$f_7(x)$	127.52	0.08	36.71	0.1229	3.47	33.70	0.0026	3.78

It is considered that the GPU implementation can conceal the latency of memory access by executing many threads in parallel, while the CPU implementation executes the GA calculation sequentially. In particular, it is notable that our implementation to parallelize the process of both individuals and their data is more effective, because the implementation enables the execution of more threads than others. In addition, most GA processes are executed on GPU. This can suppress the frequency of data transfer between the host and the device, which is probably the bottleneck to speed up by GPU.

6. Conclusion

In this paper, the implementation of GA on GPGPU using C-CUDA is carried out. The massive parallel architecture of GPU exploited to attain required speedups in GA. It shows acceleration of 1.18-4.15 times as compared to its sequential execution on CPU on variety benchmark test functions. From this result it is concluded that, the algorithm can be made more optimized for several search problems to enhance its wide variety of features. In future work, the performance of GA model will be more improved by modifying single objective GA to multi-objective GA. Further improvement of this model will be done by implementing multi-objective GA model with Fuzzy logic system which is expected to a fast parallel approach.

References

[1] L. De Giovanni and F. Pezzella, "An improved genetic algorithm for the distributed and flexible job-shop scheduling problem", European journal of operational research, vol. 200, no. 2, **(2010)**, pp. 395-408.
[2] J. H. Holland, "Genetic algorithms and the optimal allocation of trials", SIAM Journal on Computing, vol. 2, no. 2, **(1973)**, pp. 88-105.
[3] K. Ghoseiri and S. F. Ghannadpour, "Multi-objective vehicle routing problem with time windows using goal programming and genetic algorithm", Applied Soft Computing, vol. 10, no. 4, **(2010)**, pp. 1096-1107.
[4] K. P. Murphy, "Machine learning: a probabilistic perspective", MIT press, **(2012)**.
[5] H. Xing and R. Qu, "A compact genetic algorithm for the network coding based resource minimization problem", Applied Intelligence, vol. 36, no. 4, **(2012)**, pp. 809-823.
[6] S. Yang, H. Cheng and F. Wang, "Genetic algorithms with immigrants and memory schemes for dynamic shortest path routing problems in mobile ad hoc networks", Systems, Man, and Cybernetics, Part C: Applications and Reviews, IEEE Transactions on, vol. 40, no. 1, **(2010)**, pp. 52-63.
[7] A. Prakash, F. T. Chan and S. Deshmukh, "Fms scheduling with knowledge based genetic algorithm approach", Expert Systems with Applications, vol. 38, no. 4, **(2011)**, pp. 3161-3171.

[8] J. Adams, D. L. Woodard, G. Dozier, P. Miller, K. Bryant and G. Glenn, "Genetic-based type ii feature extraction for periocular biometric recognition: Less is more", Pattern Recognition (ICPR), 2010 20th International Conference on. IEEE, **(2010)**, pp. 205-208.
[9] A. Quteishat, C. P. Lim and K. S. Tan, "A modified fuzzy min–max neural network with a genetic-algorithm-based rule extractor for pattern classification", Systems, Man and Cybernetics, Part A: Systems and Humans, IEEE Transactions, vol. 40, no. 3, **(2010)**, pp. 641-650.
[10] Y. Zhang and L. Wu, "Artificial bee colony for two dimensional protein folding," Advances in Electrical Engineering Systems, vol. 1, no. 1, **(2012)**, pp. 19-23.
[11] L. Magnier and F. Haghighat, "Multiobjective optimization of building design using trnsys simulations, genetic algorithm, and artificial neural network", Building and Environment, vol. 45, no. 3, **(2010)**, pp. 739-746.
[12] S. Omkar, J. Senthilnath, R. Khandelwal, G. Narayana Naik and S. Gopalakrishnan, "Artificial bee colony (abc) for multi-objective design optimization of composite structures", Applied Soft Computing, vol. 11, no. 1, **(2011)**, pp. 489-499.
[13] F. Fabris and R. A. Krohling, "A co-evolutionary differential evolution algorithm for solving min–max optimization problems implemented on gpu using c-cuda", Expert Systems with Applications, vol. 39, no. 12, **(2012)**, pp. 10 324-10 333.
[14] O. Maitre, F. Kr¨uger, S. Querry, N. Lachiche and P. Collet, "Easea: specification and execution of evolutionary algorithms on gpgpu", Soft Computing, vol. 16, no. 2, **(2012)**, pp. 261-279.
[15] O. Maitre, N. Lachiche and P. Collet, "Fast evaluation of gp trees on gpgpu by optimizing hardware scheduling", Genetic Programming, Springer, 2010, **(2011)**, pp. 301-312.
[16] M. A. Franco, N. Krasnogor and J. Bacardit, "Speeding up the evaluation of evolutionary learning systems using gpgpus", Proceedings of the 12th annual conference on Genetic and evolutionary computation. ACM, **(2010)**, pp. 1039-1046.
[17] S. Ryoo, C. I. Rodrigues, S. S. Baghsorkhi, S. S. Stone, D. B. Kirk and W.-M. W. Hwu, "Optimization principles and application performance evaluation of a multithreaded gpu using cuda", Proceedings of the 13th ACM SIGPLAN Symposium on Principles and practice of parallel programming, ACM, **(2008)**, pp. 73-82.
[18] M. R. Noraini and J. Geraghty, "Genetic algorithm performance with different selection strategies in solving tsp", Proceedings of the World Congress on Engineering 2011, vol. II, **(2011)**.
[19] M. Oiso, T. Yasuda, K. Ohkura and Y. Matumura, "Accelerating steadystate genetic algorithms based on cuda architecture", Evolutionary Computation (CEC), 2011 IEEE Congress on. IEEE, **(2011)**, pp. 687-692.
[20] P. Posp´ıchal, J. Schwarz and J. Jaros, "Parallel genetic algorithm solving 0/1 knapsack problem running on the gpu", 16th International Conference on Soft Computing MENDEL, vol. 2, **(2010)**, pp. 64-70.
[21] R. Arora, R. Tulshyan and K. Deb, "Parallelization of binary and real-coded genetic algorithms on gpu using cuda", Evolutionary Computation (CEC), 2010 IEEE Congress, IEEE, **(2010)**, pp. 1-8.
[22] M. Oiso, Y. Matsumura, T. Yasuda and K. Ohkura, "Evaluation of generation alternation models in evolutionary robotics", Natural Computing. Springer, **(2010)**, pp. 268-275.
[23] M. Jamil and X.-S. Yang, "A literature survey of benchmark functions for global optimisation problems", International Journal of Mathematical Modelling and Numerical Optimisation, vol. 4, no. 2, **(2013)**, pp. 150-194.

Authors

Rashmi Sharan Sinha was born on Apr 6, 1987. She received her Bachelor's degree (B.Tech.) from Lala Lajpat Rai Institute of Engineering and Technology, Moga, in year 2011 and Master's degree (M.Tech.) from Shaheed Bhagat Singh State Technical Campus (formerly, SBS College of Engineering & Technology), Ferozepur, Punjab (India) with specialization in Electronics & Communication Engineering in year 2015. Her research interests include Evolutionary Algorithms and Fuzzy Logic System.

Satvir Singh was born on Dec 7, 1975. He received his Bachelor's degree (B.Tech.) from Dr. B. R. Ambedkar National Institute of Technology, Jalandhar, Punjab (India) with specialization in Electronics & Communication Engineering in year 1998, Masters degree (M.E.) from Delhi Technological University (Formerly, Delhi College of Engineering), Delhi (India) with distinction in Electronics

& Communication Engineering in year 2000 and Doctoral degree (Ph.D.) from Maharshi Dayanand University, Rohtak, Haryana (India) in year 2011.

His fields of special interest include Evolutionary Algorithms, High Performance Computing, Type-1 & Type-2 Fuzzy Logic Systems, Wireless Sensor Networks and Artificial Neural Networks for solving engineering problems. He is active member of an editorial board of International Journal of Electronics Engineering and published nearly 15 research papers in International Journals and Conferences. He has delivered nearly 15 Invited Talks during National and International Conferences, Seminar, Short Term Courses and Workshops. He completed two AICTE funded projects under MODROB Scheme worth 15 Lacs and conducted a 2-Week Staff Development Programme on "Intelligent Computational Techniques".

Sarabjeet Singh received the B.Tech degree in Computer Science & Engineering from National Institute of Technology Jalandhar, M.Tech degree in Computer Science & Engineering from Panjab University Chandigarh. He is currently working in Shaheed Bhagat Singh State Technical Campus, Ferozepur. His current research interests include Computer Graphics and High Performance Computing.

Vijay Kumar Banga received the B. Tech degree in Electronics and Communication engineering from Punjabi University Patiala, M. Tech degree in Electronics and Communication Engineering from Panjab University Chandigarh and Phd. from Thapar University Patiala. He is currently working as Principal in Amritsar College of Engineering and Technology, Amritsar. His current research interests include Soft Computing, Image Processing, Autonomous Robots.

An Adaptive Bacterial Foraging Algorithm For Color Image Enhancement

Om Prakash Verma, Rishi Raj Chopra and Abhinav Gupta
Department of Computer Science and Engineering
Delhi Technological University
Delhi, India
opverma.dce@gmail.com, rishirajchopra2@gmail.com, guptabhi123@gmail.com

***Abstract*— A new approach in spatial domain is presented for the enhancement of color images using an Adaptive Bacterial Foraging Algorithm (ABFA). The image may be classified as under-exposed or over-exposed depending upon the value of exposure. A new objective function is formulated which makes use of the fuzzy entropy. This objective function is optimized using ABFA which allows the step-size of the bacterial colony to vary dynamically over the generations. The lifetime of the bacterial colony is described by generations which are split into two phases; exploration and exploitation based on the value of step-size. Smaller step-sizes correspond to exploitation phases in which the entire bacterial colony is trying to exploit a region of interest while larger step-sizes correspond to exploration phases in which the entire bacterial colony is trying to explore the search space to find regions of interest which can then be exploited by reducing the step-size. This method is applicable on both over-exposed and under-exposed images. The proposed algorithm is found to be better and much more simplified than the existing Bacterial Foraging Algorithm (BFA) in fuzzy domain for color image enhancement upon comparison.**

Keywords—Fuzzy Entropy; Exposure; Adaptive Bacterial Foraging Algorithm; Color Image Enhancement

I. INTRODUCTION

Images often contain unnecessary details which hide its basic features and decrease image quality. Image enhancement helps us to improve the quality of the original image by addition of relevant or removal of irrelevant information from the image. Many image enhancement techniques have been implemented on grayscale images, like Histogram Equalization (HE) [1] but its results are too intense at times. An adaptive HE was proposed by Stark [2] to generalize and improve HE. Singh *et al*. [3] proposed an exposure based sub-image histogram equalization (ESIHE) technique which proved to be very effective for contrast enhancement. However, these are limited to grayscale images only and generalizing them to color images is a complex task which involves the human visual system, maintaining the color contrast of the image and selection of the color models. Moreover, color images are more desirable in the real world emphasizing the importance of color enhancement techniques.

Image enhancement techniques may be divided into two major categories namely; transformation domain and the spatial domain. The first category uses frequency transform of an image which can be very time inefficient, especially for 2D images. The second category operates on the image pixels directly. It improves the visual perception by the human eye [4]. For the enhancement of color images, it is necessary to note that the color should not change for any pixel. Changing the color means changing the hue. Thus, hue should be conserved. Gupta *et al.* [5] presented a hue preserving approach for contrast stretching for a class of color images.

There always presents ambiguity in the real world and it so does in digital images. Color properties, brightness, intensities are few of the properties which are not deterministic. In a fuzzy domain, we utilize the mathematical properties of fuzzy sets [6] to eliminate this ambiguity by introducing a user defined membership function. Smoothing in fuzzy sets in [7] is presented by Pal *et al.* for gray tone enhancements; however it is restricted to grayscale images.

In recent years, optimization based image enhancement techniques have been introduced which utilize various nature inspired algorithms, like a GA based approach to color image enhancement [8], which uses weighted transform of four types of linear transform but presents ambiguity. This ambiguity was overcome by Hanmandlu *et al.* [9] in a BFA based approach, and by Verma *et al.* [10] in an Ant Colony Optimization (ACO) based approach. The approach in [9] makes the use of visual factors and entropy for the enhancement. Minimizing entropy enhances the image by bringing out the basic features of the image. We extend this approach by simplifying the objective function used in [9]. We have removed the visual factors from the objective function. It results in a less complex objective function, and also makes the minimization of entropy less constrained. This allows the entropy of an image to further decrease making the image more pleasant. Another change made to the approach in [9] is the use of ABFA [11] instead of classical BFA [12], for better optimization. The step size used in the classical BFA is static. This step-size has been made dynamic in the proposed method to allow the algorithm to reach closer to an optima.

The criterion employed for performance analysis utilizes the Tenengrad measure and exposure, in addition to visual quality. The entropy of the original and the enhanced images from various approaches are also studied to understand the difference made.

II. ENHANCEMENT IN FUZZY DOMAIN

An image can be termed as underexposed or overexposed depending on its exposure value, defined in [9] as:

$$exposure = \frac{1}{L}\frac{\sum_{x=1}^{L} p(x).x}{\sum_{x=1}^{L} p(x)} \qquad (1)$$

978-1-4673-9457-4/16/$31.00 ©2016 IEEE

where x denotes the gray-level values of the image, $p(x)$ represents the histogram of the whole image, and L represents the total number of gray levels. A factor α defined as:

$$\alpha = \mathrm{L}.(1 - \mathrm{exposure}) \quad (2)$$

is used to divide the gray levels into two parts: [0, α-1] for the underexposed part, and [α, L-1] for the overexposed part.

The quality of an image cannot be quantified according to the visual perception of a human since it may be impressionistic. Therefore, a fuzzy approach is adopted to deal with uncertainty in images since they can quantify the uncertainty of images by assigning a degree of membership to each pixel.

A. Fuzzification

The image is divided into two parts according to exposure, and a modified Gaussian membership function [13] is employed to fuzzify the underexposed regions given as:

$$\mu_{X_u}(x) = e^{-\{\left(\frac{x_{max}-(x_{avg}-x)}{\sqrt{2}f_h}\right)^2\}} \quad (3)$$

where $\mu_{X_u}(x)$ denotes the degree of membership of a gray level x to the set of underexposed region denoted by u; x_{max} and x_{avg} are the maximum and the average intensity level in the image respectively; and f_h is called the fuzzifier, whose initial value is given by [14]:

$$f_h^2 = \frac{1}{2}\frac{\sum_{x=0}^{L-1}(x_{max}-x)^4 p(x)}{\sum_{x=0}^{L-1}(x_{max}-x)^2 p(x)} \quad (4)$$

To fuzzify the overexposed region, a triangular membership function is used, given as:

$$\mu_{X_o}(x) = \begin{cases} 0 & x < a \\ \dfrac{x-a}{L-a} & x \geq a \end{cases} \quad (5)$$

where $\mu_{X_o}(x)$ denotes the degree of membership of a gray level x to the set of overexposed region denoted by o.

B. Membership Value Enhancement

A parametric sigmoid operator is employed for the enhancement of the underexposed region, given as:

$$\mu'_{X_u}(x) = \frac{1}{1 + e^{-t(\mu_{X_u}(x)-\mu_c)}} \quad (6)$$

where t is the intensification factor, μ_c is the crossover point, and $\mu'_{X_u}(x)$ is the modified membership value of the pixel for the underexposed region.

In order to enhance the overexposed region, a power law operator is used. In the overexposed region, the intensities of pixels are all near to the highest gray level and the difference between the neighborhood pixels is low. Thus, the information content is also low. After applying the power law transformation, the information content is increased by the power of γ, given as:

$$\mu'_{X_o}(x) = K(\mu_{X_o}(x) + \epsilon)^{\gamma} \quad (7)$$

where $\mu'_{X_o}(x)$ is the modified membership value of the pixel for the overexposed region and γ is the factor by which the membership values are enhanced. It may be pointed out that if a region has all pixels at minimum or maximum intensity value then no enhancement operator can increase the information content by just working on the intensity component. These kind of regions are considered as permanently degraded areas. By manipulating the saturation component, the hidden details in such regions can be unveiled. For the enhancement of saturation in such regions, another power law operator [15] is used, given as:

$$S'(x) = [S(x)]^{(1-0.5*exposure)} \quad (8)$$

where S(x) and S'(x) are the original and the modified saturation values of the HSV color space respectively.

C. Defuzzification

Defuzzification of the modified membership values is done based on the inverse MFs, given as:

$$x'_u = \mu_u^{-1}[\mu'_{X_u}(x)] \quad (9)$$

$$x'_o = \mu_o^{-1}[\mu'_{X_o}(x)] \quad (10)$$

where x'_u and x'_o are the new values of the intensity component of the image in HSV.

III. Optimization

A. Entropy

A measure of the quality of information in an image in the fuzzy domain is given by its Entropy which makes use of Shanon's function. The entropy defines the ambiguity in the image. The entropy, E, is given as:

$$\begin{aligned} E = \frac{-1}{Lln2}[\sum_{x=0}^{\alpha-1}\Big[&\mu'_{X_u}(x)\ln\left(\mu'_{X_u}(x)\right) \\ &+ (1-\mu'_{X_u}(x))\ln(1-\mu'_{X_u}(x))\Big] \\ &+ \sum_{x=\alpha}^{L-1}[\mu'_{X_o}(x)\ln\left(\mu'_{X_o}(x)\right) \\ &+ (1-\mu'_{X_o}(x))\ln(1-\mu'_{X_o}(x))]] \end{aligned} \quad (11)$$

Minimizing the entropy helps us to reduce the effect of unnecessary features and serves as a method to calculate the optimum value of parameters (t, μ_c, f_h, γ).

B. Objective Function

The approach mentioned in [9] for the calculation of objective function makes use of visual factors along with entropy. The entropy was minimized to bring out the basic characteristics of the image and get rid of unnecessary details while the visual factors were introduced in [9] to measure the amount of enhancement caused. We removed the visual factors from the objective function to reduce the complexity. Also, the removal of visual factors allows the image to be enhanced further as the entropy could now be minimized directly with lesser constraints. However, if the entropy is allowed to go through unconstrained minimization, it would lead to a loss of critical details from the image and might render the image flat (E=0). Thus, we decided that the entropy would not reduce below Q% of the original entropy to prevent the loss of critical information from the image. The objective function is formulated as:

$$J = \left| E' - \frac{Q}{100}.E \right| \quad (12)$$

where, E and E' are the original and the minimized entropy respectively. It was observed experimentally that the best results were obtained when the entropy was allowed to be reduced till 70% of its original value, thus, the value of Q was fixed to 70.

$$J = |E' - 0.7 * E| \quad (13)$$

Minimization of the objective function helps us obtain the value of parameters t, μ_c, f_h, γ.

C. Adaptive Bacterial Foraging Algorithm (ABFA)

An ABFA given in [11] is used to optimize the objective function. BFA, motivated by E. coli bacteria was introduced by K.M. Passino in [12]. Searching the hyperspace is accomplished through three main operations, namely; chemotaxis, reproduction and elimination dispersal. The chemotaxis operation is represented as:

$$\theta^i(j+1,k,l) = \theta^i(j,k,l) + C(i)\emptyset(i) \quad (14)$$

where, $\theta^i(j+1,k,l)$ is the new position after a step of size $C(i)$, called the step-size, in the direction of the tumble for bacterium i given by $\emptyset(i)$, a direction vector, and j, k and l are indices for chemotactic, reproductive and elimination/dispersal steps respectively. We only mention the formulation of the chemotaxis step as it is useful for our discussion. Reproduction and elimination-dispersal steps are as mentioned in [9].

The chemotaxis operation of the bacteria via random motion is a powerful strategy to explore the optimum point in a search space [16]. In classical BFA, the step-size is kept static. Small step-sizes in the bacteria motion lead to high accuracy in the solution but slow convergence. On the other hand, defining large step-sizes for the motion leads to faster convergence but low accuracy. To overcome this issue, in ABFA, the step-size is made dynamic. The chemotaxis, reproduction, and elimination-dispersal steps are applied in generations, where each generation corresponds to a particular value of step-size which is dynamically adapted on the basis of the output of the previous generations. Chemotaxis in ABFA is given as:

$$\theta^i(w,j+1,k,l) = \theta^i(w,j,k,l) + C(i,w)\emptyset(i) \quad (15)$$

where w is the generation number. This splits the generations into two phases; exploration and exploitation, enabling the algorithm to modify the value of C(i,w) depending upon how close it is to an optima instead of remaining constant. The value of C(i,w) is kept large when it is exploring the search space for optima, and small when it is exploiting a region close to optima. This dynamic adaptation allows the bacteria colony to converge closer and faster to an optima. We have kept the same step-size for all the bacteria in the colony for simplification. Thus, we remove the parameter 'i' from our discussion on step-size. The new step-size is calculated after each generation as:

$$C(w+1) = \begin{cases} \frac{C(w-n)}{a} & w \bmod n = 0 \ \& f_{best} < \varphi(w) \\ C(w-n) & w \bmod n = 0 \ \& f_{best} \geq \varphi(w) \\ C(w) & otherwise \end{cases} \quad (16)$$

where, w is the generation number, C(w+1) represents the step-size for $(w+1)^{th}$ generation, f_{best} is the best fitness so far, $\varphi(w)$ is the precision value at the w^{th} generation and, a and n are user defined constants. This modification in the calculation of step-size makes sure that if a bacteria colony has reached the expected fitness for that generation, then its step-size is decreased to make it move slower, thus exploiting the optima better. The precision value for each generation is calculated as:

$$\varphi(w+1) = \begin{cases} \frac{\varphi(w-n)}{b} & w \bmod n = 0 \ \& f_{best} < \varphi(w) \\ \varphi(w-n) & w \bmod n = 0 \ \& f_{best} \geq \varphi(w) \\ \varphi(w) & otherwise \end{cases} \quad (17)$$

where, b is a user defined constant. The initial value of C(w) and $\varphi(w)$ are user-defined. After every n generations, the bacteria colony is re-initialized with the best-so-far position found by each bacterium. There are a total of N_t generations, where N_t is fixed by the user. ABFA is described by Fig 1.

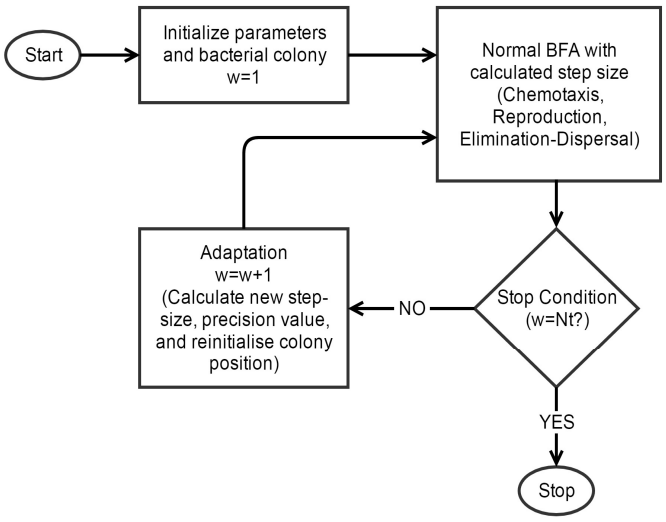

Figure 1: Flowchart of ABFA

The comparison of BFA and ABFA is shown in Fig 2 by plotting Entropy v/s Number of Chemotactic Steps in optimizing the entropy of an image using (13). ABFA starts performing better than BFA after 100 chemotaxis steps as can be seen in Fig 2 (b). The green line (ABFA) is constantly lower than the blue line (BFA) after 100 chemotactic steps. Thus, ABFA is adapted as the optimization algorithm as it converges faster than BFA to more accurate results.

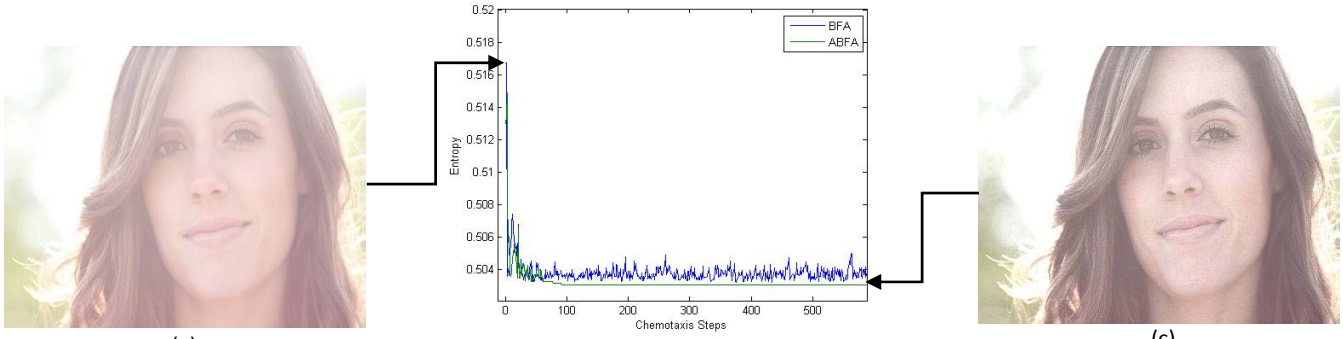

Figure 2: Chemotaxis Steps for BFA and ABFA (a) Original Image (b) Fitness graph of Entropy (c) Enhanced Image

D. *Initialization of parameters of ABFA*

The parameters of ABFA were initialized as follows:

1) Number of bacteria in the colony, $N_b = 20$
2) Number of chemotactic steps, $N_c = 20$
3) Length of swimstep, $N_s = 10$
4) Number of reproduction steps, $N_{re} = 4$
5) Number of Elimination/Dispersal steps, $N_{ed} = 6$
6) Probability for Elimination/Dispersal, $P_{ed} = 0.25$
7) Number of generations, $N_t = 10$
8) Constant n = 2, Constant a = 10, Constant b = 1.001
9) Initial value of C(w) = 0.1
10) Initial value of $\varphi(w)$ = to 0.9*(entropy of the image)

E. *Enhancement Algorithm*

The algorithm for enhancement is described as follows:

1. Convert the input image (RGB) to HSV
2. Obtain the histogram of the image p(x), x ∈ V
3. Find the values of exposure, α and f_h using (1), (2) and (4), and set the initial value of μ_c, t, and γ as 0.5, 7 and 2 respectively.
4. Obtain membership values, $\mu_{X_u}(x)$ and $\mu_{X_o}(x)$ by fuzzifying V using (4) and (6) respectively
5. Obtain the modified membership values $\mu'_{X_u}(x)$ and $\mu'_{X_o}(x)$ using (7) and (8) respectively
6. Obtain the initial value of Entropy of the image using (11)
7. Set up the objective function for optimization using (13)
8. Optimize the objective function using ABFA to get the optimized value of parameters (μ_c, t, γ, f_h)
9. Repeat step 6 to obtain the new membership values using the optimized value of parameters (μ_c, t, γ, f_h) obtained in step 8
10. Defuzzify the modified membership values $\mu'_{X_u}(x)$ and $\mu'_{X_o}(x)$ using (9) and (10)
11. Combine them based on the value of α as:

$$x' = \begin{cases} x'_u \; for \; 0 \; to \; \alpha - 1 \\ x'_o \; for \; \alpha \; to \; L - 1 \end{cases} \quad (18)$$

This gives us the enhanced intensity (V') for the image.

12. For overexposed images, modify the saturation component using (8) and then display the enhanced HSV image.

IV. RESULTS AND DISCUSSIONS

The proposed approach was implemented on MATLAB 2013. It has been applied to 40 images and the results observed were quite satisfactory. We have considered some test images to display the results here, viz, "train", "gang", "lady", "girl", "horse". The original images and the corresponding enhanced images are shown in Figs 3-7.

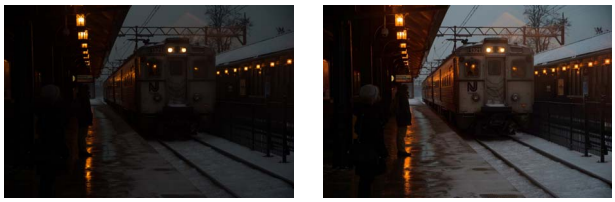

Figure 3: (a) Original Image ("train") (b) Enhanced Image

Figure 4: (a) Original Image ("gang") (b) Enhanced Image

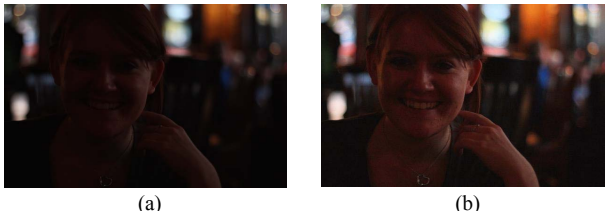

Figure 5: (a) Original Image ("lady") (b) Enhanced Image

We have used Tenengrad and Exposure as the performance measures. The result of the two measures is given in Table I.

(a) (b)

Figure 6: (a) Original Image ("girl") (b) Enhanced Image

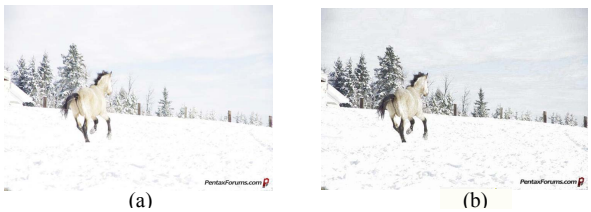

(a) (b)

Figure 7: (a) Original Image ("horse") (b) Enhanced Image

Table I: Results of Performance Measures

Image Name	Original Image		Enhanced Image	
	Tenengrad	Exposure	Tenengrad	Exposure
Train	11584	0.0893	11819	0.1820
Gang	11494	0.0370	11743	0.0621
Lady	11285	0.0887	11566	0.1644
Girl	11101	0.8479	10356	0.7995
Horse	11057	0.9382	10280	0.9013

The first three images, "train", "gang" and "lady" are underexposed, having low brightness while the last 2 images, "girl" and "horse" are overexposed, having a high brightness. It can be seen in Table I that the exposure has increased for the first three images while it has decreased for the last 2 images. Table II describes the initial value of parameters (t, μ_c, γ, f_h) and entropy of the original image. The value of f_h is higher for the last 2 images as they are overexposed. Table III describes the optimized value of parameters and entropy used to enhance the image.

Table II: Initial Values of Parameters and Entropy

Image Name	t	μ_c	γ	f_h	Entropy
Train	7.0000	0.5000	2.0000	78.8779	0.3609
Gang	7.0000	0.5000	2.0000	80.1716	0.6185
Lady	7.0000	0.5000	2.0000	78.0356	0.3278
Girl	7.0000	0.5000	2.0000	93.7889	0.6236
Horse	7.0000	0.5000	2.0000	82.9288	0.5117

Table III: Optimized Values of Parameters and Entropy

Image Name	t	μ_c	γ	f_h	Entropy
Train	6.8488	0.5924	2.3188	78.7044	0.2862
Gang	5.8335	0.5417	2.2658	92.3402	0.4724
Lady	6.7246	0.5862	2.3061	80.6726	0.2833
Girl	4.9509	0.4975	2.2278	85.5454	0.5811
Horse	3.8929	0.4196	2.1660	81.3396	0.4837

It can be seen from Table II and III that the enhanced image has a lesser value of entropy than the original image. This shows that the image features have been reduced in the enhanced image, making the image more pleasing to the human eye.

The proposed approach is compared with the approach in [9] which uses visual factors in the objective function and a static step size in the BFA for optimization and also with the HE technique [1] applied to color images by equalization of the intensity component (V) in HSV color space. Two images are shown here for comparison, namely "flowers" and "scenery" and their corresponding enhanced images are shown in Figs. 8 and 9. Table IV and V give the exposure and the entropy values respectively for the original and the enhanced images.

Table IV: Comparison of exposure values

Image Name	Original	Enhanced using visual factor approach	Enhanced using the HE approach	Enhanced using the proposed approach
Flowers	0.0545	0.2052	0.4087	0.2228
Scenery	0.1435	0.2866	0.4509	0.3015

Table V: Comparison of entropy values

Image Name	Original	Enhanced using visual factor approach	Enhanced using the HE approach	Enhanced using the proposed approach
Flowers	0.2385	0.1923	0.6381	0.1855
Scenery	0.6333	0.3265	0.6858	0.2812

As it can be seen from Table IV, the proposed approach has yielded higher exposure values than the visual factor approach but lower than the HE approach. The exposure values have increased in all the enhanced images because the original images contained more percentage of underexposed regions giving rise to low exposure values. HE over enhances the image leading to a huge difference between the exposure values of the enhanced and the original image. The proposed approach yields an optimum exposure value by effectively developing the basic features in the image. The entropy values listed in Table V show that the proposed approach obtains the lowest entropy values for enhanced images. This was expected as in the proposed approach, there are fewer constraints on the minimization of entropy in the objective function as compared to the visual factors approach [9]. The HE approach has yielded images with entropy values higher than the original images. In the "flowers" image given in Fig 8(a), histogram equalization has yielded an image with entropy value 287% times the entropy of original image. This is not desirable, as it has added a lot of unnecessary information to the image. This makes the image look over enhanced as can be seen in Fig. 8 (c). The proposed approach obtains an optimum entropy value, i.e. not lower than the 70% of original as fixed in the objective function. Thus, the proposed approach achieves slightly better results than the visual factor approach given in [9] but reduces the complexity of the objective function a lot. Also, the proposed approach outperforms the histogram equalization technique.

Figure 8: (a) Original Image ("flowers") (b) Enhanced using visual factor approach [9] (c) Enhanced using HE approach [1] (d) Enhanced using proposed approach

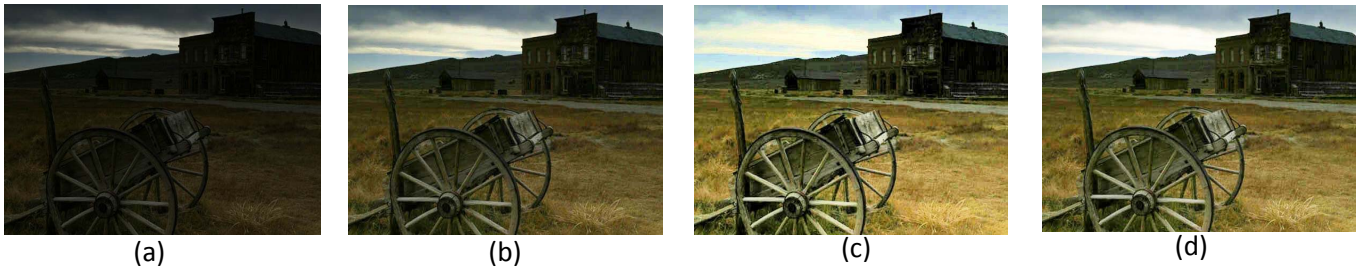

Figure 9: (a) Original Image ("scenery") (b) Enhanced using visual factor approach [9] (c) Enhanced using HE approach [1] (d) Enhanced using proposed approach

V. CONCLUSIONS

We have successfully improved the existing approach [9] on color image enhancement. The ambiguity of color intensities was surmounted using fuzzy set tools. The objective function presented here utilizes only the entropy for optimization. A simple constraint, however, was placed on the minimization of entropy so as to disallow the loss of necessary information from the image. We have also used ABFA for optimization instead of classical BFA. By determining the step size dynamically, ABFA is able to optimize the entropy better and come much closer to the optimum value.

The results of the proposed approach were satisfactory and we obtained visually enhanced images from degraded images. The pleasing nature and the original colors of the images were restored. We compared the approach with the visual factor approach and found that the results were slightly better with reduced complexity of the objective function. We also compared the approach with a classical image enhancement technique, i.e. histogram equalization. We found that histogram equalization often over enhances the image which makes it look unpleasant. The proposed approach outperformed the histogram equalization technique.

REFERENCES

[1] A. K. Jain, Fundamentals of Digital Image Processing. Englewood Cliffs, NJ: Prentice-Hall, 1989.
[2] J. Alex Stark, "Adaptive Image Contrast Enhancement Using Generalizations of Histogram Equalization," IEEE Trans. Image Processing, vol. 9, no. 5, May 2000.
[3] K Singh, R Kapoor, Image enhancement using exposure based sub image histogram equalization. Pattern Recogn. Lett. 36, 10–14 (2014)
[4] R. C. Gonzalez and R. E. Woods, Digital Image Processing. Reading, MA: Addison-Wesley, 1992.
[5] A. Gupta and B. Chanda, "A hue preserving enhancement scheme for a class of color images," Pattern Recognit. Lett., vol. 17, pp. 109–114, 1996.
[6] H. J. Jimmermann, Fuzzy Set Theory and its Applications, Second ed. Norwell, MA: Kluwer, 1991
[7] Sankar K. Pal and Robert A. King, "Image Enhancement Using Smoothing with Fuzzy Sets,"IEEE Trans. Systems, Man, And Cybernetics, Vol. SMC-1 1, no. 7, July 1981.
[8] M. Shyu and J. Leoua, "A genetic algorithm approach to color image enhancement," Pattern Recognit., vol. 31, no. 7, pp. 871–880, Jul. 1998.
[9] Madasu Hanmandlu, Om Prakash Verma, Nukala Krishna Kumar and Muralidhar Kulkarni, "A Novel Optimal Fuzzy System for Color Image Enhancement Using Bacterial Foraging," IEEE Trans Instrumentation AND Measur., Vol. 58, no. 8, August 2009.
[10] O.P. Verma, P. Kumar, M. Hanmandlu, S. Chhabra, "High dynamic range optimal fuzzy color image enhancement using Artificial Ant Colony System," Applied Soft Computing, 12 (2012), pp. 394–404
[11] Hanning Chen, Yunlong Zhu, and Kunyuan Hu, "Adaptive Bacterial Foraging Optimization," Abstract and Applied Analysis, vol. 2011, Article ID 108269, 27 pages, 2011. Doi:10.1155/2011/108269
[12] K.M. Passino, "Biomimmicry of bacterial foraging for distributed optimization and control,"IEEE Control Syst. Mag., vol.22, no. 3, pp. 52-67, Jun. 2002.
[13] M. Hammandlu and D.Jha, "An optimal fuzzy system for color image enhancement," IEEE Trans. Image Process., vol. 15, no. 10, pp. 2956-2966, Oct 2006
[14] M. Hanmandlu, M. Jha, and R. Sharma, "Color image enhancement using fuzzification," Pattern Recognit. Lett., vol. 24, no. 1-3, pp. 81-87, 2003.
[15] L. Wang, L. Wei, K. Zhou, B. Guo, and H. Shum, "High Dynamic Range Image Hallucination," in Proc. Eurographics Symp. Rendering, 2007.
[16] Ahmad N. K. Nasir, M. O. Tokhi, and N. Maniha Abd. Ghani, "Novel Adaptive Bacteria Foraging Algorithms for Global Optimization," Applied Computational Intelligence and Soft Computing, vol. 2014, Article ID 494271, 7 pages, 2014. doi:10.1155/2014/49427

Applied Soft Computing xxx (2016) xxx–xxx

Contents lists available at ScienceDirect

Applied Soft Computing

journal homepage: www.elsevier.com/locate/asoc

An empirical framework for defect prediction using machine learning techniques with Android software

Ruchika Malhotra

Department of Software Engineering, Delhi Technological University, Bawana Road, Delhi, India

ARTICLE INFO

Article history:
Received 30 November 2015
Received in revised form 20 March 2016
Accepted 26 April 2016
Available online xxx

Keywords:
Object-oriented metrics
Machine-learning
Software defect proneness
Statistical tests
Inter-release validation

ABSTRACT

Context: Software defect prediction is important for identification of defect-prone parts of a software. Defect prediction models can be developed using software metrics in combination with defect data for predicting defective classes. Various studies have been conducted to find the relationship between software metrics and defect proneness, but there are few studies that statistically determine the effectiveness of the results.

Objective: The main objectives of the study are (i) comparison of the machine-learning techniques using data sets obtained from popular open source software (ii) use of appropriate performance measures for measuring the performance of defect prediction models (iii) use of statistical tests for effective comparison of machine-learning techniques and (iv) validation of models over different releases of data sets.

Method: In this study we use object-oriented metrics for predicting defective classes using 18 machine-learning techniques. The proposed framework has been applied to seven application packages of well known, widely used Android operating system viz. Contact, MMS, Bluetooth, Email, Calendar, Gallery2 and Telephony. The results are validated using 10-fold and inter-release validation methods. The reliability and significance of the results are evaluated using statistical test and post-hoc analysis.

Results: The results show that the area under the curve measure for Naïve Bayes, LogitBoost and Multilayer Perceptron is above 0.7 in most of the cases. The results also depict that the difference between the ML techniques is statistically significant. However, it is also proved that the Support Vector Machines based techniques such as Support Vector Machines and voted perceptron do not possess the predictive capability for predicting defects.

Conclusion: The results confirm the predictive capability of various ML techniques for developing defect prediction models. The results also confirm the superiority of one ML technique over the other ML techniques. Thus, the software engineers can use the results obtained from this study in the early phases of the software development for identifying defect-prone classes of given software.

1. Introduction

In software engineering, early detection of defective portions of the software can help the software developers and engineers in proper allocation of limited resources in testing and maintenance phases of the software development. The cost of correcting the defects increases exponentially if the defects are encountered later in the software development. The software defect prediction models can be used in the early phases of software development life cycle. Further, their use reduces the testing and maintenance time, cost and effort of the project and thus improves the quality of the software [1].

In order to increase the level of automation while developing software, models are effective and are gaining importance. Moreover, defect prediction models can be developed by using software metrics in conjunction with defect data obtained from historical repositories. The models can be trained using the historical releases of the same software and validated either on the same release or the subsequent releases of the software.

There are several machine-learning (ML) techniques proposed in the literature including neural networks, Support Vector Machines, ensemble learners and decision trees. But, it is difficult to establish the superiority of one ML technique over the other techniques using multiple data sets. Hence, more and more stud-

E-mail address: ruchikamalhotra2004@yahoo.com

http://dx.doi.org/10.1016/j.asoc.2016.04.032
1568-4946/

ies should be performed in order to draw well-formed, widely acceptable and generalized conclusions based on the experimental evidence gathered from the obtained results [1]. The results from the empirical studies will help to improve, refute and validate the results obtained from the past studies.

An effective empirical framework for the development of the prediction models should focus on the following issues: (i) use of appropriate and large number data sets (ii) performance of the predicted models assessed using appropriate performance measures (iii) reliability of the results using statistical tests (iv) validating the predicted models on data different from which they are trained. Lessman et al. [3] and Malhotra [4,5] observed that, the size of the study, performance measures used to assess the predicted model performance and the statistical tests to confirm the reliability of the results are three very important factors that need to be considered while conducting an empirical study. Also, the data sets available in software engineering research are scarce. There are only few studies that use statistical tests to analyze the suitability and validity of the results in literature. The evaluation of effectiveness of the performance of the predicted models is very crucial for the assessment of practical application of any defect prediction models. The reliability of empirical experiments can only be confirmed using the statistical tests [6]. Certain studies have pointed out that the statistical significance of the obtained results is rarely examined (Menzies et al. [7], Myrtviet et al. [8]). Further, previous studies have validated the developed models using the same data, on which they were trained.

In this work, we develop defect prediction models using object-oriented (OO) metrics over multiple application packages of Android operating system, open source software. Specifically, we address the following research issues in this work: (i) low repeatability of empirical studies, (ii) less usage of statistical tests for comparing the effectiveness of different models, and (iii) non-assessment of results on different releases of the software. This study will present an empirical framework of defect prediction models using 18 ML techniques, which will yield unbiased, accurate and repeatable results. The outcome of this research is assessed over various releases of seven application packages of Android software available in the Google code repository—Contact, MMS, Bluetooth, Email, Calendar, Gallery2 and Telephony.

As there is less use of statistical tests in the literature for statistically determining the comparative difference between predictive performances of developed models. Hence, after the models are generated, we will apply statistical techniques (such as Friedman test) to statistically determine whether there is a statistical difference between the performances of different ML techniques. We will also perform post-hoc analysis (using Nemenyi test) to evaluate the pairwise comparison amongst the results of different techniques. The results are evaluated using area under the curve (AUC) obtained from Receiver Operating Characteristics (ROC) analysis. Thus, the following research questions are addressed in this work:

- RQ1: What is the overall predictive capability of various ML techniques on seven application packages of Android software using 10-fold validation?

In this question we validate the results of predicted models using 10-fold validation with the help of various performance measures. The overall capability of the 18 ML techniques is assessed based on the results obtained using seven application packages of Android software.

- RQ2: What is the performance of defect prediction models when inter-release validation is carried out?

The performance of defect prediction models is validated using inter-release validation in this question. The results are evaluated using the AUC measure obtained using ROC analysis.

- RQ3: Is the performance of defect prediction models validated using inter-release validation comparable to 10-fold validation and is it statistically different than 10-fold validation?

We compare and assess the performance of models validated using inter-release with models validated using 10-fold validation. We determine the statistical difference between the results of inter-release validation and 10-fold validation for defect prediction using Wilcoxon test.

- RQ4: Which are the best and worst ML techniques for defect prediction using OO metrics?

The best and worst ML techniques are determined using the results of both 10-fold and inter-release validation over the seven application packages of Android software. These results are based on AUC measure and derived using the statistical test, Friedman.

- RQ5: Which pairs of ML techniques are statistically different from each other for defect prediction?

In this research question, we determine the pairs of ML techniques that are statistically different than each other. The results are based on post-hoc analysis using Nemenyi test.

The initial results carried out using one application package of Android software following the proposed approach are reported in Malhotra et al. [9]. Now, we present a major extension of the preliminary results presented in our previous study by evaluating the ML techniques over six additional application packages of Android software. The results of the previous study were not generalizable as they were only based on one application package of Android software. Also, we carry out post-hoc analysis using Nemenyi test to determine the effectiveness of the results. We also determine the statistical significance of inter-release validation and compare the ML techniques on the basis of inter-release validation. There is no study to the best of the authors' knowledge that extensively compares and assesses the performance of ML techniques to analyze the relationship between OO metrics and defect prediction using statistical tests. Hence, the main contributions of this paper are summarized below:

(1) An extensive comparison of 18 popular ML techniques in the context of defect prediction.
(2) The use of data collected from seven application packages over multiple releases of widely used Android software.
(3) Statistical analysis of the obtained results for comparison of ML techniques.
(4) An inter-release validation of models developed in order to obtain unbiased and generalized results.

The rest of the paper is organized as follows: Section 2 summarizes the related work and Section 3 describes the empirical research framework followed in this paper. Section 4 presents the research methodology and Section 5 provides the answers to the research questions. The threats to validity in the current research are summarized in Section 6 and the conclusions of the work are presented in Section 7.

Please cite this article in press as: R. Malhotra, An empirical framework for defect prediction using machine learning techniques with Android software, Appl. Soft Comput. J. (2016), http://dx.doi.org/10.1016/j.asoc.2016.04.032

Table 1
Summary of studies using ML techniques using OO metrics.

Study Refs.	Data type	Performance measures	Statistical test	Validation type
Briand 2002 [24]	Proprietary	Completeness, correctness	–	10-fold
Gyimothy 2005 [25]	Open source	Accuracy, correctness, completeness	–	10-fold, inter-release
Zhou and Leung 2006 [27]	Proprietary	Accuracy, precision, completeness	–	10-fold
Kanmani 2007 [29]	Academic	Correctness, completeness	–	Random training and testing
Pai 2007 [30]	Proprietary	Specificity, sensitivity, accuracy	–	10-fold
Catal 2007 [31]	Proprietary	Recall, accuracy, precision, gmean, f-measure	–	10-fold
Singh 2009 [34]	Proprietary	Sensitivity, specificity, completeness, Accuracy, AUC	–	10-fold
Malhotra 2010 [28]	Open source	Sensitivity, specificity, completeness, accuracy, AUC	–	10-fold
Zhou 2010 [35]	Open source	AUC	Statistical test based on Mann–Whitney statistic [46]	10-fold, inter-release
Arisholm 2010 [32]	Proprietary	AUC, accuracy, precision, recall	Wilcoxon	Hold-out
Carvalho 2010 [33]	Proprietary	AUC, accuracy, precision, recall, f-measure	Wilcoxon	10-fold
Martino 2011[36]	Open source	Accuracy, recall, precision, f-measure	–	Hold-out, 10-fold
Azar 2011 [38]	Open source	Accuracy	Wilcoxon	10-fold
Malhotra 2011 [39]	Open source	Sensitivity, specificity, AUC, Accuracy	–	10-fold
Malhotra 2012 [40]	Open source	Sensitivity, specificity, AUC, Accuracy	–	10-fold
Okutan2012 [37]	Open source	AUC	*t*-test	10-fold
Yang 2012 [41]	Open source	Recall, precision, f-measure	*t*-test	5-fold cross validation
Li 2012 [42]	Open source	f-measure, balance	Mann Whitney *U*-test	Random sampling validation
Canfora 2013 [43]	Proprietary	Precision, Recall	Wilcoxon	10-fold, inter-project
Harman 2014 [44]	Open source	G-mean, recall	Wilcoxon with Holm–Bonferroni correction	Inter-release

2. Related work

There are number of studies in literature that analyze relationship between OO metrics and fault proneness using a statistical technique, logistic regression (Basili et al. [10]; Binkley and Schach [11]; Briand et al. [12]; Briandet al. [13]; Cartwright and Shepperd [14]; Chidamber et al. [15]; Harrisonet al. [16]; El Emam et al. [17]; Li and Henry [18]; Yu et al. [19]; Aggarwal et al. [20]; Li and Shatnawi [21]; Olague et al. [22]; Aggarwal et al. [23]).

There are various studies that analyze the relationship between OO metrics and defect proneness that evaluate ML techniques. Briand et al. [24] validated Multivariate Adaptive Regression Splines (MARS) technique for the construction of defect proneness models and concluded that models developed using MARS technique outperformed logistic regression (LR) technique. Gyimothy et al. [25] used Mozilla data set to validate the results to evaluate the relationship of Chidamber & Kemerer (CK) metrics [26] with defect prediction using LR and ML techniques (decision tree and neural network). The results indicated number of children (NOC) as an insignificant metric for predicting defects and showed low accuracy of models developed using ML techniques. Zhou and Leung [27] validated the results using NASA data set KC1 (written in C++ language) with respect to two severity levels of defects—high and low. They employed statistical technique (LR) and three ML techniques (Naïve Bayes, Random Forest and NNge) to evaluate the effectiveness of CK metrics for defect prediction with regard to the high and low defect severity levels. The results showed that the defect prediction models developed at high severity level of defects had less prediction accuracy. The values of performance measures for defect prediction models were low with regard to ML techniques. Singh et al. [1] validated the results on the same NASA data set KC1 with three severity levels of defects—high, medium and low. They used logistic regression, decision tree and artificial neural network techniques and used ROC analysis to evaluate and assess the performance of developed defect prediction models. The results of this study depicted better performance as compared to the results obtained by Malhotra and Singh [28], particularly with regard to the models developed at high severity level of defects. The performance of the models developed using the chosen ML techniques were also high. In another study by Kanmani et al. [29], the Support Vector Machines (SVM) technique was evaluated using the public domain NASA KC1 data set at various severity levels of defects.

Pai and Dugan [30] evaluated an approach that was based on neural networks and the results were based on the software system written in the Java programming language. The study illustrated that the performance of models developed using neural networks was high as compared to the models developed using the statistical technique. Catal et al. [31] assessed the Bayesian approach and the results were validated using the NASA KC1 data set. The results showed that the models developed using the Bayesian techniques were comparable to the existing techniques for defect prediction. In another study conducted by Arisholm et al. [32], Artificial Immune Recognition System was evaluated using NASA KC1 data set. Carvalho et al. [33] used Java Telecom system for comparing various variations of decision tree techniques. In addition to the decision tree technique (C4.5), they also evaluated neural networks, SVM and LR techniques and concluded that the model developed using the C4.5 technique showed high accuracy. The predictive ability of MultiObjective Particle Swarm Optimization technique and SVM technique (using Jedit software) were evaluated by Carvalho et al. [33] and Singh et al. [34], respectively. Zhou et al. [35] proposed the usefulness of odds ratio in predicting defective classes using CK and complexity measures. Martino et al. [36] developed model using SVM technique and the model was configured using Genetic algorithm for prediction of defective classes with regard to OO metrics. Okutan et al. [37] assessed the relationship between CK metrics and defect proneness using the Bayesian approaches. Azar and Vybihal [38] developed defect prediction models using Ant Colony Optimization (ACO) technique and concluded these models were better than decision tree (C4.5) and random guessing techniques. Studies by Malhotra and Singh [39] and Malhotra and Jain [40] developed defect prediction models on open-source data sets using 10-fold cross validation. However, Yang et al. [41] used five-fold cross validation technique for developing defect prediction models. Canfora et al. [43] developed defect prediction models using both 10-fold and inter-project results. Harman et al. [44] developed temporal defect prediction models using eight releases of open-source Hadoop software.

Table 1 provides the information about the use of data set type (Academic, proprietary or open-source), statistical test, performance measures and the type of validation in the literature. It

Please cite this article in press as: R. Malhotra, An empirical framework for defect prediction using machine learning techniques with Android software, Appl. Soft Comput. J. (2016), http://dx.doi.org/10.1016/j.asoc.2016.04.032

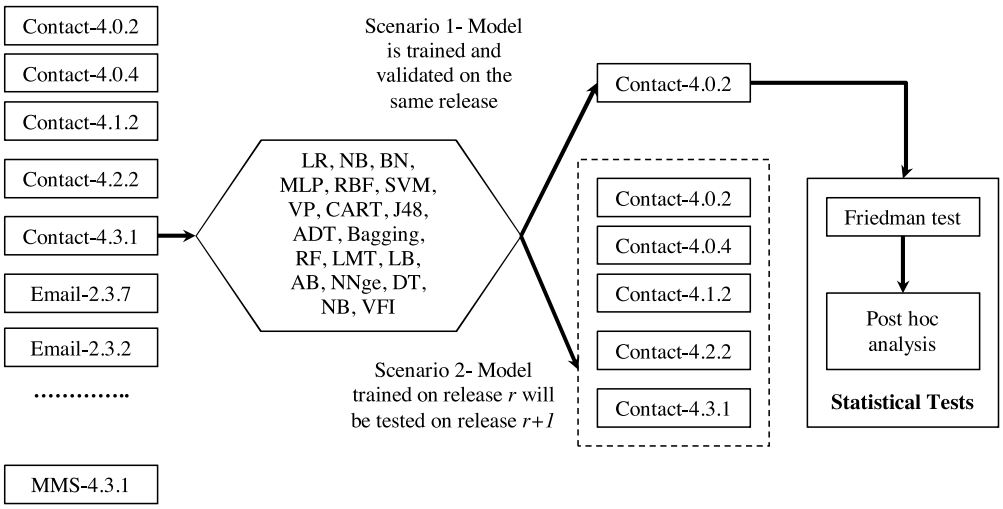

Fig. 1. Framework for defect prediction—an example using Contact.

can be seen from the table that out of 21 studies only 5 studies use inter-release validation. Though two studies in literature use *t*-test, it is not effective, as it requires a lot of pre-assumptions about the underlying data such as the data should follow normal distribution etc. Thus, the parametric nature of the test limits its applicability as it has very stringent assumptions. However, a commonly used test in literature is Wilcoxon test for ascertaining the differences amongst the performance of different techniques, but the use of Wilcoxon test without Bonferroni correction is not advisable, as it does not take into account family-wise error. The use of a *p*-value in multiple comparisons only signifies the probability of an error of a certain comparison but ignores the remaining comparisons which belong to the same family. It is important to adjust the *p*-value otherwise the probability of committing Type I error is quite high. Demšar recommends the use of Nemenyi test as a post-hoc test for comparing the pairwise differences amongst the performance of different techniques [45] as it reduces family-wise error. It is also advocated by Lessmann et al. [3].

Although, the above studies use ML techniques to evaluate the relationship between OO metrics and defect prediction, however there are no studies to the best of the author's knowledge that extensively compares the ML techniques to evaluate the relationship between OO metrics and defect prediction. In this study we not only compare and assess the effectiveness of the 18 ML techniques for defect prediction, we also use appropriate statistical tests to evaluate the statistical significant differences amongst the ML techniques. We also perform inter-release validation on various releases of seven application packages of Android software. Hence, we provide a completely generalizable framework and repeatable results in this study.

3. Empirical research framework

This section presents the empirical research framework followed in this work in order to conduct the extensive comparison and assessment of ML techniques. Fig. 1 presents the framework for development of defect prediction models for application package 'contact' of Android software. The figure depicts that various releases of application packages of Android software are analyzed using 18 ML techniques. It also shows that two types of validations (scenario 1 and 2) are carried out. In scenario 1, each version of contact is used and the predicted model is trained and validated on the same release of the software. In scenario 2, the model is trained on release *r* and validated on the subsequent release *r*+1. For example, model is trained using Contact-4.0.2 and validated on Contact-4.0.4. Similarly, model is trained using Contact-4.0.4 and validated on Contact-4.1.2. The procedure is repeated over all the releases of seven application packages of Android software.

The subsequent sub sections describe the procedure of data collection and independent and dependent variables used in this study.

3.1. Data collection procedure

Smartphones have revolutionized the modern day scenario as they can easily perform a number of tasks with increase in there computing and communication facilities [47]. Recent studies like Espada et al. [48], focus on improving user experience for smartphones. In this study, the empirical results are computed using various application packages of widely used Android operating system, which is popularly used in smartphones. The Android OS has six releases with three code names namely—Ginger Bread (2.3.2 and 2.3.7), Ice Cream Sandwich (4.0.2 and 4.0.4) and JellyBean (4.1.2, 4.2.2 and 4.3.1). The data has been collected using seven application packages of Android operating system namely—Contact, MMS, Bluetooth, Email, Calendar, Gallery2 and Telephony. The source code of various releases of these application packages has been obtained from Google's Git repository (https://android.googlesource.com). The characteristics of the seven application packages over various releases are given in Table 2.

Fig. 2 shows the procedure for data collection in this study. The open source repositories are used to extract the source code with OO metrics using Chidamber and Kemerer Java Metrics (CKJM) tool. The defects are collected from open sources bug repository, GIT. Defect Collection and Reporting System (DCRS) tool developed at the Delhi Technological University [49] in the Java language is used for collection of the defects. After following the procedure described below, finally the data is collected for each application package of Android operating system over various releases.

Table 2 presents the total classes, LOC, number of defects and percentage of defective classes in each release of the seven application packages of Android software. The steps stated below are followed to collect the defects from the open source software defect logs [9,49]:

(1) *Step 1: obtain change logs*: The DCRS obtains change logs from Git repository of two predetermined consecutive releases. The change may occur due to defect occurrence, improvement in

Please cite this article in press as: R. Malhotra, An empirical framework for defect prediction using machine learning techniques with Android software, Appl. Soft Comput. J. (2016), http://dx.doi.org/10.1016/j.asoc.2016.04.032

Table 2
Summary of various releases of Android software over application packages.

Data set name	Version	Total classes	Total LOC	Defective #	Defective %
Gallery2	4.0.2	305	18,853	24	7.86
	4.0.4	310	19,290	69	22.25
	4.1.2	330	20,446	170	51.51
	4.2.2	374	28,223	93	24.86
	4.3.1	647	50,168	130	20.09
Contact	2.3.7	85	7788	29	34.11
	4.0.2	325	22,722	19	5.84
	4.0.4	331	22,834	107	32.32
	4.1.2	357	24,644	35	9.80
	4.2.2	375	25,860	14	3.73
	4.3.1	210	14,807	98	46.66
Email	2.3.2	385	25,760	21	5.45
	2.3.7	394	26,839	41	10.41
	4.0.2	469	33,730	17	3.62
	4.0.4	624	43,147	274	43.91
	4.1.2	475	34,255	61	12.84
	4.2.2	472	34,025	7	1.48
	4.3.1	472	34,037	77	16.31
MMS	2.3.7	195	13,157	54	27.69
	4.0.2	201	13,538	11	5.47
	4.0.4	206	13,804	68	33.01
	4.1.2	223	14,759	42	18.83
	4.2.2	225	14,932	12	5.33
	4.3.1	224	14,915	23	10.27
Calendar	4.0.2	77	8042	22	28.57
	4.0.4	78	8216	45	57.69
	4.1.2	86	9285	12	13.95
	4.2.2	88	9465	41	46.59
Bluetooth	4.1.2	39	2517	15	38.46
	4.2.2	63	6246	10	15.87
	4.3.1	72	7550	13	18.05
Telephony	4.2.2	249	30,325	137	55.02
	4.3.1	224	28,331	154	68.75

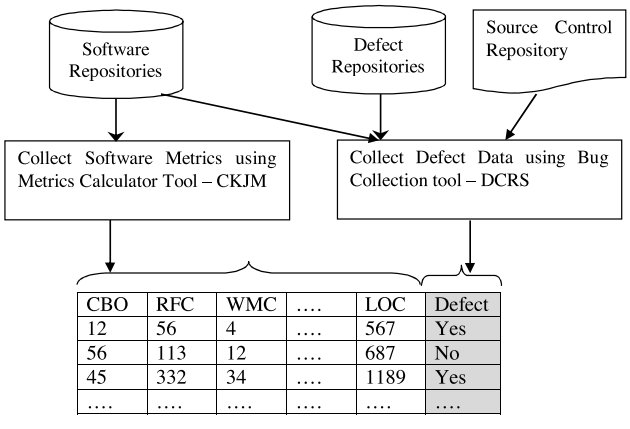

Fig. 2. The procedure for defect data collection.

quality of the software, or new functionality add-on. A single change record represents a change. A change record includes unique identifier, timestamp of committing, description of change (optional), and a list of modified lines of source code. The change logs of the available releases (Android 2.3.2, Android 2.3.7, Android 4.0.2, Android 4.0.4, Android 4.1.2, Android 4.1.2, Android 4.2.2 and Android 4.3.1) of seven application packages of Android software were obtained from the repository. The releases that did not have any change or were not available are not included in this analysis.

(2) *Step 2: process the changes related to defects*: The relevant information is extracted by preprocessing of changes related to fixed defects. The change log consists of information related to defects from the beginning (i.e., the first release of the software). Hence, preprocessing is required as in this study defects that are encountered from the immediate previous release to the subsequent release are only considered. For example, the defects between Contact 2.3.7 and 4.0.2 were taken into account; the defects between Contact 4.0.2 and 4.0.4 were taken into account and so on. The records of defects are retrieved by searching defect-Ids and if defect-Ids are not found to be present then keywords "issue"; "fault"; "bug" or "defect" are searched in the given description of the change.

(3) *Step 3: calculating OO metrics with respect to each Java file*: The open source CKJM tool (http://gromit.iiar.pwr.wroc.pl/p_inf/ckjm/metric.html) is used for computing the values of OO metrics (indicated in Section 3.2). The Java source code files are only considered in this step and all the other types of files are ignored. The OO metrics were calculated for each of the Java class with respect to each release of the specified package.

(4) *Step 4: associating or linking defects to the Java classes*: The collected defects in step 2 are finally linked to the Java classes in the source code. Hence, each class found in step 3 is related to defect count corresponding to that class. The classes in each release of the application package of the Android software are related with the defects fixed from the current release that is being considered to the immediate successive release (i.e., defects obtained from current release to next succeeding release).

3.2. Variables

The independent variables (used in this study) are the OO metrics. The metrics used in this project, are the ones, which are most commonly used by various researchers, to account for software

Please cite this article in press as: R. Malhotra, An empirical framework for defect prediction using machine learning techniques with Android software, Appl. Soft Comput. J. (2016), http://dx.doi.org/10.1016/j.asoc.2016.04.032

characteristics such as size, coupling, cohesion and inheritance. In addition to the metrics proposed by Chidamber and Kemerer [26] we also used the metrics proposed by Henderson-Sellers [50] and Bansiya and Davis [51]. The dependent variable of the study is defect proneness, which is defined as probability of occurrence of defect in a class [1]. The OO metrics used in this work are summarized below:

Chidamber & Kemerer metrics [26]:

- Coupling between objects (CBO): counts number of other classes to which a class is coupled with.
- Response for a class (RFC): counts number of external and internal classes.
- Lack of cohesion in methods (LCOM): measures dissimilarity of methods in a class.
- Number of children (NOC): counts number of descendants of a class.
- Depth of inheritance (DIT): measures number of ancestor classes.
- Weighted methods per class (WMC): counts number of methods in a class weighted by complexity.

Henderson-Sellers metric [50]:

- Lack of cohesion in methods (LCOM3): $\text{LCOM3} = \frac{\frac{1}{N}\sum_{i=1}^{n}\mu(D_i)-m}{1-m}$.

Martin's metrics [52]:

- Afferent couplings (Ca): counts how many other classes use a given class.
- Efferent Couplings (Ce): counts the number of classes, a class is dependent upon.

QMOOD metrics suite (Bansiya and Davis [51])

- Number of public methods (NPM): counts the number of public methods in a class.
- Data Access Metric (DAM): defined as the number of private methods divided by the total number of methods.
- Measure of Aggregation (MOA): counts the number of abstract data types in a class.
- Measure of Functional Abstraction (MFA): defined as the number of inherited methods divided by total number of methods accessible by its member functions.
- Cohesion Among Methods of Class (CAM): based upon the parameters in a method.

Tang et al. metrics [53]:

- Inheritance Coupling (IC): it is based upon inheritance-based coupling.
- Coupling Between Methods (CBM): counts the newly added functions with which inherited based methods are coupled.
- Average Method Complexity (AMC): counts average size of method in a class.

LOC: it counts the number of lines of source code.

4. Experimental setup

In order to answer the research questions formed in this work the following steps must be conducted in an empirical framework:

1. Selection of feature section technique as described in Section 4.1.
2. Selection of appropriate data analysis techniques.
3. Selection of performance measures that can deal with imbalanced data sets for evaluating the predictive capability of data analysis techniques selected at step 2 (refer Section 4.3).
4. Use of efficient validation methods to determine the true applicability of the models predicted.
5. Selection of appropriate statistical tests to determine the superiority of one ML technique over the other ML techniques.

After the above steps have been conducted, an empirical methodology is followed that includes (i) feature sub selection (ii) model training (iii) model validation (iv) model evaluation and (v) statistical evaluation of predicted models.

In the subsequent sections, we describe the feature selection method, ML techniques, performance measures, validation methods and statistical tests used to carry out the empirical study.

4.1. Feature selection method

In this work, 18 OO metrics have been used for defect prediction. It is essential to select relevant and important attributes out of these OO metrics so that only uncorrelated and relevant OO metrics are included in the construction of defect prediction models. In order to achieve this aim, we used Correlation based Feature Selection (CFS) method for feature selection. The CFS method is simple, fast and is widely used with ML techniques for selecting features [54]. In this method a subset of attributes is selected by searching the best combination of attributes [54]. The CFS method is a supervised technique that is based on the evaluation of correlation between independent variables and the dependent variable. The method follows the principle for selecting the independent variables that are highly correlated with the dependent variable and uncorrelated with each other [54]. Thus, in this case OO metrics that are highly correlated with defect prediction are selected and the OO metrics that are highly correlated with each other are avoided. Hence the CFS method removes irrelevant and redundant OO metrics.

4.2. ML techniques

We have carefully selected the ML techniques from each of the categories as shown in Table 3.

4.3. Performance measures

In order to evaluate the learning process, various performance measures need to be analyzed which indicate the effectiveness of the developed defect prediction models. These performance measures include specificity, sensitivity, and Area Under the Receiver Operating Characteristics (ROC) Curve amongst others. A high value for these performance measures denotes a good prediction model.

Sensitivity: It is defined as the ratio of correctly predicted defect-prone classes to the total number of classes.

Specificity: It is defined as the ratio of correctly predicted non defect-prone classes to the total number of classes.

The data having disproportionate ratio of defective and not defective classes is often known as imbalanced data. Given the imbalanced nature of the data sets, the ROC analysis is a commonly used performance measure [7,55]. The ROC analysis is one of the most popular techniques used to determine the accurateness of the prediction model. It determines how well the model has worked on the validation data [55]. It is a plot of sensitivity and '1-specificity' at various cutoff points. Here, sensitivity is plotted on *y*-axis and '1-specificity' is plotted on *x*-axis. In ROC analysis, the optimal cutoff

Please cite this article in press as: R. Malhotra, An empirical framework for defect prediction using machine learning techniques with Android software, Appl. Soft Comput. J. (2016), http://dx.doi.org/10.1016/j.asoc.2016.04.032

Table 3
Description of ML techniques used in the study.

Machine learning technique		Description
Statistical classifier		
LR	Logistic regression	LR uses statistical method to estimate the response. NB assumes interdependence of various attributes and uses Bayes theorem. BN uses conditional probability with K2 as a search technique.
NB	NaiveBayes	
BN	Bayesian networks	
Neural networks		
MLP	Multilayer perceptron	MLP uses two separate passes i.e. backward and forward which is formally known as the back propagation method for learning. A learning rate of 0.3 with 500 epochs was used. RBF uses Gaussian radial basis function which is normalized.
RBF	Radial basis function	
Support Vector Machines based		
SVM	Support Vector Machines	These techniques use the concept of a hyperplane to distinguish the data set into defective and not defective instances. In case of a nonlinear region, a kernel function is used appropriate mapping. Both SVM and VP techniques use a polynomial kernel function.
VP	Voted perceptron	
Decision tree methods		
CART	Classification & regression trees	These techniques involve successful construction of trees where attributes that are most efficient at classifying the defective classes are chosen at each node, based on the splitting criteria. C4.5 uses entropy and information gain, while CART uses Gini Index for splitting criteria.
J48	C4.5 based technique	
ADT	Alternating decision trees	
Ensemble learning		
Bag	Bagging	These techniques are meta learning in nature and use voting in order to effectively classify a class as defect or not defective. The CART technique is used by RF and the LR technique is used by LMT as base learners. Both LB and AB techniques use decision stump i.e. one level decision tree algorithm as boosting algorithms. LB is said to perform additive logistic regression.
RF	Random forest	
LMT	Logistic model trees	
LB	Logit boost	
AB	Ada boost	
Rule based learning		
NNge	Nearest neighbour with generalised exemplars	NNge is a nearest-neighbor technique that formulates if-then rules. DTNB is hybrid in nature as it incorporates the strengths of DT as well as NB techniques for all the attributes at each step.
DTNB	Decision table Naïve Bayes	
Miscellaneous		
VFI	Voting feature intervals	This technique establishes intervals specific to each attribute for classifying each class.

point is chosen that maximizes the values of both sensitivity and specificity measures.

AUC computed using ROC analysis is used to determine the accuracy of the predicted model. Carvalho et al. [33] advocated AUC to be the relevant criterion for dealing with unbalanced and noisy data as AUC is insensitive to the changes in distribution of class. He and Garcia [56] have recommended the use of AUC for dealing the issues of imbalanced data as with regard to class distributions, it provides a visual representation of the relative trade-offs between the advantages (represented by true positives) and costs (represented by false positives) of classification. Thus, in order to determine the performance of the ML techniques we used AUC measure derived using ROC analysis.

4.4. Validation methods

In any empirical study it is essential to obtain unbiased and generalizable results that can be applied to future releases and unseen similar-natured projects. Thus, it is important to validate the models predicted on different data set from which they are trained. In this study we used two validation methods—10-fold cross validation and inter-release validation. In 10-fold cross validation, the data is divided into 10 folds where each time nine parts are used for training purpose and one part is used for validation purpose. This procedure is repeated 10 times and the results from each fold are combined to produce the model validation results [57].

In inter-release validation, the model is trained using a specific release and validated on its immediate release. Thus, we used each release of application packages of Android software and constructed models and validated these models on the subsequent releases. For example, MMS-2.3.7 release was used to train the model using ML techniques and the developed model is henceforth validated on MMS-4.0.2 release.

4.5. Statistical tests

In order to statistically analyze the results, we use Friedman test, which is followed by post-hoc Nemenyi test. Both the tests are non-parametric in nature and are advocated by Demšar [45] and Lessmann et al. [3] to compare the effectiveness of various techniques. The tests used do not require the underlying data to follow normal distribution.

The Friedman [58] test allocates mean ranks to all the techniques based on their performance, which is evaluated using the AUC measure. It is used to ascertain whether the performance of different techniques differs significantly when compared with each other or not. The technique achieving the lowest rank is termed as the best performing technique. The Friedman test statistic has $n-1$ degrees of freedom and is based on chi-square distribution, where n is the total number of compared techniques. The Friedman statistic is calculated on the basis of the given formula, where k corresponds to the number of data sets, R_i is the rank allocated to the ith technique by the Friedman test.

$$\chi 2 = \frac{12}{nk(k+1)} \sum_{i=1}^{k} {R_i}^2 - 3n(k+1)$$

If Friedman test yields significant results, we perform post-hoc Nemenyi test to compare pairwise differences amongst the performance of various techniques, based on AUC performance measure. The Nemenyi test involves computation of a critical distance, which is then compared with the difference between mean ranks allocated to the two techniques using Friedman test. In case, the difference amongst mean ranks of the two compared ranks is greater than or equal to computed the critical distance, we conclude that the performance of the compared techniques differs significantly at the chosen significance level (α). The critical distance for the Nemenyi test is based on the following formula.

$$\text{Critical Distance} = q_\alpha \sqrt{\frac{n(n+1)}{6k}}$$

Here n corresponds to the number of compared techniques, k corresponds to the number of data sets on which the comparison is based and q_α is the studentized range statistic divided by $\sqrt{2}$. The study also evaluates whether there is any significant difference between the results obtained using 10-fold validation and inter-release val-

Please cite this article in press as: R. Malhotra, An empirical framework for defect prediction using machine learning techniques with Android software, Appl. Soft Comput. J. (2016), http://dx.doi.org/10.1016/j.asoc.2016.04.032

idation using Wilcoxon test. The test evaluates the significance by computing the difference amongst the results of the two validation techniques and then ranking them on the basis of their absolute values.

5. Experimental results

This section presents the results of comparison of ML techniques using OO metrics for defect prediction. The reliability of the results is assessed using the Friedman Test followed by post-hoc analysis using Nemenyi test as described in Section 4.5. The first step is data preprocessing that includes summarizing the descriptive statistics of the data sets and reducing the number of OO metrics by applying CFS method (refer Section 4.1). The effectiveness of predicted models is analyzed using 10-fold validation and inter-release validation.

5.1. Data preprocessing results

The number of OO metrics were reduced by applying the CFS method. Table 4 presents the relevant OO metrics selected after applying CFS method over all the releases of seven application packages of Android software. It can be seen that LOC, CAM, WMC, Ce and LCOM3 are commonly found relevant metrics related to defect proneness of classes in most of the releases of seven application packages of Android software.

Table 4
Metrics selected across Data sets using CFS Method.

Data set name	Release	OO metrics selected
Gallery2	4.0.2	Ce, LCOM3, LOC, MOA, CAM
	4.0.4	WMC, Ce, NPM, LOC, CAM
	4.1.2	WMC, CBO, RFC, Ce, LOC, AMC
	4.2.2	NPM, LOC, CAM
	4.3.1	Ce, NPM, LOC, MOA, CAM
Contact	2.3.7	DIT, NPM
	4.0.2	WMC, RFC, Ce, LOC, CAM
	4.0.4	Ce, LOC, DAM, CAM
	4.1.2	WMC, CBO, Ce, NPM, LOC, CAM
	4.2.2	LOC
	4.3.1	WMC, DIT, CBO, NPM, LCOM3, LOC, MOA, AMC
Email	2.3.2	NPM, LCOM3, LOC, DAM, CAM
	2.3.7	DIT, LOC, CAM
	4.0.2	CAM
	4.0.4	CAM
	4.1.2	DIT, LCOM3, DAM, CAM
	4.2.2	WMC
	4.3.1	CAM
MMS	2.3.7	Ce, LCOM3, LOC, DAM, MOA, CAM, AMC
	4.0.2	WMC, RFC, LCOM, LCOM3, DAM
	4.0.4	Ce, NPM, LCOM3, LOC, DAM, CAM
	4.1.2	Ce, CAM
	4.2.2	DAM
	4.3.1	Ce, LOC, DAM, MOA
Calendar	4.0.2	WMC, CAM
	4.0.4	WMC, DIT, RFC, LOC, MOA, CAM
	4.1.2	WMC, DIT, RFC, LOC, MOA, CAM
	4.2.2	WMC, RFC, Ce, CAM
Bluetooth	4.1.2	CBO, Ce
	4.2.2	LOC, CAM
	4.3.1	WMC, LOC, CAM
Telephony	4.2.2	WMC, CBO, LCOM3, LOC, MFA
	4.3.1	CBO, LCOM3, LOC, MFA,CAM

5.2. RQ1—what is the overall predictive capability of various ML techniques on seven application packages of Android software using 10-fold validation?

After applying CFS method, the models are predicted using 18 ML techniques and the predicted models are validated using 10-fold validation. We used ROC analysis to obtain the balance between sensitivity and specificity over multiple cutoff points. The value of sensitivity (sen.) and specificity (sp.) over appropriate cutoff point is shown in Tables 5–11 . The results are presented over various releases for each application package of Android data set viz. Contact, MMS, Bluetooth, Email, Calendar, Gallery2 and Telephony.

The performance of the defect prediction models is evaluated using AUC obtained using ROC analysis as shown in Table 12a and b. The AUC of most of the models predicted using the ML techniques is 0.7, which highlights the predictive capability of the ML techniques. The last column depicts the average AUC over all the releases of each application package of the Android software. The ML technique yielding the best AUC for a given release is depicted in bold. The results show that the model predicted using the NB, AB, RBF, Bag, ADT, MLP, LB and RF techniques have AUC greater than 0.7 corresponding to most of the releases of the application packages of Android software. Fig. 3 depicts the average AUC values of each ML technique on all the seven corresponding data sets.

From Fig. 3, it can be clearly seen that NB, LR, MLP, LB and Bagging techniques show the highest performance. The average AUC of NB

Table 5
Sensitivity and specificity values of Gallery2 data set.

Dataset	Gallery2-4.0.2		Gallery2-4.0.4		Gallery2-4.1.2		Gallery2-4.2.2		Gallery2-4.3.1	
Tech.	Sen.	Sp.	Sen.	Sp.	Sen.	Sp.	Sen.	Sp.	Sen.	Sp.
LR	70.8	72.1	71.0	70.5	68.2	67.5	60.2	57.2	61.5	64.2
NB	75.0	74.0	68.1	67.2	60.5	60.0	53.7	57.2	59.2	59.7
BN	66.7	68.7	72.5	72.6	70.6	70.6	54.8	50.2	66.2	63.4
MLP	70.8	69.8	69.6	70.1	66.5	68.7	59.1	61.2	60.7	62.2
RBF	75.0	75.0	71.0	71.0	65.8	69.3	55.9	59.7	62.3	59.3
SVM	100.0	0.0	1.4	99.6	59.4	63.7	0.0	100.0	0.0	100.0
VP	100.0	0.0	2.9	99.2	81.7	40.6	0.0	100.0	0.0	100.0
CART	50.0	39.5	63.8	55.2	69.4	70.6	51.6	54.1	0.0	100.0
J48	37.5	57.3	59.4	61.4	67.6	70.0	55.9	45.1	64.6	41.3
ADT	54.2	53.7	68.1	69.3	70.5	71.2	52.6	52.3	63.0	65.3
Bag	62.5	61.9	72.5	72.6	74.1	71.2	58.0	59.4	63.8	63.0
RF	70.8	69.8	72.5	72.2	71.7	75.6	60.2	61.9	72.3	59.3
LMT	66.7	65.8	73.9	73.9	68.2	68.7	61.2	59.4	64.6	62.2
LB	66.7	68.0	71.0	70.5	75.8	72.5	56.9	56.2	64.6	64.4
AB	62.5	63.7	68.	69.7	71.1	71.8	59.1	52.6	63.0	60.3
Nnge	16.7	95.7	46.4	90.0	66.4	63.1	35.4	79.7	36.9	87.2
DTNB	37.5	57.7	73.9	73.0	69.4	70.6	53.8	58.7	74.6	31.9
VFI	58.3	64.1	73.9	32.0	55.3	63.7	76.3	25.9	67.6	53.7

Please cite this article in press as: R. Malhotra, An empirical framework for defect prediction using machine learning techniques with Android software, Appl. Soft Comput. J. (2016), http://dx.doi.org/10.1016/j.asoc.2016.04.032

Table 6
Sensitivity and specificity values of Contact data set using 10-fold validation.

Dataset	Contact-2.3.7		Contact-4.0.2		Contact-4.0.4		Contact-4.1.2		Contact-4.2.2		Contact-4.3.1	
Tech.	Sen.	Sp.	Sen.	Sp.	Sen.	Sp.	Sen.	Sp.	Sen.	Sp.	Sen.	Sp.
LR	48.2	47.2	73.6	76.0	70.1	72.3	71.4	70.2	64.3	62.3	70.4	67.9
NB	51.7	50.9	73.6	71.4	72.9	69.6	74.3	73.0	57.1	60.7	68.4	66.1
BN	48.2	45.4	73.6	70.1	69.2	72.3	65.7	66.1	35.7	45.2	70.4	67.9
MLP	58.6	56.3	68.4	71.8	69.2	70.1	65.7	68.3	64.3	62.0	72.4	70.5
RBF	62.1	61.8	68.4	70.8	71.0	72.8	71.4	68.0	64.3	64.0	66.3	67.0
SVM	100.0	0.0	0.0	100.0	20.6	97.8	0.0	100.0	0.0	100.0	51.0	85.7
VP	6.8	89.1	0.0	100.0	45.8	62.5	0.0	100.0	0.0	100.0	96.9	24.1
CART	37.9	60.0	89.4	17.7	59.8	63.8	28.6	68.3	42.9	39.9	66.3	69.6
J48	37.9	60.0	89.4	15.7	59.8	66.1	34.3	59.6	42.9	39.9	71.4	71.4
ADT	65.5	60.0	73.6	76.3	69.2	70.1	57.1	57.1	64.3	62.6	70.4	70.5
Bag	58.6	63.6	68.4	66.8	70.1	71.9	65.7	64.3	50.0	66.5	74.5	70.5
RF	62.1	63.6	78.9	79.0	65.4	71.9	60.0	64.0	28.6	87.3	66.3	74.1
LMT	48.2	50.9	63.1	62.9	69.2	66.5	68.6	72.4	64.3	62.9	70.4	67.9
LB	65.5	61.8	73.6	74.4	70.1	73.2	68.6	68.0	57.1	59.6	68.4	69.6
AB	55.1	63.6	73.6	76.7	67.3	66.5	68.6	66.8	57.1	57.6	64.3	66.1
Nnge	48.2	65.4	36.8	95.7	57.9	77.2	8.6	94.4	0.0	94.5	67.3	69.6
DTNB	37.9	60.0	52.6	69.1	70.1	73.2	60.0	53.7	42.9	39.9	68.4	70.5
VFI	51.7	60.0	68.4	60.3	68.2	67.0	77.1	62.1	57.1	57.9	60.2	60.7

Table 7
Sensitivity and specificity values of MMS data set.

Dataset	MMS-2.3.7		MMS-4.0.2		MMS-4.0.4		MMS-4.1.2		MMS-4.2.2		MMS-4.3.1	
Tech.	Sen.	Sp.	Sen.	Sp.	Sen.	Sp.	Sen.	Sp.	Sen.	Sp.	Sen.	Sp.
LR	68.5	64.5	63.6	58.9	75.0	79.0	69.0	72.4	50.0	54.0	60.9	63.7
NB	74.1	70.9	63.6	64.2	77.9	76.8	69.0	68.0	58.3	51.6	73.9	70.6
BN	68.5	66.0	81.8	10.0	76.5	73.2	61.9	70.2	25.0	69.0	60.9	40.3
MLP	66.7	63.8	63.6	66.8	73.5	74.6	69.0	70.7	58.3	53.5	65.2	63.7
RBF	63.0	64.5	63.6	63.7	73.5	70.3	66.7	69.1	66.7	68.1	60.9	59.7
SVM	5.6	99.3	0.0	100	66.2	86.2	0.0	100.0	0.0	100.0	0.0	100.0
VP	59.3	53.2	27.3	90.5	92.6	39.1	14.3	97.8	0.0	100.0	0.0	100.0
CART	72.2	73.0	75.0	14.3	70.6	66.7	69.0	66.9	66.7	19.7	60.9	29.9
J48	59.3	61.7	45.5	49.5	72.1	69.6	57.1	66.3	66.7	19.7	47.8	45.8
ADT	70.4	68.8	63.6	67.4	76.5	78.3	64.3	64.6	50.0	54.0	60.9	64.7
Bag	72.2	69.5	72.7	61.1	73.5	73.9	66.7	66.3	66.7	59.2	65.2	66.2
RF	70.4	66.7	45.5	78.9	70.6	74.6	61.9	59.7	58.3	59.2	73.9	67.7
LMT	74.1	70.9	72.7	51.1	76.5	78.3	66.7	67.4	50.0	54.0	69.6	71.1
LB	72.2	71.6	72.7	75.8	75.0	74.6	59.5	68.0	58.3	59.6	60.9	62.2
AB	68.5	69.5	63.6	63.7	67.6	71.0	64.3	63.0	58.3	62.0	60.9	60.7
Nnge	51.9	85.8	9.1	97.4	66.2	83.3	42.9	89.5	41.7	87.8	8.7	93.5
DTNB	66.7	70.2	45.5	50.0	75.0	77.5	61.9	66.9	66.7	19.7	65.2	56.2
VFI	63.0	68.1	72.7	65.8	64.7	65.2	54.8	62.4	66.7	69.5	65.2	66.7

Table 8
Sensitivity and specificity values of Email data set using 10-fold validation.

Dataset	Email-2.3.2		Email-2.3.7		Email-4.0.2		Email-4.0.4		Email-4.1.2		Email-4.2.2		Email-4.3.1	
Tech.	Sen.	Sp.	Sen.	Sp.	Sen.	Sp.	Sen.	Sp.	Sen.	Sp.	Sen.	Sp.	Sen.	Sp.
LR	76.2	79.9	68.3	67.4	88.2	85.0	54.0	57.4	70.5	69.1	57.1	66.9	59.1	62.6
NB	81.0	81.0	73.2	72.0	82.4	85.6	56.6	54.3	68.9	66.4	57.1	61.9	58.3	60.9
BN	81.0	83.2	68.3	70.5	82.4	84.7	55.5	44.9	67.2	66.7	0.0	69.7	55.1	54.8
MLP	76.2	78.3	70.7	71.1	88.2	84.5	52.2	55.1	67.2	71.0	71.4	68.0	58.3	61.7
RBF	71.4	75.0	70.7	69.1	82.4	86.1	54.0	55.7	68.9	69.1	57.1	55.5	58.3	61.4
SVM	0.0	100.0	0.0	100.0	0.0	100.0	0.0	100.0	0.0	100.0	0.0	100.0	0.0	100.0
VP	0.0	100.0	0.0	100.0	0.0	100.0	4.7	94.6	0.0	100.0	0.0	100.0	0.0	100.0
CART	85.7	9.9	29.3	69.4	17.6	69.7	49.3	56.9	83.6	16.7	0.0	77.8	56.7	44.6
J48	66.7	64.3	29.3	69.4	17.6	69.7	49.6	53.4	50.8	55.3	0.0	69.7	48.8	49.3
ADT	76.2	79.7	68.3	71.4	76.5	78.1	51.8	52.6	70.5	69.3	57.1	60.2	57.5	50.7
Bag	76.2	78.0	70.7	69.1	82.4	86.1	48.5	52.3	72.1	71.3	71.4	55.5	55.9	57.7
RF	71.4	79.9	65.9	64.9	29.4	87.6	49.6	46.3	62.3	76.1	28.6	82.2	52.0	55.7
LMT	76.2	77.2	56.1	57.8	88.2	82.1	55.8	52.9	65.6	66.4	71.4	69.5	56.7	59.4
LB	71.4	74.7	70.7	72.2	82.4	84.7	48.9	49.4	73.8	70.5	57.1	64.9	55.9	54.5
AB	81.0	78.8	68.3	71.1	82.4	84.7	48.2	53.1	65.6	68.4	57.1	45.4	58.3	55.1
NNge	9.5	97.3	12.2	89.8	0.0	96.2	41.6	56.9	31.1	91.1	28.6	97.8	30.7	78.0
DTNB	38.1	59.3	68.3	30.0	17.6	69.7	49.6	53.4	68.9	35.0	0.0	69.7	38.6	59.4
VFI	66.7	69.2	68.3	55.8	70.6	55.1	47.1	53.4	72.1	64.7	42.9	54.0	50.4	47.5

Please cite this article in press as: R. Malhotra, An empirical framework for defect prediction using machine learning techniques with Android software, Appl. Soft Comput. J. (2016), http://dx.doi.org/10.1016/j.asoc.2016.04.032

Table 9
Sensitivity and specificity values of Calendar data set using 10-fold validation.

Dataset	Calendar-4.0.2		Calendar-4.0.4		Calendar-4.1.2		Calendar-4.2.2	
Tech.	Sen.	Sp.	Sen.	Sp.	Sen.	Sp.	Sen.	Sp.
LR	63.6	67.3	75.6	78.8	66.7	73.0	68.3	66
NB	63.6	67.3	73.3	75.8	58.3	64.9	63.4	59.6
BN	59.1	58.2	64.4	63.6	33.3	60.8	53.7	51.1
MLP	63.6	67.3	75.6	72.7	58.3	62.2	68.3	66
RBF	72.7	70.9	64.4	66.7	75.0	78.4	63.4	61.7
SVM	4.5	100	88.9	36.4	0.0	100	34.1	87.2
VP	50.0	52.7	0.0	100.0	0.0	98.6	92.7	8.5
CART	54.5	52.7	73.3	66.7	50.0	47.3	58.5	59.6
J48	63.6	60	55.6	57.6	50.0	47.3	61	57.4
ADT	59.1	60	68.9	66.7	66.7	64.9	51.2	53.2
Bag	68.2	69.1	73.3	75.8	66.7	67.6	63.4	61.7
RF	63.6	61.8	71.1	72.7	66.7	63.5	53.7	61.7
LMT	63.6	65.5	73.3	75.8	75.0	78.4	63.4	59.6
LB	54.5	58.2	71.1	72.7	66.7	66.2	58.5	61.7
AB	54.5	60	66.7	66.7	66.7	70.3	68.3	66
NNge	54.5	81.8	73.3	60.6	33.3	95.9	58.5	59.6
DTNB	59.1	52.7	57.8	72.7	50.0	45.9	58.5	53.2
VFI	40.9	50.9	66.7	66.7	66.7	59.5	63.4	59.6

Table 10
Sensitivity and specificity values of Bluetooth data set using 10-fold validation.

Dataset	Bluetooth-4.1.2		Bluetooth-4.2.2		Bluetooth-4.3.1	
Tech.	Sen.	Sp.	Sen.	Sp.	Sen.	Sp.
LR	46.7	45.8	70.0	73.6	76.9	79.7
NB	53.3	54.2	70.0	71.7	76.9	79.7
BN	33.3	41.7	70.0	67.9	69.2	72.9
MLP	40.0	45.8	70.0	66.0	76.9	79.7
RBF	60.0	58.3	70.0	67.9	69.2	72.9
SVM	26.7	100.0	0.0	100.0	23.1	100
VP	66.7	58.3	10.0	90.6	46.2	55.9
CART	66.7	54.2	30.0	66.0	46.2	45.8
J48	46.7	41.7	30.0	64.2	53.8	54.2
ADT	53.3	50.0	60.0	62.3	61.5	64.4
Bag	46.7	54.2	70.0	64.2	69.2	69.5
RF	53.3	54.2	70.0	73.6	61.5	64.4
LMT	40.0	37.5	70.0	64.2	76.9	79.7
LB	53.3	50.0	70.0	64.2	69.2	72.9
AB	33.3	29.2	70.0	67.9	69.2	64.4
NNge	33.3	45.8	30.0	86.8	23.1	93.2
DTNB	53.3	54.2	20.0	77.4	69.2	74.6
VFI	46.7	50.0	80.0	71.7	61.5	62.7

Table 11
Sensitivity and specificity values of Telephony data set using 10-fold validation.

Dataset	Telephony-4.2.2		Telephony-4.3.1	
Tech.	Sen.	Sp.	Sen.	Sp.
LR	68.6	68.8	78.6	78.6
NB	70.1	67.9	75.3	75.7
BN	68.6	67.0	75.3	74.3
MLP	67.2	67.9	77.9	78.6
RBF	62.0	63.4	72.1	72.9
SVM	89.8	40.4	90.9	61.4
VP	0.0	100.0	0.0	100.0
CART	68.6	69.6	72.1	65.7
J48	68.6	68.8	77.3	75.7
ADT	70.1	67.0	74.0	78.6
Bag	65.7	65.2	77.3	77.1
RF	59.9	59.8	79.2	78.6
LMT	67.9	67.9	76.0	75.7
LB	73.0	72.3	76.0	75.7
AB	71.5	68.8	70.8	68.6
NNge	56.9	58.0	85.7	60.0
DTNB	68.6	68.8	72.1	72.9
VFI	69.3	62.5	79.2	74.3

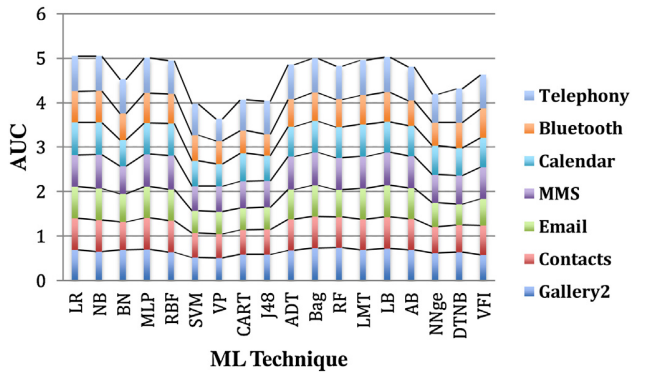

Fig. 3. Average AUC values of each ML technique on corresponding data sets using 10-fold validation.

technique with respect to Gallery2, Contact, Email, MMS, Calendar, Bluetooth and Telephony data sets is 0.65, 0.71, 0.71, 0.76, 0.73, 0.71 and 0.78, respectively. The average AUC of MLP technique is 0.70, 0.71, 0.70, 0.73, 0.70, 0.68 and 0.79 with respect to Gallery2, Contact, Email, MMS, Calendar, Bluetooth and Telephony data sets. Similarly, LB technique shows good values of average AUC over all the Android data sets (between 0.69 and 0.79).

Fig. 3 also depicts that defect prediction models constructed using VP technique over seven application packages of Android data sets showed the lowest performance. The results show that the average AUC of VP technique is around 0.5 for all the data sets that proves the poor or no predictive capability of VP technique. SVM and decision tree based techniques (CART and J48) follows VP technique.

5.3. RQ2—what is the performance of defect prediction models when inter-release validation is carried out?

The performance of defect prediction models was also evaluated using inter-release validation (refer Section 4.5). In order to do so, a model developed using a specific release was validated on its immediate subsequent release. The procedure for inter-release validation was performed for all the data sets. Table 15a and b present the results of inter-release validation in terms of AUC performance measure. As mentioned earlier that this measure has been recommended in literature for dealing with imbalanced data.

The tables show that the average AUC values for Gallery2 data set are in the range 0.50–0.65, with the MLP technique showing the best AUC value. Similarly, the Contact data set show average inter-release AUC values as 0.53–0.72, with NB, MLP, LMT and LR techniques showing the best AUC values for the data set. The inter-release AUC values for Email and MMS data sets are in the range 0.50–0.73 and 0.58–0.78, respectively. The NB and MLP techniques show the best inter-release results on Email data set and the Bagging technique on the MMS data set. An average inter-release AUC of 0.55–0.77 was obtained on Calendar data set with ADT and LMT showing the best results. The inter-release AUC results for Bluetooth and Telephony data sets were in the range 0.55–0.79 and 0.59–0.90 for Bluetooth and Telephony data sets respectively. The LMT technique was the best performing technique for Bluetooth data set and both the LMT and Bag techniques gave an AUC of 0.90 for telephony data set. It is observed from the tables that the models developed using NB, MLP, RBF, ADT, LMT, Bag, LB and AB techniques showed an AUC of 0.7 in most of the data sets. This reinforces the effective capability of ML techniques for developing defect prediction models.

Fig. 4 depicts the cumulative average AUC over all the ML techniques for all application packages of Android software. The figure

Please cite this article in press as: R. Malhotra, An empirical framework for defect prediction using machine learning techniques with Android software, Appl. Soft Comput. J. (2016), http://dx.doi.org/10.1016/j.asoc.2016.04.032

Table 12
AUC values of data sets using 10-fold validation.

(a)

Dataset	Gallery2						Contact							Email							
Tech.	4.0.2	4.0.4	4.1.2	4.2.2	4.3.1	Avg	2.3.7	4.0.2	4.0.4	4.1.2	4.2.2	4.3.1	Avg	2.3.2	2.3.7	4.0.2	4.0.4	4.1.2	4.2.2	4.3.1	Avg
LR	0.76	0.74	0.67	0.62	0.67	0.69	0.48	0.77	0.76	0.76	0.71	0.75	**0.71**	0.84	0.73	0.84	0.57	0.74	0.68	0.60	**0.71**
NB	0.78	0.71	0.56	0.58	0.64	0.65	0.56	0.77	0.74	0.76	0.66	0.75	**0.71**	0.83	0.79	0.84	0.57	0.72	0.65	0.60	**0.71**
BN	0.70	0.77	0.77	0.55	0.68	0.69	0.46	0.72	0.76	0.68	0.40	0.75	0.63	0.83	0.74	0.77	0.50	0.66	0.35	0.58	0.63
MLP	0.75	0.76	0.73	0.61	0.65	**0.70**	0.65	0.77	0.74	0.69	0.68	0.75	**0.71**	0.81	0.72	0.82	0.55	0.72	0.65	0.63	**0.70**
RBF	0.50	0.76	0.71	0.61	0.64	0.64	0.67	0.78	0.74	0.71	0.64	0.73	**0.71**	0.78	0.73	0.85	0.56	0.71	0.65	0.62	**0.70**
SVM	0.50	0.50	0.61	0.50	0.50	0.52	0.50	0.50	0.59	0.50	0.50	0.68	0.55	0.50	0.50	0.50	0.50	0.50	0.50	0.50	0.50
VP	0.45	0.51	0.61	0.50	0.50	0.51	0.48	0.64	0.53	0.50	0.50	0.61	0.54	0.50	0.50	0.50	0.50	0.50	0.50	0.50	0.50
CART	0.49	0.66	0.75	0.53	0.50	0.59	0.50	0.54	0.65	0.50	0.41	0.71	0.55	0.48	0.49	0.44	0.54	0.51	0.43	0.52	0.49
J48	0.49	0.67	0.72	0.54	0.55	0.59	0.49	0.54	0.66	0.48	0.41	0.77	0.56	0.66	0.49	0.44	0.53	0.56	0.35	0.49	0.50
ADT	0.67	0.72	0.78	0.58	0.66	0.68	0.62	0.77	0.73	0.63	0.67	0.77	**0.70**	0.81	0.75	0.78	0.53	0.73	0.52	0.58	0.67
Bag	0.71	0.79	0.80	0.65	0.68	**0.73**	0.61	0.76	0.75	0.68	0.64	0.79	**0.71**	0.81	0.72	0.86	0.50	0.73	0.66	0.60	**0.70**
RF	0.77	0.80	0.80	0.64	0.71	**0.74**	0.64	0.79	0.71	0.66	0.56	0.80	0.69	0.78	0.63	0.57	0.44	0.74	0.58	0.55	0.61
LMT	0.66	0.76	0.74	0.63	0.67	0.69	0.46	0.72	0.74	0.75	0.71	0.73	0.69	0.81	0.66	0.84	0.57	0.66	0.73	0.58	0.69
LB	0.75	0.78	0.79	0.59	0.68	**0.72**	0.66	0.77	0.76	0.73	0.59	0.77	**0.71**	0.84	0.76	0.83	0.52	0.74	0.65	0.61	**0.71**
AB	0.69	0.75	0.78	0.59	0.65	0.69	0.66	0.79	0.74	0.70	0.62	0.71	**0.70**	0.82	0.72	0.81	0.54	0.66	0.65	0.61	0.69
NNge	0.56	0.68	0.65	0.57	0.62	0.62	0.56	0.66	0.68	0.51	0.47	0.68	0.59	0.53	0.51	0.48	0.49	0.61	0.63	0.54	0.54
DTNB	0.49	0.78	0.78	0.61	0.56	0.64	0.49	0.67	0.76	0.60	0.41	0.75	0.61	0.48	0.49	0.44	0.51	0.54	0.35	0.49	0.47
VFI	0.58	0.51	0.65	0.50	0.64	0.58	0.61	0.64	0.72	0.67	0.62	0.70	0.66	0.71	0.62	0.65	0.51	0.71	0.51	0.49	0.60

(b)

Dataset	MMS							Calendar					Bluetooth				Telephony		
Tech.	2.3.7	4.0.2	4.0.4	4.1.2	4.2.2	4.3.1	Avg	4.0.2	4.0.4	4.1.2	4.2.2	Avg	4.1.2	4.2.2	4.3.1	Avg	4.2.2	4.3.1	Avg
LR	0.76	0.66	0.85	0.73	0.56	0.68	**0.71**	0.66	0.80	0.82	0.69	**0.74**	0.49	0.79	0.81	**0.70**	0.73	0.85	**0.79**
NB	0.79	0.73	0.84	0.76	0.62	0.80	**0.76**	0.70	0.80	0.71	0.69	**0.73**	0.53	0.74	0.85	**0.71**	0.73	0.83	**0.78**
BN	0.76	0.46	0.84	0.73	0.43	0.52	0.62	0.58	0.70	0.51	0.56	0.59	0.37	0.73	0.71	0.60	0.70	0.83	**0.77**
MLP	0.75	0.71	0.85	0.71	0.61	0.76	**0.73**	0.65	0.80	0.69	0.65	**0.70**	0.46	0.78	0.80	0.68	0.72	0.85	**0.79**
RBF	0.74	0.76	0.80	0.74	0.76	0.74	**0.76**	0.71	0.73	0.75	0.69	**0.72**	0.52	0.70	0.80	0.67	0.69	0.81	**0.75**
SVM	0.52	0.50	0.76	0.50	0.50	0.50	0.55	0.52	0.63	0.50	0.61	0.57	0.63	0.50	0.62	0.58	0.65	0.76	**0.71**
VP	0.58	0.59	0.67	0.56	0.50	0.50	0.57	0.51	0.50	0.49	0.51	0.50	0.56	0.50	0.50	0.52	0.50	0.50	0.50
CART	0.77	0.45	0.75	0.74	0.43	0.45	0.60	0.56	0.73	0.58	0.63	0.63	0.57	0.48	0.49	0.51	0.65	0.75	**0.70**
J48	0.68	0.48	0.78	0.67	0.43	0.52	0.59	0.59	0.61	0.55	0.54	0.57	0.47	0.46	0.50	0.48	0.69	0.80	**0.75**
ADT	0.79	0.72	0.83	0.72	0.62	0.74	**0.74**	0.58	0.74	0.71	0.64	0.67	0.46	0.69	0.72	0.62	0.73	0.83	**0.78**
Bag	0.80	0.68	0.84	0.74	0.68	0.72	**0.74**	0.69	0.80	0.69	0.66	**0.71**	0.51	0.71	0.71	0.64	0.71	0.83	**0.77**
RF	0.76	0.65	0.82	0.67	0.70	0.73	**0.72**	0.64	0.78	0.72	0.61	0.69	0.49	0.68	0.71	0.63	0.65	0.85	**0.75**
LMT	0.78	0.66	0.83	0.75	0.56	0.73	**0.72**	0.65	0.81	0.79	0.63	**0.72**	0.43	0.76	0.80	0.66	0.73	0.84	**0.79**
LB	0.79	0.75	0.82	0.71	0.70	0.65	**0.74**	0.56	0.78	0.73	0.67	0.69	0.48	0.76	0.76	0.67	0.75	0.83	**0.79**
AB	0.77	0.70	0.81	0.69	0.70	0.65	**0.72**	0.57	0.71	0.75	0.69	0.68	0.31	0.72	0.68	0.57	0.72	0.80	**0.76**
NNge	0.69	0.53	0.75	0.66	0.65	0.51	0.63	0.68	0.67	0.65	0.59	0.65	0.40	0.58	0.58	0.52	0.57	0.72	0.65
DTNB	0.73	0.46	0.81	0.71	0.43	0.68	0.64	0.62	0.72	0.54	0.58	0.62	0.50	0.49	0.73	0.57	0.72	0.81	**0.77**
VFI	0.74	0.72	0.70	0.62	0.76	0.74	**0.71**	0.48	0.76	0.71	0.67	0.66	0.50	0.79	0.68	0.66	0.70	0.81	**0.76**

shows that similar to the results shown in Fig. 3, NB, LR, MLP, LB and Bagging techniques show the highest performance over all the data sets.

5.4. RQ3: is the performance of defect prediction models validated using inter-release validation comparable to 10-fold validation and is it statistically different than 10-fold validation?

We further compared the results of the defect prediction models developed using all the 18 ML techniques using 10-fold validation and inter-release validation. The comparative results using average AUC values are shown in Fig. 5. It can be observed from the figure that in majority of the cases the results of the inter-release models were found comparable or even better than 10-fold validation results. However, in certain cases such as in the case when the model developed by Contact 4.0.2 was validated on Contact 4.0.4, or another case when the model developed by Contact 4.2.2 was validated on Contact 4.3.1, there was decrease in the average AUC values. The average AUC values of 10-fold validation models were better than inter-release models in such cases. The reason for such a trend could be the ineffectiveness of the training models due to low percentage of defective classes. The percentage of defective classes in Contact 4.0.2 and Contact 4.2.2 are very less i.e. 5.84% and 3.73%,

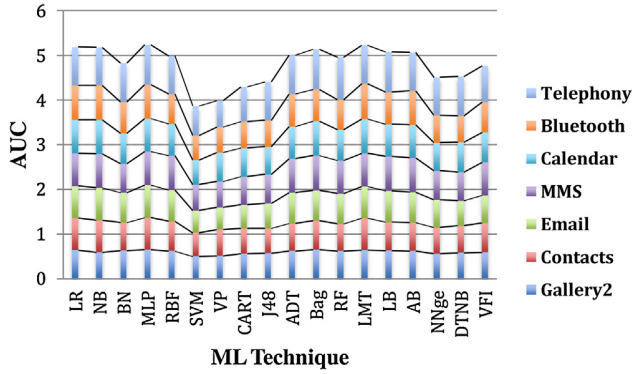

Fig. 4. Average AUC values of each ML technique on corresponding data sets using inter-release validation.

respectively as compared to the versions on which these models are validated i.e. Contact 4.0.4 has 32.32% of defective classes and Contact 4.3.1 has 46.66% defective classes. Due to low number of defective classes in the data sets, which are used for training, the models developed may not be able to learn effectively the values of OO metrics that are efficient in predicting defective classes leading to decrease in average AUC values.

Please cite this article in press as: R. Malhotra, An empirical framework for defect prediction using machine learning techniques with Android software, Appl. Soft Comput. J. (2016), http://dx.doi.org/10.1016/j.asoc.2016.04.032

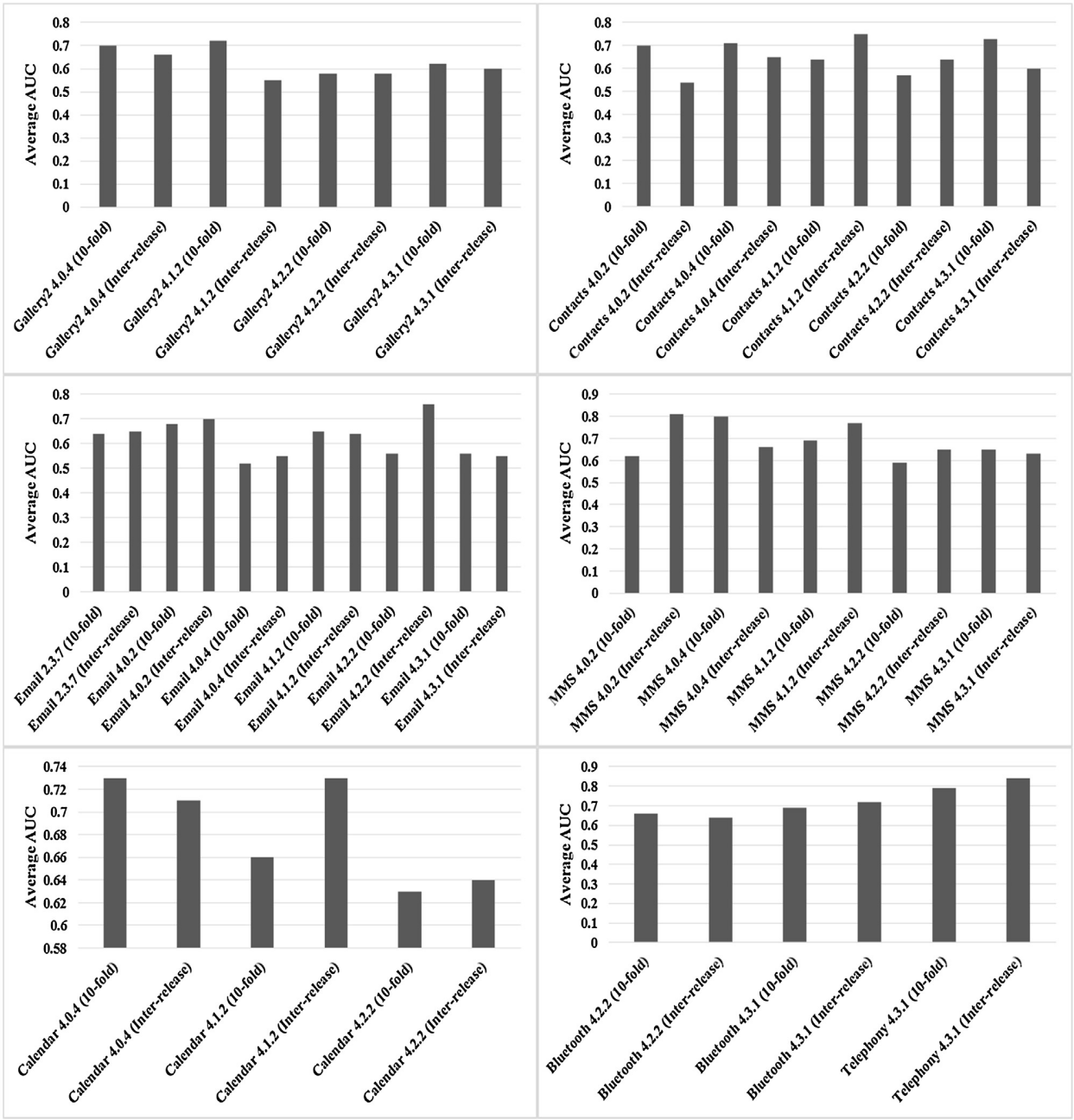

Fig. 5. Comparison of 10-fold and Inter-release validation models using average AUC values.

Moreover, we also validated whether there is any statistical difference amongst the results obtained using 10-fold and inter-release validation on all the data sets using Wilcoxon test. The average results of all the data sets on all the releases of a specific data set, were analyzed to compare the AUC obtained using 10-fold and inter-release validation. The test did not yield significant results, which means that the performance of the developed models using both 10-fold and inter-release validation is comparable to each other.

5.5. RQ4—which are the best and worst ML techniques for defect prediction using OO metrics?

The difference in performance amongst the ML techniques is assessed using Friedman test. It provides a combined ranking of the 18 ML techniques over multiple releases of seven application packages of Android data sets. This will allow us to determine whether the performance difference among the ML techniques is random or not and establish the superiority of one ML technique over the other ML techniques. The results are analyzed at the 0.5 significance level. We first obtain the average performance of each technique on each of the data set by computing the average AUC obtained on all the releases of a specific data set both using 10-fold as well as using inter-release validation. Then, each of the eighteen techniques are ranked by the Friedman test. Since, eighteen techniques are compared, the degrees of freedom is 17. The computed Friedman test statistic is 92.354. We used AUC for determining the difference in performance of the ML techniques. AUC is reported to be an appropriate measure for dealing with unbalanced and noisy data [56] as

Please cite this article in press as: R. Malhotra, An empirical framework for defect prediction using machine learning techniques with Android software, Appl. Soft Comput. J. (2016), http://dx.doi.org/10.1016/j.asoc.2016.04.032

Table 13
Friedman mean ranks of ML techniques based on AUC.

ML technique	Mean rank	ML technique	Mean rank
MLP	3.93	RF	8.50
LR, NB	4.68	BN	10.25
LB	4.71	VFI	10.64
Bag	4.82	DTNB	12.71
LMT	5.50	NNge	13.96
RBF	6.89	J48	14.79
ADT	7.71	CART	15.61
AB	7.96	SVM, VP	16.82

it is unaffected to the changes in distribution of outcome class (for example percentage of defective or non-defective classes).

The null hypothesis of the Friedman test is that there is no significant difference between the AUC of ML techniques. The results are found to be significant at 0.05 level. Hence, we reject the null hypothesis and accept the alternative hypothesis that there is a significant difference among the performance of the ML techniques. The results show that MLP is the best technique followed by NB and LR for defect prediction models. VP, SVM and CART techniques received the lowest ranks amongst the ML techniques. Hence, the results confirm the reliability of the difference amongst the ML techniques in the defect prediction models (Table 13).

The MLP technique achieved the best rank amongst all other ML techniques for developing defect prediction models using 10-fold as well as inter-release validation. MLP technique is effective and powerful as it allows insertion of a number of non-linear layers between the input and output layers. As advocated by Gondra [59], these intermediate layers allow complex interactions between the inputs and outputs that are capable of fitting complex functions. This also allows adaptiveness of the network to train new functions. The 10-fold validation results on Contact and Telephony data sets showed MLP as the best technique. Similarly, the inter-release validation results on Gallery2, Contact and Email depicted MLP as the best technique. It can be seen that in majority of the data sets except Telephony data set, the percentage of defective classes ranged from very low i.e. 1% to about 50%. Thus, MLP showed effective results with data sets having imbalanced distribution of defective classes (1%) to balanced distribution (50%). Moreover, MLP use back-propagation as a learning mechanism that allows two passes through the networks. During the forward pass of the network, the synaptic weights of the network are adjusted according to the training data, and the actual response of the network is produced. The backward pass propagates an error signal, which is the difference between the desired response and the actual response of the network. During this pass, the weights of the network are readjusted to decrease the difference between the actual and desired response. Thus, this training process helps in developing efficient models.

The average AUC of the NB model are between 0.65–0.78 for all the application packages of Android software. The results in this study confirm the previous findings that the NB technique is effective in defect prediction and may be used by researchers and practitioners in future applications. The NB technique is based on the assumption that the attributes are independent and unrelated. One of the reasons that the NB technique showed the best performance is that the features were reduced using the CFS method before applying the model prediction techniques in this work. The CFS method removes the features that are correlated with each other and retains the features that are correlated with the dependent variable. Hence, OO metrics selected by the CFS method for each data set are less correlated with each other and more correlated with the defect variable. This could be the reason that the NB technique showed the best results on data sets, which have few features, selected. For example, the 10-fold validation results on the Email 4.0.4 data set with just one feature selected (AUC—0.57), the MMS 4.1.2 data set with two features (AUC—0.76), the Email 2.3.7 data set (AUC—0.79) and the Bluetooth 4.3.1 data set (AUC—0.85) with three features each selected show the best AUC values using the NB technique. The NB technique is easy to understand and interpret (linear model can be obtained as a sum of logs) and is also computationally efficient [11,30]. However, the NB technique shows low AUC values in Email Android data set 4.0.4. This may be due to the reason the NB technique was not able to make accurate predictions of defects on the basis of only one OO metric (CAM). Thus, data sets with few features should use NB technique for developing defect prediction models.

Also, ensemble learners like RF, Bag, LB, AB and LMT show very good results on a number of data sets. For example, RF shows best results on Email 4.1.2, Contact 4.3.1, Gallery2 4.3.1 with AUC values of 0.74, 0.80 and 0.71 respectively. LB shows best results on Contact 4.0.4 with an AUC of 0.79 and Email 2.3.2 with an AUC of 0.84. Bag also exhibits best results on Email 4.0.2 data set with an AUC of 0.86 and so do LMT and AB on a number of data sets. Ensemble learners develop effective prediction models as they use a number of learning techniques together to obtain better predictive performance than constituent learning techniques. Thus, these techniques can also be used on various data sets for developing defect prediction models.

Table 14
Nemenyi test results.

	NB	Bag	RBF	ADT	LB	MLP	LR	LMT	AB	RF	VFI	BN	DTNB	NNge	CRT	J48	SVM	VP
NB		↑	↑	↑	↑	↓	=	↑	↑	↑	↑	↑	‡	‡	‡	‡	‡	‡
Bag			↑	↑	↓	↓	↓	↑	↑	↑	↑	↑	‡	‡	‡	‡	‡	‡
RBF				↑	↓	↓	↓	↓	↑	↑	↑	↑	↑	‡	‡	‡	‡	‡
ADT					↓	↓	↓	↑	↑	↑	↑	↑	↑	↑	‡	‡	‡	‡
LB						↓	↓	↓	↑	↑	↑	↑	‡	‡	‡	‡	‡	‡
MLP							↑	↑	↑	↑	↑	↑	‡	‡	‡	‡	‡	‡
LR								↑	↑	↑	↑	↑	‡	‡	‡	‡	‡	‡
LMT									↑	↑	↑	↑	‡	‡	‡	‡	‡	‡
AB										↑	↑	↑	↑	↑	‡	↑	‡	‡
RF											↑	↑	↑	↑	‡	↑	‡	‡
VFI												↓	↑	↑	↑	↑	↑	↑
BN													↑	↑	↑	↑	↑	↑
DTNB														↑	↑	↑	↑	↑
NNge															↑	↑	↑	↑
CART																↓	↑	↑
J48																	↑	↑
SVM																		=
VP																		

Please cite this article in press as: R. Malhotra, An empirical framework for defect prediction using machine learning techniques with Android software, Appl. Soft Comput. J. (2016), http://dx.doi.org/10.1016/j.asoc.2016.04.032

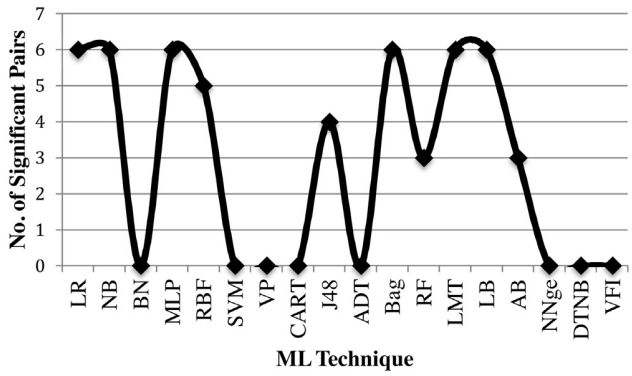

Fig. 6. Number of significant pairs corresponding to each ML technique.

Support Vector Machines like SVM and VP do not show good performance in terms of AUC for most of the data sets. This could be because these techniques are efficient in handling high dimensional data sets with redundant features. Since, we have applied CFS to the features before developing models using ML techniques, very few features (on an average 3–5) are left to develop the model. However, in certain data sets where after feature reduction, the number of features is 6–7, the SVM and VP techniques give better results. For example, in 10-fold validation results of Contact 4.3.1 data set with seven features, the SVM technique shows an AUC of 0.68 and the VP technique shows an AUC of 0.61, which is much higher than an AUC of 0.50 shown by SVM and VP in most other versions of Contact data set. Similarly, in MMS 4.0.4 data set, six features are used to develop models for 10-fold validation. The AUC of SVM was 0.76 and that of VP was 0.67, which is much higher than an AUC of 0.50–0.58, obtained by SVM and VP techniques in other MMS data sets. Thus, SVM and VP techniques are better suited to data sets with high dimensionality and redundant features.

5.6. RQ5—which pairs of ML techniques are statistically different from each other for defect prediction?

After obtaining significant results using the Friedman test, we performed post-hoc analysis using the Nemenyi test. The Nemenyi test was used to examine the statistical difference between the pairs of different ML techniques. The critical distance computed for Nemenyi test was 6.97 at $\alpha = 0.05$. The distance between the mean ranks allocated by the Friedman test to each of the techniques is computed for each pair of techniques and compared with this critical distance. If the computed difference is greater than or at least equal to the critical distance, the performance of pair of techniques is said to differ significantly at the significance level $\alpha = 0.05$.

The results of the pair-wise comparisons of the ML techniques are shown in Table 14. Out of 153 pairs of ML techniques, 51 were found to have significant results. The results shown in Table 14 depict that MLP, NB, LR, LB, Bagging and LMT techniques are significantly superior to six techniques namely DTNB, NNge, J48, CART, SVM and VP techniques. Similarly, RBF technique is significantly superior to NNge, J48, CART, SVM and VP techniques, whereas J48 technique is significantly superior to J48, CART, SVM and VP techniques. AB and RF techniques are significantly superior to CART, SVM and VP techniques. Hence, the results show that 51 pairs of ML techniques depict significant results. It also confirms that MLP, NB, LR, LB, Bagging and LMT are top six ML techniques with maximum number of significant pairs. Fig. 6 depicts the number of pairs corresponding to each ML technique, in which it performs significantly better. For example, LR performs significantly better than four other ML techniques when pairwise comparisons were performed using Nemenyi test.

6. Threats to validity

This section describes the various threats to validity of the study.

6.1. Conclusion validity

All possible threats that may bias the results and affect the relationship of dependent and independent variables pose a threat to conclusion validity [61]. Conclusion validity also concerns itself with statistical validity of the results. This study involves use of non-parametric tests i.e. Friedman and Nemenyi, which are carefully chosen as these tests do not require certain data pre-conditions to be fulfilled such as data normality, homogeneity of variances etc. The study also evaluates its results at a widely acceptable cut-off value of $\alpha = 0.05$. The results are also evaluated using post-hoc analysis, which reinforces confidence in the results of the study. Moreover, the use of 10-fold validation omits validation bias.

6.2. Internal validity

The threat to internal validity is present if there is "causal effect" of the OO metrics on defect proneness attribute. However, in order to determine this effect, it is necessary to perform experiments where values of other OO metrics are controlled in order determine the "causal effect" of one OO metric [13]. But such experiments are difficult to perform. Since, the objective of the study was not to determine the causal effect, this threat exists in the study.

6.3. Construct validity

Construct validity is used to ascertain whether the dependent and independent variables accurately represent the concepts they are supposed to measure. The dependent variable of the study is computed by the DCRS tool, which is efficient in extracting defect information from change logs. Thus, the dependent variable is accurately measured. Moreover, certain researchers have performed extensive experiments to validate the accurateness of certain OO metrics used in the study [12,62,63], which further reduces this threat for the independent variables of the study.

6.4. External validity

The extent to which the results of the study are generalizable aids the external validity of the study [64]. Since, the study uses seven application packages of widely used mobile operating system Android, the results of the study are widely acceptable and can be used in similar scenarios. Furthermore, the data sets used in the study are open source on nature, which aids the replicability of the study. However, future studies should evaluate the results on software which are not operating systems to increase the generalizability of the obtained results.

7. Conclusions

Development of a defect prediction model helps in ascertaining software quality attributes and focused use of constraint resources. They also guide researchers and practitioners to perform preventive actions in the early phases of software development and commit themselves for creation of better quality software. In this work, we not only conduct an extensive empirical experimentation on publically available application packages of Android software systems but also provide a repeatable and pragmatic approach to achieve such models. Specifically, the main contributions of the paper are: (i) create defect prediction models using various ML techniques on collected multiple data sets from the Google code repository for the Android platform, (ii) pre-process the data using

Please cite this article in press as: R. Malhotra, An empirical framework for defect prediction using machine learning techniques with Android software, Appl. Soft Comput. J. (2016), http://dx.doi.org/10.1016/j.asoc.2016.04.032

Table 15
AUC values of data sets using inter-release validation.

(a)

Dataset	Gallery2					Contact						Email						
Tech.	4.0.2 on 4.0.4	4.0.4 on 4.1.2	4.1.2 on 4.2.2	4.2.2 on 4.3.1	Avg	2.3.7 on 4.0.2	4.0.2 on 4.0.4	4.0.4 on 4.1.2	4.1.2 on 4.2.2	4.2.2 on 4.3.1	Avg	2.3.2 on 2.3.7	2.3.7 on 4.0.2	4.0.2 on 4.0.4	4.0.4 on 4.1.2	4.1.2 on 4.2.2	4.2.2 on 4.3.1	Avg
LR	0.77	0.55	0.54	0.68	0.64	0.61	0.72	0.77	0.77	0.73	**0.72**	0.73	0.85	0.58	0.72	0.78	0.63	**0.72**
NB	0.75	0.49	0.44	0.67	0.59	0.62	0.74	0.76	0.75	0.73	**0.72**	0.71	0.82	0.58	0.72	0.89	0.63	**0.73**
BN	0.76	0.55	0.61	0.61	0.63	0.50	0.70	0.77	0.67	0.50	0.63	0.73	0.81	0.57	0.64	0.77	0.5	0.67
MLP	0.77	0.65	0.51	0.68	0.65	0.62	0.75	0.76	0.76	0.73	**0.72**	0.74	0.86	0.58	0.72	0.83	0.63	**0.73**
RBF	0.76	0.53	0.57	0.63	0.62	0.50	0.74	0.74	0.75	0.64	0.67	0.73	0.76	0.58	0.73	0.78	0.61	**0.70**
SVM	0.50	0.50	0.49	0.50	0.50	0.50	0.50	0.66	0.50	0.50	0.53	0.50	0.50	0.50	0.50	0.50	0.50	0.50
VP	0.50	0.51	0.53	0.50	0.51	0.72	0.50	0.73	0.50	0.50	0.59	0.50	0.50	0.50	0.50	0.50	0.50	0.50
CART	0.50	0.58	0.59	0.57	0.56	0.61	0.50	0.72	0.50	0.50	0.57	0.50	0.50	0.50	0.66	0.50	0.50	0.53
J48	0.50	0.60	0.61	0.57	0.57	0.61	0.50	0.71	0.50	0.50	0.56	0.54	0.50	0.50	0.64	0.69	0.50	0.56
ADT	0.74	0.50	0.63	0.60	0.62	0.43	0.66	0.77	0.62	0.61	0.62	0.72	0.80	0.57	0.65	0.84	0.55	0.69
Bag	0.78	0.57	0.63	0.63	0.65	0.42	0.66	0.77	0.74	0.66	0.65	0.77	0.78	0.56	0.59	0.86	0.52	0.68
RF	0.68	0.58	0.61	0.60	0.62	0.44	0.66	0.79	0.61	0.53	0.61	0.74	0.76	0.53	0.63	0.93	0.50	0.68
LMT	0.72	0.55	0.63	0.65	0.64	0.61	0.75	0.76	0.74	0.73	**0.72**	0.62	0.85	0.58	0.73	0.83	0.63	**0.71**
LB	0.73	0.51	0.63	0.65	0.63	0.41	0.68	0.76	0.69	0.64	0.64	0.73	0.83	0.58	0.66	0.83	0.58	**0.70**
AB	0.73	0.55	0.64	0.57	0.62	0.41	0.67	0.73	0.73	0.66	0.64	0.71	0.77	0.58	0.67	0.77	0.58	0.68
NNge	0.54	0.56	0.57	0.56	0.56	0.57	0.56	0.73	0.57	0.50	0.59	0.60	0.56	0.51	0.66	0.88	0.50	0.62
DTNB	0.50	0.58	0.61	0.61	0.58	0.59	0.67	0.77	0.50	0.50	0.61	0.50	0.50	0.50	0.64	0.73	0.50	0.56
VFI	0.65	0.65	0.52	0.55	0.59	0.52	0.71	0.71	0.69	0.66	0.66	0.70	0.57	0.55	0.54	0.75	0.60	0.62

(b)

Dataset	MMS						Calendar				Bluetooth			Telephony	
Tech.	2.3.7 on 4.0.2	4.0.2 on 4.0.4	4.0.4 on 4.1.2	4.1.2 on 4.2.2	4.2.2 on 4.3.1	Avg	4.0.2 on 4.0.4	4.0.4 on 4.1.2	4.1.2 on 4.2.2	Avg	4.1.2 on 4.2.2	4.2.2 on 4.3.1	Avg	4.2.2 on 4.3.1	Avg
LR	0.81	0.80	0.80	0.66	0.58	**0.73**	0.81	0.79	0.66	**0.75**	0.72	0.82	**0.77**	0.86	**0.86**
NB	0.83	0.83	0.78	0.68	0.70	**0.76**	0.80	0.78	0.70	**0.76**	0.71	0.83	**0.77**	0.85	**0.85**
BN	0.85	0.50	0.78	0.63	0.50	0.65	0.72	0.78	0.55	0.68	0.60	0.79	**0.70**	0.87	**0.87**
MLP	0.85	0.82	0.81	0.68	0.58	**0.75**	0.81	0.76	0.65	**0.74**	0.65	0.87	**0.76**	0.89	**0.89**
RBF	0.82	0.75	0.78	0.72	0.80	**0.77**	0.76	0.74	0.63	**0.71**	0.48	0.86	0.67	0.85	**0.85**
SVM	0.68	0.50	0.71	0.50	0.50	0.58	0.51	0.63	0.51	0.55	0.59	0.50	0.55	0.66	0.66
VP	0.70	0.50	0.71	0.50	0.50	0.58	0.79	0.51	0.64	0.65	0.63	0.50	0.57	0.59	0.59
CART	0.80	0.50	0.71	0.63	0.50	0.63	0.66	0.71	0.55	0.64	0.68	0.50	0.59	0.78	**0.78**
J48	0.84	0.50	0.77	0.63	0.50	0.65	0.59	0.72	0.55	0.62	0.68	0.50	0.59	0.86	**0.86**
ADT	0.83	0.69	0.81	0.74	0.71	**0.76**	0.70	0.78	0.68	**0.72**	0.62	0.84	**0.73**	0.87	**0.87**
Bag	0.85	0.72	0.79	0.72	0.81	**0.78**	0.83	0.74	0.75	**0.77**	0.61	0.81	**0.71**	0.90	**0.90**
RF	0.88	0.61	0.82	0.68	0.71	**0.74**	0.65	0.74	0.68	0.69	0.60	0.74	0.67	0.95	**0.95**
LMT	0.81	0.79	0.80	0.74	0.58	**0.74**	0.80	0.79	0.73	**0.77**	0.73	0.85	**0.79**	0.86	**0.86**
LB	0.85	0.69	0.81	0.69	0.80	**0.77**	0.71	0.76	0.68	**0.72**	0.63	0.81	**0.72**	0.90	**0.90**
AB	0.82	0.78	0.78	0.66	0.80	**0.77**	0.72	0.79	0.70	**0.74**	0.68	0.84	**0.76**	0.86	**0.86**
NNge	0.78	0.54	0.71	0.65	0.56	0.65	0.67	0.60	0.62	0.63	0.57	0.64	0.61	0.85	**0.85**
DTNB	0.80	0.52	0.77	0.63	0.50	0.64	0.66	0.81	0.55	0.67	0.68	0.50	0.59	0.88	**0.88**
VFI	0.84	0.79	0.72	0.58	0.78	**0.74**	0.48	0.76	0.71	0.67	0.50	0.79	0.68	0.70	**0.81**

Please cite this article in press as: R. Malhotra, An empirical framework for defect prediction using machine learning techniques with Android software, Appl. Soft Comput. J. (2016), http://dx.doi.org/10.1016/j.asoc.2016.04.032

the attribute reduction techniques, (iii) empirically validate the constructed models on various releases of the application packages of Android data sets in order to obtained generalized results, (iv) perform statistical tests to evaluate the significance of the obtained results and, (v) analyze the outcomes to deduce meaningful and generalized conclusions. The results are based on AUC and the primary results of the paper are as follows:

1. The LOC, CAM, WMC, Ce and LCOM3 metrics were found to be significant predictors over the various releases of seven application packages of the Android software using the CFS method.
2. The work confirms the overall predictive ability of the various ML techniques including MLP, NB, AB, ADT, Bagging, LB and RF techniques (AUC greater than 0.7 in most cases) for defect prediction. The results are confirmed using both 10-fold and inter-release validation.
3. The results of inter-release validation depict comparable results with 10-fold validation. This conforms the generalizability of the results with respect to the defect prediction models developed in this work.
4. The results of the comparison of ML techniques evaluated using Friedman test show the superiority of the MLP, LB, LR and NB technique in defect prediction. The MLP technique is found to be the best followed by NB and LR techniques. On the other hand, support vector based techniques namely SVM and VP show the worst performance for predicting defective classes. They are followed by two decision tree based techniques CART and J48 among the lowest rankers.
5. The statistical test, Nemenyi, depict that there is significant difference between the performances of 51 pairs (out of 153) of the ML techniques, i.e. about 33.3%.

Thus, we conclude that the ML techniques have predictive capability and the empirical framework proposed in this paper is repeatable and the results can be generalized on future releases of Android software and similar natured software. Moreover, the study statistically examines the results using Friedman and Nemenyi test (RQ4 and RQ5), thus overcoming the weakness of low use of statistical tests in the previous literature studies.

Once a defect prediction model is trained it can be used for quality assessment and for predictions on future unseen data. The predictions of this work can be utilized for assessing software quality processes and procedures as we evaluate the software products that are a result of these processes. The defect prediction models are efficient and effective, can be used by researchers and practitioners to quickly identify defect-prone classes and will aid any software organization to reduce associated costs, time of development and allow an efficient allocation of available resources. In future, we propose to replicate the work done in this paper using metaheuristic techniques and hybridized algorithms.

Acknowledgement

The author is thankful to Ms. Megha Khanna, Research Scholar, Department of Software Engineering, Delhi Technological University, India for her research inputs and scholarly discussions.

References

[1] Y. Singh, A. Kaur, R. Malhotra, Empirical validation of object-oriented metrics for predicting fault proneness models, Softw. Qual. J. 18 (2010) 3–35.
[3] S. Lessmann, B. Baesens, C. Mues, S. Pietsch, Benchmarking classification models for software defect prediction: a proposed framework and novel findings, IEEE Trans. Softw. Eng. 34 (2008) 485–496.
[4] R. Malhotra, Empirical Research in Software Engineering—Methods, Techniques and Applications, CRC Press, USA, 2015.
[5] R. Malhotra, A systematic review of machine learning techniques for software fault prediction, Appl. Soft Comput. 27 (2015) 504–518.
[6] A. Arcuri, L. Briand, A practical guide for using statistical tests to assess randomized algorithms in software engineering, Proceedings of the 33rd International Conference on Software Engineering (2011) 1–10.
[7] T. Menzies, J. Greenwald, A. Frank, Data mining static code attributes to learn defect predictors, IEEE Trans. Softw. Eng. 33 (2007) 2–13.
[8] I. Myrtveit, E. Stensrud, M. Shepperd, Reliability and validity in comparative studies of software prediction models, IEEE Trans. Softw. Eng. 31 (2005) 380–391.
[9] R. Malhotra, R. Raje, An empirical comparison of machine learning techniques for software defect prediction, Proceedings of the 8th International Conference on Bioinspired Information and Communications Technologies (2014) 320–327.
[10] V. Basili, L. Briand, W. Melo, A validation of object-oriented design metrics as quality indicators, IEEE Trans. Softw. Eng. 22 (1996) 751–761.
[11] A. Binkley, S. Schach, Validation of the coupling dependency metric as a risk predictor, Proceedings of the International Conference on Software Engineering (1998) 452–455.
[12] L.C. Briand, J. Wust, J.W. Daly, D.V. Porter, Exploring the relationships between design measures and software quality in object-oriented systems, J. Syst. Softw. 51 (2000) 245–273.
[13] L. Briand, J. Wüst, H. Lounis, Replicated case studies for investigating quality factors in object-oriented designs, Empir. Softw. Eng.: Int. J. 6 (2001) 11–58.
[14] M. Cartwright, M. Shepperd, An empirical investigation of an object-oriented software system, IEEE Trans. Softw. Eng. 26 (1999) 786–796.
[15] S. Chidamber, D. Darcy, C. Kemerer, Managerial use of metrics for object-oriented software: an exploratory analysis, IEEE Trans. Softw. Eng. 24 (1998) 629–639.
[16] R. Harrison, S.J. Counsell, R.V. Nithi, An evaluation of MOOD set of object-oriented software metrics, IEEE Trans. Softw. Eng. 24 (1998) 491–496.
[17] K. El Emam, S. Benlarbi, N. Goel, S. Rai, The confounding effect of class size on the validity of object-oriented metrics, IEEE Trans. Softw. Eng. 27 (2001) 630–650.
[18] W. Li, S. Henry, Object-oriented metrics that predict maintainability, J. Syst. Softw. 23 (1993) 111–122.
[19] P. Yu, T. Systa, H. Muller, Predicting fault-proneness using OO metrics: an industrial case study, in: Proceedings of Sixth European Conference on Software Maintenance and Reengineering, Budapest, Hungary, 2002, pp. 99–107.
[20] K.K. Aggarwal, Y. Singh, A. Kaur, R. Malhotra, Investigating the effect of coupling metrics on fault proneness in object-oriented systems, Softw. Qual. Prof. 8 (2006) 4–16.
[21] W. Li, R. Shatnawi, An empirical study of the bad smells and class error probability in the post-release object-oriented system evolution, J. Syst. Softw. 80 (2007) 1120–1128.
[22] H. Olague, L. Etzkorn, S. Gholston, S. Quattlebaum, Empirical validation of three software metrics suites to predict fault-proneness of object-oriented classes developed using highly iterative or agile software development processes, IEEE Trans. Softw. Eng. 33 (2007) 402–419.
[23] K.K. Aggarwal, Y. Singh, A. Kaur, R. Malhotra, Empirical analysis for investigating the effect of object-oriented metrics on fault proneness: a replicated case study, Softw. Process Improv. Pract. 14 (2009) 39–62.
[24] L.C. Briand, W. Melo, J. Wuest, Assessing the applicability of fault-proneness models across object-oriented software projects, IEEE Trans. Softw. Eng. 28 (July (7)) (2002).
[25] T. Gyimothy, R. Ferenc, I. Siket, Empirical validation of object-oriented metrics on open source software for fault prediction, IEEE Trans. Softw. Eng. 31 (2005) 897–910.
[26] S.R. Chidamber, C.F. Kemerer, A metrics suite for object oriented design, IEEE Trans. Softw. Eng. 20 (1994) 476–493.
[27] Y. Zhou, H. Leung, Empirical analysis of object-oriented design metrics for predicting high and low severity faults, IEEE Trans. Softw. Eng. 32 (2006) 771–789.
[28] R. Malhotra, Y. Singh, A. Kaur, Empirical validation of object-oriented metrics for predicting fault proneness at different severity levels using support vector machines, Int. J. Syst. Assur. Eng. Manag. 1 (2010) 269–281.
[29] S. Kanmani, V.R. Uthariaraj, V. Sankaranarayanan, P. Thambidurai, Object-oriented software fault prediction using neural networks, Inf. Softw. Technol. 49 (2007) 483–492.
[30] G.J. Pai, J.B. Dugan, Empirical analysis of software fault content and fault proneness using Bayesian methods, IEEE Trans. Softw. Eng. 33 (2007) 675–686.
[31] C. Catal, B. Diri, B. Ozumut, An artificial immune system approach for fault prediction in object-oriented software, 2nd Int. Conf. Dependability Comput. Syst. (2007) 1–8.
[32] E. Arisholm, L.C. Briand, E.B. Johannessen, A systematic and comprehensive investigation of methods to build and evaluate fault prediction models, J. Syst. Softw. 83 (2010) 2–17.
[33] A.B. Carvalho, A. Pozo, S.R. Vegilio, A symbolic fault-prediction model based on multiobjective particle swarm optimization, J. Syst. Softw. 83 (2010) 868–882.
[34] Y. Singh, A. Kaur, R. Malhotra, Software fault pronennes prediction using support vector machines, Procedings World Congr. Eng. (2009) 240–245.
[35] Y. Zhou, B. Xu, H. Leung, On the ability of complexity metrics to predict fault-prone classes in object-oriented systems, J. Syst. Softw. 83 (2010) 660–674.

Please cite this article in press as: R. Malhotra, An empirical framework for defect prediction using machine learning techniques with Android software, Appl. Soft Comput. J. (2016), http://dx.doi.org/10.1016/j.asoc.2016.04.032

[36] S. Martino, F. ferrucci, C. Gravino, F. Sarro, A genetic algorithm to configure support vetcor machine for predicting fault prone components, Product Focus Software Process Improvement (2011) 247–261.
[37] A. Okutan, O.T. Yıldız, Software defect prediction using Bayesian networks, Empir. Softw. Eng. 19 (2012) 154–181.
[38] D. Azar, J. Vybihal, An ant colony optimization algorithm to improve software quality prediction models: case of class stability, Inf. Softw. Technol. 53 (2011) 388–393.
[39] R. Malhotra, Y. Singh, On the applicability of machine learning techniques for object-oriented software fault prediction, Softw. Eng. Int. J. 1 (2011) 24–37.
[40] R. Malhotra, A. Jain, Fault prediction using statistical and machine learning methods for improving software quality, J. Inf. Process. Syst. 8 (2012) 241–262.
[41] Y. Yang, Z. He, F. Shu, M. Li, Q. Wang, An investigation on the feasibility of cross-project defect prediction, Autom. Softw. Eng. 19 (2012) 167–199.
[42] M. Li, H. Zhang, R. Whu, Z. Zhou, Sample-based software defect prediction with active and semi-supervised learning, Autom. Softw. Eng. 19 (2012) 201–230.
[43] G. Canfora, A.D. Lucia, M.D. Penta, R. Oliveto, A. Panichella, S. Panichella, Multi-objective cross-project defect prediction, Proceedings of 6th International Conference on Software Testing, Verification and Validation, Luxembourg (2013) 252–261.
[44] M. Harman, S. Islam, Y. Jia, L.L. Minku, F. Sarro, K. Sirivisut, Less is more: temporal fault predictive performance over multiple hadoop releases, in: Proceedings of 6th International Symposium on Search Based Software Engineering, Fortaleza, 2014, pp. 240–246.
[45] J. Demšar, Statistical comparisons of classifiers over multiple data sets, J. Mach. Learn. Res. 7 (2006) 1–30.
[46] E.R. Delong, D.M. Delong, D.L. Clarke-Pearson, Comparing the areas under two or more correlated receiver operating characteristic curves: a nonparametric approach, Biometrics 44 (1998) 837–845.
[47] J.P. Espada, V.G. Diaz, R.G. Crespo, O.S. Martinez, B.C.P. G-Bustelo, J.M.C. Lovella, Using extended web technologies to dvelop bluetooth multi-platform mobile applications for interact with smart things, Inf. Fusion 21 (2015) 30–41.
[48] J.P. Espada, V.G. Diaz, R.G. Crespo, B.C.P. G-Bustelo, J.M.C. Lovella, An intelligent mobile web browser to adapt the mobile web as a function of the physical environment, IEEE Latin Am. Trans. 13 (2015) 503–509.
[49] R. Malhotra, K. Nagpal, P. Upmanyu, N. Pritam, Defect collection and reporting system for git based open source software, ICACCI (2014).
[50] B. Henderson-Sellers, Object-Oriented Metrics: Measures of Complexity, Prentice-Hall, Inc., Upper Saddle River, NJ, USA, 1996.
[51] J. Bansiya, A. Davis, A hierarchical model for object-oriented design quality assessment, IEEE Trans. Softw. Eng. 28 (2002) 4–17.
[52] R. Martin, OO design quality metrics—an analysis of dependencies, Workshop Pragmatic and Theoretical Directions in Object-Oriented Software Metrics, OOPSLA'94 (1994).
[53] M.H. Tang, M.H. Kao, M.H. Chen, An empirical study on object-oriented metrics, Proceedings of Metrics (1999) 242–249.
[54] M. Hall, Correlation-based feature selection for discrete and numeric class machine learning, Proceedings of the 17th Int. Conference on Machine Learning (2007) 359–366.
[55] J. Hanley, B.J. McNeil, The meaning and use of the area under a receiver operating characteristic ROC curve, Radiology 143 (1982) 29–36.
[56] H. He, E.A. Garcia, Learning from imbalanced data, IEEE Trans. Knowl. Data Eng. 21 (2009) 1263–1284.
[57] M. Stone, Cross-validatory choice and assessment of statistical predictions, J. R. Soc. Ser. B 36 (2) (1974) 111–114.
[58] M. Friedman, A comparison of alternative tests of significance for the problem of m rankings, Ann. Math. Stat. 11 (1940) 86–92.
[59] I. Gondra, Applying machine learning to software fault-proneness prediction, J. Syst. Softw. 81 (2008) 186–195.
[61] T.M. Khoshgoftaar, N. Seliya, N. Sundaresh, An empirical study of predicting faults with case-based reasoning, Softw. Qual. J. 14 (2006) 85–111.
[62] L. Briand, J. Daly, J. Wust, A unified framework for cohesion measurement in object-oriented systems, Empir. Softw. Eng. 3 (1998) 65–117.
[63] L. Briand, J. Daly, J. Wust, A unified framework for coupling measurement in object-oriented systems, IEEE Trans. Softw. Eng. 25 (1999) 91–121.
[64] R. Malhotra, Comparative analysis of statistical and machine learning methods for predicting faulty modules, Appl. Soft Comput. 21 (2014) 286–297.

Please cite this article in press as: R. Malhotra, An empirical framework for defect prediction using machine learning techniques with Android software, Appl. Soft Comput. J. (2016), http://dx.doi.org/10.1016/j.asoc.2016.04.032

International Journal of Innovative
Computing, Information and Control
Volume **12**, Number **2**, April **2016**

ICIC International ©2016 ISSN 1349-4198
pp. 615–634

BENCHMARKING FRAMEWORK FOR MAINTAINABILITY PREDICTION OF OPEN SOURCE SOFTWARE USING OBJECT ORIENTED METRICS

Anuradha Chug[1] and Ruchika Malhotra[2]

[1]University School of Information and Communication Technology
Guru Gobind Singh Indraprastha University
Sector 16-C, Dwarka, New Delhi 110077, India
anuradha@ipu.ac.in

[2]Department of Software Engineering
Delhi Technological University
Bawana Road, Delhi 110042, India
ruchikamalhotra2004@yahoo.com

Received October 2015; revised January 2016

Abstract. *Software maintainability is measured as the ease with which the existing software could be modified and often predicted during the development stage on the basis of some measurable design characteristics. Controlling the software maintainability and understandability of any open source software (OSS) system is extremely challenging because it is written and constantly modified by the developers located all over the world. The current study analyzes the effectiveness of machine learning (ML) techniques for the maintainability prediction of OSS systems. In this work large-scale empirical comparisons of thirteen classifiers over seven open source datasets were conducted followed by extensive statistical tests and post hoc analysis to establish the confidence on the performance of one ML technique over another. The results show two important findings: firstly, we observed that overall good prediction accuracy is achieved by almost all ML techniques; secondly the prediction models using genetically adaptive learning ML technique and group method of data handling (GMDH) technique perform better than the other ML techniques in the context of OSS systems. The outcome of this investigation would be helpful for developers in order to predict maintenance behavior of the software at the earlier stages of software development lifecycle (SDLC). Accordingly, they can optimize their resource allocations, prioritize maintenance tasks and produce high-quality low maintenance software systems. Additionally, it also has numerous other applications such as schedule planning, cost estimation, quality assurance testing, software debugging, budget preparation, and software performance optimization.*

Keywords: Empirical validation, Software maintainability prediction, Object-oriented metrics, Open source software, Friedman test, Post hoc analysis, Feature subselection

1. **Introduction.** Software maintenance is an important phase in software development life cycle (SDLC) as it plays a determinant role in finding the total project cost of any software [1]. Maintainability of the software cannot be measured until the software system reaches to the operational phase; however, by then it would be too late to rectify and optimize the quality. In this regard, it has become increasingly important to develop maintenance prediction models to assess accurate maintainability during the early phases of the SDLC. This can be done with the help of some measurable software design characteristics such as cohesion, coupling, abstraction, complexity and inheritance [2,3]. In open source software (OSS), practitioners across the globe are allowed to change, expand and redistribute the newly created version without any requirement of the license [4]. Changes

in OSS are made continuously in order to remove defects, improve functionalities, and increase usefulness [5]. Estimating the maintainability of OSS becomes more challenging due to the lack of technical support and the absence of adequate documentation. Although various maintainability prediction models using statistical and machine learning (ML) techniques have been developed in past [6-25], to the best of authors' knowledge, studies on observing the maintainability of OSS systems are very limited except one conducted by Zhou and Xu [16]. Even though Ramil et al. [17] have compiled many empirical studies on OSS, all the studies focused on intuitively judging the software maintainability instead of creating a mathematical prediction model. Myrtveit et al. [18] have also raised an important issue that more reliable research procedures must be developed before believing on the outcome of any one of the prediction models. In order to address these issues an effort has been made in this study to find the answer of the following three research questions:

- **RQ1**: Does the impact of object-oriented (OO) metrics on maintainability exist in the context of OSS?
- **RQ2**: What is the comparative performance of ML techniques for maintainability prediction using OSS?
- **RQ3**: Which pairs of ML techniques perform significantly different from each other in terms of prediction accuracy measures?

We extensively compare the experimental results of thirteen ML classifiers over seven OSS using statistical test followed by post hoc analysis to scrutinize if there exists a significant difference among the performance of any particular ML technique. The thirteen selected classifiers include Linear Regression (LR), M5Rules, Decision Tree (DT), Support Vector Machine (SVM), KStar, Bagging, Jordan Elman Recurrent Network (JERN), Back Propagation Network (BPN), Kohonen Network (KN), Probabilistic Neural Network (PNN), Group Method of Data Handling (GMDH), General Regression Neural Networks (GRNN), and GRNN with Genetic Adaptive Learning (GGAL). The source code of seven OSS Drumkit, OpenCV, Abdera, Ivy, Log4j, JEdit and JUnit is obtained from http://sourceforge.net and https://apache.org to carry out this widespread investigation.

The rest of the paper is organized as follows. Section 2 summarizes the related work and Section 3 describes the independent variables, dependent variables and the process of empirical data collection. Section 4 presents research methodology adopted in the current study. Section 5 describes the results and analysis. Threats to validity are discussed in Section 6 and finally Section 7 concludes the paper with future directions.

2. **Related Work.** Predicting the maintainability during early phases of SDLC helps in better planning and appropriate allocation of resources for reducing maintenance effort of the software and therefore remained the prime subject of research. Extensive research has been carried out in the past to empirically prove that software metrics can be used to determine maintainability of a software at early stages of the SDLC by various statistical and ML techniques [6-15]. Various information about the studies is compiled in Table 1, such as the type of the dataset used, validation method, ML technique, statistical test, and performance measures.

Li and Henry [8] attempted as early as in the year 1993 to validate linear regression model using two proprietary datasets, User Interface Management System (UIMS) and Quality Evaluation System (QUES) for evaluating the relationship between Chidamber and Kemerer (C&K) [26] metrics suite and maintainability. The results indicated that a total of 90% and 87% total variance in maintenance effort is accounted by C&K metrics for UIMS and QUES systems respectively. Koten and Gray [12] further validated Bayesian Belief Network using 10-cross validation on the same dataset and found it to

TABLE 1. Salient details of prediction models used by researchers in software maintainability

Study	Dataset	Metric suite	Prediction Model	Validation Method	Prediction Accuracy Measure
Li and Henry [8]	UIMS and QUES dataset	C&K metric suite	Multiple linear regression (MLR)		
Koten and Gray [12]	UIMS and QUES dataset [8]	DIT, NOC, MPC, RFC, LCOM, DAC, WMC, NOM, Size1, Size2	Linear Rgression, Bayesian Belief Network (BBN)	10-cross Validation	Absolute RES, MRE, MMRE, Pred(q)
Elish and Elish [13]	UIMS and QUES dataset [8]	C&K metric suite	Tree Nets classifier	Leave-one-out cross Validation	MRE, MMRE, Pred(q), Overestimate, Underestimate
Jin and Liu [14]	Programs developed by the students in C++	LCOM, NOC, DIT, WMC, RFC, DAC, MPC, NOM	Support Vector Machine (SVM)	none	MARE, MRE, p-value, r
Kaur et al. [15]	UIMS and QUES dataset [8]	LCOM, DIT, WMC, NOC, RFC, DAC, MPC, NOM	ANN, Fuzzy Inference Systems (FIS) and Adaptive Neuro FIS (ANFIS)	Hold-out	MARE, MRE, p-value, r
Zhou and Xu [16]	Open Source Software	NPAVGC, OSAVG, CSAO, CSA, SDIT, SLCOM, SRFC, SWMC, SNOC, MHF, POF, NCLASS, MNETH, PDIT	Univariate and Multivariate Regression Analysis	Leave-one-out cross Validation	R2, p-value, Std. Error
Zhou and Leung [19]	UIMS and QUES dataset [8]	WMC, DIT, NOC, RFC, LCOM, MPC, DAC, NOM, Size1, Size2	MLR, ANN, RT, SVM, MARS	Leave-one-out cross Validation	RES, ARE, MRE, MMRE
Malhotra and Chug [21]	Proprietary systems namely FLM, and EASY	WMC, DIT, NOC, RFC, LCOM, MPC, DAC, NOM, Size1, Size2	GRNN, FF3LBPNN, and GMDH	Hold-out	MRE, MMRE, Pred(q), Overestimate, Underestimate
Malhotra and Chug [23]	Proprietary systems namely FLM, EASY, SMS, IMS and ABP System	WMC, DIT, NOC, CBO, RFC, LCOM, SCCR, NODBC, MI, Cyclomatic Complexity	GMDH	10 fold cross validation	MRE, MMRE, Pred(q)
Malhotra and Chug [24]	UIMS and QUES dataset [8]	WMC, DIT, NOC, RFC, LCOM, MPC, DAC, NOM, Size1, Size2	GMDH, GA, PNN	Hold-out	MRE, MMRE, Pred(q), R-Square, p-value

be significantly better model in terms of precise prediction accuracy. Elish and Elish [13] corroborate relatively new Technique, TreeNets for software maintainability Predictions. They compared their results with other prevalent models and found them to be least cost effective with more prediction accuracy on UIMS and QUES datasets. The results were analyzed using various prediction accuracy measures such as Magnitude of Relative Error (MRE), Mean Magnitude of Relative Error (MMRE) and Prediction accuracy with less than 25% error (Pred 0.25).

Further, in the year 2010, Kaur et al. [15] conducted the study and analyzed the prediction capability of the Adaptive Neuro Fuzzy Inference System (ANFIS) technique on UIMS and QUES dataset using Hold-out validation and the outcome showed better performance as compared to previous studies. In another study conducted by Malhotra and Chug [21], the predicted capability of the Group Method of Data Handling (GMDH) technique was analyzed using the UIMS and QUES dataset using MRE, MMRE, Pred(0.25) and Mean Absolute Relative Error (MARE) measures. The results indicated that the hybrid models such as GMDH has enhanced capabilities to capture the design characteristics using C&K metrics and hence results were found to be more precise. Dagpinar and Jhanke [10] suggested that instead of designing level metrics of structure languages, OO metrics should be used for precise capturing while making any prediction model. Further, they also recorded the significant impact of direct coupling metric and size metric on software maintainability instead of other metrics such as cohesion, inheritance and indirect coupling. Aggarwal et al. [25] in his study suggested that since maintainability is very subjective in nature, the use of the fuzzy model for its measurement would be more appropriate.

Overall, the studies reported on the subject reveal that C&K metric suite [26] is quite popular and used extensively in most studies [10-13,19,21] because of its research focus and capability of capturing the OO metrics more accurately. The researchers are always constrained against non-availability of genuine datasets to conduct their validation studies and test newer prediction models of determining maintainability. However, the datasets of two proprietary software systems comprising of UIMS and QUES made public by Li and Henry [8] opened the doors for additional research studies to validate the maintainability prediction models and therefore majority of researchers used the datasets in their experiments [10-13,19,21].

We also found that in two research studies [14,20], datasets developed from the students' software was used to validate their prediction models. In the first study, Jun and Liu [14] validated their prediction model using the datasets collected from the software systems developed by graduate students. Their results show that when Support Vector Machine (SVM) is combined with clustering for the purpose of maintenance effort predictions, correlation between C&K metric suite and maintainability was found to be as high as 0.769 which is statistically quite significant. In the second study, Misra [20] used the datasets collected from a pool of 50 C++ programmes and deployed them in LR classifier as well as intuitive analysis based model using more than twenty design and code measures.

Although many maintainability prediction models have been proposed in the literature, almost all of them have used either the traditional dataset given by Li and Henry [8] in the year 1993 or used the students' programmes to compare the performance of ML techniques. The only exception reported in literature on OSS was by Zhou and Xu [16] but they analyze only statistical regression based model for the correct estimation of maintainability. As the interest for OSS has been rising across the globe, a powerful customized ML technique based prediction model for OSS was seen as the potential scope of research. In order to get unbiased, accurate and repeatable maintainability prediction model for OSS, the current study attempts to create an empirical framework using 13

ML techniques. Outcome of the current research has been further assessed over various releases of seven OSS comprising of Drumkit, OpenCV, Abdera, Ivy, Log4j, JEdit and JUnit available at http://www.github.com and http://www.sourceforge.net repositories.

3. **Research Background.** This section presents the selection of dependent and independent variables and subsequently the process of collecting the empirical data for the validation of ML techniques. Our goal was to capture the various attributes of OO paradigm such as size, coupling, cohesion, abstraction, complexity and inheritance. In the current study, we have used C&K metric suite which is very common and used by various researchers [10-13,19,21]. In one of our previous studies [23] we realized few shortcomings in C&K metric suite such as it does not take into account the structural complexity of the software and any metric on account of the amount of database handling. In order to overcome such shortcomings, in addition to C&K metric suite, we have also included the metric suites proposed by Henderson-Sellers [27] and Bansiya and Davis [28].

The dependent variable is 'Change' defined as the number of changes in source code in terms of addition, deletion or modification in the lines of code. In Subsection 3.1, independent variables are explained, in Subsection 3.2, we have discussed the dependent variable and Subsection 3.3 give details of the process of empirical data collection.

3.1. **Independent variables.** Various OO metrics were carefully selected from the metric suites proposed by researchers [26-28] to capture all the design attributes such as coupling, cohesion, inheritance, abstraction and complexity of OO paradigm as summarized in Table 2.

3.2. **Dependent variables.** The dependent variable in the current study is maintenance effort measured by observing the number of changes made between two consecutive versions and it is counted in terms of a number of lines of source code added, deleted or modified in the newer version with respect to the older version for each class. We identify the common classes between two consecutive versions and compute the exact number of lines where change is performed. Any addition or deletion of a line in the current version with respect to an older version is counted as one change whereas any modification of the line is counted as two changes. The value of each OO metric for each class is calculated and combined with the respective changes made into that class to generate the data points. Same approach is adopted by many researchers [6-15,19,21-24].

3.3. **Empirical data collection.** We explore open source repositories for collecting the empirical data keeping in mind two important characteristics which include that it should follow OO paradigm and it should have a high number of downloads in recent times (last 12 months) as it is a clear indication that there are active users contributing constantly.

The details of the selected OSS systems in terms of versions, release date, size, number of classes, etc. are summarized in Table 3 and their functioning in brief are explained as below:

- Drumkit is a Java Mobile based game on JAVA-JME platform. (https://github.com/nokia-developer/drumkit-jme)
- OpenCV stands for Open Source Computer Library designed for providing computational efficiency with a main focus on real-time applications. (http://sourceforge.net/projects/opencvlibrary)
- Abdera is an open source Atom parser generator used for client and server to build high-performance functionality of Internet by producing high quality designed documents. (https://git.apache.org/abdera)

- Ivy is a set of open source libraries and programs that allow applications to broadcast information through text messages, with a subscription mechanism based on regular expressions. (https://git.apache.org/ivy)
- Log4j allows the developer to control which log statements are output with arbitrary granularity. It is fully configurable at runtime using external configuration files. (https://git.apache.org/Log4j)
- JEdit is a highly customizable text editor written in Java and runs on any operating system. It can be extended with macros written in scripting languages. (https://jedit.svn.sourceforge.net/svnroot/jedit)

TABLE 2. Independent variables

Metrics	Ref	Definition
WMC (Weighted Methods per Class)	[26]	It counts the sum of McCabe's Cyclomatic complexities of all local methods in a class.
DIT (Depth of Inheritance Tree)	[26]	It calculates the depth of the said class in inheritance from the root class.
NOC (Number of Children)	[26]	It counts the number of immediate subclasses', i.e., number of children of the said class in the inheritance hierarchy.
RFC (Response For a Class)	[26]	It counts the number of local methods and the number of nonlocal methods which are called by the local methods.
DAM (Data Access Metric)	[28]	It is calculated as the ratio of private + protected attributes of the said class to the total number of attributes defined in that class.
MOA (Measure Of Aggression)	[28]	It counts the percentage of user defined data declared in the said class.
MFA (Method of Functional Abstraction)	[28]	It is counted as the ratio between the inherited methods and the total number of methods in the said class.
CAM (Cohesion Among the Methods of a Class)	[28]	Based on the signatures of the methods, this metric computes the similarity among various methods of the said class.
AMC (Average Method Complexity)	[27]	It is computed as the average of McCabe's Cyclomatic Complexity of all method.
CBO (Coupling Between Object)	[26]	It is computed by counting the number of other classes to which said the class is coupled.
LCOM (Lack of Cohesion of Methods)	[26]	It is calculated by counting the number of disjoint sets of local methods in a class.
LCOM3 (Lack of Cohesion Among Methods of a Class)	[27]	Proposed by Henderson-sellers to remove some of the disadvantages of LCOM.
NPM (Number of Public Methods)	[28]	It is computed by counting the number of public methods in a given class.
Ca (Afferent Couplings)	[27]	It is counted as the number of classes calling the said class.
Ce (Efferent Couplings)	[27]	It is counted as the number of other classes called by said class.
IC (Inheritance Coupling)	[27]	It is counted as the number of parent classes to which a class is coupled.
LOC (Lines of code)	[27]	It counts the number of lines of code. Comments lines and blank lines are simply ignored.

TABLE 3. Characteristics of open source software

Software	Version	Release Date	No. of Classes	% change
Drumkit	1-0.5.0 to 1-0.6.0	25 Apr 2014	101 classes	20.34
OpenCV	2.4.10 to 3.0	12 Sept 2014	143 Classes	16.29
Abdera	1.1.2 to 1.1.3	08 Jan 2014	686 Classes	61.88
Ivy	2.2.0 to 2.3.0	21 June 2013	614 Classes	74.76
Log4j	1.2.16 to 1.2.17	31 Mar 2010	351 classes	34.50
JEdit	5.1 to 5.2	28 July 2013	417 classes	24.96
JUnit	4.10 to 4.11	29 Sept 2011	251 classes	14.644

- JUnit is an open source framework for writing and executing unit tests and defining test suite. They provide compatibility with almost all IDEs and inbuilt test drivers; hence only tests case needs to be written. (http://sourceforge.net/projects/junit/)

4. **Research Methodology.** Basically, there are two broad approaches in which the maintainability of a software can be measured, firstly through the measurement of external quality factors such as understandability, analyzability, modifiability and secondly through the measurement of internal quality metrics and use them for making software maintainability prediction model. In the first approach, external factors can only be measured by collecting the opinion from the developers who participate in writing the source code of the open source software. Conducting such surveys is not only time-consuming and involves high cost but also produces different opinions due to the subjective nature of external quality factors. The second approach of measuring the internal quality attributes through OO metrics suite has been used in many empirical studies [3,6-16]. Almost all of the studies showed the existence of the relationship between OO metrics suite and maintainability. In the current empirical investigation, the second approach is used and the adopted research methodology is shown in Figure 1.

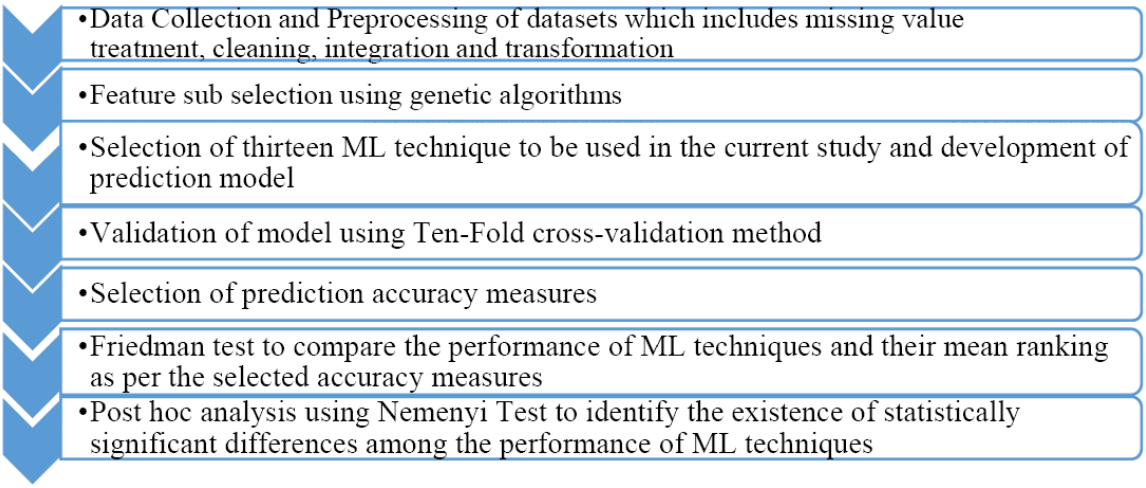

FIGURE 1. Proposed research methodology

4.1. **Data pre-processing.** Git repository mining tool 'Defect Collection and Reporting System' (DCRS) developed in the Java language at Delhi Technological University by Malhotra et al. [29] has been used for the purpose of empirical data collection from two repositories http://www.github.com and http://www.sourceforge.net. It processes the repositories and reads the change descriptions such as timestamp of committing the

incurred change, unique change identifier, type of change (defective, perfective or corrective), change descriptions, list of changes and counting the line of code where changes took place and generates the reports containing detailed information for each class. It also calculates a total number of changes, values of the OO metrics for each class and provides insight such as cloning of Git Repositories and Self Loggings. For example, if Abdera 1.1.2 (older version) and Abdera 1.1.3 (newer version) are being analyzed in DCRS, processing the change logs generates the number of changes performed from older version to newer version per class. Similarly, processing the classes in older version generates the class wise values of each OO metric. Finally, both are combined for each class to generate the data points. Figure 2 graphically summarizes the changes made into each system selected in the current study.

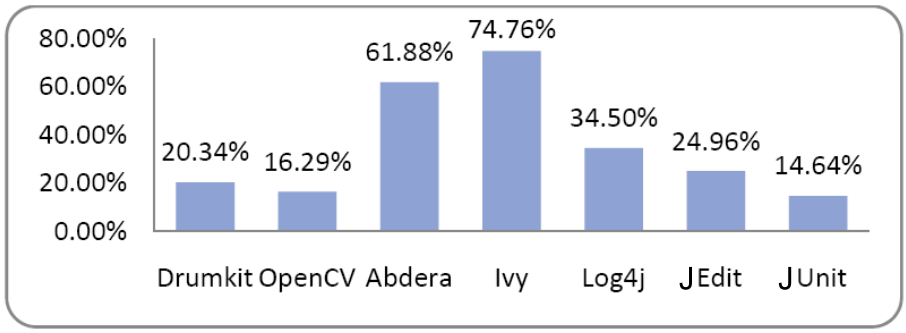

FIGURE 2. Summary of changes made into each dataset

During the preprocessing we extract those classes which are common in current as well as the previous version for each software system. Classes either added in latest version or deleted from the older version are simply discarded. Library classes, as well as interface classes, are also excluded from the list.

4.2. **Feature sub-selection.** The aim for carrying out the feature sub-selection process is to remove irrelevant and redundant independent variables from the dataset before it can be used further by the seventeen classifiers selected in the current study for training purpose as suggested by Donell [30]. This dimensionality reduction process not only reduces the unnecessary attributes and irrelevant noisy data, but it also enhances the execution time, improves the quality of datasets and thereof amplifies the accuracy of the prediction process. Kohavi and John [31] explained the feature selection algorithms and categorized them in two types: Wrappers and Filters. While evaluating the most valued subset from a given set of attributes, filter method does not require the classification algorithms whereas wrappers method needs them. In this empirical investigation, genetic algorithms (GA) are used for feature sub-selection process as suggested by Yang and Honavar [32]. GA is deployed using three operators: selection, crossover and mutation. In selection operation, every solution is evaluated on the basis of predefined fitness function and good solutions are picked up to breed new generations. In crossover operations, these good solutions are combined to generate better off springs. In mutation operation, solution string is mutated to maintain genetic diversity from one generation to the next. In each generation, the population is evaluated against the predefined fitness function to test if the termination criterion is met or not. This genetic cycle of applying all three operators on the population and re-evaluation continues until a specific termination criterion is achieved.

TABLE 4. Description of the machine learning techniques

Name of the ML Technique	Reference	Description
Linear regression (LR)	Hoffmann and Shafer [38]	LR first determines the percent of variance occurring in the dependent variable due to each independent variable separately and further used this knowledge to predict the dependent variable.
M5Rules	Kohavi and Sommerfield [39]	Accurate and compact rule sets are generated using separate-and-conquer paradigm in this technique. Initially, the rules are induced and later on revised using complex global optimization procedure to build a model tree and further used for predictions.
Decision Tree (DT)	Kohavi and Sommerfield [39]	It creates a decision tree based on the concept of entropy and information gain. During the construction as per the pre-specified splitting criterion, the most qualified independent variable is selected at the node.
Support Vector Machine (SVM)	Cortes and Vapnik [40]	Although SVM was originally developed for solving the binary classification problems, later on it was also extended to solve the regression problems. Hyperplane is created in this method to separate the data into the nonlinear region and finally with the help of kernel function data points are mapped into different dimensional space.
K-Star	Lee and Song [41]	It is an instance-based classifier that uses similarity function from the training set to classify the test set. This method uses entropy based distance function and missing values are averaged by column entropy curves.
Bagging	Brieman [42]	Developed by Leo Breiman to increase the accuracy of regression models, it reduces the variance and helps to avoid the problems associated with over-fitting. The idea is to build various similar training sets and train a new function for each of them.
Jordan Elman Recurrent Network (JERN)	Lee and Song [41]	It is special kind of ANN with the recurrent network in which hidden layers are fed directly into the input layers. Although slower but the recurrent network has the ability to learn sequences. It is a very powerful learning as the hidden layer is fed back into the input layer, so features detected in all previous patterns are fed into the network with each new pattern.
Back Propagation Network (BPN)	Specht and Shapiro [43]	It is a supervised learning process in which a new pattern is presented to the network through a forward activation flow of outputs in each cycle and the backward error propagation of weight adjustments is performed.
Kohonen Network (KN)	Kohonen [44]	It is an unsupervised learning network which neither uses any sort of activation function nor bias. It does not use any hidden layer. When a pattern is presented to a Kohonen network, only one of the output neurons is selected as the winner.
Probabilistic Network (PNN)	Specht [45]	PNN consists of several sub-networks in which the input nodes are the set of measurements, second layer consists of the Gaussian functions formed using the given set of data points as centers, the third layer performs an average operation of the outputs from the second layer for each class and the fourth layer performs a vote, selecting the largest value to determine the associated class label.
Group Method of Data Handling (GMDH)	Ivakhnenko and Koppa [46]	It is ideal for complex, unstructured system where the investigator is only interested in obtaining a high order input-output relationship. It can build a multinomial of a degree in hundreds whereas standard multiple regression exhausted in computation.
General Regression Neural Networks (GRNN)	Specht [47]	It is a memory-based network with one-pass learning technique with a highly parallel structure which provides smooth transitions from one observed value to another even with sparse data in a multidimensional measurement space.
GRNN Genetic Adaptive Learning (GGAL)	Specht [47]	By simulating the biological evolution, this genetic inspired neural network method has the ability to search large and complex spaces to determine near optimal solutions in time and space efficient manner.

4.3. **Machine learning techniques.** This section presents the definition of all thirteen ML techniques used in the current study as compiled in Table 4 for making prediction models. All the ML techniques are divided into two sets, and first set contains all those ML techniques which are basic in nature and non-bioinspired such as LR, M5Rules, DT, SVM, KStar, and Bagging. Second set consists of classifiers based on the bio-inspired nonlinear statistical data modeling technique such as ANN. In this set all ML techniques explored the complex relationships between inputs and outputs to identify the patterns during the training process and further used the same knowledge for predictions process such as JERN, BPN, KN, PNN, GMDH, GRNN, and GGAL.

4.4. **Ten-fold cross-validation.** Ten-fold cross-validation scheme is used to train and validate the software maintainability prediction model. In this technique, the data is divided into ten random partitions. Each classifier trains itself from 9 partitions of the datasets and validates itself on the remaining 10^{th} partition. The process is repeated 10 times and the results of all folds are combined to produce the final result. It ensures that the training of the model from the dataset remains unbiased and accurate.

4.5. **Prediction accuracy measures.** Estimating the accuracy of the predicted model is a very important step in any empirical study. Each time the predicted value of the dependent variable is generated from the model, which is compared with the respective actual value to find the errors. Although many types of residual-based measures have been recommended in literature to evaluate the prediction accuracy of any given model, however, following three prevalent measures suggested by Kitchenham et al. [33] and Conte et al. [34] are used to compare the performance of various ML techniques used in the current study.

4.5.1. *Mean absolute error.* Mean absolute error (MAE) is a normalized measure to detect the discrepancy between actual and predicted value of dependent variable (maintenance effort in this case). In MAE first the difference between the actual and predicted value is calculated and the result is divided by the actual value. Then, the absolute value for each data point is summed and is divided by the total number of data points. MAE is defined as follows:

$$\text{MAE} = \frac{1}{N}\sum_{i=1}^{N}\frac{|\text{Actual Value} - \text{Predicted Value}|}{(\text{Actual Value})} \tag{1}$$

where N is the number of classes.

4.5.2. *Root mean squared error.* Another measure used to compare the ML techniques is the root mean squared error (RMSE) defined as the square root of the variance of the residual value. In RMSE, the difference between the predicted values with actual values for each class is squared then averaged and finally the square root of this average value is taken. The RMSE measure is defined as:

$$\text{RMSE} = \sqrt{\frac{1}{N}\sum_{i=1}^{N}(\text{Actual Value} - \text{Predicted Value})^2} \tag{2}$$

This method gives comparatively high weightage to large errors as the differences are squared before they are averaged. It is chosen when large errors are most undesirable. Lower values of RMSE indicate better fitness of the model used for predictions.

4.5.3. Pred(q). Another prediction accuracy measure, selected to compare the performance of ML technique is Pred(0.25), i.e., at 25%. It calculates the proportions of the result that has MAE less than 0.25 to the total number of observations made. It is given as:

$$\text{Pred}(q) = \frac{K}{N} \tag{3}$$

where q is the specified value, K is a number of observations whose MAE is less than or equal to q and N is the total number of classes.

4.6. **Friedman test to rank the performance.** The Friedman's test [35] is a kind of non-parametric statistical test, which is used to find if there exists significant difference among the performance of ML techniques and rank them accordingly. The following hypothesis is formed before conducting the Friedman test on results.

Null Hypothesis (H0): There is no significant difference among the performance of participant ML techniques.

Alternate Hypothesis (H1): There exists significant difference among the performance of participant ML Techniques.

As suggested by Demsar [36], when performances of multiple classifiers needed to be compared on multiple datasets, it is one of the best techniques. The Friedman measure is defined as follows:

$$\chi_r^2 = \left(\frac{12}{Nk(k+1)} \sum_{i=1}^{k} R^2 \right) - 3N(k+1) \tag{4}$$

where R is the average rank of the individual method, N is the number of datasets; k is number of ML techniques considered for ranking. The value of $\chi_{\text{calculated}}$ is calculated from the given Equation (4) and compared with $\chi_{\text{tabulated}}$ using chi-square distribution table. If the value of Friedman Measure, i.e., $\chi_{\text{calculated}}$ lies in the critical region, Null hypothesis is rejected, alternate hypothesis is accepted and it is concluded that there exists significant difference among the performance of participant ML techniques. Otherwise Null hypothesis is accepted, alternate hypothesis is rejected and concluded that there does not exist significant difference between the performance of participant ML techniques.

Further, individually every technique is also ranked using Friedman's Individual Rank (FIR) based on undermentioned Equation (5).

$$\text{Friedman's Individual Rank (FIR)} = \frac{C}{N} \tag{5}$$

where C is the cumulative rank and N is number of datasets. FIR for each technique is calculated and the technique which scores lowest value of FIR is considered as the best performer and the technique achieving the highest rank is termed as worst performer. If the results based on the mean rank achieved using FIR for both the performance measure MAE or RMSE is found to be significant, it is advisable to check whether the difference in mean rank is statistically significant or not by means of post hoc analysis using Nemenyi test.

4.7. **Post hoc analysis using Nemenyi test.** When the sample size is equal and the data is not normalized, Nemenyi test is a very powerful test for post hoc analysis [37]. It is used to compare the performance of ML models for finding the existence of statistically significant difference among themselves. First of all critical difference (CD) is calculated using Equation (6) which depends upon the number of techniques, number of datasets

and the level of significance.

$$CD = q_\alpha \sqrt{\frac{k(k+1)}{6N}} \tag{6}$$

where k means the number of techniques, N is the number of the data sample. The value of q_α is based on Studentized range statistics for a given level of significance as defined by Demsar [36]. While comparing the performance of two ML techniques during post hoc analysis, the difference between their respective FIR values is calculated. If this difference is greater than or equal to the value of CD, it is concluded that the performance of two ML techniques is statistically significant at the selected significance level α. If the difference is less than the value of CD, it is concluded that the difference between their performances is not statistically significant.

5. **Result Analysis.** This section presents the prediction results of various classifiers based on ML techniques for maintainability prediction using OO metrics.

5.1. **Feature sub selection (FSS).** The first step in the empirical study was FSS; in which irrelevant and unimportant features were removed using GA. Table 5 summarizes the relevant metrics found after applying FSS using GA over all the releases of seven datasets selected in the current study. In total 17%, 17%, 41%, 35%, 23%, 41% and 35% reductions were observed for Drumkit, OpenCV, Abdera, Ivy, Log4j, JEdit and JUnit datasets respectively. On an average 24% saving is observed for all datasets.

Out of the seventeen independent variables, we found that LCOM3, LOC and DIT are the most commonly selected OO metrics in the current study. Efferent coupling Ce is also found to be significant in Abdera and Log4j Systems. We also found that the results obtained using reduced set of independent variables after applying FSS were slightly better as compared to the results obtained using all independent variables in prediction models. Similar observations were made by Kohavi and John [31] as well as Yang and Honavar [32] that not only the impact of FSS on the accuracy is minimal but they are also capable of capturing all the characteristics irrespective of the size of the extracted subset. Moreover, the time consumed by prediction model on newly reduced dataset using FSS is comparatively lesser than the time consumed on actual dataset.

Table 5. Metrics obtained using feature sub-selection using GA algorithm

Software Name	Selected Relevant OO Attributes
Drumkit	WMC, RFC, DIT, LCOM3
OpenCV	CBO, DIT, LCOM3, LOC
Abdera	Ce, NPM, LOC, LCOM3, DAM, CAM
Ivy	LCOM3, LOC, DAM, MOA, CAM, AMC
Log4j	NPM, Ce, LOC, LCOM3, DIT, MOA, CAM
JEdit	WMC, LOC, DIT, DAM, CAM, AMC
JUnit	RFC, CBO, LCOM, LCOM3, NPM, IC

RQ1: Does the impact of OO metrics on maintainability exist in the context of OSS?

To assess the outcome of ML techniques based prediction models, their prediction accuracy was measured through MAE, RMSE, Pred(0.25) and Pred(0.75). Their values were evaluated as per criterion set by previous researchers [33,34] that any prediction model is considered accurate if its MAE values are less than 0.40 also the value of Pred(0.25) should always be greater than Pred(0.75).

TABLE 6. MAE values over seven datasets

Dataset	Drumkit	OpenCV	Abdera	Ivy	Log4j	JEdit	JUnit
LR	0.57	0.48	0.41	0.29	0.36	0.38	0.54
M5Rule	0.49	0.52	0.43	0.37	0.38	0.41	0.52
DT	0.58	0.57	0.44	0.39	0.42	0.45	0.49
SVM	0.43	0.64	0.46	0.49	0.46	0.61	0.52
KStar	0.45	0.62	0.51	0.33	0.48	0.42	0.43
Bagging	0.51	0.45	0.43	0.41	0.47	0.52	0.44
JERN	0.53	0.54	0.41	0.59	0.51	0.52	0.44
BPN	0.42	0.58	0.61	0.37	0.35	0.42	0.47
KN	0.56	0.49	0.37	0.41	0.43	0.52	0.50
PNN	0.38	0.42	0.38	0.53	0.37	0.41	0.47
GMDH	0.49	0.37	0.32	0.34	0.32	0.30	0.35
GRNN	0.38	0.42	0.45	0.41	0.32	0.49	0.48
GGAL	0.33	0.31	0.29	0.36	0.28	0.34	0.36

Firstly, we present the results of all 13 ML techniques for maintainability prediction models validated using 10-fold cross validation on seven OSS. Difference between the predicted value and actual value is compared and analyzed using various accuracy measures such as MAE, RMSE, Pred(25%) and Pred(75%) using Equations (1), (2) and (3) respectively.

The MAE values of each ML technique for all seven datasets used in the study are summarized in Table 6. For example, it is observed that when LR technique was applied on JEdit datasets, it gave an accuracy of 62% (since the error is 0.38, accuracy is 100-38). Similarly, we found 67% accuracy when GGAL technique applied on Drumkit datasets respectively. The accuracy of all the ML techniques w.r.t. MAE on all seven selected datasets lies between the ranges of 39-77% which is quite encouraging. Thus, it highlights the capability of ML technique for effective maintainability predictions of OSS.

The value of RMSE is obtained using Equation (2) after performing ten runs of ten-fold cross-validation for each ML technique on each dataset tabulated in Table 7. Each row represents the RMSE value of a particular technique on specific datasets. For example, first row compiles the value of RMSE when LR technique is used with all seven datasets and generates values as 0.66, 0.56, 0.61, 0.58, 0.49, 0.42 and 0.47 respectively.

Prediction accuracy of each classifier on each dataset is calculated at 25% as well as at 75% and the results are compiled in Table 8. While compiling the results for each ML technique, each dataset is divided in two sub-columns; first column contains the values of Pred(0.25), i.e., 25% and second column contains the values of Pred(0.75), i.e., 75%. It also helps in determining whether the results are as per the criterion set by [33,34] that any prediction model is considered accurate if the value of (0.25) is less than Pred(0.75). As per the results presented in Tables 6, 7, and 8 for the respective values of MAE, RMSE, Pred(25%) and Pred(75%), we found that even though the prediction models for software maintainability usually attain less accuracy [10-13,19,21], in the current study we found their reasonable values.

When we analyzed the values of pred(0.25) and pred(0.75) from Table 8, it is recorded in the range of 72-78% for Pred(25%) and 66-89% for Pred(75%) which is quite reassuring that ML techniques are very effective. With respect to Pred(0.25), GMDH is found to be most accurate with Log4j dataset and JUnit dataset, i.e., 79% accuracy (entries are highlighted in Table 8). We also observe that GMDH method achieved more than 70% accuracy with four out of seven datasets. Similarly, if Pred(0.75) is taken as accuracy

TABLE 7. RMSE values over seven datasets

Dataset	Drumkit	OpenCV	Abdera	Ivy	Log4j	JEdit	JUnit
LR	0.66	0.56	0.61	0.58	0.49	0.42	0.47
M5Rule	0.72	0.38	0.30	0.37	0.41	0.56	0.63
DT	0.86	0.74	0.41	0.34	0.43	0.47	0.58
SVM	0.64	0.67	0.47	0.42	0.39	0.48	0.54
KStar	0.67	0.77	0.55	0.38	0.39	0.56	0.61
Bagging	1.23	1.52	0.59	0.39	0.47	0.59	0.43
JERN	0.53	0.54	0.41	0.59	0.47	0.39	0.48
BPN	0.42	0.58	0.61	0.33	0.41	0.42	0.51
KN	0.56	0.48	0.37	0.40	0.35	0.43	0.52
PNN	0.38	0.42	0.33	0.53	0.43	0.53	0.41
GMDH	0.23	0.37	0.32	0.34	0.37	0.38	0.42
GRNN	0.38	0.42	0.45	0.41	0.32	0.49	0.47
GGAL	0.33	0.41	0.49	0.36	0.28	0.37	0.32

TABLE 8. Results of Pred(25%) and Pred(75%) over seven datasets

Dataset	Drumkit		OpenCV		Abdera		Ivy		Log4j		JEdit		JUnit	
	25%	75%	25%	75%	25%	75%	25%	75%	25%	75%	25%	75%	25%	75%
LR	62	67	58	71	56	66	61	71	63	73	59	70	54	64
M5Rule	63	69	49	69	57	76	59	74	65	75	51	73	57	55
DT	70	78	53	72	49	63	57	87	68	78	61	71	63	69
SVM	65	76	47	67	51	72	52	82	73	81	42	64	49	66
KStar	68	88	55	75	52	69	58	78	72	88	57	72	61	69
Bagging	75	79	51	69	59	72	65	77	69	**89**	43	61	38	52
JERN	68	88	69	73	72	74	62	71	74	81	61	69	52	64
BPN	62	86	57	77	62	81	73	79	77	87	49	57	60	77
KN	67	87	63	79	53	83	48	69	73	81	58	65	52	72
PNN	51	83	61	73	59	79	64	71	73	85	59	66	61	75
GMDH	69	77	73	78	65	74	78	88	**79**	86	73	84	68	**79**
GRNN	65	81	59	83	65	75	68	73	71	84	75	80	62	73
GGAL	72	85	67	82	73	72	75	69	69	88	70	83	74	81

measure, Bagging is found to be most accurate with Log4j dataset, i.e., 89% accuracy. GGAL is also found to be the best ML technique because more than 80% accuracy is achieved with five out of seven datasets at Pred(0.75). When we closely observe the range of accuracies, GGAL has performed outstandingly. Results are in the range of 67-75% across all datasets which are quite close to the criterion set by Kitchenham et al. [33] and Conte et al. [34].

Further, Figures 3(a) and 3(b) depict the MAE and RMSE values obtained by each ML technique on all the seven datasets correspondingly. Figure 3(a) clearly shows that GMDH and GGAL ML techniques have performed highest over all seven datasets. It is also evident from Figure 3(a) that minimum values recorded for MAE on all seven datasets were within the range of 0.28-0.36.

Additionally, with respect to RMSE as depicted in Figure 3(b), we found that mean values of RMSE range from 0.23-0.63. It is also observed that four ML techniques PNN, GMDH, GRNN and GGAL have achieved less than 30% error which is considered to be excellent.

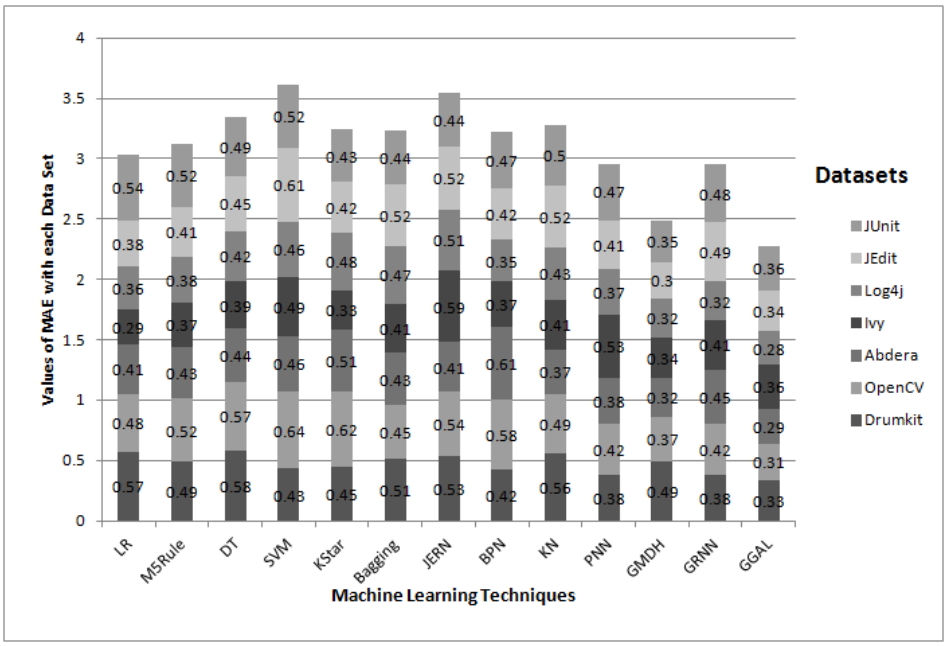

(a)

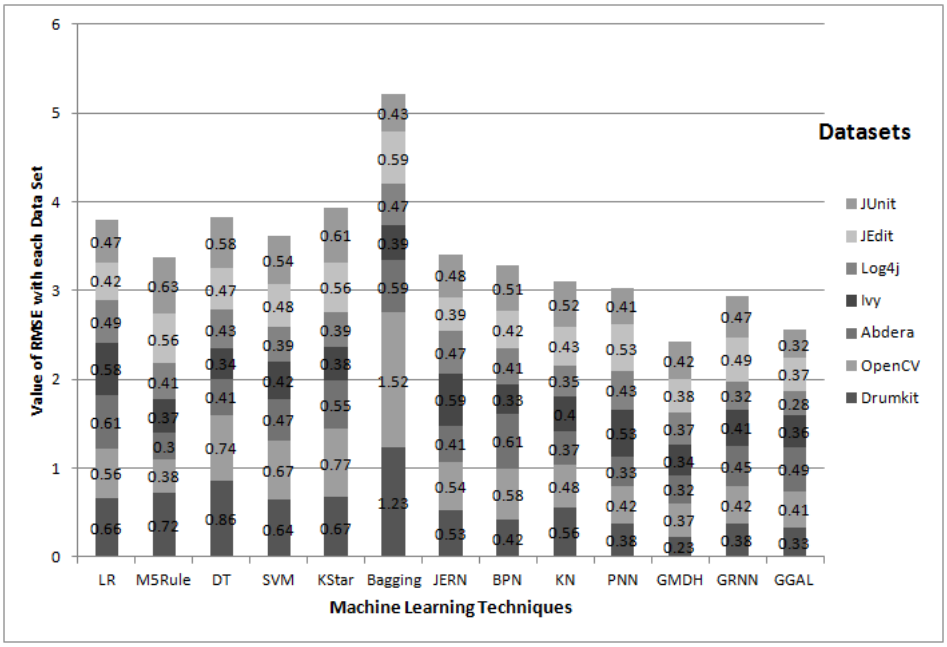

(b)

FIGURE 3. (a) MAE values of each ML technique on corresponding datasets using 10-fold cross validation, (b) RMSE values of each ML technique on corresponding datasets using 10-fold cross validation

On judging the overall performance of all ML techniques using four measures in the current study, it clearly satisfies the criteria laid down by [33,34], and hence we conclude that the impact of OO metrics on maintainability indeed exists in the perspective of OSS; *thus ML techniques can be successfully applied for their maintainability prediction using OO metrics suite.*

RQ2: What is the comparative performance of ML techniques for maintainability prediction of OSS?

We applied extensive statistical tests in order to check whether the performances of proposed ML techniques are significantly different or not. As per Demsar [36], non-parametric tests are safer as they do not assume normal distribution or homogeneity of variance in the data. In the current investigation, Friedman test was used to compare the performance of thirteen ML techniques on seven datasets. We calculate the value of critical region at 5% significance level and degree of freedom 12 (i.e., for 13 ML techniques-1). The value of $\chi_{\text{tabulated}}$ is obtained from Chi-square table where the degree of freedom is twelve (for thirteen ML techniques) and level of significance was 95%.

The null hypothesis of the Friedman test states that there is no significant difference between the performance of ML techniques. We found that at significant level 0.05 calculated value of Friedman measure, i.e., $\chi_{\text{calculated}}$ lies in the critical range for MAE as well as RMSE; hence, the *Null hypothesis is rejected and alternative hypothesis is accepted and it is concluded that significant difference exists among the performance of participant ML techniques.*

Further, in order to rank the performance of each of the ML technique, their FIR is calculated using Equation (5) and compiled in Table 9 and Table 10 for MAE and RMSE respectively. As discussed earlier, lower the mean rank means better the performance. The outcome of the Friedman test using FIR for ranking as compiled in Table 9 with respect to MAE measure indicates that the performance of *GGAL technique is the best and GMDH is the second best technique.*

TABLE 9. Mean ranking of ML techniques by applying Friedman test on MAE

ML Tech	GGAL	GMDH	PNN	GRNN	LR	BPN	M5Rule	KStar	Bagging	KN	DT	JERN	SVM
Mean Rank	1.79	2.71	3.57	4.36	5.36	6.64	7.14	8.57	9.1	9.43	10.6	11.28	11.57

TABLE 10. Mean ranking of ML techniques by applying Friedman test on RMSE

ML Tech	GMDH	GGAL	GRNN	KN	PNN	BPN	M5Rule	JERN	DT	SVM	LR	KStar	Bagging
Mean Rank	1.21	2.08	3.79	4.14	5.79	7.28	7.87	8.32	8.5	9.21	9.57	10.36	11.58

With respect to RMSE from Table 10, we observe that GMDH technique is the second best and GGAL as the best technique for the maintainability prediction of OSS on the basis of their mean rank.

In order to ascertain whether the performance differences which exist between FIR values of various ML techniques are statistically significant or not, we proceed towards post hoc analysis in RQ3.

RQ3: In terms of performance, which ML technique is significantly better than the other techniques?

In RQ2, with the help of Friedman test, we concluded that there exists a significant difference among the performance of ML technique; hence we proceed towards post hoc analysis using Nemenyi test to determine whether the difference is actually statistically significant between the performances of ML techniques or not.

The value of CD is calculated as 6.8 after putting the values of n as 13 (number of ML techniques) and value of k as 7 (number of datasets) into Equation (6). Next, we make a pair for each ML technique with every other to calculate their rank differences (FIR) and compiled in Tables 11 and 12 for MAE and RMSE, respectively. In total, 78 such pairs were formed as we have used 13 ML techniques in our study.

In Table 11, we have highlighted those entries which have values greater than CD. It is quite evident that out of 78 pairs of ML techniques, 13 pairs (bold entries) were found to have significant differences among their performances. One pair between GGAL and KStar has attained the difference (6.78) almost touching the critical difference (6.8). Hence, 14 pairs out of 78 means, *the performance of 17.9% of pairs was found to be significantly different using statistical test and not coincidental.*

Results shown in Table 11 also depict that GGAL performed better than KStar, Bagging, KN, DT, JERN and SVM whereas GMDH performed better than DT, JERN and SVM. *Hence, on the basis of post hoc analysis of MAE, we conclude that GMDH and GGAL outperformed other ML techniques.* The difference between the performance of all other ML techniques was not found to be significant.

We performed the same procedure for RMSE and the rank difference of each pair was calculated and compiled in Table 12. Highlighted entries in Table 12 indicate that the difference of FIR between that pair of ML technique is greater than CD.

It is observed that out of 78 pairs of ML techniques, 12 pairs (bold entries) were found to have significant differences among their performances. *So, with the help of Nemenyi*

TABLE 11. Computation of pairwise rank difference amongst all ML techniques in terms of MAE

ML Tech	GGAL	GMDH	PNN	GRNN	LR	BPN	M5Rule	KStar	Bagging	KN	DT	JERN	SVM
GGAL	–	0.92	1.78	2.57	3.57	4.85	5.35	**6.78**	**7.31**	**7.64**	**8.81**	**9.49**	**9.78**
GMDH		–	0.86	1.65	2.65	3.93	4.43	5.86	6.39	6.72	**7.89**	**8.57**	**8.86**
PNN			–	0.79	1.79	3.07	3.57	5.00	5.53	5.86	**7.03**	**7.71**	**8.00**
GRNN				–	1.00	2.28	2.78	4.21	4.74	5.07	6.24	**6.92**	**7.21**
LR					–	1.28	1.78	3.21	3.74	4.07	5.24	5.92	6.21
BPN						–	0.5	1.93	2.46	2.79	3.96	4.64	4.93
M5Rule							–	1.43	1.96	2.29	3.46	4.14	4.43
KStar								–	0.53	0.86	2.03	2.71	3.00
Bagging									–	0.33	1.5	2.18	2.47
KN										–	1.17	1.85	2.14
DT											–	0.68	0.97
JERN												–	0.29
SVM													–

TABLE 12. Computation of pairwise rank difference amongst all ML techniques in terms of RMSE

ML Tech	GMDH	GGAL	GRNN	KN	PNN	BPN	M5Rule	JERN	DT	SVM	LR	KStar	Bagging
GMDH	–	0.87	2.58	2.93	4.58	6.07	6.66	**7.11**	**7.29**	**8.00**	**8.36**	**9.15**	**10.37**
GGAL		–	1.71	2.06	3.71	5.2	5.79	6.24	6.42	**7.13**	**7.49**	**8.28**	**9.5**
GRNN			–	0.35	2	3.49	4.08	4.53	4.71	5.42	5.78	6.57	**7.79**
KN				–	1.65	3.14	3.73	4.18	4.36	5.07	5.43	6.22	**7.44**
PNN					–	1.49	2.08	2.53	2.71	3.42	3.78	4.57	5.79
BPN						–	0.59	1.04	1.22	1.93	2.29	3.08	4.3
M5Rule							–	0.45	0.63	1.34	1.7	2.49	3.71
JERN								–	0.18	0.89	1.25	2.04	3.26
DT									–	0.71	1.07	1.86	3.08
SVM										–	0.36	1.15	2.37
LR											–	0.79	2.01
KStar												–	1.22
Bagging													–

test conducted on RMSE measure, 12 pairs were found to be significantly different out of 78 pairs which is almost 15.3% of the total pairs.

It is also quite apparent that GMDH-JERN, GMDH-DT, GMDH-SVM, GMDH-LR, GMDH-KStar and the GMDH-Bagging pair were found to be significant as they have a value greater than CD. GGAL was found to be performing significantly superior to SVM, LR, KStar and Bagging. GRNN and KNN also performed better than Bagging technique.

Hence, we conclude that the difference in the performances of GGAL and GMDH were statistically different significantly as well as better than other ML techniques and the difference among the performance of all other ML techniques is not found to be significant.

6. **Threats to Validity.** This empirical investigation is carried out on OSS which may not be the true representative of all those softwares used in industry but with the help of ten-fold cross-validation and repetition of same ML technique for training over seven datasets with different individuality, we have tried our best to obtain as much unbiased and generalized results as possible. The results of this study would be incomplete without the discussion of all three types of threats to validity present in every empirical investigation: External, Internal and Construct Validity.

External validity means the degree with which the results of this empirical study can be generalized. By taking seven OSS with different sizes, different characteristics, different maintenance requirements, we have reduced this threat to its minimum.

Internal validity is defined as the degree with which conclusions can be drawn about the consequence of independent variables on dependent variables. We have minimized this threat by successfully applying FSS using GA and further exploring the cumulative effects of all the selected independent variables on maintainability.

Construct validity represents the extent to which the OO characteristics are accurately captured through the independent and dependent variables used in any study. We have not stuck to only one metric suite in our study, instead seventeen different metrics were selected to capture the OO characteristics proposed by well-tested metrics suite from Chidamber and Kemerer [26], Bansiya and Davis [27], and Henderson-Sellers [28]; hence, it is reasonable to claim that this threat is also minimized.

7. **Conclusion and Future Direction.** The objective of the study was to analyze the effectiveness of ML techniques for predicting software maintainability and the results are validated using dataset collected from open source software. An extensive empirical comparison of thirteen ML techniques on seven datasets obtained from open source code repositories is conducted. Prediction models were developed using seventeen most commonly used OO metrics. We further compared the performance of ML techniques using four prediction accuracy measures MAE, RMSE, Pred(0.25) and Pred(0.75). The variations amongst the performance of various ML techniques were further evaluated for significance using Friedman test. Post hoc analysis using Nemenyi test was also conducted to identify whether there exists the statistical difference of performance between the pair of different ML techniques. The main findings of the work are summarized below.

- Feature subselection using GA was used and it could successfully reduce the dimensions by almost 26.6%.
- To measure the residual error, MAE and RMSE prediction accuracy was used and we found that GGAL and GMDH techniques perform better than other ML techniques.
- The work also confirms that ML techniques have overall fare predictive ability as Pred(0.25) values are more than 60% in all cases; hence, they can be used for making the prediction model for software maintainability of OSS.

- The superiority of GGAL and GMDH techniques over other ML techniques in the context of maintainability prediction of OSS was further confirmed by the results of Friedman test and post hoc analysis.

Hence, ML techniques based prediction models can be used to decide the ideal time for throwing away the old system and replace it by the whole new system. The results of this study are exploratory and indicative. Moreover, there might be a number of other factors that may possibly affect the results and limit their generalization. We plan more studies in future work validated on industrial software systems.

REFERENCES

[1] IEEE Std 828-1998, *IEEE Standard for Software Configuration Management Plans*, Standard, 1998.

[2] M. Jorgensen, Experience with the accuracy of software maintenance task effort prediction models, *IEEE Trans. Software Engineering*, vol.21, no.8, pp.674-681, 1995.

[3] A. D. Lucia, E. Pompella and S. Stefanucci, Assessing effort estimation models for corrective maintenance through empirical studies, *Journal of Information and Software Technology*, vol.47, no.1, pp.3-15, 2005.

[4] W. Scacchi, Understanding the requirements for developing open source software systems, *IEE Proceedings Software*, vol.149, no.1, pp.24-39, 2002.

[5] I. Samoladas, I. Stamelos, L. Angelis and A. Oikonomou, Open source software development should strive for even greater code maintainability, *Communications of the ACM*, vol.47, no.10, pp.83-87, 2004.

[6] R. K. Bandi and V. K. Vaishnavi, Turk DE: Predicting maintenance performance using object-oriented design complexity metrics, *IEEE Trans. Software Engineering*, vol.29, no.1, pp.77-87, 2003.

[7] V. R. Basili, L. C. Briand and W. L. Melo, A validation of object-oriented design metrics as quality indicators, *IEEE Trans. Software Engineering*, vol.22, no.10, pp.751-761, 1996.

[8] W. Li and S. Henry, Object-oriented metrics which predict maintainability, *Journal of Systems and Software*, vol.23, no.2, pp.111-122, 1993.

[9] F. Fioravanti and P. Nesi, Estimation and prediction metrics for adaptive maintenance effort of an object-oriented system, *IEEE Trans. Software Engineering*, vol.27, no.12, pp.1062-1084, 2001.

[10] M. Dagpinar and J. H. Jhanke, Predicting maintainability with object-oriented metric – An empirical comparison, *Proc. of the 10th Working Conference on Reverse Engineering*, pp.155-164, 2003.

[11] M. M. T. Thwin and T. S. Quah, Application of neural networks for software quality prediction using object-oriented metrics, *Journal of Systems and Software*, vol.76, no.2, pp.147-156, 2005.

[12] C. V. Koten and A. R. Gray, An application of Bayesian network for predicting object-oriented software maintainability, *Information and Software Technology*, vol.48, no.1, pp.59-67, 2006.

[13] M. O. Elish and K. O. Elish, Application of tree net in predicting object-oriented software maintainability: A comparative study, *Proc. of European Conference on Software Maintenance and Reengineering*, Kaiserslautern, Germany, pp.69-78, 2009.

[14] C. Jin and J. A. Liu, Applications of support vector machine and unsupervised learning for predicting maintainability using object-oriented metrics, *Proc. of the 2nd International Conference on Multi-Media and Information Technology*, pp.24-27, 2010.

[15] A. Kaur, K. Kaur and R. Malhotra, Soft computing approaches for prediction of software maintenance effort, *International Journal of Computer Applications*, vol.1, no.16, pp.339-515, 2010.

[16] Y. Zhou and B. Xu, Predicting the maintainability of open source using design metrics, *Wuhan University Journal of Natural Sciences*, vol.13, no.1, pp.14-20, 2008.

[17] F. J. Ramil, A. Lozano, M. Wermelinger and A. Capiluppi, Empirical studies of open source evolution, *Software Evolution*, pp.263-288, 2008.

[18] I. Myrtveit, E. Stensrud and M. Shepperd, Reliability and validity in comparative studies of software prediction models, *IEEE Trans. Software Engineering*, vol.31, no.5, pp.380-391, 2005.

[19] Y. Zhou and H. Leung, Predicting object-oriented software maintainability using multivariate adaptive regression splines, *Journal of Systems and Software*, vol.80, no.8, pp.1349-1361, 2007.

[20] S. C. Misra, Modeling design/coding factors that drive maintainability of software systems, *Software Quality Journal*, vol.13, pp.297-320, 2005.

[21] R. Malhotra and A. Chug, Application of group method of data handling model for software maintainability prediction using object oriented systems, *International Journal of System Assurance Engineering and Management*, vol.5, no.2, pp.165-173, 2014.

[22] K. K. Aggarwal, Y. Singh, A. Kaur and R. Malhotra, Application of artificial neural network for predicting maintainability using an object-oriented metric, *Trans. Engineering, Computing and Technology*, vol.15, pp.285-289, 2008.
[23] R. Malhotra and A. Chug, An empirical study to redefine the relationship between software design metrics and maintainability in high data intensive applications, *Lecture Notes in Engineering and Computer Science: Proc. of the World Congress on Engineering and Computer Science (WCECS)*, San Francisco, USA, pp.61-66, 2013.
[24] R. Malhotra and A. Chug, Software maintainability prediction using machine learning algorithm, *Software Engineering: An International Journal*, vol.2, no.2, pp.9-36, 2012.
[25] K. K. Aggarwal, Y. Singh, P. Chandra and M. Puri, Measurement of software maintainability using a fuzzy model, *Journal of Computer Sciences*, vol.1, no.4, pp.538-542, 2005.
[26] S. R. Chidamber and C. F. Kemerer, Towards a metrics suite for object oriented design, *Proc. of the 6th ACM Conference on Object-Oriented Programming, Systems Languages, and Applications*, Phoenix, AZ, 1991.
[27] B. Henderson-Sellers, *Object-Oriented Metrics: Measures of Complexity*, Englewood Cliff, Upper Saddle River, NJ, USA, Prentice-Hall Inc., 1996.
[28] J. Bansiya and C. G. Davis, A hierarchical model for object-oriented design quality assessment, *IEEE Trans. Software Engineering*, vol.28, no.1, pp.4-17, 2002.
[29] R. Malhotra, N. Pritam, K. Nagpal and P. Upmanyu, Defect collection and reporting system for GIT based open source software, *Proc. of International Conference on Data Mining and Intelligence Computing*, New Delhi, India, pp.1-7, 2014.
[30] G. M. Donell, Establishing relationships between specification size and software process effort in case environment, *Information and Software Technology*, vol.39, no.1, pp.35-45, 1997.
[31] R. Kohavi and G. H. John, Wrappers for feature subset selection, *Journal of Artificial Intelligence*, vol.97, no.2, pp.273-324, 1997.
[32] J. Yang and V. Honavar, Feature subset selection using genetic algorithm, *IEEE Intelligent System and Their Applications*, vol.13, no.2, pp.44-49, 1998.
[33] B. Kitchenham, L. M. Pickard, S. G. MacDonell and M. L. Shepperd, What accuracy statistics really measure, *IEE Proceedings Software*, vol.148, no.3, pp.81-85, 2001.
[34] S. Conte, H. Dunsmore and V. Shen, *Software Engineering Metrics and Models Book*, Benjamin-Cummings Publishing Co., Menlo Park, CA, 1986.
[35] M. Friedman, A comparison of alternative tests of significance for the problem of m rankings, *The Annals of Mathematical Statistics*, vol.11, no.1, pp.86-92, 1940.
[36] J. Demsar, Statistical comparison on classifier over multiple datasets, *Journal Machine of Learning Research*, vol.7, pp.1-30, 2006.
[37] S. Lessmann, B. Baesens, C. Mues and S. Pietsch, Benchmarking classification models for software defect prediction: A proposed framework and novel findings, *IEEE Trans. Software Engineering*, vol.34, no.4, pp.485-496, 2008.
[38] J. P. Hoffmann and K. Shafer, *Linear Regression Analysis, Assumptions, and Applications*, NASW Press, 2015.
[39] R. Kohavi and D. Sommerfield, Targeting business users with decision table classifiers, *Proc. of IEEE Symposium on Information Visualization*, pp.102-105, 1998.
[40] C. Cortes and V. Vapnik, Support-vector networks, *Machine Learning*, vol.20, no.3, pp.273-297, 1995.
[41] S. W. Lee and H. H. Song, A new recurrent neural network architecture for visual pattern recognition, *IEEE Trans. Neural Networks*, vol.8, no.2, pp.331-340, 1997.
[42] L. Brieman, Bagging predictors, *Machine Learning*, vol.24, no.2, pp.123-140, 1996.
[43] D. Specht and P. Shapiro, Generalization accuracy of probabilistic neural networks compared with back-propagation networks, *Proc. of the International Joint Conference on Neural Networks*, pp.887-892, 1991.
[44] T. Kohonen, The self-organizing map, *Proc. of the IEEE*, vol.78, no.9, pp.1464-1480, 1990.
[45] D. F. Specht, Probabilistic neural networks, *Journal of Neural Networks*, vol.3, no.1, pp.109-118, 1990.
[46] A. G. Ivakhnenko and Y. U. Koppa, Regularization of decision functions in the group method of data handling, *Soviet Automatic Control*, vol.15, no.2, pp.28-37, 1970.
[47] D. F. Specht, General regression neural networks, *IEEE Trans. Neural Networks*, vol.2, no.6, pp.568-576, 1991.

ASIAN JOURNAL OF MANAGEMENT RESEARCH
Online Open Access publishing platform for Management Research

Research Article **ISSN 2229 – 3795**

Beyond the bond: Psychological contracts in Indian startups

Rajat Kumar Sharma, Nimisha Bansal, Shikha N. Khera
Delhi School of Management, Delhi Technological University,
New Delhi – 42, India
amkumar615@gmail.com

ABSTRACT

Purpose: Key purpose of this paper is to explore the difference in the needs of the employees working in the Indian startup industry on the basis of gender, qualification and work experience they have acquired during the course of their career. Level of mutual understanding, existing between employees and employers in startup industry, is also one of the major findings of this study.

Design/methodology: Exploratory study was done to study the mutual expectations of employers and employers on an ordinal ranking scale. Simple random sampling was used to select the respondents from lower (employees) and top (employers) managerial levels from startup organizations. A total of 165 questionnaires were distributed and 105 valid responses collected.

Findings: It was found that no significant difference exists in the needs of the employees working in the Indian startup industry on the basis of gender, qualification and work experience (on the basis of Kendall's coefficient of corcodance and wilxocon test). Moreover it was found that employees are better able to understand employer's expectations (92.86%) as compared to employers understanding their expectations (77.78%).

Practical Implications: Special focus is required on behalf of top management of Indian startups to ensure provision of opportunities of promotion and career growth, fair and equitable salary as per the industry standards, and safe and healthy work environment, as these have been identified as top 3 factors rated by the employees working across startup organizations. Similarly employees should also take care of factors like flexibility in accepting variety of roles and responsibilities, honesty and up-to-mark performance (in terms of quality and quantity), as they have been rated highest by the startup employers.

Social Implications: In order to create a coherent working environment in one of the country's biggest industry, both employers and employees need to be aware of their mutual expectations. This would ultimately lead to optimal employee performance and job satisfaction, leading to high profitability of such ventures.

Keywords: Psychological Contracts, Employee Expectations, Indian Startups, Mutual Obligations

1. Introduction

There has always been some difference in the expectations of the employees and employers across all kinds of organizations and industries in this entire world. Amidst the day to day

hectic tasks of any job, an employer and employee hardly find any time to understand these mutual expectations, which keep on changing with the course of time. There are a lot of instances when both these parties are not even aware about the existence of such expectations or obligations from the other side and both parties feel that they are fulfilling their part of responsibilities with complete dedication, but in reality they are hardly accomplishing any of the unsaid or 'hidden' expectations of the other side. To reveal those unsaid and 'hidden' expectations of one party to other, a detailed study needs to be carried out to specify what are those mutual obligations which exist between an employer and employees, and how do they change with the course of time.

Since India is emerging as one of the major start-up hubs on the globe, there is a crucial need to identify the psychological contracts that exist between the employer and employees in such setups. Entities such as VP Funding, Angel Investors, and Seed Funding and so on, have revolutionized the startup industry to make it third largest startup ecosystem on the globe. Any startup, you consider in a global context, is a result of enthusiasm and innovation of some likeminded brains. After some time that association of a very few people germinates into a bigger unit with various technical, sales and administrative staff coming into the picture. And if startup is good enough to serve the customer needs and strong enough to sustain the competitive pressure over a sustained period of time, it blossoms into a larger establishment having a specialized functional unit for all its processes. So from an enthusiastic association, it moves towards becoming a customer serving unit and from there a profit-making venture.

But the big question that arises here is: What after this? Is profit making the only aim of a startup, for which it uses its human resources like machines. What is the fate of those employees who get associated with a startup in its initial phase? Are there any values, commitments and citizenship that exist across startups or are they just a part time earning source for the jobless youth of our country, who just expects a good enough paycheck and nothing more from these startups. The current study focuses upon the factors, both from employee and employer perspective, which help in shaping the work-relation between these two irreplaceable entities at work. Through this study we aim at illustrating the most critical employee needs, which should be catered by the employers in order to fetch the maximum productivity from their employees. Similarly we also aim to provide the factors that should be kept in mind by the employees in order to serve their employers effectively.

This study intends to explore the difference in the needs of the employees working in the Indian startup industry on the basis of gender, qualification and work experience they have acquired in the course of their career. Level of mutual understanding, existing between employees and employers in startup industry, is also one of the major findings of this study.

2. Literature Review

2.1 Early Studies

Though Argyris (1960) is believed to be the originator of the concept of Psychological Contract, but the earlier works from various researchers such as Barnard (1938), and March and Simon (1958) can be considered as initial writings on the concept of employment relationship. Barnard's (1938) theory of equilibrium clearly cited the significance of organizational rewards in continued and sustainable employee relationship with his/her organization. March and Simon's (1958) inducement-contribution model illustrated this idea

of exchange relationship further as they said that a greater inducement on behalf of the organization, motivates employees for better contribution. The same theory puts forward the organization's perspective by illustrating that a considerable amount of employee's contribution is a pre-requisite for any inducement from organization's part.

Argyris (1960) conceptualization of Psychological Contract made it appear like an exchange of tangible and primarily economic resources, where it focused on higher productivity and lower grievances from employees in return of sufficient wages and job security from their employers. Argyris (1960) model focused mainly on the mutual needs of the employees and their foreman, who represented the organization. Later Levinson et al. (1962) expanded the horizon of Psychological Contract by introducing intangibles into it, which was more or less inspired from the work of Menninger (1958). Menninger (1958) advocated the exchange of intangibles in an employee-employer relationship, and cited mutual satisfaction as one of the key ingredients of a sustainable work relationship.

Levinson et al (1962) focused on the significance of reciprocity in an employee-employer relationship, where employees would feel motivated to serve the needs of organization, if organization fulfills their needs in turn. In Levinson et al's (1962) study, organization was represented by its managers who would set the expectations to employees, where expectations can range from being very specific to very generic in nature. These expectations are bound to be modified along with the course of time, which in turn would bring a change in the psychological contract between two parties.

Later on Schein (1965) further elaborated Levinson et al's (1962) viewpoint of reciprocity, as he laid considerable emphasis on matching of expectations between employees and organizations. Unlike previous studies on Psychological Contract, Schein (1965) laid considerable emphasis on organizational perspective in terms of expectations from their employees, which might be illustrated through organizational culture. Schein (1980, p.99) has later emphasized on the fact that psychological contract cannot be understood by keeping a single perspective in frame, for which he says' "We cannot understand the psychological dynamics if we look only to the individual's motivations or only to the organizational conditions and practices. The two interact in a complex fashion that demands a systems approach, capable of handling interdependent phenomena".

2.2 Re-conceptualization

Denise Rousseau (1989) is credited with the re-conceptualization of psychological contract with her seminal article, which laid the foundation of further contemporary researches on the topic. Rousseau's (1989) work differs from her former counterparts as she defined psychological contract in terms of mutual obligations, while Levinson et al (1962) and Schein (1965) expressed psychological contract as a function of mutual expectations, which arise out of needs. Rousseau's (1989) emphasis on 'obligations' seems to be greatly inspired from Blau's (1964) social exchange theory. Though there are significant differences between the conventional and contemporary works on the subject of psychological contract, but researchers have always discovered the nature of exchange as the core foundation of the subject.

Rousseau's (1989) work stands apart in one more sense from the early researchers of the topic as it describes psychological contract from the beholder's point of view. Whereas Schein (1965) focused on matching of expectations between employees and his/her

organization, Rousseau (1989) laid significant emphasis on individual's perception of agreement. This shifted the focus of psychological contract from being a bipartite to a unilateral entity, which was a result of individual's perception of the obligations existing between two parties viz. employee and employer.

While Levinson (1962) and Schein (1965) viewed expectations as a result of needs, Rousseau (1989) replaced those needs with promises. Rousseau (1989) highlighted perceived promises, where she talks about the impact of organization's implicit and explicit signals that play a crucial role in shaping an individual's psychological contract. Most distinguishing feature of Rousseau's (1989) re-conceptualization of the topic is her focus on the individual level of perception, where an individual's psychological contract is a result of how he/she perceives the set of obligations existing between him/her and organization.

3. Framework for determinants of psychological contracts

As Conway & Briner (2005) draw upon the findings of the survey held by Herriot, Manning and Kidd (1997), where they interviewed UK employees and managers, and tried to reveal the mutual expectations existing between employees and their organizations. The study clearly states factors such as safe environment, fair salary, adequate training, and job security and so on, as, have a crucial significance on drafting an individual's psychological contract. As clear from their research, they not only laid stress on the factors related to employees' psychological contract, but also gave equal significance to the expectations of employers, which mainly constituted top-level managers and organization's board of directors.

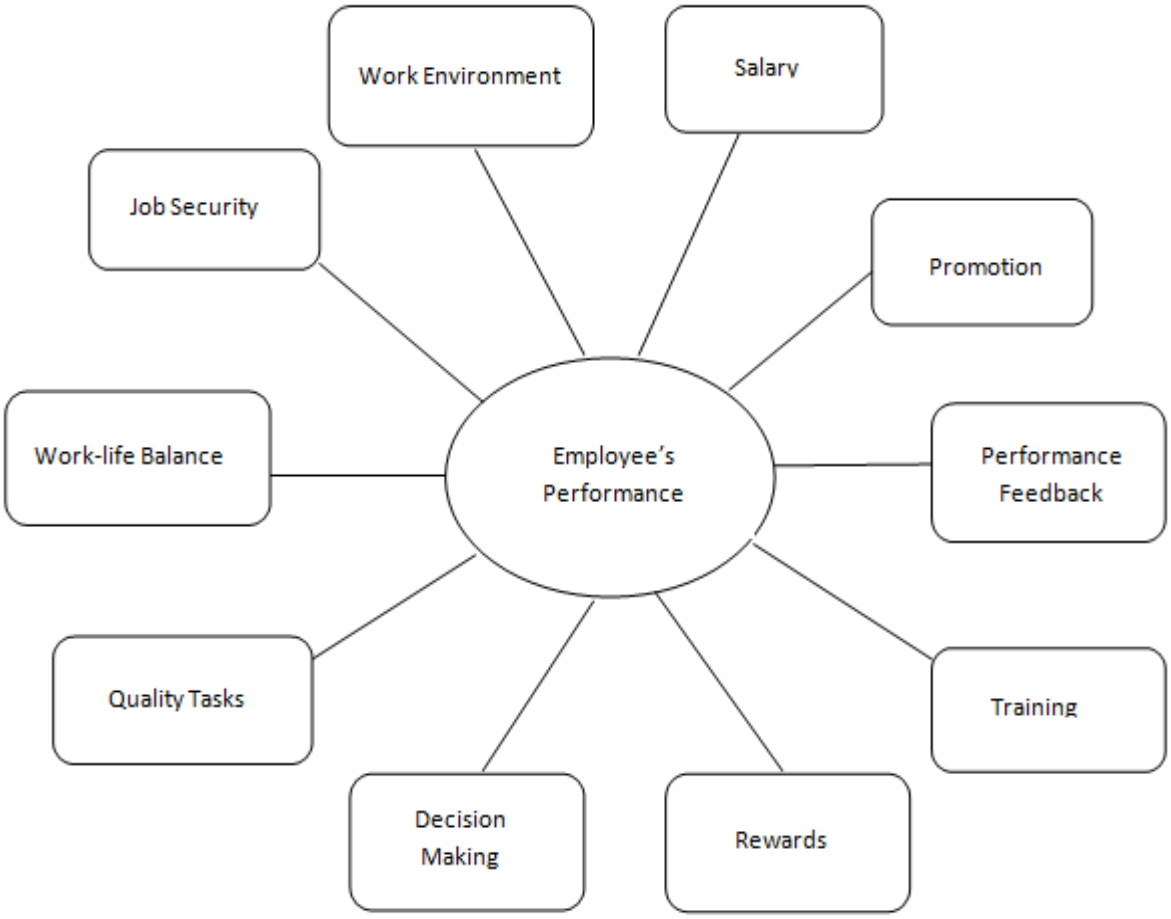

Figure 1: Framework for employee's psychological contract

Factors undertaken for the employers' psychological contract included honesty, loyalty, flexibility, working for contracted hours and so on, which were expected from the employees. This study gave a new turn to the field of psychological contract, by bringing both employees' and employers' expectations on same canvas. It depicted the value of each attribute (in percentage), as per the importance given to it by the survey takers.

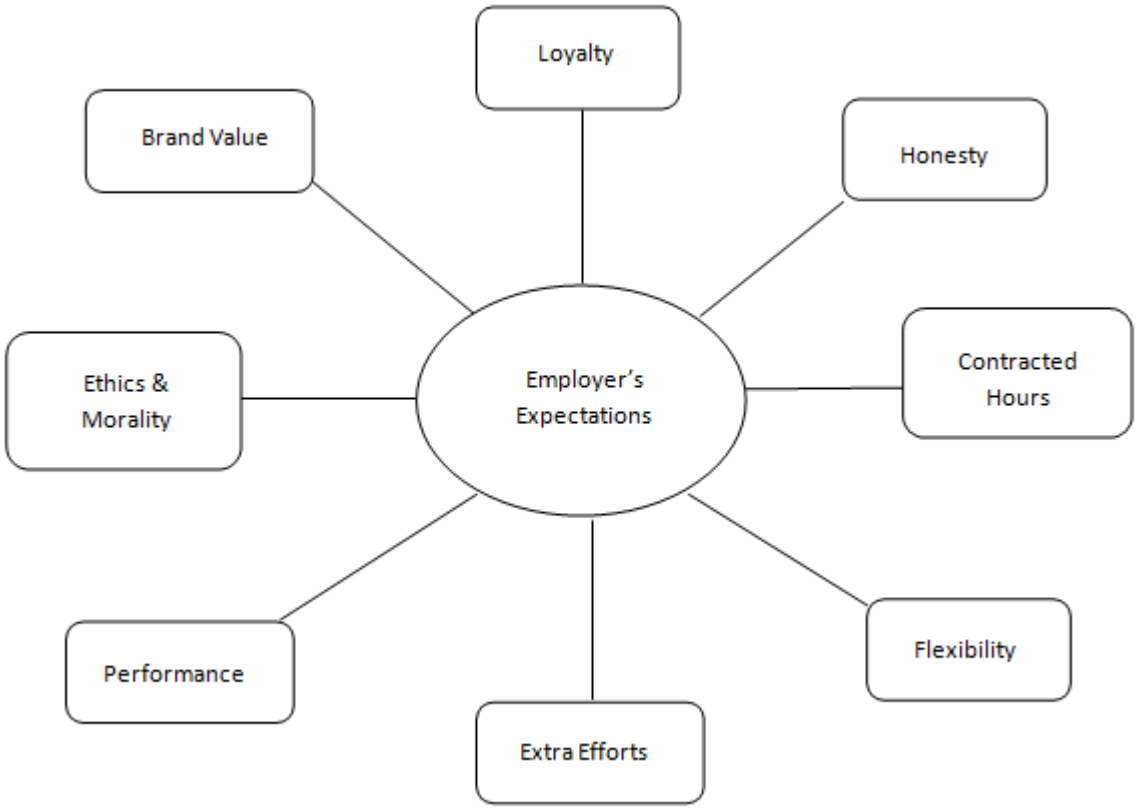

Figure 2: Framework for employer's psychological contract

3.1 Objectives

1. To identify the difference in the expectations of employees joining a startup venture on the basis of their highest level of educational qualification

Though it is usually perceived that startup ventures attract their employee workforce from a cadre of undergraduate/graduate youth, but if any employee with a higher qualification joins the venture, so is there any difference in the expectations of the workers with different level of educational qualifications.

H0: There is no difference in the expectation level of people joining start ups on the basis of their educational qualification

H1: There is a difference in the expectation level of people joining start ups on the basis of their educational qualification

2. To identify the difference in the expectations of male and female employees working in a startup venture

As males, in Indian social context, are considered to be more career oriented as compared to their female counterparts, due to the personal responsibilities they need to cater, so does it imply a different set of expectations or priorities as compared to their female colleagues working in the startup ventures.

H0: There is no difference in the expectation level of people joining start ups on the basis of their gender.

H1: There is a difference in the expectation level of people joining start ups on the basis of their gender.

3. To identify the relationship between the work experience and salary (monetary) expectations of an employee working in a startup venture.

As it is widely known that with the increase in job tenure or experience, incumbent's monetary expectations tend to take an upward turn as compared to other perks and benefits. But the primary question is whether it is only the monetary expectations that increase with the time or non-monetary expectations also take the same direction.

H0: There is a negative correlation between work experience and the relative importance that individual attaches to the salary component.

H1: There is a positive correlation between work experience and the relative importance that individual attaches to the salary component.

4. Methodology

4.1 Instrument development

Two survey questionnaires were designed, where first one intended to identify the expectations of employees from their employers through parameters such as safe and healthy work environment, proper work-life balance, fair and equitable salary as per the industry standards, opportunities of promotion and career growth, feedback for performance at regular intervals, adequate training as per professional needs, rewards and recognition for special contributions, challenging and quality tasks that frame career in a positive manner, job security even during the distressed times of economic depression or recession and opportunity to get involved in organizational decision making.

The instrument also aimed to measure what employees think about their employer's expectations from them. The parameters used for measuring such expectations are loyalty, honesty, flexibility, extra efforts during the hour of need or organizational distress, up to mark performance in terms of quality and quantity, moral values and ethical behavior, uplift organization's brand value through work and code of conduct. Respondents (employees) were asked to rank each item from 1 to 10 in first questionnaire and 1 to 8 in second questionnaire (vice versa for employers). The instrument was validated using pilot data from 30 respondents. Reliability of the various factors through the instrument was found to be statistically significant.

4.2 Sampling and data collection

As the reliability coefficients were statistically significant, the instrument was used for the main data collection. Simple random sampling was used to select the employees from start-up organizations, which were registered on or after 2008. Since the research required responses from both employees and employers of start-up organizations, so every care was taken in recording the responses only from those organizations from which both employees' and employers' data was collected. A total of 200 questionnaires were distributed and mailed, and 105 valid responses were collected, resulting in a 52 per cent response rate.

4.3 Analysis

Data analysis was carried out using the correlation analysis technique to identify the correlation between experience and the influence of salary on an employee. Non-parametric

tests, such as Wilcoxon signed rank test and Kendals test, were also used to identify the difference in expectations of two dissimilar groups.

4.3.1 Test for Normality

A Shapiro – Wilk's test (Shapiro & Wilk, 1965; Razali & Wah, 2011) and a visual inspection of their histograms, normal q-q plots and box plots showed that the data for the various factors is not normally distributed for both males and females.

Test 1:

H0: Distribution of sample data is normal
H1: Distribution of sample data is not normal

We found that Kolmogorov-Smirnov test of normality had the significance value for all the variables under consideration less than 0.05 at 5% level of significance. Thus we failed to accept the null hypothesis so we went ahead for non-parametric tests. Hence we got the result that the data gathered from both the genders is not normal.

4.3.2 Non-parametric tests

Here we have tried to find out whether the expectations of employees change with respect to the following parameters:

Gender

H0: There is no difference in the expectation level of people joining start ups on the basis of their gender.
H1: There is a difference in the expectation level of people joining start ups on the basis of their gender.

To test this hypothesis two tests were performed which showed that expectations of employees do not change with respect to gender. Kendall's coefficient of corcodance and wilxocon test gave the result that there is no difference in the expectation level of employees from their employers on the basis of gender i.e. the parameters identified in the research are free from gender bias. The significance value for Wilcoxon comes out to be .811 while for Kendall's coefficient of concordance comes out to be 1, which clearly indicates that there is no difference in the distribution of data of males and females.
Result: Null hypothesis is to be retained.

4.4 Educational qualification

Similar tests were conducted to check whether educational qualification has an impact on the expectation level of employees. Test for checking the normality of the data gives the following results.

H0: There is no difference in the expectation level of people joining start ups on the basis of their qualification.
H1: There is a difference in the expectation level of people joining start ups on the basis of their qualification

Kendall's coefficient of corcodance and wilxocon test gave the result that there is no difference in the expectation level of employees from their employers on the basis of gender i.e. the parameters identified in the research remain unaffected from educational qualification. The significance value for Wilcoxon comes out to be .679 while for Kendall's

coefficient of concordance comes out to be .637, which clearly indicates that there is no difference in the distribution of data among employees with different educational backgrounds.

Result: Null hypothesis is to be retained.

4.5 Experience and Monetary Expectations

Correlation analysis was performed to study relation between the work experience of employees working in start-up industry and their monetary expectations.

H0: There is a negative correlation between experience and the relative importance that individual attaches to the salary component
H1: There is a positive correlation between experience and the relative importance that individual attaches to the salary component

Work experience and salary expectations are negatively correlated which states that as work experience increases employees consider salary as a secondary factor and begin focusing on other parameters which provide them satisfaction.

Result: Null hypothesis is to be retained.

4.6 Employer-Employee Relationship

Study reveals that there is considerable gap in the understanding level of employees and employers towards each other. Analysis of the sample taken shows that employees understand the employer needs regarding work and culture, to a better extent, as compared to employers understanding employees' needs.

Table 1: Employee understands

Extent to which employees understand employer's expectations (percentage)	**92.86%**
Extent to which employers understand employees' expectations (percentage)	**77.78%**

This difference in level of understanding exists because employees give more importance to rewards and recognition as compared to the employers. There is a clear mismatch in the thinking of employer and employees on this parameter. Hence employers should focus on improving the level of rewards and recognition given to employees as compared to current industry norms.

4.7 Other findings

Furthermore we were interested to know the parameters that employees expect the most. That s provided by the following table.

4.8 Result

Employees keep opportunities of promotion and career growth as their first and topmost priority expectation from the employers which are followed by fair and equitable salary as per the industry standards. A very interesting point discovered here was, employees working

in start-up organizations ranked job security at ninth position (cumulative), which means that unlike previous baby boomers and generation-x, they do not consider job security to be a crucial parameter in their work life.
Data regarding the expectation of organization from the employees was also analyzed which revealed the following results.

Table 2: Expectation of organization from the employees

Items	Ranking
Opportunities of promotion and career growth	1
Fair and equitable salary as per the industry standards	2
Safe and healthy work environment	3
Proper work-life balance	4
Adequate training as per my professional needs	5
Challenging and quality tasks that frame my career in a positive manner	6
Feedback for my performance at regular intervals	7
Rewards and recognition for my special contributions	8
Job security even during the distressed times of economic depression or recession	9
Opportunity to get involved in organizational decision making	10

Table 3: Expectation of organization from the employees

Items	Rank
Be flexible in accepting variety of roles and responsibilities	1
Remain honest in all my transactions, internal or external to the organization	2
Perform up to mark in terms of quality and quantity	3
Put in extra efforts during the hour of need or organizational distress	4
Be loyal, in terms of my tenure with the organization	5
Understand moral and ethical responsibilities as an organizational citizen	6
Uplift organization's brand value through work and code of conduct	7
Work for contracted hours	8

4.9 Result

Employees think that their employers want them to take up a wide variety of roles and responsibilities because generally start ups have lesser number of positions and thus responsibilities are high on those positions.

5. Recommendations

Though we started with 10 parameters viz. safe and healthy work environment, proper work-life balance, fair and equitable salary as per the industry standards, opportunities of promotion and career growth, feedback for performance at regular intervals, adequate training as per professional needs, rewards and recognition for special contributions, challenging and quality tasks that frame career in a positive manner, job security even during the distressed times of economic depression or recession and opportunity to get involved in

organizational decision making, which seemed to be affecting employees' performance working in start-up industry but after analyzing the feedback collected from employees currently working in the industry we found that most critical factors affecting employees' performance are: *opportunities of promotion and career growth, fair and equitable salary as per the industry standards, and safe and healthy work environment.*

5.1 Appendix

5.1.1 Instrument for recording employee's responses

Table 4: I want my organization to provide me:

Items	Ranking
Safe and healthy work environment	
Proper work-life balance	
Fair and equitable salary as per the industry standards	
Opportunities of promotion and career growth	
Feedback for my performance at regular intervals	
Adequate training as per my professional needs	
Rewards and recognition for my special contributions	
Challenging and quality tasks that frame my career in a positive manner	
Job security even during the distressed times of economic depression or recession	
Opportunity to get involved in organizational decision making	

Table 5: I think my organization expects me to:

Items	Ranking
Be loyal, in terms of my tenure with the organization	
Remain honest in all my transactions, internal or external to the organization	
Work for contracted hours	
Be flexible in accepting variety of roles and responsibilities	
Put in extra efforts during the hour of need or organizational distress	
Perform up to mark in terms of quality and quantity	
Understand moral and ethical responsibilities as an organizational citizen	
Uplift organization's brand value through work and code of conduct	

5.1.2 Instrument for recording employer's responses

Table 6: I expect my employees to

Items	Ranking
Be loyal, in terms of tenure with the organization	
Remain honest in all their transactions, internal or external to the organization	
Work for contracted hours	
Be flexible in accepting variety of roles and responsibilities	
Put in extra efforts during the hour of need or organizational distress	

Perform up to mark in terms of quality and quantity	
Understand moral and ethical responsibilities as an organizational citizen	
Uplift organization's brand value through work and code of conduct	

Table 7: I think my employees expect me to provide:

Items	Ranking
Safe and healthy work environment	
Proper work-life balance	
Fair and equitable salary as per the industry standards	
Opportunities of promotion and career growth	
Feedback for their performance at regular intervals	
Adequate training as per their professional needs	
Challenging and quality tasks that frame their career in a positive manner	
Job security even during the distressed times of economic depression or recession	
Opportunity to get involved in organizational decision making	

Therefore employers and top management of start-up organizations must work towards facilitating these afore mentioned factors to their employees, in order to fetch the most optimal performance out of them. As seen from the analysis, there is no significant difference in the expectations of male and female employees working in the Indian startups, which signifies that employers do not need to craft some special policies for enhancing the employee's productivity on the basis of gender. Rather they should try to focus upon the top three critical factors viz. opportunities for career growth, salary and safe & healthy work environment, without discriminating between male and female employees. Moreover, no difference has been observed in the expectations of employees on the basis of highest level of educational qualification acquired by them. It shows that though startup industry is characterized by a significant number of undergraduates and recently graduated young professionals, but there hardly seems to be any difference in the expectations of a postgraduate and an undergraduate employee working in the industry. Thus startup industry should focus upon catering to the employee needs uniformly, irrespective of the highest degree attained by the incumbent.Most critical aspect of this study, which intended to determine the relation between work experience of the employees and their monetary expectations from their employers, revealed a noticeable and distinguishing observation. It has been observed that with an increase in the number of years of work experience, non-monetary expectations of the employees increase rather than the monetary counterpart. So instead of just providing only the salary increments, with an increase in employees' experience, employers should also try to focus upon ensuring improved non-monetary aspects such as healthy and safe work environment, work-life balance and so on. Thus employee dissatisfaction or decreased productivity should not always be countered through monetary pumping rather other non-monetary aspects should also be considered as per respective work style and settings. A significant difference has also been observed in the level of understanding of mutual expectations between employees and employers, which is mainly due to employers' ignorance towards providing appropriate rewards and recognition for their special contribution on required occasions. Thus employers should not just focus on timely monthly salary and periodic salary increments, but should also put in a little bit extra effort in giving them due recognition for their above the line contributions towards the organization.

5.1 Limitations

Sample size for this study can be considered a critical limitation, as a sample of 105 is not a big number for this kind of extensive study on an emerging industry in Indian business context. Moreover such study can be conducted across different states or regions of the country, to get a better hold of the employee and employer expectations, and thus derive a nation-wide perception on psychological contracts in Indian startups.

5.2 Future Scope

This study can be extended to a larger set of sample, in order to obtain a better view of the scenario of employee-employer mutual understanding in the startup industry. Such kind of studies can also be carried out across other industries present in the country, to get further understanding of psychological contracts persistent amidst them. Since the sample for this study were mainly collected from startups in North Indian region, this study can be extended to the rest of the country and across the globe as well, to obtain clear insight of employee-employer relations in startup organizations.

6. References

1. Argyris C., (1960), Understanding Organizational Behavior. Homewood, IL: Dorsey Press.

2. Barnard C.I., (1938), The functions of the executive. Cambridge, MA: Harvard.

3. Blau, P., (1964), Exchange and power in social life. Wiley: New York.

4. Conway Neil & Briner Rob B., (2005) Understanding Psychological Contracts at Work: A Critical Evaluation of Theory and Research. Oxford: Oxford University Press.

5. Herriot P., Manning W, Kidd J., (1997) The Content of the Psychological Contract' British Journal of Management, 8, pp 151-162.

6. Levinson H., Price C.R, Munden K.J., Mandl H.J, Solley C.M., (1962), Men, Management and Mental Health. Boston: Harvard University Press.

7. Marc, J.G., Simon H.A., (1958), Organizations. New York.

8. Menninger K., (1958), Theory of psychoanalytic technique. New York: Basic Books, Inc.

9. Rousseau D.M., (1989), Psychological and implied contracts in organizations. Employee Responsibilities and Rights Journal, 2, pp 121-139.

10. Schein E.H., (1965), Organizational psychology. Englewood Cliffs, NJ: Prentice Hall.

11. Schein E.H., (1980), Organizational psychology. 3rd edition. Englewood Cliffs, NJ: Prentice Hall.

Appl. Phys. A (2016)122:605
DOI 10.1007/s00339-016-0134-4

Applied Physics A
Materials Science & Processing

Chirped photonic crystal with different symmetries for asymmetric light propagation

Brahm Raj Singh[1] · Swati Rawal[1] · R. K. Sinha[2,3]

Received: 6 April 2016 / Accepted: 12 May 2016

Abstract In the present paper, we have carried out analysis of asymmetric light propagation in a chirped photonic crystal waveguide. The designed structures have hexagonal arrangement and square arrangement of silicon rods in air substrate. Dimensions of the defect rods are tailored, so that the proposed design structure works as an optical isolator. The transmission analysis of the structure reveals that it can act as an optical diode. We have plotted the extinction ratio and transmission analysis graphs for the structure, and it has been observed that the maximum output is obtained for telecom wavelength of 1.55 μm. Dispersion curves are obtained using the plane wave expansion method, and the transmission is simulated using finite element method. The proposed structures are applicable for photonic integrated circuits due to their simple and clear operating principle.

This work is carried out at Jaypee Institute of Information Technology, Noida and "TIFAC Centre of Relevance and Excellence in Fiber Optics and Optical Communication in Delhi Technological University (Formerly Delhi College of Engineering, Delhi University), Delhi" through the "Mission Reach" program of Technology Vision-2020, Government of India.

✉ Swati Rawal
swati.rawal@yahoo.com

[1] Department of Physics and Material Science Engineering, Jaypee Institute of Information Technology, Noida 201307, India

[2] TIFAC—Centre of Relevance and Excellence in Fiber Optics and Optical Communication, Department of Applied Physics, Delhi Technological University (Formerly Delhi College of Engineering, Delhi University), Delhi 110042, India

[3] CSIR—Central Scientific Instruments Organisation (CSIO), Sector-30C, Chandigarh 160030, India

1 Introduction

In recent years, photonic crystals (PhCs) have gained much attention due to their potential for controlling the propagation of light. These are periodic dielectric structures which can trap light and hence does not allow frequencies of certain range, known as photonic bandgap (PBG) to pass through [1, 2]. This unconventional guiding of light in PhCs provides a platform for the design of integrated circuits. Silicon-based photonic devices and circuits have offered a great means to revolutionize signal processing, information processing and computing technologies [3, 4]. Optical isolators, in which light can propagate only in one direction, plays a crucial role in information processing systems. Although widely used in lasers and optical communication, these devices are still lacking in semiconductor integrated photonic circuits because of challenges, mainly in the material integration and device design. There are number of methods to achieve asymmetric light propagation based on photonic crystals. An electro-tunable optical isolator based on liquid–crystal heterojunctions, showing nonreciprocal transmission of circularly polarized light in photonic bandgap regions, has been reported in the literature [5]. In another example, using liquid–crystals, linearly polarized light is used for realization of the device [6], whereas in many attempts on magneto-optical materials [7–10], optical isolators have also been fabricated using nonlinear optical processes [11, 12], and electro-absorption modulators [13]. A theoretical scheme of optical isolation is achieved by dynamically inducing indirect photonic transitions in an appropriately designed photonic structure [14]. A photonic crystal-based heterojunction diode [15, 16] was made of two types of square lattice photonic crystals with different radii of dielectric rods in air substrate. The unidirectional optical diode is achieved

Published online: 23 May 2016

with the concept of directional bandgap of the photonic crystals. One researcher presented a different approach to obtain asymmetric light propagation with graded photonic crystal waveguides [17]. The horizontal period of the photonic crystal was changed linearly, and the asymmetric light propagation was achieved.

We here present, photonic crystal-based optical isolator, to achieve asymmetric light propagation in optical communication window of electromagnetic spectrum. We have considered hexagonal and square symmetry PhC structure with silicon rods in air. The design and analysis of the proposed isolators were carried out using plane wave expansion (PWE) method. PWE method calculates the photonic bandgap and the existence of guided modes in different waveguides, while the finite element method (FEM) method demonstrates, how asymmetric propagation of light is taking place in the designed PhC. Transmittance and Extinction ratio has been calculated to check the cross talk among the ports.

2 Structure design

In the proposed paper, we have designed an optical diode in the photonic crystal with hexagonal and square lattice arrangement of silicon ($n = 3.42$) rods in air ($n = 1$). Figure 1 shows the schematic of two-dimensional photonic crystal structure (with hexagon symmetry) that provides asymmetric light propagation. Two cases have been considered; first, when Port A acts as an input source for left-to-right transmission, output from Port B becomes high. Second, when Port B acts as an input source for the right-to-left transmission, output at Port A becomes low and the remaining energy is lost in the photonic crystal as dispersion. The working region chosen here is the C band of electromagnetic spectrum with wavelength range varying from 1.53 to 1.57 μm. The lattice constant and radius for the structure were chosen, so as to provide photonic bandgap for the TM polarization at the telecom wavelength, 1.55 μm. COMSOL Multiphysics software has been used for analysis of electric field distribution. Free triangular meshing is used in the designing of the structure.

2.1 Phc-based optical isolator with hexagonal arrangement of silicon rods in air

An optical diode is designed in a regular hexagon lattice PhC, with Si ($n = 3.42$) rods in air. The proposed optical diode is designed to exhibit bandgap for the TM mode of the telecom wavelength, 1.55 μm ($a/\lambda = 0.4387$). Lattice constant (a) and radius of the rods (r) chosen here is 0.68 and 0.23 μm, respectively. Figure 1a shows that the PBG exist for the TM modes in normalized frequency range; $0.3801 \leq a/\lambda \leq 0.4731$. A PhC waveguide is then created by removing a row of rods and chirping the neighboring rods, as shown in Fig. 1b. The radius of the chirped rods is; $r_1 = 0.220$ μm, $r_2 = 0.209$ μm and $r_3 = 0.197$ μm.

The designed PhC structure consists of two ports and both the ports can act as input and output port. When propagation of light is considered from Port A to Port B, output from port B is highly illuminated, however when propagation of light takes place from Port B to Port A, the output obtained at Port A is low. In a normal photonic crystal waveguide, light propagation at a frequency corresponding to the PhC waveguide mode within the bandgap region propagates in both directions and the amount of transmitted power in both the directions is nearly the same. To break this symmetry in the structure, we purposely removed few rods and changed the radii of few rods (chirping) near to PhC W1 waveguide (Fig. 1b). The

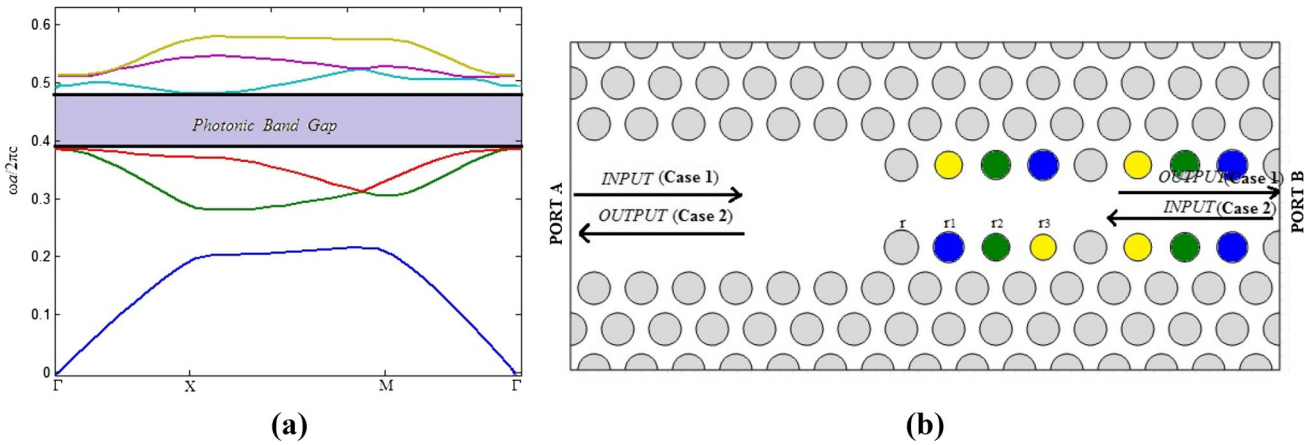

Fig. 1 **a** Band structure for TM modes in hexagonal lattice arrangement of Si rods where rod radius $r = 0.23$ μm and $a = 0.68$ μm. **b** Schematic diagram of the proposed optical diode having chirped silicon rods with $r_1 = 0.220$ μm, $r_2 = 0.209$ μm and $r_3 = 0.197$ μm

electric field propagation is then carried out from different ports. Case I: When light propagates from left to right (Port A to Port B), Fig. 2a, it propagates mostly along the central region of PhC waveguide, i.e. along the optical axis of the designed structure and exit at Port B, i.e. a high field output is obtained from Port B in left-to-right propagation. Figure 2b shows the transverse field profile along the right end of the structure for first case. Case II: When light propagates from right to left (Port B to Port A) direction, along the designed photonic crystal, the guiding of light wave is lost toward the end of the structure, i.e. at the left end (Port A), output obtained is low (Fig. 2d). Hence, field leakage in the designed structure leaves weak field amplitude along the optical axis along which light is propagating. Figure 2c shows transverse field profile along the left end of the structure for the second case. The electric field profiles support asymmetric light propagation in both the direction, i.e. left to right (Port A to Port B), right to left (Port B to Port A).

2.2 Phc-based optical isolator with square arrangement of silicon rods in air

The proposed optical diode is designed to exhibit bandgap for TM mode of the telecom wavelength, 1.55 μm ($a/\lambda = 0.4580$). Lattice constant (a) and radius of the rods (r) chosen here is 0.71 and 0.22 μm, respectively. Figure 3a shows that the PBG exist for TM modes in

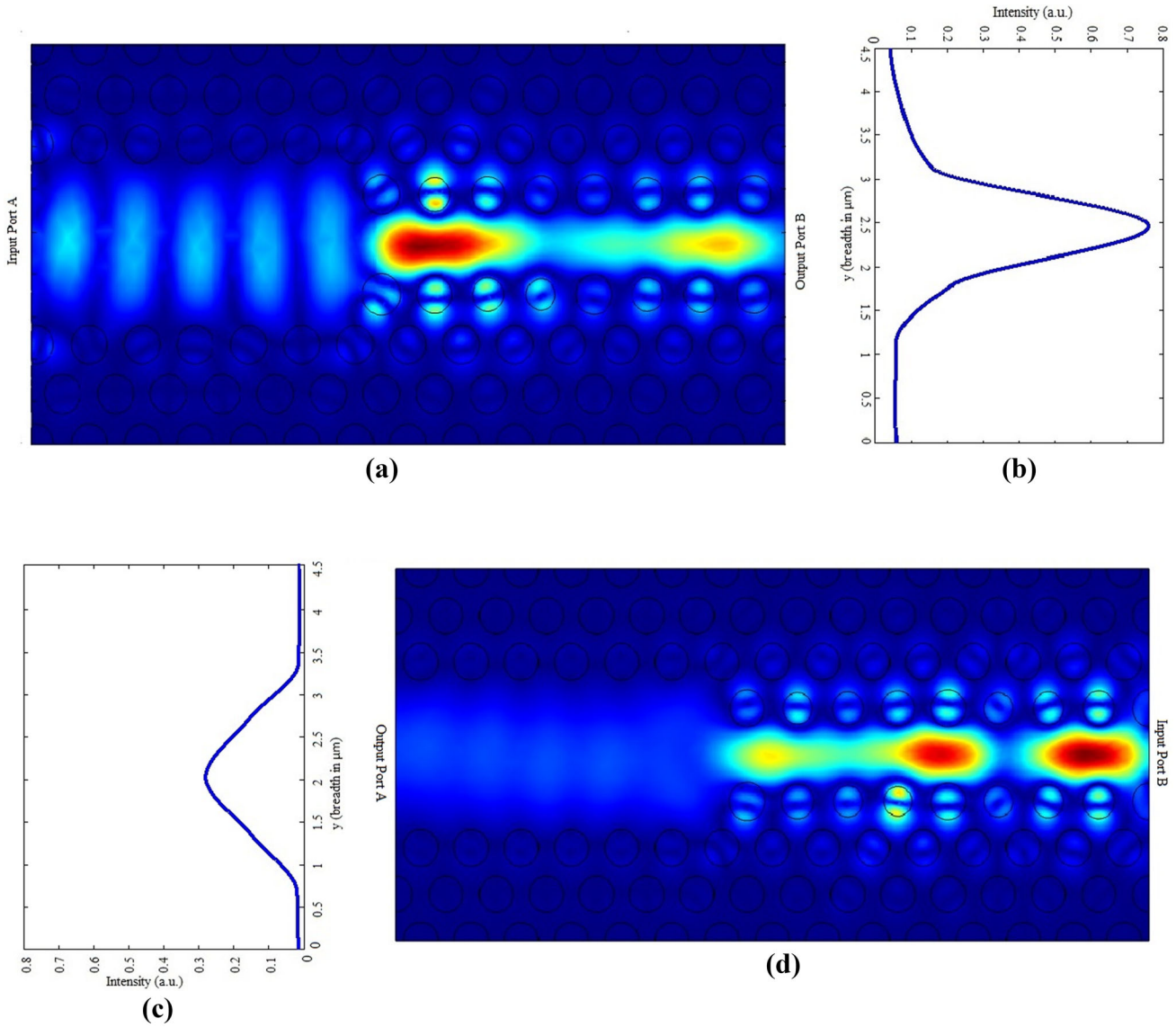

Fig. 2 **a** Time-domain snapshot of propagation of light ($\lambda = 1.55$ μm) from input Port B to output Port A (*left* to *right*). **b** The transverse field profile *across the right end* (Case I) face of the structure. **c** The transverse field profile *across the left side* (Case II) of the structure. **d** Time-domain snapshot of light ($\lambda = 1.55$ μm) propagation from input Port B to output Port A (*right to left*)

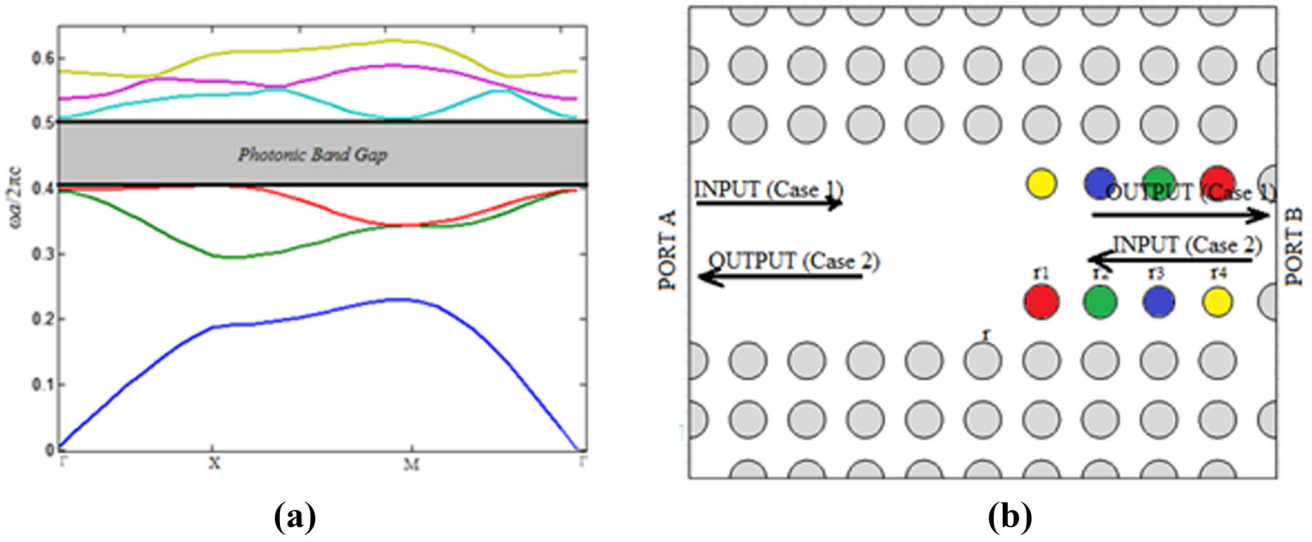

Fig. 3 **a** Band structure for TM modes for square lattice having Si rod radius $r = 0.22$ μm and $a = 0.71$ μm. **b** Schematic diagram of the proposed optical diode having chirped silicon rods with $r_1 = 0.21$ μm, $r_2 = 0.20$ μm, $r_3 = 0.19$ μm, $r_4 = 0.17$ μm

normalized frequency range $0.3971 \leq a/\lambda \leq 0.5024$. The optical diode is designed in a regular square lattice PhC, with Si ($n = 3.42$) rods in air. PhC W1 waveguide is created by removing the rows of rods and chirping the neighboring rods as shown in Fig. 3b. The radius of the chirped rods is; $r_1 = 0.21$ μm, $r_2 = 0.20$ μm, $r_3 = 0.19$ μm, $r_4 = 0.17$ μm.

Similar to the previous case, the designed square symmetry PhC optical diode consists of two ports and both the ports act as input and output port. When propagation of light is considered from Port A to Port B, output from port B is low, while when propagation of light takes place from Port B to Port A, the output obtained at Port A is highly illuminated. Figure 4 shows the electric field propagation of square lattice PhC-based optical isolator. Case I: When light propagates from left to right (Port A to Port B), Fig. 4a shows that the guiding of light wave is lost toward the end of the structure, i.e. toward the right end (output Port B). Hence, field leakage in the designed structure leaves weak field amplitude along the optical axis, along which light is propagating. Figure 4b shows the transverse field profile along the right end of the structure for first case. Case II: When light propagates from right to left (Port B to Port A) direction along the designed photonic crystal waveguide, it propagates mostly along the central region of PhC waveguide, i.e. along the optical axis of the designed structure and exit at Port A, i.e. a high field output is obtained from Port A in right-to-left propagation. Figure 4c shows the transverse field profile along the right end of the structure for second case. Hence, the electric field profiles support asymmetric light propagation in both the directions, i.e. left to right (Port A to Port B), right to left (Port B to Port A).

3 Transmittance

Transmittance (TR) of the designed optical isolator is defined as the ratio of output power to the input power and mathematically it can be written as

$$\mathrm{TR} = P_{\mathrm{OUT}}/P_{\mathrm{IN}} \tag{1}$$

where P_{OUT} is the power at either of the output port and P_{IN} is the power at the input port.

Figures 5 and 6 show the plot of transmittance with wavelength for hexagonal lattice arrangement-based PhC isolator and square lattice arrangement-based PhC isolator, respectively, for both cases. Wavelength range taken here is the C-Band, i.e. 1540–1560 nm. It is observed from both the curves, maximum output is obtained at 1550 nm, i.e. both the structures work well as optical isolator at telecom wavelength of 1550 nm.

4 Extinction ratio

Extinction ratio (ER) can be defined as:

$$\mathrm{ER} = 10\log_{10}(P_1/P_0) \tag{2}$$

where P_1 is the power obtained from the desired output port and P_0 is power obtained from the other output port. The extinction ratio (ER) is used to describe the efficiency

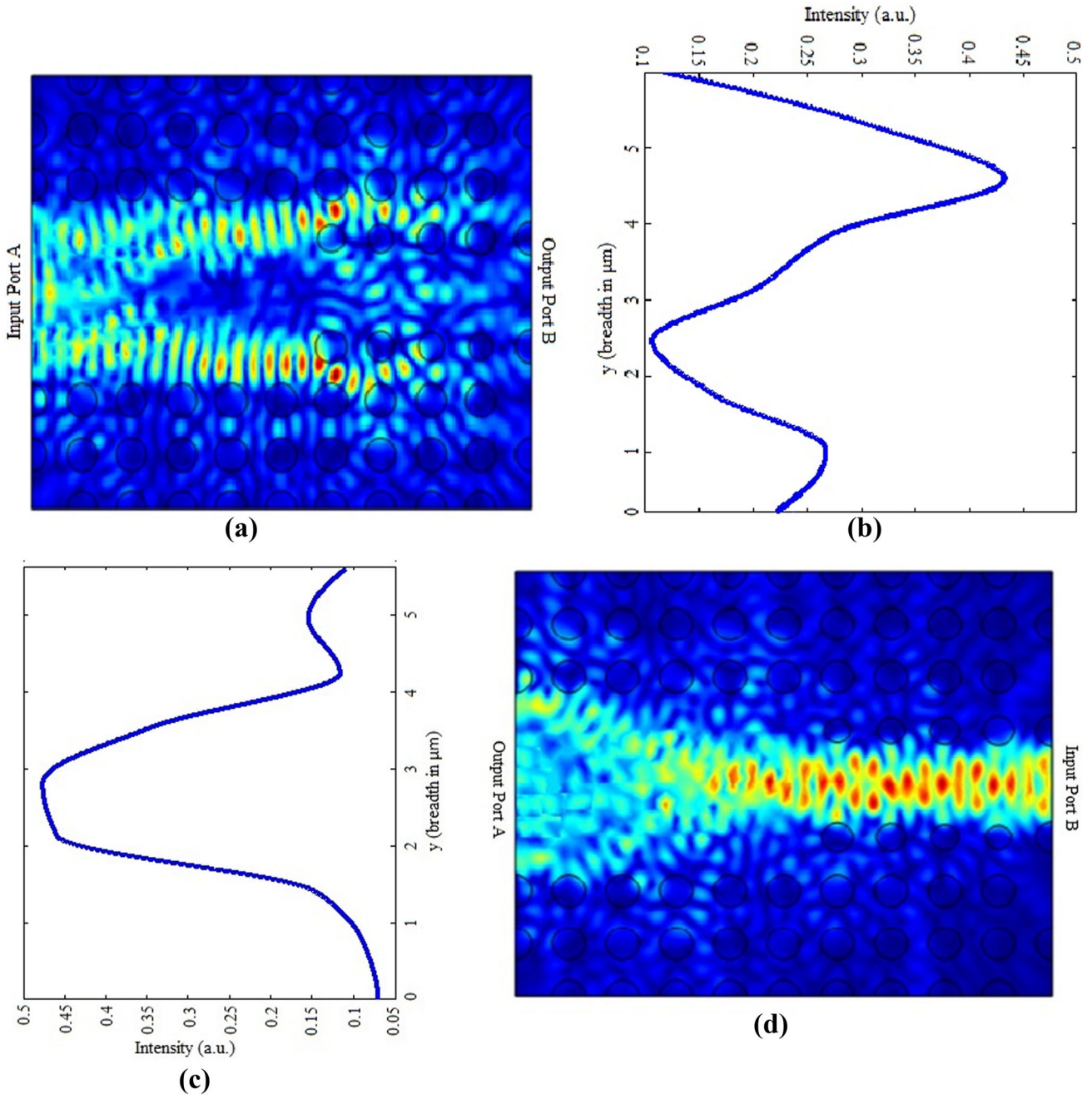

Fig. 4 **a** Time-domain snapshot of propagation of light ($\lambda = 1.55$ μm) from *right* to *left*. **b** The transverse field profile *across the right end* face of the structure. **c** The transverse field profile *across the left end* side of the structure. **d** Time-domain snapshot propagation of light ($\lambda = 1.55$ μm) from *left* to *right*

with which the transmitted optical power is modulated over the designed waveguide. The wavelength variation considered here is 1530–1570 nm. It is observed from the Fig. 7a, b that extinction ratio for hexagonal arrangement is better than square arrangement for the desired wavelength range 1530–1570 nm.

5 Results and conclusion

To conclude, the aim of this work was to obtain an optical diode-like structure by utilizing chirped photonic crystal waveguide. For this goal, the radius of the rods in the neighboring column of PhC W1 waveguide in both

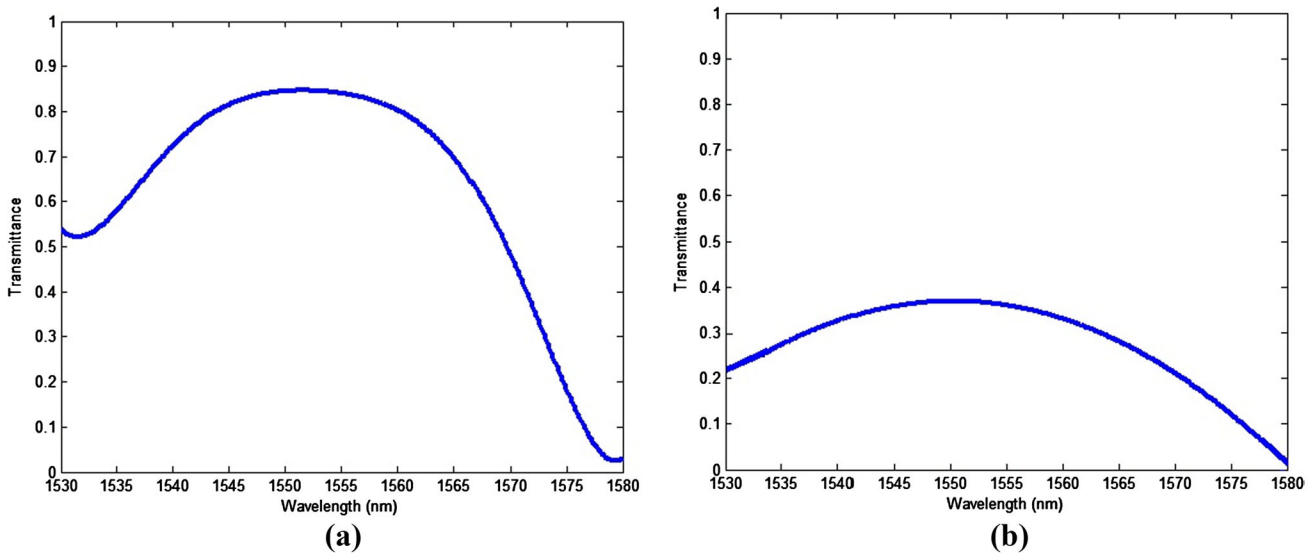

Fig. 5 Transmittance curve for hexagonal arrangement optical isolator **a** for high output (input Port A to output Port B) and **b** for low output (input Port B to output Port A)

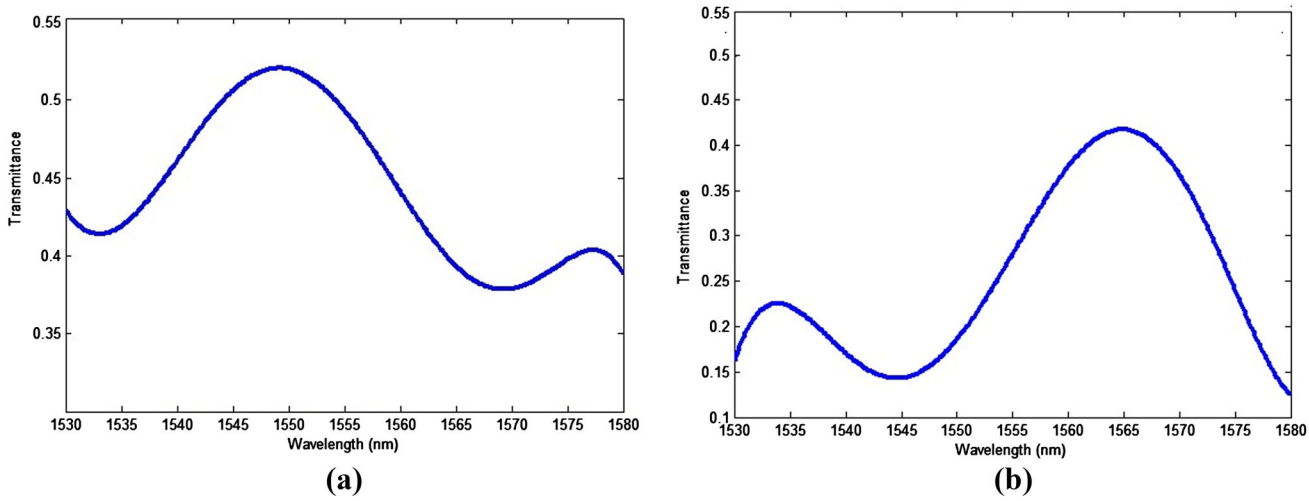

Fig. 6 Transmittance curve for square arrangement **a** for high output (input Port B to output Port A) and **b** for low output (input Port A to output Port B)

hexagonal lattice and square lattice photonic crystal is modified, to obtain a chirped device. The wavelength region considered is the C Band (1530–1570 nm) of the electromagnetic spectrum. The standard W1 waveguide shows no diode-like behavior due to the symmetry of the structure as the optical pulse propagates identically in either direction in a standard waveguide. However, the chirped designed PhC waveguide can be used for asymmetric light propagation. This can be observed from the transmission time-domain snapshots along the proposed optical diode structures both in hexagonal and square lattice arrangement. As observed from the transmission graphs of hexagon lattice-based optical isolator, nearly 82 % transmittance is obtained at 1.55 μm, which corresponds to high output electric field intensity, while when the transmission of light take places from other direction, the transmittance obtained is nearly 35 % which corresponds to low electric field intensity. The square arrangement-based optical isolator is having transmittance 52 % for high output (at $\lambda = 1.55$ μm) and 18 % for low output electric field intensity (at $\lambda = 1.55$ μm). Extinction ratio achieved for hexagonal-based optical isolator is nearly 5.5 dB (at $\lambda = 1.55$ μm) and for square arrangement-based optical isolator is nearly 4.1 dB (at $\lambda = 1.55$ μm). The

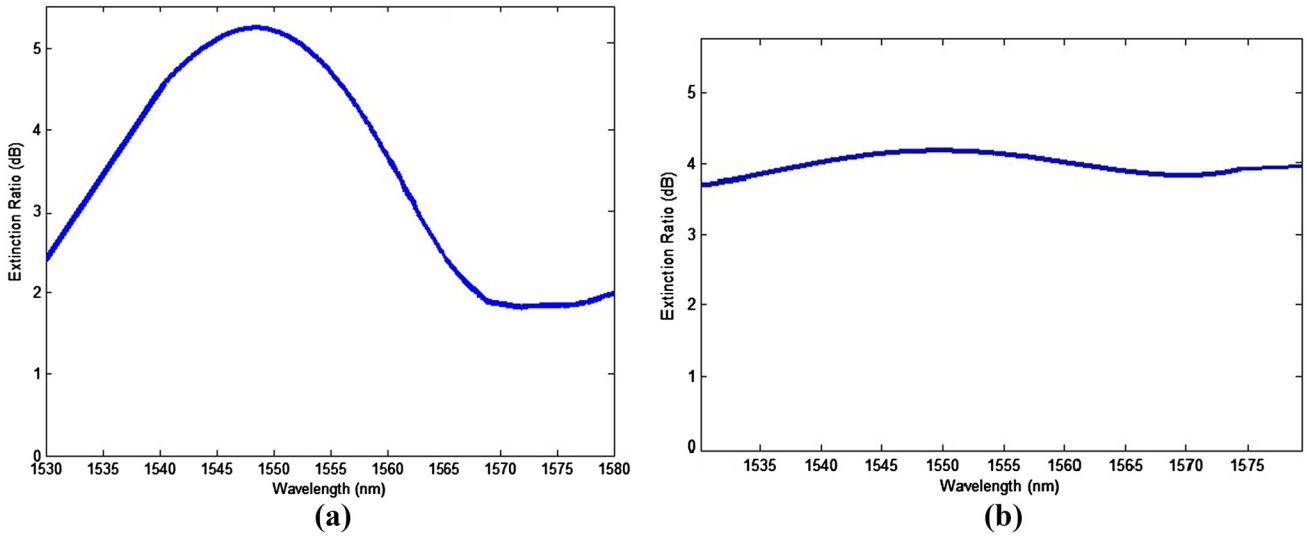

Fig. 7 Extinction ratio curve **a** for hexagonal lattice arrangement optical isolator and **b** for square lattice arrangement optical isolator

engineering of the chirped rods radii and refractive index parameters may further enhance the performance of the optical diode in photonic crystal waveguides.

Acknowledgments The authors Swati Rawal and Brahm Raj Singh acknowledge JIIT Noida, for providing research support for the present research work. The authors gratefully acknowledge the initiatives and support toward establishment of "TIFAC Centre of Relevance and Excellence in Fiber Optics and Optical Communication at Delhi Technological University (Formerly Delhi College of Engineering), Delhi" through "Mission REACH" program of Technology Vision-2020, Government of India.

References

1. E. Yablanovitch, Phys. Rev. Lett. **58**, 2059 (1987)
2. S. John, Phys. Rev. Lett. **58**, 2486 (1987)
3. C. Wang, C.-Z. Zhou, Z.Y. Li, Opt. Expr. **19**(27), 26948 (2011)
4. M. Scalora, J.P. Dowling, C.M. Bowden, M.J. Bloemer, J. Appl. Phys. **76**(4), 2023 (1994)
5. V.R. Almeida, C.A. Barrios, R.R. Panepucci, M. Lipson, Nature **431**(7012), 1081 (2004)
6. J.Y. Chen, L.W. Chen, Opt. Expr. **14**(22), 10733 (2006)
7. R.L. Espinola, T. Izuhara, M.C. Tsai, R.M. Osgood Jr, H. Dötsch, Opt. Lett. **29**(9), 941 (2004)
8. M.A. Levy, J. Opt. Soc. Am. B **22**(1), 254 (2005)
9. T.R. Zaman, X. Guo, R.J. Ram, Appl. Phys. Lett. **90**(2), 023514 (2007)
10. H. Dötsch, N. Bahlmann, O. Zhuromskyy, M. Hammer, L. Wilkens, R. Gerhardt, P. Hertel, A.F. Popkov, J. Opt. Soc. Am. B. **22**(1), 240 (2005)
11. K. Gallo, G. Assanto, K.R. Parameswaran, M.M. Fejer, Appl. Phys. Lett. **79**(3), 314 (2001)
12. M. Soljačić, C. Luo, J.D. Joannopoulos, S. Fan, Opt. Lett. **28**(8), 637 (2003)
13. S.K. Ibrahim, S. Bhandare, D. Sandel, H. Zhang, R. Noe, Electron. Lett. **40**(20), 1293 (2004)
14. Z. Yu, S. Fan, Nat. Photon. **3**(2), 91 (2009)
15. S. Zhaojian He, Y. Peng, Z. Ye, C. Dai, M. Qiu, Z.Liu. Ke, Appl. Phys. Lett. **98**, 083505 (2011)
16. C. Wang, X.L. Zhong, Z.Y. Li, Sci. Rep. **2**, 674 (2012)
17. H. Kurt, D. Yilmaz, A.E. Akosman, E. Ozbay, Opt. Expr. **20**(18), 20635 (2012)

Title: Compatibility issues of cement with water reducing admixture in concrete

Author: A.K. Shrivastava Munendra Kumar

PII: S2213-0209(16)30077-5
DOI: http://dx.doi.org/doi:10.1016/j.pisc.2016.04.055
Reference: PISC 225

To appear in:

Received date: 20-1-2016
Accepted date: 7-4-2016

Please cite this article as: Shrivastava, A.K., Kumar, M.,Compatibility issues of cement with water reducing admixture in concrete, *Perspectives in Science* (2016), http://dx.doi.org/10.1016/j.pisc.2016.04.055

Compatibility issues of cement with water reducing admixture in concrete

A.K. Shrivastava[1], Munendra Kumar[2]
[1]*Department of Civil Engineering, Delhi Technological University, Delhi-42*,M: 9818162728, email:aksrivastava@dce.ac.in
[2]*Department of Civil Engineering, Delhi Technological University, Delhi-42, email:mkumar66@gmail.com*

Abstract
Multiple brand of cement and water reducing admixtures are available in the market, even though these cements and admixture comply with the respective codal provisions there performance are not same in the concrete for each and every brand of cement and water reducing admixture, even if quality and source of other ingredients of concrete is kept same. This has created a lot of confusion among the user about what type/ brand of admixture is used with what type/brand of cement and what should be optimum dose of admixture. Common problem associated with incompatibility issue is flash setting, delayed setting, rapid slump loss, improper strength gain and cracking, these not only effect the strength of the concrete but also the durability of the structure. Hence, in the present study different brand/ type of cement and water reducing admixture available in the market is used to find study the compatibility issue and optimum doase of admixture. To achieve this marsh cone test has been performed. Test results indicate that the optimum doase of admixture vary from 0.9 to 1.1 % of the weight of cement with different type/ brand of cement and type/brand of admixture.

Need of the study
The demand of concrete is increasing day by day in India, as it is a developing country. The increase in demand has come up with number of challenges in concreting like production of higher grade of concrete, retaining the slump of the concrete for higher duration and pumping the concrete at greater height. Efficiently these requirements can be fulfilled by utilization of proper admixture like plasticizer or super plasticizer. Hence now various type of plasticizer and super plasticizer available in the market and they are manufactured by number of companies. It is observed in the field that behavior of one brand of admixture is varying with other brand of admixture even though there chemical family are same for a given cement, the same variation is

seen when cement brand is changed. It has created lot of discomfort and confusion in the mind of concrete producer, because it is difficult to maintain the brand of cement and admixture same during the whole construction process. As these materials cannot be procured and stored for as per the whole project requirement, because of lesser expiry period, require huge storage space and higher initial investment. It is general practice at the site to use any of easily available cement and admixture keeping their chemical family same. But these practices have caused lots of problem in concreting not only in terms of strength and durability but also workability. This results into operation problem like chowking of pipe line because of dry, bleeded or segrated concrete. Keeping this in mind in the present study compatibility issue of different brand of cement with different brand of super plasticizing admixture is studied and a small test method is suggested that can even be done at the site to get the optimum doase, so as to avoid any problem like strength and workability issue at site.

IS 456: 2000 allow use of different type of cement like, **33** Grade ordinary Portland cement, 43 Grade ordinary Portland cement, 53 Grade ordinary Portland cement, Rapid hardening Portland cement, Portland slag cement, Portland pozzolana cement (fly ash based), Portland pozzolana cement (calcined clay based), Hydrophobic cement, Low heat Portland cement, Sulphate resisting Portland cement other combinations of Portland cement with mineral admixtures for the manufacturing of concrete. All these cement is manufactured by the name of different brand and uses different source of raw material.

Super Plasticizer in concrete

Similarly the different types of super plasticizing admixture are having the base like: Lignosulphonates, Sulphonated melamine formaldehyde (SMF), Sulphonated naphthalene formaldehyde (SNF) and Polycarboxylic ether (PCE) and different manufacturers are available for each. These all admixtures comply with codal provision laid down by IS 9103. This super plasticizer is used in the manufacturing of concrete: 1. To produce flowable concrete 2. To produce concrete with very low water-cement ratio 3. To produce high performance concrete

Compatibility issue in concrete

The common problem associated with incompatibility of concrete is : Flash setting, Delayed setting, Rapid slump loss, Improper strength gain and Cracking etc. These effects not only strength of concrete but also the durability of concrete.

The factors affecting the compatibility is

1. Composition of cement, specially tri calcium aluminate C_3A, when the C_3A content of cement is high and the availability of sulphate is low, super plasticizer will cause rapid loss in slump.
2. Fineness of cement, the amount of super plasticizer required for certain workability would be higher for a finer cement (Jolicoeur et al., 1994), the adsorption of super plasticizer is more for finer cement.
3. Nature of the calcium sulphate used during the clinker grinding
4. Soluble alkalis (alkali sulphates)
5. Chemical family of Super plasticizer
6. Chain length of Super plasticizer
7. Dosage of Super plasticizer
8. Temperature of concreting
9. Molecular weight of the polymer

Keeping this in mind in the present study compatibility issue of different brand of cement with different brand of super plasticizing admixture is studied and a small test method is suggested that can even be done at the site to get the optimum doase, so as to avoid any problem like strength and workability issue at site. The various methods available for finding out the compatibility and optimum dose of super plasticizer are: Marsh cone test, Mini slump test and Flow table test.

In the present test marsh cone test set up is fabricated as shown in Fig.1 to find the saturation or optimum doase of admixture. Cement paste by keeping water cement ratio of 0.45 is made with varying the doase of admixture in % by weight of cement. Time in seconds required to flow out 1000 cc of cement slurry from cone is find out and referred as marsh cone time in seconds. The doase of admixture after which no significant reduction in marsh cone time is observed that doase of admixture is called as saturation doase or optimal doase. The same test is repeated after different interval of time like 5 , 30, 60, 120 and 240 min to understand the slump retention capability of the admixture and cement and optimal doase of admixture for a given slump retention period. The test result is as shown in Fig.2 and 3. For a given PPC cement for one

brand of SNF base admixture is 0.9% for almost all slump retention period but for the same PPC on second brand of SNF base admixture it is 1.1%. Now if 0.9% admixture is used for second brand of admixture concrete will be dry and it can not be pumped, where as 1.1 % doase of first brand of admixture is used for concreting the concrete may bleed and segregate making concreting difficult. Hence it is advised to perform

Fig.1 Marsh cone test set up

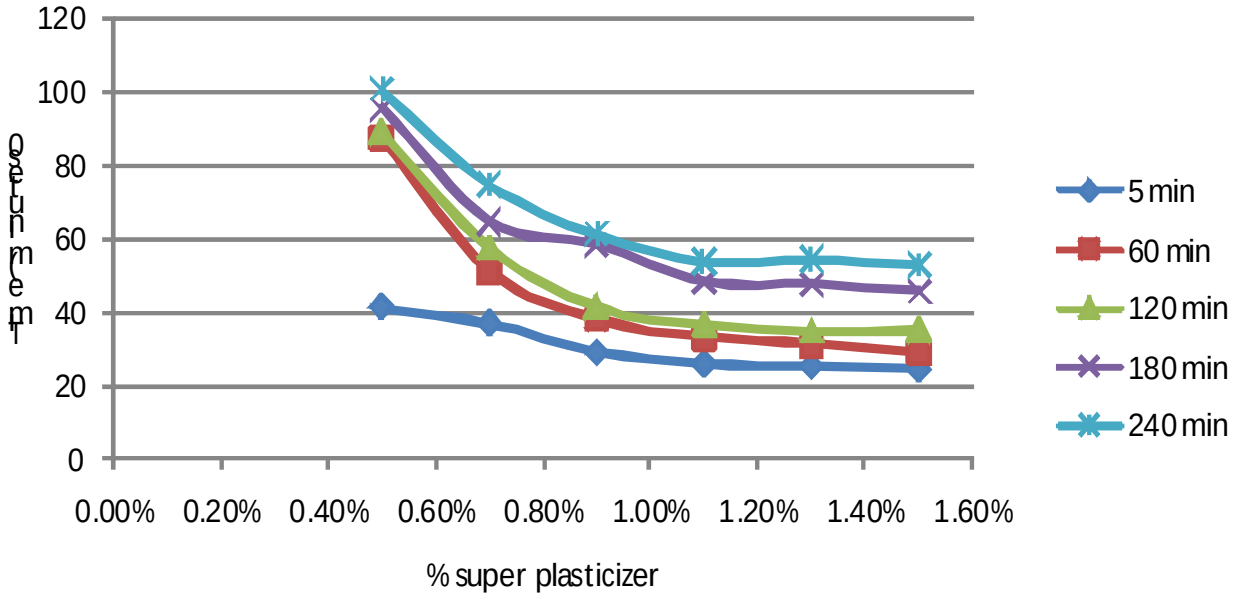

Fig.2 PPC with one brand of SNF base admixture

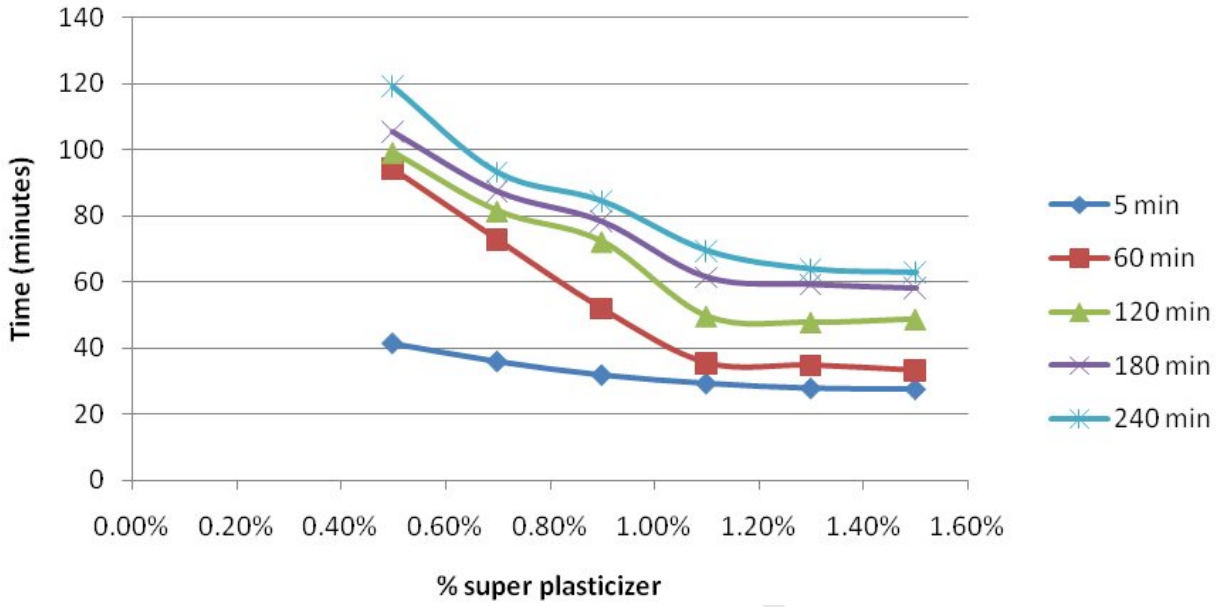

Fig.3 PPC with second brand of SNF base admixture

compatibility test at site to get optimum doase of admixture for a workable concrete for a given brand of cement and admixture.

Conclusion

The marsh cone compatibility test must be done at the site to find out the optimum or saturation doase of admixture for a given brand of cement and admixture to get proper strength, durable and workable concrete.

Bibliography

1. IS 456: 2000, “Palne and reinforced concrete – code of practice”, Berau of Indian standard, Delhi, PP1-99.

2. IS 9103: 1999, “Concrete admixtures: specification”, Berau of Indian standard, Delhi, PP1-14.

3. C. Jolicoeur, P.-C. Nkinamubanzi, M. A. Simard, and M. Piotte, “Progress in Understanding the Functional Properties of Superplasticizer in Fresh Concrete,” ACI SP-148 (1994) 63 – 88.

Int.J.Curr.Microbiol.App.Sci (2016) *5*(5): 138-152

International Journal of Current Microbiology and Applied Sciences
ISSN: 2319-7706 **Volume 5 Number 5 (2016) pp. 138-152**
Journal homepage: http://www.ijcmas.com

Original Research Article http://dx.doi.org/10.20546/ijcmas.2016.505.015

Degradation of Lindane by Sludge Enriched on Mixed Commercial Formulations of Organophosphate and Pyrethroid Pesticides

Satish Kumar, Rajkumar Bidlan* and Jai Gopal Sharma

Department of Biotechnology, Delhi Technological University, Delhi- 110042, India
**Corresponding author*

Keywords

HCH, Lindane, Biodegradation, Microbial Consortium, Pesticide, Organophosphate, Pyrethroid, Organochlorine.

Article Info

Accepted:
12 April 2016
Available Online:
10 May 2016

A B S T R A C T

Lindane (γ–Hexachlorocyclohexane) is detected in the environment even after three decades of its cessation of use. It is also found in milk, blood and food samples indicating the vastness of biomagnification. Organophosphates and pyrethroids are the other classes of pesticides being used frequently nowadays leading to further risk enhancement. Microbial degradation is the cost effective and safe strategy that can be developed and adapted for improving the environmental health by remediating lindane contamination. We enriched a bacterial population consisting of morphologically 47 distinct bacteria using commercial formulations of organophosphates and pyrethroids mixture. This consortium showed 55.6% - 90.45 % degradation of 5-30ppm lindane by 6 days. The temperature and pH optima were found to be 30^{o}C and 6 respectively. When this consortium was induced with lindane in broth only four cultures survived while 24 isolates showed the ability to clear lindane film on a nutrient agar plate. This is the first report with a microbial population enriched completely on mixtures of commercial formulations of organophosphate and pyrethroid classes of pesticides and used for degrading a pure isomer of an organochlorine pesticide.

Introduction

Among all classes of synthetic pesticides, organochlorines have found indiscriminate applications in the last century. DDT (dichlorodiphenyltrichloroethane) and HCH (hexachlorocyclohexane) were the major OCP (organochlorine pesticides) used by many developed and developing countries. Lindane (γ- HCH) and DDT were detected in the water, sediments and biota of certain provinces in China even after 30 years of their ban (Grung *et al*., 2015). According to an estimate by Weber *et al*. (2008), approximately 6 million tonnes of HCH isomers have been dumped into the environment. Vankarand Sahu (2011) have detected the average lindane levels of 10.03 ppm in a study conducted near the HCH dumping site by an HCH manufacturing unit in the Lucknow district (Uttar Pradesh state) of India. Lindane has been a causative agent to many health problems including respiratory disorders (Simonich and Hites, 1995; ATSDR, 2005; Ye *et al*., 2013). GABA neurotransmitter is influenced by lindane, affecting the vital organs like liver, kidney and the nervous system (Agrawal

and Shahi, 2015). Reduction ingermination of certain food crops in thepresence of HCH was observed by Bidlan *et al*., (2004). Lindane was also found in coffee samples of Romania (Stanciu *et al*., 2008). Nitrifying and denitrifying bacteria are also negatively affected by the presence of lindane (Tolido *et al*., 1993; Saez *et al*., 2006). Severe toxicity of lindane in fishes and gilthead seabream was demonstrated by Johnson and Finley (1980) and Oliva *et al*. (2008) respectively. Reports in the year 2000 (Cerkvenik *et al*.; Noren and Meironyte) showed the presence of organochlorine pesticides in cow and human milk from Slovenia and Sweden respectively. Concentrations exceeding the WHO/FDA limits of lindane have been detected in at least 50% of the of buffalo milk samples in national capital regions of India (Aslam *et al*., 2013). Similarly, milk samples from Lucknow (Uttar Pradesh state of India) were shown to have more than the maximum residue limit (MRL) of HCH (Nigam and Siddiqui, 2001); an increase by three times from the earlier studies by Saxena and Siddiqui (1982) indicating the increasing levels of HCH in the environment with time due to its liberal applications. According to a report from Centre for Science and Environment (CSE, India) 100% samples of blood from villages of Punjab state of India harboured lindane (Mathur *et al*., 2005). The use of pesticides seems to be unavoidable in the present scenario where new and resistant insect population is developing leading to heavy crop and economic losses.

The new generation of pesticides is also being brought into the market to combat this problem. Overall, the crops and health in all the biotic spheres areaffected negatively by the use of synthetic pesticides. Thus, it becomes imperative to develop strategies that can take care of these unprecedented levels of pesticides in our environment and help keep the nature clean and green. Here we report enriching a bacterial population that is resistant to a mixture of commercial formulations of non-organochlorine classes of pesticides and its efficacy towards lindane mineralisation.

Materials and Methods

Chemicals

Lindane (97%) was procured from Sigma Aldrich Co. (USA). Chlorpyriphos, propenofos cypermethrin, deltamethrin-triazophos and lambda-cyhalothrin were procured from Hindustan Pulverising Mills (HPM) Chemicals & Fertilizers Ltd. (India). Dichlorvos and cypermethrin were purchased from insecticide India Ltd (India) and Bharat Insecticides Limited (India) respectively. o-tolidine was purchased from Thomas Baker. All other chemicals were of analytical grade and purchased from standard companies.

Minimal Medium

The minimal medium was prepared according to Bidlan and Manonmani (2002).

Sample Collection and Preparation

Sewage and sludge were collected from surrounding areas of Delhi Technological University, Delhi, India (77.217 E long./ 28.667 N lat.), considering the fact that the wastes/effluents are dumped into these water bodies by almost every sector. The samples were maintained cold (4 ^{o}C) until further processing. Samples were mixed thoroughly just before use and filtered through Whatman No.1 filter paper. The filtrate was used as the source of native microbial population for the enrichment of pesticide tolerant microbes.

Enrichment of Consortium

To 20 ml sewage filtrate 80 ml distilled water and 0.5 g peptone was added. After shaking (120 rpm) for 24 h at room temperature (RT, 25- 30 ^{o}C), 2 ppm (2 mgL^{-1}) of each pesticide's EC was added and kept for shaking for 1 week. The cells were harvested and placed into a fresh 0.2% peptone with 2 ppm pesticide formulation mixture and kept shaking at RT. This process continued for a month with a gradual reduction in the supplied peptone concentration to 0.05%. After a month's treatment under these conditions, the pesticide concentrations were increased gradually up to 500 ppm of each of the commercial formulations. This process took 9 months. The viability of the microbes was regularly checked during the complete course of the process.

Inoculum for Degradation Studies

The consortium enriched by gradually increasing concentrations of commercial formulations of organophosphate and pyrethroid pesticides with naturally established ratio (after 9 months), was inoculated into nutrient broth (NB) and incubated for 24 h at RT. 5 ppm of lindane (as Dimethyl formamide solution, DMF) was added to the growing culture and was induced for 72 h at RT. This was harvested by centrifugation, washed twice in minimal medium and used as inoculum for degradation studies.

Effect of Temperature on the Degradation of Lindane

The induced consortium was inoculated to 20ppm lindane in minimal medium (in triplicates) maintained and incubated at temperatures 10^{o}C through 50^{o}C for 0, 3 and 6 days. The growth and degradation of the added 20ppm lindane were analysed for optimum temperature.

Effect of pH on Degradation of Lindane

0.1M phosphate buffers with pH 5, 6, 7 and 8 were prepared. 5 ml of each buffer was placed separately in triplicate test tubes and 10 ppm lindane (as DMF solution) was added. The induced consortium was inoculated to these tubes and incubated at RT. Controls for each pH and sampling periods were also placed without inoculum. The residual lindane and the growth were analysed.

Screening for Lindane-degrading Strains on Solid Medium

The pure cultures were isolated from the 9-month enriched consortium by repeated streaking on nutrient agar plates. Each culture was streaked for dense growth onto a fresh nutrient agar and allowed to grow for 24h. The plates were then sprayed with 0.5% lindane (in acetone) under aseptic conditions; acetone was allowed to evaporate leaving a thin lindane film behind. The plates were incubated at RT for another 48 h and observed for the zone of clearance in the lindane film dueto degradation by respective cultures.

Establishment of Cultures in Broth

The pure cultures from the original (9-month enriched) consortium were remixed in equal proportions of OD_{600} and allowed to grow at RT in 1/50 nutrient broth for 72 h so that the natural proportion is established amongst the populations. At the end of 72 h of growth, 5 ppm of lindane (as DMF solution) was added to the culture. This was further incubated at RT for 72 h. The process was repeated for 3 cycles. The culture was streaked on nutrient agar plates for growth for 24-48 h to obtain the finally enriched lindane tolerant bacteria.

Analytical

Determination of Growth

One ml of sample was taken for spectrophotometry (Perkin-Elmer UV-Vis-NIR lambda950) and read at 600 nm against minimal media blank.

Extraction of Lindane

The samples were first acidified by adding 2-3 drops of concentrated HCl immediately after the sampling. The acidified sample was transferred into a glass separating funnel and extracted twice with equal volume of dichloromethane. The organic layer, carrying lindane, was passed through anhydrous sodium sulphate after standing for 5 minutes to separate the two layers. The organic layers for each sample were pooled and allowed to evaporate at RT followed by transferring to a microcentrifuge tube using acetone. The acetone was allowed to evaporate. The residual lindane was re-dissolved in a known volume of acetone for analysis by chromatography.

Thin Layer Chromatography

The residual lindane was estimated by using thin layer chromatography on silica gel G coated plates. The 20 x 20 cm^2 plates were prepared by spreading a uniform layer of 0.25 mm thickness silica gel G using a spreader. The plates were allowed to dry at RT and activated at 105 ^oC for one hour. A predetermined volume of the extracted lindane (in acetone) was spotted, developed in cyclohexane: n-hexane (4:1) solvent system as mobile phase till the solvent front reached 2/3 height of the plate. The plates were removed and the solvent was allowed to evaporate at RT. Lindane spots were detected by spraying 2% o-tolidine (in acetone) and exposing the plates to bright sunlight. The spots, peacock- green in colour, were delineated using a needle and the intensity observed and the spot area calculated. The square root of the area under each spot was linearly related to the logarithm of lindane concentration. The known amounts of lindane were spotted as standards for generating the reference curve.

Gas Chromatography

The residual lindane was confirmed and quantified by injecting known volume of appropriately diluted sample- extract dissolved in acetone into the gas chromatograph (Fison 1000 series) equipped with ^{63}Ni electron capture detector and SS column (200 cm x 2 mm) packed with 1.5% OV-17 plus 1.95 QF-1 on chromosorb- W, 80-100 mesh. The column, injector and detector were maintained at 230, 230 and 320 ^oC respectively with a flow rate of carrier gas nitrogen at 50 ml min^{-1}. Under these conditions, the retention time of lindane was 3.99 min. The detection limit of lindane by GC is 2 pg and above under the given set of conditions.

Results and Discussion

Enriched Population

At the end of 9 months of enrichment, morphologically 47 distinct bacteria were obtained on nutrient agar plates. These were purified by repeated streaking and maintained on nutrient agar with 5 ppm pesticide- mixture. All the 47 isolates were again mixed in equal quantities to reconstitute the consortium (undefined) and used for screening.

Degradation of Lindane by the Original Consortium

The consortium showed 55.61% - 90.35% degradation of lindane (Fig.1). The initial concentration of 5 ppm lindane was reduced

to 9.65% at the end of 144 h of incubation while initially added higher concentrations of 10, 15, 20, 25 and 30 ppm were reduced to 10.65, 29.21, 29.94, 39.25 and 44.39% during the same time. The corresponding growth of the microbial consortium is shown in Fig. 2(a &b). It was observed that the growth of the consortium increased drastically with increasing concentrations of lindane. The six- fold increase in growth on 30ppm lindane by 18 h is a reflection of utilisation of lindane as acarbon source by the members of the consortium (Fig. 2b).

It was observed that the growth followed a zig-zag pattern with the initial increase and then decrease and again an increase. At the end of 144 h, the final growth was approximately 2 ½ - 3 ½ folds with respect to the initial inoculum (Fig. 2a).

There appeared to be a direct correlation between the concentration and the time for degrading the initially supplied lindane. The other common trend observed was that when growth reduced, the degradation also diminished in that phase. This was an indication of the direct relationship between consortium growth and lindane degradation. Similar observations were made by Jilani (2013).

Lindane Degradation at Different Temperatures

The initially added 20 ppm of lindane was degraded by 13.89% at both 10 ^{o}C and 20 ^{o}C while 23.6% and 36.2% degradation was observed at 40 ^{o}C and 50 ^{o}C respectively (Fig. 3a).

Maximum degradation of 64.9% was seen at 30 ^{o}C (Fig. 3a). The corresponding growth is shown in Fig. 3b. Overall growth was observed only at 30 ^{o}C with 6.67% increase and at 40 ^{o}C with 34.6% increase in 6 days of incubation. The added inoculum decreased at other temperatures. Even though the growth was better at 40 ^{o}C than 30 ^{o}C, degradation was better in the latter case. The reason may be the temperature optima for catabolic enzymes is in favour of the 30 ^{o}C. With 46% reduction in the inoculum at 50 ^{o}C, degradation was more effective than 40^{o}C. This may be because of the higher inoculum size provided to 50^{o}C and also certain catabolic enzymes (from certain member(s) of the consortium) might have higher temperature optima.

The consortium comprises of different cultures that may have different behaviour at different temperatures andpH. In an earlier study, Bidlan and Manonmani (2002) have earlier detected the deradation of DDT from 4^{o}C to 50^{o}C but the most efficient degradation was shown to be at 30^{o}C while the efficient growth was observed at 37 ^{o}C.

Lindane Degradation at Different pH

The consortium could degrade the initially provided 10 ppm lindane by 13.9%, 18.9%, 23.6% and 50.5% at pH 5, pH 6, pH 7 and pH 8 respectively by the end of 144 h (6 days) of incubation (Fig. 4a). The corresponding growth pattern is shown in Fig. 4b.

It was observed that the growth increased by 42.86%, 52.17%, 39.13% and 86.96% in the first 3 days of incubation at pH 5, pH 6, pH 7 and pH 8 respectively that reduced to 14.29% for pH 5 and to 26.09% for other 3 pH respectively by the end of 6th day of incubation with respect to the initial inoculum level. The maximum growth increment in the first 3 days was at pH 8 followed by pH 6, pH 5 and pH 7 respectively while the reduction in next 3 days was least at pH 7 followed by pH 6, pH 5 and pH 8 with 33.33%, 50%, 66.67% and

70% reduction respectively. The degradation of lindane was more effective with an increase in pH indicating a direct correlation between studied pH levels and lindane degradation.

Even though the growth in pH 8 decreased maximum in last three days, yet the degradation was more efficient suggestive towards the secretory enzymes/enzyme systems involved in lindane degradation (this is our hypothesis and need further studies to prove; though it is believed that the degradative enzymes are non-secretory through experiments with Pseudomonas paucimobilis).

Bidlan and Manonmani (2002) and Bidlan (2003) have earlier shown that the pH 7- 7.5 was more favourable for bioremediation of DDT by *Serratia marcescens* DT-1P, *Pseudomonas aeruginosa* DT- ct1 and *Pseudomonas aeruginosa* DT- ct2. Sreedharan *et al*. (1999) demonstrated the degradation of HCH in acidic soils with pH above 3 using Pseudomonas paucimobilis. More growth during the first 3 days in pH 8 in our case, could have enhanced the enzyme production that continued to act during the subsequent three days of incubation, thereby degrading almost 87.29% of lindane as compared to first three days. At pH 6 the degradation in last three days was 225.32% as compared to the first three days. Since the growth in pH 6 was second to that of pH 8, the greater degradation percentage in thesecond half as compared to the first half might be due to the pH optima for the catabolic enzymes. The culture can be grown at pH 8 initially and then the pH 6 can be provided for efficient degradation. The pH 7 showed the least increase in biomass in the first half but it also showed the least decrease in the biomass in thesecond half; thereby giving the consortium optimum condition to degrade 69.89% lindane in last three days as compared to the first three days. Yet, the most efficient degradation among different pH provided was at pH 8. Earlier, Bidlan and Manonmani (2002) found that the degradation and growth reduced at pH greater than 7.5.

Screening of the Individual Isolates for Lindane Degradation on Agar

Cultures 3, 5, 6, 7, 9, 10, 11, 14, 15, 18, 19, 20, 22, 23, 26, 28, 29, 30, 33, 35, 36, 38, 44 and 46 showed clearance of lindane film (Fig. 5). This was an indication that the cultures have the potential for degrading lindane.

Screening of the Individual Isolates for Lindane Degradation in Broth

It was observed that the lindane- induced consortium had dominatingly 4 distinct cultures. These cultures were purified, designated as LR1, LR2, LR3 and LR4 respectively (Fig. 6) and maintained on minimal agar supplemented with 1/50 NB and 5 ppm lindane for future studies later.

Most reports show that the enrichment is done with the same (parent) compound (Manonmani *et al*., 2000; Bidlan, 2003; Bidlan *et al*., 2004; Nagpal and Paknikar, 2006; Murthy and Manonmani, 2007; Deepthi *et al*., 2007; Pannu and Kumar, 2014) or the analogues of the compound (Focht and Alexander, 1970; Bartha, 1990) that needs to be degraded by the microbes. In contrast to the basic practice, our approach was to adapt a technique that could be beneficial in the present and future scenario, keeping in view that most parts of the world are now applying the organophosphates and pyrethroids instead of organochlorine pesticides.

Amyotrophic Lateral Sclerosis (ALS), a progressive fatal neurodegenerative human disease has been associated with pesticide exposure especially with organochlorines, pyrethroids, herbicides and fumigants (Kamel *et al*., 2012) and organophosphates (Chen, 2012). Slotkin and Seidler (2009) have demonstrated the neurological and neurotoxic effects of organophosphates while David *et al*. (2014) discussed the teratogenic effect of paraoxon, an organophosphate, on neurodifferentiation.We wish to establish a population tolerant to the existing concentrations of non- organochlorine pesticides in the environment and probably still higher concentrations in future. Being tolerant to these other classes of pesticides will help the application of our cultures as they would stay active and remediate the organochlorine load already present in nature. Apart from this, the same culture might be able to remediate the loads from other classes of pesticides.

Grung *et al*. (2015) stressed the need for research on organophosphates since they are the dominating group being used at present. Viel *et al*. (2015) discussed the cognitive developmental disabilities in post- natal stages of children due to the exposure of pyrethroids leading to an urgent realisation of considering the remediation for this pesticide class as well. Our cultures from the consortium may act upon these pesticides as they were enriched by the mixture of organophosphates and pyrethroids. The probability of the application of our consortium towards simultaneous degradation of different classes of pesticides cannot be ruled out. Selvi *et al*. (2013) worked with DDT- degrading consortium to study the degradation of the pesticide isoprothiolane. Pino and Penuela (2011) developed a microbial consortium with 12 different bacterial strains through enrichment technique that could degrade 150 ppm each of chlorpyrifos and methyl-parathion separately as well as simultaneously. Liu *et al*. (2009) engineered strain LZ1 of Stenotrophomonas species that could produce the enzyme organophosphorus hydrolase (OPH). This enzyme was capable of degrading p-nitrophenol substituted organophosphates and their products. The three organophosphates paraoxon, parathion and methylparathion degradation was enhanced in the presence of 4-chlorophenol. Yang *et al*. (2012) could co-express the lin A_{and}mpdgenes in a cloned E. coli for simultaneous degradation of organochlorine (lindane) and organophosphate (methyl parathion). This clone is good to work in a bioreactor as it also expresses the green fluorescent protein for detection. Our consortium on the other hand, with longer acclimatisation, may work in-situ. The need of acclimatisation (pre-exposure or induction) in bioremediation was earlier emphasised by many researchers in the past as well (Bidlan and Manonmani, 2002; Bidlan, 2003; Jilani, 2013). Sonkong *et al*. (2008) also demonstrated the effectiveness of 72 h induction of inoculum to DDT in the presence of glucose and yeast extract for enhancing the degradation of DDT. Successive exposure of culture to lindane improved its ability to degrade the pesticide (Wada *et al*., 1989; Bhuyan *et al*., 1992) while the same with DDT did not yield any improvement (Bidlan and Manonmani, 2002).

Microorganisms transform the complex organic compounds to CO_2 or other simple organic compounds through their metabolic enzymes. This reducing equivalents from the oxidation are assimilated and results in the growth of organisms that work out the degradation (Latha, 2012). Our results also reflect the similar view along with the other hypothesis proposed here by us that the degradation during the decline phase of

growth may be due to the enzyme/ enzyme systems already synthesised by the microbial cells during their active growth phase (need further studies to prove). Baczynski *et al*. (2010) noted the initial increase in growth with substantial decrease and then the biomass remaining constant until the end of the studies. The zig- zag pattern of growth as in the present study was also observed by Sander *et al*. (1991), Bidlan and Manonmani (2002), Sonkong*et al*. (2008) and Jilani (2013). Jilani (2013) discussed the decline in the viable count due to non- acclimation of the culture to the pesticides while we hypothesise it differently here; further studies might establish the fact.

Fig.1 Degradation of Lindane by the Consortium Enriched on Mixture of Organophosphate and Pyrethroid Pesticide (Commercial Formulation)

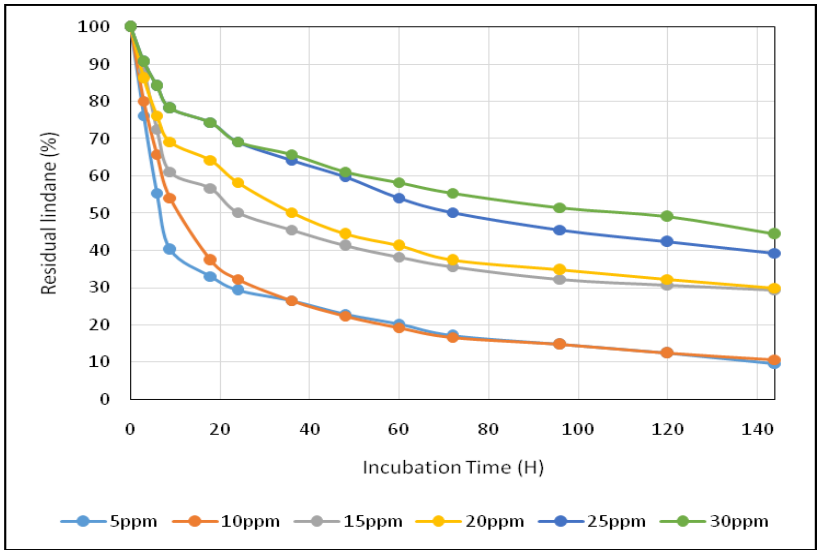

Fig.2a Growth of the Consortium on Different Concentrations of Lindane. The Consortium is Enriched on Mixture of Organophosphate and Pyrethroid Pesticide (Commercial Formulation)

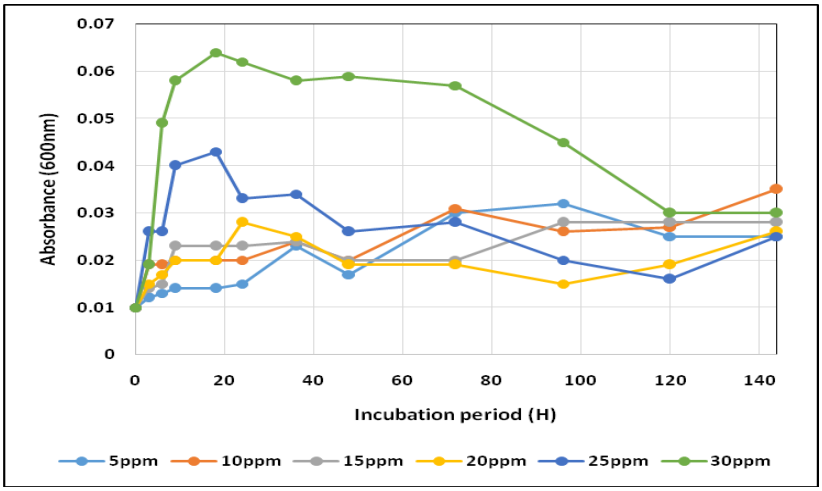

Fig.2b Growth of the Consortium on Different Concentrations of Lindane During the First 24 h

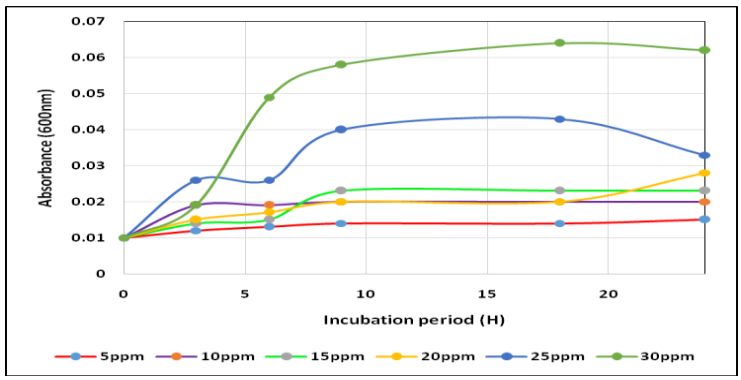

Fig.3a Degradation of Lindane by the Consortium. The Consortium was Inoculated to 20ppm Lindane in MM and Samples were Drawn at 0 Days, 3 Days and 6Days for Analysis

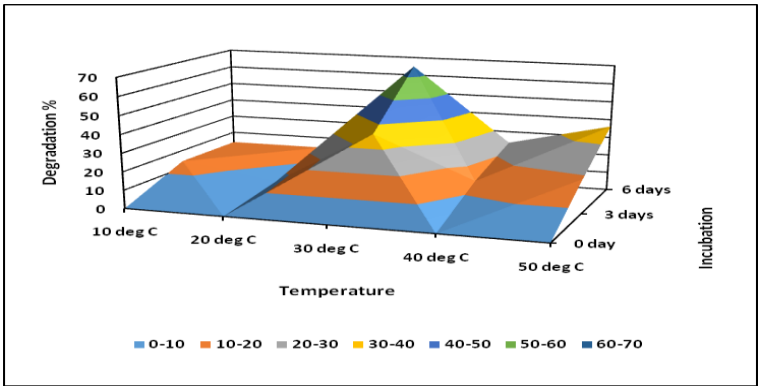

Fig.3b Growth of the Consortium at Different Temperatures. The Consortium was Inoculated to 20ppm Lindane in MM and Samples were Drawn at 0 Days, 3 Days and 6Days for Analysis

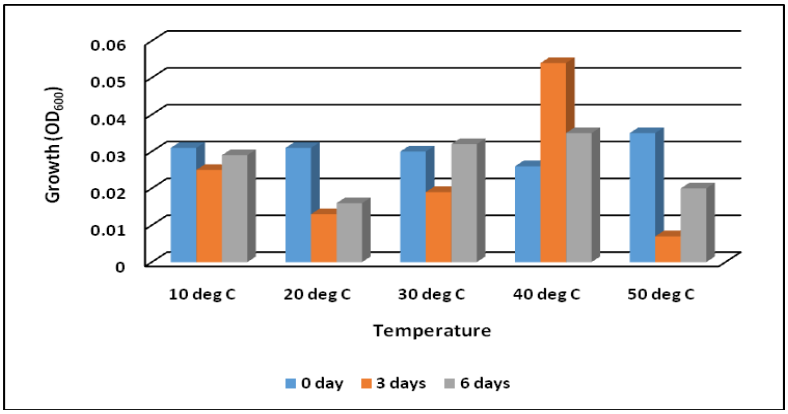

Fig.4a Effect of pH on Lindane Degradation by the Consortium. The Consortium was Inoculated to 10ppm Lindane in MM and Samples were Drawn at 0 Days, 3 Days and 6Days for Analysis

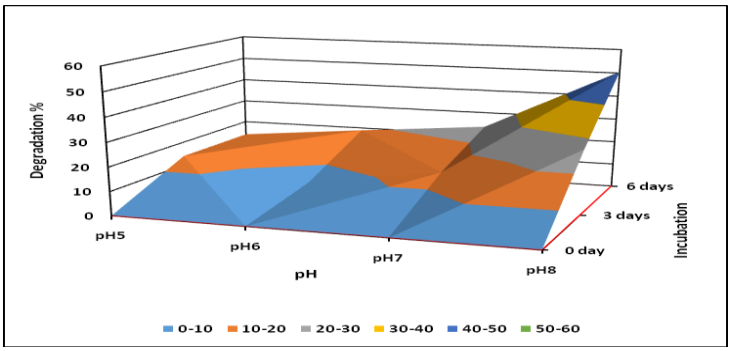

Fig.4b Effect of ph on Consortium (Biomass). the consortium was Inoculated to 10ppm Lindane in MM and Samples were Drawn at 0 Days, 3 Days and 6Days for Analysis

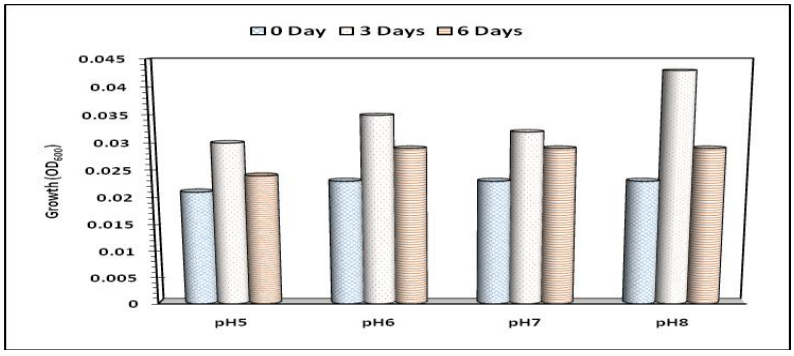

Fig.5 Individual Strains were Sprayed with 0.5% Lindane Solution to form a Thin Film and Incubated at R.T. The Cultures that have the Potential for Degrading Lindane Cleared the Film

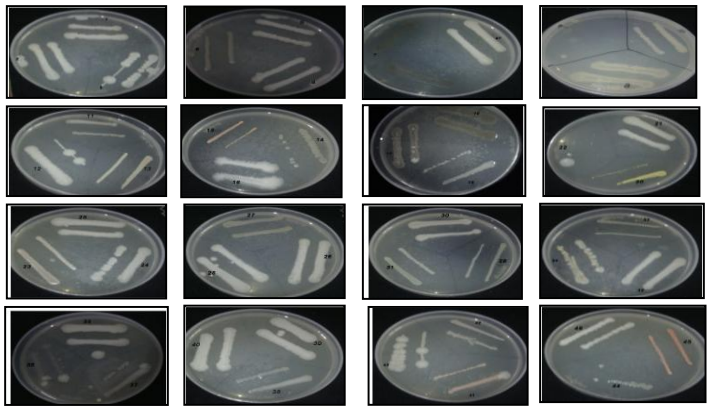

Fig.6 Individual Strains that Ultimately Survived the Lindane Enrichment

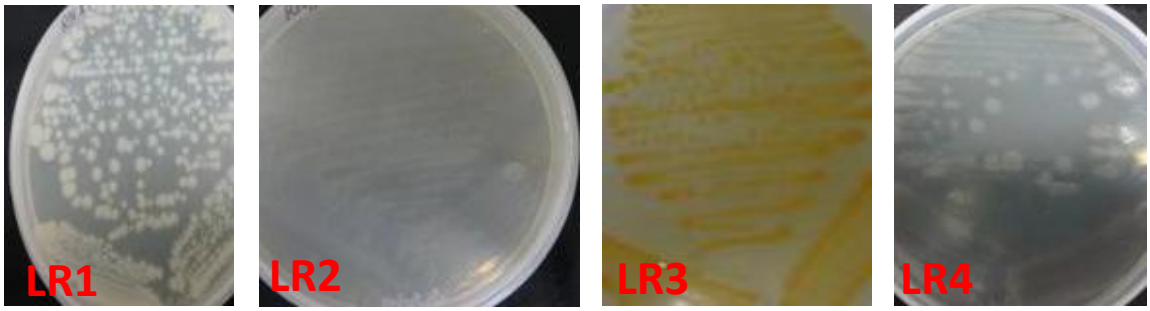

Acclimation of consortium for DDT degradation by Bidlan and Manonmani (2002) also resulted in the ultimate survival of four strains comprising *Serratia marcescens* DT- 1P and other three Pseudomonas strains. Pannu and Kumar (2014) isolated 78 strains out of which only 9 strains could clear the lindane film after 7 days of incubation and only 3 strains RP-1, RP-3and RP-9 were able to withstand 100 ppm of this insecticide. The other strains were able to tolerate lindane concentrations from 20- 60 ppm (parts per million= 1 x 10^{-6}). Similar observations with limiting cadmium were described by Kumar *et al*.(2010). The cultures in pure form were able to degrade lindane in agar medium while in the broth where the cultures were in mixed form, the total number of surviving/ actively growing cultures were observed to be only four (Fig. 6). This might be due to the interaction between the various types of bacteria present. The two cultures viz. RL2 and RL4 were dominating and appeared indiscriminately, overcasting the other members of the consortium. This might be due to the antibiotic or inhibitory factors produced by the two cultures. The other two cultures (RL1 &RL3) were able to resist these factors along with the lindane; hence survived.

The degradations of pesticides have been achieved in many works in the past 50- 60 years. The time required and the percentage of degradation varied from case to case. The microbe used and the type of pesticide under study play a vital role than the other parameters like pH and temperature. Many times the significant parameter described is the inoculum size (Bidlan and Manonmani, 2002; Selvi *et al*., 2013). There might also be the effect of a threshold level of the initial pesticide concentration necessary for the degradation below which the culture induction is not possible. More investigations may further support the findings.

In conclusion, this is the first report of its kind with a microbial population enriched completely on mixtures of commercial formulations of organophosphate and pyrethroid classes of pesticides used for degrading a pure isomer of an organochlorine pesticide. The fact that our consortium could degrade substantially the initially supplied lindane concentrations from 5 ppm through 30 ppm in a short period of 6 days is a positive sign to apply it for remediation of contaminated water bodies; of course, after further vigorous training (acclimation) of the consortium with lindane in presence of the organophosphates and pyrethroids. The future environmental problem may arise through the indiscriminate use of organophosphates and pyrethroid pesticides.

For such conditions prevailing in future, our consortium and its application can become the master stroke. The avenues are still open for a better combinatorial bioremediation strategy to save our biosphere in a healthy way for the future generations.

Acknowledgement

The authors would like to thank the Hon'ble Vice Chancellor, Registrar, Dean-PG, Dean-IRD and AR-IRD, Head of Biotechnology, all from Delhi Technological University for their constant support and encouragement during this work. We also thank Mr. Jitendra Singh and Mr. Chhail Bihari of Biotechnology, DTU for their timely support. The first two authors thank the University Grants Commission, India for providing the junior research fellowship and post- doctoral fellowship respectively. Most of the work could be conducted from the contingency grants of UGC fellowships.

References

Agrawal, N., Shahi, S.K. 2015. An environmental clean-up strategy-Microbial transformation of xenobiotic compounds. *Int. J. Curr. Microbiol. App. Sci.*, 4(4): 429-461.

Aslam, M., Rais, S., Alam, A. 2013. Quantification of organochlorine pesticide residues in the buffalo milk samples of Delhi city, India. *J. Environ. Protec.*, 4: 964- 974. DOI: http://dx.doi.org/10.4236/jep.2013.49111

ATSDR. Agency for Toxic Substances and Disease Registry. 2005. ToxFAQs for hexachlorocyclohexane. Hexa-chlorocyclohexane (HCH). Atlanta, USA. (http://www.atsdr.cdc.gov/toxfaqs/tf.asp?id=753&tid=138)

Baczynski, T., Pleissner, D., Grotenhuis, T. 2010. Aerobic biodegradation of organochlorine pesticides in contaminated soil- Significance of temperature and availability. *Chemosphere*, 78(1): 22-28. DOI: http://dx.doi.org/10.1016/j.chemosphere.2009.09.058.

Bartha, R. 1990. Isolation of microorganisms that metabolize xenobiotic compounds. In: Labeda D. P., editor. Isolation of Biotechnological Organisms from Nature. New York: Mc Graw Hill. 283- 305.

Bhuyan, S., Sahu, S.K., Adhya, T.K., Sethunathan, N. 1992. Accelerated aerobic degradation of □-HCH in suspensions of flooded and non-flooded soils pretreated with HCH. *Biol. Fert. Soils.*, 12(4): 279- 284. doi: http://dx.doi.org/10.1007/BF00336044

Bidlan, R. 2003. Studies on DDT degradation by Bacterial strains. In: Isolation, purification and identification of microbes capable of DDT-degradation. Ph.D. thesis, University of Mysore, India. pp 90-142.

Bidlan, R., Manonmani, H.K. 2002. Aerobic degradation of dichlorodiphenyltrichloroethane (DDT) by *Serratia marcescens* DT-1P. *Process Biochem.*, 38: 49-56. DOI: http://dx.doi.org/10.1016/S0032-9592(02)00066-3.

Bidlan, R., Afsar, M., Manonmani, H.K. 2004. Bioremediation of HCH-contaminated soil: elimination of inhibitory effects of the insecticide on radish and green gram seed germination. *Chemosphere*, 56: 803-811. doi: http://dx.doi.org/10.1016/j.chemosphere.2004.01.015.

Cerkvenik, V., Doganoc, D.Z., Jan, J. 2000. Evidence of some trace elements, organochlorine pesticides and PCBs in Slovenian cow's milk. *Food Technol. Biotechnol.*, 38(2): 155-160.

Chen, Y. 2012. Organophosphate- induced brain damage: mechanisms, neuropsychiatric and neurological consequences and potential

therapeutic strategies. *Neurotoxicol.*, 33: 391- 400. DOI: http://dx.doi.org/10.1016/j.neuro.2012.03.011.

David, P., Sogorb, M.A., Fabbri, M., Gribaldo, L., Collotta, A., Scelfo, B., Vilanova, E., Harris, G., Price, A.B. 2014. Genomic and phenotypic alterations of the neuronal- like cells derived from human embryonal carcinoma stem cells (NT2) caused by exposure to organophosphorus compounds paraoxon and mipafox. *Int. J. Mol. Sci.*, 15: 905-926. DOI: http://dx.doi.org/10.3390/ijms15010905.

Deepthi, N., Rastogi, N.K., Manonmani, H.K. 2007. Degradation of DDT by a defined microbial consortium: optimization of degradation conditions by response surface methodology. *Res. J. Microbiol.*, 2: 315- 326. DOI: http://dx.doi.org/10.3923/jm.2007.315.326.

Focht, D.D., Alexander, M. 1970. DDT metabolites and analogs: ring fission by Hydrogenomonas. Science. 170(3953): 91-92. DOI: http://dx.doi.org/10.1126/science.170.3953.91.

Francis, A.J., Spanggord, R.J., Ouchi, G.I. 1975. Degradation of lindane by Escherichiacoli. *App. Microbiol.*, 29(4): 567- 568.

Grung, M., Lin, Y., Zhang, H., Steen, A.O., Huang, J., Zhang, G., Larssen, T. 2015. Pesticide levels and environmental risk in aquatic environments in China — A review. *Environ. Int.*, 81: 87–97. DOI: http://dx.doi.org/10.1016/j.envint.2015.04.013.

Jilani, S. 2013. Comparative assessment of growth and biodegradation potential of soil isolate in the presence of pesticides. *Saudi J. Biol. Sci.*, 20: 257-264. DOI: http://dx.doi.org/10.1016/j.sjbs.2013.02.007.

Johnson, W.W., Finley, M.T. 1980. Handbook of acute toxicity of chemicals to fish and aquatic invertebrates. Resource publication 137. Washington DC: U.S. Department of interior fish and wildlife service. pp. 6-56.

Kamel, F., Umbach, D.M., Bedlack, R.S., Richards, M., Watson, M., Alavanja, M.C.R., Blair, A., Hoppin, J.A., Schimdt, S., Sandler, D.P. 2012. Pesticide exposure and amyotrophic lateral sclerosis. *Neurotoxicol.*, 33(3): 457-462. DOI: http://dx.doi.org/10.1016/j.neuro.2012.04.001.

Kumar, A., Cameotra, S.S., Gupta, S. 2010. Screening and characterization of potential cadmium biosorbent Alcaligenes strain from industrial effluent. *J. Basic Microbiol.*, 51: 1-7.

Latha, R. 2012. Biochemical and molecular characterization of DDT- degrading dehalogenase from Pseudomonas Spp. In: Review of literature. Ph.D. thesis. University of Mysore, Mysore, India. pp 9-105.

Liu, Z., Yang, C., Jiang, H., Mulchandani, A., Chen, W., Qiao, C. 2009. Simultaneous degradation of organophosphates and 4- substituted phenols by Stenotrophomonas Species LZ-1 with surface- displayed organophosphorus hydrolase. *J. Agric. Food Chem.*, 57: 6171- 6177. DOI: http://dx.doi.org/10.1021/jf804008j.

Manonmani, H.K., Chandrashekaraiah, D.H., Reddy, S.N., Elcey, C.D., Kunhi, A.A.M. 2000. Isolation and acclimation of a microbial consortium for improved aerobic degradation of □- hexachlorocyclohexane. *J. Agric. Food Chem.*, 48: 4341–4351. DOI**:** http://dx.doi.org/10.1021/jf990712c.

Mathur, H.B., Agarwal, H.C., Sapna Johnson, Nirmali Sarikia. 2005. CSE India Report: Analysis of Pesticide Residues In Blood Samples From Villages of Punjab. CSE/PML/PR-21/2005.

Murthy, H.M.R., Manonmani, H.K. 2007. Aerobic degradation of technical hexachlorocyclohexane by a defined microbial consortium. *J. Hazard. Mater.*, 149(1): 18-25. DOI: http://dx.doi.org/10.1016/j.jhazmat.2007.03.053.

Nagpal, V., Paknikar, K.M. 2006. Integrated approach for the enhanced degradation of lindane. *Indian J. Biotechnol.*, 5(Suppl): 400-405.

Nigam, U., Siddiqui, K.J. 2001. Organochlorine insecticide residues in dairy milk samples collected in Lucknow, India. *Bull. Environ. Contam. Toxicol.*, 66: 678-682.

Noren, K., Meironyte, D. 2000. Organochlorine and organobromine contaminating Swedish human milk in perspective of past 20- 30 years. *Chemosphere*, 44: 1111-1123. DOI: http://dx.doi.org/10.1016/S0045-6535(99)00360-4.

Oliva, M., Garrido, C., Sales, D., Canales, M.L.G. 2008. Lindane toxicity on early life stages of gilthead seabream (Sparus aurata) with a note on its histopathological manifestations. *Environ. Toxicol. Pharmacol.*, 25(1): 94-102. DOI: http://dx.doi.org/10.1016/j.etap.2007.09.005.

Pannu, R., Kumar, D. 2014. Biodegradation study of □- hexachlorocyclohexane using selected bacteria from agricultural soil. *Afr. J. Microbiol. Res.*, 8(36): 3335-3346. DOI: http://dx.doi.org/10.5897/AJMR2014.6842.

Pino, N., Penuela, G. 2011. Simultaneous degradation of the pesticides methyl parathion and chlorpyrifos by an isolated bacterial consortium from a contaminated site. *Int. Biodeter. Biodegr.*, 65: 827-831. DOI: http://dx.doi.org/10.1016/j.ibiod.2011.06.001.

Saez, F., Pozo, C., Gomez, M.A., Toledo, M.V.M., Rodelas, B., López, J.G. 2006. Growth and denitrifying activity of Xanthobacter autotrophicus CECT 7064 in the presence of selected pesticides. *Appl. Microbiol. Biotechnol.*, 71: 563-567. DOI: http://dx.doi.org/10.1007/s00253-005-0182-8.

Sander, P., Wittich, R.M., Fortnagel, P., Wilkes, H., Francke, W. 1991. Degradation of 1,2,4- Trichloro- and 1,2,4,5- Tetrachlorobenzene by Pseudomonas strains. *Appl. Environ. Microbiol.*, 57(5): 1430-1440. (0099-2240/91/051430-11$02.00/0).

Saxena, M.C., Siddiqui, M.K.J. 1982. Pesticide pollution in India: Organochlorine pesticides in milk of women, buffalo and goat. *J. Dairy Sci.*, 65: 430-434. DOI: http://dx.doi.org/10.3168/jds.S0022-0302(82)82209-1.

Selvi, A.A., Rastogi, N.K., Manonmani, H.K. 2013. Degradation of isoprothiolane by a defined microbial consortium using response surface methodology. *J. Environ. Biol.*, 34: 545-554.

Simonich, L.S., Hites, R.A. 1995. Global distribution of persistent organochlorine compounds. *Sci.*, 269: 1851–1854.

Slotkin, T., Seidler, F. 2009. Transcriptional profiles reveal similarities and differences in the effects of developmental neurotoxicants on differentiation into neurotransmitter phenotypes in PC12 cells. *Brain Res. Bull.*, 78(4-5): 211-225. DOI: http://dx.doi.org/10.1016/j.brainresbull.2008.08.021.

Sonkong, K., Prasertsan, P., Sobhon, V. 2008. Screening and identification of p, p'-DDT degrading soil isolates. *J. Sci. Technol.*, 30(Suppl.1): 103- 110.

Sreedharan, B., Singh, N., Sethunathan, N. 1999. Aerobic degradation of soil-sorbed isomer of hexachlorocyclohexane by Pseudomonaspaucimobilis. In: Abstract book, Abstract No. TRC 2.

2nd Int. Conf. On Contam. *Soil Environ.*, In Australasia-pacific regions. 12- 17 Dec. 1999, New Delhi, pp. 109-/110.

Stanciu, G., Dobrinas, S., Birghila, S., Popescu, M. 2008. Determination of organic compounds from different types of coffee by HPLC and GC-ECD analysis. *Environ. Engg. Mgmt J.*, 7(6): 661-666.

Toledo, M.V.M., Salmeron, V., Rodelas, B., Pozo, C., Lopez, J.G. 1993. Studies on the effects of a chlorinated hydrocarbon insecticide, lindane, on soil microorganisms. *Chemosphere*, 27(11): 2261-2270. DOI: http://dx.doi.org/10.1016/0045-6535(93)90137-T.

Vankar, P.S., Sahu, R. 2011. Lindane levels in the dumping grounds in Chinhat area, Lucknow, India. *Electron. J. Environ. Agri. Food Chem.*, 10(4): 2081-2089.

Viel, J.F., Warembourg, C., Idrissi, G.L.M., Lacroix, A., Limon, G., Rouget, F., Monfort, C., Durand, G., Cordier, S., Chevrier, C. 2015. Pyrethroid insecticide exposure and cognitive development disabilities in children: The PELAGIE mother- child cohort. Environ. Int. 82:69-75 DOI: http://dx.doi.org/10.1016/j.envint.2015.05.009.

Wada, H., Senoo, K., Takai, Y. 1989. Rapid degradation of □-HCH in upland soil after multiple applications. *Soil Sci. Plant Nutr.*, 35(1): 71-77. DOI: http://dx.doi.org/10.1080/00380768.1989.10434738.

Weber, R., Gaus, C., Tysklind, M., Johnston, P., Forter, M., Hollert, H., Heinisch, H., Holubek, I., Lloyd- Smith, M., Masunaga, S., Moccarelli, P., Santillo, D., Seike, N., Symons, R., Torres, J.P.M., Verta, M., Barbelow, G., Vijgen, J., Watson, A., Costner, P., Woelz, J., Wycisk, P., Zennegg, M. 2008. Dioxin- and POP- contaminated sites- contemporary and future relevance and challenges. *Environ. Sci. Poll Res.*, 15: 363-393. DOI: http://dx.doi.org/10.1007/s11356.008.0024-1.

Yang, J., Liu, R., Song, W., Yang, Y, Cui, F., Qiao, C. 2012. *Appl. Biochem. Biotechnol.*, 166: 590-598. DOI: http://dx.doi.org/10.1007/s12010-011-9450-5.

Ye, M., Beach, J., Martin, J.W., Senthilselvan, A. 2013. Occupational pesticide exposures and respiratory health. *Int. J. Environ. Res. Public Health*, 10: 6442-6471. DOI: http://dx.doi.org/10.3390/ijerph10126442.

How to cite this article:

Satish Kumar, Rajkumar Bidlan and Jai Gopal Sharma. 2016. Degradation of Lindane by Sludge Enriched on Mixed Commercial Formulations of Organophosphate and Pyrethroid Pesticides. *Int.J.Curr.Microbiol.App.Sci.* 5(5): 138-152.
doi: http://dx.doi.org/10.20546/ijcmas.2016.505.015

Optics Communications 374 (2016) 148–155

Contents lists available at ScienceDirect

Optics Communications

journal homepage: www.elsevier.com/locate/optcom

Design and analysis of polarization independent all-optical logic gates in silicon-on-insulator photonic crystal

Preeti Rani, Yogita Kalra, R.K. Sinha *

TIFAC-Centre of Relevance and Excellence in Fiber Optics and Optical Communication, Department of Applied Physics, Delhi Technological University (Formerly Delhi College of Engineering, University of Delhi), Bawana Road, Delhi 110042, India

ARTICLE INFO

Article history:
Received 25 January 2016
Received in revised form
5 April 2016
Accepted 16 April 2016

Keywords:
Photonic crystal
Polarization independent
Optical logic device
Interference
Optoelectronics

ABSTRACT

In this paper, we have reported design and analysis of polarization independent all optical logic gates in silicon-on-insulator photonic crystal consisting of two dimensional honeycomb lattices with two different air holes exhibiting photonic band gap for both TE and TM mode in the optical communication window. The proposed structures perform as an AND optical logic gate and all the optical logic gates based on the phenomenon of interference. The response period and bit rate for TE and TM polarizations at a wavelength of 1.55 μm show improved results as reported earlier.

1. Introduction

In recent years various schemes have been employed for the designing of optical logic gates using optical fibers [1–5] and waveguides [6–8], but they have certain limitations like low speed, big size and difficult to perform on chip integration. Recently, two dimensional (2D) photonic crystal (PhC) slab structures have attracted wide attention due to their ease of fabrication as compared to three dimensional structures. The 2D PhC structures provide versatile platform for on-chip device design and present an alternative to the existing electronic circuitry. In general, these 2D PhC structures are operational for only one specific polarization that limits the light coupling to localized optical modes and extraction of light from the slab. However, polarization independent wave guiding in 2D PhC structures with complete photonic band gap (i.e. photonic band gap for both transverse electric (TE) and transverse magnetic (TM) mode) may overcome this limitation [9–12]. Optical switches and logic gates have emerged as an important part of optoelectronic and integrated devices and have several applications.

To our knowledge, only single polarization based logic gates have been reported so far [13–17]. Optical logic gates on SOI platform lead to certain applications like the ultrafast operation of the devices as compared to the traditional electronic devices, data-integrity verification, packet header modification etc. The reported optical logic gates are 2D structures operational for single polarization [18–22]. In this paper, we propose the design of polarization independent AND optical logic gate and all optical logic gates in silicon-on-insulator (SOI) platform based on the light beam interference effect. The structure for AND gate consists of symmetric Y branch waveguide so that light beams interfere constructively whereas for all optical logic gates one additional reference waveguide has been created. The light beams interfere either constructively or destructively for both the polarizations based on the phase angle of the light beam launched at reference waveguide. Phase angle of the input light beam can be varied as demonstrated by Birr et al. [23]. The proposed design consists of honey comb lattice arrangement with two different air holes in SOI substrate. The honey comb arrangement on SOI platform has been chosen because this arrangement supports both the polarizations. The honey comb structure of such type can be easily implemented on SOI substrate using recently available technology. The structure has been optimized for both the polarizations (TE and TM mode) at 1.55 μm wavelength. The contrast ratio and bit rate have been calculated for TE and TM modes separately and it has been found that the proposed designs behave as AND optical logic gate and all optical logic gates. The contrast ratio defined as $10\log(P_1/P_0)$ (dB) has been calculated for both TE and TM polarizations separately, where P_1 represents power for logic-1 and P_0 represents the power for logic-0 obtained at the output port. The response time [24,25] for both the polarizations has been

* Corresponding author.
E-mail address: dr_rk_sinha@yahoo.com (R.K. Sinha).

http://dx.doi.org/10.1016/j.optcom.2016.04.037
0030-4018/

evaluated using the finite difference time domain (FDTD) method. The calculated results i.e. response period and bit rate are improved than that reported in the previous papers [18,19,25].

2. Device design, optimization and simulation results

In this paper, the design for AND optical logic gate and all optical logic gates constructed on SOI substrate has been presented. The proposed design consists of honey comb lattice of air holes of two different radii in silicon slab as shown in Fig. 1(a). The radii of two different air holes have been chosen, so as to achieve complete photonic band gap. The radii of two air holes has been taken as $r_b=0.36a$ (radius of bigger air hole) and $r_s=0.16a$ (radius of smaller air hole), where '$a=570$ nm' is the lattice constant. The smaller air holes have been placed exactly at the center of the bigger air holes. An asymmetrical silicon ($n_{Si}=3.5$) slab of thickness 250 nm has been taken which has air as upper cladding and silica ($n_{Sio_2}=1.45$) as lower cladding layer. The 3D calculations consume more time and memory, so, we have employed 2D analysis with effective index method. The effective index of the slab for TE and TM modes has been calculated to be n_{eff} (TE)=2.89 and n_{eff} (TM)=2.15 at 1.55 μm wavelength, respectively using Finite Element Method (FEM) [12]. Using plane wave expansion (PWE) method, it has been observed that there exists a complete photonic band gap in the normalized frequency range of 0.3520–0.3836 (a/λ), as shown in Fig. 1(b).

2.1. For AND optical logic gate

2.1.1. Design

For AND optical logic gate three waveguides have been created in the proposed structure to act as input and output waveguides. The design consists of a Y branch photonic crystal waveguide having three arms out of which two behave as input ports (Input A and Input B) and the third one acts as an output port as shown in Fig. 2. The region on both sides of the waveguides has mirror image symmetry so that the maximum light remains confined within the waveguide region. Further, the output waveguide has been modified by addition of the extra air holes of smaller radii at the two boundaries of the output waveguide. A hole has been introduced at the center of the three waveguides, which has been optimized for both the TE and TM modes. Due to the symmetric waveguide structure the light interferes constructively at the intersection of the three waveguides, when both the signals are launched simultaneously in both the input waveguides. As a result, the maximum value of power is obtained. However, there is branching of signals through the other path when either one of the two signals is present. As a result, low value of power is obtained in the output waveguide. Thus, leading the proposed design to operate as an AND optical logic gate.

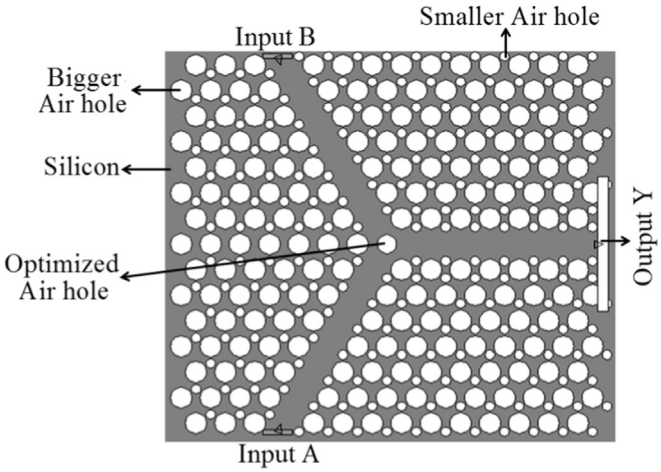

Fig. 2. Schematic representation of AND optical logic gate.

2.1.2. Optimization of the radius of the central hole for AND optical logic gate

The radius of the central hole has been optimized at the center of the Y branch to enhance the performance of the proposed logic gate for both the TE and TM modes separately. Fig. 3 shows the variation of ratio of output power to the input power (P_{out}/P_{in}) versus radius of the central hole for both the polarizations at single input and both input signals. For TE mode, it has been observed that as the radius of the central hole increases the ratio of output power to input power increases and then decreases whereas the variation remains same for TM mode. A common region has been chosen for optimization of the radius of central hole where output for single input as well as for both input signals is maximum for TE and TM polarizations. Hence, the optimized radius of the central hole has been taken as 0.30a.

2.1.3. Simulation results and discussion for and gate

The optimized structure has been analyzed to perform as AND optical logic gate for both TE and TM modes using FDTD method.

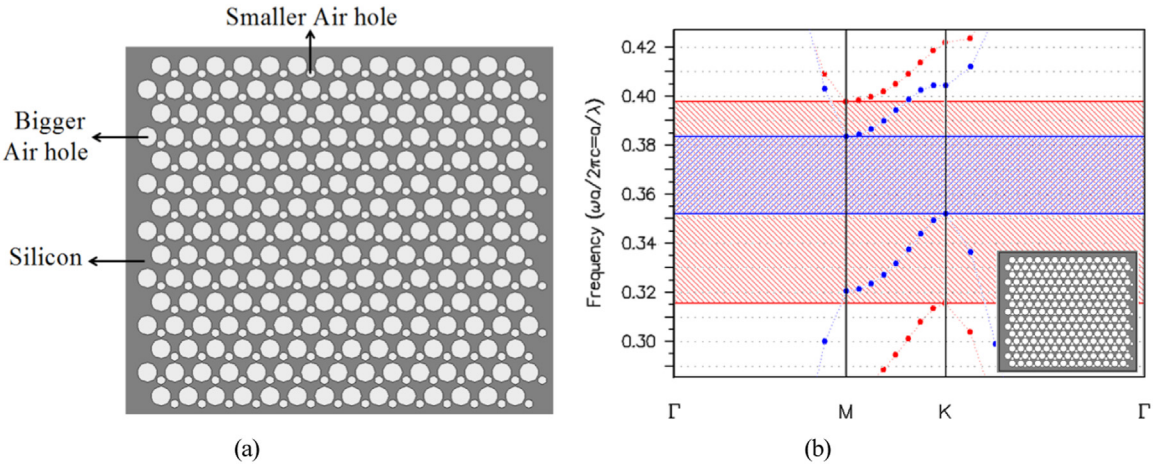

Fig. 1. (a) Schematic representation of honey comb photonic crystal (b) complete band gap for honey comb lattice arrangement where red curves correspond to the TE modes and blue curves correspond to the TM modes. (For interpretation of the references to color in this figure legend, the reader is referred to the web version of this article).

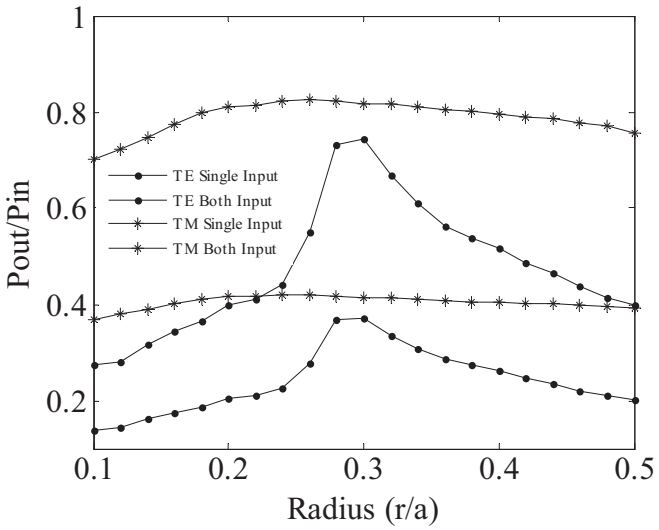

Fig. 3. Power transmittance with radius of central hole both for TE and TM mode with respect to the single input and both inputs.

Table 1
Truth table for AND optical logic gate for TE and TM polarizations at 1.55 μm wavelength where output power Y is in terms of input power P_a.

AND gate				
Input A	Input B	Logic output	Output Y (TE)	Output Y (TM)
0	0	0	0	0
0	1	0	0.372 P_a	0.414 P_a
1	0	0	0.372 P_a	0.414 P_a
1	1	1	1.485 P_a	1.630 P_a

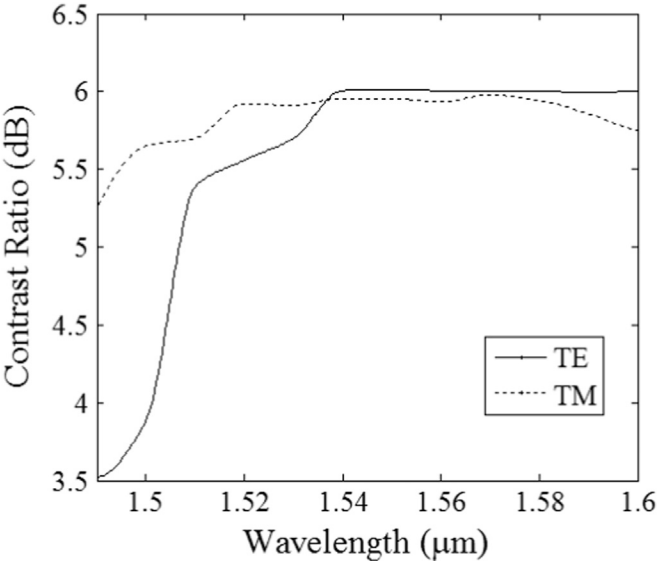

Fig. 4. Contrast ratio for both TE and TM polarizations in the complete band gap range.

Both the TE polarized and TM polarized light has been launched at input ports A and B. When input power P_a is launched at input port A or at port B separately, then the power at output port remains low. When power is launched at both the ports A and B simultaneously, then maximum power is obtained at the output port for both TE and TM polarizations as mentioned in Table 1. The results calculated in Table 1 indicate that the design can work as AND optical logic gate for both TE and TM polarizations based on

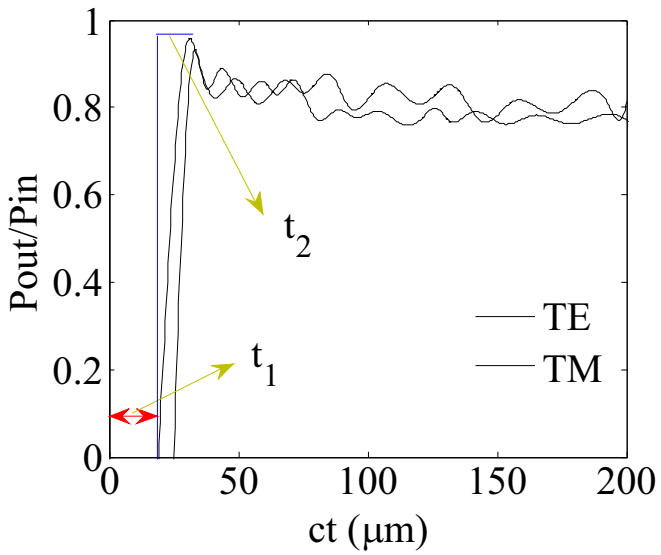

Fig. 5. Response time in terms of time evolution of the output power for both TE and TM polarizations.

the phenomenon of interference. The contrast ratio for both TE and TM polarizations has been calculated as the ratio of the power for logic-1 to the power for logic-0 i.e. Contrast Ratio = 10 log(P_1/P_0) (dB), where P_1 represents power for logic-1 and P_0 represents power for logic-0 and has been found out to be 6 dB at 1.55 μm wavelength as shown in Fig. 4. Fig. 4 shows the variation of the contrast ratio for both the TE and TM polarizations in the entire range of complete band gap. The response time which is defined as the switching time of the device between the OFF and ON state for both TE and TM polarizations has been determined using time evolving curve of the output power as shown in Fig. 5. For TE polarized mode, at steady-state, the time taken to reach output power from 0% to 90% of the average output power (P_{av}) is ct=32.8 μm or t=0.316 ps, where 'c' is the speed of light in medium. This time consists of two parts one of which is time due to transmission delay i.e. t_1=0.241 ps and another is time taken by output power to climb from 0.1% to 90% of P_{av} i.e. t_2=0.075 ps. It has been expected that the falling time from P_{av} to 10% of P_{av} is approximately equal to t_2. Thus, a narrow pulse width of $2t_2$ =0.150 ps can be produced and hence the response time of 0.300 ps has been achieved if the ON and OFF time of the signal is same. Further, bit rate which is defined as the inverse of the response time has been calculated to be 3.33 Tbit/s for TE polarized mode. Similarly, response period and bit rate has been calculated for TM polarized mode using Fig. 5. For TM polarized mode, ct=30.3 μm or t=0.27 ps, t_1=0.136 ps, t_2=0.081 ps, $2t_2$=0.162 ps and the response period of 0.324 ps and a bit rate of 3.09 Tbit/s have been obtained. Hence, we have achieved the improved values of bit rate and response period as reported earlier [18,19,25]. The field distribution profiles at steady state for both TE and TM polarized modes as shown in Fig. 6 and the results mentioned in Table 1 for both TE and TM polarizations at a wavelength of 1.55 μm, indicate that the design behaves as AND optical logic gate.

2.2. For all optical logic gates

2.2.1. Device design

In the proposed design for all optical logic gates, four waveguides have been created out of which two behave as input ports (Input A and Input B) and the third one acts as a reference port (R) and fourth as an output port Y as shown in Fig. 7. The reference port with reference/control signal has been used to create phase

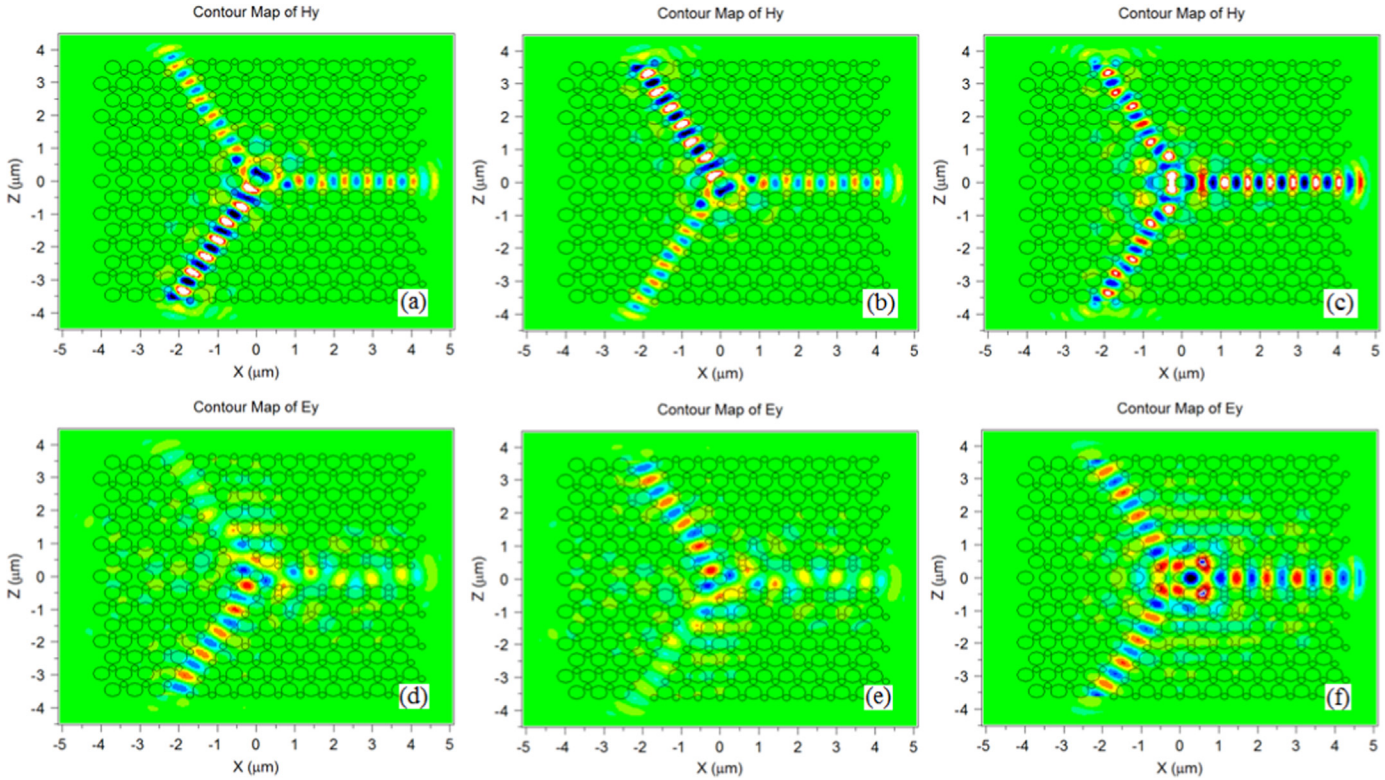

Fig. 6. Field distributions at steady state of the "AND" logic gate at 1.55 μm wavelength for TE polarization at (a) A=1, B=0 (b) A=0, B=1 (c) A=1, B=1 and for TM polarization at (d) A=1, B=0 (e) A=0, B=1 (f) A=1, B=1.

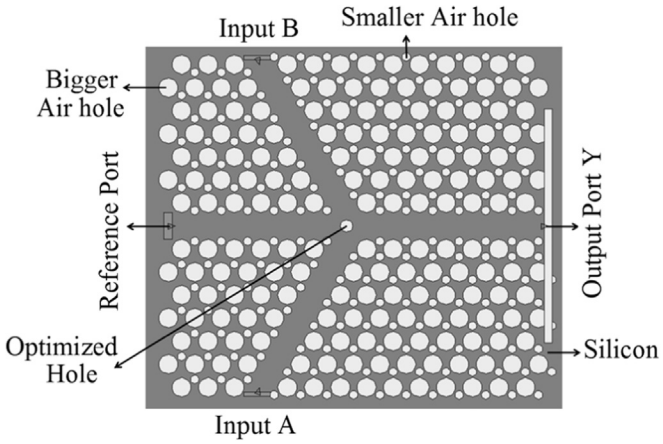

Fig. 7. Schematic representation of all optical logic gates.

difference between the input signals which results into constructive as well as destructive interference depending on the phase angle of the reference/control signal. In this structure also mirror image symmetry has been considered so that the maximum light remains confined within the waveguide region. A hole has been introduced at the center of the four waveguides, which has been optimized for both the TE and TM polarized modes. The light interferes constructively at the intersection of the four waveguides as the addition of signals that are in-phase, when either of the input signals or both the input signals are launched simultaneously in both the input waveguides. As a result, maximum value of power is obtained. However, there is a destructive interference when signals are out of phase resulting into low value of power in the output waveguide. Thus, the proposed design can be used for the realization of all optical logic gates.

2.2.2. Optimization of the radius of the central hole for all optical logic gates

The radius of the central hole has been optimized at the center of the four waveguides to enhance the performance of the proposed design for both the TE and TM polarized modes separately. Fig. 8 shows the variation of ratio of output power to the input power (P_{out}/P_{in}) versus radius of the central hole for both the polarizations at single input (along with the reference signal) and both input signals (along with the reference signal). For TE polarized mode, it has been observed that as the radius of the central

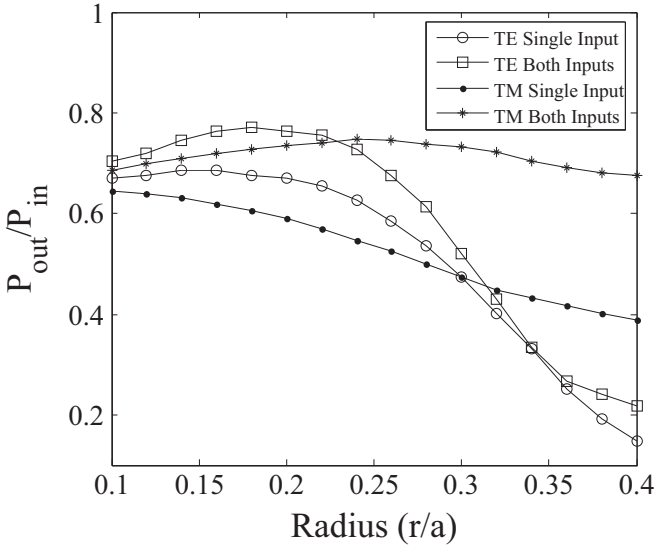

Fig. 8. Power transmittance with radius of central hole for all optical logic gates for both TE and TM polarized modes with respect to the single input and both inputs along with the reference/control signal.

hole increases the ratio of output power to input power increases and then decreases. For TM mode it increases first and then decreases for both inputs whereas it keeps on decreasing for single input. A common region has been chosen for the optimization of the radius of central hole where output for both input signals (along with the reference signal) crosses each other for TE and TM polarizations. Hence, the optimized radius of the central hole has been taken as 0.23*a*.

2.2.3. Results and discussion

The optimized structure has been analyzed to perform as AND, OR, NOT, NAND, NOR, XOR, XNOR all-optical logic gates for both TE and TM polarized modes using FDTD method. Both the TE polarized and TM polarized light has been launched at the input ports A and B and at reference port. The logic operations has been performed as follows: (i) when either of the input ports A and B or both the input ports A and B has been excited with light signal having phase angle $\varphi = 0^{\circ}$ and the reference port with reference/control signal having phase angle $\varphi = 0^{\circ}$ then logic 1 is obtained at the output port Y. (ii) when either input ports A and B or both the input ports A and B are excited with light signals having phase angle $\varphi = 0^{\circ}$ and reference port with control signal having phase angle $\varphi = \pi$ then logic 0 is obtained at the output port Y. (iii) When only the control signal at reference port with $\varphi = 0^{\circ}$ or $\varphi = \pi$ has been excited then maximum power is obtained at the output port as shown in Figs. 9 and 10. Fig. 9 represents the field distribution pattern for TE polarized mode and Fig. 10 corresponds to the TM polarized mode. The logic behaviors have been analyzed at a wavelength of 1.55 μm for both the TE and TM polarizations.

2.2.3.1. AND gate. The AND optical logic gate operations is as follows (i) when A=1, B=0 at $\varphi = 0^{\circ}$and R=1 at $\varphi = \pi$ then output Y=0 due to destructive interference. (ii) When A=0, B=1 at $\varphi = 0^{\circ}$ and R=1 at $\varphi = \pi$ the also output Y=0. (iii) When A=1, B=1 at $\varphi = 0^{\circ}$ and R=1 at $\varphi = 0^{\circ}$ then output Y=1 due to constructive interference. The results have been compared and summarized in Table 2 for all possible combinations for both TE and TM polarizations. Fig. 9(c)–(e) shows the field distribution for TE polarization. The field distribution for TM polarization has been shown in Fig. 10(c)–(e). The calculated value of contrast ratio is found out to be 10 dB.

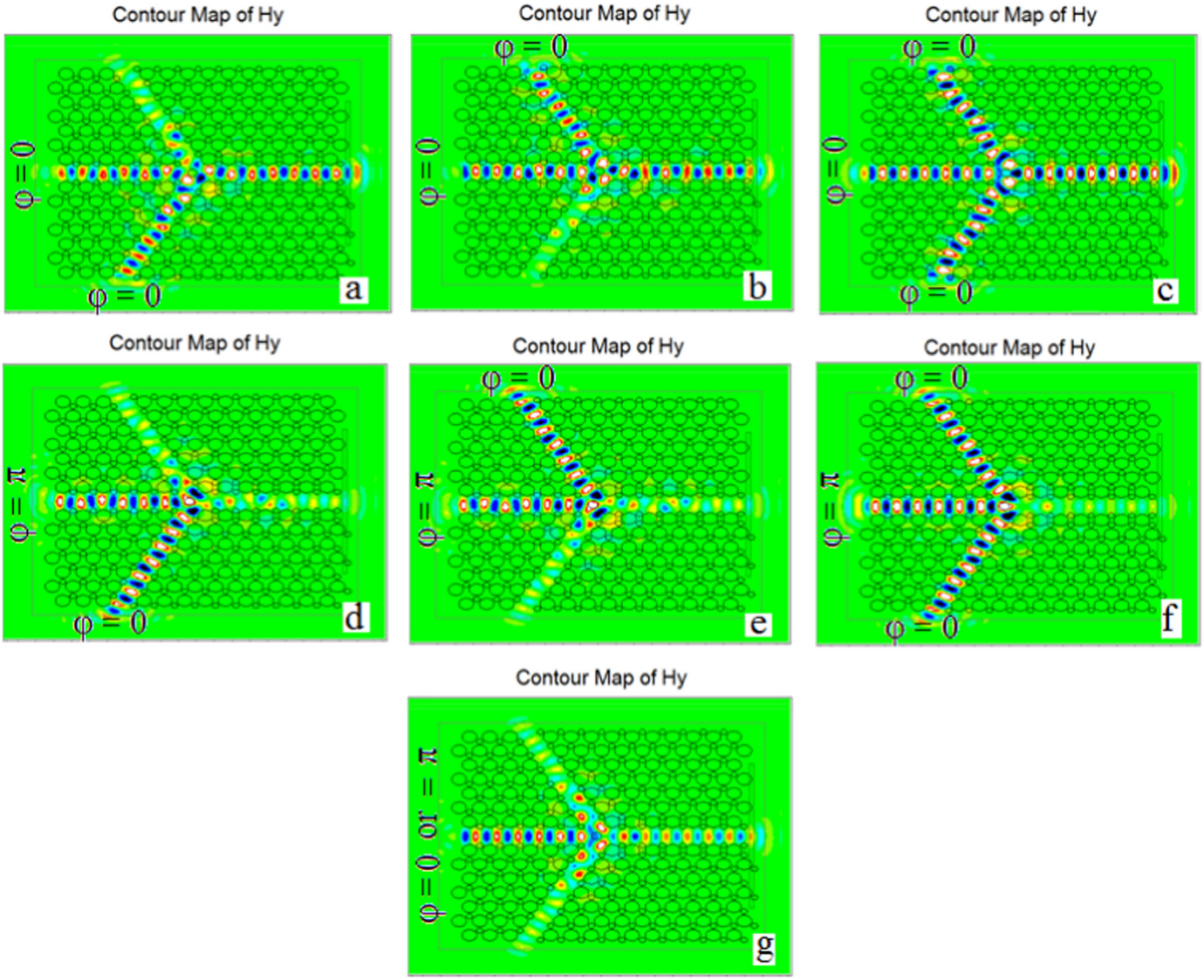

Fig. 9. Field distributions at steady state for all optical logic gates at 1.55 μm wavelength for TE like polarization at (a) A=1, B=0 at $\varphi = 0^{\circ}$, R=1 at $\varphi = 0^{\circ}$ (b) A=0, B=1 at $\varphi = 0^{\circ}$, R=1 at $\varphi = 0^{\circ}$ (c) A=1, B=1 at $\varphi = 0^{\circ}$, R=1 at $\varphi = 0^{\circ}$(d) A=1, B=0 at $\varphi = 0^{\circ}$, R=1 at $\varphi = \pi$ (e) A=0, B=1 at $\varphi = 0^{\circ}$, R=1 at $\varphi = \pi$ (f) A=1, B=1 at $\varphi = 0^{\circ}$, R=1 at $\varphi = \pi$ (g) A=0, B=0, R=1 at $\varphi = 0^{\circ}$ or π.

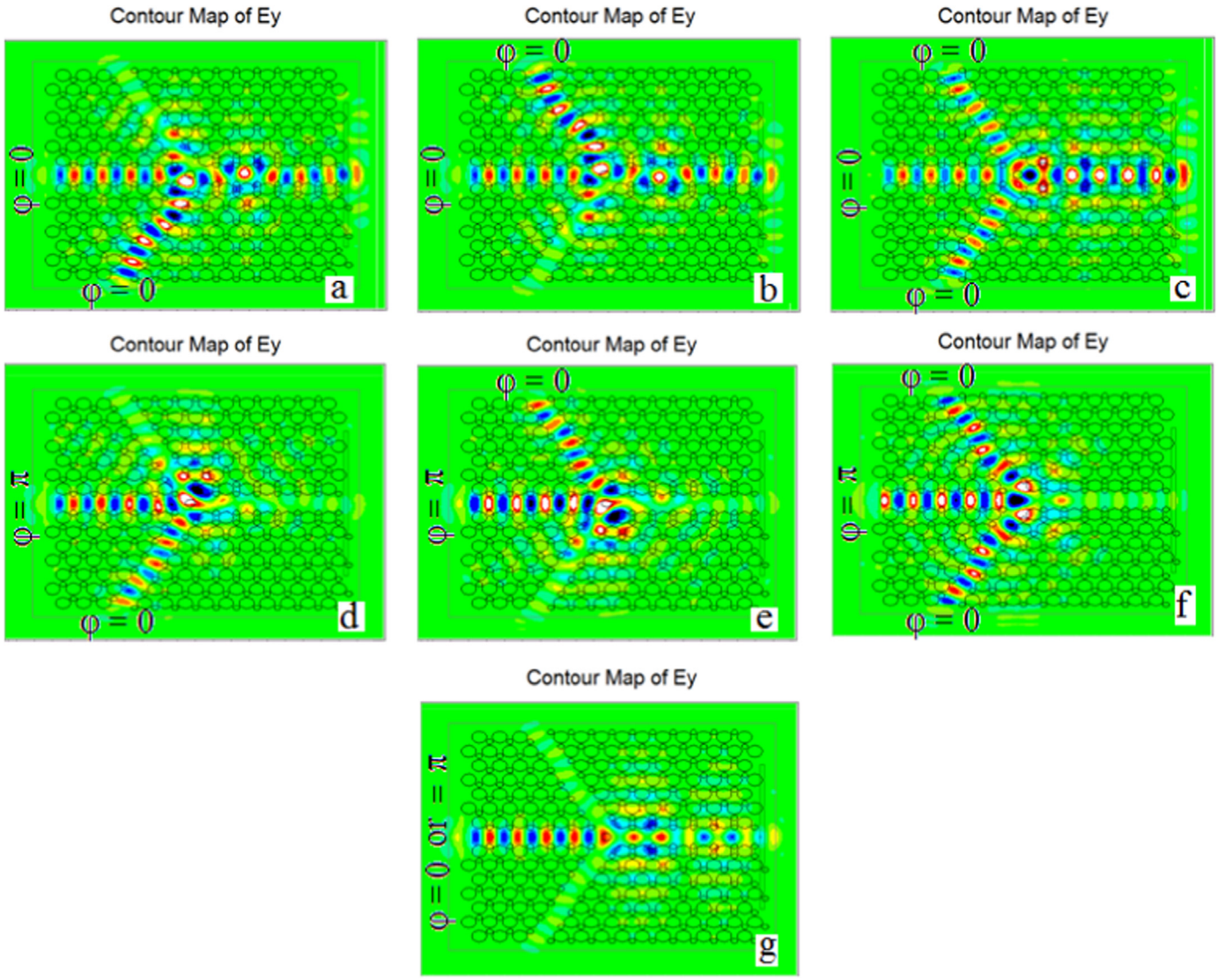

Fig. 10. Field distributions at steady state for all optical logic gates at 1.55 μm wavelength for TM like polarization at (a) A=1, B=0 at $\varphi = 0^{\circ}$, R=1 at $\varphi = 0^{\circ}$ (b) A=0, B=1 at $\varphi = 0^{\circ}$, R=1 at $\varphi = 0^{\circ}$ (c) A=1, B=1 at $\varphi = 0^{\circ}$, R=1 at $\varphi = 0^{\circ}$ (d) A=1, B=0 at $\varphi = 0^{\circ}$, R=1 at $\varphi = \pi$ (e) A=0, B=1 at $\varphi = 0^{\circ}$, R=1 at $\varphi = \pi$ (f) A=1, B=1 at $\varphi = 0^{\circ}$, R=1 at $\varphi = \pi$ (g) A=0, B=0, R=1 at $\varphi = 0^{\circ}$ or π.

Table 2
Truth table for AND optical logic gate for TE and TM polarizations at 1.55 μm wavelength where normalized output power Y is in terms of input power P_a.

AND gate					
Input A ($\varphi = 0^{\circ}$)	Input B ($\varphi = 0^{\circ}$)	Reference signal (R)	Logic output	Normalized output Y (TE)	Normalized output Y (TM)
0	0	0	0	0	0
0	1	1 ($\varphi = \pi$)	0	0.1716 P_a	0.0902 P_a
1	0	1 ($\varphi = \pi$)	0	0.1722 P_a	0.0920 P_a
1	1	1 ($\varphi = 0^{\circ}$)	1	0.7448 P_a	0.7453 P_a

Table 3
Truth table for OR optical logic gate for TE and TM polarizations at 1.55 μm wavelength where normalized output power Y is in terms of input power P_a.

OR gate					
Input A ($\varphi = 0^{\circ}$)	Input B ($\varphi = 0^{\circ}$)	Reference signal (R)	Logic output	Normalized output Y (TE)	Normalized output Y (TM)
0	0	0	0	0	0
0	1	1 ($\varphi = 0^{\circ}$)	1	0.6407 P_a	0.5629 P_a
1	0	1 ($\varphi = 0^{\circ}$)	1	0.6391 P_a	0.5572 P_a
1	1	1 ($\varphi = 0^{\circ}$)	1	0.7448 P_a	0.7453 P_a

2.2.3.2. OR gate. The optimized structure can be operated as OR gate for both TE and TM polarizations and explained as follows: (i) when A=1, B=0, or A=0, B=1, at $\varphi = 0^{\circ}$ and R=1 also at $\varphi = 0^{\circ}$ then Y=1 i.e. logic 1 is obtained at the output port Y due to the constructive interference. (ii) When A=1, B=1, at $\varphi = 0^{\circ}$ and reference port with reference/control signal R=1 is also having phase angle $\varphi = 0^{\circ}$ then logic 1 is obtained at the output port Y due to the phase matching condition. For the OR gate realization, the phase angle between the input signals and control signal has been taken as same which results into the constructive interference and satisfying the logic output of the OR gate. The field distribution at steady state for TE polarization has been shown in Fig. 9(a)–(c) and for TM polarization in Fig. 10(a)–(c). The results mentioned in Table 3 clearly shows that the proposed structure can function as OR optical logic gate.

Table 4
Truth table for NOT optical logic gate for TE and TM polarizations at 1.55 μm wavelength where normalized output power Y is in terms of input power P_a.

NOT gate				
Input A ($\varphi = 0^\circ$)	Reference signal (R)	Logic output	Normalized output Y (TE)	Normalized output Y (TM)
0	1 ($\varphi = \pi$)	1	0.6562 P_a	0.4244 P_a
1	1 ($\varphi = \pi$)	0	0.1722 P_a	0.0920 P_a

2.2.3.3. NOT gate. In the proposed structure, for NOT gate one input has been taken at the input port A and other at the reference port as control signal. The switching from off to on state has been maintained by phase difference of π between the input signal and control signal. The output remains high when only control signal is present with phase angle of $\varphi = \pi$ i.e. A=0, R=1and is low when input signal and the control signal are out of phase i.e. A=1 at $\varphi = 0^\circ$, R=1 at $\varphi = \pi$ as indicated in Table 4 for both TE and TM polarizations at a wavelength of 1.55 μm. The contrast ratio for NOT gate is 6 dB. The Table 4 and field distributions shown in Fig. 9 (d) and (g), 10(d) and (g) clearly indicate that the proposed structure can be used as a NOT gate.

2.2.3.4. NAND gate. The universal NAND gate is the inverse of the AND gate. The NAND gate optical logic behavior for both the TE and TM polarizations has been explained as follows: (i) When control signal is launched at the reference port with phase angle $\varphi = 0^\circ$ i.e. R=1 and none of the signals is launched at the input ports, i.e. A=0, B=0 then the output obtained at the output port Y is logically '1'. (ii) When either of the input ports have been excited with the input signals i.e. A=1, B=0 or A=0, B=1 with $\varphi = 0^\circ$ and control signal R=1 with $\varphi = 0^\circ$ then also the output obtained is logically '1'. (iii) When A=1, B=1 with phase $\varphi = 0^\circ$ and reference port with control signal R=1 with $\varphi = \pi$ then logic '0' is obtained at the output port Y. The results have been summarized in Table 5 and the simulations shown in Fig. 9(a), (b), (f) and (g) for TE polarization and Fig. 10(a), (b), (f) and (g) for TM polarization clearly indicate that the structure could really behave as NAND optical logic gate. The contrast ratio for NAND gate is found out to be 7 dB.

2.2.3.5. NOR gate. The inverse of OR gate leads to the universal NOR logic gate which can further be used to design other devices. The NOR logic operation is as follows (i) when only the control signal is applied at the reference port with phase angle $\varphi = \pi$ then only the output is logically in the ON state. (ii) When the input signal is applied at either of the input ports or at both the input port with phase angle $\varphi = 0^\circ$ but control signal is applied at the reference port with phase angle $\varphi = \pi$ then the output at the output port is always zero i.e. in OFF state. The logic output for both TE and TM polarizations have been compared in Table 6 and

Table 6
Truth table for NOR optical logic gate for TE and TM polarizations at 1.55 μm wavelength where normalized output power Y is in terms of input power P_a.

NOR gate					
Input A ($\varphi = 0^\circ$)	Input B ($\varphi = 0^\circ$)	Reference signal (R)	Logic output	Normalized output Y (TE)	Normalized output Y (TM)
0	0	1($\varphi = \pi$)	1	0.6562 P_a	0.4244 P_a
0	1	1($\varphi = \pi$)	0	0.1716 P_a	0.0902 P_a
1	0	1($\varphi = \pi$)	0	0.1722 P_a	0.0920 P_a
1	1	1($\varphi = \pi$)	0	0.1236 P_a	0.1215 P_a

can be easily verified from the simulation figures shown in Figs. 9 and 10.

2.2.3.6. XOR gate. The output in XOR logic gate is logically "1" if only one of the two inputs is high (1) and logically "0" if both the inputs are high (1) or low (0). The working of XOR logic gate has been explained as follows: (i) when one of the input signals is applied along with the control signal i.e. A=1, B=0, R=1 or A=0, B=1, R=1 with phase angle $\varphi = 0^\circ$ then the output is logically high. (ii) The output is logically low when none of the input ports and reference port have been excited or both the input ports have been excited with the light signal having phase angle $\varphi = 0^\circ$ and reference port with the reference light signal having phase angle $\varphi = \pi$ i.e. A=0, B=0, R=0 or A=1, B=1, R=1. The simulation Fig. 9 (a), (b) and (f) for TE polarization and Fig. 10(a), (b) and (f) for TM polarization show that the proposed structure could really work as XOR logic gate. The truth table for TE and TM polarizations has been compared in Table 7. The calculated value of contrast ratio for XOR logic gate has been found out to be 5 dB.

2.2.3.7. XNOR gate. The XNOR optical logic gate is inverse of the XOR optical logic gate and can be easily verified as mentioned in Table 8 for both the polarizations. The field distribution shown in Fig. 9(c)–(e) and (g) for TE polarization and Fig. 10(c)–(e) and (g) for TM polarization proves that the proposed design can be efficiently used as XNOR optical logic gate.

The response time of the all optical logic gate device for both TE and TM polarized modes has also been determined in a similar manner as done for AND optical logic gate design using time evolving curve of the output power as shown in Fig. 11. For TE mode, at steady-state, ct=37.4 μm or t=0.360 ps, time due to transmission delay is t_1=0.245 ps and time taken by output power to climb from 0.1% to 90% of P_{av} is t_2=0.115 ps, a narrow pulse width of $2t_2$=0.230 ps. Thus, the response time of 0.460 ps has been achieved which leads to a bit rate of 2.17 Tbit/s. Similarly, for TM mode, ct=32.0 μm or t=0.230 ps, t_1=0.114 ps, t_2=0.116 ps, $2t_2$ =0.232 ps and the response period of 0.464 ps and a bit rate of 2.15 Tbit/s have been obtained. Hence, we have achieved the

Table 5
Truth table for NAND optical logic gate for TE and TM polarizations at 1.55 μm wavelength where normalized output power Y is in terms of input power P_a.

NAND gate					
Input A ($\varphi = 0^\circ$)	Input B ($\varphi = 0^\circ$)	Reference signal (R)	Logic output	Normalized output Y (TE)	Normalized output Y (TM)
0	0	1 ($\varphi = 0^\circ$)	1	0.6562 P_a	0.4244 P_a
0	1	1 ($\varphi = 0^\circ$)	1	0.6407 P_a	0.5629 P_a
1	0	1 ($\varphi = 0^\circ$)	1	0.6391 P_a	0.5572 P_a
1	1	1 ($\varphi = \pi$)	0	0.1236 P_a	0.1215 P_a

Table 7
Truth table for XOR optical logic gate for TE and TM polarizations at 1.55 μm wavelength where normalized output power Y is in terms of input power P_a.

XOR gate					
Input A ($\varphi = 0^\circ$)	Input B ($\varphi = 0^\circ$)	Reference signal (R)	Logic output	Normalized output Y (TE)	Normalized output Y (TM)
0	0	0 ($\varphi = 0^\circ$)	0	0	0
0	1	1 ($\varphi = 0^\circ$)	1	0.6407 P_a	0.5629 P_a
1	0	1 ($\varphi = 0^\circ$)	1	0.6391 P_a	0.5572 P_a
1	1	1 ($\varphi = \pi$)	0	0.1236 P_a	0.1215 P_a

Table 8
Truth table for XNOR optical logic gate for TE and TM polarizations at 1.55 μm wavelength where normalized output power Y is in terms of input power P_a.

XNOR gate					
Input A ($\varphi = 0^\circ$)	Input B ($\varphi = 0^\circ$)	Reference signal (R)	Logic output	Normalized output Y (TE)	Normalized output Y (TM)
0	0	1 ($\varphi = \pi$)	1	0.6562 P_a	0.4244 P_a
0	1	1 ($\varphi = \pi$)	0	0.1716 P_a	0.0902 P_a
1	0	1 ($\varphi = \pi$)	0	0.1722 P_a	0.0920 P_a
1	1	1 ($\varphi = 0^\circ$)	1	0.7448 P_a	0.7453 P_a

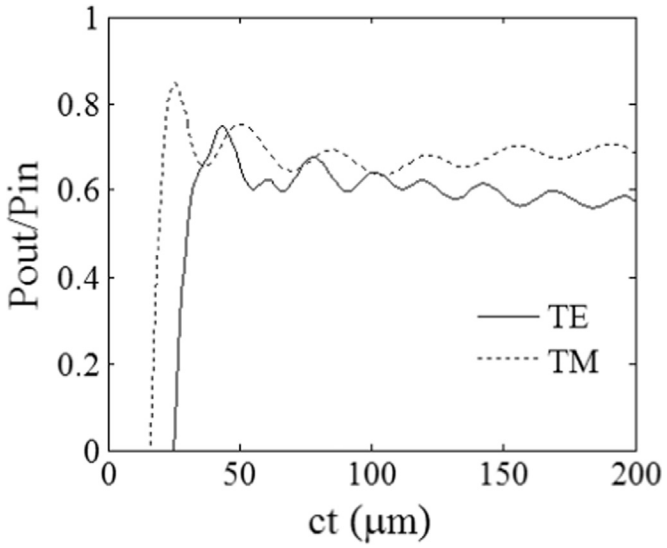

Fig. 11. Response time in terms of time evolution of the output power for all optical logic gate design for both TE and TM polarizations.

improved values of bit rate and response period for both TE and TM modes at a wavelength of 1.55 μm. The results indicate that the proposed design behaves as all-optical logic gates.

3. Conclusion

In this paper, we have reported the design and performance characteristics of polarization independent AND optical logic gate in Y shaped and all optical logic gates in three port waveguide shaped honey comb photonic crystal which yields complete photonic band gap in the range of optical communication window around 1.55 μm. The PWE and FDTD methods have been utilized to determine the optimized parameters. The contrast ratios for both TE and TM modes are comparable at 1.55 μm wavelength which makes this suitable for c-band device design. The response time and bit rate have been calculated for the designs for both the polarizations. The proposed structures are easier to fabricate than alternating slabs conducive to TE and TM band gaps and hence could be a strong candidate for future polarization independent all optical integrated devices.

Acknowledgments

The authors gratefully acknowledge the initiatives and support towards the establishment of "TIFAC Centre of Relevance and Excellence in Fiber Optics and Optical Communication at Delhi Technological University, formerly Delhi College of Engineering" through "Mission REACH" program of Technology vision-2020, Government of India.

References

[1] J.R.R. Sousa, A.F.G.F. Filho, A.C. Ferreira, G.S. Batista, C.S. Sobrinho, A.M. Bastos, M.L. Lyra, A.S.B. Sombra, Generation of logic gates based on a photonic crystal fiber Michelson interferometer, Opt. Commun. 322 (2014) 143–149.
[2] Alex S. Clark, J.érémie Fulconis, John G. Rarity, William J. Wadsworth, Jeremy L. O'Brien, All-optical-fiber polarization-based quantum logic gate, Phys. Rev. A 79 (2009) 030303 R.
[3] K.H. Ahn, X.D. Cao, Y. Liang, B.C. Barnett, S. Chaikamnerd, M.N. Islam, Cascadability and functionality of all-optical low-birefringent non-linear optical loop mirror: experimental demonstration, J. Opt. Soc. Am. B 14 (1997) 1228–1236.
[4] A. Bogoni, L. Poti, R. Projetti, G. Meloni, F. Ponzini, P. Ghelfi, Regenerative and reconfigurable all-optical logic gates for ultra-fast applications, Electron. Lett. 41 (2005) 435–436.
[5] J.W.M. Menezes, W.B. Fraga, A.C. Ferreira, K.D.A. Saboia, A.F.G.F. Filho, G. F. Guimaraes, J.R.R. Sousa, H.H.B. Rocha, A.S.B. Sombra, Logic gates based in two-and three-modes nonlinear optical fiber couplers, Opt. Quantum Electron. 39 (2007) 1191–1206.
[6] Yabu Tetsuro, Geshiro Masahiro, Kitamura Toshiaki, Nishida Kazuhiro, Sawa Shinnosuke, All-optical logic gates containing a two-mode nonlinear waveguide, IEEE J. Quantum Electron. 38 (2002) 37–46.
[7] Wu Yaw-Dong, All-optical logic gates by using multi branch waveguide structure with localized optical nonlinearity, IEEE J. Sel. Top. Quantum Electron. 11 (2005) 307–312.
[8] Wu Yaw-Dong, Shih Tien-Tsorng, Chen Mao-Hsiung, New all-optical logic gates based on the local nonlinear Mach–Zehnder interferometer, Opt. Express 16 (2008) 248–257.
[9] H. Wu, D.S. Citrin, L. Jiang, X. Li, Polarization independent single mode wave guiding with honey comb photonic crystals, IEEE Photonics Technol. Lett. 27 (8) (2015) 840–843.
[10] H. Sei-ichi Takayama, Y. Kitagawa, T. Tanaka, Asano, S. Noda, Experimental demonstration of complete photonic bandgap in two dimensional photonic crystal slabs, Appl. Phys. 87 (2005) 061107.
[11] F. Wen, S. David, X. Checoury, M.E. Kurdi, P. Boucaud, Two dimensional photonic crystals with large complete photonic band gaps in both TE and TM polarizations, Opt. Express 16 (16) (2008) 12278–12289.
[12] R.K. Sinha, Y. Kalra, Design of optical waveguide polarizer using photonic band gap, Opt. Express 14 (22) (2006) 10790–10794.
[13] L. Zhang, J. Ding, Y. Tian, R. Ji, L. Yang, H. Chen, P. Zhou, Y. Lu, W. Zhu, R. Min, Electro-optic directed logic circuit based on micro ring resonators for XOR/XNOR operations, Opt. Express 20 (11) (2012) 11605–11614.
[14] J.Y. Kim, J.M. Kang, T.Y. Kim, S.K. Han, 10 Gbit/s all-optical composite logic gates with XOR, NOR, OR and NAND functions using SOA-MZI structures, Electron. Lett. 42 (5) (2006) 303–304.
[15] T. Fujisawa, M. Koshiba, All-optical logic gates based on nonlinear slot-waveguide couplers, J. Opt. Soc. Am. B 23 (4) (2006) 684–691.
[16] S.K. Tripathy, S. Sahu, C. Mohapatro, S.P. Dash, Implementation of optical logic gates using closed 2D photonic crystal structure, Opt. Commun. 285 (13–14) (2012) 3234–3237.
[17] C. Husko, T.D. Vo, B. Corcoran, J. Li, T.F. Krauss, B.J. Eggleton, Ultracompact all-optical XOR logic gate in a slow-light silicon photonic crystal waveguide, Opt. Express 19 (21) (2011) 20681–20690.
[18] P. Rani, Y. Kalra, R.K. Sinha, Realization of AND gate in Y shaped photonic crystal waveguide, Opt. Commun. 298 (2013) 227–231.
[19] P. Rani, Y. Kalra, R.K. Sinha, Design of all optical logic gates in photonic crystal waveguides, Optik 126 (2015) 950–955.
[20] P. Andalib, N. Granpayeh, All-optical ultra compact photonic crystal AND gate based on nonlinear ring resonators, J. Opt. Soc. Am. B 26 (1) (2009) 10–16.
[21] Y. Tian, L. Zhang, R. Ji, L. Yang, P. Zhou, H. Chen, J. Ding, W. Zhu, Y. Lu, L. Jia, Q. Fang, M. Yu, Proof of concept of directed OR/NOR and AND/NAND logic circuits consisting of two parallel micro ring resonators, Opt. Lett. 36 (9) (2011) 1650–1652.
[22] Y. Ishizaka, Y. Kawaguchi, K. Saitoh, M. Koshiba, Design of ultra compact all-optical XOR and AND logic gates with low power consumption, Opt. Commun. 284 (14) (2011) 3528–3533.
[23] Tobias Birr, Urs Zywietz, Parva Chhantyal, Boris N. Chichkov, Carsten Reinhardt, Ultrafast surface plasmon-polariton logic gates and half-adder, Opt. Express 23 (25) (2015) 31755–31765.
[24] Z. Zang, Numerical analysis of optical bistability based on fiber Bragg grating cavity containing a high nonlinearity doped-fiber, Opt. Commun. 285 (5) (2012) 521–526.
[25] C.J. Wu, C.P. Liu, Z. Ouyang, Compact and low-power optical logic NOT gate based on photonic crystal waveguides without optical amplifiers and nonlinear materials, Appl. Opt. 51 (5) (2012) 680–685.

Design and analysis of trench-assisted leaky channel waveguide for high power applications

Himanshu Pandey, Than Singh Saini, and Ajeet Kumar

Citation: AIP Conference Proceedings **1728**, 020376 (2016); doi: 10.1063/1.4946427
View online: http://dx.doi.org/10.1063/1.4946427
View Table of Contents: http://scitation.aip.org/content/aip/proceeding/aipcp/1728?ver=pdfcov
Published by the AIP Publishing

Design and Analysis of Trench-assisted Leaky Channel Waveguide for High Power Applications

Himanshu Pandey[1], Than Singh Saini[1], Ajeet Kumar[1, a)]

[1] *Department of Applied Physics, Delhi Technological University (Formerly Delhi College of Engineering) Delhi- 110042, India.*

[a)]Corresponding author: ajeetdph@gmail.com

Abstract. We purpose a leaky channel waveguide design that supports a single guided mode. The waveguide works on the principle of higher-order mode discrimination. The cladding of waveguide is formed by alternate low and high index regions, which helps to leak out of higher-order modes while retaining the fundamental mode over the entire length of the waveguide. The Structure is analysed by the finite element method 'Comsol Multiphysics' and the leakage losses of the modes along with effective mode area have been calculated. We show that a waveguide formed in silica with core width 6 μm can be designed to exhibit single mode operation at 1550 nm wavelength. The Fundamental loss E_{11} = 0.076 dB/mm and the higher order loss E_{21} = 11.4 dB/mm with the rectangular core area as large as 50 μm^2. Such large-core-area waveguide structure efficiently suppresses unwanted non-linear optical effects and is suitable for high power devices such as high power Waveguide Laser and Amplifier.

INTRODUCTION

Integrated optic waveguide lasers have always been a subject of interest in the research and scientific community [1]. Innumerable efforts have already been made to increase the output power of waveguide lasers. Use of suitable rare earth metals, efficient pumping schemes and geometrically shaped waveguide designs for large-core single-mode (SM) operation are various schemes and method to increase the output power of waveguide laser. Waveguide lasers and amplifiers preferably require the structures that support a single guided mode to avoid inter-modal dispersion, since material dispersion and waveguide dispersion play an integral role in single-mode waveguide devices [2, 3]. Significant efforts have been made to design the waveguides that support SM operation even with large-core-area in rectangular geometry [4-7]. These structures are based on higher-mode discrimination for achieving SM operation as the lower order modes travel faster than higher modes in an optical waveguide [8-10]. We have designed and analysed a trench-assisted channel waveguide that works on the principle of mode filtering. The waveguide design is optimized to obtain high leakage loss to higher order modes and nominal loss to the fundamental mode. We have thus calculated the leakage loss and effective mode area using finite element method. The structure has been simulated using commercially available software 'Comsol Multiphysics'. Our analysis shows that present design provides better flexibility in designing the structure for effective SM operation.

LMA CHANNEL WAVEGUIDE DESIGN

Figure.1 shows the cross-sectional view of the proposed channel waveguide, which consists of a rectangular core and a geometrically shaped trench-assisted cladding in the *y*-direction. The core has a refractive index n_1, thickness h_0 and width 2a, and is formed on a substrate with a lower refractive index n_2. The region on each side of the core consists of alternatively shaped two low-index trenches of depths h_1 and h_2. The entire structure is covered by another low index material n_3. Rectangular perfectly matched layers have been bounded by the channel waveguide structure for calculating accurate confinement loss. To facilitate the discussion, width of cladding layers have been defined as d_1 = b-a, d_2 = c-b. Such structure supports leaky modes. Leakage loss that plays a crucial role in higher-order mode filtering has been calculated by solving the waveguide by well-established finite element method.

International Conference on Condensed Matter and Applied Physics (ICC 2015)
AIP Conf. Proc. 1728, 020376-1–020376-4; doi: 10.1063/1.4946427
Published by AIP Publishing. 978-0-7354-1375-7/$30.00

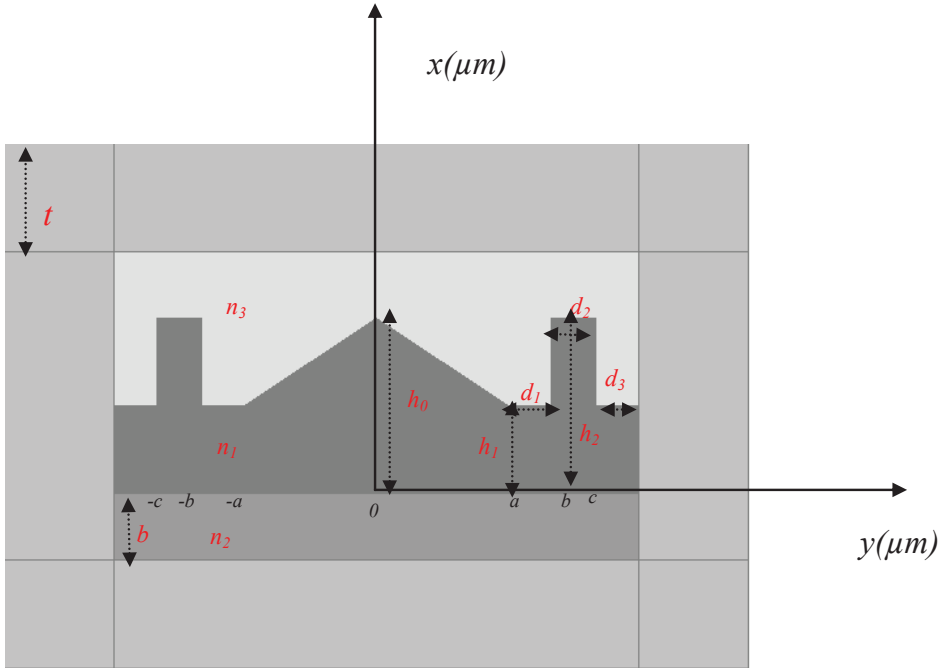

FIGURE 1 The Transverse Cross-sectional view of proposed leaky channel waveguide

NUMERICAL RESULTS AND ANALYSIS

We have carried out numerical calculations for the following parameters: $n_1 = 1.542$, $n_2 = 1.444$, $n_3 = 1.512$, a = 6 μm and $h_0 = 8$ μm, which are typical of a polymer waveguide fabricated on a silica substrate. Geometrically shaped cladding parameters (i.e., d_1, d_2, d_3, h_0, h_1, h_2) which define the shape of multi-layered cladding are used to control the leakage loss of the modes. In this paper, we have investigated the effect of a core width and cladding parameter h_2 on single mode operation of the waveguide. Our study shows that these parameters have effective control on the leakage loss and can be used to design LMA SM channel waveguide. These cladding parameters also give us the freedom to optimize further the design for SM operation in accordance with the change in core parameters and operating wavelength.

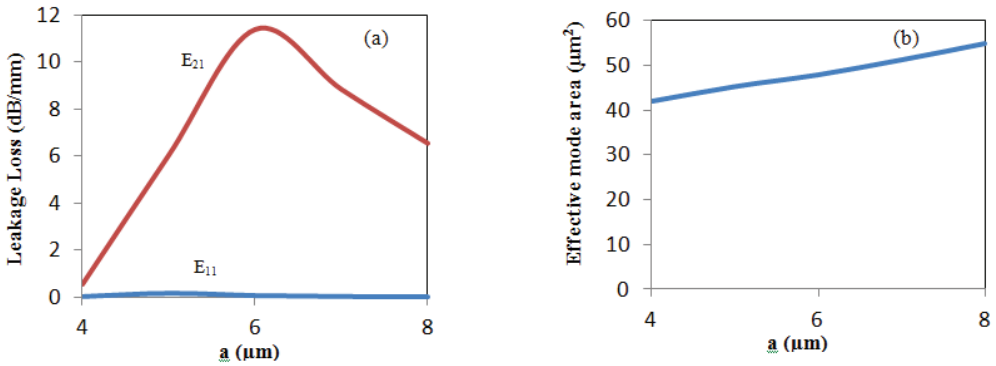

FIGURE 2 (a) Effect of 'a' on leakage loss of first two modes. (b) Effect of 'a' on effective mode area of E_{11}^{x} i.e., fundamental modes.

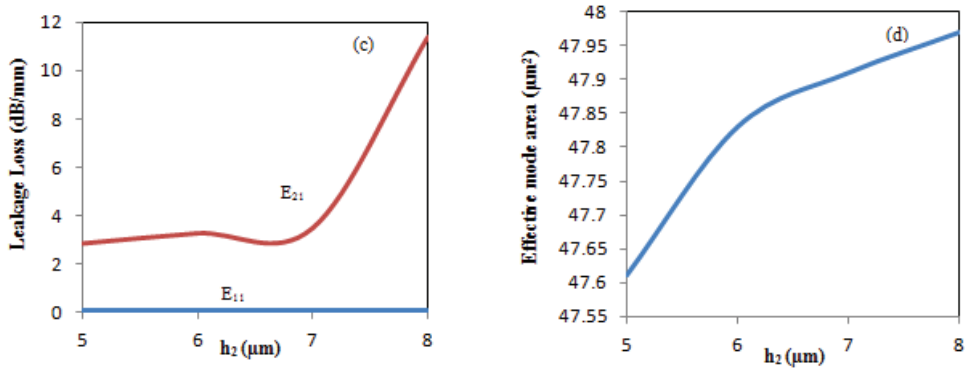

FIGURE 3 (a) Effect of 'h_2' on leakage loss of first two modes. (b) Effect of 'h_2' on effective mode area of E_{11}^x i.e., fundamental modes.

To make a detailed study of these cladding parameters, we have studied the effect of h_2 on the leakage losses of first two modes and shown in the Fig. 2(a), 2(b), 3(c), 3(d). It is clear from these figures that leakage losses of the modes increase with mode order at a wavelength 1.55 μm. The differential leakage loss of the first two modes, however, increases with h_2. When h_2 = 8 μm, the waveguide introduces 0.076 dB/mm and 11.4 dB/mm losses to E_{11}^x and E_{21}^x modes respectively. Thus, a 1.75 mm length of a waveguide can strip off all higher modes to ensure effective SM operation. A smaller value of h_2 < 7 ?m introduce low leakage loss to E_{21}^x, however, it does not increase the loss of fundamental mode beyond 1 dB/mm. The intensity contour plot of the fundamental mode and next higher mode is shown along with the transverse cross-section of the channel waveguide in Fig. 4(a), 4 (b). The Fundamental mode is well confined in the core with a mode area of 50 μm^2.

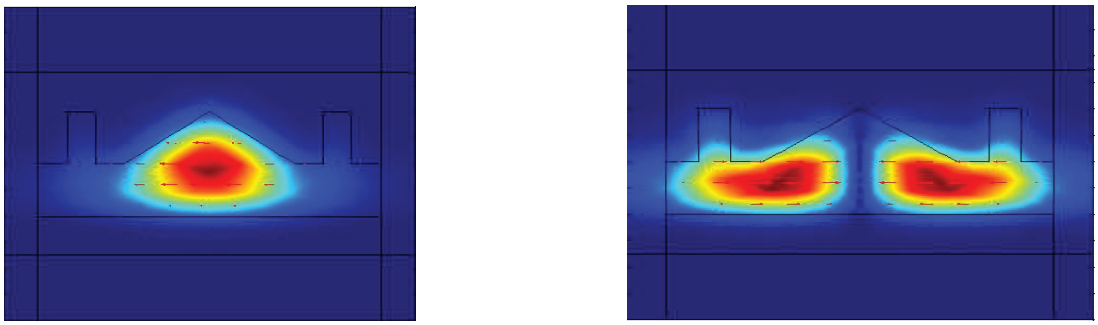

(a) (b)

FIGURE 4 (a) The contour plot of the E_{11}^x mode, (b) The contour plot of the E_{21}^x mode when a = 6 μm, h_0 = 8 μm, h_1 = 4 μm, h_2 = 8 μm and t = 1.55 μm at λ =1.55 μm.

CONCLUSION

We have proposed an integrated optical channel waveguide for LMA with the single-mode operation. Such waveguide utilizes a trench-assisted cladding which can be easily fabricated by reactive ion etching technique. Our numerical results show the effective single-mode operation of the structure with a mode area larger than 50 μm^2. With such a large mode area, the proposed waveguide can efficiently suppress the non-linear effects and can be useful for designing the higher-power waveguide devices.

ACKNOWLEDGEMENTS

This work has been partially supported by the DST Fast track project on "Speciality large mode area rectangular waveguides and fibres for high power Applications".

REFERENCES

1. J. M. Eggleston, T. J. Kane, K. Kuhn, R. L. Byer, and J. Unternahrer, "The slab geometry laser I-Theory," IEEE J. Quantum Electron. **20**, 289-301 (1984).
2. A. Kumar, V. Rastogi, "Multilayer cladding leaky planar waveguide for high power applications", Appl. Phys B **92**, 577-583 (2008).
3. A. Kumar and V. Rastogi, "Design and analysis of dual-shape core large mode area optical fiber", App. Opt. **50**, E119-E124 (2011).
4. A. Kumar, V. Rastogi, C. Kakkar, and B. Dussardier, "Coaxial dual core resonant leaky fibre for optical amplifier," J. Opt. A Pure Appl. Opt. **10**, 115306 (2008).
5. T. S. Saini, A. Kumar, V. Rastogi and R. K. Sinha "Selectively filled large-mode-area photonic crystal fiber for high power applications" Proceeding of SPIE Optics + Photonics 2013, USA, Vol. 8847, No. **61** (2013).
6. A. Kumar and V. Rastogi, "Design and analysis of a multilayer cladding large mode area optical fiber", J. Opt. A. Pure Appl. Opt. **10**, 015303 (2008).
7. J. N. Walpole, J.P. Donelly, P. J. Taylor, L. J. Missaggia, C. T. Harris, R. J. Bailey, A. Napoleone, S.H. Groves, S.R. Chin, R. Huang, J. Plant, IEEE Photon. Technol. Lett. **14**, 756 (2002).
8. R. K. Huang, L.J. Missaggia, J.P. Donnelly, C.T. Harris, G.W. Turner, IEEE Photon. Technol. Lett. **17**, 959 (2005).
9. S. Yin, K.W. Chung, H. Liu, P. Kurtz, K.Reichard, Opt. Commun. **177**. 225 (2000).
10. N. G. R. Broderick, H. L. Offerhaus, D. J. Richardson, R. A. Sammut, J. Caplen, L. Dong, Opt. Fiber Technol. **5**. 185 (1999).
11. Y. Jeong, J. K. Sahu, D. N. Payne, J. Nilsson, Opt. Express **12**, 6088 (2004).

Design and Performance Analysis of Solar Parabolic Trough for Cooking Application

Shubham Gupta*, Prof. R. S. Mishra

Department of Mechanical Engineering Delhi Technological University, Delhi-110042.

**Post Graduate Student*

Abstract: **- Solar Thermal technology is widely popular and used. Solar thermal technology helps in maintaining the ecological balance as it saves Co_2 emissions. It is necessary to design the technology for specific application and to have high efficiency. Solar parabolic trough has various application in the field of cooking, hotels, laundry, textiles, etc. and provides saving in non-renewable fuels. But however in this paper only cooking application is focussed.**

Key Words**: Solar Thermal, Parabolic Trough, Cooking, Concentrator**

I. INTRODUCTION

Intense hot gases prevail in the blackbody Sun of temperature 5778 K & diameter 13.9 million KM. While at Centre temperature is very High. Continuously Hydrogen is converted to Helium as Sun acts as a large fusion reactor. Total Energy output of the sun can be considered as 63 MW/m2 on the sun's surface which is radiated outwards. Thermal or heat energy from the sun can be utilized or converted in one form or another to meet the suitable requirement or application such as cooking, electricity generation, etc. there are two types of radiation that we deal in Solar Thermal Designing: DNI (Direct Normal Incidence) & GHI (Global Horizontal Incidence). Water Heating Parabolic-trough is a proficient technology of renewable energy for heating applications. In India Direct Normal Incidence is also high which makes this technology much more suitable. Hot water applications can be used at various places such as temples (Meal preparation), Hotels, etc. This technology has a good payback as compared to Solar PV technology. There are various types of Solar concentrating thermal technologies which includes Linear Fresnel, compound parabolic, paraboloid dish, solar tower, flat plate collector.

II. SOLAR CONCENTRATOR PARABOLIC TROUGH

Solar thermal collectors can be considered as a heat exchanger which transforms solar direct irradiation to enthalpy of the fluid medium in the tube.Following are the main components of Solar Thermal Collector.

- Collector: Receives or collects the sun radiation convert it to heat and directs or concentrates it to the receiver
- Receiver: It is a glass tube in working fluid which circulates and gains the heat from the collectors and transfers it to the desired equipment or heat storage tank
- Fluid: It can be organic fluids, water, heating oil, etc.
- Tracking: E-W tracking or N-S tracking or both can be done to increase the efficiency of parabolic trough
- Storage tank: In case of cloudy, rainy & non-sunshine conditions heat can be stored in a storage tank.

III. LITERATURE REVIEW

A. ValanArsau et.al (2007) [1] designed the parabolic trough with rim angle 90^o with the use of reinforced fibreglass and provide the manufacture techniques. This modal has very low drag coefficient in the acceptable range. Standard deviations of the of the parabolic surface error distribution was in the limit range of accuracy. Kalogirou et.al (2004) [2] Explains the importance of renewable energy considering environmental factors as a major issue. Author also discussed various solar thermal technologies such as flat plate collector, parabolic troughs, etc. and their applications. Krishnamurthy et.al (2012) [3]Focuses on economic evaluation of the solar thermal parabolic trough technology considering various factors such as rate of equity, discount rate, capital cost, generation cost, solar insolation and various modals are compared.Omid karimisadaghiyani et.al (2014) [4] Designed two solar collectors and evaluate and compared performance characteristics by using CFD and MATLAB.S. D.Odeh (1998) [5] Evaluate the performance characteristics of parabolic trough by considering absorber wall temperature instead of fluid bulk temperature to provide flexibility of use of any working fluid. Author used Syltherm 800 as a working fluid for experimental work. Vinay V Gadikar et.al (2016) [6] Assesses the Solar concentrator technology use in laundry purposes at Goa by detail specification discussion and also discussed about the problems and challenges faced and performance evaluation is also done.Richter et.al (1996) [7] provides the methods to improve the optical efficiency of parabolic trough which plays a great role in overall efficiency of the solar thermal technology.

IV. CASE STUDY UNDERTAKEN

Bangalore city is considered for the case study. It has good DNI. A mess of approximately 250 people is considered for the case study in this paper. Meal includes Breakfast, Lunch, Evening Snacks & Dinner. In a day in total 3 Meals for person is considered.

Table 1: Quantity of meal items used.

S.No.	Item	Dry Wt (in Kg) per Meal
1.	Rice	25
2.	Dal	13
3.	Vegetables	13

V. METHODOLOGY

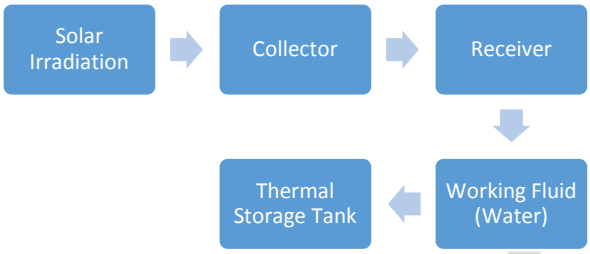

Fig 1: Methodology used in Solar Parabolic Trough

VI. DESIGN CONSIDERATIONS

Longitude: 12.9716^{o} N

Latitude: 77.5946^{o} E

No. of people in mess: 250

No. of Meals Daily: 3 per person

Shade free Area available for Solar Concentrator Technology installation: 80 square meters

No. of operational Hours in a year: 2100

Operating temperature: 170^{o} C

Operating pressure: 10 bar

Table 2: Ambient Conditions Considered

Ambient Conditions		
Parameters	**Units**	
Wind Speed	m/s	3
Irradiation	W/m2	1000
Tilt Factor		1.02

Table 3: Fluid Specifications Considered

Fluid Specifications		
Parameters	**Units**	**Vapour**
Mass Flow Rate	Kg/s	0.25
Density	Kg/m3	5.147
Heat Capacity	KJ/Kg-K	2.5944
Thermal Conductivity	W/m-k	0.0364
Kinematic Viscosity	m2/s	2.91948E-06
Dynamic Viscosity	Kg/m-s	1.50E-05

Table 4: Parabolic Trough Specifications

Parabolic Trough Specifications		
Parameters	**Units**	
Outer Diameter	m	0.03
Inner Diameter	m	0.025
Outer Diameter Glass Cover	m	0.055
Inner Diameter Glass Cover	m	0.05
Aperture	m	1.5
Length	m	4
Aperture Area	m2	5.88
Avg. Value transmissivity- Absorbivity product for beam radiation		0.9
Specular Reflectivity of the concentrator Surface		0.95
Intercept factor (The fraction of the reflected radiation intercepted by the absorber tube)		0.95
Temperature Outlet	Celsius	80
Temperature Inlet	Celsius	40

VII. COMPUTATION OF ENERGY POTENTIAL

Table 5: Monthly Thermal Output Generation

Parameters	Units	Jan	Feb	Mar	Apr	May	Jun	Jul	Aug	Sep	Oct	Nov	Dec	Annual Average
Incident Beam radiation	W/m2	1000	1000	1000	1000	1000	1000	1000	1000	1000	1000	1000	1000	1000
DNI	KWh/day	7.28	7.48	6.50	5.83	5.94	4.15	2.99	3.13	4.35	3.99	5.74	6.57	5.32
Tilt Factor		1.02	1.02	1.02	1.02	1.02	1.02	1.02	1.02	1.02	1.02	1.02	1.02	
Avg. Value transmissivity - absorbivity product for beam radiation		0.9	0.9	0.9	0.9	0.9	0.9	0.9	0.9	0.9	0.9	0.9	0.9	
Aperture of Parabolic Trough	meters	1.5	1.5	1.5	1.5	1.5	1.5	1.5	1.5	1.5	1.5	1.5	1.5	
Absorber Outer Diameter	meters	0.03	0.03	0.03	0.03	0.03	0.03	0.03	0.03	0.03	0.03	0.03	0.03	
Length of Parabolic Trough	meters	4	4	4	4	4	4	4	4	4	4	4	4	
Specular Reflectivity of the concentrator Surface		0.95	0.95	0.95	0.95	0.95	0.95	0.95	0.95	0.95	0.95	0.95	0.95	
Overall Loss Coefficient	W/m2-K	24.8	24.8	24.8	24.8	24.8	24.8	24.8	24.8	24.8	24.8	24.8	24.8	
Useful Heat Gain	W	3672	3672	3672	3672	3672	3672	3672	3672	3672	3672	3672	3672	3672
Thermal Units/Day	KWh	11.04	16.73	21.34	21.86	22.12	16.38	12.06	13.55	17.56	19.14	12.5	12.23	16.38
Thermal Units/ Day	Kcal	9505.48	14400.39	18368.01	18810.33	19040.66	14097.4	10379.06	11666	15117.58	16468.88	10755.67	10524.08	14094.45
No. of Modules		6	6	6	6	6	6	6	6	6	6	6	6	6
Total Thermal Units	Kcal/day	57032	86402	110208	112862	114243	84584	62274	69995	90705	98813	64534	63144	84566

VIII. RESULTS & DISCUSSION

84566 Kcal/day is produced from 6 parabolic troughs with 36 square meters of reflective area. Collector efficiency is 60 %. Concentration ratio is 15. This energy is enough to prepare meal for 3 times for 250 people. In overall 10 Kg/day of LPG gas is saved which provides of annual saving of 3000 Kg of LPG gas.

IX. CONCLUSION

Since because of various factors like clouds, dust, etc. Sun's rays reach the earth in a diffuse manner a less Direct rays is received. Solar PV technology works on GHI. While Solar thermal works on DNI. So if we use the Solar thermal output as a heat it will be more useful gain as in converting electricity much more losses occur in concentrating solar thermal technology. A fluid run through a pipe line continuously and gain heat from concentrated sun's rays by parabolic trough. Parabolic trough concentrator is such designed to achieve desire temperature difference. This fluid after gaining heat moves to storage tank where it can be utilized. After utilization again it moves to make up tank then to inlet of Parabolic Trough.Price.H et.al (2002) [8]stated at low working temperature difference Concentrating solar thermal technology works with high efficiency. Many design considerations can also be improved to improve the efficiency.

REFERENCES

[1]. A. ValanArsau, T. S. (2007). Design, manufacture and testing of fiberglass reinforced parabola trough for parabolic trough solar collectors. Solar Energy, 1273-1279.

[2]. Kalogirou, S. A. (2004). Solar thermal collectors and applications. Progress in Energy and combustion science, 231-295.
[3]. Krishnamurthy, P. M. (2012). An analysis of costs of parabolic trough technology in India. Energy Policy, 407-419.
[4]. Omid KARIMI SADAGHIYANI, M. B. (2014). Two new designs of Parabolic solar collectors. Thermal Science, 323-334.
[5]. S. D. ODEH, G. L. (1998). Modelling of parabolic trough through direct steam generation solar collectors. Solar Energy, 395-406.
[6]. Vinay V Gadikar, S. D. (2016, Jan-Mar). CST BEING USED IN LAUNDRY AT LAKAKI DRYCLEANERS, GOA . Sun Focus, pp. 15-17.
[7]. Richter, J. L. (1996), Optics of a Two-trough Solar Concentrator, Solar Energy, pp. 191-198
[8]. Price, H., et al. (2002), Advances in Parabolic Trough Solar Power Technology, Journal of Solar Energy Engineering, pp. 109-125.

International Journal of Science and Research (IJSR)
ISSN (Online): 2319-7064
Index Copernicus Value (2013): 6.14 | Impact Factor (2015): 6.391

Designing an In-Silico Mimetic for Thrombopoietin Using Combinatorial Library

Vimal Kishor Singh[1], Ishita Goyal[2], Abhishek Saini[3], Neeraj Kumar[4], Manisha Kalsan[5], Ramesh Chandra[6]

[1, 2, 3]Stem Cell Research Laboratory, Department of Biotechnology, Delhi Technological University, Delhi, India

[4, 5, 6]Department of Chemistry, University of Delhi, Delhi, India

Abstract: ***Differentiation and proliferation of megakaryocytic progenitor cells into mature platelets is triggered and activated upon binding of Thrombopoietin Receptor (TPOR), a cytokine receptor protein, to thrombopoietin (TPO), a 95 KD glycoprotein hormone.TPO plays a very important role as it can easily direct Hematopoietic Progenitor Cells into the megakaryocytic lineage but even then very few mimetic have been reported, Agonists such as Romiplostim and Electrombopag are reported, recombinant TPO mimetic are also available but structural mimetic is only TMP, so the scope of further research is available. A promising approach for designing a mimetic can be targeting the binding site of the receptor such that the mimetic peptide has similar agonist activity as the ligand. Diverse libraries can be created using in-silico approaches and they are analyzed to bind receptor efficiently. In this study efforts are made for the development of TPO mimetic with therapeutic potential. TPO increases its number, prevent apoptosis, and thereby increases platelet production. Activation of TPO receptor leads to phosphorylation of the cytoplasmic domain as well as downstream activation of JAK2, STAT5, and other anti-apoptotic pathways. This increases the viability of stem cells and precursors of all lineages. The anti-apoptotic effect of TPO is probably important in patients with ITP: bone marrow megakaryocytes and megakaryocyte precursors are already increased but these cells are undergoing apoptosis mediated by anti-platelet IgG and T cells, thereby limiting platelet production. Administration of TPO decreases the apoptotic rate of the megakaryocyte precursors and thereby enhance the platelet production. Once produced, platelets are still affected by TPO. TPO's new Combinatorial library was designed by interaction sites of TPOR with TPO and previously reported TPO mimetic peptide (TMP), further screening of combinatorial library was done and an efficient mimetic was chosen based on scoring function commonly called Energy. Energy is calculated in terms of KJ/mol, based on the orientations generated by docking ligand with the receptor, the most efficient ligand has the most stable conformation with minimum energy value. In this study docking of TPO and TPOR has a minimum energy value of -518.20; TPOR and mimetic designed has a total score of -456.55which is better than the known mimetic TMP, which has an energy score of -170.17 with TPOR. Computational approaches confirmed that the resulting peptide mimetic was stable and similar in nature to TPO. Further Ex-vivo study of designed mimetic can confirm its role in regenerative medicine, increasing the shelf life of platelet to improve cellular viability of platelet by preventing programmed cell death, i.e. apoptosis, which can be achieved by adding TPO during storage since TPO levels increase when platelet count is low, to stimulate additional production. TPO is absorbed by transfused platelets, which may decrease available TPO level or in the disease condition.***

Keywords: Thrombopoietin, Thrombopoietin receptor, Mimetic, Library designing, Docking

1. Introduction

Platelets are the smallest cells in the blood. These cells are enucleated, discoid in shape and size ranges from 1-2 µm. Platelets play an important role in maintaining homeostasis, healing wounds, and stop bleeding. Number of Platelet varies from 1.5 – 4 x 10^6 cells per microliter (per mcL) of blood.The average platelet count in women is considerably higher than men. Platelets are generated from megakaryocytes in the bone marrow and highly regulated by various growth factors [1]. The importance of the maintenance of both number of platelets and their functionality may be understood from the most common diseases associated with them, e.g.

- Thrombocythemia and reactive Thrombocytosis - Abnormal increase in platelets; if blood has too many platelets, one may have a higher risk of blood clots.
- Thrombocytopenia - Decrease in platelets; if blood has a low number of platelets, one can be at risk of bleeding.
- Platelet dysfunction - The platelets are unable to stick together or attach to blood vessel walls hampering their normal function and this can cause excessive bleeding e.g. von Willebrand Disease.

In any of these conditions, hemostatic balance is disturbed and may lead to bleeding.

Disease condition where a patient is deficient in TPO, this approach can be miraculous.TPO plays an important role in hematopoiesis, any change in the hormone or to its receptor may trigger any congenital or acquired disease state of thrombocytopenia, thrombocytosis or aplastic anemia. Apart from the disease conditions, TPO can also help in improving the quality of platelet during storage condition. Platelets are generated from megakaryocytic cells in the bone marrow using a number of growth factors such as TPO, IL-2,3,6,11 surprisingly Hematopoietic Progenitor Cells can easily be directed into the megakaryocytic lineage by using only a single growth factor i.e. Thrombopoietin. TPO can improve cellular viability of platelet by preventing programmed cell death, i.e. apoptosis; and perhaps this could be helpful in achieving prolonged shelf life by adding TPO during storage since

a) TPO levels increase when the platelet count is low, to stimulate additional production.
b) TPO is absorbed by transfused platelets, which may decrease available TPO levels [2].

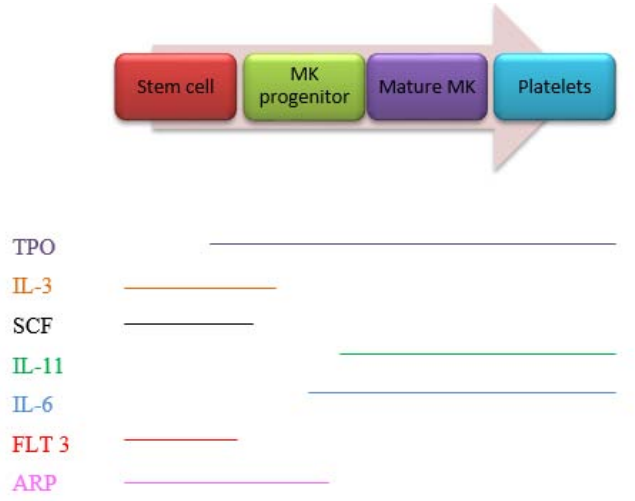

Figure 1: *Regulation of megakaryocytopoiesis by various hematopoietic growth factors. Figure explains that amongst all the growth factors completing the process of megakaryocytopoiesis, TPO plays an important role at every stage. Through the process of platelet production, various growth factors play a role but TPO plays a very important role at all the stages beginning from Stem cell to MK progenitor cell to Mature MK to Platelets.*

TPO is primarily synthesized in human liver parenchymal cells and kidney. It's a 353 amino acid protein which on the removal of the signal peptide of 21 amino acid forms a mature molecule. The mature molecule consists of two domains: receptor binding and carbohydrate rich region. Levels of TPO increase with a decline in platelet mass and remain elevated throughout thrombocytopenia. Structure-function analysis of TPO has revealed that the thrombopoietin effect of the molecule is present in the N-terminal i.e. first 153 amino acids only and it is all that is required for the activity but this truncated molecule has a reduced circulatory half-life, thus, it is presumed that the glycosylated second region provides stability and prolongs the circulatory half-life [3-5]

An experimental study in mice showed that mice deficient in TPO show a reduction of 90% in bone marrow megakaryocytes and circulating platelets quantity; and administration of TPO to normal mice increases platelet count almost 200%, 500 % increase in megakaryocytes and 1000% increase in bone marrow colony-forming unit megakaryocytes [6-7].

TPO is a 95 kDa glycoprotein. It possesses 2 domain structures - Cytokine domain at the N-terminal,Carbohydrate domain at C-terminal. The cytokine domain comprises of first 153 amino acids up till Arg 153 followed by the carbohydrate domain which starts from Arg 154 till 332nd amino acid. The carbohydrate domain shows no biological activity but still assists TPO to be soluble. It is also prototypically cleaved from the protein before it binds to its receptor.

TPO receptor (C-mpl) is a 635 amino acid protein. It has an extracellular domain of 485 amino acid starting from 26th amino acid and ends at 491st amino acid. TPO interacts with c-MPL in the extracellular domain only. C-mpl has two extracellular subunits, namely subunit I from 26 – 277 amino acids and subunit II from 253 – 491. Subunit I shows greater interaction with the ligand [8].

The specific interaction of TPO with c-MPL triggers a cascade of cellular signal, which involves,

- JAK2 and TYK2 pathways
- Mitogen-activated protein kinase pathway
- Phosphatidylinositol 3-kinase pathway
- Nuclear factor kappa B pathway (Kuter D., 1995)

Initially, a recombinant form of human TPO was developed as a first generation thrombopoietic agent, but their development was terminated because cross-reactivity was observed with endogenous TPO. Now second generation thrombopoiesis stimulating, these have distinguished pharmacological properties and show no homology to Thrombopoietin. Romiplostim and Eltrombopag are two agents which have completed phase III trials and they have been authorized for marketing for the use of disease purpose. There are very few peptides mimetic available for TPO so the efforts are being made for the same.

Numbers of previously reported TPO mimetic are very limited and thus, the scope of improving is more. New and improved approach for ligand discovery, based on combinatorial procedures of assembling a number of compounds to produce diverse molecules for binding molecular targets with higher specificity and efficiency can prove to be miraculous. Based on this same approach, we have designed a combinatorial library, consisted of oligopeptides. It was formed by oligopeptides derived from interaction sites TPOR with TPO and TMP and literature survey. TPO and TMP bind to TPOR in the extracellular domain and activate it in order to regulate thrombocytosis. Randomly varying various combinations of the peptides obtained is a possible approach to design a mimetic.

2. Method and Methodology

2.1 Library Formation

In this study, a peptide library was formed on the basis of interaction studies of TPOR with TPO and TMP (known mimetic) and literature survey. Interaction studies were used for library formation. Random changes of the amino acid at the different location were done for making various combinations of oligopeptide library.

2.2 Receptor Protein Preparation

TPO binds to TPOR on extracellular domain region (ECD). The 3D structure of TPOR was not available on RSCB protein data bank. So from NCBI protein sequence was retrieved and homology search was done. BLASTp using Protein data bank database was used for homology study. The result showed a maximum similarity of 24% with EPO, which was not enough for predicting structure, so using structure prediction tool phyre 2, based on *ab-initio* search and fold recognition, was used. Binding site (Extracellular

region) of TPOR protein was selected. Native TPOR protein was prepared for docking analysis using maestro. TPOR protein chains were identified for finding any duplication, duplicated chains were removed. Hydrogen was added to the protein molecule and then protein structure was selected for energy minimization and followed by optimization for docking analysis.

Table 1: Servers, databases, and software used in this study

Tools	*Function*	*Application*
BLAST	For searching similar protein or nucleotide sequences.	BLAST was used to determine homology of TPOR with the database.
Cell predictor	Determines the sub-cellular localization of target protein.	Shortlisted peptides were run through this tool for predicting the subcellular localization.
Hex 8.0.0	Protein –protein docking server.	Peptide sequences were docked with the receptor.
Pep fold	Tool for prediction of the de novo 3D structure of oligopeptides.	Pep fold was used for predicting the 3D structure of the peptide sequences.
Phyre2	Tool for prediction of the de novo 3D structure of proteins.	Phyre2 was used for predicting the 3D structure of protein sequences.
Protein Data Bank (PDB)	PDB consists of a 3D structure of biomolecules and their complexes.	The 3D structure of protein were retrieved from PDB and used for determining physicochemical properties.
Protein peptide calculator	Identifies various properties of a peptide sequence.	Shortlisted peptide sequences were run through the Protein peptide calculator for determining physiochemical properties.
ProtParam	Identifies various properties of a peptide sequence.	Shortlisted peptide sequences were run through the ProtParam for determining physiochemical properties.
Pymol	For a 3D view of proteins and analysis of PDB structure.	TPO-TPOR & TMP-TPOR complexes and other 3D structure viewed and analysed.

2.3 TMP, Known mimetic preparation

Known mimetic, TMP, was reported to mimic the role of TPO for activation and dimerization of TPOR. The 3D structure of the known mimetic was retrieved from Pepfold (mobyle server) in PDB format. For docking analysis, known mimetic was prepared by extracting water. PDB file was imported into Maestro workspace and prepared.

2.4 Interaction analysis of TPOR with TMP and TPO

PDB files of TPOR and TMP were imported into HEX 8.0.0 for docking analysis. Similar docking analysis was done for TPOR and TPO.

2.5 Ligand preparation of peptide sequences

Based on the interaction sites and literature survey a peptide library was generated. Random changes of the amino acid at different locations are done for making various combinations of oligopeptide library. In Peptide Library, first, the 3D structure was predicted by Pep fold peptide structure prediction server. Different peptides imported in the workspace of Pep fold and saving the project name and sequence and format allowed to run. Pep fold returned PDB file, which was processed further using Prep wizard.

2.6 Interaction analysis of TPOR and combinatorial library of peptides-

For peptide library (peptide sequences) binding energy is analysed by using the docking tool HEX 8.0.0. This required prepared receptor and ligand in PDB format. The receptor and ligand PDBs were imported into the workspace of HEX 8.0.0.HEX 8.0.0 gives binding energy in terms of E_{total} score. Top 10 results were chosen for further analysis.

2.7 Physiochemical and biological activity prediction-

Selected mimetics were further analysed for physicochemical and Biological properties. Physiochemical properties & Biological properties are determined using Peptide protein calculator, ProtParam, RAMPAGE and Cello server.

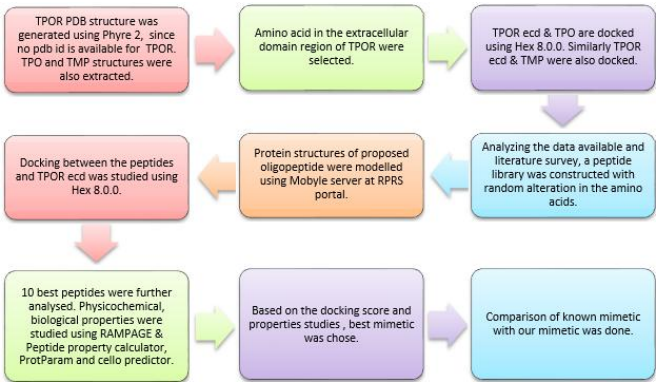

Table 2 *Methodology used to design TPO mimetic. TPO-TPOR complex was analysed to determine the interaction site was generated. A combinatorial library was generated by previously known mimetic and TPO and literature survey. Prepared receptor protein and library compounds were docked. Compounds were shortlisted on the basis of their docking results and further analysed for the physicochemical and biological properties.*

3. Results

3.1 Receptor Preparation

TPOR BLAST result: BLASTp analysis, using protein data bank database, of TPOR sequence revealed that it has a maximum identity of 24% with EPOR, which is not enough to make a 3D structure based on homology alone. TPOR 3D structure Analysis- Literature study defined TPOR having two similar chains in pairs A, B and C, D binding to TPO.

Receptor-ligand binding critically depends on the orientation of interaction. Both pairs of chains of TPOR have similar amino acid sequences so for docking analysis duplicated chain C & D is removed from the receptor protein. Protein is prepared using Prep wizard by importing receptor file and minimizing and optimizing the receptor protein.

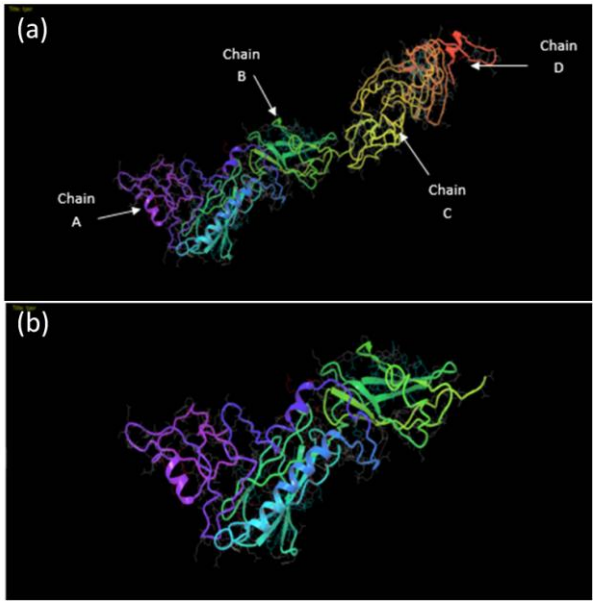

Figure 2 *a) The 3D structure of TPOR indicating various chains in the structure. Chain A & chain B are identical to chain C & chain D so only one set of chains are considered for further study. b) 3D structure of TPOR, representing chains A & B. (after removing duplicate chains C & D and water molecules)*

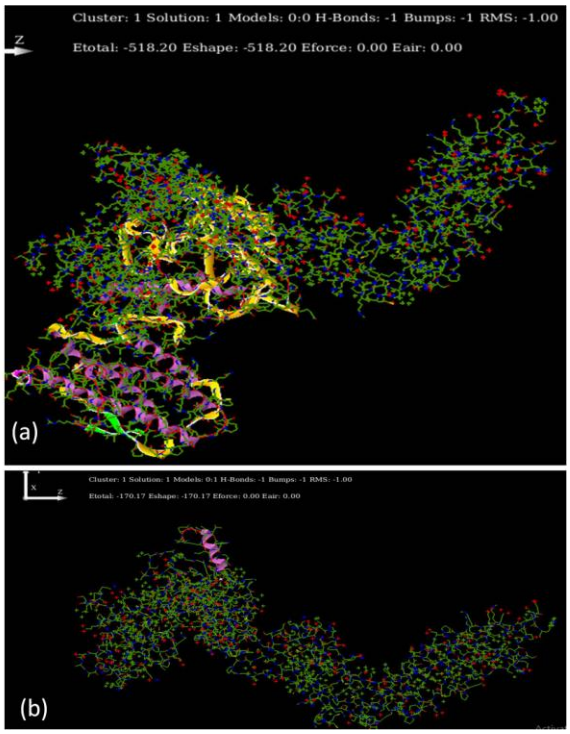

Figure 3 *a) Interacting TPO-TPOR and showing binding sites. Docking study gave an E_{total} of -518.20.Identified residues which are interacting were – V44, D45, F46, S47, L48, E50, A126, L129, Q132, H133, R140, F141, and L144. b) docking analysis of TPOR-TMP. E_{total} of -170.17 was observed in when TPOR and TMP were docked using HEX 8.0.0.*

3.2 Interaction analysis of TPOR with TPO & TMP

Prepared receptor protein TPOR was docked with TPO and known mimetic TMP using HEX 8.0.0 server. PDB files of receptor and ligand imported and interaction domain and number out coming result 10 were selected. Best resulting PDB of ligand and receptor analysed to determining binding sites. Random combination of these amino acids made and peptide sequences predicted.

3.3 Library formation- Peptide mimetic predication

Peptide sequences were predicted on the basis of binding site of TPO and TMP with TPOR. First protein is prepared and docking is allowed.

3.4 Library Generation

Pepfold a de-novo peptide structure prediction tool was used to predict 3D structures of peptides Peptide sequences were pasted on the workspace and allowed to run which gives 3D structure in PDB format. PDB files imported to Maestro and Prepwizard used to prepare structures.

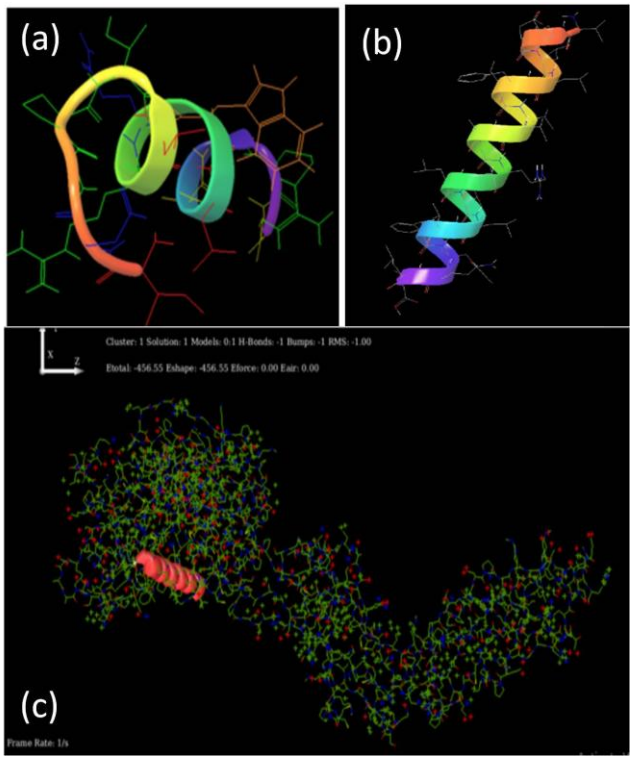

Figure 4: *a) 3D structure for TMP retrieved from Pep fold. b) Peptide 1 retrieved from pep fold and processed in maestro, c) Peptide 1 interacting to its target TPOR*

3.5 Interaction analysis of TPOR and combinatorial library of peptides-

A combinatorial library of peptides interaction with TPOR was analysed using HEX 8.0.0 software. Initially, receptor and ligand were prepared for removing water and unwanted ligands then PDBs of receptor and ligand peptides were

uploaded to the software. Parameters of interaction analysis calculation device number of results and domain of interaction are selected and then the programme was run. Hex returned the E_{total} score and best PDBs for the interaction of receptor and ligand were obtained. (Table: 3)

Table 3: E_{total} score of TPOR and peptide library using HEX 8.0.0. Known and Unknown peptide mimetic with their scores. Peptide-1 has better Energy total score than other peptides.

S.No	Oligopeptides	E_{total}
Known mimetic		
0	IEGPTLRQWLAARA(TMP)	-170.17
Unknown mimetic		
1	VLDLLFTVLAARLLVLLFFQLL	-456.55
2	LLELLFIVLAARLLVLLFFQLL	-333.85
3	LLSLIVLAARLLVLLFFQLLLF	-299
4	LLSLLFIVLAADELVLLFFQLL	-333.66
5	SPAPPACQVHPLPTPVLLPAVDFSLG	-356.03
6	LLSLLFIVLAARLLVLLFFQLL	-340.91
7	LLSLLFIVLAAHLLVLLFFQLH	-333.51
8	SPAPPACQVHPLPTPVLLPAVDF	-300.07
9	LLSLLFIVLAAHLLVLLFFQLH	-315.22
10	LLSLLFIVLEAHLLVLLDFQLH	-330.2
11	SPACQVHLTDFGEWKQMIRQ	-300.44
12	EDKRKHTQRRNH	-252.85
13	THRRKKRDGWEQNH	-252.85
14	WQDRKPELLRKLRNH	-194.78
15	SPAPPACQVHPLPTPVLLPA	-256.49
16	SPAPPACQVHPLPTPVL	-138.59
17	CRNEAESHYCYYNNASHL	-209.83
18	NQDRKPELLRKLRNH	-225.85
19	LLSLLFRVLAADELVLLKFQLL	-276.24
20	LLSLLFIVADRLLVLLFFQLL	-233.35
21	ILVGTLIVLIPVLIVLVFLYWQ	-266.99

3.6 Physicochemical properties of peptide

Peptide mimetic with better binding energy value was further evaluated for physicochemical properties using Protein peptide calculator and Protparam. The results obtained from the software were the physiochemical parameters such as molecular weight, isoelectric pH, nature and charge of the peptides, estimated half-life, and instability index.

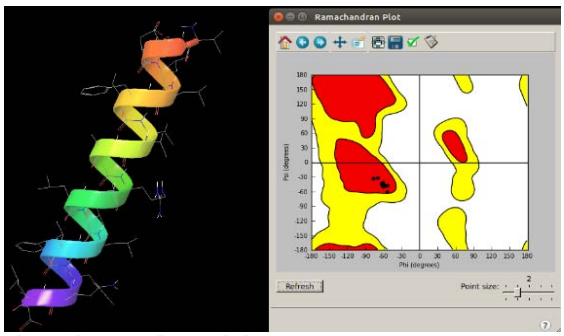

Figure 5: *Ramachandran plot generated for Peptide 1 along with details of residues by RAMPAGE.*

Table 4 *Peptide 1 parameters identification using protein peptide calculator and ProtParam. Various parameters studied were Molecular weight, Isoelectric pH– The value of pH at which a particular molecule carries no net electrical charge, Charge, Nature, Estimated half-life- It is basically a prediction of time for half of the amount of protein in a cell to disappear after its synthesis. ProtParam place reliance on the "N-end rule", in which the half-life of a protein relies on its N-terminal residue; the prediction is given for 3 model organisms namely, human, yeast and E.coli. The N-terminal residue of a protein also plays an important role in determining its stability in vivo, Instability index – It determines whether it will be stable in a test tube. If the index is greater than 40, then it is probably unstable in the test tube.*

Parameters	Values for Peptide-1	Values for TMP
Molecular weight	2543.24	1581.8
Isoelectric pH	6.23	10.45
Charge	0	1
Nature	Neutral	basic
Estimated half-life	100 hours (mammalian reticulocytes, in vitro). >20 hours (yeast, in vivo). >10 hours (Escherichia coli, in vivo).	20 hours (mammalian reticulocytes, in vitro). 30 min (yeast, in vivo). >10 hours (Escherichia coli, in vivo).
Instability index	5.69 (This classifies the protein as stable)	77.00 (This classifies the protein as unstable)

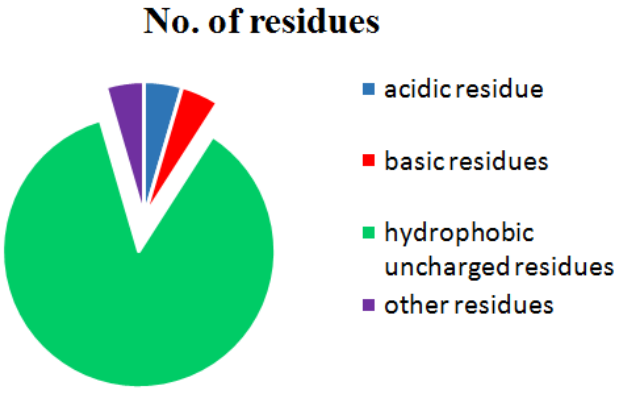

Figure 6: *Hydrophilicity analysis of peptide 1 obtained from protein peptide calculator. We can conclude that the number of uncharged hydrophobic residues are maximum in number i.e. 19 and the other three namely acidic residue, basic residue, other residues are 1 each. With the colour code, the sequence will be written as VLDLLFIVLAARLLVLLFFQLL.*

3.7 Biological properties of peptide

Cello predictor server is used for the Subcellular localization of the peptide-1. Subcellular localization can be correlated to the biological function of a protein It determines the localization of peptides after secretory pathway.

Table 5 Cello predictor results of Peptide-1 for determining the localization in the cell.

Extracellular	1.266	Peroxisomal	0.034
Nuclear	1.134	ER	0.028
Mitochondrial	0.891	Golgi	0.019
Chloroplast	0.759	Cytoskeletal	0.018
Cytoplasmic	0.496	Vacuole	0.018
Plasma Membrane	0.320	Lysosomal	0.017

4. Discussion

Designing an in-silico mimetic for Thrombopoietin to improve the cellular viability of platelet by preventing programmed cell death, i.e. apoptosis or to treat platelet-associated diseases like aplastic anemia, etc., via a combinatorial library of peptide sequence derived from binding sites of TPOR with TPO and known mimetic and literature survey is created. The library was tested for interaction analysis with TPOR extracellular domain region for binding and regulation of thrombopoiesis. For the interaction study, first in the receptor, TPOR, extracellular domain region was prepared by structure prediction method via phyre 2 and then by removing water structure was prepared. A similar procedure was followed for TPO since PDB structures for both the proteins is not available. The TPO-TPOR active site is analyzed using PDB structure of the complex obtained from docking results by HEX 8.0.0 in maestro server. TPOR found to interact with two regions in TPO forming the receptor dimer. Hydrophobic amino acids, namely, His133, Lys14, Lys138, and Phe141 are present in the receptor binding site. Peptide mimetic 1 has an E_{total} value of -456.55 which is better than the E_{total} value of known mimetic TMP, -170.17. Lead Peptide mimetic was further analyzed for physicochemical properties and stability. Peptide mimetic showed higher hydrophobicity which is similar to natural TPO variant and is necessary to the membranes. Lead peptide hydrophilic and hydrophobic nature may have an important role in binding to TPOR as we had seen polar and non-polar both interactions involved in binding of TPO-TPOR complex. Cello predictor results showed that peptide localization by secretary pathway is to the cytoplasm where it can bind to its receptor and activate the signaling further for platelet formation. In future, further *Ex-vivo* study of designing mimetic with TPOR can confirm its role in increasing the shelf life of the platelet by acting as an anti-apoptotic agent or in the diseased condition and more importantly can be used for ex vivo platelet generation and in many other applications in the field of regenerative medicine.

5. Conclusion

Peptides are conveniently modified using computational tools for *in-silico* study. *In silico* study helps in improving peptide in terms of stability, to further enhance the therapeutic potential. This would reduce the time and expenses of *in vivo* and *in-vitro* experiments. In this study, using computational tools an attempt was made to design novel TPO mimetic which would activate TPOR cytokine protein and consequent signaling. TPO is an essential factor for platelet, MK progenitor cells viability, and proliferation. We identified that peptide 1 from the library generated has a high binding affinity towards TPOR. On studying physiochemical and biological properties the predicted mimetic was acceptable with high stability. In future, the designed mimetic would be a promising candidate for treating aplastic anemia, thrombocytopenia, Thrombocythemia, and other platelet dysfunctional diseases. Mimetic can play an important role in increasing the shelf life of platelet by acting as an anti-apoptotic agent.

References

[1] Machlus KR, Italiano JE Jr. The incredible journey: From megakaryocyte development to platelet formation. J Cell Biol. 2013 Jun 10;201(6):785-96. doi: 10.1083/jcb.201304054

[2] Christian H, Rüster B, Seifried E, Henschler R. . Platelet precursor cells can be generated from cultured human CD34+ progenitor cells but display recirculation into hematopoietic tissue upon transfusion in mice. Transfus. Med. Hemother. 2010. 37, 185–190. 10.1159/000316975

[3] Kuter DJ, Rosenberg RD. The reciprocal relationship of thrombopoietin (c-Mpl ligand) to changes in the platelet mass during busulfan-induced thrombocytopenia in the rabbit. Blood. 1995 May 15;85(10):2720-30.

[4] Kuter DJ. Thrombopoietin and thrombopoietin mimetics in the treatment of thrombocytopenia. Annual Review of Medicine, 2009, 60, 193–206. http://doi.org/10.1146/annurev.med.60.042307.181154

[5] Kuter DJ. Review article New thrombopoietic growth factors 2015, 109(11), 4607–4617. http://doi.org/10.1182/blood-2006-10-019315.

[6] Chen WM, Yu B, Zhang Q, & Xu P. Identification of the residues in the extracellular domain of thrombopoietin receptor involved in the binding of thrombopoietin and a nuclear distribution protein (human NUDC). Journal of Biological Chemistry, 2010, 285(34), 26697–26709. http://doi.org/10.1074/jbc.M110.120956

[7] Harker LA, Hunt P, Marzec UM, Kelly AB, Tomer A, Hanson SR, Stead RB. Regulation of platelet production and function by megakaryocyte growth and development factor in nonhuman primates. Blood. 1996 Mar 1;87(5):1833-44.

[8] Hsieh DPH, Huxtable S, Ng K F, Chen HM, Tsang PWK, Wang J, & Xu P. Determination of interactions between human thrombopoietin and its receptor MPL by yeast two-hybrid system and affinity biosensor. International Journal of Biochemistry and Cell Biology, 2000, 32(5), 481–488. http://doi.org/10.1016/S1357-2725 (99)00132-6.

Author Profile

Dr. Vimal Kishor Singh received the M.Sc. in Bio-Medical Sciences from University of Delhi. PhD from Institute of Nuclear Medicine and Allied Sciences (DRDO)/University of Delhi Founder and O/I of **Stem Cell Research Laboratory**, Dept. of Biotechnology, Delhi Technological University

Ishita Goyal received the M.Tech degree in Bioinformatics from Delhi Technological University in 2015. Her area of interest lies in computational biology, protein-protein docking.

Abhishek Saini received the B.Sc. Microbiology (H) degree from Delhi University and M.Sc. in Biotechnology from TERI University. At present pursuing Ph.D. from Delhi Technological University.

Neeraj Kumar received the B.Sc. degree in Chemistry from Delhi University and the M.Sc. degree in Biochemistry from Jamia Millia Islamia University and M.Tech degree in Bioinformatics from Delhi Technological University. Presently, pursuing his Ph.D. from Delhi University.

Manisha Kalsan received a B. Tech degree in Biotechnology from D. C. R. University of Science and Technology, Murthal and an M. Tech degree in Bioinformatics from Delhi Technological University and is presently pursuing her PhD from University of Delhi.

Prof Ramesh Chandra is founder Director of ACBR, University of Delhi. Former Vice-Chancellor, Bundelkhand University Professor, Department of Chemistry, University of Delhi.

Effective relative permittivity and characteristic impedance of graphene loaded microstrip line by scalar S-parameters

Kamlesh Patel, Neha, and Pawan K. Tyagi

Citation: AIP Conference Proceedings **1728**, 020617 (2016); doi: 10.1063/1.4946668
View online: http://dx.doi.org/10.1063/1.4946668
View Table of Contents: http://scitation.aip.org/content/aip/proceeding/aipcp/1728?ver=pdfcov
Published by the AIP Publishing

Effective relative permittivity and characteristic impedance of graphene loaded microstrip line by scalar S-parameters

Kamlesh Patel[1, 2, a)], Neha[1] and Pawan K. Tyagi[2, b)]

[1]*Department of Electronic Science, University of Delhi, Benito Juarez Road, New Delhi 110021, India*
[2]*Department of Applied Physics, Delhi Technological University, Bawana Road, Delhi 110042, India*

[a)]Corresponding author: kpatel@south.du.ac.in
[b)]pawan.phy@dce.edu

Abstract. Graphene film has particular applications at the microwave frequencies because as the number of layers increases, the permittivity and conductivity are modulated. Particularly, an effective relative permittivity of graphene is of high interest. In the present work, effective relative permittivity and characteristic impedance for three kind of structures where microstrip line is either in air or loaded by glass or by graphene film on the glass substrate have been determined. The scalar S-parameters have been measured by adopting both transmission- reflection and short-open methods. The propagation constant and effective relative permittivity have been calculated and found to be nearly same for the both methods with maximum difference of 0.27% and 1.87%, respectively. However, the characteristic impedance values have significant variations as high as 12.13%. Enhanced effective relative permittivity in the range of 3.7 to 4.12 has been observed in the frequency range 1 to 8 GHz, if graphene film on the glass substrate has been loaded on top of the microstrip line. In this value the contribution of stripline substrate includes. Relative permittivity of only monolayer graphene film on the glass substrate is determined in the range of 1.62 to 4.05, and dispersive in nature.

INTRODUCTION

An effective relative permittivity (ε_{reff}) of the microstrip line exhibits due to the different modes propagate in the microstrip line and these modes called quasi-transverse electromagnetic (quasi-TEM) mode. In this mode of propagation, the electromagnetic (EM) fields exist in the top and bottom regions of the top conductor line due to quasi-TEM mode. If any unknown material placed on the top conductor in microstrip line, then EM fields disturbed. This changed the values of Propagation constant (γ) and characteristic impedance (Z_0) in the modified structure. A change in these parameters can be used to quantitively measured the EM properties of the unknown superstrate material placed on top of the microstrip line. In this manuscript, word 'superstrate' is used for the material placed on the top of microstrip. Adopting this approach, a microstrip line can be used as a sensor and the material properties have been extracted.[1]

Experimentally, γ and Z_0 can be evaluated from the scattering (S) -parameters of the microstrip line structure. These S-parameters can obtain using transmission-reflection method and short-open method by a network analyzer.[2,3] The ratio of propagation constant with an unknown material on top of the microstrip line to the free space propagation constant gives the experimental value of the effective relative permittivity (ε_{reff}).[4] Graphene is a planar single atomic thick layer of carbon atoms bonded in a hexagonal structure, i.e. a monolayer of sp^2 –bonded carbon atoms arranged in a honeycomb crystal lattice.[5] Recently, several applications of graphene have been explored to use it as a versatile material in a wide frequency range (from the microwave to Terahertz-THz) like in field-effect transistor (FET), phase shifter, graphene based IC etc. [6,7,8] In many of these applications, electromagnetic (EM) properties of graphene are of interest for its optimum utilization. To understand the EM properties of graphene and its related applications, graphene needs to be characterized at the microwave range. The effective permittivity of graphene is reported to be in between 2 to 16 in 5- 40 GHz and 3 to 5.5 in 0.5 - 6 GHz range.[7,8] In present work, we

International Conference on Condensed Matter and Applied Physics (ICC 2015)
AIP Conf. Proc. 1728, 020617-1–020617-6; doi: 10.1063/1.4946668
Published by AIP Publishing. 978-0-7354-1375-7/$30.00

have studied the properties of graphene using three simple structures where microstrip line is either in air or loaded by glass or by graphene film on the glass substrate (graphene/substrate). From the measured S-parameters, the values of γ, Z_0 and ε_{reff} have determined for the three structures by adopting both the methods and compared. In addition, the estimated value of combined relative permittivity of monolayer graphene on the glass has been also extracted.

TRANSMISSION-REFLECTION (T-R) AND SHORT-OPEN (S-O) METHODS

From the measured reflection and transmission parameters, S_{11} and S_{21}, respectively, by using transmission-reflection method, the characteristic impedance (Z_C) and the propagation constant γ of line can be obtained using the Equations (1) and (2).[2]

$$Z_C = Z_0 \sqrt{\frac{(1+S_{11})^2 - S_{21}^2}{(1-S_{11})^2 - S_{21}^2}} \quad \textbf{(1)}$$

$$\gamma l = \ln\left(\frac{1 - S_{11}^2 + S_{21}^2 \pm \sqrt{(1 - S_{11}^2 + S_{21}^2)^2 - 4S_{11}^2}}{2S_{21}^2} \right) \quad \textbf{(2)}$$

where Z_0 is the reference impedance (~50 Ω) and l is the length of transmission line.

To remove any ambiguity in γ, we define a term X as a hyperbolic tangency of the propagation constant in T-R method, multiplied by line length, $\gamma_{TR}l$ as mentioned in equation (3).

$$X = \tanh(\gamma_{TR} l) \quad \textbf{(3)}$$

If the microstrip line is terminated with the coaxial short and open standards, one port S-parameter, $S_{11short}$ and S_{11open} can be measured using the network analyzer, respectively. The short circuit impedance Z_{SC} and open circuit impedance Z_{OC} are obtained from the measured values of $S_{11short}$ and S_{11open} .[3, 4] The characteristic impedance of the microstrip line is obtained from the equations (4),

$$Z_C = \sqrt{Z_{SC} Z_{OC}} \quad \textbf{(4)}$$

We define a term Y as a hyperbolic tangency of γ_{SO}l in the S-O method and which is given by,

$$Y = \tanh(\gamma_{SO} l) = \sqrt{\frac{Z_{SC}}{Z_{OC}}} \quad \textbf{(5)}$$

Now, the values of γ can be calculated by using the following equation (6),[9]

$$\gamma = \frac{1}{l}\left[\pi.k + \tan^{-1}(X)\right] = \frac{1}{l}\left[\pi.k + \tan^{-1}(Y)\right] \quad \textbf{(6)}$$

where k is a number having values of 0, 0.1, 0.2, 0.3, ...

The value of k is estimated from the approximate value of the propagation constant γ_{approx} $(= 2\pi.f\sqrt{\varepsilon_r}/c)$. Here, c is the velocity of light (m/s), f is the frequency (Hz) and ε_r is the dielectric constant of the substrate material.The k value is chosen to provide the calculated γ using the equation (6) to be close to the approximate value of γ.

The effective relative permittivity (ε_{reff}) is the function of the physical dimensions of transmission line and substrate and superstrate parameters.[10] Alternatively, the effective relative permittivity (ε_{reff}) can then obtained from the ratios of corresponding γ to free space propagation constant γ_0, using the following equation (7), [4,8]

$$\varepsilon_{reff} = \left(\frac{\gamma}{\gamma_0}\right)^2 = \left(\frac{\gamma.c}{2\pi\pi}\right)^2 \quad \textbf{(7)}$$

Statically, the effective relative permittivity ε_{reff} can be expressed in terms of the relative permittivity (ε_r) of the substrate, the relative permittivity (ε^*) of the superstrate, width (W) of microstrip line, total height (h) of substrate and superstrate.[11,12] By re-arranging the static formula, $\varepsilon^*$of the superstrate can be given by the Equation (8),

$$\varepsilon^* = \frac{2\varepsilon_{reff} - \varepsilon_r\left[1+\left(1+12\frac{h}{W}\right)^{-0.5}\right]}{\left[1-\left(1+12\frac{h}{W}\right)^{-0.5}\right]} \quad \textbf{(8)}$$

This ε^* is a frequency dependent estimate of the combined relative permittivity of the superstrate and the dielectric constant of the air on the top of microstrip line as the equation (8) doesn't involve their dimensions.

The percent difference in values obtained for three structures using two methods can help to estimate the amount of error in the evaluation. The percent difference between the two evaluated values of γ from T-R and S-O methods is obtained using the following standard expression [13],

$$\text{Difference in } \gamma\,(\%) = \frac{\left|\gamma_{SO} - \gamma_{TR}\right|}{\left(\frac{\gamma_{SO} + \gamma_{TR}}{2}\right)} \quad \textbf{(9)}$$

where γ_{SO} and γ_{TR} are the propagation constant obtained using the short-open and transmission-reflection methods, respectively.

RESULTS FROM THE MEASUREMENTS

A microstrip line of length 50.8 mm has been fabricated on glass-reinforced epoxy laminate (flame-retardant FR4) substrate of dielectric constant (ε_r) of 4.2 and height (h) of 1.5 mm with a copper thickness (t) of 18 μm and characteristic impedance of 50 Ω. The glass and graphene on the glass substrate were purchased from M/s Graphene Laboratories Inc., USA. From the three sets of measured S-parameters for the T-R and S-O methods using scalar network analyzer HP 8757A in a frequency range of 1 to 8 GHz with a step of 500 MHz, the values of γ and Z_C for air-loaded microstrip line, γ_{Gl} and $Z_{C,Gl}$ for glass- loaded microstrip line and γ_{Gr} and $Z_{C,Gr}$ for graphene/substrate - loaded microstrip line, were calculated by using the equations (1) to (6) for both methods. The values of effective relative permittivity (ε_{reff}) are then found from the evaluated propagation constant for three structures using equation (7) and represented in Fig. 1 (i). Ironically, the values of ε_{reff} are obtained in the comparable range for three different structures using both T-R and S-O methods. The variations with frequencies are found to be asymmetric, which indicates that S-O method gives results with greater accuracy than T-R method. Higher values of ε_{reff} indicate that the monolayer graphene has higher ε_r than the air and near about of glass (≈5.25) and FR4 (≈ 4.4) substrate. These values have been found to be less dispersive in the measurement frequency range. Using the both T-R and S-O methods, the values of propagation constant and effective relative permittivity are found almost same.

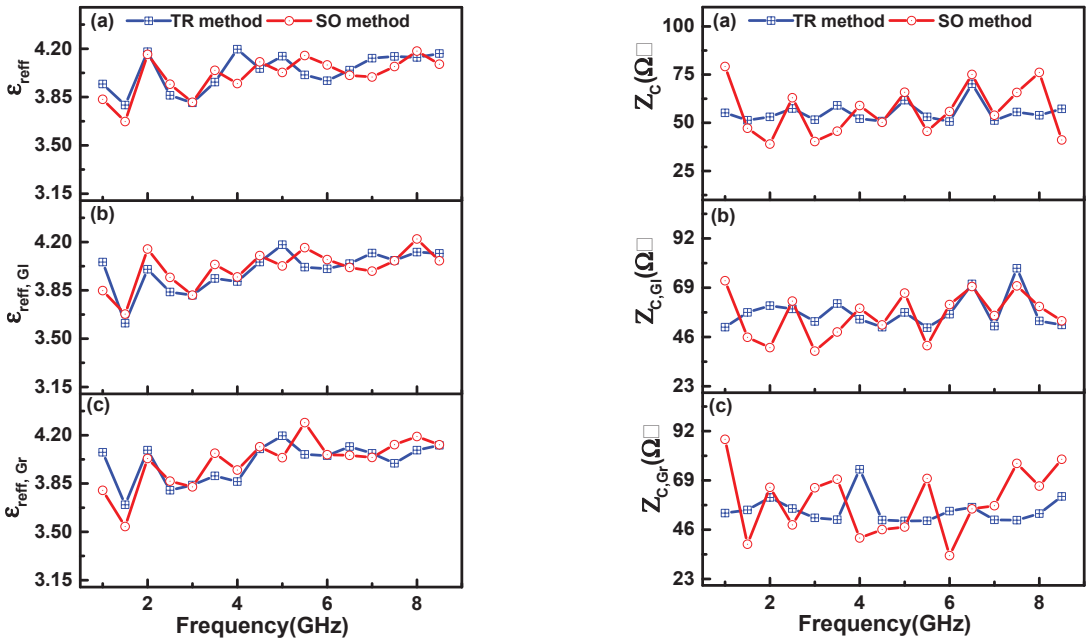

FIGURE 1. (i) Effective relative permittivity (ε_{reff}) and (ii) characteristic impedance (Z_C) in T-R and S-O methods (a) microstrip line, (b) glass-loaded microstrip line, and (c) graphene/substrate-loaded microstrip line.

Fig. 1 (ii) illustrates the characteristic impedance variation obtained by T-R and S-O methods for the three structures. If Z_C values are calculated from the data obtained by adopting S-O method, more variations observed and these variations are significant for the air-loaded as well as graphene/substrate loaded microstrip line. However, glass loading somehow increases the matching condition of the line from the air-loading case. In case of graphene/substrate, the impedance matching deteriorates at the lower frequencies and becomes better at the higher frequencies. Thus, among the structures, Z_C changes value with superstrate loading of glass and graphene/substrate. In comparison to T-R method, the extra variability in Z_C values obtained from the S-O method. This represents two time loading effect as signals travel over the transmission line after reflected from open and short terminations also.The percent difference between these parameters are obtained using equation (9) for two methods and shown in Fig. 2 (i). The percent difference for γ is lower for three structures and almost linear in the measurement frequency range. The higher differences in Z_C values obtained specially for the structure loaded with graphene/substrate. Similarly, percent differences for ε_{reff} are higher for the graphene/substrate-loaded structure, which shows the monolayer graphene has the significant dielectric properties. The results indicated that the measurement method for evaluation of these parameters can also impact their values as the percent difference were not found zero in most frequency points.

The relative permittivity of superstrate material ε^* were estimated for three structures from the respective evaluated ε_{reff} values using equation (8) and shown in Fig. 6. In case of glass-loaded superstrate, glass thickness of 0.7 mm was added to the height of substrate. An additional thickness of 0.335 nm for monolayer graphene is further added to the combined height of glass and stripline substrate. The ε^* values of structures have the similar variation with frequency as of ε_{reff} values of these structures, but of lower values and showing the removal of the substrate contribution i.e. FR4. Hence ε^* are found in the minimum and maximum values of 2.05 to 3.74 for air, 1.86 to 3.69 for glass and 1.62 to 4.05 for graphene/substrate. We observed that for all three structures, these minimum and maximum values were found at the same frequencies. With loading, the minimum value decreases and the maximum value increases except for maximum value for glass-loading. The values obtained from the T-R method

are higher than those from the S-O method at most of frequencies. Also ε* values are becoming more dispersive with the loading, which derived from the effective relative permittivity of the structures.

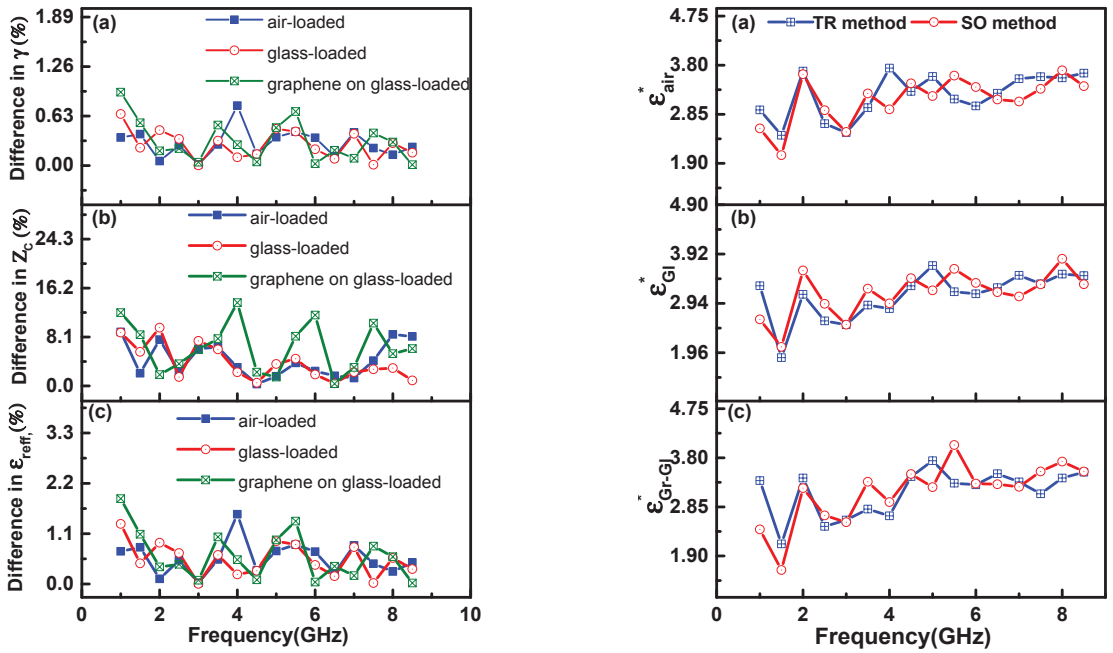

FIGURE 2. (i) Percent difference between T-R and S-O methods, (a) in propagation constant, (b) in characteristic impedance and (c) in the effective relative permitivity for three structures, and (ii) the relative permittivity of the superstrate on top of microstrip line (a) air, (b) glass with air and (c) graphene/substrate with air.

CONCLUSION

We have evaluated the propagation constant (γ), characteristic impedance (Z_C) and effective relative permittivity (ε_{reff}) of microstrip line with three kinds of loading. Two methods, the transmission-reflection and short-open methods, have given similar results for γ and ε_{reff}, but Z_C values have found of different values. The reduced values of γ indicate that the dielectric loading is increased for glass and graphene/substrate. The correct evaluation of the propagation constant depends on the physical length (l) of transmission line, where $l < \lambda/4$. Also such evaluation has been obtained at the discrete frequency points.[4,8] We have experimentally confirmed that the propagation constant can be obtained for any length of a transmission line in a broad frequency range by properly selecting the values of k. The present study showed that the electromagnetic signals while travelling through the graphene experience the significant changes due to its material properties. The variations obtained in our results could be helpful in order to design and tune the specifications of the developed microwave components, if any change in design frequency or component specification is required without making a new component.

ACKNOWLEDGMENTS

We acknowledge the financial support from R & D Scheme 2014-15 of University of Delhi. K. Patel thanks Dr. Harsupreet Kaur for useful discussions on the manuscript and the Head, Department of Electronic Science for the support of the work.

REFERENCES

1. P. Queffelec, P. Gelin, J. Gieraltowski, and J. Loaec, IEEE Trans. Magnetics **30** (2), pp. 224-231 (1994).
2. J. Zhang and T. Y. Hsiang, PIERS Online **3**(7), pp. 1102-1106 (2007).
3. J. Ou and M. F. Caggiano, in *Proceedings of 55th IEEE Electronic Components and Technology Conference* **2**, Florida, USA, 31 May – 3 June 2005, pp. 1765-1768.
4. R. G. Arnaudov, R. B. Borisov, in *Proceedings of 19th Telecommunications forum (TELFOR 2011)*, Serbia, Belgrade, 22 – 24 November 2011, pp. 900- 903.
5. A. K. Geim and K. S. Novoselov, Nature Mater. **6**, pp.183-191 (2007).
6. M. Dragoman, D. Neculoiu, D. Dragoman, G. Deligeorgis, G. Konstantinidis, A. Cismaru, F. Coccetti, and R. Plana, IEEE Microwave Magazine **11** (7), pp. 81-86 (2010).
7. M. Dragoman, A. Cismaru, A. Stefanescu, A. Dinescu, D. Dragoman, in *Proceedings of The 43rd European Microwave Conference,* Nuremberg, Germany, 7- 10 October 2013, pp. 530-532.
8. Y. Wu, Y. Xu, Z. Wang, C. Xu, Z. Tang, Y. Chen, and R. Xu, Appl. Phy. Letters **101**, 053110-1-3 (2012).
9. A. Kumar, *Microwave Techniques: Transmission Lines* (New Age Publications, 1998), pp. 49-50.
10. D. M. Pozar, *Microwave Engineering* (John Wiley & Sons, Inc., 2012), pp.8-10.
11. K. C. Gupta, R. Garg, and I. J. Bahl, *Microstrip Lines and Slotlines* (Artech House, 1979), pp.147-149.
12. R. B. Keam and W. S. Holmes, in *Proceeding of International Microwave and Optoelectronics Conference (SBMO/IEEE MTT-S IMOC'95)* **1**, Rio de Janeiro, Brazil, 24 – 27 July 1995, pp. 137-142.
13. G. A. Carlson, Experimental Errors and Uncertainty, 2000 - 2002, pp. 1- 6 (www.ece.rochester.edu).

Oper Res Int J
DOI 10.1007/s12351-016-0245-x

ORIGINAL PAPER

Energy planning problems with interval-valued 2-tuple linguistic information

Anjali Singh[1] · **Anjana Gupta**[1] · **Aparna Mehra**[2]

Received: 29 May 2015 / Revised: 4 April 2016 / Accepted: 8 April 2016

Abstract In this paper, we address to the concern as to which alternative is most suitable for energy production in a new power plant set up in India. We model this problem as a multi-criteria group decision making problem where the criteria values are described in terms of interval-valued 2-tuple linguistic variables. We propose to solve this model by extending the PROMETHEE II method to interval-valued 2-tuple linguistic variables where the criteria weights in the PROMETHEE II method are supplied using the entropy measure. A small example is presented to illustrate the practicality and usefulness of the proposed method.

Keywords Multi-criteria group decision problems · Energy planning problem · PROMETHEE II · Interval-valued 2-tuple linguistic variable · Score function · Accuracy function

1 Introduction

Energy systems are vital for the economic and social development of a country and the quality of life. An adequate, affordable, clean and equitable energy supply is essential. It is now well acknowledged that the conventional energy resources are depleting at a fast rate. Moreover the environmental impact of their usage are now well recognized (Simpson and Edwards 2011). There is an increasing need to develop and employ alternative energy technologies that can lessen the dependency on the conventional energy resources and reduce the negative environmental

✉ Anjana Gupta
anjanagupta@dce.ac.in

[1] Department of Applied Mathematics, Delhi Technological University, Shahbad, Daulatpur, Bawana Road, Rohini 110042, Delhi, India

[2] Department of Mathematics, Indian Institute of Technology Delhi, Hauz Khas, New Delhi 110016, India

Published online: 07 May 2016

impacts. These objectives lead to the question as to which alternative energy technologies should be pursued by the country? The potential technologies need to be compared on a platform based on their technical, environmental, and economic performance before arriving at a conclusion.

According to Ministry of New and Renewable Energy of India, the impressive rate of growth of India is 8.2 % (Access to Clean Energy 2010). The country ranks sixth in the world in terms of total energy consumption and needs to accelerate development of the energy sector to meet its growth aspirations. According to International Energy Agency, India is the fourth largest consumer of crude oil and natural gas after China, the United States and Russia in 2011 (Ahn and Graczyk 2012). Hence, like any other developing country, a reliable and adequate supply of clean energy is the necessity for India's continued economic development.

Since the energy planning problems are subject to many sources of uncertainty, large investments, long term planning featuring multiple decision makers (DMs) and many conflicting criteria, these have been modeled in MCGDM framework. MCGDM is an integral part of the modern decision sciences. It has received great attention in last few decades (Herrera and Martinez 2000; Martinez and Herrera 2012; International Journal of Uncertainty 2009; Mi et al. 2009; Pang and Liang 2012; Zhang 2012). In the foregoing literature about MCGDM problems, DMs are asked to provide assessment for all alternatives on each criterion. Until now, the studies of MCGDM in energy planning considered models describing criteria values that are either crisp or fuzzy (Goumas and Lygerou 2000; Pohekar and Ramachandran 2004; T et al. 2009). The DMs may however be reluctant or unable to assign precise numeric evaluation to comparison judgments due to inherent subjective nature of human thinking. Hence quantitative values are not adequate enough to model such decision problems. A possible way to overcome this is to use the linguistic approach wherein the information is represented in qualitative terms by means of linguistic variables.

The 2-tuple linguistic model proposed by Herrera and Martinez (2000, 2001) has the capability of expressing any counting of information in the universe of discourse. But sometimes the subjectivity of the linguistic terms in the linguistic term set is not complete to cater to the granularity of uncertainty in assessment on some criteria. Of course, one can always put forth an argument that the linguistic term set can be enlarged by including more linguistic terms with different refined granularity of uncertainty for better information expressions; this amounts to increasing tedious calculations in aggregating the large sets of information (Zhang 2012). Zhang (2012) introduced a new version of linguistic representation model using interval-valued 2-tuple linguistic variables. In this model, the judgements of DMs are expressed with interval-valued 2-tuple terms from the predefined linguistic terms set. Some authors Beg and Rashid (2014), Ruan et al. (2013), Wang et al. (2015) and Zhang (2013) investigated and proposed new aggregation operators for interval-valued 2-tuple linguistic variables. Liu et al. (2013) presented an interval 2-tuple linguistic VIKOR method for solving the material selection problem. You et al. (2015) extended the VIKOR method for group multi-criteria supplier selection problem under incomplete information scenario using interval-valued 2-tuple linguistic information. Liu et al. (2009) presented a novel FMEA (failure mode and

effect analysis) approach by combining interval-valued 2-tuple linguistic variables with gray relational analysis to improve the effectiveness of the traditional FMEA.

Another widely used outranking method to solve multi-criteria decision problems is PROMETHEE (Preference Ranking Organization Method for Enrichment Evaluations) method, introduced by Brans (1983) and extended by Vincke and Brans (1985) and Brans et al. (1986). Since its inception, the method is successively applied in various fields including environment management, energy management, investment planning, agriculture, logistics and transportation, medicine, to name a few. For instance, one can refer to Aldavi et al. (2007), Mareschal (1998), Mareschal and Brans (1988, 1991), Oberschmidt et al. (2010) and Yan et al. (2007), to cite a few. A survey paper by Behzadiana et al. (2010) highlights the development and research on PROMETHEE in great details. Halouani et al. (2009) proposed PROMETHEE method to deal with multigranular linguistic information. Chen et al. (2009) used crisp values to express quantitative information and 2-tuple linguistic variables to express qualitative information along with linguistic PROMETHEE in personnel evaluation and selection of candidates.

The significance of various criteria in a multi-criteria problem is described by associating weights with them. PROMETHEE II assumes that these weights can be prescribed by DMs, a rather stringent assumption. On the other hand, a good number of techniques exist in literature to obtain the criteria weights in a judicious way. They are broadly classified into two categories: subjective methods and objective methods (Wang and Lee 2009). The subjective methods determine the criteria weights based on the preferences of DMs, like analytical hierarchy process, whereas the objective methods utilize mathematical models, such as entropy measure, to find these weights. Since all criteria in a MCGDM problem may not transmit same level of information to elucidate the best alternative, entropy is a well suited measure to determine the relative intensities of the criteria (Zeleny 1996).

In this paper, we aim to model an energy planning problem of India as a MCGDM problem where the DMs provide their preferences on alternatives with respect to various criteria using interval-valued 2-tuple linguistic variables. In order to solve this model, we propose to apply the PROMETHEE II method after suitably modifying it for interval-valued 2-tuple linguistic variables. The two principal requirements of PROMETHEE II method are single assessment matrix of criteria-alternatives, and the criteria weights. The former is achieved by aggregating various assessment matrices of criteria-alternatives provided by the DMs using weights of each DM on each criterion-alternative pair. And next the criteria weights, for aggregating information on each alternative over various criteria, are computed using entropy measure. Thereafter, we proceeded with the PROMETHEE II method to rank the alternatives.

The remainder of this paper is set out as follows. Section 2 presents a brief description of linguistic variables with some arithmetic operations. Section 3 introduces PROMETHEE II method for ranking alternatives in MCGDM problems with interval-valued 2-tuple linguistic information. Section 4 presents an example for energy planning problem of selecting the best renewable energy resource for India. The paper concludes in Sect. 5.

2 Preliminaries

This section provides the retrospective view of 2-tuple linguistic variables and interval-valued 2-tuple linguistic variables and their arithmetic.

A 2-tuple linguistic variable, denoted by (s_i, α), comprises of a linguistic term s_i and a real number α where s_i represents the linguistic label from a predefined linguistic term set and α is the symbolic translation.

Let $LT = \{s_i : i = 0, 1 \ldots, g\}$ be a finite and totally ordered discrete linguistic term set with following characteristics:

1. $s_i \geq s_j$ if $i \geq j$ (i.e., the set is ordered); (i.e., the set is ordered);
2. $\max(s_i, s_j) = s_i$ if $s_i \geq s_j$ and $\min(s_i, s_j) = s_i$ if $s_i \leq s_j$;
3. Negation: $\text{neg}(s_i) = s_j$ where $j = g - i$.

2.1 A 2-tuple linguistic model

The 2-tuple linguistic representation model was firstly presented in Herrera and Martinez (2000). Chen et al. (2009) and Tai and Chen (2009) proposed the generalized 2-tuple linguistic model.

Definition 1 Let $\beta \in [0, 1]$ be the result of an aggregation of the indices of a set of labels assessed in LT having cardinality $g + 1$. Suppose $i = \text{round}(\beta g)$, (where round $(\cdot)$ is the usual round operation) and $\alpha = \beta - \frac{i}{g}$, be such that $i \in \{0, 1, \ldots, g\}$ and $\alpha \in \left[\frac{-1}{2g}, \frac{1}{2g}\right)$, then α is called the *symbolic translation*.

Note β above is relevant to the granularity of the linguistic term set.

Definition 2 Let $LT = \{s_i : i = 0, 1, \ldots, g\}$ be a linguistic term set and $\beta \in [0, 1]$ represents the result of a symbolic aggregation. The equivalent 2-tuple linguistic variable can be obtained using the function $\Delta : [0, 1] \to LT \times \left[\frac{-1}{2g}, \frac{1}{2g}\right)$, defined as,

$$\Delta(\beta) = (s_i, \alpha_i) \quad \text{where} \quad i = \text{round}(\beta g) \text{ and } \alpha_i = \beta - \frac{i}{g}.$$

The function Δ is bijection, its inverse is given by

$$\Delta^{-1} : LT \times \left[\frac{-1}{2g}, \frac{1}{2g}\right) \to [0, 1] \quad \text{as} \quad \Delta^{-1}(s_i, \alpha_i) = \alpha_i + \frac{i}{g} = \beta.$$

Clearly, $\Delta\left(\frac{i}{g}\right) = (s_i, 0)$ and $\Delta^{-1}(s_i, 0) = \frac{i}{g}$.

Herrera and Martinez (2000, 2001) defined ranking in 2-tuple linguistic variables using the lexicographic order.

Definition 3 Let (s_i, α_i) and (s_j, α_j) be two 2-tuple linguistic variables.

1. If $i < j$ then $(s_i, \alpha_i) < (s_j, \alpha_j)$.
2. If $s_i = s_j$, then
   (a) if $\alpha_i = \alpha_j$ then $(s_i, \alpha_i) = (s_j, \alpha_j)$;
   (b) if $\alpha_i > \alpha_j$ then $(s_i, \alpha_i) > (s_j, \alpha_j)$;
   (c) if $\alpha_i < \alpha_j$ then $(s_i, \alpha_i) < (s_j, \alpha_j)$.

In earlier literature, authors Chen et al. (2009), Ju and Wang (2013) and Wei (2010) had worked with linguistic variables by converting them to their equivalent numeric values using Δ and Δ^{-1} functions. We shall be defining some arithmetic operators that directly operate on linguistic variables so that the entire discussion can be carried out on the same domain of linguistic variables.

2.1.1 Arithmetic operators on 2-tuple linguistic variables

Let $LT = \{s_i : i = 0, 1, \ldots, g\}$ be the linguistic term set. The 2-tuple linguistic variable is of the form (s_i, α_i), where $s_i \in LT$, $\alpha_i \in \left[\frac{-1}{2g}, \frac{1}{2g}\right)$, for all $i = 1, \ldots, g-1$, $0 \le \alpha_0 < \frac{1}{2g}$, $\frac{-1}{2g} \le \alpha_g \le 0$.

Distance The distance between two 2-tuple linguistic variables (s_i, α_i) and (s_j, α_j) is defined as follows:

$$d((s_i, \alpha_i), (s_j, \alpha_j)) = (s_k, \alpha_k), \text{ where } k = \text{round } (|i - j + (\alpha_i - \alpha_j)g|) \text{ and}$$
$$\alpha_k = \left(\left|\left(\frac{i}{g} + \alpha_i\right) - \left(\frac{j}{g} + \alpha_j\right)\right|\right) - \frac{k}{g}.$$

Scalar multiplication For a scalar a, $0 \le a \le 1$, define

$$a(s_i, \alpha_i) = (s_k, \alpha_k), \text{ where } k = \text{round } (ia + \alpha_i ag) \text{ and } \alpha_k = a\left(\frac{i}{g} + \alpha_i\right) - \frac{k}{g}.$$

Multiplication

$$(s_i, \alpha_i) * (s_j, \alpha_j) = (s_k, \alpha_k), \text{ where } k = \text{round } \left(\left(\frac{i}{g} + \alpha_i\right)\left(\frac{j}{g} + \alpha_j\right)g\right) \text{ and}$$
$$\alpha_k = \left(\frac{i}{g} + \alpha_i\right)\left(\frac{j}{g} + \alpha_j\right) - \frac{k}{g}.$$

Arithmetic mean (AM) Let (s_{r_i}, α_{r_i}), $i = 1, \ldots, q$, $r_i \in \{0, 1, \ldots, g\}$, be a set of 2-tuple linguistic information. Then

$$AM((s_{r_i}, \alpha_{r_i}) : i = 1, \ldots, q) = (s_k, \alpha_k),$$

where

$$k = \text{ round } \left(\frac{1}{q}\sum_{i=1}^{q} r_i + \frac{g}{q}\sum_{i=1}^{q} \alpha_{r_i}\right) \quad \text{and} \quad \alpha_k = \frac{q}{g}\sum_{i=1}^{q} r_i + \frac{1}{q}\sum_{i=1}^{q} \alpha_{r_i} - \frac{k}{g}.$$

Weighted average (WA) Let (s_{r_i}, α_{r_i}); $r_i \in \{1, \ldots, g\}$, $i = 1, \ldots, q$, be a set of 2-tuple linguistic information and $w = \{w_1, \ldots, w_q\}^T$ be the weight vector satisfying $0 \le w_i \le 1$, $i = 1, \ldots, q$, and $\sum_{i=1}^{q} w_i = 1$. Then

$$WA((s_{r_i}, \alpha_{r_i}) : i = 1, \ldots, q) = (s_k, \alpha_k),$$

where

$$k = \text{ round } \left(\sum_{i=1}^{q} w_i (r_i + \alpha_{r_i} g)\right), \quad \alpha_k = \sum_{i=1}^{q} w_i \left(\frac{r_i}{g} + \alpha_{r_i}\right) - \frac{k}{g}.$$

2.2 An interval-valued 2-tuple linguistic model

Zhang (2012) proposed an interval-valued 2-tuple linguistic representation model as an extension of 2-tuple linguistic model.

Definition 4 Zhang (2012) Let $LT = \{s_i : i = 0, 1, \ldots, g\}$ be a linguistic term set. An interval-valued 2-tuple linguistic variable comprises of two 2-tuple linguistic terms, denoted by $[(s_i, \alpha_i), (s_j, \alpha_j)]$ where $i \le j$. Here s_i and s_j represent the linguistic labels from LT and α_i and α_j are the symbolic translations.

Analogous to the Δ and Δ^{-1} functions defined in Definition 2, Zhang (2012) proposed a bijection $\Delta : [0, 1] \times [0, 1] \to \left(LT \times [\frac{-1}{2g}, \frac{1}{2g})\right) \times \left(LT \times [\frac{-1}{2g}, \frac{1}{2g})\right)$, such that the interval-valued 2-tuple linguistic information that represents the equivalent information to an interval $[\beta_1, \beta_2]$ ($\beta_1, \beta_2 \in [0, 1], \beta_1 \le \beta_2$) can be derived as follows.

$$\Delta([\beta_1, \beta_2]) = [(s_i, \alpha_i), (s_j, \alpha_j)] \quad \text{where} \quad \begin{cases} s_i & i = \text{ round } (\beta_1 g) \\ \alpha_i = \beta_1 - \dfrac{i}{g} & \alpha_i \in \left[\dfrac{-1}{2g}, \dfrac{1}{2g}\right) \\ s_j & j = \text{ round } (\beta_2 g) \\ \alpha_j = \beta_2 - \dfrac{j}{g} & \alpha_j \in \left[\dfrac{-1}{2g}, \dfrac{1}{2g}\right). \end{cases}$$

Also an interval-valued 2-tuple linguistic variable can be converted into an interval $[\beta_1, \beta_2]$, $\beta_1, \beta_2 \in [0, 1], \beta_1 \le \beta_2$, as follows.

$$\Delta^{-1}\left([(s_i, \alpha_i), (s_j, \alpha_j)]\right) = \left[\frac{i}{g} + \alpha_i, \frac{j}{g} + \alpha_j\right] = [\beta_1, \beta_2].$$

Remark 1 If $s_i = s_j$, then $[(s_i, \alpha_i), (s_j, \alpha_j)]$ reduces to $(s_i, [\alpha_i, \alpha_j])$, where s_i is a linguistic label from LT and $[\alpha_i, \alpha_j]$ is an interval symbolic translation with $\alpha_i \leq \alpha_j$, $\alpha_i, \alpha_j \in \left[\frac{-1}{2g}, \frac{1}{2g}\right)$.

Remark 2 If $s_i = s_j$ and $\alpha_i = \alpha_j$, then the interval-valued 2-tuple linguistic variable reduces to 2-tuple linguistic variable.

Interval-valued 2-tuple linguistic variables are ranked using score and accuracy functions. We recall the two concepts from Zhang (2012).

Definition 5 For an interval-valued 2-tuple linguistic variable $A = [(s_i, \alpha_i), (s_j, \alpha_j)]$, the 2-tuple linguistic score function is defined as

$$S(A) = (s_k, \alpha_k), \quad \text{where } k = round\left(\frac{i + j + (\alpha_i + \alpha_j)g}{2}\right),$$
$$\alpha_k = \left(\frac{i + j + (\alpha_i + \alpha_j)g}{2g}\right) - \frac{k}{g}.$$

and the accuracy function is defined as,

$$H(A) = \left(\frac{j}{g} + \alpha_j\right) - \left(\frac{i}{g} + \alpha_i\right).$$

The scheme to compare any two interval-valued 2-tuple linguistic variables is summarized as follows:

Definition 6 Let A = $[(s_i, \alpha_i), (s_j, \alpha_j)]$ and B = $[(s_{i'}, \alpha_{i'}), (s_{j'}, \alpha_{j'})]$ be two interval-valued 2-tuple linguistic variables.

1. If $S(A) > S(B)$ then A > B.
2. If $S(A) < S(B)$ then A < B.
3. If $S(A) = S(B)$ then,
   (a) if $H(A) > H(B)$ then $A < B$;
   (b) if $H(A) < H(B)$ then $A > B$;
   (c) if $H(A) = H(B)$ then $A = B$, that is, both A and B represent same information.

Note that while comparing $S(A)$, we need to invoke Definition 3.

We now define some arithmetic operators on interval-valued 2-tuple linguistic variables that can directly operate on them without converting them into numerics.

Definition 7 Let $X = \{[(s_{r_i}^{(L)}, \alpha_{r_i}^{(L)}), (s_{r_i}^{(U)}, \alpha_{r_i}^{(U)})];\ r_i \in \{0, 1, \ldots, g\},\ i = 1, 2, \ldots, q\}$ be a set of interval-valued 2-tuple linguistic information and $w = (w_1, \ldots, w_q)^T$ be

the weight vector, with $w_i \in [0,1], i = 1,\ldots,q,\ \sum_{i=1}^{q} w_i = 1$. The Interval-valued 2-tuple Weighted Average (IWA) of X is defined as follows:

$$\begin{aligned} &IWA([(s_{r_i}^{(L)}, \alpha_{r_i}^{(L)}), (s_{r_i}^{(U)}, \alpha_{r_i}^{(U)})] :\ i = 1,2,\ldots,q) \\ &\quad = w_1[(s_{r_1}^{(L)}, \alpha_{r_1}^{(L)}), (s_{r_1}^{(U)}, \alpha_{r_1}^{(U)})] \oplus w_2[(s_{r_2}^{(L)}, \alpha_{r_2}^{(L)}), (s_{r_2}^{(U)}, \alpha_{r_2}^{(U)})] \oplus \cdots \oplus \\ &\qquad w_q[(s_{r_q}^{(L)}, \alpha_{r_q}^{(L)}), (s_{r_q}^{(U)}, \alpha_{r_q}^{(U)})] \\ &\quad = [(s_{k^{(L)}}, \alpha_{k^{(L)}}), (s_{k^{(U)}}, \alpha_{k^{(U)}})] \end{aligned}$$

where

$$k^{(L)} = \text{round}\left(\sum_{i=1}^{q} w_i\left(r_i^{(L)} + \alpha_{r_i}^{(L)} g\right)\right), \quad \alpha_k^{(L)} = \sum_{i=1}^{q} w_i\left(\frac{r_i^{(L)}}{g} + \alpha_{r_i}^{(L)}\right) - \frac{k^{(L)}}{g},$$

and

$$k^{(U)} = \text{round}\left(\sum_{i=1}^{q} w_i\left(r_i^{(U)} + \alpha_{r_i}^{(U)} g\right)\right), \quad \alpha_k^{(U)} = \sum_{i=1}^{q} w_i\left(\frac{r_i^{(U)}}{g} + \alpha_{r_i}^{(U)}\right) - \frac{k^{(U)}}{g}.$$

If $w = \left(\frac{1}{q},\ldots,\frac{1}{q}\right)^T$, then IWA of X reduces to the Interval-valued 2-tuple Arithmetic Mean (IAM) operator of X.

Definition 8 Let $[(s_i, \alpha_i), (s_j, \alpha_j)]$ and $[(s_{i'}, \alpha_{i'}), (s_{j'}, \alpha_{j'})]$ be two interval-valued 2-tuple linguistic variables. The 2-tuple linguistic distance operator between them is defined as

$$D([(s_i, \alpha_i), (s_j, \alpha_j)], [(s_{i'}, \alpha_{i'}), (s_{j'}, \alpha_{j'})]) = (s_k, \alpha_k) \tag{1}$$

where

$$\begin{aligned} k &= \text{round}\left(0.5\left(\left|(i + \alpha_i g) - (i' + \alpha_{i'} g)\right| + \left|(j + \alpha_j g) - (j' + \alpha_{j'} g)\right|\right)\right) \\ \alpha_k &= \left(\frac{|(i + \alpha_i g) - (i' + \alpha_{i'} g)| + |(j + \alpha_j g) - (j' + \alpha_{j'} g)|}{2g}\right) - \frac{k}{g}. \end{aligned}$$

3 PROMETHEE-II method for interval-valued 2-tuple linguistic variables

Several versions of PROMETHEE had been developed over the years but all of them require knowledge of criteria weights. Herein, we shall first be using entropy measure to evaluate the normalized weights of the criteria and subsequently apply these weights in the PROMETHEE-II method to rank the alternatives.

3.1 Entropy method with interval-valued 2-tuple linguistic variables

Suppose we have a panel of t DM (or experts) to evaluate m alternatives based on n criteria using linguistic term set $LT = \{l_0, l_1, \ldots, l_g\}$ to rank the alternatives.

Step 1 Each DM provides a linguistic decision matrix $R_{(k)} = (r_{ij_{(k)}})_{m\times n} = [l_{ij_{(k)}}^{(L)}, l_{ij_{(k)}}^{(U)}]$; $i = 1, \ldots, m$; $j = 1, \ldots, n$ and $k = 1, \ldots, t$, by pairwise comparing different alternatives with prevalent criteria on linguistic scale LT, where $l_{ij_{(k)}}^{(L)}, l_{ij_{(k)}}^{(U)} \in LT$. Convert the matrices $R_{(k)}$ into interval-valued 2-tuple linguistic decision matrices $\widetilde{R}_{(k)} = (\widetilde{r}_{ij_{(k)}})_{m\times n} = ([(l_{ij_{(k)}}^{(L)}, 0), (l_{ij_{(k)}}^{(U)}, 0)])$.

Step 2 Aggregate these opinions to construct an aggregated interval-valued 2-tuple linguistic decision matrix $\widetilde{R} = (\widetilde{r}_{ij})_{m\times n}$ using IAM operator (Definition 7).

$$\begin{aligned}\widetilde{r}_{ij} &= [(l_{ij}^{(L)}, \alpha_{ij}^{(L)}), (l_{ij}^{(U)}, \alpha_{ij}^{(U)})] \\ &= IAM\Big(\big[(l_{ij_{(1)}}^{(L)}, 0), (l_{ij_{(1)}}^{(U)}, 0)\big], \big[(l_{ij_{(2)}}^{(L)}, 0), (l_{ij_{(2)}}^{(U)}, 0)\big], \ldots, \big[(l_{ij_{(t)}}^{(L)}, 0), (l_{ij_{(t)}}^{(U)}, 0)\big]\Big).\end{aligned}$$

Step 3 Construct the distance matrix $\widetilde{P}_{(k)} = (l_{ij_{(k)}}, \alpha_{ij_{(k)}})$ of each DM's decision matrix $\widetilde{R}_{(k)}$ from the aggregated matrix $\widetilde{R}$ using 2-tuple linguistic distance function for interval-valued 2-tuple linguistic variables (Definition 8).

$$(l_{ij_{(k)}}, \alpha_{ij_{(k)}}) = D\big(\big[(l_{ij_{(k)}}^{(L)}, \alpha_{ij_{(k)}}^{(L)}), (l_{ij_{(k)}}^{(U)}, \alpha_{ij_{(k)}}^{(U)})\big], \big[(l_{ij}^{(L)}, \alpha_{ij}^{(L)}), (l_{ij}^{(U)}, \alpha_{ij}^{(U)})\big]\big).$$

Step 4 Compute the similarity matrix $S_{(k)} = \big[(s_{ij_{(k)}}, \beta_{ij_{(k)}})\big]_{m\times n}$, using distance function $d(\cdot, \cdot)$ of 2-tuple linguistic variables,

$$(s_{ij_{(k)}}, \beta_{ij_{(k)}}) = d\big((l_g, 0), (l_{ij_{(k)}}, \alpha_{ij_{(k)}})\big).$$

Step 5 Now the weight matrix $(w_{ij_{(k)}})_{m\times n}$ of kth DM is determined as follows

$$w_{ij_{(k)}} = \frac{\Delta^{-1}(s_{ij_{(k)}}, \beta_{ij_{(k)}})}{\sum_{k=1}^{t} \Delta^{-1}(s_{ij_{(k)}}, \beta_{ij_{(k)}})}.$$

Note that each DM has a different importance according to his/her expertise in criteria domains. The closer the value of $\widetilde{r}_{ij_{(k)}}$ to the mean value $\widetilde{r}_{ij}$, the higher is the value of the similarity degree, consequently higher value of $w_{ij_{(k)}}$. In other words, the more precise and informative decision a DM provides for a particular criterion-alternative pair, the more is the weight(importance) of his/her judgement for that particular pair.

Step 6 Construct the collective decision matrix $\widetilde{R}_{coll}$ using IWA operator (Definition 7).

$$\begin{aligned}\widetilde{R}_{coll} &= \left[\left[(r_{ij}^{(L)}, \mu_{ij}^{(L)}), (r_{ij}^{(U)}, \mu_{ij}^{(U)})\right]\right]_{m\times n} \\ &= \left[\left[IWA\left(\left[(l_{ij_{(1)}}^{(L)}, 0), (l_{ij_{(1)}}^{(U)}, 0)\right], \left[(l_{ij_{(2)}}^{(L)}, 0), (l_{ij_{(2)}}^{(U)}, 0)\right], \ldots, \left[(l_{ij_{(t)}}^{(L)}, 0), (l_{ij_{(t)}}^{(U)}, 0)\right]\right)\right]\right],\end{aligned}$$

where weights are taken from Step 5.

Step 7 Convert the matrix $\widetilde{R}_{coll}$ into the numeric matrix.

$$R_{coll} = \left[[p_{ij}, q_{ij}]\right]_{m\times n} = \left[[\Delta^{-1}(r_{ij}^{(L)}, \mu_{ij}^{(L)}), \Delta^{-1}(r_{ij}^{(U)}, \mu_{ij}^{(U)})]\right].$$

Step 8 Compute the criteria weights via an exact model of entropy proposed by Lotfi and Fallahnejad (2010). Calculate the lower bounds $h_j^{(L)}$ and the upper bounds $h_j^{(U)}$ of the interval entropy as follows

$$h_j^{(L)} = \min\left\{-h_0\sum_{i=1}^{m} p_{ij}\ln p_{ij}\,, -h_0\sum_{i=1}^{m} q_{ij}\ln q_{ij}\right\}, \quad j = 1, \ldots, n,$$

and

$$h_j^{(U)} = \max\left\{-h_0\sum_{i=1}^{m} p_{ij}\ln p_{ij}, -h_0\sum_{i=1}^{m} q_{ij}\ln q_{ij}\right\}, \quad j = 1, \ldots, n,$$

where $h_0 = (\ln m)^{-1}$ and $p_{ij}\ln p_{ij} = 0$ or $q_{ij}\ln q_{ij} = 0$ if $p_{ij} = 0$ or $q_{ij} = 0$.

Step 9 Calculate the jth criterion weight, w_j as,

$$w_j = \frac{1}{2}\left(\frac{1 - h_j^{(U)}}{n - \sum_{j=1}^{n} h_j^{(L)}} + \frac{1 - h_j^{(L)}}{n - \sum_{j=1}^{n} h_j^{(U)}}\right), \quad j = 1, \ldots, n.$$

Normalize the weights using,

$$W_j = \frac{w_j}{\sum_{j=1}^{n} w_j}, \quad j = 1, \ldots, n.$$

As argued earlier, these weights depict importance of the criteria. We supply them to the PROMETHEE II method for ranking the alternatives.

3.2 PROMETHEE II with interval-valued 2-tuple linguistic variables

This section presents the PROMETHEE II method for interval-valued 2-tuple linguistic variables in following steps.

Step 1 Recall the $m \times n$ collective matrix $\widetilde{R}_{coll} = \left[\left[(r_{ij}^{(L)}, \mu_{ij}^{(L)}), (r_{ij}^{(U)}, \mu_{ij}^{(U)})\right]\right]$ in Step 6 from previous subsection. Calculate the linguistic score values and accuracy values using Definitions 5. Denote the matrices of score values and accuracy values of $\widetilde{R}_{coll}$ by $\widetilde{S}$ and H, respectively. Note each entry in $\widetilde{S}$ is a 2-tuple linguistic variable, while each entry in H is a real number.

Step 2 Compute score values and accuracy values of preference indices as follows.

$$P_j^{(s)}(A_i, A_{i'}) = \begin{cases} \text{score} = d(\widetilde{S}_{ij}, \widetilde{S}_{i'j}), & \widetilde{S}_{ij} > \widetilde{S}_{i'j} \\ \text{score} = 0, & \widetilde{S}_{ij} \leq \widetilde{S}_{i'j}; \quad i, i' = 1, \ldots, m \text{ and } j = 1, \ldots, n \end{cases}$$

$$P_j^{(a)}(A_i, A_{i'}) = \begin{cases} \text{accuracy} = H_{ij} - H_{i'j}, & \widetilde{S}_{ij} > \widetilde{S}_{i'j} \\ \text{accuracy} = H_{ij} - H_{i'j}, & \widetilde{S}_{ij} = \widetilde{S}_{i'j} \\ \text{accuracy} = 0, & \widetilde{S}_{ij} < \widetilde{S}_{i'j}; \quad i, i' = 1, \ldots, m \text{ and } j = 1, \ldots, n \end{cases}$$

Step 3 Compute the cumulative preference indices for score values and accuracy values respectively as follows.

$$\pi^{(s)}(A_i, A_{i'}) = \sum_{j=1}^{n} W_j(\text{score of } P_j(A_i, A_{i'})), \quad i, i' = 1, \ldots, m,$$

and

$$\pi^{(a)}(A_i, A_{i'}) = \sum_{j=1}^{n} W_j(\text{accuracy of } P_j(A_i, A_{i'})), \quad i, i' = 1, \ldots, m.$$

Step 4 Determine the outgoing flows $\Phi^+(A_i)$ and the incoming flows $\Phi^-(A_i)$, $i = 1, \ldots, m$, as follows.

Flow	Score	Accuracy
$\Phi^+(A_i) \ : i = 1, \ldots, m$	AM $[\pi^{(s)}(A_i, A_{i'}) \ : \ i' = 1, \ldots, m, \ i \neq i']$	$\frac{1}{m-1} \sum_{\substack{i'=1 \\ i \neq i'}}^{m} \pi^{(a)}(A_i, A_{i'})$
$\Phi^-(A_i) \ : i = 1, \ldots, m$	AM $[\pi^{(s)}(A_{i'}, A_i) : i' = 1, \ldots, m, i \neq i']$	$\frac{1}{m-1} \sum_{\substack{i'=1 \\ i \neq i'}}^{m} \pi^{(a)}(A_{i'}, A_i)$

Step 5 Let $I_{(a)}$ be the set of indices of alternatives for which the score value of the outgoing flow is greater than or equal to the score value of its incoming flow. Calculate the score and accuracy of net flow for alternatives with indices $i \in I_{(a)}$ as follows.

$$\begin{aligned} \text{score of } \Phi(A_i) &= d(\text{score of } \Phi^+(A_i), \text{ score of } \Phi^-(A_i)), \quad i \in I_{(a)}, \\ \text{accuracy of } \Phi(A_i) &= \text{accuracy of } \Phi^+(A_i) - \text{accuracy of } \Phi^-(A_i), \quad i \in I_{(a)}. \end{aligned}$$

Step 6 Rank the alternatives using the 2-tuple linguistic score values and accuracy values of net flow $\Phi(A_i), i \in I_{(a)}$, as described in Definition 6.

4 Energy planning: choosing best renewable energy resource for India

India is undergoing rapid economic development and a part of the population is experiencing a rapid increase in prosperity. Today, India is the ninth largest economy in the world with GDP growth 8.7 % in five years (Energy Statistics 2013). India's energy generation is primarily driven by coal power so much so that other renewables such as wind, geothermal, hydroelectricity hold only 2 % while nuclear power contributes 1 % only to it. The power sector in India had an installed capacity of 236.38 Gigawatt (GW) as of March 2012 recording an increase of 14 % over that of March 2011 (Energy Statistics 2013).

As prosperity continues to grow, we will arrive at a point where the demand for energy outstrips supply. Besides conservation and efficient usage of energy, a definite need is there to explore and fully utilize the potential renewable energy from various sources like wind, solar, biomass, small hydro-plants. The total potential for renewable power generation in India as on March 2012 is estimated at 89,774 MW (Energy Statistics 2013). All energy sources have an impact on environment. Concerns about the greenhouse effect and global warming, air pollution, and energy security have led to increasing interest and more development in renewable energy sources.

In this section, we validate the proposed method via a problem from energy sector to select the most appropriate energy resource that can be used in the new power plant in India based on certain predetermined factors. Herein the example considered is hypothetical and data is populated synthetically to illustrate the proposed methodology. However, it is not hard to implement these thoughts on real data.

Suppose a three members expert committee is constituted by the Department of Energy (DoE) of India to study and recommend the best energy resource among the 7 renewable alternatives: biomass, solar energy, geothermal, hydro power, wind energy, ocean energy and nuclear energy. The criteria under which the alternatives are evaluated are as follows.

C_1 is the regional factor that includes proximity of the plant to the sources of raw materials.
C_2 includes cost of the resource along with the transportation cost.
C_3 concerns with an easy availability of the raw materials.
C_4 signifies commitment to green environment. The fuel sources affect on the environment since diverse types of fuels contribute to greenhouse gas emissions and the possibility of contaminating land, water and air with radioactive waste. This criterion looks out for clean energy resources.
C_5 is the energy produced per unit resource consumption.
C_6 includes government regulations pertaining to fuel sources as these are probably one of the biggest factors affecting the energy industry. Emissions standards, taxes, market directives and specific fuel guidelines are but some of the mandates that directly impact fuel sources.
C_7 is the available infrastructure.
C_8 is concerned with dumping or recycling waste materials produced from resources.
C_9 involves safety of workforce and people in neighborhood of the energy source.

The three DMs are asked to give their preferences using a predefined linguistic term set

$$LT = \{l_0 : \mathrm{W},\ \mathrm{l}_1 : \mathrm{Lab},\ \mathrm{l}_2 : \mathrm{LVs},\ \mathrm{l}_3 : \mathrm{LEs},\ \mathrm{l}_4 : \mathrm{LWk},\ \mathrm{l}_5 : \mathrm{Eq},\ \mathrm{l}_6 : \mathrm{Wk},\ \mathrm{l}_7 : \mathrm{Es},\ l_8 : \mathrm{Vs},\ \mathrm{l}_9 : \mathrm{Ab}\},$$

where W: worst, Lab: less absolutely preferred, LVs: less very strongly preferred, LEs: less extremely preferred, LWk: less weakly preferred, Eq: equally preferred, Wk: weakly preferred,Es: extremely preferred, Vs: very strongly preferred, Ab: absolutely preferred.

The three DMs are not restricted to provide only interval linguistic information but can give preferences in linguistic term l_{ij} or 2-tuple linguistic (l_{ij}, α_{ij}) or an interval linguistic $[l_{ij}^{(L)}, l_{ij}^{(U)}]$, where $l_{ij}, l_{ij}^{(L)}, l_{ij}^{(U)} \in LT$ and $\alpha_{ij} \in \left[\frac{-1}{18}, \frac{1}{18}\right)$, or no judgement. In no judgement case, we use an interval with range $[l_0, l_9]$ where l_0 is the minimum and l_9 is the maximum linguistic term in LT. The decision matrices given by the DMs are as follows:

$$R_1$$

$$\begin{bmatrix}
[LVs, LEs] & [LEs, LWk] & LVs & Vs & [LEs, LWk] & Eq & [Eq, Wk] & [W, Ab] & [W, LVs] \\
[W, Ab] & [Eq, Es] & [W, Ab] & [Lab, LVs] & LVs & [Vs, Ab] & [W, Lab] & Wk & [Lab, LVs] \\
[LWk, Eq] & [LVs, LEs] & [Lab, LVs] & [LEs, Eq] & [Eq, Wk] & [Eq, Wk] & Eq & [LWk, Eq] & LWk \\
W & [LEs, Eq] & [Wk, Vs] & LWk & [Lab, LVs] & LWk & [Eq, Wk] & [W, Lab] & LVs \\
[LEs, Wk] & [LWk, Eq] & Wk & [W, Lab] & Lab & [LVs, LEs] & Wk & Eq & [Vs, Ab] \\
[Eq, Wk] & Eq & [LVs, LEs] & [Lab, LVs] & [W, LVs] & LEs & [W, Lab] & Wk & [Eq, Wk] \\
[LVs, Eq] & [Lab, LVs] & LEs & [Wk, Es] & W & LVs & [LEs, LWk] & [Lab, LVs] & [Lab, LVs]
\end{bmatrix}$$

$$R_2$$

$$\begin{bmatrix}
Lab & LWk & [Lab, LVs] & [Wk, Es] & [LEs, LWk] & [LWk, Eq] & Lab & Wk & W \\
[LEs, LWk] & [LVs, LEs] & [Wk, Es] & [LWk, Eq] & W & LWk & [LVs, LEs] & W & [Eq, Wk] \\
Wk & LVs & Lab & LVs & Eq & Eq & W & [Lab, LVs] & [LWk, Eq] \\
[Lab, LVs] & [LVs, LWk] & [Vs, Ab] & [LVs, LEs] & Lab & [Eq, Wk] & [LVs, LEs] & [Wk, Es] & LEs \\
LEs & [LVs, LEs] & [W, Lab] & Wk & [LEs, LWk] & [Es, Vs] & [Lab, LVs] & LWk & LWk \\
[W, Ab] & [LEs, LWk] & [LEs, LWk] & Vs & LEs & LVs & [Es, Vs] & [LVs, LEs] & [LVs, LEs] \\
LVs & W & LVs & [Vs, Ab] & [W, Ab] & [W, Lab] & Wk & Es & [LVs, LEs]
\end{bmatrix}$$

$$R_3$$

$$\begin{bmatrix}
Eq & Wk & [W, Lab] & Es & W & W & Vs & Lab & [W, Ab] \\
[LEs, LWk] & [Vs, Ab] & Ab & [LWk, Eq] & [W, Lab] & [LVs, LEs] & [Es, Vs] & Es & [Eq, Wk] \\
W & [Eq, Wk] & [LEs, LWk] & Wk & [Lab, LVs] & [Es, Vs] & [W, Lab] & [LVs, LEs] & Vs \\
[Eq, Wk] & LEs & [Eq, Wk] & [Eq, Wk] & LVs & Ab & [Vs, Ab] & LEs & [Vs, Ab] \\
LVs & W & [W, Lab] & [LWk, Eq] & Ab & [LEs, LWk] & Ab & [LVs, LEs] & W \\
Lab & Eq & Lab & [LWk, Eq] & [LEs, LWk] & [Es, Vs] & [W, Lab] & [Wk, Es] & LEs \\
Es & [W, Lab] & Ab & Eq & Wk & Es & [LWk, Eq] & Es & [Es, Vs]
\end{bmatrix}$$

Converting these matrices into 2-tuple interval valued linguistic information.

$$\widetilde{R}_1$$

$$\begin{bmatrix}
[(l_2,0),(l_3,0)] & [(l_3,0),(l_4,0)] & [(l_2,0),(l_2,0)] & [(l_8,0),(l_8,0)] & [(l_3,0),(l_4,0)] & [(l_5,0),(l_5,0)] & [(l_5,0),(l_6,0)] & [(l_0,0),(l_9,0)] & [(l_0,0),(l_2,0)] \\
[(l_0,0),(l_9,0)] & [(l_5,0),(l_7,0)] & [(l_0,0),(l_9,0)] & [(l_1,0),(l_2,0)] & [(l_2,0),(l_2,0)] & [(l_8,0),(l_9,0)] & [(l_0,0),(l_1,0)] & [(l_6,0),(l_6,0)] & [(l_1,0),(l_2,0)] \\
[(l_4,0),(l_5,0)] & [(l_2,0),(l_3,0)] & [(l_1,0),(l_2,0)] & [(l_3,0),(l_5,0)] & [(l_5,0),(l_6,0)] & [(l_5,0),(l_6,0)] & [(l_5,0),(l_5,0)] & [(l_4,0),(l_5,0)] & [(l_4,0),(l_4,0)] \\
[(l_0,0),(l_0,0)] & [(l_3,0),(l_5,0)] & [(l_6,0),(l_8,0)] & [(l_4,0),(l_4,0)] & [(l_1,0),(l_2,0)] & [(l_4,0),(l_4,0)] & [(l_5,0),(l_6,0)] & [(l_0,0),(l_1,0)] & [(l_2,0),(l_2,0)] \\
[(l_3,0),(l_6,0)] & [(l_4,0),(l_5,0)] & [(l_6,0),(l_6,0)] & [(l_0,0),(l_1,0)] & [(l_1,0),(l_1,0)] & [(l_2,0),(l_3,0)] & [(l_6,0),(l_6,0)] & [(l_5,0),(l_5,0)] & [(l_8,0),(l_9,0)] \\
[(l_5,0),(l_6,0)] & [(l_5,0),(l_5,0)] & [(l_2,0),(l_3,0)] & [(l_1,0),(l_2,0)] & [(l_0,0),(l_2,0)] & [(l_3,0),(l_3,0)] & [(l_0,0),(l_1,0)] & [(l_6,0),(l_6,0)] & [(l_5,0),(l_6,0)] \\
[(l_2,0),(l_5,0)] & [(l_1,0),(l_2,0)] & [(l_3,0),(l_3,0)] & [(l_6,0),(l_7,0)] & [(l_0,0),(l_0,0)] & [(l_2,0),(l_2,0)] & [(l_3,0),(l_4,0)] & [(l_1,0),(l_2,0)] & [(l_1,0),(l_2,0)]
\end{bmatrix}$$

$$\widetilde{R}_2$$

$$\begin{bmatrix}
[(l_1,0),(l_1,0)] & [(l_4,0),(l_4,0)] & [(l_1,0),(l_2,0)] & [(l_6,0),(l_7,0)] & [(l_3,0),(l_4,0)] & [(l_4,0),(l_5,0)] & [(l_1,0),(l_1,0)] & [(l_6,0),(l_6,0)] & [(l_0,0),(l_0,0)] \\
[(l_3,0),(l_4,0)] & [(l_2,0),(l_3,0)] & [(l_6,0),(l_7,0)] & [(l_4,0),(l_5,0)] & [(l_0,0),(l_0,0)] & [(l_4,0),(l_4,0)] & [(l_2,0),(l_3,0)] & [(l_0,0),(l_0,0)] & [(l_5,0),(l_6,0)] \\
[(l_6,0),(l_6,0)] & [(l_2,0),(l_2,0)] & [(l_1,0),(l_1,0)] & [(l_2,0),(l_2,0)] & [(l_5,0),(l_5,0)] & [(l_5,0),(l_5,0)] & [(l_0,0),(l_0,0)] & [(l_1,0),(l_2,0)] & [(l_4,0),(l_5,0)] \\
[(l_1,0),(l_2,0)] & [(l_2,0),(l_4,0)] & [(l_8,0),(l_9,0)] & [(l_2,0),(l_3,0)] & [(l_1,0),(l_1,0)] & [(l_5,0),(l_6,0)] & [(l_2,0),(l_3,0)] & [(l_6,0),(l_7,0)] & [(l_3,0),(l_3,0)] \\
[(l_3,0),(l_3,0)] & [(l_2,0),(l_3,0)] & [(l_0,0),(l_1,0)] & [(l_6,0),(l_6,0)] & [(l_3,0),(l_4,0)] & [(l_7,0),(l_8,0)] & [(l_1,0),(l_2,0)] & [(l_4,0),(l_4,0)] & [(l_4,0),(l_4,0)] \\
[(l_0,0),(l_9,0)] & [(l_3,0),(l_4,0)] & [(l_3,0),(l_4,0)] & [(l_8,0),(l_8,0)] & [(l_3,0),(l_3,0)] & [(l_2,0),(l_2,0)] & [(l_7,0),(l_8,0)] & [(l_2,0),(l_3,0)] & [(l_2,0),(l_3,0)] \\
[(l_2,0),(l_2,0)] & [(l_0,0),(l_0,0)] & [(l_2,0),(l_2,0)] & [(l_8,0),(l_9,0)] & [(l_0,0),(l_9,0)] & [(l_0,0),(l_1,0)] & [(l_6,0),(l_6,0)] & [(l_7,0),(l_7,0)] & [(l_2,0),(l_3,0)]
\end{bmatrix}$$

$$\widetilde{R}_3$$

$$\begin{bmatrix}
[(l_5,0),(l_5,0)] & [(l_6,0),(l_6,0)] & [(l_0,0),(l_1,0)] & [(l_7,0),(l_7,0)] & [(l_0,0),(l_0,0)] & [(l_0,0),(l_0,0)] & [(l_8,0),(l_8,0)] & [(l_1,0),(l_1,0)] & [(l_0,0),(l_9,0)] \\
[(l_3,0),(l_4,0)] & [(l_8,0),(l_9,0)] & [(l_9,0),(l_9,0)] & [(l_4,0),(l_5,0)] & [(l_0,0),(l_1,0)] & [(l_2,0),(l_3,0)] & [(l_7,0),(l_8,0)] & [(l_7,0),(l_7,0)] & [(l_5,0),(l_6,0)] \\
[(l_0,0),(l_0,0)] & [(l_5,0),(l_6,0)] & [(l_3,0),(l_4,0)] & [(l_6,0),(l_6,0)] & [(l_1,0),(l_2,0)] & [(l_7,0),(l_8,0)] & [(l_0,0),(l_1,0)] & [(l_2,0),(l_3,0)] & [(l_8,0),(l_8,0)] \\
[(l_5,0),(l_6,0)] & [(l_3,0),(l_3,0)] & [(l_5,0),(l_6,0)] & [(l_5,0),(l_6,0)] & [(l_2,0),(l_2,0)] & [(l_9,0),(l_9,0)] & [(l_8,0),(l_9,0)] & [(l_3,0),(l_3,0)] & [(l_8,0),(l_9,0)] \\
[(l_2,0),(l_2,0)] & [(l_0,0),(l_0,0)] & [(l_0,0),(l_1,0)] & [(l_4,0),(l_5,0)] & [(l_9,0),(l_9,0)] & [(l_3,0),(l_4,0)] & [(l_9,0),(l_9,0)] & [(l_2,0),(l_3,0)] & [(l_0,0),(l_0,0)] \\
[(l_1,0),(l_1,0)] & [(l_5,0),(l_5,0)] & [(l_1,0),(l_1,0)] & [(l_4,0),(l_5,0)] & [(l_3,0),(l_4,0)] & [(l_7,0),(l_8,0)] & [(l_0,0),(l_1,0)] & [(l_6,0),(l_7,0)] & [(l_3,0),(l_3,0)] \\
[(l_7,0),(l_7,0)] & [(l_0,0),(l_1,0)] & [(l_9,0),(l_9,0)] & [(l_5,0),(l_5,0)] & [(l_5,0),(l_6,0)] & [(l_7,0),(l_7,0)] & [(l_4,0),(l_5,0)] & [(l_7,0),(l_7,0)] & [(l_7,0),(l_8,0)]
\end{bmatrix}$$

The above decision matrices are aggregated using IAM operator. The aggregated matrix $\widetilde{R}$ is as follows.

$$\widetilde{R} = \begin{bmatrix}
[(l_3,-0.037),(l_3,0)] & [(l_4,0.037),(l_5,-0.037)] & [(l_1,0),(l_2,-0.037)] & [(l_7,0),(l_7,0.037)] & [(l_2,0),(l_3,-0.037)] \\
[(l_2,0),(l_6,-0.037)] & [(l_5,0),(l_6,0.037)] & [(l_5,0),(l_8,0.037)] & [(l_3,0),(l_4,0)] & [(l_1,-0.037),(l_1,0)] \\
[(l_3,0.037),(l_4,-0.037)] & [(l_3,0),(l_4,-0.037)] & [(l_2,-0.037),(l_2,0.037)] & [(l_4,-0.037),(l_4,0.037)] & [(l_4,-0.037),(l_4,0.037)] \\
[(l_2,0),(l_3,-0.037)] & [(l_3,-0.037),(l_4,0)] & [(l_6,0.037),(l_8,-0.037)] & [(l_4,-0.037),(l_4,0.037)] & [(l_1,0.037),(l_2,-0.037)] \\
[(l_3,-0.037),(l_4,-0.037)] & [(l_2,0),(l_3,-0.037)] & [(l_2,0),(l_3,-0.037)] & [(l_3,0.037),(l_4,0)] & [(l_4,0.037),(l_5,-0.037)] \\
[(l_2,0),(l_5,0.037)] & [(l_4,0.037),(l_5,-0.037)] & [(l_2,0),(l_3,-0.037)] & [(l_4,0.037),(l_5,0)] & [(l_2,0),(l_3,0)] \\
[(l_4,-0.037),(l_5,-0.037)] & [(l_0,0.037),(l_1,0)] & [(l_5,-0.037),(l_5,-0.037)] & [(l_6,0.037),(l_7,0)] & [(l_2,-0.037),(l_5,0)]
\end{bmatrix}$$

$$\begin{bmatrix}
[(l_3,0),(l_3,0.037)] & [(l_5,-0.037),(l_5,0)] & [(l_2,0.037),(l_5,0.037)] & [(l_0,0),(l_4,-0.037)] \\
[(l_5,-0.037),(l_5,0.037)] & [(l_3,0),(l_4,0)] & [(l_4,0.037),(l_4,0.037)] & [(l_4,-0.037),(l_5,-0.037)] \\
[(l_6,-0.037),(l_6,0.037)] & [(l_2,-0.037),(l_2,0)] & [(l_2,0.037),(l_3,0.037)] & [(l_5,0.037),(l_6,-0.037)] \\
[(l_6,0),(l_6,0.037)] & [(l_5,0),(l_6,0)] & [(l_3,0),(l_4,-0.037)] & [(l_4,0.037),(l_5,-0.037)] \\
[(l_4,0),(l_5,0)] & [(l_5,0.037),(l_6,-0.037)] & [(l_4,-0.037),(l_4,0)] & [(l_4,0),(l_4,0.037)] \\
[(l_4,0),(l_4,0.037)] & [(l_2,0.037),(l_3,0.037)] & [(l_5,-0.037),(l_5,0.037)] & [(l_3,0.037),(l_4,0)] \\
[(l_3,0),(l_3,0.037)] & [(l_4,0.037),(l_5,0)] & [(l_5,0),(l_5,0.037)] & [(l_3,0.037),(l_4,0.037)]
\end{bmatrix}$$

The distance between each DMs' opinion $\widetilde{R}_k$, $k = 1, 2, 3$, from the aggregated matrix $\widetilde{R}$ is evaluated using 2-tuple distance operator $D(\cdot,\cdot)$. The distance matrices are as follows.

$$\widetilde{P}_1 = \begin{bmatrix}
(l_0,0.037) & (l_1,0) & (l_1,-0.037) & (l_1,-0.0185) & (l_1,0.0185) & (l_2,-0.0185) & (l_1,-0.037) & (l_3,0) & (l_4,-0.037) \\
(l_3,-0.037) & (l_0,0.037) & (l_3,-0.0185) & (l_2,0) & (l_1,0.0185) & (l_4,-0.0556) & (l_3,0) & (l_2,-0.037) & (l_3,-0.0556) \\
(l_1,0) & (l_1,-0.0185) & (l_1,-0.0556) & (l_1,-0.037) & (l_2,-0.0556) & (l_1,-0.0556) & (l_3,0.0185) & (l_2,-0.037) & (l_1,0) \\
(l_2,0.037) & (l_1,-0.037) & (l_0,0.037) & (l_0,0.037) & (l_0,0.037) & (l_2,0.0185) & (l_0,0) & (l_3,-0.0185) & (l_2,0) \\
(l_1,0.037) & (l_2,0.0185) & (l_4,-0.037) & (l_3,0.0185) & (l_4,-0.0556) & (l_2,0) & (l_1,-0.0556) & (l_1,0.0185) & (l_5,-0.0556) \\
(l_2,-0.0185) & (l_1,-0.0556) & (l_0,0.0185) & (l_3,0.0185) & (l_2,-0.0556) & (l_1,0.0185) & (l_2,0.037) & (l_1,0) & (l_2,-0.0556) \\
(l_1,0) & (l_1,-0.0185) & (l_2,-0.037) & (l_0,0.0185) & (l_3,0.037) & (l_1,0.0185) & (l_1,0.0185) & (l_4,-0.037) & (l_3,-0.0185)
\end{bmatrix}$$

$$\widetilde{P}_2 = \begin{bmatrix}
(l_2,-0.0185) & (l_1,-0.0556) & (l_0,0.0185) & (l_1,-0.037) & (l_1,0.0185) & (l_1,0.037) & (l_4,-0.0185) & (l_2,0.0185) & (l_3,-0.037) \\
(l_1,0.037) & (l_3,0.0185) & (l_1,0.0185) & (l_1,0) & (l_1,-0.0185) & (l_1,0) & (l_1,0) & (l_4,0.037) & (l_2,-0.0556) \\
(l_3,-0.0556) & (l_1,0.037) & (l_1,0) & (l_2,0) & (l_1,0) & (l_1,0) & (l_2,-0.0185) & (l_1,0.037) & (l_0,0.0556) \\
(l_1,-0.0185) & (l_0,0.037) & (l_2,-0.0556) & (l_2,-0.0556) & (l_1,-0.0556) & (l_1,-0.037) & (l_3,0) & (l_3,0.0185) & (l_1,0) \\
(l_1,-0.0556) & (l_0,0.0185) & (l_2,-0.0185) & (l_2,0.037) & (l_1,0) & (l_3,0) & (l_4,0) & (l_0,0.0185) & (l_0,0) \\
(l_3,-0.0185) & (l_1,0) & (l_1,0.0185) & (l_3,0.037) & (l_1,-0.0556) & (l_2,0.0185) & (l_5,-0.037) & (l_3,-0.0556) & (l_2,-0.0185) \\
(l_2,0.0185) & (l_1,-0.037) & (l_3,-0.037) & (l_2,-0.0185) & (l_3,-0.0185) & (l_3,-0.037) & (l_1,0.037) & (l_2,-0.0185) & (l_2,-0.0185)
\end{bmatrix}$$

$$\widetilde{P}_3 = \begin{bmatrix}
(l_2,0.0185) & (l_2,-0.0556) & (l_1,-0.0185) & (l_0,0.0185) & (l_2,0.037) & (l_3,0.0185) & (l_3,0.0185) & (l_3,-0.0185) & (l_7,0.0185) \\
(l_1,0.037) & (l_3,-0.0185) & (l_2,0.037) & (l_1,0) & (l_0,0.037) & (l_3,-0.0556) & (l_4,0) & (l_3,-0.037) & (l_2,-0.0556) \\
(l_4,-0.0556) & (l_2,0.0185) & (l_2,-0.0556) & (l_2,0) & (l_3,-0.0556) & (l_2,-0.0556) & (l_1,0.037) & (l_0,0.037) & (l_4,-0.037) \\
(l_3,0.0185) & (l_1,-0.037) & (l_2,-0.0556) & (l_2,-0.0556) & (l_1,-0.0556) & (l_3,-0.0185) & (l_3,0) & (l_0,0.037) & (l_5,-0.0556) \\
(l_1,0.0185) & (l_2,0.037) & (l_2,-0.0185) & (l_1,-0.0185) & (l_5,-0.0556) & (l_1,0) & (l_4,-0.0556) & (l_1,0.037) & (l_4,0) \\
(l_3,-0.037) & (l_1,-0.0556) & (l_1,0.037) & (l_0,0.0185) & (l_1,0) & (l_3,0.037) & (l_2,0.037) & (l_2,-0.0556) & (l_1,0.037) \\
(l_3,-0.0185) & (l_0,0.0185) & (l_4,0.037) & (l_2,-0.037) & (l_2,0.0185) & (l_4,-0.0185) & (l_0,0.0185) & (l_2,-0.0185) & (l_3,0.0185)
\end{bmatrix}$$

The degrees of similarity matrices $S_{(k)},\ k = 1, 2, 3,$ are next evaluated. The similarity matrices are as follows.

$$S_1 = \begin{bmatrix}
(l_9,-0.037) & (l_8,0) & (l_8,0.037) & (l_8,0.0185) & (l_8,-0.0185) & (l_7,0.0185) & (l_8,0.037) & (l_6,0) & (l_5,0.037) \\
(l_6,0.037) & (l_9,-0.037) & (l_6,0.0185) & (l_7,0) & (l_8,-0.0185) & (l_6,-0.0556) & (l_6,0) & (l_7,0.037) & (l_7,-0.0556) \\
(l_8,0) & (l_8,0.0185) & (l_9,-0.0556) & (l_8,0.037) & (l_8,-0.0556) & (l_9,-0.0556) & (l_6,-0.0185) & (l_7,0.037) & (l_8,0) \\
(l_7,-0.037) & (l_8,0.037) & (l_9,-0.037) & (l_9,-0.037) & (l_9,-0.037) & (l_7,-0.0185) & (l_9,0) & (l_6,0.0185) & (l_7,0) \\
(l_8,-0.037) & (l_7,-0.0185) & (l_5,0.037) & (l_6,-0.0185) & (l_6,-0.0556) & (l_7,0) & (l_9,-0.0556) & (l_8,-0.0185) & (l_5,-0.0556) \\
(l_7,0.0185) & (l_9,-0.0556) & (l_9,-0.0185) & (l_6,-0.0185) & (l_8,-0.0556) & (l_8,-0.0185) & (l_7,-0.037) & (l_8,0) & (l_8,-0.0556) \\
(l_8,0) & (l_8,0.0185) & (l_7,0.037) & (l_9,-0.0185) & (l_6,-0.037) & (l_8,-0.0185) & (l_8,-0.0185) & (l_5,0.037) & (l_6,0.0185)
\end{bmatrix}$$

$$S_2 = \begin{bmatrix}
(l_7,0.0185) & (l_9,-0.0556) & (l_9,-0.0185) & (l_8,0.037) & (l_8,-0.0185) & (l_8,-0.037) & (l_5,0.0185) & (l_7,-0.0185) & (l_6,0.037) \\
(l_8,-0.037) & (l_6,-0.0185) & (l_8,-0.0185) & (l_8,0) & (l_8,0.0185) & (l_8,0) & (l_8,0) & (l_5,-0.037) & (l_8,-0.0556) \\
(l_7,-0.0556) & (l_8,-0.037) & (l_8,0) & (l_7,0) & (l_8,0) & (l_8,0) & (l_7,0.0185) & (l_8,-0.037) & (l_9,-0.0556) \\
(l_8,0.0185) & (l_9,-0.037) & (l_8,-0.0556) & (l_8,-0.0556) & (l_9,-0.0556) & (l_8,0.037) & (l_6,0) & (l_6,-0.0185) & (l_8,0) \\
(l_9,-0.0556) & (l_9,-0.0185) & (l_7,0.0185) & (l_7,-0.037) & (l_8,0) & (l_6,0) & (l_5,0) & (l_9,-0.0185) & (l_9,0) \\
(l_6,0.0185) & (l_8,0) & (l_8,-0.0185) & (l_6,-0.037) & (l_9,-0.0556) & (l_7,-0.0185) & (l_4,0.037) & (l_7,-0.0556) & (l_7,0.0185) \\
(l_7,-0.0185) & (l_8,0.037) & (l_6,0.037) & (l_7,0.0185) & (l_6,0.0185) & (l_6,0.037) & (l_8,-0.037) & (l_7,0.0185) & (l_7,0.0185)
\end{bmatrix}$$

$$S_3 = \begin{bmatrix}
(l_7,-0.0185) & (l_8,-0.0556) & (l_8,0.0185) & (l_9,-0.0185) & (l_7,-0.037) & (l_6,-0.0185) & (l_6,-0.0185) & (l_6,0.0185) & (l_2,-0.0185) \\
(l_8,-0.037) & (l_6,0.0185) & (l_7,-0.037) & (l_8,0) & (l_9,-0.037) & (l_7,-0.0556) & (l_5,0) & (l_6,0.037) & (l_8,-0.0556) \\
(l_6,-0.0556) & (l_7,-0.0185) & (l_8,-0.0556) & (l_7,0) & (l_7,-0.0556) & (l_8,-0.0556) & (l_8,-0.037) & (l_9,-0.037) & (l_5,0.037) \\
(l_6,-0.0185) & (l_8,0.037) & (l_8,-0.0556) & (l_8,-0.0556) & (l_9,-0.0556) & (l_6,0.0185) & (l_6,0) & (l_9,-0.037) & (l_5,-0.0556) \\
(l_8,-0.0185) & (l_7,-0.037) & (l_7,0.0185) & (l_8,0.0185) & (l_5,-0.0556) & (l_8,0) & (l_6,-0.0556) & (l_8,-0.037) & (l_5,0) \\
(l_6,0.037) & (l_9,-0.0556) & (l_8,-0.037) & (l_9,-0.0185) & (l_8,0) & (l_6,-0.037) & (l_7,-0.037) & (l_8,-0.0556) & (l_8,-0.037) \\
(l_6,0.0185) & (l_9,-0.0185) & (l_5,-0.037) & (l_7,0.037) & (l_7,-0.0185) & (l_5,0.0185) & (l_9,-0.0185) & (l_7,0.0185) & (l_6,-0.0185)
\end{bmatrix}$$

The weight matrix $W_{(k)}\ ;\ k = 1, 2, 3,$ for each DM is given as follows.

$W_{(1)} =$

	C_1	C_2	C_3	C_4	C_5	C_6	C_7	C_8	C_9
A_1	0.3824	0.3333	0.3289	0.3224	0.3507	0.3468	0.4310	0.3158	0.3951
A_2	0.2923	0.4194	0.2984	0.3043	0.3176	0.2750	0.3158	0.4000	0.3023
A_3	0.4000	0.3603	0.3542	0.3731	0.3409	0.3542	0.2823	0.3099	0.3664
A_4	0.3226	0.3289	0.3662	0.3662	0.3377	0.3203	0.4286	0.2984	0.3590
A_5	0.3194	0.3060	0.2712	0.2823	0.3056	0.3333	0.4474	0.3219	0.2432
A_6	0.3644	0.3400	0.3630	0.2869	0.3125	0.3852	0.3774	0.3636	0.3358
A_7	0.3810	0.3224	0.4000	0.3786	0.3036	0.4052	0.3219	0.2712	0.3217

$W_{(2)} =$

	C_1	C_2	C_3	C_4	C_5	C_6	C_7	C_8	C_9
A_1	0.3162	0.3542	0.3487	0.3289	0.3507	0.3710	0.2672	0.3596	0.4691
A_2	0.3538	0.2823	0.3790	0.3478	0.3311	0.4000	0.4211	0.2545	0.3488
A_3	0.3250	0.3382	0.3333	0.3134	0.3636	0.3333	0.3468	0.3239	0.3893
A_4	0.3952	0.3421	0.3169	0.3169	0.3312	0.3906	0.2857	0.2823	0.4103
A_5	0.3542	0.3955	0.3644	0.3226	0.4444	0.2857	0.2632	0.3630	0.4865
A_6	0.3136	0.3200	0.3219	0.2787	0.3542	0.3361	0.2453	0.2955	0.3209
A_7	0.3254	0.3289	0.3455	0.3071	0.3304	0.3276	0.3151	0.3644	0.3739

$W_{(3)} =$

	C_1	C_2	C_3	C_4	C_5	C_6	C_7	C_8	C_9
A_1	0.3015	0.3125	0.3224	0.3487	0.2985	0.2823	0.3017	0.3246	0.1358
A_2	0.3538	0.2984	0.3226	0.3478	0.3514	0.3250	0.2632	0.3455	0.3488
A_3	0.2750	0.3015	0.3125	0.3134	0.2955	0.3125	0.3710	0.3662	0.2443
A_4	0.2823	0.3289	0.3169	0.3169	0.3312	0.2891	0.2857	0.4194	0.2308
A_5	0.3264	0.2985	0.3644	0.3952	0.2500	0.3810	0.2895	0.3151	0.2703
A_6	0.3220	0.3400	0.3151	0.4344	0.3333	0.2787	0.3774	0.3409	0.3433
A_7	0.2937	0.3487	0.2545	0.3143	0.3661	0.2672	0.3630	0.3644	0.3043

Construct the collective matrix using IWA operator.

$$\widetilde{R}_{coll} = \begin{bmatrix} [(l_3,-0.0458),(l_3,-0.0033)] & [(l_4,0.0324),(l_5,-0.0417)] & [(l_1,0.0007),(l_2,-0.0358)] & [(l_7,-0.0007),(l_7,0.0358)] & [(l_2,0.0116),(l_3,-0.0216)] \\ [(l_2,0.0137),(l_5,0.0513)] & [(l_5,0.0054),(l_6,0.0520)] & [(l_5,0.0197),(l_8,0.0269)] & [(l_3,0.0097),(l_4,0.0097)] & [(l_1,-0.0405),(l_1,-0.0015)] \\ [(l_4,-0.05),(l_4,-0.0056)] & [(l_3,-0.0106),(l_4,-0.0482)] & [(l_2,-0.0417),(l_2,0.0324)] & [(l_4,-0.0415),(l_4,0.0415)] & [(l_4,-0.0202),(l_4,0.0505)] \\ [(l_2,-0.0215),(l_2,0.0538)] & [(l_3,-0.0380),(l_4,0)] & [(l_6,0.0352),(l_8,-0.0352)] & [(l_4,-0.0352),(l_4,0.0352)] & [(l_1,0.0368),(l_2,-0.0368)] \\ [(l_3,-0.0363),(l_4,-0.0409)] & [(l_2,0.0017),(l_3,-0.0315)] & [(l_2,-0.0414),(l_2,0.0395)] & [(l_4,-0.0538),(l_4,0.0215)] & [(l_4,-0.0123),(l_4,0.0370)] \\ [(l_2,0.0160),(l_5,0.0367)] & [(l_4,0.04),(l_5,-0.0356)] & [(l_2,0.0008),(l_3,-0.0342)] & [(l_4,0.0282),(l_5,-0.0027)] & [(l_2,0.0069),(l_3,0.0023)] \\ [(l_3,0.0520),(l_5,-0.0432)] & [(l_0,0.0358),(l_1,-0.0007)] & [(l_4,0.0202),(l_4,0.0202)] & [(l_6,0.0333),(l_7,-0.0016)] & [(l_2,-0.0188),(l_5,0.0188)] \end{bmatrix}$$

$$\begin{bmatrix} [(l_3,0.0242),(l_4,-0.0457)] & [(l_5,-0.0182),(l_5,0.0297)] & [(l_2,0.0536),(l_5,0.0361)] & [(l_0,0),(l_2,0.0014)] \\ [(l_4,0.05),(l_5,0.0056)] & [(l_3,-0.0351),(l_4,-0.0351)] & [(l_5,-0.0202),(l_5,-0.0202)] & [(l_4,-0.0233),(l_5,-0.0233)] \\ [(l_6,-0.0417),(l_6,0.0324)] & [(l_1,0.0457),(l_2,-0.0242)] & [(l_2,0.0329),(l_3,0.0329)] & [(l_5,-0.0025),(l_5,0.0407)] \\ [(l_6,-0.0182),(l_6,0.0252)] & [(l_5,0),(l_6,0)] & [(l_3,-0.0054),(l_4,-0.0520)] & [(l_4,-0.0228),(l_4,0.0028)] \\ [(l_4,-0.0212),(l_5,-0.0212)] & [(l_6,-0.0497),(l_6,-0.0205)] & [(l_4,-0.0342),(l_4,0.0008)] & [(l_4,-0.0120),(l_4,0.0150)] \\ [(l_4,-0.0246),(l_4,0.0064)] & [(l_2,-0.0314),(l_3,-0.0314)] & [(l_5,-0.0202),(l_5,0.0505)] & [(l_3,0.0390),(l_4,0.0008)] \\ [(l_3,-0.0354),(l_3,0.001)] & [(l_4,0.0342),(l_5,-0.0008)] & [(l_5,0.0414),(l_6,-0.0395)] & [(l_3,0.0222),(l_4,0.0222)] \end{bmatrix}$$

Converting the collective decision matrix to numeric matrix using Δ^{-1} function.

$$R_{coll} = \begin{bmatrix} [0.2876, 0.3301] & [0.4769, 0.5139] & [0.1118, 0.1864] & [0.7770, 0.8136] & [0.2338, 0.3118] & [0.3575, 0.3987] \\ [0.2359, 0.6068] & [0.5609, 0.7186] & [0.5753, 0.9158] & [0.3430, 0.4541] & [0.0706, 0.1096] & [0.4944, 0.5611] \\ [0.3944, 0.4389] & [0.3227, 0.3962] & [0.1806, 0.2546] & [0.4030, 0.4859] & [0.4242, 0.4949] & [0.6250, 0.6991] \\ [0.2007, 0.2760] & [0.2953, 0.4444] & [0.7019, 0.8537] & [0.4092, 0.4797] & [0.1479, 0.1854] & [0.6484, 0.6918] \\ [0.2971, 0.4035] & [0.2239, 0.3018] & [0.1808, 0.2618] & [0.3907, 0.4659] & [0.4321, 0.4815] & [0.4233, 0.5344] \\ [0.2382, 0.5923] & [0.4844, 0.5200] & [0.2230, 0.2991] & [0.4727, 0.5528] & [0.2292, 0.3356] & [0.4199, 0.4508] \\ [0.3854, 0.5123] & [0.0358, 0.1104] & [0.4646, 0.4646] & [0.7, 0.7762] & [0.2034, 0.5744] & [0.2979, 0.3343] \end{bmatrix}$$

$$\begin{bmatrix} [0.5374, 0.5852] & [0.2758, 0.5916] & [0, 0.2236] \\ [0.2982, 0.4094] & [0.5354, 0.5354] & [0.4212, 0.5323] \\ [0.1568, 0.1980] & [0.2551, 0.3662] & [0.5530, 0.5963] \\ [0.5556, 0.6667] & [0.3280, 0.3925] & [0.4217, 0.4473] \\ [0.6170, 0.6462] & [0.4102, 0.4452] & [0.4324, 0.4595] \\ [0.1908, 0.3019] & [0.5354, 0.6061] & [0.3723, 0.4453] \\ [0.4787, 0.5548] & [0.5970, 0.6271] & [0.3556, 0.4667] \end{bmatrix}$$

The criteria weights are computed using entropy. The interval entropy $H_j = [h_j^{(L)}, h_j^{(U)}]$, $j = 1, \ldots, 9$, is evaluated using Step 8, Sect. 3.1.

H_1	H_2	H_3	H_4	H_5	H_6	H_7	H_8	H_9
$[1.2358, 1.2633]$	$[1.1347, 1.1571]$	$[0.9996, 1.0898]$	$[1.0841, 1.1645]$	$[1.1293, 1.1835]$	$[1.1595, 1.2229]$	$[1.1515, 1.1708]$	$[1.2007, 1.2395]$	$[1.1069, 1.2395]$

The criteria weights are obtained using Step 9, Sect. 3.1.

C_1	C_2	C_3	C_4	C_5	C_6	C_7	C_8	C_9
0.1776	0.1043	0.0372	0.0927	0.1137	0.1388	0.1148	0.1576	0.1305

The normalized criteria weights of the criteria are given below.

C_1	C_2	C_3	C_4	C_5	C_6	C_7	C_8	C_9
0.1664	0.0977	0.0349	0.0869	0.1065	0.1301	0.1076	0.1476	0.1223

Applying PROMETHEE method, we evaluate the score values ($\widetilde{S}$) and the accuracy values (H) of collective matrix as given in Tables 1 and 2, respectively. The score values and accuracy values of preference indices are then calculated as given in Tables 3 and 4, respectively.

Table 1 Score values of collective matrix

	C_1	C_2	C_3	C_4	C_5	C_6	C_7	C_8	C_9
A_1	$(l_3, -0.0245)$	$(l_4, 0.0509)$	$(l_1, 0.0380)$	$(l_7, 0.0175)$	$(l_2, 0.0506)$	$(l_3, 0.0448)$	$(l_5, 0.0057)$	$(l_4, -0.0107)$	$(l_1, 0.0007)$
A_2	$(l_4, -0.0231)$	$(l_6, -0.0269)$	$(l_7, -0.0323)$	$(l_4, -0.0459)$	$(l_1, -0.0210)$	$(l_5, -0.0278)$	$(l_3, 0.0205)$	$(l_5, -0.0202)$	$(l_4, 0.0323)$
A_3	$(l_4, -0.0278)$	$(l_3, 0.0261)$	$(l_2, -0.0046)$	$(l_4, 0)$	$(l_4, 0.0152)$	$(l_6, -0.0046)$	$(l_2, -0.0448)$	$(l_3, -0.0227)$	$(l_5, 0.0191)$
A_4	$(l_2, 0.0161)$	$(l_3, , 0.0365)$	$(l_7, 0)$	$(l_4, 0)$	$(l_2, -0.0556)$	$(l_6, 0.0035)$	$(l_6, -0.0556)$	$(l_3, 0.0269)$	$(l_4, -0.01)$
A_5	$(l_3, 0.0170)$	$(l_2, 0.0406)$	$(l_2, -0.0009)$	$(l_4, -0.0161)$	$(l_4, 0.0123)$	$(l_4, 0.0344)$	$(l_6, -0.0351)$	$(l_4, -0.0167)$	$(l_4, 0.0015)$
A_6	$(l_4, -0.0292)$	$(l_5, -0.0533)$	$(l_2, 0.0388)$	$(l_5, -0.0428)$	$(l_3, -0.0509)$	$(l_4, -0.0091)$	$(l_2, 0.0241)$	$(l_5, 0.0152)$	$(l_4, -0.0357)$
A_7	$(l_4, 0.0044)$	$(l_1, -0.0380)$	$(l_4, 0.0202)$	$(l_7, -0.0397)$	$(l_4, -0.0556)$	$(l_3, -0.0172)$	$(l_5, -0.0388)$	$(l_6, -0.0546)$	$(l_4, -0.0333)$

Table 2 Accuracy values of collective matrix

	C_1	C_2	C_3	C_4	C_5	C_6	C_7	C_8	C_9
A_1	0.0425	0.0370	0.0746	0.0365	0.0779	0.0412	0.0479	0.3158	0.2236
A_2	0.3709	0.1577	0.3405	0.1111	0.0390	0.0667	0.1111	0.0000	0.1111
A_3	0.0444	0.0735	0.0741	0.0829	0.0707	0.0741	0.0412	0.1111	0.0433
A_4	0.0753	0.1491	0.1518	0.0704	0.0375	0.0434	0.1111	0.0645	0.0256
A_5	0.1065	0.0779	0.0810	0.0753	0.0494	0.1111	0.0292	0.0350	0.0270
A_6	0.3540	0.0356	0.0761	0.0801	0.1065	0.0310	0.1111	0.0707	0.0730
A_7	0.1270	0.0746	0.0000	0.0762	0.3710	0.0364	0.0761	0.0301	0.1111

Table 3 Score values of preference indices in interval-valued 2-tuple PROMETHEE II

	C_1	C_2	C_3	C_4	C_5	C_6	C_7	C_8	C_9
$\omega_j \rightarrow$	0.1664	0.0977	0.0349	0.0869	0.1065	0.1301	0.1076	0.1476	0.1223
$P^{(s)}(A_1, A_2)$	$(l_0, 0)$	$(l_0, 0)$	$(l_0, 0)$	$(l_4, -0.0477)$	$(l_2, -0.0395)$	$(l_0, 0)$	$(l_2, -0.0147)$	$(l_0, 0)$	$(l_0, 0)$
$P^{(s)}(A_1, A_3)$	$(l_0, 0)$	$(l_1, 0.0248)$	$(l_0, 0)$	$(l_3, 0.0175)$	$(l_0, 0)$	$(l_0, 0)$	$(l_3, 0.0505)$	$(l_1, 0.0120)$	$(l_0, 0)$
$P^{(s)}(A_1, A_4)$	$(l_1, -0.0406)$	$(l_1, 0.0144)$	$(l_0, 0)$	$(l_3, 0.0175)$	$(l_1, -0.0050)$	$(l_0, 0)$	$(l_0, 0)$	$(l_1, -0.0376)$	$(l_0, 0)$
$P^{(s)}(A_1, A_5)$	$(l_0, 0)$	$(l_2, 0.0103)$	$(l_0, 0)$	$(l_3, 0.0337)$	$(l_0, 0)$	$(l_0, 0)$	$(l_0, 0)$	$(l_0, 0.0060)$	$(l_0, 0)$
$P^{(s)}(A_1, A_6)$	$(l_0, 0)$	$(l_0, 0)$	$(l_0, 0)$	$(l_3, -0.0508)$	$(l_0, 0)$	$(l_0, 0)$	$(l_3, -0.0184)$	$(l_0, 0)$	$(l_0, 0)$
$P^{(s)}(A_1, A_7)$	$(l_0, 0)$	$(l_4, -0.0222)$	$(l_0, 0)$	$(l_1, -0.0539)$	$(l_0, 0)$	$(l_1, -0.0491)$	$(l_0, 0.0446)$	$(l_0, 0)$	$(l_0, 0)$
$P^{(s)}(A_2, A_1)$	$(l_1, 0.0014)$	$(l_1, 0.0333)$	$(l_5, 0.0408)$	$(l_0, 0)$	$(l_0, 0)$	$(l_1, 0.0385)$	$(l_0, 0)$	$(l_1, -0.0095)$	$(l_3, 0.0316)$
$P^{(s)}(A_2, A_3)$	$(l_0, 0.0047)$	$(l_3, -0.0530)$	$(l_5, -0.0276)$	$(l_0, 0)$	$(l_0, 0)$	$(l_0, 0)$	$(l_2, -0.0458)$	$(l_2, 0.0025)$	$(l_0, 0)$
$P^{(s)}(A_2, A_4)$	$(l_2, -0.0392)$	$(l_2, 0.0477)$	$(l_0, 0)$	$(l_0, 0)$	$(l_0, 0)$	$(l_0, 0)$	$(l_0, 0)$	$(l_2, -0.0471)$	$(l_0, 0.0423)$
$P^{(s)}(A_2, A_5)$	$(l_1, -0.0401)$	$(l_3, 0.0436)$	$(l_5, -0.0313)$	$(l_0, 0)$	$(l_0, 0)$	$(l_0, 0.0489)$	$(l_0, 0)$	$(l_1, -0.0035)$	$(l_0, 0.0308)$
$P^{(s)}(A_2, A_6)$	$(l_0, 0.0061)$	$(l_1, 0.0265)$	$(l_4, 0.0400)$	$(l_0, 0)$	$(l_0, 0)$	$(l_1, -0.0187)$	$(l_1, -0.0036)$	$(l_0, 0)$	$(l_1, -0.0432)$
$P^{(s)}(A_2, A_7)$	$(l_0, 0)$	$(l_5, 0.0111)$	$(l_3, -0.0525)$	$(l_0, 0)$	$(l_0, 0)$	$(l_2, -0.0105)$	$(l_0, 0)$	$(l_0, 0)$	$(l_1, -0.0455)$
$P^{(s)}(A_3, A_1)$	$(l_1, -0.0033)$	$(l_0, 0)$	$(l_1, -0.0426)$	$(l_0, 0)$	$(l_2, -0.0354)$	$(l_3, -0.0494)$	$(l_0, 0)$	$(l_0, 0)$	$(l_4, 0.0184)$
$P^{(s)}(A_3, A_2)$	$(l_0, 0)$	$(l_0, 0)$	$(l_0, 0)$	$(l_0, 0.0459)$	$(l_3, 0.0362)$	$(l_1, 0.0231)$	$(l_0, 0)$	$(l_0, 0)$	$(l_1, -0.0132)$
$P^{(s)}(A_3, A_4)$	$(l_2, -0.0439)$	$(l_0, 0)$	$(l_0, 0)$	$(l_0, 0)$	$(l_3, -0.0404)$	$(l_0, 0)$	$(l_0, 0)$	$(l_0, 0)$	$(l_1, 0.0291)$
$P^{(s)}(A_3, A_5)$	$(l_1, -0.0448)$	$(l_1, -0.0145)$	$(l_0, 0)$	$(l_0, 0.0161)$	$(l_0, 0.0028)$	$(l_2, -0.0390)$	$(l_0, 0)$	$(l_0, 0)$	$(l_1, 0.0176)$
$P^{(s)}(A_3, A_6)$	$(l_0, 0.0014)$	$(l_0, 0)$	$(l_0, 0)$	$(l_0, 0)$	$(l_2, -0.0450)$	$(l_2, 0.0045)$	$(l_0, 0)$	$(l_0, 0)$	$(l_1, 0.0547)$
$P^{(s)}(A_3, A_7)$	$(l_0, 0)$	$(l_3, -0.0470)$	$(l_0, 0)$	$(l_0, 0)$	$(l_1, -0.0404)$	$(l_3, 0.0126)$	$(l_0, 0)$	$(l_0, 0)$	$(l_1, 0.0524)$
$P^{(s)}(A_4, A_1)$	$(l_0, 0)$	$(l_0, 0)$	$(l_6, -0.0380)$	$(l_0, 0)$	$(l_0, 0)$	$(l_3, , -0.0413)$	$(l_0, 0.0498)$	$(l_0, 0)$	$(l_3, -0.0107)$
$P^{(s)}(A_4, A_2)$	$(l_0, 0)$	$(l_0, , 0)$	$(l_0, 0.0323)$	$(l_0, 0.0459)$	$(l_1, -0.0345)$	$(l_1, 0.0312)$	$(l_2, 0.0351)$	$(l_0, 0)$	$(l_0, 0)$

Table 3 continued

	C_1	C_2	C_3	C_4	C_5	C_6	C_7	C_8	C_9
$P^{(s)}(A_4, A_3)$	$(l_0, 0)$	$(l_0, 0.0104)$	$(l_5, 0.0046)$	$(l_0, 0)$	$(l_0, 0)$	$(l_0, 0.0081)$	$(l_4, -0.0108)$	$(l_0, 0.0496)$	$(l_0, 0)$
$P^{(s)}(A_4, A_5)$	$(l_0, 0)$	$(l_1, -0.0041)$	$(l_5, 0.0009)$	$(l_0, 0.0161)$	$(l_0, 0)$	$(l_2, -0.0309)$	$(l_0, 0)$	$(l_0, 0)$	$(l_0, 0)$
$P^{(s)}(A_4, A_6)$	$(l_0, 0)$	$(l_0, 0)$	$(l_5, -0.0388)$	$(l_0, 0)$	$(l_0, 0)$	$(l_2, 0.0126)$	$(l_3, 0.0314)$	$(l_0, 0)$	$(l_0, 0.0257)$
$P^{(s)}(A_4, A_7)$	$(l_0, 0)$	$(l_3, -0.0365)$	$(l_3, -0.0202)$	$(l_0, 0)$	$(l_0, 0)$	$(l_3, 0.0207)$	$(l_1, -0.0167)$	$(l_0, 0)$	$(l_0, 0.0234)$
$P^{(s)}(A_5, A_1)$	$(l_0, 0.0415)$	$(l_0, 0)$	$(l_1, -0.0390)$	$(l_0, 0)$	$(l_2, -0.0382)$	$(l_1, -0.0104)$	$(l_1, -0.0408)$	$(l_0, 0)$	$(l_3, 0.0008)$
$P^{(s)}(A_5, A_2)$	$(l_0, 0)$	$(l_0, 0)$	$(l_0, 0)$	$(l_0, 0.0298)$	$(l_3, 0.0334)$	$(l_0, 0)$	$(l_3, -0.0556)$	$(l_0, 0)$	$(l_0, 0)$
$P^{(s)}(A_5, A_3)$	$(l_0, 0)$	$(l_0, 0)$	$(l_0, 0.0037)$	$(l_0, 0)$	$(l_0, 0)$	$(l_0, 0)$	$(l_4, 0.0097)$	$(l_1, 0.0059)$	$(l_0, 0)$
$P^{(s)}(A_5, A_4)$	$(l_1, 0.0008)$	$(l_0, 0)$	$(l_0, 0)$	$(l_0, 0)$	$(l_3, -0.0432)$	$(l_0, 0)$	$(l_0, 0.0205)$	$(l_1, -0.0436)$	$(l_0, 0.0115)$
$P^{(s)}(A_5, A_6)$	$(l_0, 0)$	$(l_0, 0)$	$(l_0, 0)$	$(l_0, , 0)$	$(l_2, -0.0478)$	$(l_0, 0.0435)$	$(l_3, 0.0519)$	$(l_0, 0)$	$(l_0, 0.0372)$
$P^{(s)}(A_5, A_7)$	$(l_0, 0)$	$(l_2, -0.0325)$	$(l_0, 0)$	$(l_0, 0)$	$(l_1, -0.0432)$	$(l_1, , 0.0516)$	$(l_1, 0.0037)$	$(l_0, 0)$	$(l_0, 0.0348)$
$P^{(s)}(A_6, A_1)$	$(l_1, -0.0047)$	$(l_0, 0.0069)$	$(l_1, 0.0008)$	$(l_0, 0)$	$(l_0, 0.0096)$	$(l_1, -0.0539)$	$(l_0, 0)$	$(l_1, 0.0259)$	$(l_3, -0.0363)$
$P^{(s)}(A_6, A_2)$	$(l_0, 0)$	$(l_0, 0)$	$(l_0, 0)$	$(l_1, 0.0031)$	$(l_2, -0.0299)$	$(l_0, 0)$	$(l_0, 0)$	$(l_0, 0.0354)$	$(l_0, 0)$
$P^{(s)}(A_6, A_3)$	$(l_0, 0)$	$(l_1, 0.0316)$	$(l_0, 0.0434)$	$(l_1, -0.0428)$	$(l_0, 0)$	$(l_0, 0)$	$(l_1, -0.0422)$	$(l_2, 0.0378)$	$(l_0, 0)$
$P^{(s)}(A_6, A_4)$	$(l_2, -0.0453)$	$(l_1, 0.0212)$	$(l_0, 0)$	$(l_1, -0.0428)$	$(l_1, 0.0046)$	$(l_0, 0)$	$(l_0, 0)$	$(l_2, -0.0117)$	$(l_0, 0)$
$P^{(s)}(A_6, A_5)$	$(l_1, -0.0462)$	$(l_2, 0.0171)$	$(l_0, 0.0398)$	$(l_1, -0.0267)$	$(l_0, 0)$	$(l_0, 0)$	$(l_0, 0)$	$(l_1, 0.0319)$	$(l_0, 0)$
$P^{(s)}(A_6, A_7)$	$(l_0, 0)$	$(l_4, -0.0153)$	$(l_0, 0)$	$(l_0, 0)$	$(l_0, 0)$	$(l_1, 0.0081)$	$(l_0, 0)$	$(l_0, 0)$	$(l_0, 0)$
$P^{(s)}(A_7, A_1)$	$(l_1, 0.0289)$	$(l_0, 0)$	$(l_3, -0.0178)$	$(l_0, 0)$	$(l_1, 0.0050)$	$(l_0, 0)$	$(l_0, 0)$	$(l_2, -0.0439)$	$(l_3, -0.0340)$
$P^{(s)}(A_7, A_2)$	$(l_0, 0.0275)$	$(l_0, 0)$	$(l_0, 0)$	$(l_3, 0.0062)$	$(l_3, -0.0345)$	$(l_0, 0)$	$(l_1, 0.0518)$	$(l_1, -0.0344)$	$(l_0, 0)$
$P^{(s)}(A_7, A_3)$	$(l_0, 0.0322)$	$(l_0, 0)$	$(l_2, 0.0248)$	$(l_3, -0.0397)$	$(l_0, 0)$	$(l_0, 0)$	$(l_3, 0.0060)$	$(l_3, -0.0319)$	$(l_0, 0)$
$P^{(s)}(A_7, A_4)$	$(l_2, -0.0117)$	$(l_0, 0)$	$(l_0, 0)$	$(l_3, -0.0397)$	$(l_2, 0)$	$(l_0, 0)$	$(l_0, 0)$	$(l_2, 0.0296)$	$(l_0, 0)$
$P^{(s)}(A_7, , A_5)$	$(l_1, -0.0126)$	$(l_0, 0)$	$(l_2, 0.0211)$	$(l_3, -0.0236)$	$(l_0, 0)$	$(l_0, 0)$	$(l_0, 0)$	$(l_2, -0.0379)$	$(l_0, 0)$
$P^{(s)}(A_7, A_6)$	$(l_0, 0.0336)$	$(l_0, 0)$	$(l_2, -0.0186)$	$(l_2, 0.0031)$	$(l_1, -0.0046)$	$(l_0, 0)$	$(l_2, 0.0482)$	$(l_0, 0.0413)$	$(l_0, 0.0023)$

Table 4 Accuracy values of preference indices in interval-valued 2-tuple PROMETHEE II

	C1	C2	C3	C4	C5	C6	C7	C8	C9
$\omega_j \rightarrow$	0.1664	0.0977	0.0349	0.0869	0.1065	0.1301	0.1076	0.1476	0.1223
$P^{(a)}(A_1, A_2)$	0	0	0	−0.0746	0.0389	0	−0.0632	0	0
$P^{(a)}(A_1, A_3)$	0	−0.0365	0	−0.0464	0	0	0.0067	0.2047	0
$P^{(a)}(A_1, A_4)$	−0.0328	−0.1121	0	−0.0339	0.0404	0	0	0.2513	0
$P^{(a)}(A_1, A_5)$	0	−0.0409	0	−0.0387	0	0	0	0.2808	0
$P^{(a)}(A_1, A_6)$	0	0	0	−0.0436	0	0	−0.0632	0	0
$P^{(a)}(A_1, A_7)$	0	−0.0375	0	−0.0396	0	0.0048	−0.0282	0	0
$P^{(a)}(A_2, A_1)$	0.3285	0.1207	0.2659	0	0	0.0254	0	−0.3158	−0.1125
$P^{(a)}(A_2, A_3)$	0.3265	0.0842	0.2664	0	0	0	0.0699	−0.1111	0
$P^{(a)}(A_2, A_4)$	0.2957	0.0086	0	0	0	0	0	−0.0645	0.0855
$P^{(a)}(A_2, A_5)$	0.2645	0.0798	0.2595	0	0	−0.0444	0	−0.0350	0.0841
$P^{(a)}(A_2, A_6)$	0.0169	0.1222	0.2644	0	0	0.0357	0	0	0.0381
$P^{(a)}(A_2, A_7)$	0	0.0831	0.3405	0	0	0.0303	0	0	0
$P^{(a)}(A_3, A_1)$	0.0020	0	−0.0005	0	−0.0072	0.0329	0	0	−0.1803
$P^{(a)}(A_3, A_2)$	0	0	0	−0.0282	−0.0015	0.0074	0	0	−0.0679
$P^{(a)}(A_3, A_4)$	−0.0308	0	0	0.0125	0.0332	0	0	0	0.0176
$P^{(a)}(A_3, A_5)$	−0.0620	−0.0044	0	0.0076	0.0213	−0.0370	0	0	0.0162
$P^{(a)}(A_3, A_6)$	−0.3096	0	0	0	−0.0358	0.0431	0	0	−0.0297
$P^{(a)}(A_3, A_7)$	0	−0.0010	0	0	−0.3003	0.0377	0	0	−0.0679
$P^{(a)}(A_4, A_1)$	0	0	0.0772	0	0	0.0022	0.0632	0	−0.1980
$P^{(a)}(A_4, A_2)$	0	0	−0.1887	−0.0407	−0.0015	−0.0233	0	0	0
$P^{(a)}(A_4, A_3)$	0	0.0756	0.0777	−0.0125	0	−0.0307	0.0699	−0.0466	0
$P^{(a)}(A_4, A_5)$	0	0.0712	0.0708	−0.0048	0	−0.0677	0	0	0

Table 4 continued

	C1	C2	C3	C4	C5	C6	C7	C8	C9
$P^{(a)}(A_4, A_6)$	0	0	0.0757	0	0	0.0124	0	0	−0.0473
$P^{(a)}(A_4, A_7)$	0	0.0746	0.1518	0	0	0.0070	0.0350	0	−0.0841
$P^{(a)}(A_5, A_1)$	0.0640	0	0.0064	0	−0.0286	0.0699	−0.0187	0	−0.1966
$P^{(a)}(A_5, A_2)$	0	0	0	−0.0358	0.0103	0	−0.0819	0	0
$P^{(a)}(A_5, A_3)$	0	0	0.0069	0	0	0	−0.0120	−0.0761	0
$P^{(a)}(A_5, A_4)$	0.0312	0	0	0	0.0119	0	−0.0819	−0.0295	0.0014
$P^{(a)}(A_5, A_6)$	0	0	0	0	−0.0571	0.0801	−0.0819	0	−0.0459
$P^{(a)}(A_5, A_7)$	0	0.0034	0	0	−0.3216	0.0747	−0.0469	0	−0.0841
$P^{(a)}(A_6, A_1)$	0.3116	−0.0015	0.0015	0	0.0285	−0.0103	0	−0.2451	−0.1506
$P^{(a)}(A_6, A_2)$	0	0	0	−0.0310	0.0674	0	0	0.0707	0
$P^{(a)}(A_6, A_3)$	0	−0.0380	0.0020	−0.0028	0	0	0.0699	−0.0404	0
$P^{(a)}(A_6, A_4)$	0.2788	−0.1136	0	0.0097	0.0690	0	0	0.0062	0
$P^{(a)}(A_6, A_5)$	0.2476	−0.0424	−0.0049	0.0049	0	0	0	0.0357	0
$P^{(a)}(A_6, A_7)$	0	−0.0390	0	0	0	−0.0054	0	0	0
$P^{(a)}(A_7, A_1)$	0.0845	0	−0.0746	0	0.2931	0	0	−0.2857	−0.1125
$P^{(a)}(A_7, A_2)$	−0.2440	0	0	−0.0349	0.3320	0	−0.0350	0.0301	0
$P^{(a)}(A_7, A_3)$	0.0825	0	−0.0741	−0.0067	0	0	0.0349	−0.0810	0
$P^{(a)}(A_7, A_4)$	0.0517	0	0	0.0058	0.3335	0	0	−0.0344	0
$P^{(a)}(A_7, A_5)$	0.0205	0	−0.0810	0.0009	0	0	0	−0.0049	0
$P^{(a)}(A_7, A_6)$	−0.2271	0	−0.0761	−0.0040	0.2646	0	−0.0350	−0.0406	0.0381

The 2-tuple linguistic score values and accuracy values of cumulative preference indices are given below.

$\pi^{(s)}(A_1, A_2) = (l_1, -0.0349)$	$\pi^{(s)}(A_2, A_1) = (l_1, 0.0216)$	$\pi^{(s)}(A_3, A_1) = (l_1, 0.0226)$	$\pi^{(s)}(A_4, A_1) = (l_1, -0.0064)$
$\pi^{(s)}(A_1, A_3) = (l_1, -0.0079)$	$\pi^{(s)}(A_2, A_3) = (l_1, -0.0124)$	$\pi^{(s)}(A_3, A_2) = (l_1, -0.0383)$	$\pi^{(s)}(A_4, A_2) = (l_1, -0.0516)$
$\pi^{(s)}(A_1, A_4) = (l_1, -0.0345)$	$\pi^{(s)}(A_2, A_4) = (l_1, -0.0233)$	$\pi^{(s)}(A_3, A_4) = (l_1, -0.0331)$	$\pi^{(s)}(A_4, A_3) = (l_1, -0.0355)$
$\pi^{(s)}(A_1, A_5) = (l_0, 0.0555)$	$\pi^{(s)}(A_2, A_5) = (l_1, -0.0181)$	$\pi^{(s)}(A_3, A_5) = (l_1, -0.0494)$	$\pi^{(s)}(A_4, A_5) = (l_1, -0.0550)$
$\pi^{(s)}(A_1, A_6) = (l_1, -0.0527)$	$\pi^{(s)}(A_2, A_6) = (l_1, -0.0479)$	$\pi^{(s)}(A_3, A_6) = (l_1, -0.0422)$	$\pi^{(s)}(A_4, A_6) = (l_1, -0.0202)$
$\pi^{(s)}(A_1, A_7) = (l_1, -0.0520)$	$\pi^{(s)}(A_2, A_7) = (l_1, -0.0104)$	$\pi^{(s)}(A_3, A_7) = (l_1, -0.0106)$	$\pi^{(s)}(A_4, A_7) = (l_1, -0.0121)$
$\pi^{(s)}(A_5, A_1) = (l_1, -0.0206)$	$\pi^{(s)}(A_6, A_1) = (l_1, -0.0238)$	$\pi^{(s)}(A_7, A_1) = (l_1, -0.0015)$	
$\pi^{(s)}(A_5, A_2) = (l_1, -0.0396)$	$\pi^{(s)}(A_6, A_2) = (l_0, 0.0356)$	$\pi^{(s)}(A_7, A_2) = (l_1, -0.0164)$	
$\pi^{(s)}(A_5, A_3) = (l_1, -0.0448)$	$\pi^{(s)}(A_6, A_3) = (l_1, -0.0439)$	$\pi^{(s)}(A_7, A_3) = (l_1, 0.0094)$	
$\pi^{(s)}(A_5, A_4) = (l_1, -0.0480)$	$\pi^{(s)}(A_6, A_4) = (l_1, -0.0194)$	$\pi^{(s)}(A_7, A_4) = (l_1, 0.0103)$	
$\pi^{(s)}(A_5, A_6) = (l_1, -0.0409)$	$\pi^{(s)}(A_6, A_5) = (l_1, -0.0471)$	$\pi^{(s)}(A_7, A_5) = (l_1, -0.0321)$	
$\pi^{(s)}(A_5, A_7) = (l_1, -0.0476)$	$\pi^{(s)}(A_6, A_7) = (l_1, -0.0537)$	$\pi^{(s)}(A_7, A_6) = (l_1, -0.0320)$	

$\pi^{(a)}(A_1, A_2) = -0.0091$	$\pi^{(a)}(A_2, A_1) = 0.0187$	$\pi^{(a)}(A_3, A_1) = -0.0182$	$\pi^{(a)}(A_4, A_1) = -0.0144$	$\pi^{(a)}(A_5, A_1) = -0.0091$
$\pi^{(a)}(A_1, A_3) = 0.0233$	$\pi^{(a)}(A_2, A_3) = 0.0630$	$\pi^{(a)}(A_3, A_2) = -0.0099$	$\pi^{(a)}(A_4, A_2) = -0.0133$	$\pi^{(a)}(A_5, A_2) = -0.0108$
$\pi^{(a)}(A_1, A_4) = 0.0221$	$\pi^{(a)}(A_2, A_4) = 0.0510$	$\pi^{(a)}(A_3, A_4) = 0.0016$	$\pi^{(a)}(A_4, A_3) = 0.0057$	$\pi^{(a)}(A_5, A_3) = -0.0123$
$\pi^{(a)}(A_1, A_5) = 0.0341$	$\pi^{(a)}(A_2, A_5) = 0.0602$	$\pi^{(a)}(A_3, A_5) = -0.0107$	$\pi^{(a)}(A_4, A_5) = 0.0002$	$\pi^{(a)}(A_5, A_4) = -0.0065$
$\pi^{(a)}(A_1, A_6) = -0.0106$	$\pi^{(a)}(A_2, A_6) = 0.0333$	$\pi^{(a)}(A_3, A_6) = -0.0534$	$\pi^{(a)}(A_4, A_6) = -0.0015$	$\pi^{(a)}(A_5, A_6) = -0.0101$
$\pi^{(a)}(A_1, A_7) = -0.0095$	$\pi^{(a)}(A_2, A_7) = 0.0239$	$\pi^{(a)}(A_3, A_7) = -0.0355$	$\pi^{(a)}(A_4, A_7) = 0.0070$	$\pi^{(a)}(A_5, A_7) = -0.0395$
$\pi^{(a)}(A_6, A_1) = -0.0011$	$\pi^{(a)}(A_7, A_1) = -0.0132$			
$\pi^{(a)}(A_6, A_2) = 0.0149$	$\pi^{(a)}(A_7, A_2) = -0.0076$			
$\pi^{(a)}(A_6, A_3) = -0.0023$	$\pi^{(a)}(A_7, A_3) = 0.0024$			
$\pi^{(a)}(A_6, A_4) = 0.0444$	$\pi^{(a)}(A_7, A_4) = 0.0396$			
$\pi^{(a)}(A_6, A_5) = 0.0426$	$\pi^{(a)}(A_7, A_5) = -0.0001$			
$\pi^{(a)}(A_6, A_7) = -0.0045$	$\pi^{(a)}(A_7, A_6) = -0.0177$			

The outgoing flow, the incoming flow and the net flow for each alternative is depicted below.

Outgoing flow	Score value	Accuracy value
$\phi^+(A_1)$	$(l_1, -0.0396)$	0.0084
$\phi^+(A_2)$	$(l_1, -0.0151)$	0.0417
$\phi^+(A_3)$	$(l_1, -0.0252)$	0.0417
$\phi^+(A_4)$	$(l_1, -0.0301)$	−0.0027
$\phi^+(A_5)$	$(l_1, -0.0402)$	−0.0147
$\phi^+(A_6)$	$(l_1, -0.0439)$	0.0157
$\phi^+(A_7)$	$(l_1, -0.0104)$	0.0006

Incoming flow	Score value	Accuracy value
$\phi^-(A_1)$	$(l_1, -0.0013)$	−0.0063
$\phi^-(A_2)$	$(l_1, -0.0427)$	−0.0060
$\phi^-(A_3)$	$(l_1, -0.0225)$	0.0133
$\phi^-(A_4)$	$(l_1, -0.0247)$	0.0254
$\phi^-(A_5)$	$(l_1, -0.0429)$	0.0211
$\phi^-(A_6)$	$(l_1, -0.0393)$	−0.0100
$\phi^-(A_7)$	$(l_1, -0.0311)$	−0.0097

The net flow is evaluated only for those alternatives that have outgoing flow greater than its incoming flow. As the outgoing flows for A_2, A_5 and A_7 are greater than their respective incoming flows, hence the net flows for these alternatives are obtained.

Net flow	Score value	Accuracy value
$\phi(A_2)$	$(l_0, 0.0276)$	0.0476
$\phi(A_5)$	$(l_0, 0.0026)$	−0.0358
$\phi(A_7)$	$(l_0, 0.0207)$	0.0102

The net flow of the alternatives are compared on the basis of their score values and accuracy values. The alternative with greater score value is preferred and if two alternatives have same score values then their accuracy values are compared and the lesser one is preferred. In above example, alternative A_2 (solar energy) is best one followed by A_7 (nuclear energy) and A_5 (wind energy) for energy production in the new plant under consideration.

5 Concluding remarks

The interval-valued 2-tuple linguistic model provides a useful framework to work with qualitative information in decision situations where DMs have apprehension in assessing criteria-alternatives with precise numeric or even a single linguistic information. In this paper, the weighted matrix of each DM is evaluated for each pair of criterion-alternative to avoid unduly high or low evaluation values that can be induced by DMs' knowledge. Further, the notion of entropy is extended to interval-valued 2-tuple linguistic variables and applied to compute the criteria weights which are subsequently supplied to the main PROMETHEE II method. The PROMETHEE II method is suitably modified for interval-valued 2-tuple linguistic variables and is then used to choose the best alternative energy resources for a new plant set-up in India.

The present study assumes that all DMs have a uniform linguistic term set and all of them represent their uncertain preference information on criteria-alternatives using interval-valued 2-tuple linguistic variables. This limitation can be overcome by building a MCGDM model where DMs are allowed to express their preferences using one of many frameworks (fuzzy, linguistic, multi-granular linguistic) for representing uncertainty, like in Alonso et al. (2010).

An improvement in the line can be to include a consistency check on the assessment matrices of criteria-alternatives of the DMs'. The matrices failing to achieve the threshold consistency level can either be discarded from the analysis or can be asked to revise by the corresponding DM. We can also include some group consensus support model in the present study. The weights of the DMs can be determined based on their participation in group consensus process; the dissenting DMs can be given lesser weights in the analysis (Xu and Wu 2013). We can also

broaden the framework of present study to include different uncertainty structures like hesitant fuzzy linguistic term sets (Wei et al. 2014).

Acknowledgments The authors would like to thank the referees for their constructive suggestions.

References

Access to Clean Energy (2010) A glimpse of off grid projects in India, Government of India Ministry of New and Renewable Energy, http://www.undp.org/content/dam/india/docs/access_to_clean_energy

Ahn SJ, Graczyk D (2012) Understanding energy challenges in India: policies. Players and issues, International Energy Agency

Aldavi A, Chaharsooghi SK, Esfahanipour A (2007) Decision making in stock trading, an application of PROMETHEE. Eur J Oper Res 177:673–683

Alonso S, Herrera-Viedma E, Chiclana F, Herrera F (2010) A web based consensus support system for group decision making problems and incomplete preferences. Inf Sci 180:4477–4495

Beg I, Rashid T (2014) Aggregation operators of interval-valued 2-tuple linguistic information. Int J Intell Syst 29:63–667

Behzadiana M, Kazemzadehb RB, Albadvi A, Aghdasi M (2010) PROMETHEE: a comprehensive literature review on methodologies and applications. Eur J Oper Res 200:198–215

Brans JP (1983) Lingenierie de la decision. Elaboration dinstruments daide a la decision. Methode PROMETHEE. In: Nadeau R, Landry M (eds) Laide a la Decision: Nature, Instrument s et Perspectives Davenir. Presses de Universite Laval, Quebec, pp 183–214

Brans JP, Vincke Ph, Mareschal B (1986) How to select and how to rank projects: the PROMETHEE method. Eur J Oper Res 24(2):228–238

Chen CT, Hwang YC, Hung WZ (2009) Applying multiple linguistic PROMETHEE method for personnel evaluation and selection. In: Proceedings of the IEEE IEEM, pp 1312–1316, ISBN:978-1-4244-4870-8/09

Energy Statistics (2013) Central Statistics Office National Statistical Organisation Ministry of Statistics and Programme Implementation, Government of India, 2013. http://mospi.nic.in/mospi_new/upload/Energy_Statistics_2013

Goumas M, Lygerou V (2000) Theory and methodology : an extension of the PROMETHEE method for decision making in fuzzy environment: ranking of alternative energy exploitation projects. Eur J Oper Res 123:606–613

Halouani N, Martinez L, Chabchoub H, Martel JM, Liu J (2009) A multi-granular linguistic promethee model, IFSA-EUSFLAT , pp 213–218, ISBN:978-989-95079-6-8

Herrera F, Martinez L (2000) A 2-tuple fuzzy linguistic representation model for computing with words. IEEE Trans Fuzzy Syst 8:746–752

Herrera F, Martinez L (2001) A model based on linguistic 2-tuples for dealing with multigranuality hierarichal linguistic contexts in multi-expert decision making. IEEE Trans Syst Man Cybern B Cybern 31:227–234

Ju Y, Wang A (2013) Extension of VIKOR method for multi-criteria group decision making problem with linguistic information. Appl Math Model 37:3112–3125

Li DF (2009) Multiattribute group decision making method using extended linguistic variables. Int J Uncertain Fuzziness Knowl Based Syst 17:793–806

Liu HC, Li P, Youa JX, Chena YZ (2009) A novel approach for FMEA: combination of interval 2-tuple linguistic variables and gray relational analysis. Qual Reliabil Eng Int Online. doi:10.1002/qre.1633

Liu HC, Liu L, Wuc J (2013) Material selection using an interval 2-tuple linguistic VIKOR method considering subjective and objective weights. Mater Des 52:158–167

Lotfi FH, Fallahnejad R (2010) Imprecise Shannon's entropy and multi attribute decision making. Entropy 12:53–62

Mareschal B, Brans JP (1988) Geometrical representations for MCDA. Eur J Oper Res 34:69–77

Mareschal B, Brans JP (1991) Bankadviser, an industrial evaluation system. Eur J Oper Res 54(3):318–324

Mareschal B (1998) Weight stability intervals in multicriteria decision aid. Eur J Oper Res 33:54–64

Martinez L, Herrera F (2012) An overview on the 2-tuple linguistic model for computing with words in decision making: extensions, applications and challenges. Inf Sci 207:1–18

Mi C, Liu S, Dang Y, Wang J, Wu Z (2009) Study on 2-tuple linguistic assessment method based on grey cluster with incomplete atrribute weight informatoin. In: IEEE international conference on systems, man and cybernetics, San Antonio, TX, USA

Oberschmidt J, Geldermann J, Ludwig J, Schmehl M (2010) Modified PROMETHEE approach for assessing energy technologies. Int J Energy Sect Manag 4(2):183–212

Pang J, Liang J (2012) Evaluation of the results of multi-attribute group decision-making with linguistic information. Omega 40:294–301

Pohekar SD, Ramachandran M (2004) Application of multi-criteria decision making to sustainable energy planning—a review. Renew Sustain Energy Rev 8:365–381

Ruan Y, Pei Z, Gao Z (2013) Linguistic interval 2-tuple power aggregation operators and their applications. Int J Comput Intell Syst 6(2):381–395

Simpson AP, Edwards CF (2011) An energy-based framework for evaluating environmental impact. Energy 36:1442–1459

Tai WS, Chen CT (2009) A new evaluation model for intellectual capital based on computing with linguistic variable. Expert Syst Appl 36(2):3483–3488

T Tsoutsos, Drandaki M, Frantzeskaki N, Iosifidis E, Kiosses I (2009) Sustainable energy planning by using multi-criteria analysis application in the island of Crete. Energy Policy 37:1587–1600

Vincke Ph, Brans JP (1985) A preference ranking organization method: the PROMETHEE method for multiple criteria decision-making. Manag Sci 31(6):647–656

Wang JQ, Wang DD, Zhang HY, Chen XH (2015) Multi-criteria group decision making method based on interval 2-tuple linguistic information and Choquet integral aggregation operators. Soft Comput 19:389–405

Wang TC, Lee HD (2009) Developing a fuzzy TOPSIS approach based on subjective weights and objective weights. Expert Syst Appl 36:8980–8985

Wei C, Zhao N, Tang X (2014) Operators and comparisons of hesitant fuzzy linguistic term sets. IEEE Trans Fuzzy Syst 22(3):575–585

Wei GW (2010) Extension of TOPSIS method for 2-tuple linguistic multiple attribute group decision making with incomplete weight information. Knowl Inf Syst 25:623–634

Xu J, Wu Z (2013) A maximizing consensus approach for alternative-selection based on uncertain linguistic preference relations. Comput Ind Eng 64:999–1008

Yan J, Dagang T, Yue P (2007) Ranking environmental projects model based on multicriteria decision-making and the weight sensitivity analysis. J Syst Eng Electron 18(3):534–539

You XY, You JX, Liu HC, Zhen L (2015) Group multi-criteria supplier selection using an extended VIKOR method with interval 2-tuple linguistic information. Expert Syst Appl 42:1906–1916

Zeleny M (1996) Multiple-criteria decision making. Springer, New York

Zhang H (2012) The multiattribute group decision making method based on aggregation operators with interval-valued 2-tuple linguistic information. Math Comput Model 56:27–35

Zhang H (2013) Some interval-valued 2-tuple linguistic aggregation operators and application in multiattribute group decision making. Appl Math Model 37:4269–4282

Available online at www.sciencedirect.com

ScienceDirect

Procedia Engineering 144 (2016) 1451 – 1458

12th International Conference on Vibration Problems, ICOVP 2015

Experimental Investigation of Vibration Analysis of Multi-Crack Rotor Shaft

Anuj Kumar Jain[a]*, Vikas Rastogi[b], Atul Kumar Agrawal[c]

[b,c]*Department of Mechanical, Production, Industrial and Automobile Engineering, Delhi Technological University, Delhi–110042, India*
[*a]*Deparment of Mechanical Engineering, The Northcap University (Formerly ITM University), Gurgaon–122017, India*

Abstract

In recent years, the dynamic behaviour and diagnostic of cracked rotor have been gained momentum. In literature, several studies are available for cracked rotor systems, however very few authors have addressed the issue of multi-cracked rotor system. This paper deals with the nonlinear dynamic behaviour of multi cracked rotor system, which is analyzed experimentally and analytically with the considerations of the effects of the crack depth, crack location and the shaft's rotational speed. A new extension of Lagrangian method is used for analyzing the dynamic behaviour of a multi-cracked rotor system through Umbra Lagrangian formalism. The effects of crack depth on the shaft's stiffness and natural frequencies are analyzed experimentally. Natural frequencies have been obtained through vibration analyzer using impact hammer test under static conditions. This analysis also includes the dynamic response of rotor with breathing crack by using data acquisition system called OROS. It has been noticed that the stress concentration on the first crack has increased due to the presence of the second crack. Another interesting phenomenon is the influence of one crack over the other crack for mode shapes and for threshold speed limits. All such analysis has been carried out on experimental test rig consist of a symmetrical system, which has mild steel shaft between a pair of identical self-aligned double groove high speed bearings. The experimental results can be further validated with the analytical results.

Peer-review under responsibility of the organizing committee of ICOVP 2015

Keywords: Multi cracked rotor; Crack depth; Impact hammer test

* Corresponding author. Tel.: +91-750-378-1979.
E-mail address: anujjainkanbay@gmail.com

Peer-review under responsibility of the organizing committee of ICOVP 2015
doi:10.1016/j.proeng.2016.05.177

Nomenclature

A_n	amplitude of rotor
R_c	damping coefficient of dissipative coupling
Ω	excitation frequency
Ω_n	natural frequency of the rotor shaft
Δk	change in stiffness due to crack
L	length of the rotating shaft
μ_i	internal damping of the rotor
n	mode number and
λ	position of the discrete damper

1. Introduction

Heavy loaded rotating components of various machines (such as steam and gas turbine, pumps, generators and high speed compressor etc.) being diversely used in various fields such as aircraft, automobile and power generation. Rotor shaft is considered as one of the important part of various rotating machines. Due to manufacturing defect or cyclic loading, fatigue crack frequently appears in rotating shaft. Fatigue crack is considered as one of the main reasons for catastrophic failures in rotating shaft. In thermal machinery such as steam turbines, thermal stresses and thermal shocks are also accountable factors for high stress intensity which is also a cause of crack initiation and its propagation. This failure may cause human injury, great economic loss and equipment loss etc. Due to this reason, cracked rotors have attracted the attention of researchers since the last 50 years.

Important progress has been shown in the last 40 years in cracks detection. Since 1970, a large number of research papers on crack detection and its effects have been published. Various review papers have also been published periodically by various researchers like Wauer [1], Gasch [2], Dimarogonas [3], Sabnavis et al. [4] etc. Some recent papers were presented by Papadopoulos [5], Kumar et al. [6] and Sekhar [7]. Sekhar and Balaji [8] worked on dynamic analysis of a rotor system considering a slant crack in the shaft. They considered FEM analysis of the rotor bearing system for flexural vibrations. Reduction in the eigen frequencies of all the modes with an increased crack depth has been observed. For the same crack location, it is also observed that change in eigen frequencies is smaller in slant crack compared to transverse crack. Sekhar [9] has worked on vibration characteristics of a cracked rotor with two open cracks and applied finite element analysis on a rotor system having two transverse open cracks for flexural vibration. He noticed that in the case of two cracks of different depths, the larger crack has more significant effect on the eigen frequency.

In present study, the effect of crack depth on the shaft's stiffness and natural frequencies are investigated using experimentally. Natural frequencies have been obtained through vibration analyzer system (OROS system) system using impact hammer test under static conditions. This work also includes the dynamic response of rotor with breathing crack, which has been addressed in this paper by using the data acquisition system called OROS.

2. Methodology

The concept of extended Lagrangian Hamilton mechanics has been used to diagnose the dynamic of cracked rotor system by Mukherjee et al. [13, 14 and 15] and Rastogi et al. [16]. Umbra–Lagrangian density function has been used to describe the motion of such continuous rotor system instead of Umbra–Lagrangian by Mukherjee et al [17].

As a case study, one dimensional rotor shaft with internal and external damping along with transverse crack in middle span has discussed. The rotor is symmetrical, which is to be driven by a constant speed source through a dissipative coupling by Kumar [18]. Further, another crack has been generated and an amplitude equation has been established considering extension of Noether's theorem over manifolds.

The given amplitude may be written as:

$$A_n = \sqrt{\frac{2R_c\left[\Omega - \min\Omega_n\left\{1+\frac{2\Delta kL^3}{\mu_i n^4\pi^4}Sin^2\frac{n\pi}{L}\lambda\right\}\right]}{\xi_n\Omega_n}} \quad (1)$$

Where $\xi_n = \frac{\mu_i n^4\pi^4}{L^4}$

3. Experimental Study

3.1. Experimental setup

Experiment study has been conducted to analyze the multi-crack system. The schematic diagram of experimental setup for stiffness measurement is shown in Fig. 1. Test rig shown in Fig. 2 has been used for experimentation and analysis is carried out using OROS-36. Various components of the Test rig are shown in Fig. 2. All the components are connected to each other as per requirement so that they can share output signals generated during the experiment. In experimental testing, one may use symmetrical system which has a mild steel rotor shaft between a pair of identical self aligning bearing. The shaft has constant circular cross section which is fitted with a DC motor by using a flexible coupling to reduce the vibration transfer from a motor to the rotor. The maximum rotation speed of the motor is 6000 rpm. Impact hammer test is also carried out to find the natural frequency in static condition as shown in Fig. 2 (b).

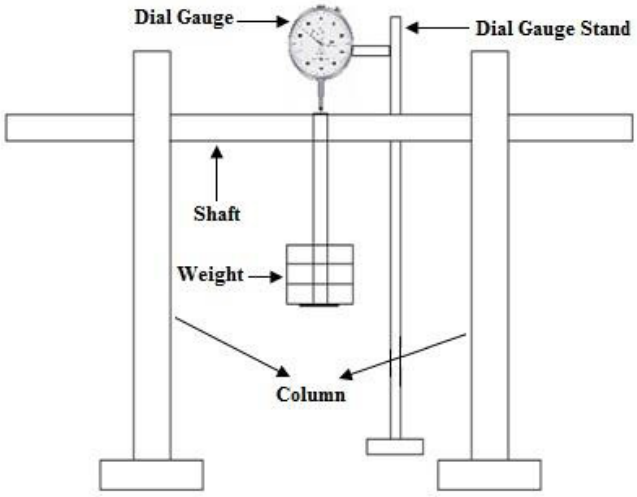

Fig. 1. Schematic diagram of experimental setup for stiffness measurement.

3.2. Test specimen

The material of shaft was chosen based on the criteria that it is referred by American Society for Testing Material Engineering (ASTM) as standard for the shaft material (0.3-0.6%). Test specimens used for analysis are made from mild steel. The schematic diagrams of single crack and multi crack specimens are shown in Fig. 3 and Fig. 4 respectively.

3.3. Experimental procedure

Creating the artificial transverse crack is one of the most challenging tasks in the present study. It is made in shaft by using very fine jewel saw. Initially the dimension of crack was considered 1mm depth and width 0.2mm. Therefore, the single crack has a range of depth between 0 to 23% (5mm) of diameter. Moreover, the following crack depths were considered for analysis: 4.54% (1mm), 9.09% (2mm), 13.64% (3mm), 18.18% (4mm) and 22.73% (5mm). First crack was formed at the centre of the two bearing support. Stiffness of the intact shaft and single cracked shaft has been determined on experimental set up as shown in Fig. 1. A known weight is applied on specimen. With the help of dial gauge indicator, deflection of shaft due to known load is measured. After this, using relation '$K=F/x$', stiffness has been determined for various crack depth. Shaft has been divided into 12 sections on the circumference having 30^o angular interval simultaneously. The arrangement of shaft at first position is shown in Fig. 5.

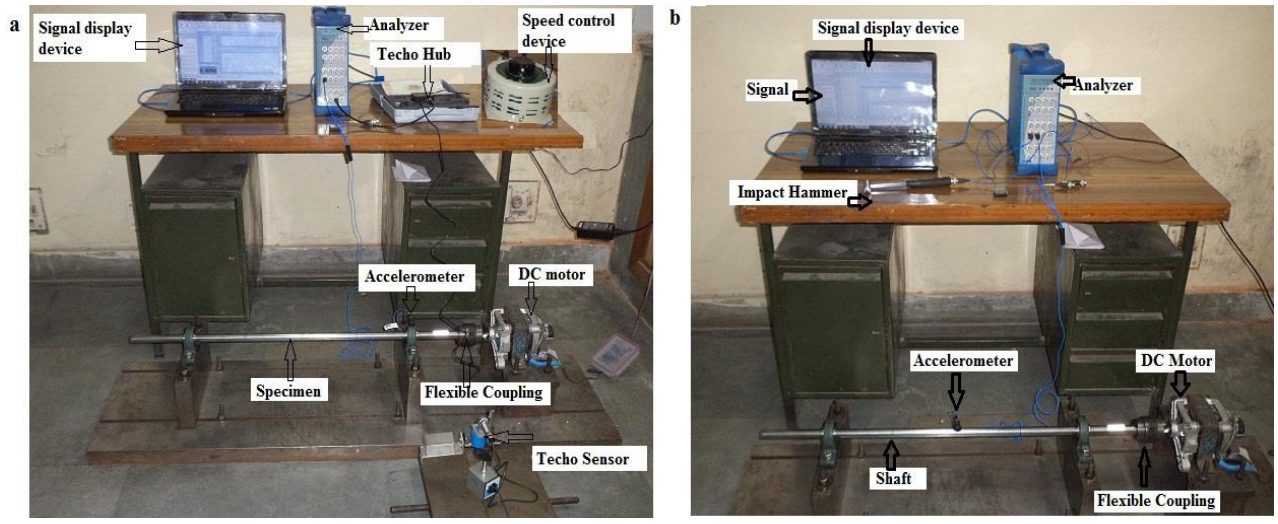

Fig. 2. (a) Experimental Setup of Dynamic Test; (b) Experimental Setup of Impact Hammer Test.

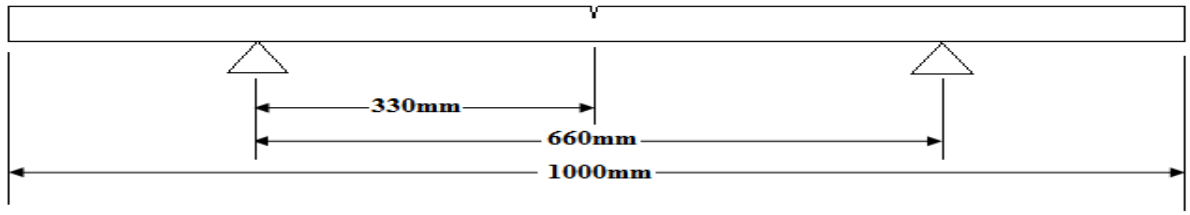

Fig. 3. Schematic diagram of single crack test specimen.

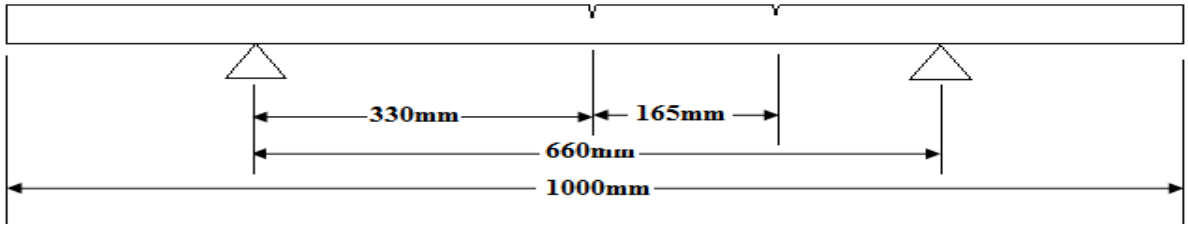

Fig. 4. Schematic diagram of multi crack test specimen.

The arrangement of second transverse crack is shown in Fig. 4. In this case, depth varies in range 0 to 13.64% (3mm) of diameter. Further, the following crack depths were considered for analysis: 4.54% (1mm), 9.09% (2mm), 13.64% (3mm). This crack is generated at the distance of 165 mm from the middle crack. Stiffness of the double cracked shaft has been evaluated through experiments and used in analytical formulation of amplitude equation.

Table 1. Details of test specimen.

Shaft specification	
Shaft material	Steel
Effective length (Bearing to bearing)	660 mm
Overhang (Each side)	175 mm
Diameter of shaft	22 mm
Weight of shaft	1.83 Kg
Density	7850 Kg/m^3
Ixx and Iyy	11503 mm^4
Stiffness	285 N/mm

The shafts are rotated at various speeds in range 1200-5500 rpm, which is used for dynamic investigation. The signal is transformed into signal analyzer which is further analyzed through NVGate® software. It has been found from literature that probes are placed near the bearing or over the bearing for analysing shaft behaviour as per the Tong Zhou et al. [19]. The accelerometer is attached on the top of bearing for capturing a signal and transmitted to display monitor.

Furthermore, impact hammer test has been conducted to find out static natural frequencies. This test performed through equipment OR36 (maximum range 20 KHz) integrate with compact real time multi-analyzer. A single accelerometer is used which mounted at mid of the shaft. Experiment has been conducted on the un-cracked, single cracked and multi cracked shafts. Each specimen (shaft) is hit by the hammer (with ICP coupling) at the centre of the shaft to create a force and vibration which is captured by OROS hammer and accelerometer respectively. For each shaft the input force, the trigger levels and accelerometer response had to be calibrated in the NVGate® analyzer project for measurement and analysis.

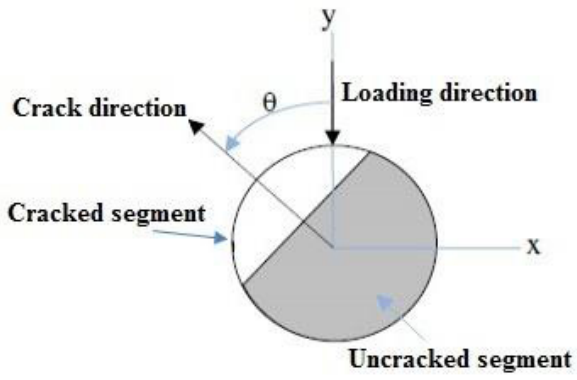

Fig. 5. Cross sectional view of rotating angle between crack and loading direction.

4. Results and Discussion

Experimental results are presented in Figs (6-9). Figure 6(a) shows the variation in stiffness with the single crack depth variation. It shows that the stiffness variation increases with increase in crack depth. Figure 6(b) shows the variation in stiffness due to second crack. Different positions of rotating cracked shaft are shown in Fig. 7. For

different crack depths, the slope of the curve decreased as the shaft rotated from fully closed (0^o and 360^o) to partially closed (90^o and 270^o) to fully open (180^o), which is termed as breathing phenomenon.

The variation of stiffness of single cracked rotor and multi cracked (two crack) shafts at different angles are shown in Fig. 8. It is evident from the plots that the stiffness of the shaft decreases with increase in crack depth. In multi crack analysis, the change in stiffness is marginal as compared to single crack propagation. Therefore, stress concentration increases rapidly at one point in case of single crack but the effect of stress concentration at the same point is marginal due to creation of other crack. The peaks indicating the amplitude of acceleration are shown in Fig. 9. These are used to find natural frequencies for cracked and un-cracked shaft.

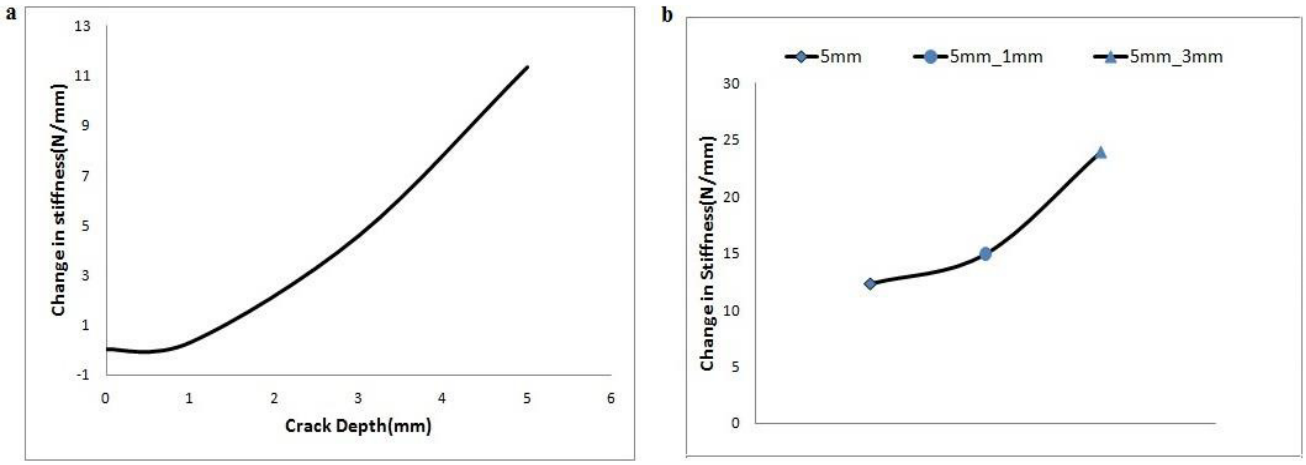

Fig. 6. (a) Variation in stiffness with the single crack depth; (b) Variation in stiffness with the Multi crack depth.

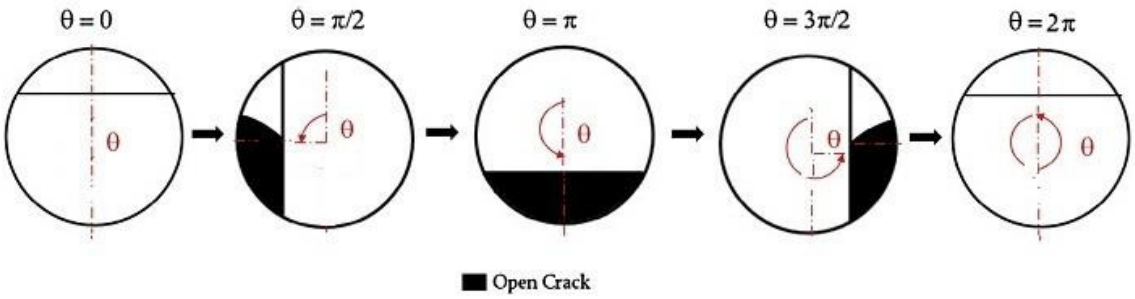

Fig. 7. Some of the angular positions of the crack during one rotation of the shaft.

In multi crack shaft, slope of the stiffness curve decreases due to second crack as compare to single crack shaft. Thus, increase in the stress concentration is marginal near the first (middle) crack as compare to the middle crack depth.

The natural frequencies at various crack depth have also been obtained from Fig. 9. For a single crack, natural frequency of the shaft decreases rapidly, which is clearly observed in Fig. 9(a). In case of multi-crack, the changes in natural frequency are marginal observed. In Fig. 9(b), first natural frequency comes out to be 114.5Hz for intact shaft and 90.5Hz for 1mm cracked shaft, 86Hz for 3 mm cracked shaft, 85Hz for 5 mm cracked shaft. In Fig. 9(b) natural frequency comes out to be 84.5Hz for multi-cracked shaft (5 mm and 1 mm crack) and 83.5 Hz for second case of multi-cracked shaft (5 mm and 3 mm crack).

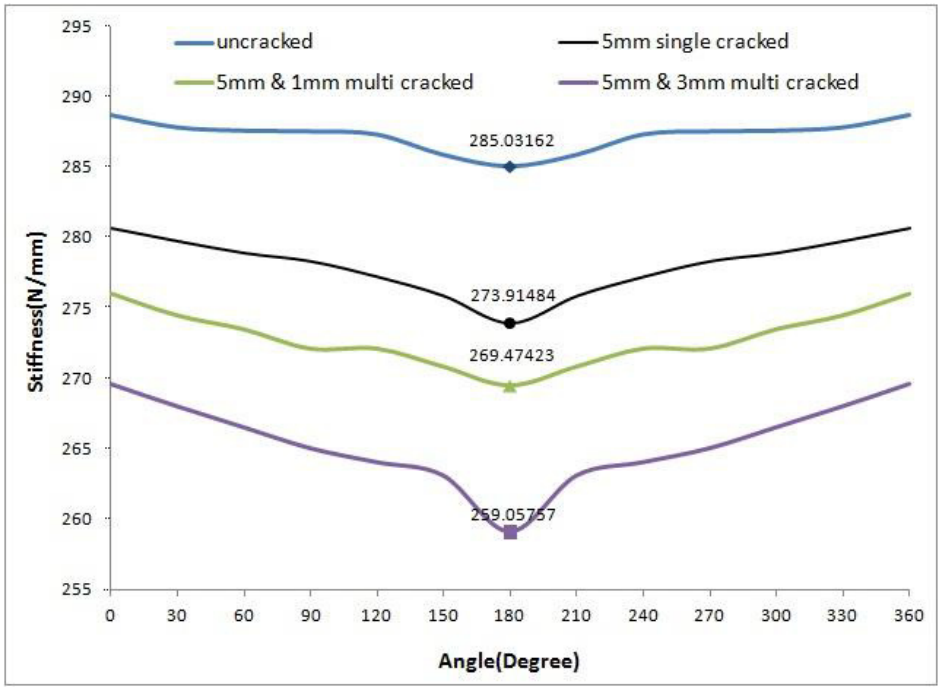

Fig. 8. Stiffness of cracked rotor at different angle.

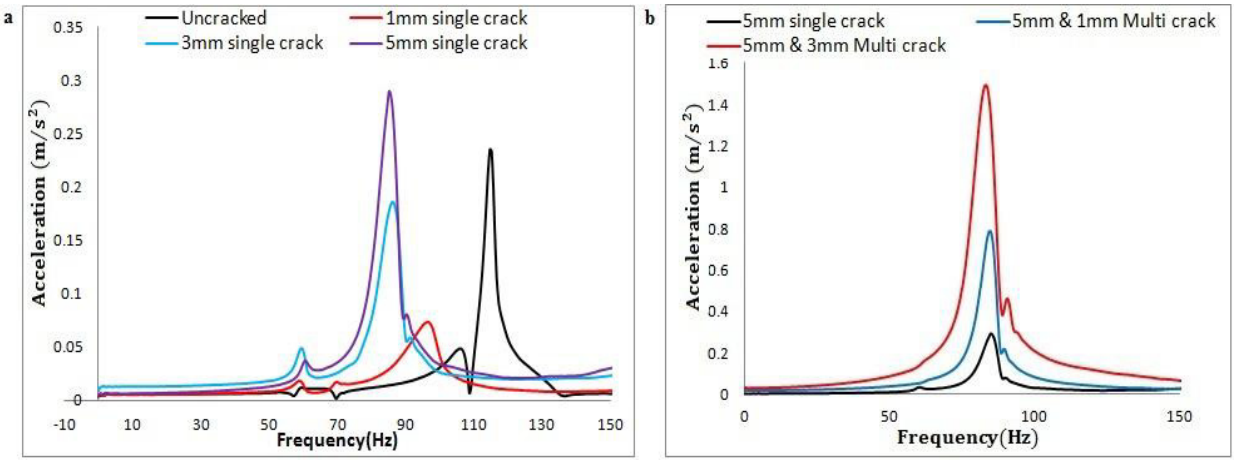

Fig. 9. (a) Frequency Vs acceleration for un-cracked shaft and single cracked shaft; (b) Frequency Vs acceleration for multi-cracked shaft.

5. Conclusion

Experimental investigations of vibration have been successfully conducted and validated through analytical equation of crack rotor system. The following conclusions have been drawn:

- Variation in stiffness has been observed clearly with the increase in crack depth whereas the stiffness of un-cracked rotor is optimum. However, when the depth of crack increases, the stiffness of the shaft drastically reduces.
- After creating the second crack, stiffness also reduces but the effect of second crack on the stiffness is found marginal. Stress concentration for the shaft is marginally affected at the middle crack.
- It has been observed that larger crack depth has the more significant effect on the shaft.

- Crack at mid of the rotor shaft has optimum effect on the stiffness as compared to the second crack, created at any other position of the shaft. Position of crack plays a significant parameter in multi-crack rotor detection.
- Since the damaged rotor shaft contains a component of nonlinearity, OROS system can even give better results when may be used for a real system.
- It has been clearly demonstrated that the natural frequency is reduced with the reduction in stiffness which may also cause resonance at very low excitation speed of the motor.
- The use of OROS system for crack detection can be conveniently applied with nonlinear models of multi-cracked rotor system.

References

[1] J. Wauer, On the dynamics of cracked rotors: a literature survey, Applied Mechanics Reviews 43 (1990) 13–17.
[2] R. Gasch, A survey of the dynamic behavior of a simple rotating shaft with a transverse crack, Journal of Sound and Vibration 160 (1983) 313–332.
[3] A.D. Dimarogonas, Vibration of cracked structure: a state of the art review, Engineering Fracture Mechanics, 55 (1996) 831-857.
[4] G. Sabnavis, R. G. Kirk, M. Kasarda, D Quinn, Cracked shaft detection and diagnosis: a literature review, Shock and Vibration digest, 36 (2004) 287-296.
[5] C.A. Papadopoulos, The strain energy release approach for modeling cracks in rotors: a state of the art review, Mechanical Systems and Signal Processing, 22 (2008) 763–789.
[6] C. Kumar, V. Rastogi, A brief review on dynamics of a cracked rotor, Inter-national Journal of Rotating Machinery, 2009, http://dx.doi.org/10.1155/2009/758108.
[7] Sekhar, A.S., Some recent studies on cracked rotors, IUTAM Symposium on Emerging Trends in Rotor Dynamics, IUTAM Conference Proceeding, 2011, pp. 491-503.
[8] A. S. Sekhar and P. Balaji Prasad, Dynamic analysis of a rotor system considering a slant crack in the shaft, Journal of Soundand Vibration, 208 (1997) 457–473.
[9] A. S. Sekhar, Vibration characteristics of a cracked rotor with two open cracks, Journal of Sound and Vibration, 223 (1999) 497–512.
[10] Mayes I. W., Davies W. G. R., Analysis of the Response of a Multi-Rotor-Bearing System Containing a Transverse Crack in a Rotor, Journal of Vibration, Acoustics, Stress, and Reliability in Design, 106 (1984) 139–145.
[11] A.C. Chasalevris, C.A. Papadopoulos, A continuous model approach for cross-coupled bending vibrations of a rotor-bearing system with a transverse breathing crack, Mechanism and Machine Theory, 44 (2009) 1176–1191.
[12] Zhou Tong, Xu Jianxue, Sun Zhengce, Dynamics of a Cracked Rotor with Some Comments on Crack Diagnosis, ASME Journal of Vibration and Acoustics, 123 (2001) 539–543.
[13] Amalendu Mukherjee, Vikas Rastogi, Anirvan Dasgupta, A Methodology for Finding Invariants of Motion for Asymmetric Systems with Gauge-Transformed Umbra Lagrangian Generated by Bond Graphs, Simulation, 82 (2006) 207-226.
[14] Amalendu Mukherjee, Vikas Rastogi, Anirvan Dasgupta, A Study of a Bi-symmetric Electro-mechanical System through Umbra-Lagrangian Generated by Bondgraphs, and Noether's Theorem, Simulation, 83 (2007) 611-630.
[15] Amalendu Mukherjee, Vikas Rastogi, Anirvan Dasgupta, Conservation laws for a gauge-variant umbra-Lagrangian in classical mechanics using bond graphs, 87 (2010) 301-312.
[16] Chandan Kumar, Vikas Rastogi, Vibration analysis of multi-rotor system through extended Lagrangian formalism, World Journal of Modelling and Simulation, 8 (2012) 103-110.
[17] Amalendu Mukherjee, Vikas Rastogi, Anirvan Dasgupta, Extension of Lagrangian–Hamiltonian mechanics for continuous systems-investigation of dynamics of a one-dimensional internally damped rotor driven through a dissipative coupling, Nonlinear Dynamics, 58 (2009) 107-127.
[18] Chandan Kumar, Investigation of Dynamics of cracked rotor through Extended Lagrangian Mechanics, Ph.D Thesis, SLIET, Longowal (2013)
[19] Tong Zhou, Zhengce Sun, Jianxue Xu and Weihua Han, Experimental analysis of cracked rotor, Journal of Dynamic Systems, Measurement and Control, 127(3) (2004) 313-320

J. Inst. Eng. India Ser. C
DOI 10.1007/s40032-016-0234-0

ORIGINAL CONTRIBUTION

Finite Element Modeling and Analysis of Powder Stream in Low Pressure Cold Spray Process

Tarun Goyal[1] · Ravinderjit Singh Walia[2] · Prince Sharma[3] · Tejinder Singh Sidhu[4]

Received: 10 September 2012 / Accepted: 15 April 2016

Abstract Low pressure cold gas dynamic spray (LPCGDS) is a coating process that utilize low pressure gas (5–10 bars instead of 25–30 bars) and the radial injection of powder instead of axial injection with the particle range (1–50 μm). In the LPCGDS process, pressurized compressed gas is accelerated to the critical velocity, which depends on length of the divergent section of nozzle, the propellant gas and particle characteristics, and the diameters ratio of the inlet and outer diameters. This paper presents finite element modeling (FEM) of powder stream in supersonic nozzle wherein adiabatic gas flow and expansion of gas occurs in uniform manner and the same is used to evaluate the resultant temperature and velocity contours during coating process. FEM analyses were performed using commercial finite volume package, ANSYS CFD FLUENT. The results are helpful to predict the characteristics of powder stream at the exit of the supersonic nozzle.

Keywords LPGDS · FEM · Modeling · CFD

✉ Tarun Goyal
goyaltarun1@gmail.com

[1] Shaheed Udham Singh (SUS) College of Engineering and Technology, Tangori, Mohali 140306, Punjab, India

[2] Delhi Technological University, New Delhi 110042, Delhi, India

[3] ISGEC Heavy Engineering Limited, Yamunanagar 135001, Haryana, India

[4] Shaheed Bhagat Singh State Technical Campus (SBSSTC), Ferozepur 152004, Punjab, India

Abbreviations

LPGDS	Low pressure gas dynamic spray
FEM	Finite element modeling
CGDS	Cold gas dynamic spray
CFD	Computational fluid dynamics

Notation

D_i	Inlet diameter
D_e	Outlet diameter
D_t	Throat diameter
L_u	Convergent length
L_d	Divergent section length
A, B, C, D, E, F, G, H	Key points for nozzle
Ω_f	Fluid region
Ω_e	Typical element
ρ_g	Density of the gas
δ_{ij}	Components of the identity tensor (Kronecker delta)
v_j	Velocity vector in the jth direction
τ_{ij}	The stress
g_i	The gravitational acceleration
μ_t	The turbulent viscosity
μ	The molecular viscosity
k_t	The kinetic energy of turbulence
ε	The dissipation of kinetic energy of turbulence
ω_i	The weight function
P_i	Pressure applied at the inlet of the nozzle MPa
x_1, x_2	Variable functions of the position at the axis
χ, α, Ψ	(Column) vectors of interpolation (shape) functions

Published online: 05 May 2016

Introduction

The cold-gas dynamic-spray process, often referred to as simply "cold spray," is a high-rate material deposition process in which fine, solid powder particles (generally 1–50 μm in diameter) are accelerated in a supersonic jet of compressed (carrier) gas to velocities in a range between 500 and 1000 m/s. As the solid particles impact the target surface, they undergo plastic deformation and bond to the surface, rapidly building up a layer of deposited material. A simple schematic of a typical cold-spray device is shown in Fig. 1.

In this process, pressurized compressed gas enters the device and flows through a converging/diverging nozzle to attain a supersonic velocity. The solid powder particles are metered into the gas flow upstream (high-pressure cold spray) or downstream (low-pressure cold spray) of the converging section of the nozzle and are accelerated by the rapidly expanding gas. To achieve higher gas flow velocities in the nozzle, the compressed gas is often preheated. However, while preheat temperatures as high as 900 K are sometimes used, due to the fact that the contact time of spray particles with the hot gas is quite short and that the gas rapidly cools as it expands in the diverging section of the nozzle, the temperature of the particles remains substantially below the initial gas preheat temperature and, hence, below the melting temperature of the powder material. The theory of bonding of particle/substrate and particle/particle is supported by a number of experimental findings such as:

- A wide range of ductile (metallic and polymeric) materials can be successfully cold-sprayed while non-ductile materials such as ceramics can be deposited only if they are co-cold-sprayed with a ductile (matrix) material [1].
- The mean deposition particle velocity should exceed a minimum (material-dependent) critical velocity to achieve deposition which suggests that sufficient kinetic energy must be available to plastically deform the solid material and/or disrupt the surface film [2].
- The particle kinetic energy at impact is typically significantly lower than the energy required to melt the particle suggesting that the deposition mechanism is primarily, or perhaps entirely, a solid-state process [3–6].

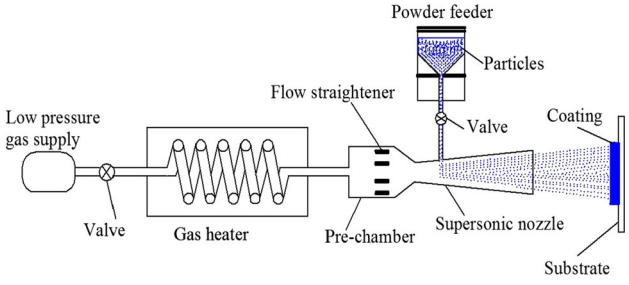

Fig. 1 Schematic of cold spray process [1]

Cold spray process have found wide applications in various types of the protective coating that provides a unique combination of properties which cannot be achieved by traditional structural materials. The cold spray process has good equipment performance, reliability and life expectancy. One of the promising methods of protection against environmental degradation such as wear, corrosion, erosion, abrasion, surface fatigue, oxidation etc. in modern engineering is CGDS [7]. In this research paper, finite element modeling (FEM) of adiabatic gas flow and expansion of gas occurring in uniform manner is made and the same is used to evaluate the resultant temperature, pressure and velocity contours during coating process. FEM analyses were performed using a commercial finite element package, ANSYS12.0 CFD FLUENT. The results obtained through the analyses are compared with the data available in the literature.

Modelling the Flow of Media in the lpgds Process Using Finite Element Modelling

The idea of using the CGDS as a coating technology was initially developed in the mid-1980s at the Institute for Theoretical and Applied Mechanics of the Siberian Division of the Russian Academy of Science in Novosibirsk [1, 8]. The Russian scientists successfully deposited a wide range of pure metals, metallic alloys, polymers, and composites onto a variety of substrate materials. In addition, they demonstrated that very high coating deposition rates of the order of 5 m^2/min ($\sim$300 ft^2/min) are attainable using the cold-spray process.

Dykhuizen and Smith [9] used an isentropic one-dimensional gas-flow model to calculate the particle velocity at the exit of the nozzle. A detailed analysis of the effects that the type of the carrier gas, the inlet gas temperature and the shape of the cold-spray nozzle have on the impact velocity of the feed-powder particles is carried out. While the one-dimensional model of Dykhuizen and Smith [9] has been found to be quite successful, its numerical nature does not enable an easy establishment of the relationships between the gas, process and feed-powder parameters on one side and the gas and the particle velocities at the nozzle exit and the velocity at which particles impact the substrate surface, on the other. The research also provides analytical equations that can be used to estimate the gas dynamics of the cold-spray process. Equations are also presented that allow calculation of the particle velocity. It is shown how the spray particle velocity depends on particle size and density, gas stagnation pressure, total gas temperature, gas

molecular weight, and nozzle shape. Use of the equations derived in this research allows determination of an optimal nozzle shape given the gas conditions, particle properties, and nozzle length. However, it is shown that the spray particle velocity is relatively insensitive to the nozzle shape. Thus, a single nozzle can be used for a variety of operational conditions.

Alkhimov et al. [10] derived an empirical equation for particle velocity based on the experimental data. Numerical and experimental research of wedge-shaped nozzles shows different types of nozzle dimensions for a given type of particles that produces the maximum possible particle velocity at the moment of impact on a target surface.

Grujicic et al. [11] were able to employ a one-dimensional model to predict the particle velocity at nozzle exit and particle behavior upon impact with a substrate during CGDS. One-dimensional models generally used to analyze the dynamics of dilute two-phase (feed-powder particles suspended in a carrier gas) flow during the cold-gas dynamic-spray process; require the use of numerical procedures to obtain solutions for the governing equations. The researchers also found that a relatively simple function is defined which relates the gas velocity at the nozzle exit with the nozzle expansion ratio and the carrier gas stagnation properties.

Li and Li [12] conducted numerical analysis for the accelerating behavior of spray particles in cold spraying using a computational fluid dynamics program, FLUENT. The optimal design of the spray gun nozzle is achieved based on simulation results to solve the problem of coating for the limited inner wall of a small cylinder or pipe. They found that the nozzle expansion ratio, particle size, accelerating gas type, operating pressure, and temperature are main factors influencing the accelerating behavior of spray particles in a limited space. Owing to the axi-symmetrical characteristic of the flow in this study, a two-dimensional model was used in this paper.

Jen et al. [13] reported the effect of friction on the gas dynamic flow through the CD nozzle. The effect of particle size on the acceleration of the particles was also reported. The acceleration process of micro scale and sub-micro scale copper (Cu) and platinum (Pt) particles inside and outside De-Laval-type nozzle is investigated. A numerical simulation is performed for the gas-particle two phase flows with particle diameter ranging from 100 nm to 50 μm, which are accelerated by carrier gas nitrogen and helium in a supersonic De-Laval-type nozzle. The carrier gas velocity and pressure distributions in the nozzle and outside the nozzle are illustrated.

Raletz et al. [14] begins with an overview of critical particle velocity under cold spray conditions. The system described in study makes it possible to simultaneously measure particle velocity and number of rebounds. They concluded that the particle velocities calculated with the one-dimensional isentropic model under the same operating conditions are close to the values found in the literature. The difference between predicted and experimental values arises from the use of real powders in the experiments and not ideal ones used in the model.

Li [15] made the comparison between the Convergent-Barrel (CB) and Convergent-Divergent (CD) nozzle. Nitrogen (N_2) was employed as driving gas at a pressure of 1.4 MPa and a temperature of 460 °C, and the spherical Cu particles of 20 μm in diameter were used. Author found that the main factors influencing significantly the particle velocity and temperature include the length and diameter of the barrel section, the nature of the accelerating gas its operating pressure and temperature, and the particle size when using a Convergent-Barrel (CB) nozzle. Particles achieve a relatively lower velocity but a higher temperature using the CB nozzle than a Convergent-Divergent (CD) nozzle under the same gas inlet pressure. The gas flow rate, and subsequently the operating cost for cold spraying, could be reduced.

Jodoin et al. [16] describes a framework for cold spray modeling and validation using an optical diagnostic method. In this study, an axi-symmetric two-dimensional mathematical model is presented which was used to predict the flow inside a cold spray nozzle as well as the particle velocity in the vicinity of the nozzle exit. The model results are compared with those obtained using the one-dimensional isentropic theory and with particle velocity measurements (using laser diagnostic techniques) made on a commercial cold spray system. The study has allowed coming to the following conclusions: The measured nozzle mass flow rate follows closely the overall behavior predicted by the one-dimensional isentropic theory. The predictions of the axi-symmetric two-dimensional mathematical model are more accurate than the one-dimensional approach due to the inclusion of viscous effects in the model. The proposed model is more accurate than the one dimensional theory in predicting the particle velocity inside the nozzle and in the free exiting jet. It is concluded that this is due to the proper treatment of the shock waves in the nozzle by the proposed model. For the two propellant gases used (helium and nitrogen), the proposed model predicts oblique shock waves in the diverging section of the nozzle. The shocks reduce drastically the gas velocity and Mach number while the gas temperature and pressure are increased sharply. The proposed model results reveal that the maximum gas velocity is always reached just in front of the first oblique shock wave. With the use of nitrogen as the propellant gas, the jet has a lower gas velocity and takes longer to reach the aerodynamic equilibrium state (jet pressure equal to external pressure). The experimental study reveals that increasing the stagnation temperature or pressure leads to an increase in particle velocity. The values predicted by the proposed model are close to the measured

ones, confirming that the mathematical model is accurate even in the presence of shock waves.

Li [17] carried out simulations using FLUENT to study the effect of throat & exit area and diverging section length on the particle flow and to optimize the nozzle design for different inlet conditions. Numerical modeling was performed by using commercial software FLUENT (Ver. 6.1) to determine the flow field of driving gas inside and outside the nozzle, and subsequently the acceleration of particles in cold spraying. It was concluded that the optimization of nozzle exit diameter is influenced by the gas conditions, particle size, and nozzle divergent section length and throat diameter.

Pardhasaradhi et al. [18] employs a one-dimensional isentropic gas flow model in conjunction with a particle acceleration model to calculate particle velocities. A laser illumination-based optical diagnostic system is used for validation studies to determine the particle velocity at the nozzle exit for a wide range of process and feedstock parameters such as stagnation temperature, stagnation pressure, powder feed rate, particle size and density. The relative influence of process and feedstock parameters on particle velocity is presented in this work. It was found that the stagnation temperature have greater influence on particle velocity in comparison to stagnation pressure and powder feed rate (particle loading) have negligible effect on particle velocity for the range employed in the present study due to the lower particle concentrations in the present study.

Lupoi and O'Neill [19] analyzed the powder stream characteristics in CGS supersonic nozzles. The powder injection location was varied within the carrier gas flow, along with the geometry of the powder injector, in order to identify their relation with particles trajectories. Computational fluid dynamic (CFD) results are presented along with experimental observations. Three nozzles configurations were examined, characterized by a different acceleration channel lengths and powder injector's geometry and locations. When powder is released axially and upstream the nozzle throat, particles trajectories do not stay close to the centre line, but tend to spread over the entire volume of the channel. The particle stream diameter at impact with substrate is comparable with the nozzle exit cross-section diameter. A theoretical (CFD) analysis has shown that one of the reasons for this effect is a relatively high gas turbulence level generated at the vicinity of the nozzle throat. The beam geometry by the CFD results compares well against experimental observations. On the other hand, when powder is released axially and straight into the supersonic region of the nozzle, a more focused stream can be achieved. In this case, CFD results were in accordance with the experiments, but failed to provide an accurate prediction of the powder beam geometry.

The mathematical representation of the flow through nozzle in the LPGDS process involves the continuity, momentum, and constitutive equations [1, 20]. The following assumptions are made to simplify the analysis in the present research:

Assumptions

The gas flow model uses isentropic relationships and linear nozzle geometry. The assumptions for the calculation are as follows:

1. The gas obeys the ideal gas law.
2. There is no friction impeding the gas flow.
3. The gas flow is adiabatic, i.e., no heat exchange occurs with the surroundings.
4. Steady-state conditions exist.
5. Expansion of the gas occurs in a uniform manner without shock or discontinuities.
6. Flow through the nozzle is one-dimensional.
7. Particles do not influence gas conditions.
8. Collision between particles is neglected.
9. The effect of the presence of particles does not affect the space charge.
10. The formation of thin coating does not affect thermo fluid field locally in the impinging region.

The equations are written for a fluid region Ω_f using the Cartesian coordinate system x_i in Eulerian reference frame, with the subscript (or index), $i = 1, 2, 3$ or 1 and 2 for two-dimensional problems, where all the variables may be functions of the position $x = x_1, x_2$.

The Governing Equations for Flow Through the Nozzle in LPGDS Process

The following governing equations are used for finite element modeling (FEM) for the flow in the LPGDS process [3].

Continuity Equation (Conservation of Mass)

According to the law of conservation of mass, the total time rate of change of mass in a fixed region is zero. The conservation equations used for turbulent flow are obtained from those of laminar flow using a time averaging procedure commonly known as Reynolds averaging [20]. It can be stated as

$$\left(\frac{\partial}{\partial x_j}\left(\rho_g v_j\right)\right) = 0 \tag{1}$$

where ρ_g is the density of the gas, and v_j is the velocity vector in the jth direction.

Momentum Equation (Conservation of Momentum)

The law of conservation of linear momentum states that the total time rate of change of linear momentum is equal to

the sum of the external forces acting on the region. Appling this law for the LPGDS process gives:

$$\rho_g\left(\frac{\partial V_i}{\partial t}+v_j\frac{\partial V_i}{\partial X_j}\right)=-\frac{\partial p}{\partial x_j}+\frac{\partial \tau_{ij}}{\partial x_j}+\rho_g g_i \tag{2}$$

where τ_{ij} is the stress and g_i is the gravitational acceleration.

Constitutive Equation

It is necessary to specify the relation between the state of stress and the history of the flow in order to obtain a closed set of equations. Such a relation is known as a constitutive equation. In the case of a Newtonian fluid, the state of stress depends only on the instantaneous local rate of strain; the extra stress is proportional to the rate of strain tensor.

The stress is given by

$$\tau_{ij}=\left[(\mu+\mu_t)\left[\frac{\partial V_i}{\partial X_j}+\frac{\partial V_j}{\partial X_i}\right]-\frac{2}{3}\mu_t\frac{\partial V_i}{\partial X_i}.\,\delta i_j\right] \tag{3}$$

where μ is the molecular viscosity and $\delta_{ij}=1$ for $i=j$; otherwise $\delta_{ij}=0$. μ_t is the turbulent viscosity given by $\mu_t=\rho_g C\mu\frac{K_t^2}{\varepsilon}$ where $C=0.09$ is a constant, k_t is the kinetic energy of turbulence, and ε is the dissipation of kinetic energy of turbulence. This constitutive equation predicts, in particular, that the stress responds instantaneously to any deformation and has no memory; the stress vanishes as soon as the driving motion has ceased.

$$\rho_{g.}\frac{\partial V_j}{\partial x_j}=0 \tag{4}$$

From Eqs. (2) and (3), we get as

$$\rho_g\left(\frac{\partial V_i}{\partial t}+V_j\frac{\partial V_i}{\partial X_j}\right)+\frac{\partial p}{\partial x_j}-\frac{\partial}{\partial x_j}\left[(\mu+\mu_t)\left[\frac{\partial V_i}{\partial X_j}+\frac{\partial V_j}{\partial X_i}\right]-\frac{2}{3}\mu_t\frac{\partial V_i}{\partial X_i}.\,\delta_{ij}\right]-\rho_{g.}g_i=0$$

On solving we get:

$$\rho_g\left[V_j.\frac{\partial V_i}{\partial X_j}\right]+\frac{\partial p}{\partial x_j}-\frac{\partial}{\partial x_j}\left[(\mu+\mu_t)\left[\frac{\partial V_i}{\partial X_j}+\frac{\partial V_j}{\partial X_i}\right]\right]-\rho_g g_i=0 \tag{5}$$

Mixed Finite Element Model

Weak Form

The starting point for the development of the finite element models of Eqs. (4), (5) to (3) is their weak form, where ω_i is the weight function, which will be equated, in the Rayleigh–Ritz–Galerkin finite element models to the interpolation function used for (p, u, t) respectively [21, 22]. The weighted integral statements of two equations over a typical element Ω_e are given by

$$\int\rho_g\frac{\partial v_j}{\partial x_j}\cdot\,\omega_1.dx=0 \tag{6}$$

The weak form for = n 5 is written as:

$$\int_{\Omega_e}\omega_2\left[\rho_g\left(\frac{\partial V_i}{\partial t}+V_j\frac{\partial V_i}{\partial X_j}\right)+\frac{\partial p}{\partial x_j}-\frac{\partial}{\partial x_j}\left[(\mu+\mu_t)\left[\frac{\partial V_i}{\partial X_j}+\frac{\partial V_j}{\partial X_i}\right]-\frac{2}{3}\mu_t\frac{\partial V_i}{\partial X_i}\delta_{ij}\right]-\rho_g g_i\right].dx=\int_{\Omega_e}\Gamma\omega_2.ds \tag{7}$$

$$\int_{\Omega_e}\omega_2\rho_g V_j\frac{\partial V_i}{\partial X_j})+\int_{\Omega_e}\frac{\partial\omega_2}{\partial x_j}.p.dx-\int_{\Omega_e}\frac{\partial\omega_2}{\partial x_j}(\mu+\mu_t)\frac{\partial V_i}{\partial X_j}.dx-\int_{\Omega_e}\frac{\partial\omega_2}{\partial x_j}(\mu+\mu_t)\frac{\partial V_j}{\partial X_i}.dx-\int_{\Omega_e}\omega_2\rho_g g_i.dx=\int_{\Omega_e}\Gamma\omega_2.ds \tag{8}$$

On constitutive equation:

$$\int_{\Omega_e}\omega_3\left[\tau_{ij}-\left[(\mu+\mu_t)\left[\frac{\partial V_i}{\partial X_j}+\frac{\partial V_j}{\partial X_i}\right]+\frac{2}{3}\mu_t\frac{\partial V_i}{\partial X_i}.\delta_{ij}\right].dx=0\right. \tag{9}$$

$$\int_{\Omega_e}\omega_3\tau_{ij}.dx-\int_{\Omega_e}\omega_3\left[(\mu+\mu_t)\left[\frac{\partial V_i}{\partial X_j}\right].dx-\int_{\Omega_e}\omega_3\left[(\mu+\mu_t)\left[\frac{\partial V_j}{\partial X_i}\right].dx+\int_{\Omega_e}\omega_3\frac{2}{3}\mu_t\frac{\partial V_i}{\partial X_i}.\delta_{ij}.dx=0\right.\right. \tag{10}$$

Finite Element Model

For the Rayleigh–Ritz–Galerkin finite element models, the choice of weight functions is restricted to spaces of approximation functions used for the velocity fields, pressure, and extra stresses [21, 22]. Suppose that the dependent variables (u_i, p_i, τ_{ij}) are approximated by expressions of the form.

$$V_i=\Sigma\alpha_1 V_j=\alpha^T V_j \tag{11a}$$

$$V_j=\Sigma\alpha_1 V_i=\alpha^T V_i \tag{11b}$$

$$P_i=\Sigma\gamma_m p_m=\gamma^T p \tag{11c}$$

$$\tau_{ij}=\Sigma\Psi^n\tau_{ij}^n=\Psi^T\tau_{ij} \tag{11d}$$

The weight functions (ω_1, ω_2, ω_3) have the following correspondence:

$$\omega_1\approx\chi^m \tag{12c}$$

$$\omega_2\approx\alpha_1 \tag{12c}$$

$$\omega_3\approx\Psi^n \tag{12c}$$

Substitution of Eqs. (11) and (12) in Eqs. (6), (8), (10) results in the following finite element equations:

(a) Continuity equation:

$$\int_{\Omega_e} \rho_g \frac{\partial \alpha^T}{\partial x_j}.\gamma.dx = 0 \tag{13}$$

(b) Momentum:

$$\int_{\Omega_e}\left[\alpha\rho_g V_j \frac{\partial \alpha^T}{\partial X_j}.dx\right].V_i + \int_{\Omega_e}\left[\frac{\partial \alpha}{\partial x_j}\right]\gamma^T.dx.p - \int_{\Omega_e}\left[\frac{\partial \alpha}{\partial x_j}(\mu+\mu_t)\frac{\partial \alpha^T}{\partial x_j}.dx\right]V_j - \int_{\Omega_e}\left[\frac{\partial \alpha}{\partial x_j}(\mu+\mu_t)\frac{\partial \alpha^T}{\partial X_i}.dx\right]V_i - \int_{\Omega_e}\left[\alpha\rho_g g_i.dx\right] = \int_{\Omega_e} \Gamma\alpha.ds \tag{14}$$

(c) Constitutive:

$$\int_{\Omega_e} \Psi\Psi^T\tau_{ij}.dx - \int_{\Omega_e}\Psi\left[(\mu+\mu_t)\left[\frac{\partial \alpha^T}{\partial X_j}\right].\mathrm{dx}\right]\mathrm{V_j} - \int_{\Omega_e}\Psi\left[(\mu+\mu_t)\left[\frac{\partial \alpha^T}{\partial X_i}\right].dx\right].\mathrm{V_i} + \int_{\Omega_e}\left[\Psi\frac{2}{3}\mu_t\frac{\partial \alpha^T}{\partial X_i}\delta_{ij}.dx\right]\mathrm{V_j} = 0 \tag{15}$$

The discrete system is given by the following matrix equations, here the momentum and continuity equations are written as a single system:

$$\begin{bmatrix} c_i u_i & 0 & 0 \\ 0 & c_i u_i & 0 \\ 0 & 0 & 0 \end{bmatrix}\begin{bmatrix} V_i \\ V_j \\ p \end{bmatrix} + \begin{bmatrix} 2K_{11}+K_{22} & K_{21} & Q_1 \\ K_{22} & K_{11}+2K_{22} & Q_2 \\ Q_1^T & Q_2^T & 0 \end{bmatrix}\begin{bmatrix} V_I \\ V_J \\ p \end{bmatrix} = \begin{bmatrix} F_1 \\ F_2 \\ 0 \end{bmatrix} \tag{16}$$

And for the constitutive equation:

$$\begin{bmatrix} N & 0 & 0 \\ 0 & N & 0 \\ 0 & 0 & N \end{bmatrix}\begin{bmatrix} \tau_{11} \\ \tau_{22} \\ \tau_{12} \end{bmatrix} - \begin{bmatrix} 2L_1 & 0 & 0 \\ 0 & 2L_2 & 0 \\ 0 & 0 & 0 \end{bmatrix}\begin{bmatrix} V_i \\ V_j \\ p \end{bmatrix} + \begin{bmatrix} D_1 & 0 & 0 \\ 0 & D_2 & 0 \\ 0 & 0 & 0 \end{bmatrix}\begin{bmatrix} V_i \\ V_j \\ p \end{bmatrix} = \begin{bmatrix} 0 \\ 0 \\ 0 \end{bmatrix} \tag{17}$$

where the sum on the repeated indices is implied. The coefficient matrix shown in the Eqs. (16) and (17) are defined by:

$$\mathrm{K_{11}} = \left(2\mathrm{S}^{11}+\mathrm{S}^{22}\right)(\mu+\mu_t)$$

$$\mathrm{K_{22}} = \left(\mathrm{S}^{11}+2\mathrm{S}^{22}\right)(\mu+\mu_t)$$

$$\mathrm{K_{21}} = [\mathrm{K_{12}}]^{\mathrm{T}}$$

$$C_i U_i = \int_{\Omega_e} \alpha\rho_g V_j.\frac{\partial \alpha^T}{\partial x_j}.\mathrm{dx}$$

$$Q = \int_{\Omega_e}\left[\frac{\partial \alpha}{\partial x_j}\right]\gamma^T.dx$$

$$S_{ij}^{11} = \int_{\Omega_e}\frac{\partial \alpha}{\partial x_j}(\mu+\mu_t)\frac{\partial \alpha^T}{\partial x_j}.dx$$

$$F_i = \int_{\Omega_e}\Gamma\alpha.ds + \int_{\Omega_e}\left[\alpha\rho_g g_i.dx\right]$$

$$\mathrm{N} = \int_{\Omega_e}\Psi\Psi^T.dx$$

$$L_1 = \int_{\Omega_e}\Psi\left[(\mu+\mu_t)\left[\frac{\partial \alpha^T}{\partial X_j}\right].\mathrm{dx}\right]$$

$$D_1 = \int_{\Omega_e}\left[\Psi\frac{2}{3}\mu_t\frac{\partial \alpha^T}{\partial X_i}.\delta_{ij}.dx\right]$$

The Eqs. (16) and (17) becomes

$$\mathrm{C(u)} + \mathrm{KU} = \mathrm{F} \tag{18}$$

$$\mathrm{N}\tau - \mathrm{LU} + \mathrm{DU} = 0 \tag{19}$$

where the vector of unknowns is $\mathrm{U^T} = \{\mathrm{V_i}, \mathrm{V_j}, \mathrm{P}\}$. Equations (18) and (19) represent the finite element equation for flow through nozzle in the LPGDS process in the steady state case. Equation (18) is recognized as the standard form for a Newtonian problem used to calculate the velocity and pressure value [21, 22]. Equation (19) is the finite element analogue of the implicit constitutive equation and is seen as an equation analogue of the extra stress. A stability condition for the resulting matrix problem requires that the extra stresses be approximated to the same order as the velocity components. The Eqs. (18) and (19) are solved after substitution of the boundary conditions.

Boundary Conditions

The boundary conditions described for flow through nozzle in the LPGDS process (Fig. 2) are as given below:

1. At the inlet 1 of the nozzle:
   $\mathrm{P} = \mathrm{P_i}$, $\mathrm{T} = \mathrm{T_i}$
2. At the inlet 2 of the nozzle:
   $\mathrm{M} = \mathrm{M_i}$ with gravity feeder.
3. The outlet of nozzle:
   $\mathrm{P} = \mathrm{P_o}$, $\mathrm{V} = \mathrm{V_O}$,$\mathrm{T} = \mathrm{T_o}$
4. At the nozzle surface:
   $\mathrm{V_{x1}} = 0$

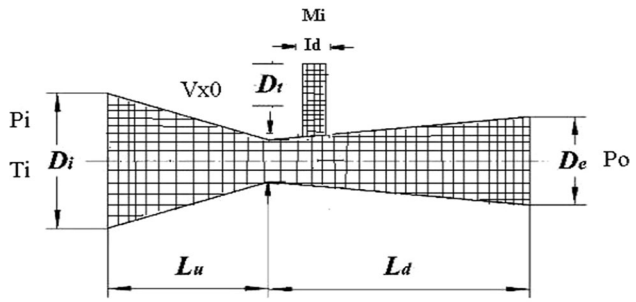

Fig. 2 Schematic flow through nozzle in LPGDS processes (domain and finite element mesh)

Nozzle Configurations

Six different types of nozzles are under investigation in this research work. In all these configurations the powder is injected axially just starting the divergent section of the nozzle. The inlet operating conditions for the entire configuration are same to measure the output conditions of different nozzle configurations (shown in Table 1).

Where Di, D_t, D_e, L_u, L_d are the inlet, throat, outlet diameter, length of convergent section and the length of the divergent sections respectively. The inlet pressure (P_i) at the nozzle is 1 MPa, and the mass flow rate (M_i) is 0.05 gs^{-1}. The nozzle surface is assumed to be the wall surface having no slip. The powder is fed through the injector by mean of gravity feeder. The pressure P_o, velocity V_o and temperature T_o is to be measured at the outlet of the nozzle.

Results and Discussion

The simulation procedure involves the determination of velocity and temperature through the nozzle. The velocity and temperature distribution were analyzed by the finite element method using the ANSYS 12.0 having module FLUENT 12.0 [23]. The resultant temperature and the velocity of flow during the process cycle were determined.

At the first instant, a model has been built using ANSYS 12.0 [24] software considering the pressure inlet for the air and the mass flow inlet for the injector. The mesh file for the nozzle was also created in ANSYS 12.0 and defining the boundary conditions. Then CFD software FLUENT 12.0 (ANSYS 12.0) was used for the solving process. Since in the finite element analysis, the results are available only on the nodes, the geometry of the problem is meshed such that the nodes can be found on the locations where the values of the degree of freedom (flow velocity and temperature) are needed. A finer meshing is required in the regions where the changes in gradients of the degree of freedom are higher. For fulfilling all these requirements, the quadilateral meshing is used for meshing the geometry. In the solution procedure, Eulerian multiphase model is used, with the viscous K-ε model.

Table 1 Nozzle configurations selected for the investigation

Configuration	Symbols	Unit	N1	N2	N3	N4	N5	N6
Inlet diameter	D_i	mm	8	16	8	22	20	8
Throat diameter	D_t	mm	4	3	2	2	4	2
Outlet diameter	D_e	mm	6	6	6	6	4.6	6.3
Convergent length	L_u	mm	50	30	28	30	17	10
Divergent length	L_d	mm	125	140	72	180	70	120
Injector diameter	Id	mm	6	4	6	2	0.9	6
Literature Reference nos.			25	12	25	19	19	26

For Nozzle N1

Velocity Distribution

The patterns of velocity distribution obtained using FLUENT 12.0 (ANSYS 12.0) shown in Fig. 3a indicates the flow with maximum velocity near the throat section of the nozzle and the velocity decreases non-linearly. Different colors (or shades) indicate different values of the velocity. Figure 3a show the distribution of the velocity in the nozzle. The velocity at the inlet of nozzle is low and has maximum value at throat section. The velocity at the outlet of the nozzle is about 945 ms^{-1}.

Temperature Distribution

Figure 3b shows the temperature distribution through the LPGDS nozzle. The contours of the temperature are shown through the nozzle. It shows that the temp at inlet is maximum and when the powder material mixes with the carrier gas, the powder is at room temperature. The critical temperature is attained at the outside of nozzle. The measured temperature at the outlet of the nozzle is 555 K.

For Nozzle N2

Velocity Distribution

Figure 4a shows the velocity distribution through the nozzle N2 having configuration in the Table 1. It shows that the velocity near about the throat is maximum and the final velocity attained is near about 700 ms^{-1}.

Temperature Distribution

Figure 4b shows the distribution of temperature through the nozzle along the length. The temperature of the carrier gas at the inlet of nozzle is about 623 K and the

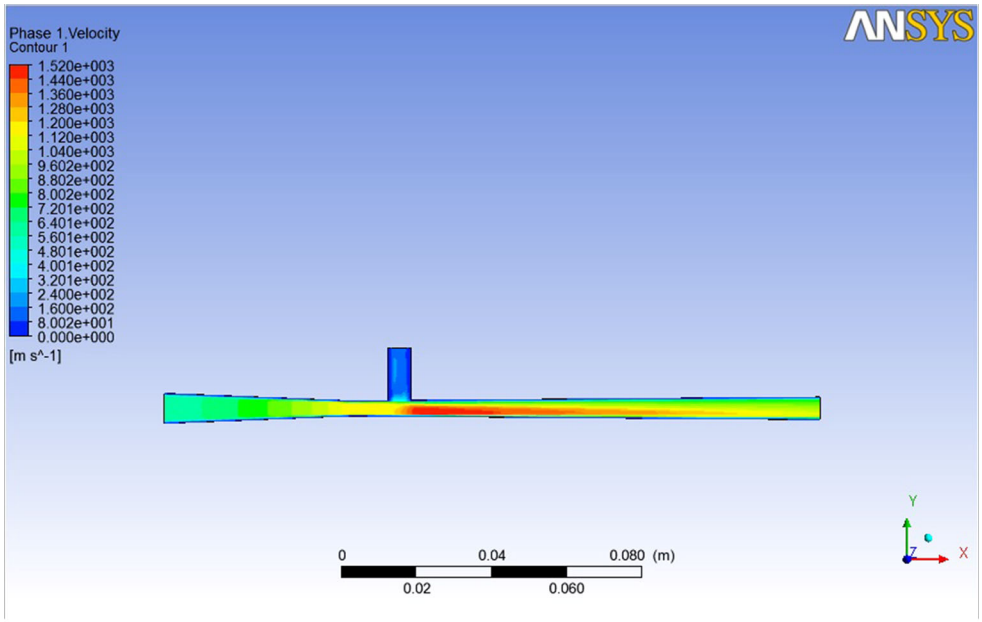

(a)

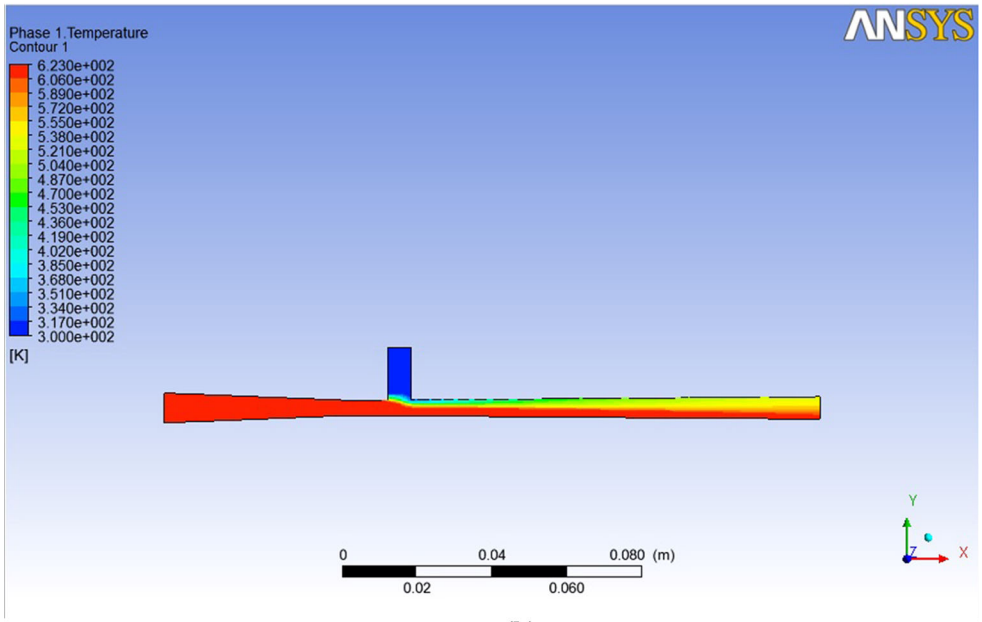

(b)

Fig. 3 Velocity and temperature distribution through the nozzle N1

powder material is at the room temperature. The outlet temperature for the mixture at the exit of the nozzle is 548 K.

For Nozzle N3

Velocity Distribution

Figure 5a shows the velocity distribution through the nozzle N3, whose geometrical configuration is discussed in Table 1. The different colors of flow through the nozzle show the values of the velocity at the various parts of the nozzle. The velocity calculated at the outlet of the nozzle is about 550 ms^{-1}.

Temperature Distribution

Figure 5b shows the temperature distribution through the nozzle at the different sections of the nozzle. It shows higher temperature at the inlet and the critical temperature at the outlet of the nozzle. The temperature at the outlet of the nozzle is about 520 K.

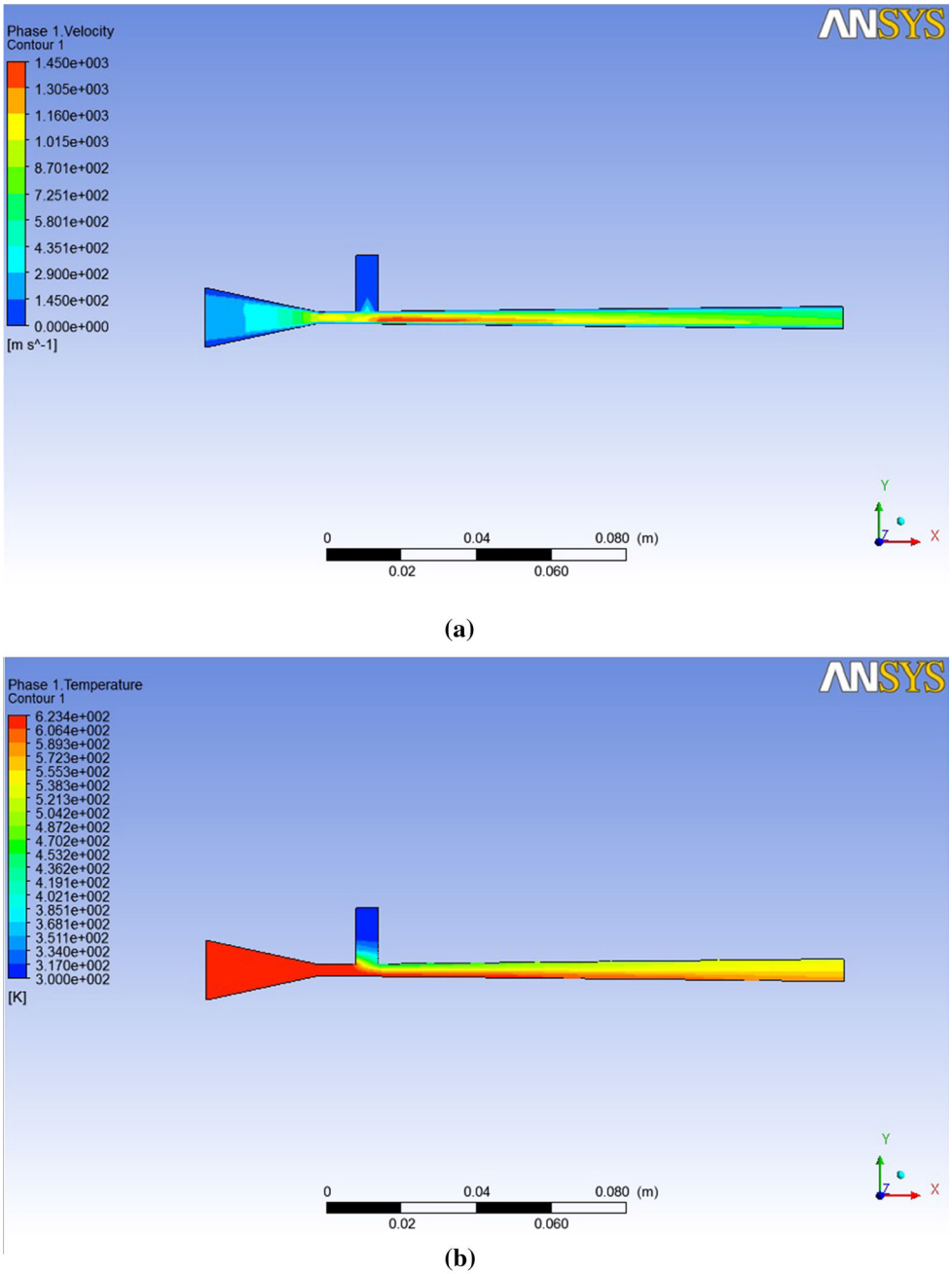

Fig. 4 Velocity and temperature distribution through nozzle N2

For Nozzle N4

Velocity Distribution

Figure 6a shows the velocity distribution through the nozzle N4. It shows that the flow attains very high velocity at the throat of the nozzle and is low at the outlet. The velocity measured at the outlet of the nozzle is about 510 ms^{-1}.

Temperature Distribution

Figure 6b shows that the inlet temperature is the temperature of the carrier gas. The powder material is mixed at room temperature with the air and the outlet temperature is less than the inlet temperature. The temperature at the outlet of the nozzle N4 is 530 K.

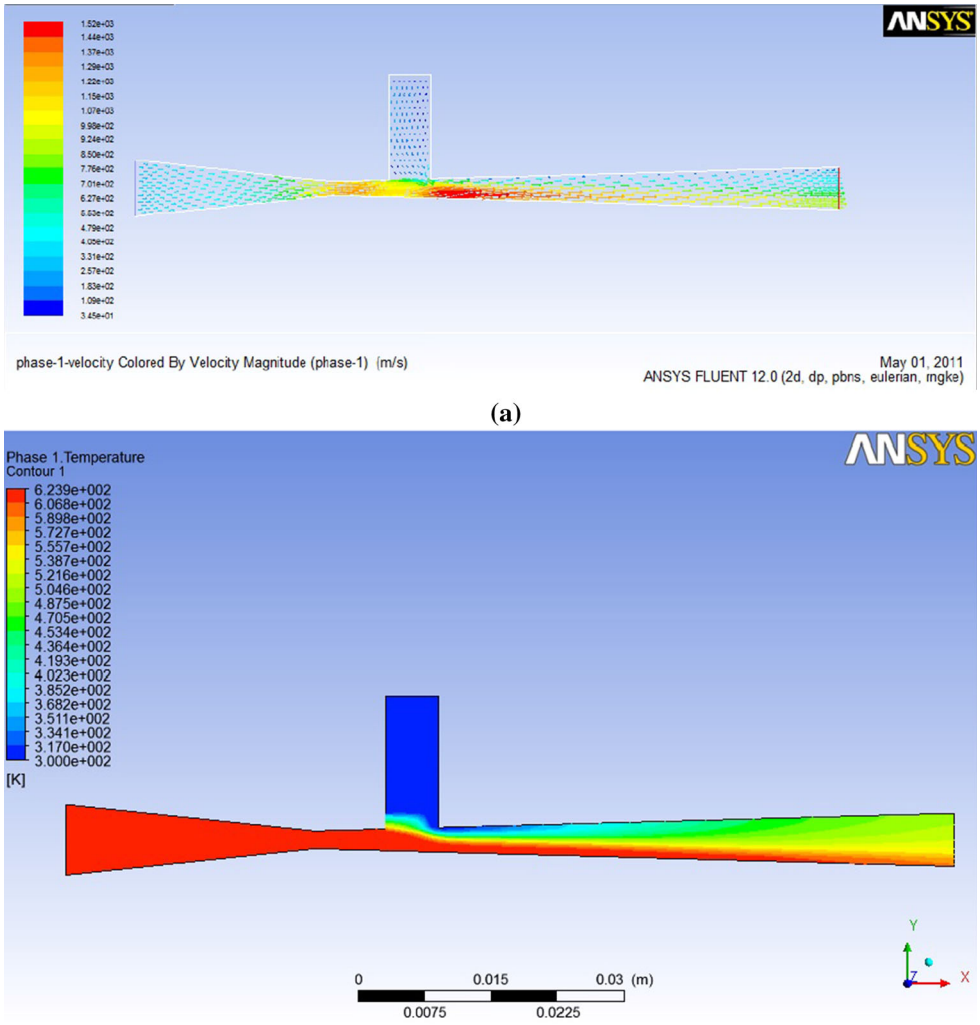

Fig. 5 Velocity and temperature distribution through the nozzle N3

For Nozzle N5

Velocity Distribution

Figure 7a shows the velocity distribution through the nozzle N5. It shows that the flow attains very high velocity at the outlet of the nozzle which is due to small injector diameter. The velocity at the outlet of the nozzle is 1100 ms^{-1}.

Temperature Distribution

Figure 7b shows the distribution of the temperature through the nozzle. The different colors show the different values of the temperature through the nozzle. Temperature at the outlet of the nozzle is 540 K.

For Nozzle N6

Velocity Distribution

Figure 8a shows the velocity distribution through the nozzle N6. The different colors show the different values of velocity at different positions. The velocity at the outlet of the nozzle is 540 ms^{-1}.

Temperature Distribution

Figure 8b shows the distribution of the temperature for the flow through the nozzle. The different colors show different values of the temperature through the nozzle. Temperature at the outlet of the nozzle is 530 K.

Table 2 presents the comparison of outlet velocity and temperature for the nozzle configurations under study.

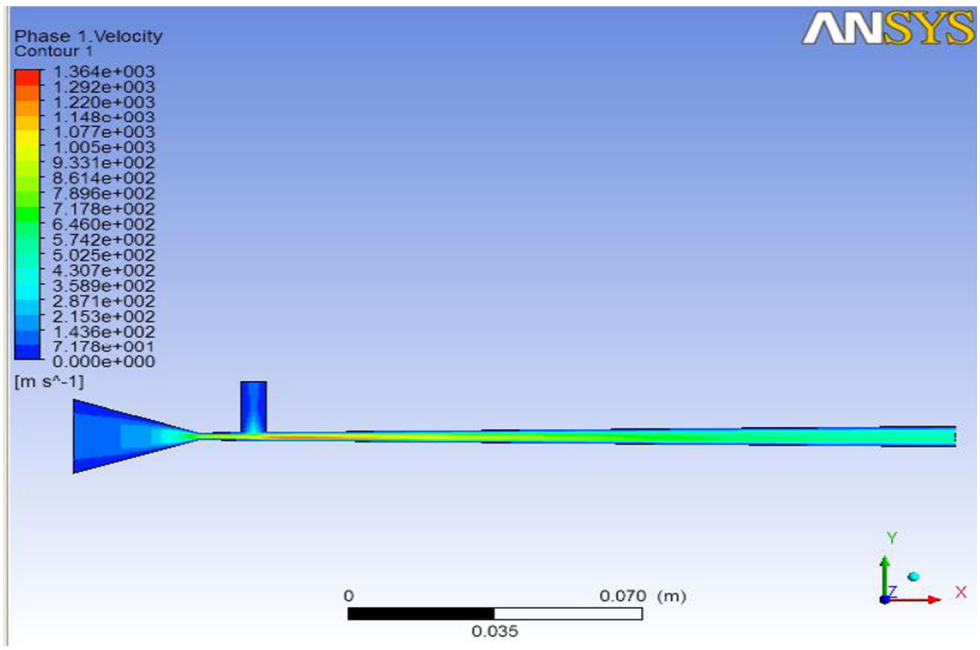

(a)

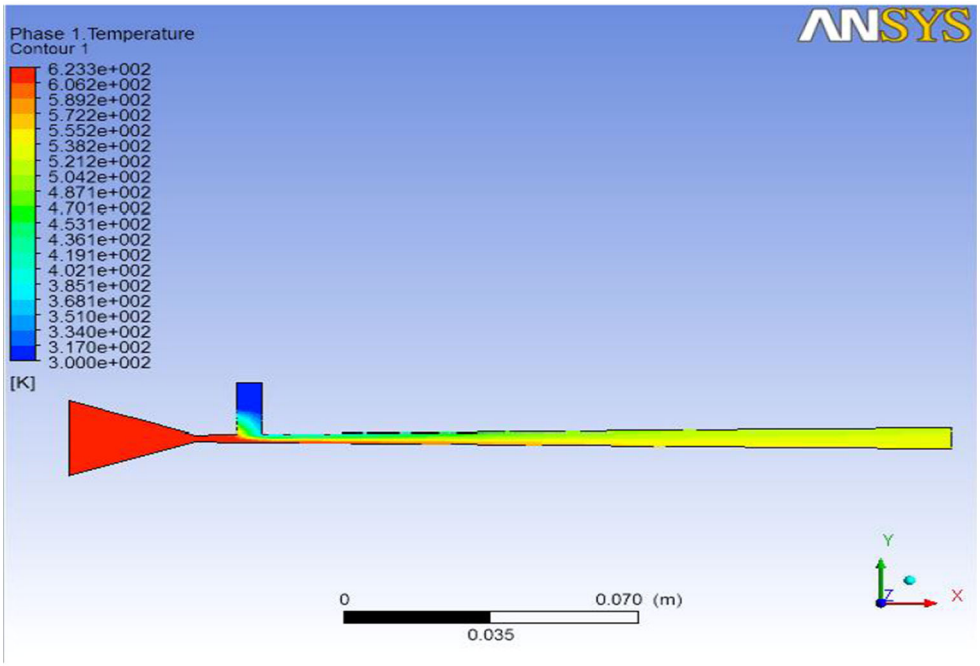

(b)

Fig. 6 Velocity and temperature distribution through the nozzle N4

From the values it had been found that nozzle N4 and N6 are optimum according to the study because there is a proper mixing of powder particles with the carrier gas as a result of which the momentum and heat transfer from the gas to the particle takes place. In the nozzle N3 there is not proper mixing of the powder material due to shorter length of the divergent section. Moreover the pressure at the section of powder injection is below atmospheric which shows that this pressure gradient helps the powder enter the nozzle from the powder feeder under the action of gravity resulting in higher velocity of the powder particles at the exit of the nozzle.

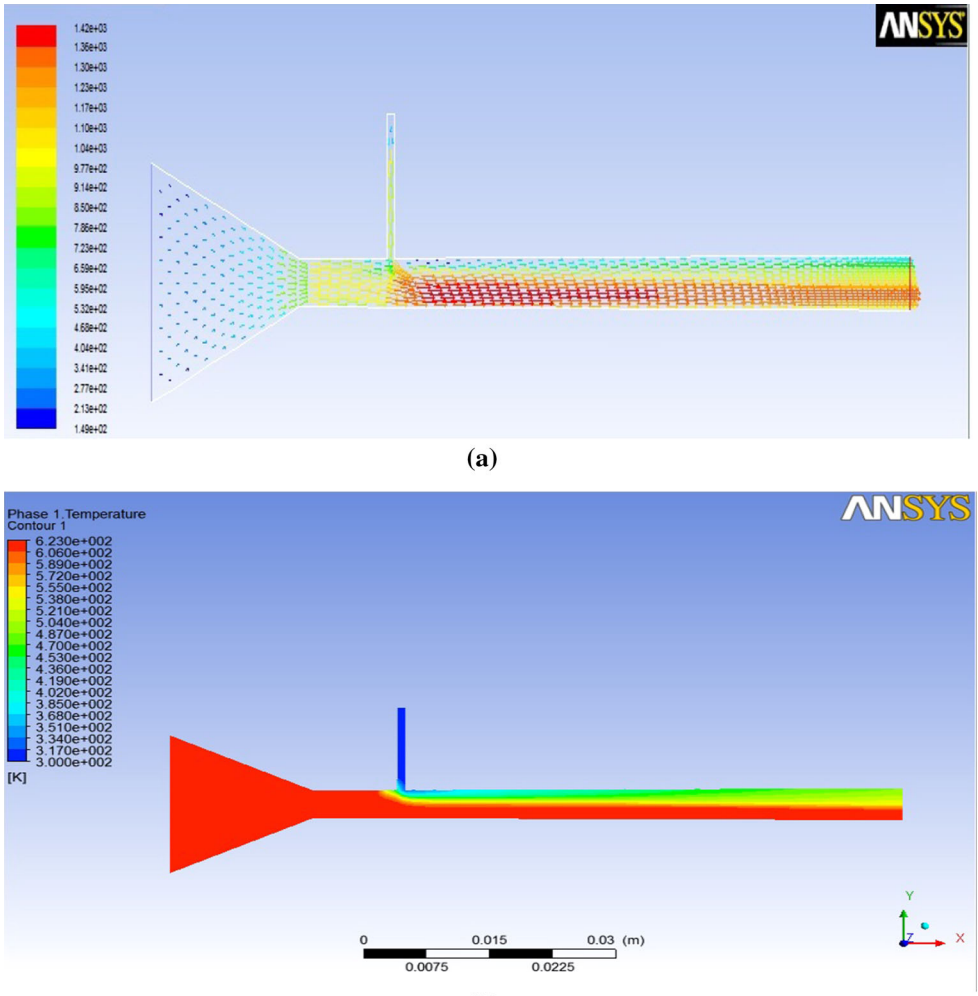

Fig. 7 Velocity and temperature distribution through the nozzle N5

Conclusion

In the present paper, a model for the flow through nozzle in LPGDS process is developed and solved by the finite element method and FLUENT 12 software respectively. The conclusions drawn from the present work are as follows:

- The results of this work show that the flow through the LPGDS process can be successfully simulated by the finite element method in predicting the resultant pressure, velocity and temperature. They can be further used to predict the coating quality during a process cycle with reasonable accuracy.
- The velocity of the carrier gas is frequently increased at the throat section, and the pressure is less than the atmospheric pressure when the powder is injected into the nozzle. The powder gets carried away with the carrier gas i.e. air.
- Model provides an estimate of velocity and temperature at the exit of the nozzle which may be validated using experimental techniques of velocity, pressure and temperature measurements.

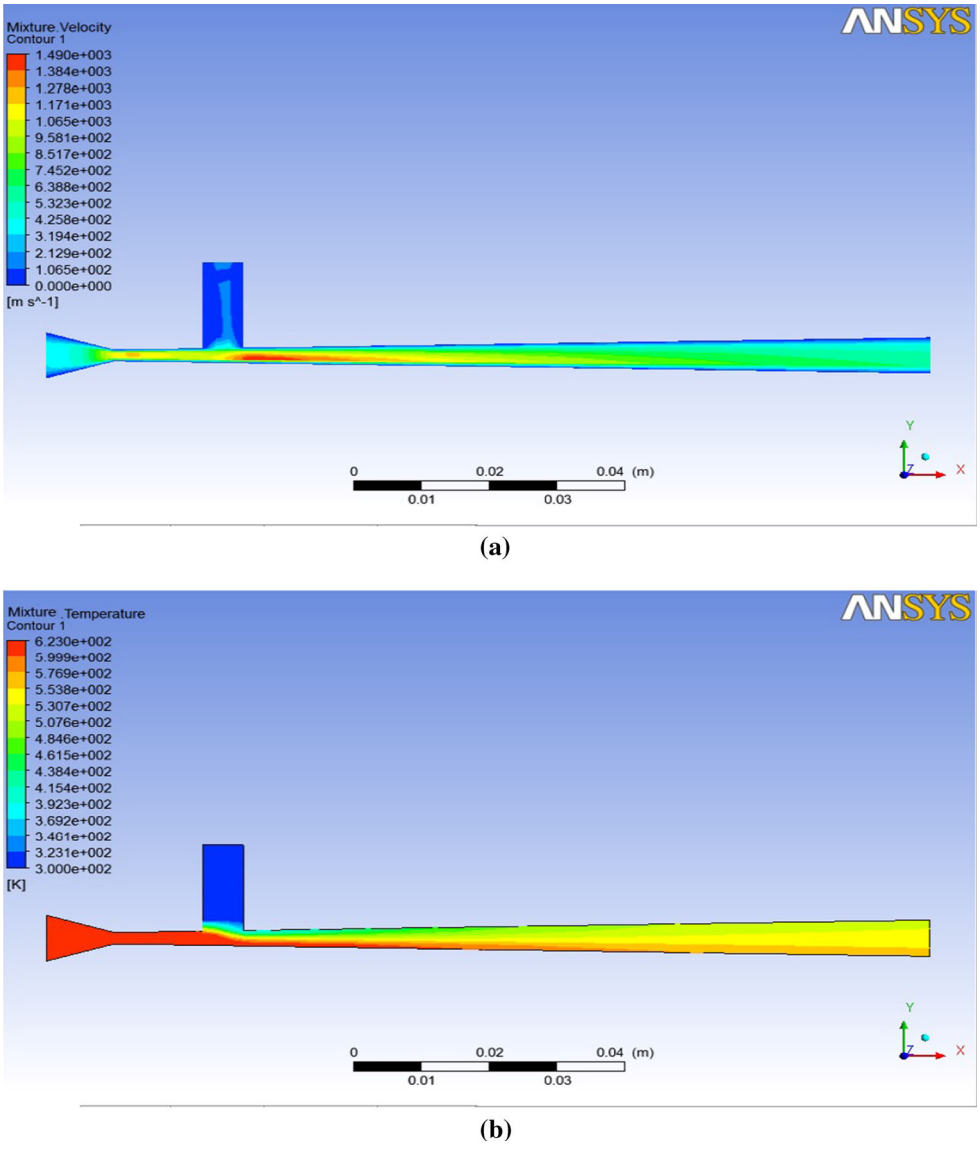

Fig. 8 Velocity and temperature distribution through the nozzle N6

Table 2 Comparison of chosen nozzles in tabular form

Nozzles	Inlet conditions at boundary 1			Inlet conditions at boundary 2				Outlet condition predicted at boundary 3	
	Carrier gas	P_i (bar)	T_i (K)	Powder material	Size (μm)	M_i (gs^{-1})	T_{i2} (K)	V_o (ms^{-1})	T_o (K)
N1	Air	10	623	Cu	50	0.05	300	945	555
N2	Air	10	623	Cu	50	0.05	300	680	548
N3	Air	10	623	Cu	50	0.05	300	550	520
N4	Air	10	623	Cu	50	0.05	300	510	530
N5	Air	10	623	Cu	50	0.05	300	1100	540
N6	Air	10	623	Cu	50	0.05	300	540	530

- Model helps to predict the velocity, and temperature at the exit of supersonic nozzle used in LPCGDS set-up. Further, the study can be extended to predict the parameter just on impact to the substrate.

References

1. A.O. Tokarev, Structure of aluminum powder coatings prepared by cold gas dynamic spraying. Met. Sci. Heat Treat. **38**(3), 136–139 (1996)
2. R.C. McCune, A.N. Papyrin, J.N. Hall, W.L. Riggs, P.H. Zajchowski, C.C. Berndt, S. Sampath, *An exploration of the cold gas-dynamic spray method for several material systems*", Thermal Spray Science and Technology; ASM International, pp. 1–5 1995
3. J. Vlcek, *A systematic approach to material eligibility for the cold spray process,* International Thermal Spray Conference and Exhibition, Orlando, Florida, 5–8 May 2003
4. D.G. McCartney, *Particle-substrate interactions in cold gas dynamic spraying*, International Thermal Spray Conference and Exhibition, Orlando, Florida, 5–8 May 2003
5. H. Assadi, F. Gärtner, T. Stoltenhoff, H. Kreye, Bonding mechanism in cold gas spraying. Acta Mater. **51**, 4379–4394 (2003)
6. F. Gärtner *Numerical and microstructural investigations of the bonding mechanisms in cold spraying*, International Thermal Spray Conference and Exhibition, Orlando, Florida, 5–8 May 2003
7. R.G.R. Maev, V. Leshchynsky, *Introduction to Low Pressure Gas Dynamic Spray Physics and Technology* (Wiley2VCH, Weinheim, 2008)
8. A.P. Alkhimov, A.N. Papyrin, V.F. Dosarev, N.I. Nestorovich, M.M. Shuspanov, *Gas dynamic spraying method for applying a coating*, U.S Patent 5, 302,414-12, April 1994
9. R.C. Dykhuizen, M.F. Smith, Gas dynamic principles of cold spray. J. Therm. Spray Technol. **7**(2), 205–212 (1998)
10. A.P. Alkhimov, V.F. Kosarev, S.V. Klinkov, The features of cold spray nozzle design. J. Therm. Spray Technol. **10**(2), 375–381 (2001)
11. M. Grujicic, W.S. DeRosset, D. Helfritch, Flow analysis and nozzle-shape optimization for the cold-gas dynamic-spray process, in *Proceedings of Institution of Mechanical Engineers* Vol. 217 *Part B: J. Engineering Manufacture*
12. W.-Y. Li, C.J. Li, Optimal design of a novel cold spray gun nozzle at a limited space. J. Therm. Spray Technol. **14**(3), 391–396 (2005)
13. T.-C. Jen, L. Li, W. Cui, Q. Chen, X. Zhang, Numerical investigations on cold gas dynamic spray process with nano and micro size particles. Int. J. Heat Mass Trans. **48**, 4384–4396 (2005)
14. F. Raletz, M. Vardelle, G. Ezo'o, Critical particle velocity under cold spray conditions. J. Surf. Coat. Technol. **201**, 1942–1947 (2006)
15. W.-Y. Li, Optimal design of a convergent-barrel cold spray nozzle by numerical method. Appl. Surf. Sci. **253**, 708–713 (2006)
16. B. Jodoin, F. Raletz, M. Vardelle, Cold spray modeling and validation using an optical diagnostic method. Surf. Coat. Technol. **200**(14–15), 4424–4432 (2006)
17. Wen-Ya. Li, Optimal design of a cold spray nozzle by numerical analysis of particle velocity. Mater. Des. **28**, 2129–2137 (2007)
18. S.P. Pardhasaradhi, V. Venkatachalapathy, S.V. Joshi, S. Govindan, Optical diagnostics study of gas particle transport phenomena in cold gas dynamic spraying and comparison with model predictions. J. Therm. Spray Technol. **17**(4), 551–563 (2008)
19. R. Lupoi, W.O'Neill, *An investigation on powder stream in Cold Gas Spray (CGS) nozzles*, V. European Conference on Computational Fluid Dynamics ECCOMAS CFD 2010, J.C.F.Pereira and A. Sequeira (Eds), Lisbon, Portugal, 14–17 June 2010
20. N. Rajaratnam, *Turbulent Jets* (Elsevier, Amsterdam, 1976)
21. J.N. Reddy, D.K. Gartling, *The Finite Element Method in Heat Transfer and Fluid Dynamics* (CRC Press, London, 1994)
22. H.C. Huang, Z.H. Li, A.S. Usmani, *Finite Element Analysis of Non-Newtonian Flow Theory and Software* (Springer, London, 1999)
23. FLUENT 12.0
24. ANSYS 12.0 software

GENERALIZED POSITIVE LINEAR OPERATORS BASED ON PED AND IPED

NAOKANT DEO AND MINAKSHI DHAMIJA

Abstract. The paper deals with generalized positive linear operators based on Pólya-Eggenberger distribution(PED) as well as inverse Pólya-Eggenberger distribution(IPED). Initially, we give the moments by using Stirling numbers of second kind and then establish direct results, convergence with the help of local and weighted approximation of proposed operators.

1. Introduction

In the year 1968, D. D. Stancu [23] introduced a new class of positive linear operators based on Pólya-Eggenberger distribution(PED) and associated to a real-valued function on $[0,1]$ as:

$$B_n^{(\alpha)}(f;x)=\sum_{k=0}^{n}\binom{n}{k}\frac{x^{[k,-\alpha]}(1-x)^{[n-k,-\alpha]}}{1^{[n,-\alpha]}}f\left(\frac{k}{n}\right), \tag{1.1}$$

where α is a non-negative parameter which may depend only on the natural number n and $t^{[n,h]}=t(t-h)(t-2h)\cdot\ldots\cdot(t-\overline{n-1}h)$, $t^{[0,h]}=1$ represents the factorial power of t with increment h.

Later on Stancu [24] introduced a generalized form of the Baskakov operators based on inverse Pólya-Eggenberger distribution(IPED) for a real-valued function bounded on $[0,\infty)$, given by

$$V_n^{(\alpha)}(f;x)=\sum_{k=0}^{\infty}\binom{n+k-1}{k}\frac{1^{[n,-\alpha]}x^{[k,-\alpha]}}{(1+x)^{[n+k,-\alpha]}}f\left(\frac{k}{n}\right). \tag{1.2}$$

Now we consider new positive linear operators $L_n^{(\alpha)}$, for each f, real valued function bounded on interval I, as:

$$L_n^{(\alpha)}(f;x)=\sum_{k}w_{n,k}^{(\alpha)}(x)f\left(\frac{k}{n}\right),\quad x\in I,\ \ n=1,2,..., \tag{1.3}$$

2010 *Mathematics Subject Classification.* 41A25, 41A36.

Key words and phrases. Generalized operators, Pólya-Eggenberger distribution, Modulus of continuity, Weighted approximation.

where $\alpha = \alpha(n) \to 0$ when $n \to \infty$, p & k are nonnegative integers and for $\lambda = -1, 0$, we have

$$\omega_{n,k}^{(\alpha)}(x) = \frac{n+p}{n+p+\overline{\lambda+1}k} \begin{pmatrix} n+p+\overline{\lambda+1}k \\ k \end{pmatrix} \frac{\prod_{i=0}^{k-1}(x+i\alpha) \prod_{i=0}^{n+p+\lambda k-1}(1+\lambda x+i\alpha)}{\prod_{i=0}^{n+p+\overline{\lambda+1}k-1}\left(1+\overline{\lambda+1}x+i\alpha\right)}$$

$$= \frac{n+p}{n+p+\overline{\lambda+1}k} \begin{pmatrix} n+p+\overline{\lambda+1}k \\ k \end{pmatrix} \frac{x^{[k,-\alpha]}(1+\lambda x)^{[n+p+\lambda k,-\alpha]}}{\left(1+\overline{\lambda+1}x\right)^{[n+p+\overline{\lambda+1}k,-\alpha]}},$$

by using the notation $\overline{m-r}\alpha = (m-r)\alpha$. Operators (1.3) is generalized form of above two operators (1.1) and (1.2) and associated with PED and IPED [7].

Kantorovich form of Stancu operators (1.1) had been given by Razi [21] and he studied its convergence properties and degree of approximation. Ispir et al. [13] also discussed the Kantorovich form of operators (1.1) and they estimated the rate of convergence for absolutely continuous functions having a derivative coinciding a.e. with a function of bounded variation. Recently, Miclaus [16] established some approximation results for the Stancu operators (1.1) and its Durrmeyer type integral modification was studied by Gupta and Rassias [12] and obtained some direct results which include an asymptotic formula, local and global approximation results for these operators in terms of modulus of continuity.

Very recently Durrmeyer type modification of generalized Baskakov operators (1.2) associated with IPED were introduced by Dhamija and Deo [6] and studied the moments with the help of Vandermonde convolution formula and then gave approximation properties of these operators which include uniform convergence and degree of approximation. Deo et al. [4] also investigated approximation properties of Kantorovich variant of operators (1.2) and they established uniform convergence, asymptotic formula and degree of approximation. Various Durrmeyer type modifications and then their local as well as weighted approximation along with some other approximation behaviour have been discussed by many authors e.g.,([3], [14], [11]).

The main object of this paper is to find moments with the help of Stirling numbers of second kind and estimate the rate of convergence of operators (1.3) by studing local and weighted approximation theorems.

Throughout this paper we consider interval $I = [0, \infty)$ for $\lambda = 0$ and $I = [0, 1]$ for $\lambda = -1$.

2. Special Cases

It is easy to understand that the special cases of operators (1.3) are as follows:

(1) For $\lambda = -1$; we have
   (i) When $\alpha \neq 0 \neq p$

$$L_n^{(\alpha)}(f;x) = \sum_{k=0}^{n+p} \begin{pmatrix} n+p \\ k \end{pmatrix} \frac{\prod_{i=0}^{k-1}(x+i\alpha) \prod_{i=0}^{n+p-k-1}(1-x+i\alpha)}{\prod_{i=0}^{n+p-1}(1+i\alpha)} f\left(\frac{k}{n}\right).$$

This leads to Schurer type Stancu operators.

(ii) When $\alpha \neq 0, p = 0$ we get alternate form of operators (1.1) as:

$$L_n^{(\alpha)}(f;x) = \sum_{k=0}^{n} \left(\begin{array}{c} n \\ k \end{array} \right) \frac{\prod_{i=0}^{k-1}(x+i\alpha) \prod_{i=0}^{n-k-1}(1-x+i\alpha)}{\prod_{i=0}^{n-1}(1+i\alpha)} f\left(\frac{k}{n}\right).$$

Particular case: when $\alpha = 1/n, p = 0$ we obtain Lupaş and Lupaş operators [15] as:

$$L_n^{(\alpha)}(f;x) = \frac{2\,(n!)}{(2n)!} \sum_{k=0}^{n} \left(\begin{array}{c} n \\ k \end{array} \right) \prod_{i=0}^{k-1}(nx+i) \prod_{i=0}^{n-k-1}(\overline{1-x}n+i) f\left(\frac{k}{n}\right).$$

(iii) When $\alpha = 0, p \neq 0$ we have Bernstein-Schurer operators [22] as:

$$L_n^{(\alpha)}(f;x) = \sum_{k=0}^{n+p} \left(\begin{array}{c} n+p \\ k \end{array} \right) x^k (1-x)^{n+p-k} f\left(\frac{k}{n}\right).$$

(iv) When $\alpha = 0, p = 0$ we obtain original Bernstein operators [2] as:

$$L_n^{(\alpha)}(f;x) = \sum_{k=0}^{n} \left(\begin{array}{c} n \\ k \end{array} \right) x^k (1-x)^{n-k} f\left(\frac{k}{n}\right).$$

(2) For $\lambda = 0$; we obtain the following operators:

(i) When $\alpha \neq 0 \neq p$ we have Stancu-Schurer operators as:

$$L_n^{(\alpha)}(f;x) = \sum_{k=0}^{\infty} \left(\begin{array}{c} n+p+k-1 \\ k \end{array} \right) \frac{\prod_{i=0}^{k-1}(x+i\alpha) \prod_{i=0}^{n+p-1}(1+i\alpha)}{\prod_{i=0}^{n+p+k-1}(1+x+i\alpha)} f\left(\frac{k}{n}\right),$$

(ii) When $\alpha \neq 0, p = 0$ we obtain alternate form of operators (1.2) as:

$$L_n^{(\alpha)}(f;x) = \sum_{k=0}^{\infty} \left(\begin{array}{c} n+k-1 \\ k \end{array} \right) \frac{\prod_{i=0}^{k-1}(x+i\alpha) \prod_{i=0}^{n-1}(1+i\alpha)}{\prod_{i=0}^{n+k-1}(1+x+i\alpha)} f\left(\frac{k}{n}\right),$$

(iii) When $\alpha = 0, p \neq 0$ we get Baskakov-Schurer operators as:

$$L_n^{(\alpha)}(f;x) = \sum_{k=0}^{\infty} \left(\begin{array}{c} n+p+k-1 \\ k \end{array} \right) \frac{x^k}{(1+x)^{n+p+k}} f\left(\frac{k}{n}\right),$$

(iv) When $\alpha = 0, p = 0$ we obtain classical Baskakov operators [1] as:

$$L_n^{(\alpha)}(f;x) = \sum_{k=0}^{\infty} \left(\begin{array}{c} n+k-1 \\ k \end{array} \right) \frac{x^k}{(1+x)^{n+k}} f\left(\frac{k}{n}\right).$$

3. Preliminary Results

In 1730, J. Stirling [25] introduced an important concept of numbers, useful in various branches of mathematics like number theory, calculus of Bernstein polynomials etc., known as Stirling numbers of first kind and afterwards Stirling numbers of second kind. Let $\mathbb{R}$ be the set of real numbers and $\mathbb{N}$, a collection of natural numbers with $\mathbb{N}_0 = \mathbb{N} \cup \{0\}$. For $x \in \mathbb{R}$ and $i, j \in \mathbb{N}_0$, let $S(j,i)$ denote the Stirling numbers of second kind then

$$x^j = \sum_{i=0}^{j} S\left(j,i\right)(x)_i,$$

with alternate form

$$x^j = \sum_{i=0}^{j-1} S\left(j,j-i\right)(x)_{j-i}, \tag{3.1}$$

and has the following properties:

$$S\left(j,i\right) := \begin{cases} 1, \text{ if } j = i = 0; j = i \text{ or } j > 1, i = 1 \\ 0, \text{ if } j > 0, i = 0 \\ 0, \text{ if } j < i \\ i.S\left(j-1,i\right) + S\left(j-1,i-1\right), \text{ if } j,i > 1. \end{cases} \tag{3.2}$$

These Stirling numbers of second kind are very useful in calculating the moments of linear positive operators especially for higher order moments. In [17, 18], Dan obtained higher order moments for Bernstein type operators by using these numbers. In what follows, we shall find the moments of $L_n^{(\alpha)}$ given by (1.3)with the help of same. Let us recall the monomials $e_j(x) = x^j, j \in \mathbb{N}_0$ be the test functions.

Lemma 3.1. *For the monomial t^j, where $j \in \mathbb{N}$, and $t, x \in I$, we have*

$$L_n^{(\alpha)}(t^j;x) = \frac{1}{n^j} \sum_{i=0}^{j-1} S\left(j,j-i\right) \phi_{n+p}^{j-i} \frac{x^{[j-i,-\alpha]}}{1^{[j-i+(\lambda+1),-\alpha]}},$$

where

$$\phi_{n+p}^{j-i} = \begin{cases} (n+p)_{(j-i)}, \ \lambda = -1 \\ (n+p)^{(j-i)}, \ \lambda = 0 \end{cases},$$

$(y)_n := \prod_{i=0}^{n-1}(y-i), (y)_0 := 1$ *and* $(y)^n := \prod_{i=0}^{n-1}(y+i), (y)^{(0)} := 1$ *are respectively the falling factorial and rising factorial with $y \in \mathbb{R}$ and $n \in \mathbb{N}$.*

Proof. Using the relation (3.1), it is easy to derive above expression on the same lines as in [19] (Page 54, Theorem 2.1.94.). □

Lemma 3.2. *For the Generalized positive linear operators* (1.3) *hold*

$$L_n^{(\alpha)}(1;x) = 1, \ \ L_n^{(\alpha)}(t;x) = \left(\frac{n+p}{n}\right) \frac{x}{\left(1 - \overline{\lambda+1}\alpha\right)},$$

$$L_n^{(\alpha)}(t^2;x) = \left(\frac{n+p}{n^2}\right) \frac{1}{\left(1-\lambda\alpha\right)\left(1-\overline{\lambda+1}\alpha\right)} \times \left[\frac{\left(n+p+\lambda+1\right)x(x+\alpha)}{1-2\overline{\lambda+1}\alpha} + x\left(1+\lambda x\right)\right],$$

$$L_n^{(\alpha)}(t^3;x)=\frac{(n+p)\,x}{n^3\left(1-\overline{\lambda+1}\alpha\right)}\left[\frac{\left(n+p+2\lambda+1\right)\left(n+p+2\overline{2\lambda+1}\right)(x+\alpha)(x+2\alpha)}{\left(1-\overline{3\lambda+2}\alpha\right)\left(1-\overline{5\lambda+3}\alpha\right)}\right.$$
$$\left.+\frac{3\left(n+p+2\lambda+1\right)(x+\alpha)}{\left(1-\overline{3\lambda+2}\alpha\right)}+1\right],$$

and

$$L_n^{(\alpha)}(t^4;x)=\frac{(n+p)\,x}{n^4\left(1-\overline{\lambda+1}\alpha\right)}$$
$$\times\left[\frac{\left(n+p+2\lambda+1\right)\left(n+p+2\overline{2\lambda+1}\right)\left(n+p+3\overline{2\lambda+1}\right)(x+\alpha)(x+2\alpha)(x+3\alpha)}{\left(1-\overline{3\lambda+2}\alpha\right)\left(1-\overline{5\lambda+3}\alpha\right)\left(1-\overline{7\lambda+4}\alpha\right)}\right.$$
$$+\frac{6\left(n+p+2\lambda+1\right)\left(n+p+2\overline{2\lambda+1}\right)(x+\alpha)(x+2\alpha)}{\left(1-\overline{3\lambda+2}\alpha\right)\left(1-\overline{5\lambda+3}\alpha\right)}$$
$$\left.+\frac{7\left(n+p+2\lambda+1\right)(x+\alpha)}{\left(1-\overline{3\lambda+2}\alpha\right)}+1\right].$$

Proof. From the definition of operators (1.3), we can obtain the moment for $j=0$, i.e.$L_n^{(\alpha)}(1;x)=1$

Also by the application of Lemma 3.1 for $j=1,2,3,4$ and taking into account the relation (3.2), we can follow the values of remaining moments. □

Further, to obtain the central moments of generalized positive operators (1.3), we use the following result:

Lemma 3.3. [10] *Let V be any linear operators then*

$$V\left((t-x)^j;x\right)=V\left(t^j;x\right)-\sum_{i=0}^{j-1}\binom{j}{i}x^{j-i}V\left((t-x)^i;x\right),$$

and in the case when $V\left(t^j;x\right)=x^j$, for $j=0,1$, then we get

$$V\left((t-x)^3;x\right)=V\left(t^3;x\right)-x^3-3xV\left((t-x)^2;x\right),$$

and

$$V\left((t-x)^4;x\right)=V\left(t^4;x\right)-x^4-4xV\left((t-x)^3;x\right)+6x^2V\left((t-x)^2;x\right).$$

Lemma 3.4. *The generalized linear positive operators* (1.3) *satisfy*

$$L_n^{(\alpha)}(t-x;x)=\frac{px+\overline{\lambda+1}\alpha}{n\left(1-\overline{\lambda+1}\alpha\right)},\tag{3.3}$$

$$L_n^{(\alpha)}((t-x)^2;x)=\frac{n+p}{n\left(1-\lambda\alpha\right)\left(1-\overline{\lambda+1}\alpha\right)}\left[\left(1-\lambda\alpha\right)\left(1-\overline{\lambda+1}\alpha\right)\frac{nx^2}{n+p}\right.$$
$$\left.+\frac{\left(n+p+\lambda+1\right)x(x+\alpha)}{n\left(1-2\overline{\lambda+1}\alpha\right)}+\frac{x\left(1+\lambda x\right)}{n}-2\left(1-\lambda\alpha\right)x^2,\right.\tag{3.4}$$

$$L_n^{(\alpha)}\left((t-x)^3;x\right)=\frac{(n+p)\,x(x+\alpha)}{n^2\left(1-\overline{\lambda+1}\alpha\right)}\left[\frac{(n+p+2\lambda+1)\left(n+p+2\overline{2\lambda+1}\right)(x+2\alpha)}{n\left(1-\overline{3\lambda+2}\alpha\right)\left(1-\overline{5\lambda+3}\alpha\right)}\right.$$
$$\left.+\frac{3\,(n+p+2\lambda+1)}{n\left(1-\overline{3\lambda+2}\alpha\right)}-\frac{3\,(n+p+\lambda+1)\,x}{(1-\lambda\alpha)\left(1-2\overline{(\lambda+1)}\alpha\right)}\right]$$
$$+\frac{(n+p)\,x}{n\left(1-\overline{\lambda+1}\alpha\right)}\left[\frac{1}{n^2}-3x\left(\frac{px+\overline{\lambda+1}\alpha}{(n+p)}\right)-\frac{3}{(1-\lambda\alpha)}\frac{x\,(1+\lambda x)}{n}\right]$$
$$-2x^3\left[2-\frac{3\,(n+p)}{n\left(1-\overline{\lambda+1}\alpha\right)}\right], \tag{3.5}$$

$$L_n^{(\alpha)}\left((t-x)^4;x\right)=\frac{(n+p)\,x(x+\alpha)}{n^2\left(1-\overline{\lambda+1}\alpha\right)}$$
$$\times\left[\frac{(n+p+2\lambda+1)\left(n+p+2\overline{2\lambda+1}\right)\left(n+p+3\overline{2\lambda+1}\right)(x+2\alpha)(x+3\alpha)}{n^2\left(1-\overline{3\lambda+2}\alpha\right)\left(1-\overline{5\lambda+3}\alpha\right)\left(1-\overline{7\lambda+4}\alpha\right)}\right.$$
$$+\frac{2\,(3-2nx)\,(n+p+2\lambda+1)\left(n+p+2\overline{2\lambda+1}\right)(x+2\alpha)}{n^2\left(1-\overline{3\lambda+2}\alpha\right)\left(1-\overline{5\lambda+3}\alpha\right)}$$
$$\left.+\frac{(7-12nx)\,(n+p+2\lambda+1)}{n^2\left(1-\overline{3\lambda+2}\alpha\right)}+\frac{6\,(n+p+\lambda+1)\,x^2}{(1-\lambda\alpha)\left(1-2\overline{(\lambda+1)}\alpha\right)}\right]$$
$$+\frac{(n+p)\,x}{n\left(1-\overline{\lambda+1}\alpha\right)}\left[\frac{1-4nx}{n^3}+8x^2\left(\frac{px+\overline{\lambda+1}\alpha}{(n+p)}\right)\frac{6x^2\,(1+\lambda x)}{n\,(1-\lambda\alpha)}\right]$$
$$+3x^4\left[3-\frac{4\,(n+p)}{n\left(1-\overline{\lambda+1}\alpha\right)}\right]. \tag{3.6}$$

Proof. The combined use of Lemma 3.2 and 3.3 will follow the proof. □

Remark 3.1. *For sufficiently large n, Lemma 3.5 gives the following inequalities:*

(i) $L_n^{(\alpha)}\left((t-x)^2;x\right)\leq A_1\frac{\left(1+x^2\right)}{n}$,

(ii) $L_n^{(\alpha)}\left((t-x)^4;x\right)\leq A_2\frac{\left(1+x^2\right)^2}{n}$,

where A_1 and A_2 are some positive constants.

Lemma 3.5. *For positive linear operators* (1.3)*, there holds,*

$$\left|L_n^{(\alpha)}(f;x)\right|\leqslant\|f\|.$$

Proof. From operators (1.3), we have

$$\left|L_n^{(\alpha)}(f;x)\right|=\left|\sum_{k=0}^{\infty}w_{n,k}^{(\alpha)}(x)f\left(\frac{k}{n}\right)\right|\leqslant\sum_{k=0}^{\infty}w_{n,k}^{(\alpha)}(x)\left|f\left(\frac{k}{n}\right)\right|$$
$$\leqslant\sum_{k=0}^{\infty}w_{n,k}^{(\alpha)}(x)\sup|f(x)|=\|f\|.$$

□

4. Direct Results

Let $C_B(I)$ be the space of all the real valued continuous and bounded functions f on the interval I, endowed with the norm

$$\|f\| = \sup_{x\in I} |f(x)|.$$

For $f \in C_B(I)$, the Peetre's $K-$functional is defined by

$$K_2(f;\delta) := \inf_{x\in C_B^2(I)} \{\|f-g\| + \delta \|g''\|\}, \ \delta > 0,$$

where $C_B^2(I) = \{g \in C_B(I) : g', g'' \in C_B(I)\}$. By DeVore and Lorentz([5], p.177. Theorem 2.4) there exists an absolute constant $C > 0$ such that

$$K_2(f;\delta) \leqslant C\omega_2\left(f;\sqrt{\delta}\right), \tag{4.1}$$

where $\omega_2\left(f;\sqrt{\delta}\right)$ is second order modulus of continuity defined by

$$\omega_2\left(f;\sqrt{\delta}\right) = \sup_{0<h<\sqrt{\delta}} \sup_{x\in I} |f(x+2h) - 2f(x+h) + f(x)|.$$

Also the first order modulus of smoothness(or simply modulus of continuity) is given by

$$\omega\left(f;\sqrt{\delta}\right) = \sup_{0<h\leqslant\sqrt{\delta}} \sup_{x\in I} |f(x+h) - f(x)|.$$

Theorem 4.1. *For $f \in C_B(I)$, we have*

$$\left|L_n^{(\alpha)}(f;x) - f(x)\right| \leqslant \omega\left(f, \frac{px+nx(\lambda+1)\alpha}{x(1-(\lambda+1)\alpha)}\right) + C\omega_2\left(f, \frac{\sqrt{\psi_{n,\lambda}^{(\alpha)}(x)}}{2}\right),$$

where C is a positive constant and

$$\psi_{n,\lambda}^{(\alpha)}(x) = L_n^{(\alpha)}\left((t-x)^2;x\right) + \left\{\frac{px+nx(\lambda+1)\alpha}{n(1-(\lambda+1)\alpha)}\right\}^2.$$

Proof. First we consider auxiliary operators

$$\hat{L}_n^{(\alpha)}(f;x) = L_n^{(\alpha)}(f;x) + f(x) - f\left(\frac{n+p}{n}.\frac{x}{1-(\lambda+1)\alpha}\right). \tag{4.2}$$

For all $x \in I$ we observed that $\hat{L}_n^{(\alpha)}(f;x)$ are linear such that

$$\hat{L}_n^{(\alpha)}(1;x) = 1 \ \textit{and} \ \hat{L}_n^{(\alpha)}(t;x) = x,$$

i. e., preserve linear functions. Therefore

$$\hat{L}_n^{(\alpha)}(t-x;x) = 0. \tag{4.3}$$

Let $g \in C_B^2(I)$ and $t, x \in I$ then Taylor's theorem implies

$$g(t) = g(x) + (t-x)g'(x) + \int_x^t (t-u)g''(u)du,$$

we can write

$$\begin{aligned}\hat{L}_n^{(\alpha)}(g;x)-g(x) &= g'(x)\hat{L}_n^{(\alpha)}((t-x);x)+\hat{L}_n^{(\alpha)}\left(\int_x^t (t-u)g''(u)du;x\right)\\ &= \hat{L}_n^{(\alpha)}\left(\int_x^t (t-u)g''(u)du;x\right)\\ &= L_n^{(\alpha)}\left(\int_x^t (t-u)g''(u)du;x\right)\\ &\quad -\int_x^{\frac{n+p}{n}\left(\frac{x}{1-(\lambda+1)\alpha}\right)}\left(\frac{n+p}{n}\frac{x}{1-(\lambda+1)\,\alpha}-u\right)g''(u)du.\end{aligned}$$

Hence we have

$$\begin{aligned}\left|\hat{L}_n^{(\alpha)}(g;x)-g(x)\right| &\leqslant L_n^{(\alpha)}\left(\left|\int_x^t (t-u)g''(u)du\right|;x\right)\\ &\quad +\left|\int_x^{\frac{n+p}{n}\left(\frac{x}{1-(\lambda+1)\alpha}\right)}\left(\frac{n+p}{n}\frac{x}{1-(\lambda+1)\,\alpha}-u\right)g''(u)du\right|. \quad (4.4)\end{aligned}$$

Since $\left|\int_x^t (t-u)g''(u)du\right| \leqslant (t-x)^2\left\|g''\right\|$ and

$$\left|\int_x^{\frac{n+p}{n}\frac{x}{1-(\lambda+1)\alpha}}\left(\frac{n+p}{n}\frac{x}{1-(\lambda+1)\,\alpha}-u\right)g''(u)du\right| \leqslant \left\{\frac{n+p}{n}\frac{x}{1-(\lambda+1)\,\alpha}-x\right\}^2\left\|g''\right\|.$$

Therefore (4.4) implies that

$$\begin{aligned}\left|\hat{L}_n^{(\alpha)}(g;x)-g(x)\right| &\leqslant \left[L_n^{(\alpha)}\left((t-x)^2;x\right)+\left\{\frac{n+p}{n}\left(\frac{x}{1-(\lambda+1)\,\alpha}\right)-x\right\}^2\right]\left\|g''\right\|\\ &\leqslant \left[L_n^{(\alpha)}\left((t-x)^2;x\right)+\left\{\frac{px+nx\,(\lambda+1)\,\alpha}{n\,(1-(\lambda+1)\,\alpha)}\right\}^2\right]\left\|g''\right\|\\ &= \psi_{n,\lambda}^{(\alpha)}(x)\left\|g''\right\|, \quad (4.5)\end{aligned}$$

Again using definition of auxiliary operators and from Lemma 3.5, we get

$$\begin{aligned}\left|L_n^{(\alpha)}(f;x)-f(x)\right| &\leqslant \left|\hat{L}_n^{(\alpha)}((f-g);x)\right|+|g(x)-f(x)|+\left|\hat{L}_n^{(\alpha)}(g;x)-g(x)\right|\\ &\quad +\left|f\left(\frac{n+p}{n}\frac{x}{1-(\lambda+1)\alpha}\right)-f(x)\right|\\ &\leqslant 4\left\|f-g\right\|+\psi_{n,\lambda}^{(\alpha)}(x)\left\|g''\right\|+\omega\left(f;\frac{px+nx\,(\lambda+1)\,\alpha}{n\,(1-(\lambda+1)\,\alpha)}\right).\end{aligned}$$

Taking infimum on both the sides over $g\in C_B^2(I)$,

$$\left|L_n^{(\alpha)}(f;x)-f(x)\right| \leqslant 4K_2\left(f;\frac{\psi_{n,\lambda}^{(\alpha)}(x)}{4}\right)+\omega\left(f;\frac{px+nx\,(\lambda+1)\,\alpha}{n\,(1-(\lambda+1)\,\alpha)}\right).$$

Hence by (4.1), we get

$$\left|L_n^{(\alpha)}(f;x)-f(x)\right| \leqslant C\omega_2\left(f;\frac{\sqrt{\psi_{n,\lambda}^{(\alpha)}(x)}}{2}\right)+\omega\left(f;\frac{px+nx\,(\lambda+1)\,\alpha}{n\,(1-(\lambda+1)\,\alpha)}\right).$$

□

We consider the following Lipschitz-type space (see [20])

$$Lip_M^*(\beta) := \left\{ f \in C_B(I) : |f(y) - f(x)| \leqslant M \frac{|y-x|^\beta}{(x+y)^{\beta/2}}; x, y \in (0,\infty) \right\},$$

where M is a positive constant and $0 < \beta \leqslant 1$.

Theorem 4.2. *For all $x \in I$ and $f \in Lip_M^*(\beta)$, $0 < \beta \in (0,1]$ we get*

$$\left| L_n^{(\alpha)}(f;x) - f(x) \right| \leqslant M \left(\frac{\phi_n^{(\alpha)}(x)}{x} \right)^{\beta/2}, \tag{4.6}$$

where $\phi_n^{(\alpha)}(x) = L_n^{(\alpha)}\left((t-x)^2; x\right)$.

Proof. Assume that $\beta = 1$. Then, for $f \in Lip_M^*(1)$, we have

$$\begin{aligned}\left| L_n^{(\alpha)}(f;x) - f(x) \right| &\leqslant \left| \sum_{k=0}^{\infty} \omega_{n,k}^{(\alpha)}(x) f\left(\frac{k}{n}\right) - f(x) \right| \\ &\leqslant \sum_{k=0}^{\infty} \omega_{n,k}^{(\alpha)}(x) \left| f\left(\frac{k}{n}\right) - f(x) \right| \leqslant M \sum_{k=0}^{\infty} \omega_{n,k}^{(\alpha)}(x) \frac{\left|\frac{k}{n} - x\right|}{\left(\frac{k}{n}+x\right)^{1/2}}.\end{aligned}$$

Applying Cauchy-Schwarz inequality for sum and $\frac{1}{\sqrt{\frac{k}{n}+x}} \leqslant \frac{1}{\sqrt{x}}$, we have

$$\begin{aligned}\left| L_n^{(\alpha)}(f;x) - f(x) \right| &\leqslant \frac{M}{\sqrt{x}} \sum_{k=0}^{\infty} \omega_{n,k}^{(\alpha)}(x) \left\{ \left(\frac{k}{n} - x\right)^2 \right\}^{1/2} \\ &\leqslant \frac{M}{\sqrt{x}} \left\{ \sum_{k=0}^{\infty} \omega_{n,k}^{(\alpha)}(x) \right\}^{1/2} \left\{ \sum_{k=0}^{\infty} \omega_{n,k}^{(\alpha)} \left(\frac{k}{n} - x\right)^2 \right\}^{1/2} \\ &\leqslant \frac{M}{\sqrt{x}} \left\{ L_n^{(\alpha)}(1;x) \right\}^{1/2} \left\{ L_n^{(\alpha)}\left((t-x)^2; x\right) \right\}^{1/2} = M \left\{ \frac{\phi_n^{(\alpha)}(x)}{x} \right\}^{1/2}.\end{aligned}$$

Therefore result is true for $\beta = 1$.

Now we prove the required result for $0 < \beta < 1$. Consider $f \in Lip_M^*(\beta)$

$$\left| L_n^{(\alpha)}(f;x) - f(x) \right| \leqslant \sum_{k=0}^{\infty} \omega_{n,k}^{(\alpha)}(x) \left| f\left(\frac{k}{n}\right) - f(x) \right| \leqslant M \sum_{k=0}^{\infty} \omega_{n,k}^{(\alpha)}(x) \frac{\left|\frac{k}{n} - x\right|^\beta}{\left(\frac{k}{n}+x\right)^{\beta/2}}.$$

Using Holder's inequality for sum with $p = 2/\beta, q = 2/(2-\beta)$ and inequality $\frac{1}{\sqrt{\frac{k}{n}+x}} \leqslant \frac{1}{\sqrt{x}}$, we have

$$\begin{aligned}\left| L_n^{(\alpha)}(f;x) - f(x) \right| &\leqslant \frac{M}{x^{\beta/2}} \sum_{k=0}^{\infty} \omega_{n,k}^{(\alpha)}(x) \left\{ \left(\frac{k}{n} - x\right)^2 \right\}^{\beta/2} \\ &\leqslant \frac{M}{x^{\beta/2}} \left\{ \sum_{k=0}^{\infty} \omega_{n,k}^{(\alpha)}(x) \left(\frac{k}{n} - x\right)^2 \right\}^{\beta/2} \left\{ \sum_{k=0}^{\infty} \omega_{n,k}^{(\alpha)}(x) \right\}^{\frac{2-\beta}{2}} \\ &\leqslant M \left\{ \frac{L_n^{(\alpha)}\left((t-x)^2; x\right)}{x} \right\}^{\beta/2} = M \left\{ \frac{\phi_n^{(\alpha)}(x)}{x} \right\}^{\beta/2}.\end{aligned}$$

□

5. Weighted Approximation

Gadjiev [8, 9] studied the weight spaces $C_\varphi(I)$ and $B_\varphi(I)$ of real valued functions defined on I with $\varphi(x) = 1 + x^2$ and proved that Korovkin's theorem in general does not hold on these spaces. Here

$$B_\varphi(I) := \{f : |f(x)| \leqslant M_f\varphi(x)\},$$

with

$$\|f\|_\varphi = \sup_{x\in I} \frac{|f(x)|}{\varphi(x)},$$

and

$$C_\varphi(I) := \{f : f \in B_\varphi(I) \text{ and } f \text{ continuous}\},$$

i.e. $C_\varphi(I) = C(I) \cap B_\varphi(I)$ is the subspace of $B_\varphi(I)$ containing continuous functions and

$$C^*_\varphi(I) := \left\{f \in C_\varphi(I) : \lim_{x\to\infty} \frac{|f(x)|}{\varphi(x)} < \infty\right\}.$$

But Korovkin's theorem holds in the space $C^*_\varphi(I)$.

The usual modulus of continuity of f on $[0, b]$ is defined as:

$$\omega_b(f, \delta) = \sup_{|t-x|\leqslant\delta\, x,t\in[0,b]} |f(t) - f(x)|.$$

Theorem 5.1. *Let $f \in C_\varphi(I)$ then for operators $L_n^{(\alpha)}(f; x)$ we have*

$$\left\|L_n^{(\alpha)}(f; x) - f(x)\right\|_{C[0,b]} \leq 4M_f\left(1 + b^2\right)\phi_n^{(\alpha)}(b) + 2\omega_{b+1}\left(f, \sqrt{\phi_n^{(\alpha)}(b)}\right), \quad (5.1)$$

where $\phi_n^{(\alpha)}(x) = L_n^{(\alpha)}\left((t - x)^2; x\right)$.

Proof. Let $x \in [0, b]$, $t \in (b + 1, \infty)$, and $t - x > 1$ we have

$$\begin{aligned}
|f(t) - f(x)| &\leqslant M_f\varphi(t - x) = M_f\left\{1 + (t - x)^2\right\} = M_f\left(1 + t^2 + x^2 - 2xt\right)\\
&\leqslant M_f\left(2 + t^2 + x^2\right) = M_f\left\{2 + 2x^2 + (t - x)^2 + 2x(t - x)\right\}\\
&\leqslant M_f(t - x)^2\left\{3 + 2x + 2x^2\right\} \leqslant 4M_f(t - x)^2\left(1 + x^2\right)\\
&\leqslant 4M_f(t - x)^2\left(1 + b^2\right). \qquad (5.2)
\end{aligned}$$

If $x \in [0, b]$ and $t \in [0, b + 1]$ then we have

$$|f(t) - f(x)| \leqslant \omega_{b+1}(|t - x|) \leqslant \left(1 + \frac{|t - x|}{\delta}\right)\omega_{b+1}(f, \delta), \delta > 0. \qquad (5.3)$$

Combining (5.2) and (5.3), we obtain

$$|f(t) - f(x)| \leqslant 4M_f\left(1 + b^2\right)(t - x)^2 + \left(1 + \frac{|t - x|}{\delta}\right)\omega_{b+1}(f, \delta).$$

Using Cauchy Schwartz inequality we get

$$\begin{aligned}\left|L_n^{(\alpha)}(t)-f(x)\right| &\leqslant 4M_f\left(1+b^2\right)L_n^{(\alpha)}\left((t-x)^2;x\right)\\ &\quad+\left(1+\frac{1}{\delta}L_n^{(\alpha)}\left(|t-x|;x\right)\right)\omega_{b+1}\left(f,\delta\right)\\ &\leqslant 4M_f\left(1+b^2\right)L_n^{(\alpha)}\left((t-x)^2;x\right)\\ &\quad+\left[1+\frac{1}{\delta}\left\{L_n^{(\alpha)}\left((t-x)^2;x\right)\right\}^{1/2}\right]\omega_{b+1}\left(f,\delta\right)\\ &\leqslant 4M_f\left(1+b^2\right)\phi_n^{(\alpha)}(b)+2\omega_{b+1}\left(f,\sqrt{\phi_n^{(\alpha)}(b)}\right).\end{aligned}$$

□

Theorem 5.2. *Let $f\in C_\varphi^*(I)$ then, we have*

$$\lim_{n\to\infty}\left\|L_n^{(\alpha)}\left(f;x\right)-f(x)\right\|_\varphi=0. \tag{5.4}$$

Proof. From [9], it's sufficient to verify the following three equations

$$\lim_{n\to\infty}\left\|L_n^{(\alpha)}\left(t^i;x\right)-t^i\right\|_\varphi=0,\ i=0,1,2. \tag{5.5}$$

Clearly equation (5.5) holds for $i=0$ as $L_n^{(\alpha)}\left(1;x\right)=1$. Now using Lemma 3.2 we have

$$\begin{aligned}\left\|L_n^{(\alpha)}\left(t;x\right)-x\right\|_\varphi &=\sup_{x\in I}\frac{1}{\varphi(x)}\left|\frac{n+p}{n}\frac{x}{\left(1-\overline{\lambda+1}\alpha\right)}-x\right|\\ &=\sup_{x\in I}\frac{x}{\varphi(x)}\left|\frac{p+\overline{\lambda+1}\alpha n}{n\left(1-\overline{\lambda+1}\alpha\right)}\right|\leqslant\frac{p+\overline{\lambda+1}\alpha n}{n\left(1-\overline{\lambda+1}\alpha\right)},\end{aligned}$$

which implies that $\lim_{n\to\infty}\left\|L_n^{(\alpha)}\left(t;x\right)-x\right\|_\varphi=0$. Similarly we have

$$\begin{aligned}&\left\|L_n^{(\alpha)}\left(t^2;x\right)-x^2\right\|_\varphi=\sup_{x\in I}\frac{1}{\varphi(x)}\left|\frac{n+p}{n^2}\frac{x}{\left(1-\lambda\alpha\right)\left(1-\overline{\lambda+1}\alpha\right)}\right.\\ &\times\left.\left[\frac{\left(n+p+\lambda+1\right)x(x+\alpha)}{1-2\overline{\lambda+1}\alpha}+x\left(1+\lambda x\right)\right]-x^2\right|\\ &\leqslant\left|\frac{n+p}{n^2}\frac{1}{\left(1-\lambda\alpha\right)\left(1-\overline{\lambda+1}\alpha\right)}\times\left[\frac{\left(n+p+\lambda+1\right)\left(1+\alpha\right)}{1-2\overline{\lambda+1}\alpha}+\lambda+1\right]-1\right|.\end{aligned}$$

Thus $\lim_{n\to\infty}\left\|L_n^{(\alpha)}\left(t^2;x\right)-x^2\right\|_\varphi=0$.
This completes the proof. □

Finally we give the rate of convergence for the generalized positive linear operators (1.3) with the help of Yüksel and Ispir [26] works. For every $f\in C_\varphi^*(I)$, the weighted modulus of continuity is defined by:

$$\Omega\left(f;\delta\right)=\sup_{x\in I,0<h\leqslant\delta}\frac{|f(x+h)-f(x)|}{1+(x+h)^2}.$$

Properties of the weighted modulus of continuity are given by the following lemma:

Lemma 5.1. [26] *Let $f \in C_{\varphi}^{*}(I)$ then we have*

(i) $\Omega(f;\delta)$ *is a monotone increasing function of* δ;
(ii) $\lim_{\delta\to 0+} \Omega(f;\delta) = 0$;
(iii) *for each* $m \in \mathbb{N}$, $\Omega(f;m\delta) = m\Omega(f;\delta)$;
(iv) *for each* $\mu \in I$, $\Omega(f;\mu\delta) = (1+\mu)\Omega(f;\delta)$.

Theorem 5.3. *Let $f \in C_{\varphi}^{*}(I)$ then for operators $L_n^{(\alpha)}(f;x)$ we have*

$$\sup_{x\in I} \frac{\left|L_n^{(\alpha)}(f;x) - f(x)\right|}{(1+x^2)^{5/2}} \leq K\Omega\left(f;\frac{1}{\sqrt{n}}\right),$$

where K is positive constant.

Proof. For $x,t \in [0,\infty)$, $\delta > 0$ and by definition of $\Omega(f;\delta)$ and Lemma 3.4, we have

$$\begin{aligned}
|f(t)-f(x)| &\leqslant \left(1+(x+|t-x|)^2\right)\Omega(f;|t-x|)\\
&\leqslant \left(1+(x+|t-x|)^2\right)\left(1+\frac{|t-x|}{\delta}\right)\Omega(f;\delta)\\
&\leqslant 2\left(1+x^2\right)\left(1+(t-x)^2\right)\left(1+\frac{|t-x|}{\delta}\right)\Omega(f;\delta).
\end{aligned}$$

Using the fact that $L_n^{(\alpha)}(f;x)$ are positive linear operators, we get

$$\begin{aligned}
\left|L_n^{(\alpha)}(f;x) - f(x)\right| &\leqslant \sum_{k=0}^{\infty} w_{n,k}^{(\alpha)}(x)\left|f\left(\frac{k}{n}\right) - f(x)\right|\\
&\leqslant 2\Omega(f;\delta)\left(1+x^2\right)\sum_{k=0}^{\infty} w_{n,k}^{(\alpha)}(x)\left\{1+\left(\frac{k}{n}-x\right)^2\right\}\left(1+\frac{\left|\frac{k}{n}-x\right|}{\delta}\right)\\
&\leqslant 2\Omega(f;\delta)\left(1+x^2\right)\left[\sum_{k=0}^{\infty} w_{n,k}^{(\alpha)}(x) + \sum_{k=0}^{\infty} w_{n,k}^{(\alpha)}(x)\left(\frac{k}{n}-x\right)^2\right.\\
&\quad \left. + \sum_{k=0}^{\infty} w_{n,k}^{(\alpha)}(x)\frac{\left|\frac{k}{n}-x\right|}{\delta} + \sum_{k=0}^{\infty} w_{n,k}^{(\alpha)}(x)\left(\frac{k}{n}-x\right)^2\frac{\left|\frac{k}{n}-x\right|}{\delta}\right]\\
&\leqslant 2\Omega(f;\delta)\left(1+x^2\right)\left[1+L_n^{(\alpha)}\left((t-x)^2;x\right)\right.\\
&\quad \left. + L_n^{(\alpha)}\left(\left(1+(t-x)^2\right)\frac{|t-x|}{\delta};x\right)\right]. \qquad (5.6)
\end{aligned}$$

Applying Cauchy Schwarz inequality and in view of Remark 3.1, we obtain

$$\begin{aligned}
&\left|L_n^{(\alpha)}(f;x) - f(x)\right| \leq 2\Omega(f;\delta)\left(1+x^2\right)\left[1+L_n^{(\alpha)}\left((t-x)^2;x\right)\right.\\
&\quad \left. + \frac{1}{\delta}\left\{\left(L_n^{(\alpha)}\left((t-x)^2;x\right)\right)^{1/2} + \left(L_n^{(\alpha)}\left((t-x)^2;x\right)\right)^{1/2}\left(L_n^{(\alpha)}\left((t-x)^4;x\right)\right)^{1/4}\right\}\right]\\
&\quad \leq K\left(1+x^2\right)^{5/2}\Omega\left(f;\frac{1}{\sqrt{n}}\right),
\end{aligned}$$

where $\delta = \frac{1}{\sqrt{n}}$ and $K = 2\left(1+A_1+\sqrt{A_1}+\sqrt{A_1A_2}\right)$. Hence the result. □

References

[1] Baskakov V. A., *An example of a sequence of linear positive operators in the space of continuous functions*, Dokl. Akad. Nauk SSSR, **113**(1957), 249-251 (in Russian).

[2] Bernstein S. N., *Démonstration du théoréme de Weierstrass fondée sur le calcul de probabilités*, Commun. Sco. Math. Charkov, **13(2)**(1912), 1-2.

[3] Deo N., *Faster rate of convergence on Srivastava-Gupta operators*, Appl. Math. Comput., **218(21)**(2012), 10486-10491.

[4] Deo N., Dhamija M. and Miclăuş D., *Stancu-Kantorovich operators based on inverse Pólya-Eggenberger distribution*, Appl. Math. Comput., **273** (2016), 281-289..

[5] DeVore R. A. and Lorentz G. G., *Constructive Approximation*, Springer, Berlin, 1993.

[6] Dhamija M. and Deo N., *Jain-Durrmeyer operators associated with the inverse Pólya-Eggenberger distribution*, Appl. Math. Comput., **286** (2016), 15-22..

[7] Eggenberger F. and Pólya G., *Uber die Statistik verkerter Vorgänge*, Z. Angew. Math. Mech., **1**(1923), 279–289.

[8] Gadjiev A. D., *The convergence problem for a sequence of positive linear operators on unbounded sets and theorems analogous to that of P P Korovkin*, English translated, Sov. Math. Dokl., **15** (1974), 5.

[9] Gadjiev A. D., *Theorems of the type of P P Korovkin type theorems*, Mat. Zametki, **20(5)** (1976), 781-786.

[10] Gonska H. H., Pitul P. and Raşa I., *On differences of positive linear operators*, Carpathian J. Math., **22**(2006), No. 1-2, 65-78.

[11] Gupta V. and Agarwal R. P., *Rate of Convergence in Simultaneous Approximation*, Springer, Switzerland, 2014.

[12] Gupta V. and Rassias T. M., *Lupaş-Durrmeyer operators based on Polya distribution*, Banach J. Math. Anal., **8** No. 2 (2014), 145–155.

[13] Ispir N., Agrawal P. N. and Kajla A., *Rate of convergence of Lupas Kantorovich operators based on Polya distribution*, Appl. Math. Comput., **261** (2015), 323-329.

[14] Jung H. S., Deo N. and Dhamija M., *Pointwise approximation by Bernstein type operators in mobile interval*, Appl. Math. Comput., **214(1)** (2014), 683-694.

[15] Lupaş L. and Lupaş A., *Polynomials of binomial type and approximation operators*, Studia Univ. Babes-Bolyai, Mathematica, **32(4)**(1987), 61-69.

[16] Miclăuş D., *On the monotonicity property for the sequence of Stancu type polynomials*, Analele Ştiinţifice Ale Universităţii "Al.i.Cuza" Din Iaşi (S.N.)(2014).

[17] Miclăuş D., *The revision of some results for Bernstein-Stancu type operators*, Carpathian J. Math., **28** No. 2 (2012), 289–300.

[18] Miclăuş D., *The moments of Bernstein-Stancu operators revisited*, Mathematica, Tome., **54(77)** No. 1 (2012), 78–83.

[19] Miclăuş D., *On the approximation order and Voronovskajas type theorem for certain linear positive operators*, *PhD. Thesis*, (2012).

[20] Özarslan M. A. and Duman O., *Local approximation behavior of modified SMK operators*, Miskolc Math. Notes, **11(1)** (2010), 8799.

[21] Razi Q., *Approximation of a function by Kantorovich type operators*, Mat. Vesnic., **41** (1989), 183–192.

[22] Schurer F., *Linear positive operators in approximation theory*, Math. Inst. Techn. Univ. Delft Report, 1962.

[23] Stancu D. D., *Approximation of functions by a new class of linear polynomial operators*, Rev. Roum. Math. Pures Appl. **13** (1968), 1173-1194.

[24] Stancu D. D., *Two classes of positive linear operators*, Anal. Univ. Timişoara, Ser. Ştin. Matem., **8**(1970), 213-220.

[25] Stirling J., *Differential Method: A Treatise of the Summation and Interpolation of Infinite Series(in Latin)*, London,(1730).

[26] Yüksel I. and Ispir N., *Weighted approximation by a certain family of summation integral-type operators*, Comput. Math. Appl., **52(10-11)** (2006), 1463-1470.

Delhi Technological University
Formerly Delhi College of Engineering
Department of Applied Mathematics
Bawana Road, 110042 Delhi, India
E-mail address: naokantdeo@dce.ac.in, dr_naokant_deo@yahoo.com
E-mail address: minakshidhamija11@gmail.com

This article has been accepted for publication in a future issue of this journal, but has not been fully edited. Content may change prior to final publication. Citation information: DOI 10.1109/TDMR.2016.2564448, IEEE Transactions on Device and Materials Reliability

Interfacial Charge Analysis of Heterogeneous Gate Dielectric - Gate All Around - Tunnel FET for Improved Device Reliability

Jaya Madan, *Student member, IEEE*, and Rishu Chaujar, *Member IEEE*

***Abstract*—In this work, we have investigated the device reliability by studying the impact of interface traps both donor (positive interface charges) and acceptor (negative interface charges) present at the Si-SiO_2 interface, on analog/RF performance and linearity distortion analysis of Hetero gate dielectric gate all around TFET (HD-GAA-TFET), which is used to enhance the tunneling current of TFET. Various figure of merits such as cut off frequency f_T, maximum oscillation frequency f_{max}, transconductance frequency product (TFP), higher order transconductance coefficients (g_{m1}, g_{m3}), VIP2, VIP3, IIP3, IMD3, zero crossover point and 1dB compression point have been investigated and the results so obtained are simultaneously compared with gate all around tunnel FET (GAA-TFET). Simulation results indicate that HD GAA TFET is more immune towards the interface trap charges present at the Si/SiO_2 interface than GAA TFET and hence can act as a better candidate for low power switching applications. All the simulations have been done on ATLAS device simulator.**

***Index Terms*—Band to band tunneling (BTBT), Heterogeneous dielectric (HD), Interface traps layer, interface trap charges (ITC), parasitic capacitance, tunneling FET (TFET).**

I. Introduction

TFET works on band to band tunneling principle and have a subthreshold swing (SS) smaller than 60mV/dec (overcome the limit of SS of MOSFET). Due to lower power dissipation, TFET has gained a lot of attraction and has become an attractive candidate for ultralow power applications. Further, TFET is immune to short channel effects and has very low OFF current, making it suitable for low power applications. However, TFET suffers from low ON state current (because of limited rate of tunneling of carrier), lower than the ITRS requirement. This makes it unsuitable for analog applications. Abundant techniques have been explored for resolving this issue such as using a smaller band gap material in the source region such as germanium [1], hetero gate dielectric TFET [2], double gate architecture [3], gate to source overlap [4], gate to drain underlap [5], dual material gate [6], n-pocket doping tunnel FET [7]. Other drawback of TFET is ambipolarity (conduction in both the directions) [8]. Many techniques were introduced to resolve this issue such as hetero gate dielectric [2], asymmetric source/drain doping [9] and hetero junction TFET [10].

The device reliability issue is always a major concern. During the device fabrication process, the process induced, stress induced and radiation induced damage results in conception of interface trap charges (ITC). It is known that the interface states causes reduction in device reliability and lifetime [11-12]. Few works on the tunnel FET reliability have been reported yet [1, 13-15]. The interface defects which is attributed to the unsaturated fourth bond present at the interface, have energy level lying in the energy band gap of the silicon (unlike in the conduction and valence band). Electrons and holes that are present in these levels cannot move freely (or are localized) due to the larger distance between the neighbouring interfacial trivalent silicon atoms. A donor type interface trap can act as a positive localized charge (when it is empty) or neutral localized charge (when it is filled with an electron). An acceptor type interface trap can act as a negative localized charge (when it is filled with an electron) or neutral localized charge (when it is empty). Donor traps usually lie near above the valence band and acceptor traps usually lies near below the conduction band.

In case of tunnel FET, higher electric field near the tunneling junction (the source channel junction) is needed for lowering of the tunneling barrier width but on the counterparts of lowering the tunneling barrier width, this high transverse field results into the generation of interface traps (donor and acceptor) and hence the localized charges (both positive and negative). Apart from the high electric field, hot carrier stress (HC) and positive bias temperature instability (PBTI) are also attributed to the generation of ITC [16]. The band to band tunneling rate is proportional to $\exp(-A/E_y)^6$, hence BTBT rate is very sensitive to electric field. But the presence of interface traps at the Si/SiO_2 interface results into degradation of electric field along the channel length at the tunneling junction and thus results in degradation of tunneling current and the analog performance of the device.

A lot of work has already been done to study the device reliability of MOSFET owed by the ITC. But there is a need to estimate the performance degradation due to the interface traps present at the Si-SiO_2 interface in TFET as the basic working principle of TFET is entirely different from that of

Manuscript submitted for review . The work of J. Madan was supported by the University Grants Commission (UGC).

J. Madan and R. Chaujar are with the Microelectronics Research Laboratory, Engineering Physics Department, Delhi Technological University, New Delhi 110042, India (e-mail: jayamadan.2012@gmail.com; rishu.phy@dce.edu).

This article has been accepted for publication in a future issue of this journal, but has not been fully edited. Content may change prior to final publication. Citation information: DOI 10.1109/TDMR.2016.2564448, IEEE Transactions on Device and Materials Reliability

the MOSFET. In this paper, the effect of ITC on two devices HD-GAA-TFET and GAA-TFET with cylindrical geometry has been compared.

II. Device Analysis And Simulation

Fig. 1 shows the simulation structure of HD-GAA-TFET. For HD-GAA-TFET region-1 consists of dielectric constant ε_1=21 HfO_2 (near the source) and region 2 consists of ε_2=3.9 (SiO_2) (near the drain) and for GAA TFET ε_1= ε_2=3.9 (SiO_2). Silicon is used as source, drain and channel material. The radius (R), channel length ($L_g=L_1+L_2$), and gate oxide thickness (t_{ox}) is 10nm, 50nm (10nm + 40nm) and 3nm, respectively for both the cases HD-GAA-TFET and GAA-TFET. The source is p^+ type doped ($1\times10^{20}cm^{-3}$), body is lightly p type doped ($1\times10^{16}cm^{-3}$) and drain is n^+ doped (5×10^{18} cm^{-3}). To constrain the ambipolarity effect, (tunneling at drain and channel junction) source and drain are doped asymmetrically [9]. The optimum value of gate metal work function has been chosen for better OFF state characteristics. Metal work function is 4.3eV for both the devices.

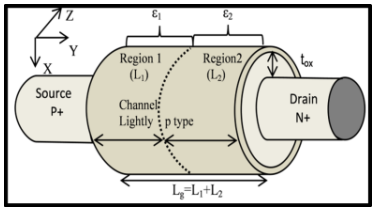

Fig. 1. Simulation structure of n-type Heterogeneous gate Dielectric-GAA-TFET (HD-GAA-TFET).

In this paper, to study the device reliability issue attributed to the interface charges, the effect of interface traps has been transmuted, into its equivalent positive localized charges (acceptor) and negative (donor) localized charges. The value of N_f is chosen on the basis of various experimental and simulation studies previously published incorporating the process damage, radiation damage and hot carrier damage resulting in trap density of 10^{11}-10^{13} $cm^{-2}eV^{-1}$ [17-18]. To investigate the minimum change we have chosen positive and negative charge density as $N_f = \pm1\times10^{12}$ cm^{-2}. Further, the effect of interface traps at the Si-SiO_2 interface is considered only near the source side for 10nm, due to the presence of high transverse electric field at the tunneling junction. Although the interface traps are also present at the interface of dielectrics in HD GAA TFET and will be absent in case of GAA TFET, but in present work we have only considered the ITCs along the channel length at the silicon and oxide interface. The main reason for neglecting the ITCs at the HfO_2/SiO_2 interface is that in case of TFETs mainly the tunneling junction and the drain junction affects the device behavior majorly so in this work we haven't considered the ITCs at the HfO_2/SiO_2 interface [19]. INTERFACE statement is used during simulation to define the density of interface fixed charges and there position present at the interface of Si-SiO_2. The distribution of interface charges is assumed to be uniform during the entire stimulation. The device reliability (to study the behavior of ITCs on device performance) is studied in terms of analog, RF and linearity figure of merits.

III. Model Validation

A. Simulation Methodology

All simulations have been performed using the ATLAS device simulator [20]. The models invoked during simulation are concentration and field dependent mobility model, Shockley-Read-Hall for carrier recombination, non-local band to band tunneling, band gap narrowing and Fermi Dirac statistics. The most important model for Tunnel FET simulations is the band-to-band tunneling (BTBT) model. Non-local models have a more physical basis and don't depend on the electric field at the individual mesh points in the simulated device structure, but rather on band diagrams calculated along cross-sections through the device. According to BBT.NONLOCAL, the tunneling happens through 1D slice, at the tunnel junction, where each slice and the tunnel junction are perpendicular to each other. These slices are parallel to themselves. Fermi Dirac statistics, the use of Fermi-Dirac statistics are essential to account for certain properties of very highly doped (degenerate) materials. Such as reduced carrier concentrations in heavily doped regions (statistical approach). As we are using heavily doped source and drain, so Fermi Dirac statistics is used. For higher doping (> $10^{18}cm^{-3}$) experimental work has shown that the p-n product in silicon becomes doping dependent. As the doping level increases, a decrease in the bandgap separation occurs. Both the numerical methods Gummel (decoupled) together with Newton's (Fully coupled) has been incorporated to mathematically solve the carrier transport equation.

B. Calibration

Before simulating the device structure, the simulation models have been calibrated with the already published results [21]. To calibrate the models the GAA TFET has been designed with the same device parameters as shown in ref [21]. To calibrate the Non-local BTBT model, the tunneling masses were tuned from their default values i.e. me.tunnel=0.322m_o and mh.tunnel=0.549m_o to make it best fit with the experimental data. Where; mo is the rest mass of electron. The adjusted value of me.tunnel=0.22m_o and mh.tunnel=0.52 m_o. Inset of Fig. 2(a) shows the transfer characteristics of the extracted data from the reference and results obtained from the simulations. The results so obtained are in close proximity, thus validates the model parameters during the simulations.

IV. Results Analysis

A. Impact of ITC on Analog and RF performance

Fig. 2(a) shows the effect of donor type traps (positive interface charges), acceptor type traps (negative interface charges) and absence of traps or interface charges on nonlocal band to band electron tunneling rate for both the aforementioned devices (GAA-TFET and HD-GAA-TFET). It is evident from the Fig. 2(a) that due to the presence of acceptor traps (negative interface charges), the band to band tunneling (BTBT) rate is decreased in both the devices and the donor traps (positive interface charges) increases the BTBT rate. This increase (decrease) is mainly attributed to the

This article has been accepted for publication in a future issue of this journal, but has not been fully edited. Content may change prior to final publication. Citation information: DOI 10.1109/TDMR.2016.2564448, IEEE Transactions on Device and Materials Reliability

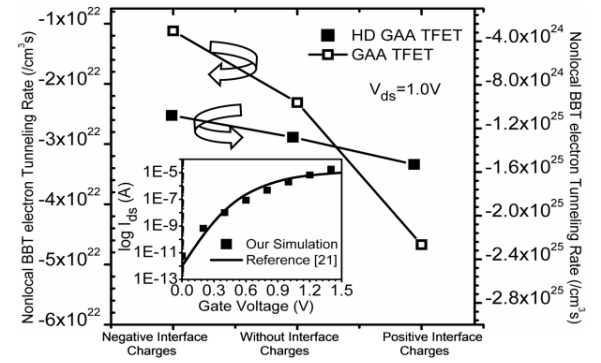

(2a)

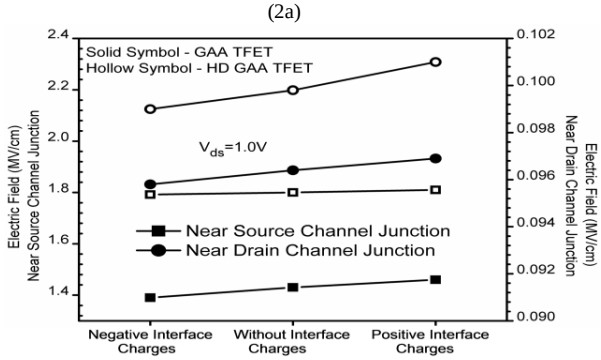

(2b)

Fig. 2(a). Nonlocal band to band tunneling rate at source-channel (tunneling) junction. Inset: Calibration with the published result, I_{ds}-V_{gs} characteristics of 200 nm gate length SiNW-TFET at V_{ds}=1.2V, t_{ox}=4.5nm, Diameter=70nm. (b) Electric Field near source and drain side of HD-GAA-TFET and GAA-TFET for acceptor, donor and absense of ITC.

lowering (enhancing) of the flat band voltage (V_{fb}), which in turn decreases (increases) the band bending of conduction and valence band. This enhanced (reduced) band bending also results into lowering (higher) of tunneling barrier width. The increase in BTBT rate results into higher tunneling current. The BTBT is almost 1000 times greater in case of HD GAA TFET as compared to GAA TFET. It should be noted that as $\Delta V_{fb}=qN_f/C_{ox}$, where ΔV_{fb} is the change in flat band voltage, q is the electronic charge, N_f is the charge density and C_{ox} is the oxide capacitance. In case of HD GAA TFET, oxide capacitance in region 1 is increased thereby reducing the ΔV_{fb}. Thus BTBT is less influenced by the interface trap charges in case of HD GAA TFET in comparison with GAA TFET. The effect of interface traps on electric field near source and drain side for both the devices is shown in Fig. 2(b). The electric field is higher at the tunneling junction (near source side) for all the cases. In case of HD GAA TFET, the dielectric near source side is replaced by a high-k and the dielectric near drain is kept same. So the effect of HD is concentrated at the tunneling junction only and field near drain side is very less affected by the application of HD. Again due to higher (lower) band bending, the electric field is enhanced (reduced) for the donor (acceptor) traps near the source channel junction. Electric field near drain side is also enhanced (reduced) for positive (negative) interface charges for both the mentioned devices. The impact of interface charges on transfer-characteristics of both the devices is shown in Fig. 3(a). As mentioned before, the donor (acceptor)

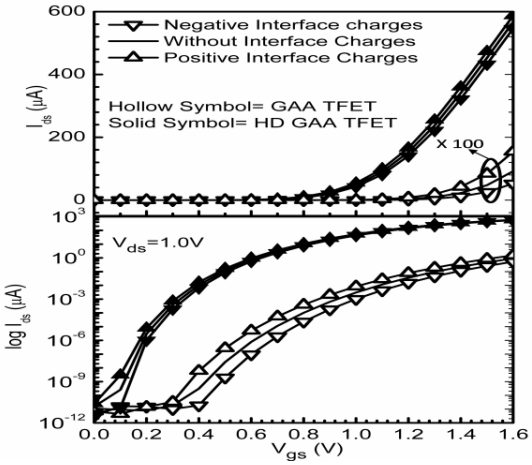

(3a)

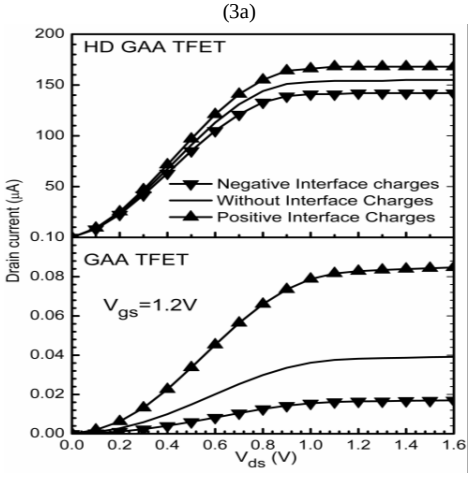

(3b)

Fig. 3 (a) Transfercharacteristic and (b) output characteristics of HD-GAA-TFET and GAA-TFET as a function of gate to source voltage for acceptor, donor and absense of ITC.

traps increases (decreases) the band bending. This increase (decrease) results in higher (lower) band to band generation rate, which finally leads to increase (decrease) in ON current. The donor (acceptor) interface traps increases (decreases) the ON current by 117% (57%) and 8.6% (8.2%) in case of GAA TFET and HD GAA TFET respectively. Furthermore the effect of interface traps is less in case of HD GAA TFET as compared to GAA TFET. This results into better device reliability in case of HD GAA TFET as compared to GAA TFET. The effect of interface traps (both donor and acceptor) on output characteristics of both the devices is shown in Fig. 3b. It is clearly shown that the donor (acceptor) traps increases (decreases) the tunneling current. Again the effect of ITCs is comparatively less in case of HD GAA TFET as compared to GAA TFET. Thus, HD GAA TFET is more reliable in comparison to GAA TFET. Another vital device design parameter is transconductance to current ratio (g_m/I_{ds}) or the device efficiency, which gives the measure of efficiency to convert current (power) into transconductance (speed). The impact of ITCs on device efficiency is shown in Fig. 4. Enhancement (reduction) in drain current and transconductance (as shown in Fig. 3(a) and Fig. 9 respectively) due to positive (negative) ITCs, results into

This article has been accepted for publication in a future issue of this journal, but has not been fully edited. Content may change prior to final publication. Citation information: DOI 10.1109/TDMR.2016.2564448, IEEE Transactions on Device and Materials Reliability

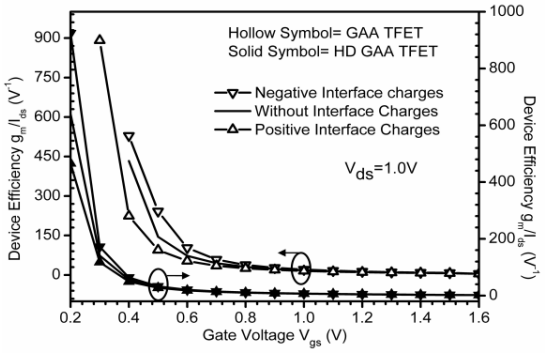

Fig. 4 Impact of ITC on device efficiency of HD-GAA-TFET and GAA-TFET.

decrease (increase) in device efficiency for both the devices. The decrease (increase) in device efficiency due to presence of positive (negative) ITCs is mainly attributed to larger deviations in drain current in comparison to transconductance. The impact of ITCs on output resistance or the drain resistance with respect to the V_{ds} is shown in Fig. 5. R_{out} is numerically equal to inverse of drain conductance $g_{d,}$ higher R_{out} is desirable for better analog performance in order to achieve higher voltage gain, $A_v=g_m*R_{out}$. It is clearly depicted in the graph that R_{out} of HD GAA TFET is many orders lower than R_{out} of GAA TFET. But the higher transconductance in case of HD GAA TFET (shown in Fig. 9) counterbalance the degradation of R_{out} and hence will stabilize the value of intrinsic gain of the device. Moreover, the presence of acceptor (donor) ITCs results into increase (decrease) of R_{out}, but again the increase/decrease in case of HD GAA TFET is very much less in comparison with GAA TFET.

After analysing the effect of trap charges on analog performance, we have investigated their influence on high frequency performance of both the devices. Numerous RF figures of merits (FOMs) and high frequency (HF) gains such as cutoff frequency $f_{T,}$ maximum oscillation frequency $f_{Max,}$ transconductance frequency product (TFP), unilateral power gain and maximum transducer power gain have been evaluated. f_T is a very vital parameter for evaluating and designing the RF performance of the device. f_T is also defined as the frequency at which short circuit current gain drops to unity (or the input and output currents are equal). f_T of both the devices has been presented in the Fig. 6(a). Numerically the cut off frequency is given by:

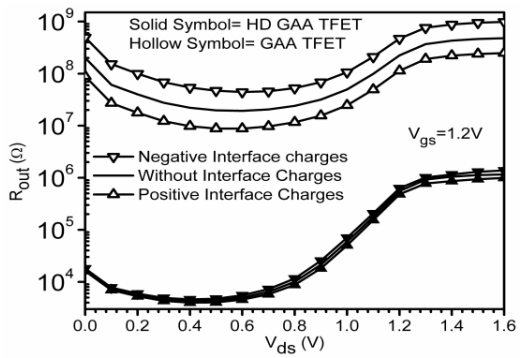

Fig. 5 Impact of ITCs on output resistance of HD-GAA-TFET and GAA-TFET.

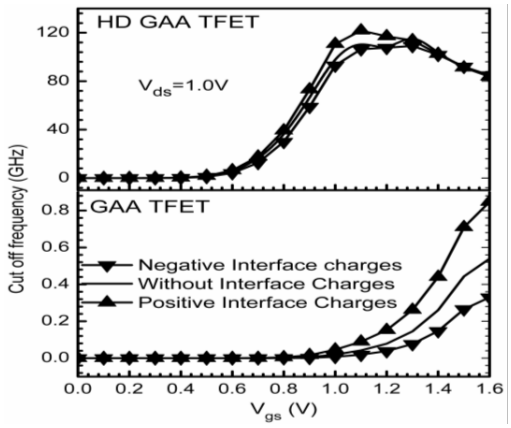

(6a)

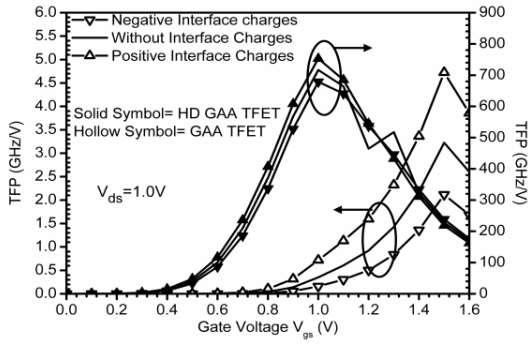

(6b)

Fig. 6 (a) Cut off frequency and, (b) transconductance frequency product (TFP) as a function of gate voltage of HD-GAA-TFET and GAA-TFET.

$$f_T = \frac{g_m}{2\pi(C_{gs}+C_{gd})} \quad (1)$$

Where; C_{gs} and C_{gd} are gate-to-source and gate-to-drain capacitance respectively. It is clearly evident that f_T of HD GAA TFET is several orders of magnitude greater than GAA TFET. Because of the increase (decrease) in transconductance due to donor (acceptor) traps, the f_T of both the devices increases (decreases) as shown in Figs. 6(a) and 9. At V_{gs}=1.2V, donor (acceptor) traps results into an increase (decrease) of 93 % (51%) and 12 % (3%) of f_T for GAA TFET and HD GAA TFET respectively. A unique FOM for high frequency performance is the transconductance frequency product (TFP), given in Eq.(2) is plotted in Fig. 6(b) for donor, acceptor and absence of ITCs.

$$TFP = (g_m/I_{ds}) \times f_T \quad (2)$$

TFP is basically the product of device efficiency and f_T. It represents a trade-off between power and bandwidth and is used for moderate to high speed designs [22]. It is clear from Fig. 6(b) that TFP of HD GAA TFET is almost 10 decades higher w.r.t TFP of GAA TFET. Further, TFP increases linearly before inversion region for both the device and after attaining a maximum value, it starts decreasing for the higher gate bias (after the inversion region is formed). Due to the presence of donor (acceptor) interface traps, TFP increases (decreases) in both the devices. At V_{gs}=1.0V, the increase (decrease) in case of GAA TFET and HD GAA TFET is by 104% (54%) and 5% (5%) respectively. Further, unilateral power gain has been extracted for determining the value of

This article has been accepted for publication in a future issue of this journal, but has not been fully edited. Content may change prior to final publication. Citation information: DOI 10.1109/TDMR.2016.2564448, IEEE Transactions on Device and Materials Reliability

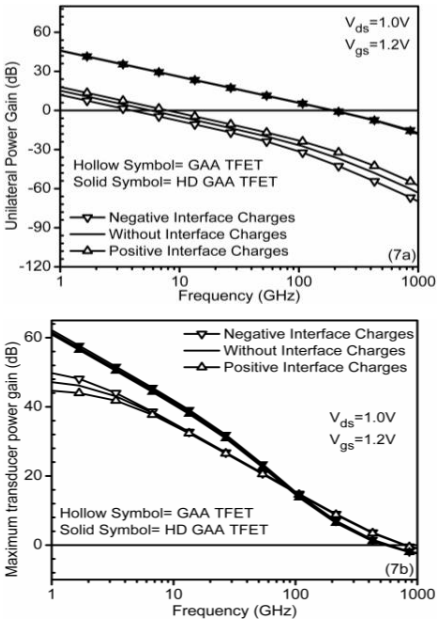

Fig. 7 (a) Unilateral power gain (b) maximum transducer power gain as a function of frequency of HD-GAA-TFET and GAA-TFET.

maximum oscillation frequency (f_{max}) and is defined as the power gain with no reverse transmission or nearly very minute reverse transmission. F_{Max} is the frequency at which the Mason's unilateral power gain drops to unity (corresponds to 0dB). Fig. 7(a) shows the effect of ITCs on unilateral power gain on both the devices. With the application of HD on GAA TFET, unilateral power gain is enhanced. The positive (negative) ITCs enhances (reduces) the unilateral power gain in case of GAA TFET, and the presence of high-k dielectric near source reduces (enhances) the unilateral power gain for positive (negative) ITCs. Moreover the effect of ITCs is very less in case of HD GAA TFET in comparison with GAA TFET. Maximum transducer power gain (G_{MT}) is basically a measure of efficacy of the two ports. In case of a two port network G_{MT} is defined as the ratio of average power delivered to the load by a source to a maximum available power from the source. Fig. 7(b) shows the effect of ITCs on G_{MT} of both HD GAA TFET and GAA TFET. Faintly degradation in the performance of GMT in case of HD GAA TFET has been obtained in comparison to GAA TFET at high frequency beyond 100GHz. The effect of ITCs is negligible less for frequency greater than 10GHz, but at lower frequencies increase (decrease) in GMT due to negative (positive) ITCs has been found.

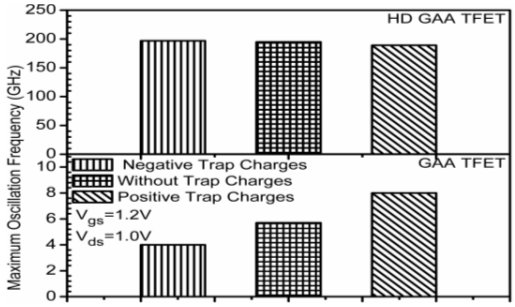

Fig. 8 Maximum oscillation frequency of HD-GAA-TFET and GAA-TFET.

Fig. 8 compare the maximum oscillation frequency f_{max} of both the devices for the donor, acceptor and absence of trap charges acquired from unilateral power gains. It is clearly evident from both the bar graphs that f_{max} for HD GAA TFET is 49.2, 34.17 and 23.62 times greater than f_{max} of GAA TFET for positive, without and negative ITCs. For HD GAA TFET f_{max} increases (decreases) by 1.02% (2.97%) for acceptor (donor) trap charges. Thus, results indicate that with the application of HD engineering, analog as well as high frequency performance of TFET is enhanced, making it a better candidate for high switching speed electronics application.

B. Effect of ITCs on linearity and distortion performance

Along with the high speed, modern communication systems must give assurance for minimum signal distortion to determine the suitability of the device for analog and RF applications. If the linearity is not maintained by a device, then the nonlinear parts at the output may swamp out the desired signal. For better linearity of a system, transconductance should be a constant over the input voltage but transconductance of a MOSFET as well as TFET depends on the input voltage, this reflects the nonlinear behaviour of a MOSFET as well as TFET. In this work, effect of ITCs on linearity and RF distortion of TFET are analysed by metrics V_{IP2}, V_{IP3}, IMD3, IIP3, g_{m3}, 1dB compression point and zero-crossover point. Which are defined as:

$$VIP2 = 4 \times \frac{g_{m1}}{g_{m2}} \qquad VIP3 = \sqrt{24 \times \frac{g_{m1}}{g_{m3}}} \tag{3}$$

$$IIP3 = \frac{2}{3} \times \frac{g_{m1}}{g_{m3} \times R_s} \qquad g_{mn} = \frac{\partial^n I_{ds}}{\partial V_{gs}^n} \tag{4}$$

$$IMD3 = \left[\frac{9}{2} \times (VIP3)^3 \times g_{m3}\right]^2 \times R_s \tag{5}$$

$$1 - dB\ compression\ point = 0.22\sqrt{\frac{g_{m1}}{g_{m2}}} \tag{6}$$

Where R_s=50Ω for most of the RF applications and V_{IP2} represents the extrapolated input voltage at which first second-order harmonic voltages are equal; V_{IP3} represents the extrapolated input voltage at which first and third-order harmonic voltages are equal; and IIP3 represents the extrapolated input power at which first and third-order harmonic powers are equal.

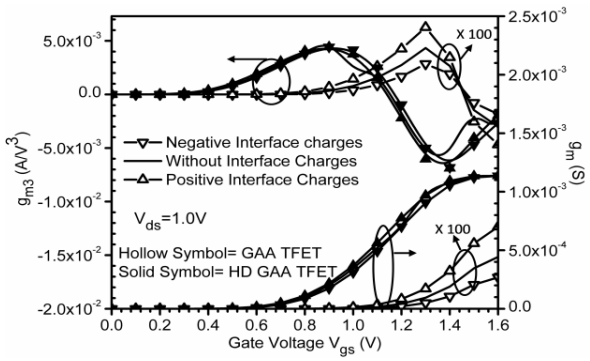

Fig. 9 g_m and g_{m3} as a function of gate bias of HD-GAA-TFET and GAA-TFET for various types of ITCs.

This article has been accepted for publication in a future issue of this journal, but has not been fully edited. Content may change prior to final publication. Citation information: DOI 10.1109/TDMR.2016.2564448, IEEE Transactions on Device and Materials Reliability

For improved linearity performance and low distortion operations, these FOMs should be as high as possible [23]. Transconductance g_m is basically the gain of the device and it also decides the current driving capability of the device. The peak value of the curve (g_m=$g_{m|max}$) gives the optimum bias point for which the device gives the maximum gain (used in case of amplifiers). Fig. 9 shows the impact of interface charges on transconductance of both the devices. As it is clearly shown that the presence of donor (acceptor) traps increases (decreases) the transconductance. Also at V_{gs}=1.2V, transconductance is enhanced (reduced) by 94 % (51%) and 13% (2.4%) for donor (acceptor) traps w.r.t the case when there are no interface traps for GAA TFET and HD GAA TFET respectively. Thus, with the application of HD onto TFET, the device reliability is also improved along with the analog performance. The higher order transconductance coefficient g_{m3} is plotted with respect to V_{gs}, as shown in Fig. 9. For better linear performance the amplitude of g_{m3} should be as low as possible. g_{m3} is mainly responsible for the distortion of fundamental amplitude via signals in the adjacent bands or the intermodulation distortions. It is clearly evident from Fig. 9 that peak of the g_{m3} is lower in case of HD GAA TFET and also shifted towards lower gate bias. Further the variation against ITCs are also less in case of HD GAA TFET.

Figs. 10(a-b) shows the effect of ITCs on V_{IP2} and V_{IP3} with respect to the variation of V_{gs} at a constant V_{ds}=1.0V for GAA TFET and HD GAA TFET. For high linearity and low distortion V_{IP2} and V_{IP3} should be as high as possible. The amplitude of V_{IP3} is higher for HD GAA TFET in comparison with GAA TFET, which shows that along with better analog performance (as shown in previous work [24]) HD engineering exhibits high linearity and low distortion in comparison with conventional TFET. Moreover the peak of the V_{IP3} is also shifted towards the lower gate bias; it implies that a lower gate drive is required to preserve linearity with the amalgamation of HD engineering onto TFET. Further, the peak value of VIP3 increases (decreases) with the presence of donor (acceptor) ITCs. V_{IP2} is used to determine the distortion characteristics for different DC parameters. As evident from graph that with the application of HD, V_{IP2} is enhanced, showing a better linearity of the device.

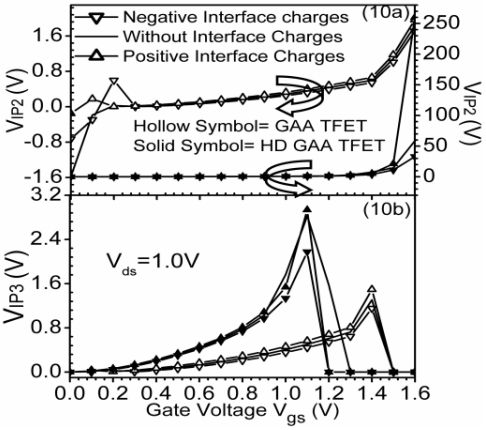

Fig. 10 (a) VIP2 and (b) VIP3 as a function of V_{gs} of HD-GAA-TFET and GAA-TFET for various types of ITCs.

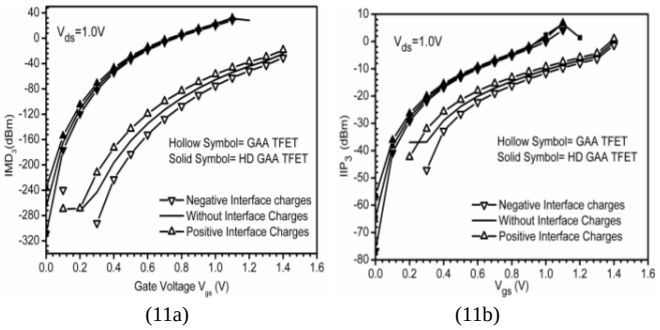

(11a) (11b)

Fig. 11 (a) IMD3 and (b) IIP3 as a function of gate bias of HD-GAA-TFET and GAA-TFET for various types of ITCs.

Figs. 11(a)-(b) illustrates the variation of third order intercept inpt power (IIP3) and third order intermodulation distortion power (IMD3) with V_{gs}. The effect of ITCs is also included in the result. When the third order nonlinearity term is equal to the fundamental term in signal power, is called the IIP3. For high linearity and lower distortion operation, IIP3 should be as high as possible and IMD3 should be as low as possible.

As reported earlier in many papers, IIP3 increases with an increase in gate bias for both aforementioned devices. As evident from 11(b) that HD GAA TFET has higher IIP3 in comparison with GAA TFET, which indicates the potential of HD for better linearity and low distortions analog and RF applications. Moreover better immunity against ITCs is gained in case of HD GAA TFET as compared to GAA TFET. 1-dB compression point (P1dB) is defined as the input power which causes the gain to drop by 1-dB (this can be considered as the onset of the distortion). P1dB gives the estimate of maximum input power, after which the gain of an amplifier decreases. Fig. 12(a) presents the impact of ITCs on 1-dB compression point for both the devices. Thus, because of reduced signal distortion and high transconductance in case of HD GAA TFET, P1dB is also enhanced in case of HD GAA TFET in comparison with GAA TFET as demonstrated in Fig. 12(a). Further, there is an increase (decrease) in P1dB due the presence of positive (negative) ITCs. The nonlinearity possessed by g_{m3} can be supressed by selecting the optimum biased point; determined by the zero crossover point (ZCP) of g_{m3}. Fig. 12(b) shows that a higher V_{gs} is needed in case of GAA TFET to achieve better linearity, in comparison with HD GAA TFET. Moreover for positive (negative) ITCs, ZCP shift towards lower (higher) gate voltages, which is desirable for better linearity and low distortion.

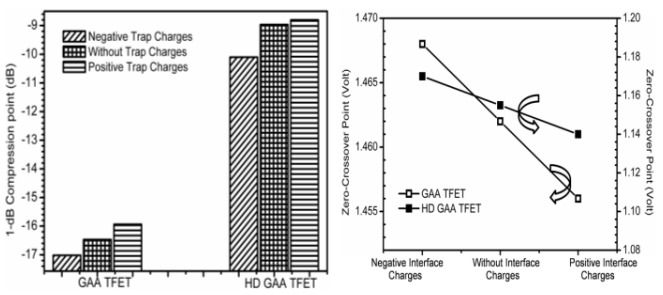

(12a) (12b)

Fig. 12 Comparison of (a) 1-dB compression point and (b)zero crossover point as a function of gate bias of HD-GAA-TFET and GAA-TFET for various types of ITCs.

This article has been accepted for publication in a future issue of this journal, but has not been fully edited. Content may change prior to final publication. Citation information: DOI 10.1109/TDMR.2016.2564448, IEEE Transactions on Device and Materials Reliability

involved in teaching the B.Tech and M.Tech courses. Her doctoral research involves modeling, design and simulation of Sub-100nm gate engineered Grooved Gate/Concave MOSFET for RFIC design and wireless applications, modeling and simulation of Insulated Shallow Extension (ISE) MOSFET for RF and microwave applications; and HEMT structures modeling for high performance microwave circuits. Her other areas of interests and activities cover VHDL implementation, solar cell modeling and simulation. She has authored or co-authored more than 149 papers in various international and national journals and conferences. She has supervised around 9-10 M.Tech students and 6 Ph.D. students are presently working under her guidance. Dr. Chaujar is an executive member of various International and Professional Societies. She is a reviewer of various International Journals and Conferences.

Optical Materials 58 (2016) 116–120

Contents lists available at ScienceDirect

Optical Materials

journal homepage: www.elsevier.com/locate/optmat

Low band gap polymeric solar cells using solution-processable copper iodide as hole transporting layer

Neeraj Chaudhary [a, b], J.P. Kesari [b], Rajiv Chaudhary [b], Asit Patra [a, *]

[a] CSIR-Network of Institutes for Solar Energy, Organic & Hybrid Solar Cells Group, Physics of Energy Harvesting Division, CSIR-National Physical Laboratory, Dr. K. S. Krishnan Marg, New Delhi 110012, India
[b] Department of Mechanical Engineering, Delhi Technological University, Delhi 110042, India

ARTICLE INFO

Article history:
Received 17 December 2015
Received in revised form
16 March 2016
Accepted 20 March 2016

Keywords:
Polymeric solar cells
Copper iodide
Hole transporting layer
Solution-processable
Optical properties

ABSTRACT

In the present work, we have shown the performance of solution-processable copper iodide (CuI) as an alternative hole transporting layer (HTL) for polymeric solar cells. Optical spectra of the CuI thin film reveal highly transparent and practically no absorption in the range vis-NIR region (450–1110 nm). X-ray diffraction (XRD) patterns of CuI exhibits as a *p*-type semiconductor as well as crystalline nature. The photovoltaic devices were fabricated using PCDTBT and PTB7 as donor materials blended with $PC_{71}BM$ as an acceptor material. The power conversion efficiencies (PCEs) based on CuI as an HTL have been achieved to up to 3.04% and 4.48% for PCDTBT and PTB7 based donor materials respectively with a configuration based on ITO/CuI(40 nm)/active layer (60 nm)/Al (120 nm). This study clearly indicated that the devices made with CuI as an HTL showed superior performance than the device fabricated from PEDOT:PSS layer as an HTL. Morphological characterization of the HTL using scanning electron microscopy (SEM) and atomic force microscope (AFM) were carried for better understanding.

1. Introduction

Polymeric solar cells have been gained a significant attention in the last two decades due to their potential advantages like mechanical flexibility, simple fabrication processes, cost effective, light weight and large area fabrication process, which are essential for bulk scale production [1,2]. Till date the power conversion efficiency (PCE) and lifetime of the photovoltaic devices are not adequate for possible commercial applications. Many attempts have been projected to optimization of photovoltaic device to reach the highest possible PCE and lifetime of the device. Among them, introduction of active materials (donor and acceptor materials) and their optimization are the most studied [3–6]. In contrast, interfacial layer (hole transport layer; HTL and electron transport layer; ETL) have received scant attention for device fabrication, while interfacial materials are playing a vital role to improve the device performance. Especially, the HTL and their deposition method have significant importance for optimal device performance to reach the highest possible PCE.

Water soluble poly(3,4-ethylenedioxythiophene):poly (styrenesulfonate) (PEDOT:PSS) is the most successfully used HTL in organic solar cells because of its excellent transporting properties, high conductivity, optical transparency in the visible range and suitable work function. While several studies have been confirmed that due to its hygroscopic, protonation and acidic nature often corrode the ITO and affects the long-term stability of the photovoltaic devices [7–10]. On the other hand PSS free organic materials like small molecules based [11], graphene-based materials [12,13] and carbon nanotubes (CNTs) etc. are also used as HTL in organic solar cells, while the photovoltaic performances of these devices are not high as compared to PEDOT:PSS as an HTL. Transition metal oxides with a high work function, namely molybdenum oxide (MoO_x), vanadium oxide (V_2O_5), nickel oxide (NiO) and tungsten oxide (WO_3) so forth have been successfully used as HTL in organic solar cells to overcome the degradation issue of PEDOT:PSS [14–21]. It is worth to mention that thermal deposition of few metal oxides such as MoO_3 was worked even better as HTL compared to solution-processed deposition.

Recently, solution-processable deposition of metal oxides with a cost-effective method has been attracted significant for solar cells applications in general. Despite the significant efforts, however, there remains a clear need for the development of new, robust, inexpensive and solution-processable HTL for cost effective

* Corresponding author.
E-mail address: apatra@nplindia.org (A. Patra).

http://dx.doi.org/10.1016/j.optmat.2016.03.040
0925-3467/

photovoltaic devices and in plastic optoelectronics more generally. Copper thiocyanate (CuSCN) was reported as an efficient solution-processable HTL in BHJ solar cells [22–24]. While, poor solubility of CuSCN has limits its applications as a solution-processable HTL for solar cells applications to the general public [22,24]. Recently, few reports have been appeared in literature for solution processed CuI as an HTL for polymeric solar cells [25–27]. Bian and co-workers demonstrated solution processable CuI as an HTL for poly(3-hexylthiophene):[6,6]-phenyl C_{61}-butyric acid methyl ester (P3HT:PC_{61}BM) [28] based polymeric solar cells and achieved to up to 4.15% PCE [25]. Alford and co-workers also reported P3HT:PC_{61}BM based solar cells employing solution-processable CuI as an HTL and compared with PEDOT:PSS [26].

Solution-processable CuI as an HTL that have replaced PEDOT:PSS for device fabrication based on P3HT:PC_{61}BM has been already reported [25,26]. Encouraged by the research of CuI over PEDOT:PSS as an HTL, we decided to explore the solution-processable CuI as an HTL for organic solar cells based on low band gap polymers for photovoltaic performances. In order to examine we have used PCDTBT [29] and PTB7 [30] as two low band gap donor materials blend with phenyl-C_{71}-butyric acid methyl ester (PC_{71}BM) as an acceptor material based on ITO/CuI/active layer/Al device configuration as shown in Fig. 1. The highest occupied molecular orbital (HOMO) and lowest unoccupied molecular orbital (LUMO) of PCDTBT, PTB7, PC_{71}BM and CuI together with the work function of ITO, PEDOT:PSS and Al are presented in Fig. 2. The work function of CuI (−5.1 eV) is slightly higher lying compared to PEDOT:PSS (−5.2 eV), which may be suggested CuI is a better hole extraction layer. Moreover, the LUMO level of CuI is about 2.0 eV, which was higher lying than the LUMO of active materials (PCDTBT, PTB7 and PC_{71}BM) and as a result easily block the electron transport to anode electrode. Additionally, CuI is a hydrophobic in nature which may provide better compatibility with hydrophobic organic materials like PCDTBT and PTB7, which improve the ordering the organic materials and reduce the contact resistance between the active layer and interfacial layer. The chemical structures of the active materials of PCDTBT, PTB7 and PC_{71}BM are presented in Fig. 3.

Here, we demonstrate that CuI as an efficient and solution-processable HTL for low band gap polymeric solar cells. Two different combinations of low band gap polymers (PCDTBT and PTB7) blended with PC_{71}BM were used as an active layer for photovoltaic device fabrication. Referential devices based on PEDOT:PSS layer as HTL have been fabricated for PCDTBT and PTB7 respectively. In this present work, the resulted HTLs were

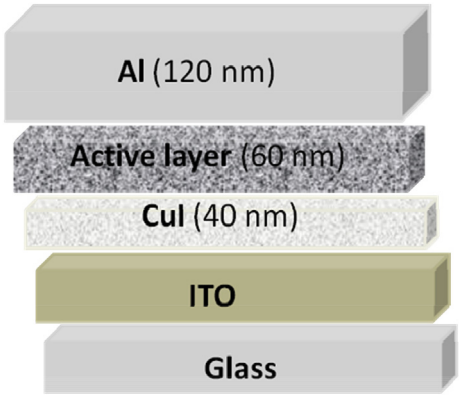

Fig. 1. Schematic diagram of the conventional polymeric solar cells in which the CuI layer is sandwiched between an ITO anode and active layer and the thickness.

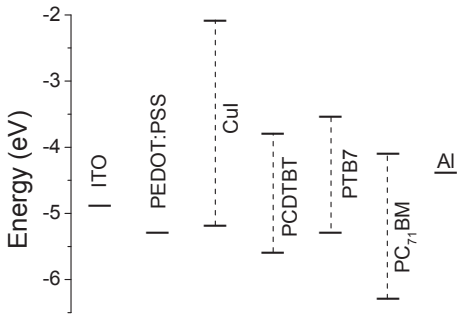

Fig. 2. Energy level diagram of the materials used in organic solar cells.

characterized by UV–vis–NIR spectroscopy, scanning electron microscope (SEM) and atomic force microscope (AFM) for better understanding to achieve the highest possible efficiency.

2. Experimental section

2.1. Materials

All chemicals and materials were purchased from Sigma–Aldrich, and Alfa-Aesar and used without further purification unless otherwise stated. PCDTBT, PTB7 and PC_{71}BM were purchased from 1-material, Canada.

2.2. Preparation of CuI thin film as an HTL

10 mg of copper(I) iodide (CuI) was dissolved in 1.0 mL of acetonitrile and the resulting suspension mixture was sonicated for 1 h at room temperature. After sonication the mixture was kept for 10 min and the resulting clear solution was used for solution-processable HTL in organic solar cells.

2.3. Preparation of PEDOT:PSS as an HTL

Around 35 nm thickness PEDOT:PSS was deposited by spin casting. After that the resulting layer was annealed at 120 °C for 15 min. Then the active layer was deposited.

2.4. Preparation of active materials

PCDTBT:PC_{71}BM: The composition ratio of PCDTBT:PC_{71}BM is1:4 that dissolved in a mixture of chlorobenzene and dichlorobenzene (1:3 ratio) in a concentration of 35 mg/mL.

PTB7:PC_{71}BM: The compositions ratio of PTB7:PC_{71}BM is 1:1.5 that dissolved in a mixture of chlorobenzene and 1,8-diiodoctane (97:3 vol%) in a concentration of 25 mg/mL.

2.5. Device fabrication

The fabrication of polymeric solar cells was done on ITO coated glass slides based on ITO/HTL/active layer/Al. First, etching of ITO slides having a suitable pattern was done by using laser scribing system. Then the slides were cleaned using soap solution followed by several rinses with deionized water. The substrates were further cleaning in boiling acetone followed by trichloroethylene and isopropanol. After annealing the slides, a thin film of CuI (40 nm) layer was deposited by spin coating over it at 3500 rpm for 60 s (10 mg CuI in 1.0 mL acetronitrile). The resulting substrates were annealed at 100 °C for 15 min followed by dried at room temperature for 1 h. For reference devices 35 nm thickness of PEDOT:PSS as an HTL layer

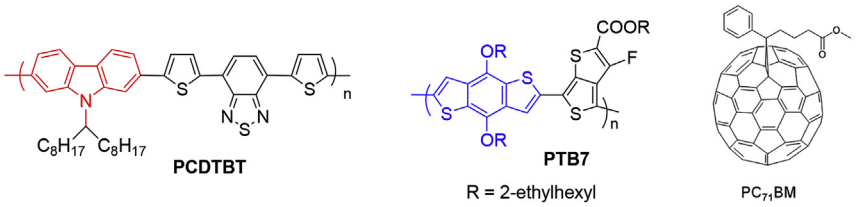

Fig. 3. Chemical structures of PCDTBT, PTB7 and $PC_{71}BM$.

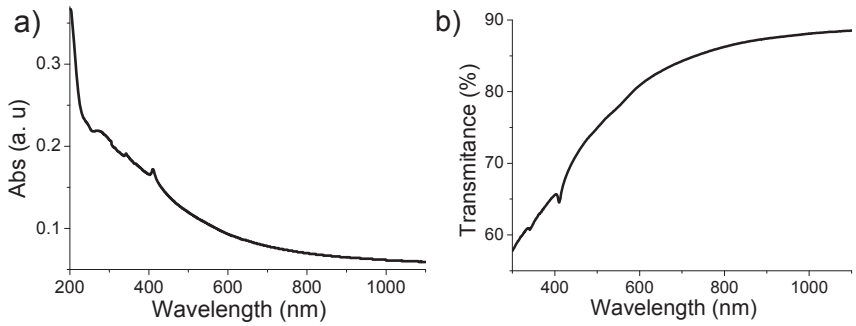

Fig. 4. Optical spectra of CuI thin films on quartz substrate, a) absorption and b) transmission.

was used for solar cells fabrication. Active materials ($PCDTBT:PC_{71}BM$ and $PTB7:PC_{71}BM$) were used and spin coated on top of CuI layer at 1000 rpm for 90 s. Then the substrates were baked using a hot plate at 70 °C for 10 min in the glove box. Finally, the devices were completed via the deposition of the aluminum layer (120 nm) as cathode within a vacuum chamber at pressure 8×10^{-6} mbar.

2.6. Device characterization

All the device measurements were performed in ambient conditions without a protective atmosphere. The current–voltage (J–V) characteristics and PCEs were measured with a computer controlled keithley 2400 source meter. To measure the current density under illumination, the devices were illuminated from the transparent ITO electrode side using solar simulator with an air mass 1.5G (AM 1.5G) (100 mW/cm^2). UV/Vis spectra were obtained on UV-1800, shimadzu spectrophotometer (spectral resolution 1.0 nm). AFM and SEM images of CuI films were obtained on model number NT-MDT Solver Pro and Zeiss EVO MA-10, variable pressure. XRD was performed using Cu Kα radiation with λ = 0.15405929 at Rigaku Miniflex-II.

3. Results and discussion

Fig. 4 displays the optical spectra of CuI thin films on quartz substrate to investigate the absorption and transmission across the range of solar spectrum [31]. CuI film shows absorption in UV region (<450 nm) and very little absorption in the range vis-NIR region (450–1110 nm). In contrast, PEDOT:PSS films exhibit significant absorption in the range vis-NIR region. Accordingly, due to lower parasitic absorption of CuI makes it's an efficient HTL in solar cells for further improvement of PCE compared to PEDOT:PSS. The transmission spectrum reveals that the CuI thin film is highly transparent in the vis-NIR region. Thus CuI thin film exhibits better transparency compared to PEDOT:PSS thin films.

The X-ray diffraction (XRD) patterns of CuI is shown in Fig. 5. The CuI exhibits an intense peak at 25.47 (2θ) corresponds to the CuI (111) reflection, which was assigned to γ-phase with zinc blende structure [31]. It is worth mentioned here that CuI has three crystalline phases of α, β and γ. Among them, γ-phase of CuI exhibits as *p*-type semiconductor. The CuI shows another weak peak at 52.35 (2θ) corresponding to CuI (222), which indicates the crystalline nature of the material.

To examine the performance of solution-processable CuI as a

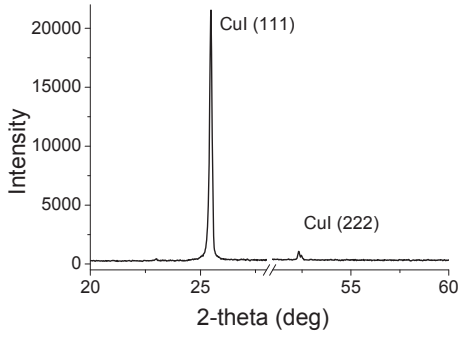

Fig. 5. XRD pattern of CuI.

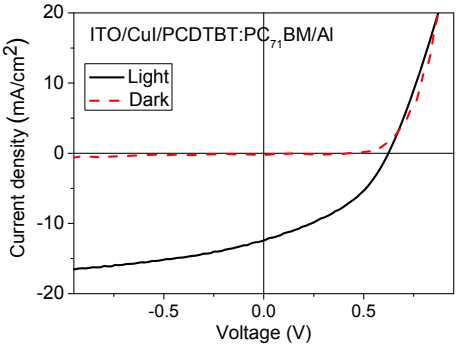

Fig. 6. Current density *versus* voltage (J–V) curves of photovoltaic device based $PCDTBT:PC_{71}BM$ active layer.

Table 1
Solar cells parameters of the devices from the solution-processable CuI as an HTL and donor materials with $PC_{71}BM$ of active area 5.0 mm^2 (average of 8 devices).

Donor materials	HTL	J_{sc} (mA/cm^2)	V_{oc} (V)	FF	PCE (%)
PCDTBT	CuI	11.93 (±0.41)	0.63 (±0.01)	0.42 (±0.03)	3.04 (±0.15)
PTB7	CuI	17.55 (±0.84)	0.63 (±0.02)	0.40 (±0.03)	4.48 (±0.21)

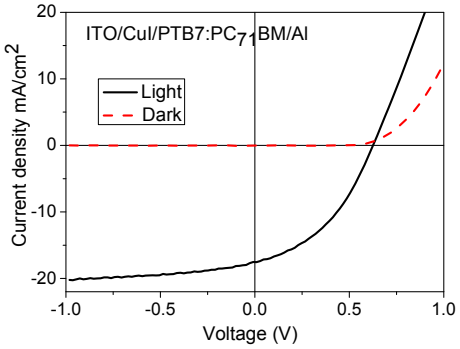

Fig. 7. Current density *versus* voltage (J–V) curves of photovoltaic device based PTB7:$PC_{71}BM$ active layer.

potential member of HTL for low band gap polymeric solar cells, we have fabricated the device based on ITO/CuI/PCDTBT:$PC_{71}BM$/Al using PCDTBT as a donor polymer with $PC_{71}BM$ as an acceptor material. The CuI as an HTL layer was deposited from a solution of acetonitrile (10 mg/mL) [32]. Then the active material PCDTBT:$PC_{71}BM$ (1.0:4.0 wt%) was deposited on the annealed HTL followed by deposition of 120 nm aluminum layer. The J–V curve in dark and light are presented in Fig. 6. The area of the active device is 5.0 mm^2 and average photovoltaic parameters of 8 devices are presented in Table 1. The dark curve shows a characteristic diode behavior. In light, we have found that the resulting devices show average PCE of 3.04% with open circuit voltage (V_{oc}), short-circuit current density (J_{sc}) and fill factor (FF) are 0.63 V, 11.93 mA/cm^2 and 0.42 respectively. In contrast, photovoltaic devices using solution-processable PEDOT:PSS as an HTL shows slightly lower performance than that of CuI as an HTL under identical conditions (Fig. 8) [33]. The lower performance of the device is mainly due to the lower in FF and J_{sc} of the device.

In order to further examine the CuI as an efficient HTL for low band gap polymer, we have considered PTB7 as a donor material blended with $PC_{71}BM$ as an acceptor. The CuI as an HTL was deposited from acetonitrile solution (10 mg/mL) on ITO coated glass and annealed. Then the active layer and metal cathode were deposited successively to complete the photovoltaic device with structure of ITO/CuI/PTB7:$PC_{71}BM$/Al. The J–V curves of dark and light are shown in Fig. 7. The resulting device exhibits PCE of 4.48% with V_{oc}, J_{sc} and FF are 0.63 V, 17.55 mA/cm^2 and 0.40 respectively (Table 1). To compare the performance of CuI as an HTL in OPV cells, we have fabricated the reference device using PEDOT:PSS as an HTL under identical conditions. The reference device exhibits lower performance as previously observed. The poor performance of the device about PCE 3.14% based on PEDOT:PSS is due significant lower FF and J_{sc} (Fig. 8) [34]. Both the results with low band gap polymeric solar cells based on PCDTBT and PTB7 clearly demonstrated that solution-processable CuI is even better HTL for photovoltaic

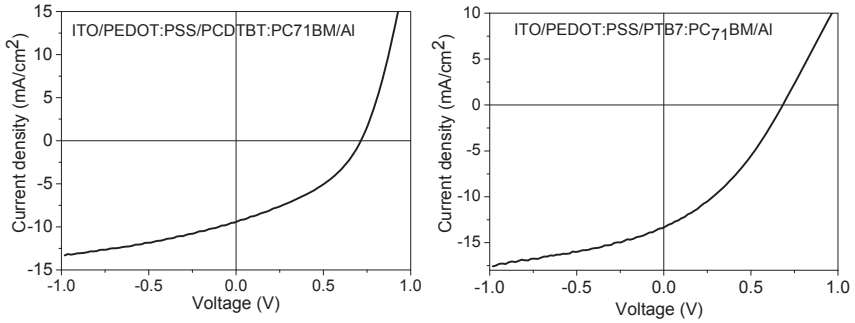

Fig. 8. J–V curves for the devices based on the structure of ITO/PEDOT:PSS/active layer/Al geometry.

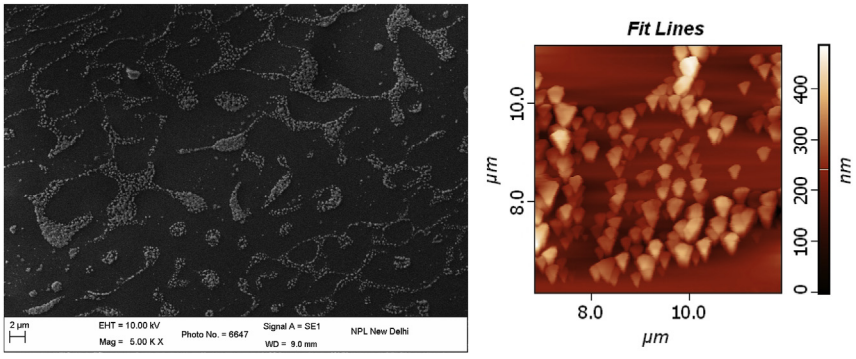

Fig. 9. (left) SEM image, (right) AFM images of CuI thin films on glass substrate.

applications.

To get a better understanding the effect of interface layer on device performance, the morphologies of the CuI layers were characterized by scanning electron microscopy (SEM) and atomic force microscope (AFM). CuI particles form a discontinuous path like CuI islands as shown in SEM image (Fig. 9). In contrast, PEDOT:PSS film exhibits a smooth surface. The AFM image of CuI film is relatively rough due to growing of CuI particles in acetronitrile. It is also noted here that PEDOT:PSS film has been reported as smoother surface.

4. Conclusion

In conclusion, we have demonstrated the efficient polymeric solar cells based on the inexpensive and solution-processable CuI as an HTL. The use of the CuI improve light absorption within the active materials and achieve to up to 3.04% and 4.48% PCEs for active materials of PCDTBT:$PC_{71}BM$ and PTB7:$PC_{71}BM$ respectively. These results are relatively better when compared to the devices fabricated using solution processed PEDOT:PSS as HTLs under similar conditions was due to the improvement of the J_{sc} and FF. We have provided further examples of solution-processable CuI as a good and inexpensive HTL over PEDOT:PSS for low band gap polymeric solar cells, in general. This study clearly demonstrates that due to non-acidic nature of CuI there is further opportunity to optimize the solution-processable CuI as an HTL to improve the PCE and lifetime of the device with a wide range of materials is under process in our laboratory.

Acknowledgments

This work is financially support by the CSIR-TAPSUN (NWP-54) programme. The authors are grateful to Jai Tawale for help with SEM measurements, to N. K. Upadhyaya for XRD measurements and to Dr. G. D. Sharma, and R. Bhardwaj for technical support.

Appendix A. Supplementary data

Supplementary data related to this article can be found at http://dx.doi.org/10.1016/j.optmat.2016.03.040.

References

[1] F. Huang, and H.-L. Yip, Y. Cao, Polymer Photovoltaics: Materials, Physics, and Device Engineering, ed. SC Polymer Chemistry Series.
[2] C. Brabec, U. Scherf, V. Dyakonov (Eds.), Organic Photovoltaics: Materials, Device Physics, and Manufacturing Technologies, second ed., Wiley-VCH Verlag GmbH & Co. KGaA, 2014.
[3] Y.-J. Cheng, S.-H. Yang, C.-S. Hsu, Chem. Rev. 109 (2009) 5868–5923.
[4] P.M. Beaujuge, J.M.J. Fréchet, J. Am. Chem. Soc. 133 (2011) 20009–20029.
[5] H. Dong, H. Zhu, Q. Meng, X. Gongb, W. Hu, Chem. Soc. Rev. 41 (2012) 1754–1808.
[6] L. Ye, S. Zhang, L. Huo, M. Zhang, J. Hou, Acc. Chem. Res. 47 (2014) 1595–1603.
[7] B. Roth, G. A. d. R. Benatto, M. Corazza, R.R. Søndergaard, S.A. Gevorgyan, M. Jørgensen, F.C. Krebs, Adv. Energy Mater. 5 (2015) 201401912.
[8] M. Jorgensen, K. Norrman, F.C. Krebs, Sol. Energy Mater. Sol. Cells 92 (2008) 686–714.
[9] B. Ecker, J. Posdorfer, E. von Hauff, B. Ecker, Sol. Energy Mater. Sol. Cells 116 (2013) 176–181.
[10] M. Jørgensen, K. Norrman, S.A. Gevorgyan, T.S. Tromholt, B. Andreasen, F.C. Krebs, Adv. Mater. 24 (2012) 580–612.
[11] A.W. Hains, C. Ramanan, M.D. Irwin, J. Liu, M.R. Wasielewski, T.J. Marks, ACS Appl. Mater. Interfaces 2 (2010) 175–185.
[12] S.-S. Li, K.-H. Tu, C.-C. Lin, C.-W. Chen, M. Chhowalla, ACS Nano 4 (2010) 3169–3174.
[13] J. Liu, Y. Xue, Y. Gao, D. Yu, M. Durstock, L. Dai, Adv. Mater. 24 (2012) 2228–2233.
[14] M.D. Irwin, D.B. Buchholz, A.W. Hains, R.P.H. Chang, T.J. Marks, Proc. Natl. Acad. Sci. 105 (2008) 2783–2787.
[15] R. Steim, F.R. Kogler, C.J. Brabec, J. Mater. Chem. 20 (2010) 2499–2512.
[16] S. Shao, J. Liu, J. Bergqvist, S. Shi, C. Veit, U. Würfel, Z. Xie, F. Zhang, Adv. Energy Mater. 3 (2013) 349–355.
[17] E.L. Ratcliff, J. Meyer, K.X. Steirer, N.R. Armstrong, D. Olson, A. Kahn, Org. Electron. 13 (2012) 744–749.
[18] Y. Sun, C.J. Takacs, S.R. Cowan, J.H. Seo, X. Gong, A. Roy, A.J. Heeger, Adv. Mater. 23 (2011) 2226–2230.
[19] P. Qin, G. Fang, F. Cheng, W. Ke, H. Lei, H. Wang, X. Zhao, ACS Appl. Mater. Interfaces 6 (2014) 2963–2973.
[20] (a) Z. Tan, L. Li, F. Wang, Q. Xu, S. Li, G. Sun, X. Tu, X. Hou, J. Hou, Y. Li, Adv. Energy Mater. 4 (2014) 1300884;
(b) V.Shrotriya, G.Li, Y.Yao, C.Chu, Y.Yang, Appl. Phys. Lett. 88 (2006) 073508.
[21] H. Pan, L. Zuo, W. Fu, C. Fan, B. Andreasen, X. Jiang, K. Norrman, F.C. Krebs, H. Chen, Org. Electron. 14 (2013) 797–803.
[22] N. Yaacobi-Gross, N.D. Treat, P. Pattanasattayavong, H. Faber, A.K. Perumal, N. Stingelin, D.D.C. Bradley, P.N. Stavrinou, M. Heeney, T.D. Anthopoulos, Adv. Energy Mater. 5 (2014) 1401529.
[23] N.D. Treat, N. Yaacobi-Gross, H. Faber, A.K. Perumal, D.D.C. Bradley, N. Stingelin, T.D. Anthopoulos, Appl. Phys. Lett. 107 (2015) 013301.
[24] N. Chaudhary, R. Chaudhary, J.P. Kesari, A. Patra, S. Chand, J. Mater. Chem. C 3 (2015) 11886.
[25] W. Sun, H. Peng, Y. Li, W. Yan, Z. Liu, Z. Bian, C. Huang, J. Phys. Chem. C 118 (2014) 16806–16812.
[26] S. Das, J.-Y. Choi, T.L. Alford, Sol. Energy Mater. Sol. Cells 133 (2015) 255–259.
[27] Y. Peng, N. Yaacobi-Gross, A.K. Perumal, H.A. Faber, G. Vourlias, P.A. Patsalas, D.D.C. Bradley, Z. He, T.D. Anthopoulos, Appl. Phys. Lett. 106 (2015) 243302.
[28] M.T. Dang, L. Hirsch, G. Wantz, Adv. Mater. 23 (2011) 3597–3602.
[29] (a) Poly[N-9′-heptadecanyl-2,7-carbazole-alt-5,5-(4′,7′-di-2-thienyl-2′,1′,3′-benzothiadiazole)] (PCDTBT). (b) S. Beaupré, M. Leclerc, J. Mater. Chem. A 1 (2013) 11097–11105.
[30] (a) Poly[[4,8-bis[(2-ethylhexyl)oxy]benzo[1,2-b:4,5-b′]dithiophene-2,6-diyl][3-fluoro-2-[(2-ethylhexyl)carbonyl]thieno[3,4-b]thiophenediyl]] (PTB7). (b) F. He, L. Yu, J. Phys. Chem. Lett. 2 (2011) 3102–3113;
(c) L. Ye, S. Zhang, W. Zhao, H. Yao, J. Hou, Chem. Mater. 26 (2014) 3603–3605.
[31] M. Grundmann, F.-L. Schein, M. Lorenz, T. Böntgen, J. Lenzner, H.V. Wenckstern, Phys. Status Solidi A 210 (2013) 1671–1703.
[32] Higher and lower concentration of CuI yielded poorer performances.
[33] For comparison purpose, we have fabricated the photovoltaic devices by using solution-processable PEDOT: PSS as HTL under similar conditions and found PCE 2.57% with J_{sc}, V_{oc} and FF are 9.36 mA/cm^2, 0.72 V and 37.9% respectively.
[34] We have fabricated the reference photovoltaic devices based on the structure of ITO/PEDOT: PSS/PTB7:$PC_{71}BM$/Al under similar conditions and found PCE 3.14% with J_{sc}, V_{oc} and FF are 13.25 mA/cm^2, 0.69 V and 34.4% respectively.

J Solid State Electrochem
DOI 10.1007/s10008-016-3244-1

ORIGINAL PAPER

Performance of the vanadium redox-flow battery (VRB) for Si-PWA/PVA nanocomposite membrane

Jay Pandey[1,2] · **Bhagya R. Tankal**[2]

Received: 17 March 2016 / Revised: 21 April 2016 / Accepted: 8 May 2016

Abstract The performance of Si-PWA/PVA nanocomposite membrane in vanadium redox-flow battery (VRB) is reported. Structurally, the membrane consisted of a dispersion of submicron-sized silica immobilized phosphotungstic acid (Si-PWA) inorganic ion-exchanging phase in the continuous phase of cross-linked poly(vinyl alcohol) (PVA). SEM micrographs indicated the defect-free top surface of membrane with similar morphology of Nafion-115. Good ion selectivity and availability of ion-exchangeable sites were observed as indicated by higher transport number (0.89) and ion-exchange capacity (IEC) (1.20 meq g^{-1}), respectively. Oxidative stability of the membrane was good in vanadium ion species (V^{4+}, V^{3+}, and V^{2+}) but its stability in V^{5+} solution and Fenton's reagent was slightly lower than Nafion-115. Vanadium ion permeability (0.69×10^{-7} cm min^{-1}) of Si-PWA/PVA membrane was significantly lower than Nafion-115. Suitability for VRB with Si-PWA/PVA membrane was assessed from open-circuit voltage (OCV) decay which was lower compared to Nafion-115. Single-cell VRB with Si-PWA/PVA membrane exhibited lower voltage during charge and higher during discharge with excellent cyclic stability compared to VRB with Nafion-115.

Keywords Nanocomposite membrane · Vanadium redox-flow battery · Oxidation stability · Vanadium permeability · OCV decay

✉ Jay Pandey
jay.pandey.iitd@gmail.com

[1] Department of Polymer Science and Chemical Technology, Delhi Technological University, Delhi 110042, India

[2] Department of Chemical Engineering, Indian Institute of Technology Delhi, Hauz Khas, New Delhi 110016, India

Introduction

Electrical energy storage technologies have a crucial role in load leveling and off-grid applications including integration of electricity grid with various renewable energy devices [1, 2]. However, storing large amount of energy and employment of renewable energy devices into large power distribution system is still one of the major challenges at this moment. In the past two decades, interest in redox-flow batteries (RFB), using different redox couples, has increased tremendously due to their high capacity of large energy storage in the range of kilowatt-hour to megawatt-hour with tunable power capacity, high energy efficiency, long cycle life, and rapid response time [3]. RFB mainly works on various redox couples like vanadium/bromide, iron/chromium, zinc/bromine, and vanadium/vanadium [4]. Among all, the vanadium/vanadium redox couples used in vanadium redox-flow battery (VRB), pioneered by Maria Skyllas Kazacos and co-workers at UNSW [4], have unique advantages of the fact that the redox couples in both half-cells involve vanadium in four different oxidation state (V^{2+}/V^{3+} and V^{4+}/V^{5+}). In addition, VRB includes high efficiency, long cycle life, deep discharge, lower cost, and flexible design over conventional redox-flow systems [5, 6].

VRB mainly employs V^{2+}/V^{3+} and V^{4+}/V^{5+} redox couples as electrolyte in negative and positive half-cells, respectively. Ion-exchange membrane (IEM), a core component of VRB, not only separates two half-cells in order to prevent mixing of electrolytic solutions but also allows selective transport of protons (H^+). An ideal membrane for VRB should possess high proton conductivity, low vanadium permeability, and good oxidative stability with low cost [7]. Nafion series membranes (Nafion-112/115/117) are preferred in VRB due to their high proton conductivity (0.1 Scm^{-1}) and excellent chemical/oxidative stability [8]. However, high vanadium ion permeability of Nafion membranes leads to lower

Published online: 18 May 2016

columbic efficiency of VRB. Additionally, Nafion membranes contribute 40 % to total VRB cost due to their high price ($600–800 m^{-2}) [9]. To overcome this problem, Nafion-117 was modified using different inorganic dopants like silica, titania, and phosphotungstic acid (PWA) to reduce its vanadium permeability [10]. Unfortunately, modification of Nafion membranes to reduce vanadium permeability led to poor proton conductivity due to blocking of ion-exchangeable sites. In continuation, sulfonated aromatic polymers were also extensively studied in VRB due to their excellent thermal and chemical stability. Chen et al. [11] have synthesized three different thickness of sulfonated fluorinated poly(arylene ether) (SFPAE) membrane for VRB and reported 95 % energy efficiency with maximum power density of 311 mW cm^{-2}. Dai et al. [12] used sulfonated poly(ether ether ketone)/graphene composite membrane in VRB and achieved maximum energy efficiency of 92.8 % with vanadium permeability of 8.9×10^{-7} cm^2 min^{-1}. In addition to lots of research work on design and synthesis of membranes for VRB, excellent review articles on the development of polymeric membranes for VRB applications were also reported by Schwenzer et al. [13] and Doan et al. [14].

Unfortunately, most of these polymeric membranes are highly prone to vanadium ion permeability resulted into poor VRB performance. Additionally, these sulfonated aromatic polymers showed poor oxidative stability due to their higher degree of sulfonation required for higher proton conductivity. Therefore, proper optimization of polymeric sulfonation is imperative if working with organic polymers.

Interestingly, the best alternative could be the use of inorganic ion-exchangers as a proton source as they possess very high oxidative stability compared to organic ion-exchangers [15]. Inorganic–organic composite ion-exchange membrane [16], synthesized by blending inorganic nanoparticles into a polymer matrix followed by the solution casting, has better mechanical, chemical, and thermal properties. Poly(vinyl alcohol) (PVA) is an attractive polymer matrix since it is biodegradable, low cost, and has high mechanical strength, chemical, and thermal stability [17]. Unfortunately, PVA-based inorganic–organic ion-exchange membranes for VRB applications have not been reported so far.

In our previous work [18], a composite ion-exchange membrane was successfully synthesized by blending the colloidal sol of sub-micron to nano-sized silica immobilized phosphotungstic acid (Si-PWA) inorganic ion-exchanger into the cross-linked PVA solution followed by solution casting to get an 80–100-μm-thick membrane film. Detailed physical (structure and morphology) and electrochemical (transport number and ion-exchange capacity (IEC)) properties of the membrane were studied using various characterization techniques (XRD, ATR-IR, SEM-EDS, TGA). Herein, our aim is to study the suitability of 125-μm-thick Si-PWA/PVA nanocomposite membrane in VRB by determining its vanadium ion permeability, oxidative stability, and open-circuit voltage (OCV) decay. Moreover, the charge–discharge rate and cyclic stability test of the single-cell VRB with the synthesized Si-PWA/PVA membrane was also performed.

Experimental

Materials and method

PVA, phosphotungstic acid ($H_3PW_{12}O_{40}.nH_2O$) and glutaraldehyde (GA) (25 vol.%), cross-linking agent, were purchased from the Central Drug House (CDH), New Delhi. Tetraethyl orthosilicate (TEOS) and vanadium sulfate ($VOSO_4$) were supplied by Alfa Aesar Pvt. Ltd., Hyderabad. All the chemicals were of AR grade (99.99 % purity), and triple deionized water was used for all the experiments.

Membrane synthesis and characterization

Si-PWA/PVA nanocomposite membrane was synthesized in simple two steps using similar procedure described in our previous work [18]. Detailed physicochemical and electrochemical characterizations (XRD, AT-IR, TGA/DSC, tensile test, and proton conductivity) were performed and analyzed for the synthesized membrane showing promising results. Here, we report few additional characterizations to determine suitability of Si-PWA/PVA membrane for VRB applications by studying membrane's oxidative stability, vanadium ion (V^{4+}) permeability, OCV decay, and charge–discharge curves. VRB performance of the synthesized membrane was also compared to the state-of-the-art Nafion-115 (125 μm) under similar conditions.

SEM and EDS

Scanning electron microscopy (SEM) coupled with energy dispersive spectroscopy (EDS) (make: ZEISS Germany, model: EVO-50) was used to study the surface morphology and elemental composition of the synthesized Si-PWA/PVA membrane, respectively. The samples were dried at 80 °C for 2 h to remove the moisture present on the surface of the membrane and then coated with gold to make the membrane sample conducting. SEM micrographs were taken at different magnifications.

Transport number

Na^+ ion transport number of the Si-PWA/PVA membrane was calculated from membrane potential measured using the diffusion cell technique as discussed in our previous publication [19]. The diffusion cell comprised of two compartments of a volume of 27 cm^3 each, separated by the membrane of circular

shape with an exposed area of 12.56 cm^2. Aqueous NaCl solutions of two different concentrations were used for the experiments. Membrane was equilibrated with NaCl solution of lower concentration for 24 h and then mounted on the cell. Lower concentration NaCl solution (0.01 M) was filled in one of the compartments first followed by filling the second compartment with higher concentration solution (0.1 M). Steady-state potential difference between the liquids in the two compartments was measured using Ag/AgCl electrodes and a multimeter (make: Mastech Inc. India, model: 3900). Transport number for the cation (Na^+) in the membrane was calculated using the Plank–Henderson equation given below,

$$E_m = \frac{RT}{nF}(2t_+\text{-}1)\ln\frac{C_1}{C_2} \quad (1)$$

E_m is the membrane potential (V), t_+ is the transport number for Na^+ ion, C_1 is the higher concentration (0.1 M), and C_2 is the lower concentration (0.01 M) of NaCl. R is the universal gas constant (8.314 $Jmol^{-1}$ K^{-1}), F is Faraday's constant (96, 485 $Cmol^{-1}$), and T is temperature (K).

Oxidative stability test

Fenton's test was done to measure the ability of the membrane to sustain the attack of radicals like hydroxyl group (*OH) and peroxide groups (*HOO) [20]. Oxidative stability of membrane sample was determined by immersing it in hot Fenton's reagent (3 % H_2O_2 aqueous solution containing 2 ppm $FeSO_4$) at 80 °C. Weight loss of the membrane in hot Fenton's reagent was measured every 1 h and till the sample started to break or dissolve in solution.

Stability in different oxidation states of vanadium

A weighed membrane sample was kept in a solution of 2 M $VOSO_4$ in 3 M H_2SO_4 (same composition used for VRB test) and the weight loss was measured. Every 24 h, the sample was taken out from the solution wiped with blotting paper and kept in oven to dry for 30 min and then the weight was measured. This was repeated till the weight of the membrane stopped changing. The same procedure was followed for measuring the degradation of membrane in different oxidation states of the electrolytic solutions, i.e., V^{+5}/V^{+4} and V^{+3}/V^{+2}.

Vanadium ion (V^{4+}) permeability test

A two-compartment diffusion cell separated by the synthesized membrane was used for vanadium ion (V^{4+}) permeability test. One side of the cell was filled with 2 M $VOSO_4$ in 3 M H_2SO_4 and the other side was filled with 2 M $MgSO_4$ in 3 M H_2SO_4. After every 1 h, the samples were collected from the compartment having $MgSO_4$, and the concentration of vanadium was measured using UV–Vis spectroscopy. Finally, the permeability was calculated by the equation given in literature [21].

$$V_R\frac{dC_R(t)}{dt} = A\frac{P}{L}[C_L - C_R(t)] \quad (2)$$

where C_L is the concentration (mol L^{-1}) of $V(V^{4+})$ ion in the left compartment and C_R is the concentration (mol L^{-1}) of $V(V^{4+})$ ion in the right compartment as a function of time in, A and L are the area (cm^2) and thickness (cm) of membrane, respectively, P is permeability (cm^2 min^{-1}) of vanadium ion, and V_R is the volume (cm^3) of each compartment.

OCV decay test and VRB cell charging–discharging

Synthesized Si-PWA/PVA membrane was mounted in a single-cell VRB as shown schematically in Fig. 1. Each of the two half-cells separated by membrane has graphite felt electrode. Vanadium sulfate (with V^{4+} oxidation state) was used as an electrolyte which was stored externally in two separate reservoirs and circulated to the cell using peristaltic pumps. Initially, both the reservoirs were filled with 2 M $VOSO_4$ in 3 M H_2SO_4. A direct current (DC) source was used to apply constant current for charging the VRB cell. During VRB charging, the V^{4+} oxidation state of the solution was changed to V^{5+} in anode compartment and V^{3+}/V^{+2} in cathode compartment. VRB charging was stopped when the cell voltage reached to a maximum of 1.8 V, and the OCV of the cell was measured for 3 h. To study the charge–discharge behavior, first, the single-cell VRB, connected to potentiostat/galvanostat (Ref 600, make: Gamry Instruments, USA) with battery testing software, was charged and discharged at a current density of 10 mA cm^{-2}. VRB cell charging and discharging voltages were limited to 1.6 and 0.9 V, respectively, to avoid the degradation of the graphite electrode.

Cyclic stability of the VRB was evaluated by studying the charge–discharge rate of single-cell VRB with Si-PWA/PVA

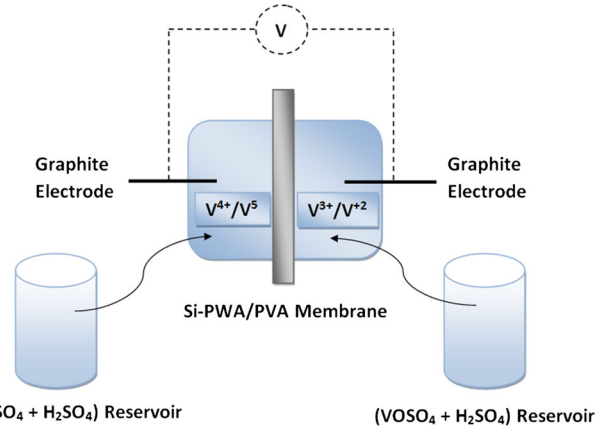

Fig. 1 Schematic of the experimental set up for single-cell VRB

membrane at a fixed current density of 10 mA cm^{-2} under repeated 10 cycles. For comparing the cyclic performance of the synthesized Si-PWA/PVA membrane in VRB, the measurements were also carried out for VRB with Nafion-115 membrane under similar conditions.

Results and discussion

Synthesized Si-PWA/PVA nanocomposite membrane has the backbone of cross-linked PVA which provides mechanical strength to the membrane and uniformly dispersed nanoparticles of Si-PWA ion-exchanger imparts ionic moieties to the membrane. Structural characterization using XRD, as reported in previous work [18], showed amorphous nature of the membrane allowing greater flexibility of the polymeric chain of the cross-linked PVA matrix and thereby enhanced proton conductivity through the membrane. The presence of Si-PWA and PVA cross-linking was confirmed using ATR-IR spectra. Si-PWA/PVA membrane showed excellent tensile strength up to 93 MPa [14] due to cross-linked PVA support.

Figure 2a, and b show the SEM morphology of the top surface of the synthesized Si-PWA/PVA membrane and Nafion-115, respectively. The morphology of the top surface of Si-PWA/PVA shows uniformly distributed Si-PWA nanoparticles (30 nm) onto the cross-linked PVA polymeric support with smooth and defect-free top surface of the membrane having similar morphology of Nafion-115. Even at higher magnification of ×20,000 magnification, any pores of submicron size were not seen which indicates the dense structure of the composite membrane which is responsible for better diffusion of ions through the membrane. Thickness of the synthesized Si-PWA/PVA membrane was 125 μm as shown in the cross-sectional image of Si-PWA/PVA membrane (Fig. 2c) and also confirmed by measuring with digital micrometer.

To confirm the uniform distribution of Si-PWA particles over cross-linked PVA matrix, EDS was performed at different regions of the membrane. The EDS spectrum, as shown in Fig. 2d, show the presence of ion-exchanging phase in the membrane indicating surface uniformity. Table 1 shows the atomic percent of the elements present in the membrane. EDS results clearly demonstrate presence of silica, tungsten, and phosphorous with W/Si ratio 0.31 indicating presence of ion-conducting phase in the membrane responsible for the ion transport.

Oxidative stability

Figure 3 shows the percentage weight loss for the Si-PWA/PVA membrane and Nafion-115, immersed in Fenton's reagent, at different time intervals. Both the membranes showed considerable weight loss up to 12 h and afterwards, there were insignificant weight losses. Total loss in weight of Si-PWA/PVA membrane was found to be 9 % whereas it was only 4 % for Nafion-115. Larger weight loss for the Si-PWA/PVA membrane was due to polymeric PVA support which is relatively weaker compared to PTFE support used in Nafion-115. It is reported that the fluorinated polymers are exceptionally resistant under strong oxidizing medium [8].

Stability in vanadium environment

Insignificant weight loss was observed for both Nafion-115 and Si-PWA/PVA membranes in V^{+4} and V^{+3}/V^{+2} solutions. However, there was a significant weight loss in V^{+5} solution (highly oxidizing in nature) for both the membranes. The weight loss for synthesized Si-PWA/PVA membrane was around 13 % whereas for Nafion-115, it was around 4.5 %. Higher weight loss for Si-PWA/PVA membrane compared to Nafion-115 was due to relatively weak chemical stability of c-PVA matrix compared to mechanically stable fluorinated backbone of conventional Nafion-115.

Transport number and IEC

Synthesized Si-PWA/PVA membrane showed counter-ion (Na^+) transport number, 0.89 and its IEC was observed 1.2 meq g^{-1}. IEC was comparable to that of the state-of-the-art Nafion-115 membrane (0.90 meq g^{-1}); however, its transport number was lower than the Nafion-115 (0.96). It is believed that lower transport number even with similar IEC could be due to higher water uptake and the associated increase in channel diameters for the Si-PWA/PVA membrane [18]. Transport number of the PVA-based membranes has not been reported in literature which is one of the basic electrochemical characterization techniques to measure the homogeneity and heterogeneity of the membrane. It was observed that the IEC of the Si-PWA/PVA membrane is considerably higher than the values (0.5–0.8 meq g^{-1}) reported in literature [17, 18]. The areal resistance of the synthesized membrane (1.34 Ω cm^2) is comparable to Nafion-115.

Transport no. and IEC are the measurement tools describing the ion transport properties and availability of ion-exchangeable sites of any ion-conducting membrane. To assess the stability of synthesized membranes in VRB environment, we measured the transport no. and IEC of Si-PWA/PVA membrane before and after performing charge–discharge cycles for VRB. Interestingly, we did not observe much variation in the transport no. and IEC values even after exposure to VRB electrolytes and repeated charging–discharging of VRB which itself indicates good stability of synthesized membrane under VRB environment.

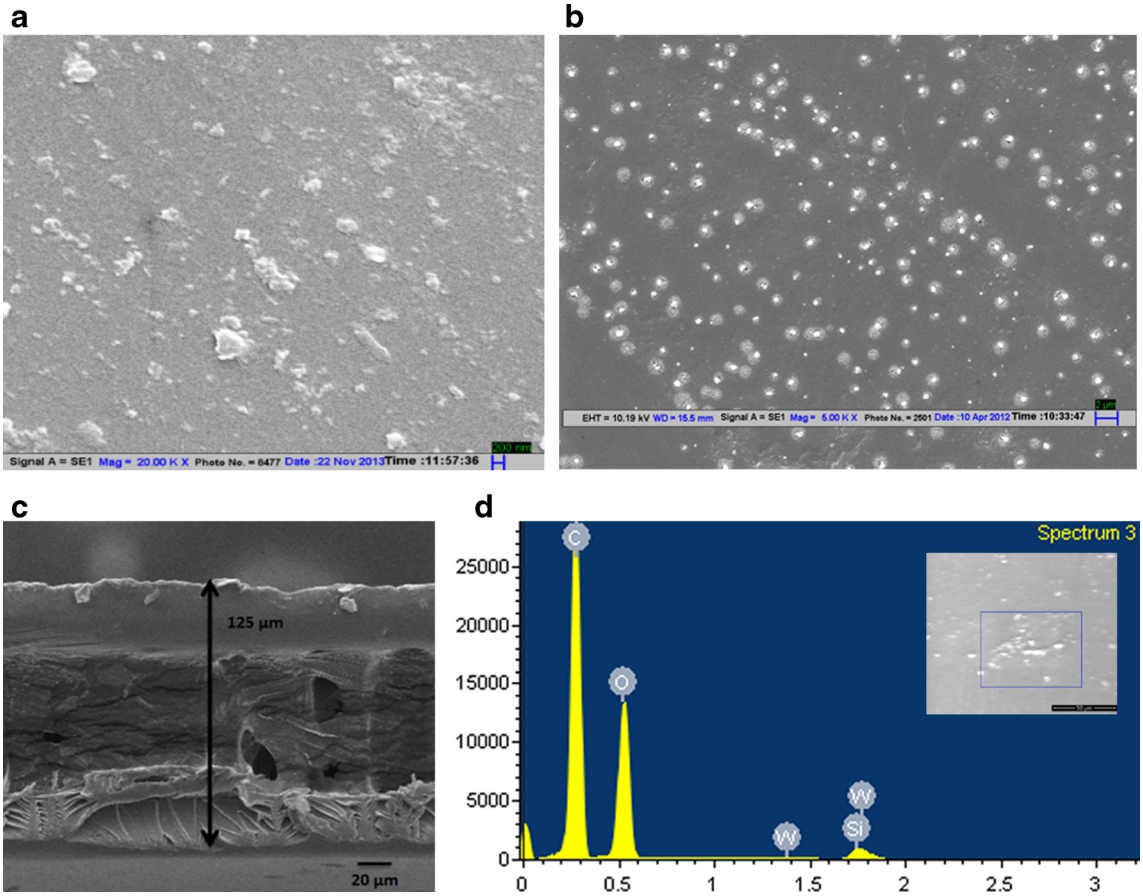

Fig. 2 SEM morphology for **a** Si-PWA/PVA membrane, **b** Nafion-115, **c** cross-sectional view of Si-PWA/PVA membrane, and **d** EDS spectrum for Si-PWA/PVA membrane

Vanadium ion permeability

Figure 4 shows the concentration of permeated vanadium ion (IV) through the synthesized Si-PWA/PVA membrane which was much smaller than Nafion-115. The calculated vanadium ion (V^{4+}) permeability for the Si-PWA/PVA membrane was 0.69×10^{-7} cm^2 min^{-1} about an order of magnitude lower than conventional Nafion-115 (5.8×10^{-7} cm2 min^{-1}). It was observed from the diffusion plot that after a certain period of permeation test, there was no significant change in the concentration of vanadium ion (V^{4+}) for the synthesized membrane; however, there was continuous little permeation in case of Nafion-115. Much lower vanadium ion permeation through Si-PWA/PVA membrane compared to Nafion-115 could be attributed to the presence of silica particles which has ability to retain vanadium (V^{4+}) ions as reported by Vijayakumar et al. [10].

Lower vanadium ion permeability though membrane not only reduces the rate of cross-contamination in VRB cell but

Table 1 EDS elemental composition for Si-PWA/PVA membrane

Element	Atomic %
C	65.44
O	32.55
Si	1.51
W	0.47
P	0.03

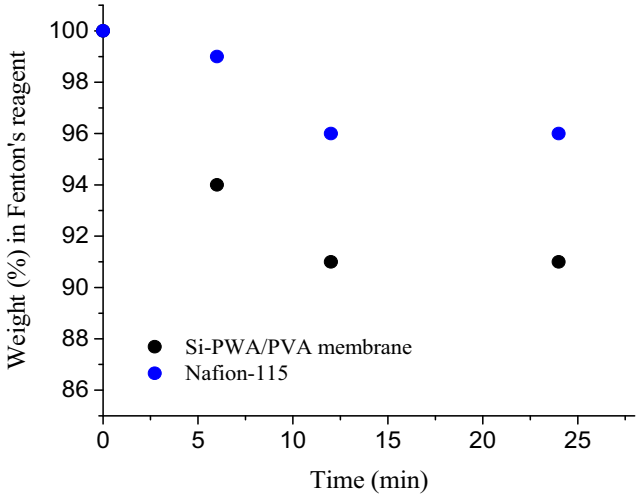

Fig. 3 Weight loss under Fenton's stability test for Si-PWA/PVA membrane and Nafion-115

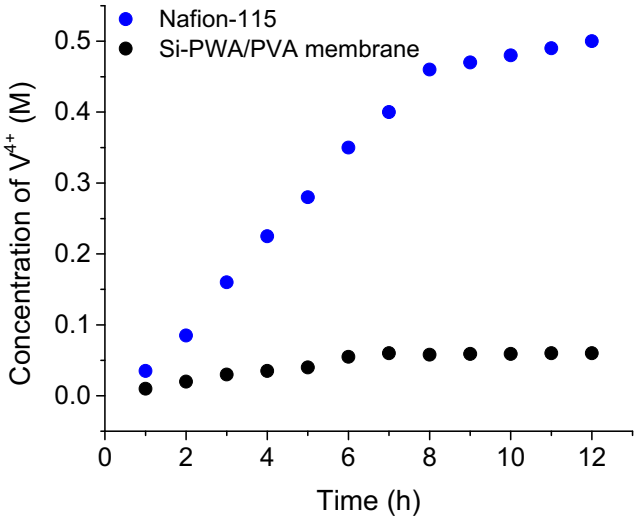

Fig. 4 Vanadium ion permeability for Si-PWA/PVA membrane and Nafion-115

also improves the columbic efficiency of the VRB. The permeability results indicated suitability of the synthesized Si-PWA/PVA membrane in single-cell VRB.

OCV decay test and charge–discharge curves for the VRB cell

Self-discharge of VRB due to cross-mixing of anolyte and catholyte was studied by monitoring open-circuit voltage (OCV) of the VRB at room temperature after it was charged. Electrolyte solutions were continuously circulated during the course of experiment. Electrolyte volume to exposed membrane area was kept low to obtain accelerated result on self-discharge. Figure 5 shows the variation of OCV with time for single cell VRB with Si-PWA/PVA membrane and Nafion-115. OCV decreased continuously with time, the rate of decrease was less rapid for initial period where after it decreased rapidly to about 1.5 V and thereafter, it continued to decrease slowly; however, the drop in OCV for the synthesized Si-PWA/PVA membrane was lower compared to Nafion-115 (1.4 V). The consistent permeation of vanadium ions through the membrane leads to the self-discharge of the VRB cell resulting into the decrease of the OCV [22]. Therefore, the change in the OCV value with time can be used to gauge columbic efficiency of the VRB. The decay in OCV was more for Nafion-115 than the Si-PWA/PVA membrane. The time of the self-discharge for the Si-PWA/PVA membrane was much longer compared to the Nafion-115 and correlates well to the lower permeability of the vanadium ions for the Si-PWA/PVA membrane.

Typical charge–discharge curves, collected at 10 mA cm^{-2} for 10 cycles, for the single-cell VRB with synthesized Si-PWA/PVA membrane and Nafion-115 are shown in Fig. 6. The charge curve shows that the cell charging is relatively faster for the VRB cell with Si-PWA/PVA membrane compared to Nafion-115. Therefore, VRB with Si-PWA/PVA membrane has lower average voltage during charge and has higher average voltage during discharge than VRB with Nafion-115. This resulted in better performance (higher energy efficiency) of VRB with Si-PWA/PVA membrane in comparison to Nafion-115.

The charge–discharge curves for VRB with Si-PWA/PVA membrane collected at different cycles do not show much appreciable change in charge–discharge curves indicating good cyclic stability of synthesized membrane in VRB environment. On the other hand, for the conventional Nafion-115, the cyclic stability was not good due to vanadium ion permeability leading to loss in VRB efficiency. The good cyclic performance of VRB with Si-PWA/PVA membrane also has good agreement with higher ion-exchange capacity and transport no. of synthesized membrane.

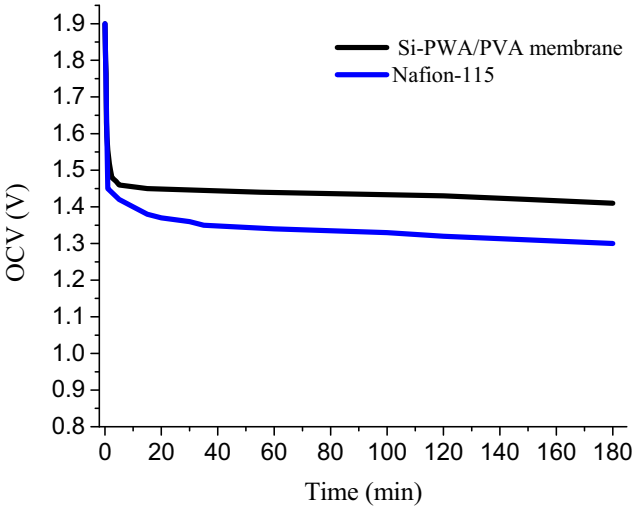

Fig. 5 OCV decay for single-cell VRB with Si-PWA/PVA membrane and Nafion-115

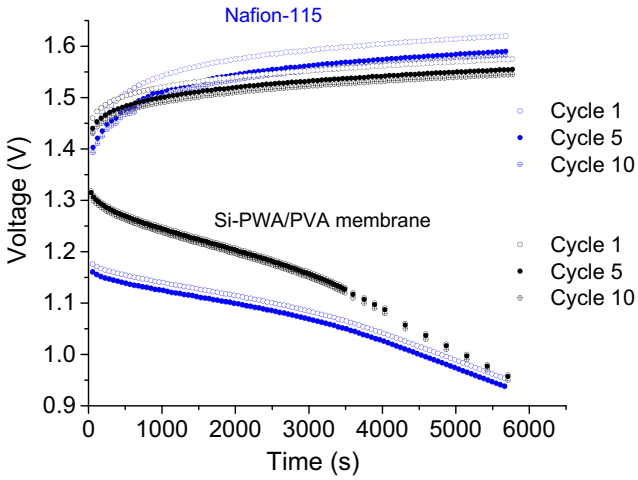

Fig. 6 Charge–discharge curves showing cyclic performance of single cell VRB with Si-PWA/PVA membrane and Nafion-115

Conclusion

Si-PWA/PVA nanocomposite membrane was synthesized using simple solution casting method under controlled thickness of 125 μm. High transport number (0.89) and IEC (1.2 meq g^{-1}) exhibited good ion selectivity and availability of ion-exchangeable sites, respectively. Oxidative stability of Si-PWA/PVA membrane was slightly lower than Nafion-115 due to the strong fluorinated backbone of Nafion-115 compared to the cross-linked PVA support for the Si-PWA/PVA membrane. Single-cell VRB with Si-PWA/PVA membrane showed lower OCV decay compared to Nafion-115 owing to reduced vanadium ion (V^{4+}) permeability through Si-PWA/PVA membrane. VRB with Si-PWA/PVA membrane demonstrated lower voltage during charge and higher during discharge with excellent cyclic stability compared to Nafion-115. Our present work suggests that the synthesized Si-PWA/PVA membrane can be utilized as a promising membrane material for VRB applications.

References

1. Alotto P, Guarnieri M, Moro F (2014) Redox flow batteries for the storage of renewable energy: a review. Renew Sust Energ Rev 29: 325–335
2. Eckroad S (2002) Electric Power Research Institute Report, 1007189, California, USA.
3. Leung P, Li X, Leon CPD, Berlouis L, Low CTJ, Walsh FC (2012) Progress in redox flow batteries, remaining challenges and their applications in energy storage. RSC Adv 2:10125–10156
4. Skyllas-Kazacos M, Rychcik M, Robins RG, Fane AG, Green MA (1986) New all vanadium redox flow cell. J Electrochem Soc 133: 1057–1058
5. Skyllas-Kazacos M, Grossmith F (1987) Efficient vanadium redox flow cell. J Electrochem Soc 134:2950–2953
6. De León CP, Frías-Ferrer A, González-García J, Szánto DA, Walsh FC (2006) Redox flow cells for energy conversion. J Power Sources 160:716–732
7. Skyllas-Kazacos M, Kazacos G, Poon G, Verseema H (2010) Recent advances with UNSW vanadium-based redox flow batteries. Int J Energy Res 34:182–189
8. Pandey J, Shukla A (2013) Synthesis and characterization of PVDF supported silica immobilised phosphotungstic acid (Si-PWA/PVDF) ion exchange membrane. Mater Lett 100:292–295
9. Weber AZ, Mench MM, Meyers JP, Ross PN, Gostick JT, Liu QH (2011) Redox flow battery: a review. J Appl Electrochem 4:1137–1164
10. Vijayakumar M, Schwenzer B, Kim S, Yang Z, Thevuthasan S, Liu J, Graff GL, Hu J (2012) Investigation of Local Environments in Nafion-SiO2 Composite Membranes used in Vanadium Redox Flow Batteries. Solid State Nucl Magn Reson 42:71–80
11. Chen D, Wang S, Xiao M, Meng Y (2010) Synthesis and properties of novel sulfonated poly (arylene ether sulfone) ionomers for vanadium redox flow battery. Energy Convers Manag 51:2816–2824
12. Dai W, Yu L, Li Z, Yan J, Liu L, Xi J, Qui X (2014) Sulfonated Poly(Ether Ether Ketone)/Graphene Co mposite Membrane for Vanadium Redox Flow Battery. Electrochem Acta 132:200–207
13. Schwenzer B, Zhang J, Kim S, Li L, Liu J, Yang Z (2011) Membrane development for vanadium redox flow batteries. Chem Sus Chem 4:1388–1406
14. Doan TNL, Hoang TKA, Chen P (2015) Recent development of polymer membranes as separators for all-vanadium redox flow batteries. RSC Adv 5:72805–72815
15. Pandey J, Mir FQ, Shukla A (2014) Performance of PVDF supported silica immobilized phosphotungstic acid membrane (Si-PWA/PVDF) in direct methanol fuel cell. Int J Hydrog Energy 39: 17306–17313
16. Nagarale RK, Shin W, Singh PK (2010) Progress in ionic organic-inorganic composite membranes for fuel cell applications. Polym Chem 1:388–408
17. Maiti J, Kakati N, Lee SH, Jee SH, Yoon YS (2011) PVA nano composite membrane for DMFC application. Solid State Ionics 201:21–26
18. Pandey J, Mir FQ, Shukla A (2014) Synthesis of silica immobilized phosphotungstic acid (Si-PWA)-poly(vinyl alcohol) (PVA) composite ion-exchange membrane for direct methanol fuel cell. Int J Hydrog Energy 39:9473–9481
19. Geise GM, Cassady HJ, Paul DR, Logan BE, Hickner MA (2014) Specific ion effects on membrane potential and the permselectivity of ion exchange membranes. Phys Chem Chem Phys 16:21673–21681
20. Smitha B, Sridhar S, Khan AA (2005) Synthesis and characterization of poly(vinyl alcohol)-based membranes for direct methanol fuel cell. J Appl Polym Sci 95:1154–1163
21. Duangkaew P, Wootthikanokkhan J (2008) Methanol permeability and proton conductivity of direct methanol fuel cell membranes based on sulfonated poly(vinyl alcohol)–layered silicate nanocomposites. J Appl Polym Sci 109:452–458
22. Xi J, Wu Z, Qiu X, Chen L (2007) Nafion/SiO2 hybrid membrane for vanadium redox flow battery. J Power Sources 166:531–536

Polyaniline modified flexible conducting paper for cancer detection

Saurabh Kumar, Anindita Sen, Suveen Kumar, Shine Augustine, Birendra K. Yadav, Sandeep Mishra, and Bansi D. Malhotra

Citation: Applied Physics Letters **108**, 203702 (2016); doi: 10.1063/1.4950961
View online: http://dx.doi.org/10.1063/1.4950961
View Table of Contents: http://scitation.aip.org/content/aip/journal/apl/108/20?ver=pdfcov
Published by the AIP Publishing

APPLIED PHYSICS LETTERS **108**, 203702 (2016)

Polyaniline modified flexible conducting paper for cancer detection

Saurabh Kumar,[1,a)] Anindita Sen,[1,a)] Suveen Kumar,[1] Shine Augustine,[1] Birendra K. Yadav,[2] Sandeep Mishra,[3] and Bansi D. Malhotra[1,b)]
[1]*Nanobioelectronics Laboratory, Department of Biotechnology, Delhi Technological University, Shahbad Daulatpur, Delhi 110042, India*
[2]*Rajiv Gandhi Cancer Institute and Research Centre, Rohini, Delhi 110085, India*
[3]*Department of Applied Physics, Delhi Technological University, Shahbad Daulatpur, Delhi 110042, India*

(Received 14 March 2016; accepted 3 May 2016; published online 19 May 2016)

We report results of studies relating to the fabrication of a flexible, disposable, and label free biosensing platform for detection of the cancer biomarker (carcinoembryonic antigen, CEA). Polyaniline (PANI) has been electrochemically deposited over gold sputtered paper (Au@paper) for covalent immobilization of monoclonal carcinoembryonic antibodies (anti-CEA). The bovine serum albumin (BSA) has been used for blocking nonspecific binding sites at the anti-CEA conjugated PANI/Au@Paper. The PANI/Au@Paper, anti-CEA/PANI/Au@Paper, and BSA/anti-CEA/PANI/Au@Paper platforms have been characterized using scanning electron microscopy, X-ray diffraction, Fourier transmission infrared spectroscopy, chronoamperometry, and electrochemical impedance techniques. The results of the electrochemical response studies indicate that this BSA/anti-CEA/PANI/Au@paper electrode has sensitivity of 13.9 μA ng^{-1} ml cm^2, shelf life of 22 days, and can be used to estimate CEA in the range of 2–20 ng ml^{-1}. This paper sensor has been validated by detection of CEA in serum samples of cancer patients via immunoassay technique. *Published by AIP Publishing.* [http://dx.doi.org/10.1063/1.4950961]

Cancer is currently the leading cause of morbidity and mortality worldwide. An estimated 14.1×10^6 new cases of cancer occurred in 2012 and it is expected to reach 22×10^6 in the next two decades.[1] The diagnosis of cancer via a biomarker has recently aroused much interest. More than 160 different types of cancer biomarkers have been identified to date.[2] Among these, carcinoembryonic antigen (CEA) is one of the most widely used cancer biomarker that has been associated with colon, ovarian, breast, and lung cancer.[3–6] Its abnormal pre- and postoperative serum levels have been correlated with the depth of tumor invasion, and these are used routinely for the prognosis of cancer. Many methods such as immunohistopathology, radioimmuno assays, enzyme linked immune sorbent assay (ELISA), reverse transcriptase polymerase chain reaction (RT-PCR), and positron emission tomography for CEA detection have been developed.[7–11] These techniques are time consuming, expensive, require expert handling, and necessitate exposure to harmful radiations. In this context, biosensors offer a number of advantages such as simplicity, high sensitivity, cost effectiveness, flexibility, and require low sample volume.[12,13] Glassy carbon, ITO, and gold coated glass electrodes are currently being used as a substrate for fabrication of desired biosensing platforms. However, the rigidity, brittleness, and cost limit their applications towards the development of a wearable, flexible, cost effective, and disposable point-of-care device. Recently, paper based electrochemical biosensors have been attracting considerable attention because of their light weight, flexibility, portability, high sensitivity, fast response time, and disposability.[14–16] Besides this, electrochemical biosensors enable miniaturization through the use of miniaturized components such as interdigitated micro-electrodes, miniaturized potentiostat, etc., that have been found to play an important role in the development of point of care devices.[17–19] Further integration of the paper based electrochemical biosensor with microfludics system is likely to minimize the problems arising due to portability, sample volume size, and excess use of power.

For the fabrication of an efficient biosensing platform, immobilizing matrix plays a crucial role. In this context, polyaniline (PANI) may serve as a promising immobilization matrix due to its solution processability, electrical conductivity, flexibility, and large surface area. Moreover, the presence of amine groups provides an additional benefit for covalent immobilization of biomolecules with enhanced biosensing characteristics.[20–22] Singh *et al.*[23] used nanostructured polyaniline and Soni *et al.*[24] utilized polyaniline-gold nanocomposite for the detection of sexually transmitted disease (gonorrhoeae). Further, Tiwari and Gong demonstrated chitosan-*co*-polyaniline (CS-*co*-PANI) copolymer for application to breast cancer biomarker (BRCA1) detection.[25] These authors used rigid and brittle glassy substrates as biosensing platforms.

We report results of studies relating to the development of a flexible, label free, and disposable electrochemical biosensor for CEA detection. The Whatman filter Paper 1 (procured from GE healthcare, UK) was used as a substrate for the fabrication of the paper based biosensing platform. Initially, a filter paper was sputtered with gold for about 4 min using ion sputtering system (Hitachi Ion Sputter E1010). Further, electropolymerization of polyaniline was accomplished by adopting cyclic voltammetry (Autolab Potentiostat/Galvanostat, Metrohm) using a conventional three-electrode cell, wherein the gold coated paper (Au@paper, 1×2.5 cm) acted as a working, platinum as an auxiliary, and Ag/AgCl as reference electrode in a solution

[a)]Saurabh Kumar and Anindita Sen contributed equally to this work.
[b)]Author to whom correspondence should be addressed. Electronic mail: bansi.malhotra@gmail.com

containing 1.4 M aniline (Merck India, Ltd.) and 1 M HCl in water. The electrochemical cell is exposed to a potential cycle (n = 10) between −0.2 V and 0.9 V with a scan rate of 20 mV/s. Thus obtained uniform green color stable film of PANI/Au@paper electrode was rinsed with milli Q water to remove any unbound polyaniline molecules. Further, for the fabrication of bioelectrode (*anti-CEA/PANI/Au@paper*), monoclonal CEA (Sigma Aldrich India, 1 mg/ml) antibodies were immobilized onto PANI/Au@paper via covalent binding using EDC-NHS chemistry. The EDC-NHS was used to activate and couple the carboxylic (-COOH) group of the antibody with amine group of polyaniline. Further, bovine serum albumin (BSA) (Sigma Aldrich India, 0.1% in phosphate buffer saline, PBS at pH 7.0) was used for blocking non-specific active sites of anti-CEA/PANI/Au@paper electrode. The fabricated BSA/anti-CEA/PANI/Au@paper bioelectrode was washed several times to remove any unbound antibodies and BSA, respectively. These bioelectrodes were stored at 4 °C until further use. Figure 1 shows the step wise fabrication of a polyaniline modified paper sensor.

The results of cyclic voltammetry studies show the formation of PANI on the surface of the gold coated paper (Au@paper) electrode (Figure S1).[33] An oxidation peak seen near 0.2 V corresponds to the formation of emaraldine, a partial oxidized form of aniline, and a peak near 0.8 V relates to the formation of perningraniline, a fully oxidized form of aniline.[26] With increase in the thickness of the film, there is a gradual shift in both the anodic and cathodic peak potential.[27] During electrochemical deposition, polyaniline is switched from its reduced form (leucoemaraldine, transparent) to its oxidized form (emaraldine/perningraniline, green), as shown in video S1.[33] The reduced form of polyaniline reveals its insulating nature, whereas the oxidized form indicates its conducting behavior. The inset of Figure S1 shows the fabricated PANI/Au@paper electrode that exhibits a green uniform deposition of PANI.[33]

The results of X-ray diffraction (XRD, Bruker D-8 Advance, Cu Kα radiation; $\lambda = 1.5406$ Å) studies of the fabricated PANI/Au@paper electrode conducted between 2θ angles 30° and 70° are shown in Figure S2(a).[33] The diffraction peaks observed at 34.2° and 46.3° correspond to (221) and (115) planes, indicating the formation of PANI over Au@paper electrode (JCPDS No.: 53–1891).[28] The surface morphology of the Au@paper, PANI/Au@paper, and anti-CEA/PANI/Au@paper electrodes was investigated via scanning electron microscopy (SEM, Hitachi S-3700 N). The SEM micrograph of the Au@paper electrode (Figure S2(b)) shows smooth and homogenous surface, whereas in Figure S2(c), the thread like porous structure appears to cover the Au@paper surface, confirming the uniform deposition of polyaniline.[33] However, after anti-CEA immoblization (Figure S2(d)), the surface morphology of the PANI/Au@paper electrode shows the filled pores in the fibrous structure of PANI with shiny appearance.[33]

Fourier transmission infrared spectroscopy (FT-IR) (Bruker Optics, Vertex 70 V) spectra of the PANI/Au@paper and anti-CEA/PANI/Au@paper are shown in Figures S3(a) and S3(b), repectively.[33] The FTIR spectrum of the PANI/Au@paper exhibits characterstic absorption band near 1466 and 1618 cm^{-1}, representing benzenoid and quinoid ring of PANI.[29] The other high intensity peak found at 1108 cm^{-1} corresponds to C-H in the plane bending motion of the quinoid ring. The peak present at 1298 cm^{-1} indicates C-N stretching of aromatic amine, whereas the broad band at

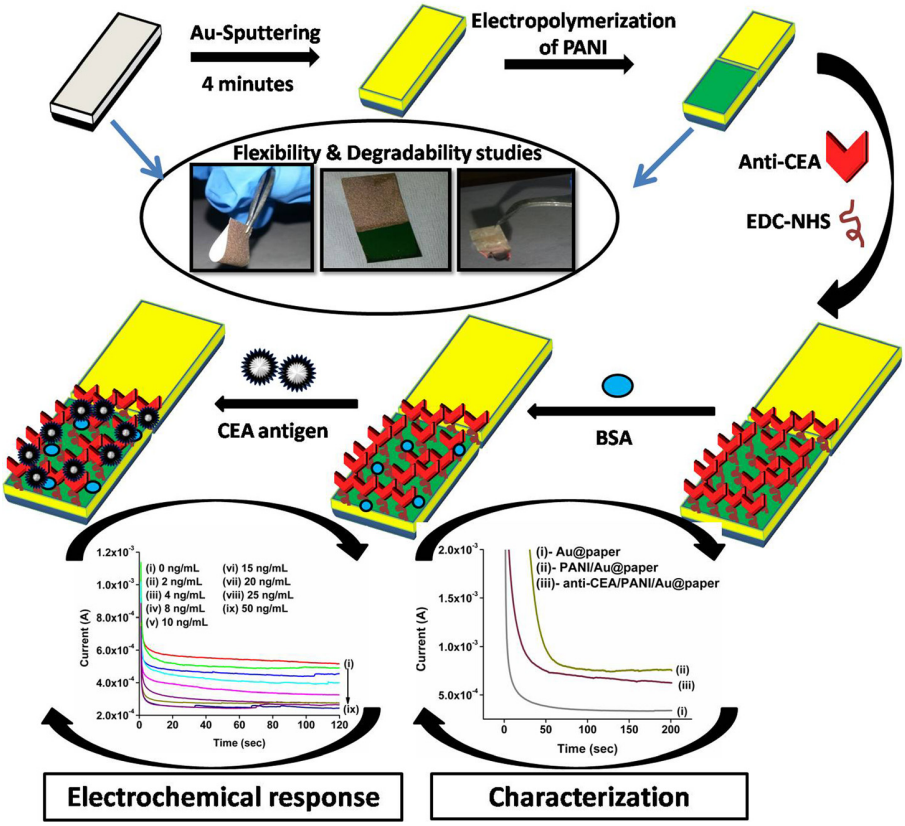

FIG. 1. Schematic relating to fabrication of the anti-CEA/PANI/Au@paper electrode.

3440 cm^{-1} is due to N-H stretching of -NH_2 group present in PANI that helps in covalent immobilization of antibodies.[30] After the anti-CEA immobilization, the peak observed at 1531 cm^{-1} corresponds to C–N bond formed between -NH_2 group of PANI and –COOH groups of F_c region of antibodies, indicating covalent immobilization of anti-CEA.[22] The additional peaks found at 1700 cm^{-1} and 3300 cm^{-1} may be attributed to C=O stretching for amide I and –NH stretch in the amide II group of protein (anti-CEA), respectively.

The results of flexibility studies of the PANI/Au@paper electrode are shown in Figure 2. The optical image at Figure 2(a) exhibits green colour coating of PANI over the Au@paper with a high degree of flexibility. The SEM image in Figure 2(b) shows the dark and light areas of PANI and Au, respectively, at the PANI/Au@paper electrode, revealing successful coverage of PANI over the modified paper fibers (Au@paper). The after effect of bending (+180° and −180°) of the Au@paper electrode results in the formation of cracks along the line of bending, as shown in the SEM micrograph (Figure 2(c)). This may perhaps be attributed to the deformation mismatch between the metal (Au) and the paper substrate when subjected to stress.[31] It appears that the PANI modified Au@paper overcomes this problem by conferring improved flexibility to the Au@paper electrode, as shown in Figure 2(d). Further, it was found that no cracks developed during bending of the PANI/Au@paper electrode. This clearly proves that PANI provides a strong hold over the sputtered gold layer to prevent the delamination of Au from the paper surface.

Electrochemical impedance spectroscopy (EIS) is an effective tool for the investigation of the interfacial properties of the surface modified electrodes. In order to study the charge transfer phenomena occurring at the paper/solution interface, the EIS studies were carried out (Autolab Potentiostat/Galvanostat, Metrohm). Figure 3(a) shows the Nyquist plot obtained for Au@paper, PANI/Au@paper, and anti-CEA/PANI/Au@paper at 0.03 V biasing potential conducted in the frequency range of 100 kHz to 0.1 Hz. The diameter of the semicircle in the Nyquist plot gives the magnitude of charge transfer resistance (R_{ct}) of the electrode that depends on the dielectric characteristics of the electrode/electrolyte interface. The curve fitting has been done assuming Randles circuit [$R_s(R_{ct}C_{dl})$] of the electrochemical cell. The R_{ct} value obtained for the PANI/Au@paper electrode (∼20.6 Ω, curve ii) is found to be lower than that of the Au@paper electrode (∼268Ω, curve i). These results suggest that deposition of PANI onto the Au@paper surface enhances the electron transfer kinetics between the electrolyte and Au@paper electrode, resulting in the enhancement of the electrochemical properties of the PANI/Au@paper electrode. However, the observed R_{ct} value (24.6 Ω, curve iii) for the anti-CEA/PANI/Au@paper electrode is higher than that of the PANI/Au@paper electrode (∼20.6 Ω, curve ii). The significant increase in the R_{ct} value is attributed to the immobilization of anti-CEA that causes the hindrance due to macromolecular structure of antibodies that in turn are likely to obstruct electron transfer owing to their insulating nature. The heterogenous electron transfer rate constant (Kct) value of the Au@paper, PANI/Au@paper, and anti-CEA/PANI/Au@paper electrodes has been estimated to be 1.98×10^{-4} cm s^{-1}, 2.5×10^{-3} cm s^{-1}, and 2.1×10^{-3} cm s^{-1}, respectively. (See the supplementary material for Kct calculation). This indicates that the PANI/Au@paper electrode exhibits faster electron transfer kinetics as compared to the anti-CEA/PANI/Au@paper and Au@paper electrode. Interestingly, Kct of the PANI/Au@paper electrode is found to be nearly 2 orders of magnitude higher compared to our previous works.[15,32]

Figure 3(b) shows results of the chronoamperometric studies (current versus time, Autolab Potentiostat/Galvanostat, Metrohm) obtained for (i) Au@paper, (ii) PANI/Au@paper, and (iii) anti-CEA/PANI/Au@paper, at 0.5 V on every 0.1 s.

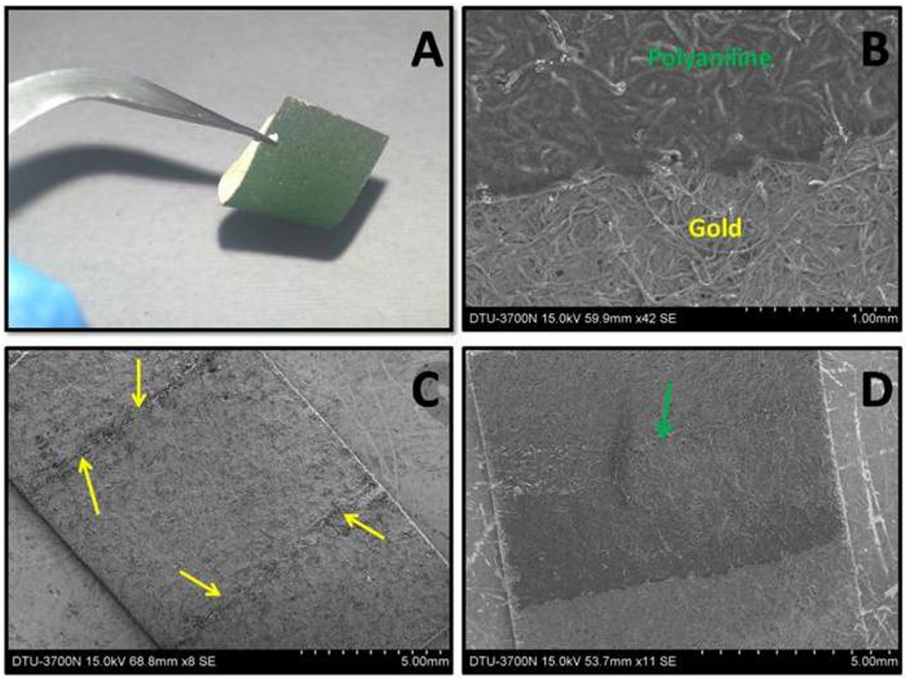

FIG. 2. (a) Optical image of PANI/Au@paper, showing flexible nature. The SEM images of (b) Au@paper and PANI/Au@Paper, confirm uniform deposition of PANI that tightly bound the modified paper fibers. (c) Au@paper electrode after folding (+180° and −180°) developed cracks along the line of folding indicated by the yellow arrows and (d) PANI/Au@paper electrode, no cracks are visible along the line of folding after deposition of PANI.

The observed increase in the value of the electrochemical current of the PANI/Au@paper electrode (~0.76 mA) than that of the Au@paper electrode (~0.34 mA) confirms polymerization of PANI on the Au@paper surface, resulting in enhanced permeability of the redox couple $[Fe(CN)_6]^{3-/4-}$. The decrease in the electrochemical response current of the anti-CEA/PANI/Au@paper electrode (~0.68 mA) than that of the PANI/Au@paper electrode (~0.76 mA) is due to immobilization of the anti-CEA which perhaps hinders the electron transport owing to its insulating and macromolecular nature.

The electrochemical response of the anti-CEA/PANI/Au@paper electrode (Figure 3(c)) was conducted as a function of carcinoembryonic antigen (CEA) concentration (2–50 ng/ml) in PBS (50 mM, pH 7.4, 0.9% NaCl) containing 5 mM $[Fe(CN)_6]^{3-/4-}$ using chronoamperometry with an incubation time of 10 min. For this purpose, bovine serum albumin (0.1% in PBS) was dispensed onto the anti-CEA/PANI/Au@paper electrode to block the non-specific sites. After rinsing with PBS, the electrode was used for sensing studies. The magnitude of the current was measured on addition of each CEA concentration. It was found that the current decreased on addition of CEA due to the formation of electrically insulating antigen-antibody complexes caused by specific interaction of the CEA and the anti-CEA that perhaps diminishes the charge transfer via $[Fe(CN)_6]^{3-/4}$, leading to the reduction in amperometric current at the paper electrode surface. Figure 3(d) shows the calibration curve obtained between the response current and CEA concentration in the range of 2–50 ng/ml. The variation of current with concentration follows:

$$I(A) = -13.9\,\mu\text{A ml ng}^{-1}\text{x [CEA concentration]} + 549\,\mu\text{A; R}^2 = 0.99. \quad (1)$$

The value of sensitivity is obtained as 13.9 μA ng^{-1} ml cm^{-2}. A control experiment was performed to check cross reactivity of the PANI/Au@paper with CEA antigen (in the absence of antibodies). However, no significant change in current response was observed for the PANI/Au@paper in the absence of antibodies as a function of CEA concentration (Figure S4(a)), which clearly indicated the absence of cross reactivity.[33]

The reproducibility, selectivity, and stability of the BSA/PANI/Au@paper electrode were studied (Figures S4(b)–S4(d)) and found to be reasonably reproducible (relative standard deviation (RSD) less than 5%) and stable up to 22 days.[33] The selectivity of the BSA/anti-CEA/PANI/Au@paper electrode was investigated in the presence of other analyte such as cardiac troponin 1 (cTn-1), endotheline-1 (ET-1), and cytokeratin-19 fragment (CYFRA-21-1) (2 ng/ml). We did not observe any significant change in electrochemical current. However, on addition of carcinoembryonic antigen (CEA) (2 ng/ml), we observed a significant change in electrochemical current response, indicating that the BSA/anti-CEA/PANI/Au@paper electrode is highly specific for CEA and does not cross react with other interferants. Further, the BSA/anti-CEA/PANI/Au@paper electrode was validated using CEA concentration obtained by serum samples of cancer patients via immunoassay technique. The sensing results obtained (Table ST1) using the fabricated paper electrode are in accordance with results of the immunoassay.[33]

The sensing characteristics of the BSA/anti-CEA/PANI/Au@paper electrode along with those reported in literature are summarized in Table ST2.[33] It can be seen that the fabricated electrode is more efficient than those reported using the conventional electrodes and is much higher in comparison to the paper electrode. This electrode could be easily decomposed by simple incineration (Figure S5).[33] The resulting ash was examined by energy dispersive X-ray (EDX) technique. The results of EDX analysis confirm the absence of any toxic or pernicious elements in this conducting paper ash (Figure S6).[33]

In conclusion, we have demonstrated a flexible, lightweight, and disposable paper sensor based on a polyaniline

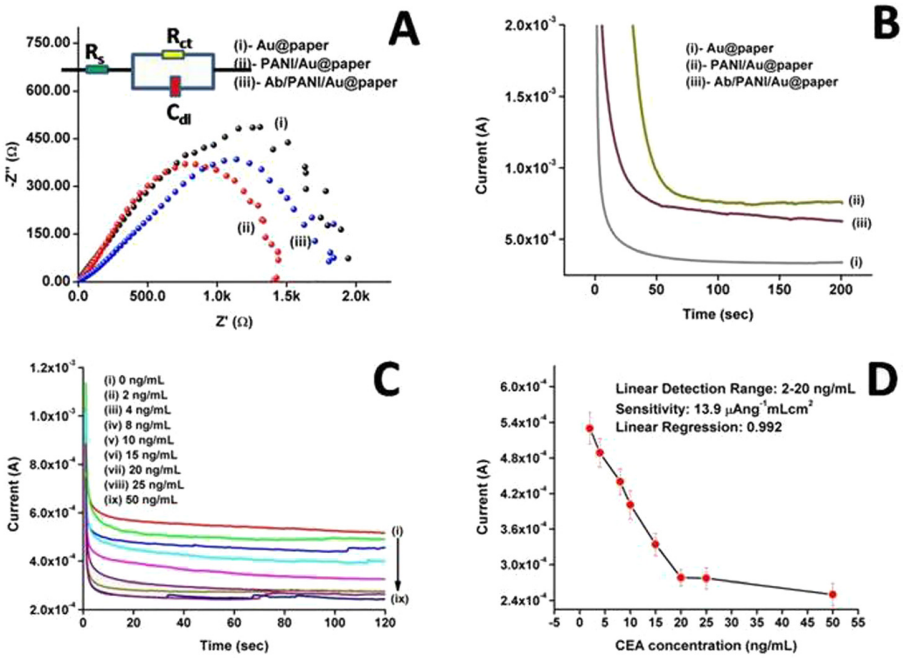

FIG. 3. Electrochemical studies conducted on modified paper electrode. (a) Electrochemical impedance spectra and (b) chronoamperometry plot obtained for (i) Au@paper (ii) PANI/Au@paper (iii) anti-CEA/PANI/Au@paper. (c) Electrochemical response studies of anti-CEA immobilized conducting electrode (BSA/anti-CEA/PANI/Au@paper) at different concentrations of CEA. (d) Calibration plot between magnitudes of current as a function of CEA concentration.

modified paper. It has been found that the polyaniline modified paper exhibits improved flexibility, high heterogenous electron transfer rate constant, large surface area, and provides a suitable matrix for covalent immobilization of biomolecules. The fabricated BSA/anti-CEA/PANI/Au@paper electrode has been used for cancer biomarker (CEA) detection, and is found to be highly sensitive (13.9 μA ng^{-1} ml cm^{-2}) with good linearity in the physiological range of (2–20) ng ml^{-1} and a lower detection limit of 1.36 ng ml^{-1}. This simple, flexible, lightweight platform has immense potential for smart point-of-care devices, gas sensors, strain sensors, and flexible electronics.

We thank Professor Yogesh Singh, Vice Chancellor, Delhi Technological University (DTU), Delhi, India, for providing the facilities. S.K. and A.S. are thankful to DTU for the award of research fellowship. We thank Dinesh C. Doval, Director (Research) Rajiv Gandhi Cancer Institute & Research Centre for providing patient samples and Dr. Chandra Mouli Pandey, DTU for discussions.

[1]World Cancer Report 2014, edited by B. W. Stewart and P. Christopher (International Agency for Research on Cancer, 2014).
[2]S. Kumar, S. Kumar, Md. Ali, P. Anand, V. V. Agrawal, R. John, S. Maji, and B. D. Malhotra, Biotechnol. J. **8**(11), 1267 (2013).
[3]H. J. Wanebo, B. Rao, C. M. Pinsky, R. G. Hoffman, M. Stearns, M. K. Schwartz, and H. F. Oettgen, New England J. Med. **299**(9), 448 (1978).
[4]S. S. Sørensen and B. J. Mosgaard, Dan. Med. Bull. **58**(11), A4331 (2011).
[5]R. E. Myers, D. J. Sutherland, J. W. Meakin, J. A. Kellen, D. G. Malkin, and A. Malkin, Cancer **42**(S3), 1520 (1978).
[6]J. Kulpa, E. Wójcik, M. Reinfuss, and L. Kołodziejski, Clin. Chem. **48**(11), 1931 (2002).
[7]D. M. Goldenberg, R. M. Sharkey, and F. J. Primus, Cancer **42**(S3), 1546 (1978).
[8]D. M. P. Thomson, J. Krupey, S. O. Freedman, and Ph. Gold, Proc. Natl. Acad. Sci. **64**(1), 161 (1969).
[9]F. Zhou, M. Wang, L. Yuan, Z. Cheng, Z. Wu, and H. Chen, Analyst **137**(8), 1779 (2012).
[10]Y. Yonemura, Y. Endou, T. Fujimura, S. Fushida, E. Bandou, K. Kinoshita, K. Sugiyama, T. Sawa, B.-S. Kim, and T. Sasaki, ANZ J. Surg. **71**(9), 521 (2001).
[11]F. L. Flanagan, F. Dehdashti, O. A. Ogunbiyi, I. J. Kodner, and B. A. Siegel, Ann. Surg. **227**(3), 319 (1998).
[12]B. D. Malhotra and A. Chaubey, Sens. Actuators, B **91**(1), 117 (2003).
[13]A. J. Bandodkar and J. Wang, Trends Biotechnol. **32**(7), 363 (2014).
[14]C. Desmet, C. A. Marquette, L. J. Blum, and B. Doumèche, Biosens. Bioelectron. **76**, 145 (2016).
[15]S. Kumar, S. Kumar, S. Srivastava, B. K. Yadav, S. H. Lee, J. G. Sharma, D. C. Doval, and B. D. Malhotra, Biosens. Bioelectron. **73**, 114 (2015).
[16]Yi.-H. Chen, Z.-K. Kuo, and C.-M. Cheng, Trends Biotechnol. **33**(1), 4 (2015).
[17]A. F. Diaz Cruz, N. Norena, A. Kaushik, and S. Bhansali, Biosens. Bioelectron. **62**, 249 (2014).
[18]A. Kaushik, A. Yndart, R. Dev Jayant, V. Sagar, V. Atluri, S. Bhansali, and M. Nair, Int. J. Nanomed. **10**, 677 (2014).
[19]A. Vasudev, A. Kaushik, Y. Tomizawa, N. Norena, and S. Bhansali, Sens. Actuators, B **182**, 139 (2013).
[20]C. Crean, E. Lahiff, N. Gilmartin, D. Diamond, and R. O'Kennedy, Synth. Met. **161**(3), 285 (2011).
[21]C. Dhand, M. Das, M. Datta, and B. D. Malhotra, Bios. Bioelectron. **26**(6), 2811 (2011).
[22]S. Kumar, K. K. Jagadeesan, A. G. Joshi, and G. Sumana, RSC Adv. **3**(29), 11846 (2013).
[23]R. Singh, R. Prasad, G. Sumana, K. Arora, S. Sood, R. K. Gupta, and B. D. Malhotra, Bios. Bioelectron. **24**(7), 2232 (2009).
[24]A. Soni, C. M. Pandey, S. Solanki, and G. Sumana, RSC Adv. **5**(57), 45767 (2015).
[25]A. Tiwari and S. Gong, Talanta **77**(3), 1217 (2009).
[26]G. S. Akundy, R. Rajagopalan, and J. O. Iroh, J. Appl. Polym. Sci. **83**(9), 1970 (2002).
[27]Y. Atassi and M. Tally, arXiv:1307.5668 [cond-mat.mtrl-sci] (2013).
[28]E. Subramanian, R. Dhana Ramalakshmi, N. Vijayakumar, and G. Sivakumar, Indian J. Eng. Mater. Sci. **19**(4), 237 (2012).
[29]K. K. Jagadeesan, S. Kumar, and G. Sumana, Electrochem. Commun. **20**, 71 (2012).
[30]F. Xu, G. Zheng, D. Wu, Y. Liang, Z. Li, and R. Fu, Phys. Chem. Chem. Phys. **12**(13), 3270 (2010).
[31]A. C. Siegel, S. T. Phillips, M. D. Dickey, N. Lu, Z. Suo, and G. M. Whitesides, Adv. Funct. Mater. **20**(1), 28 (2010).
[32]S. Kumar, M. Willander, J. G. Sharma, and B. D. Malhotra, J. Mater. Chem. B **3**(48), 9305 (2015).
[33]See supplementary material at http://dx.doi.org/10.1063/1.4950961 for a video demonstrating the different forms of PANI, result of electrochemical polymerization of aniline (CV), XRD, SEM, FTIR, and EDX studies of the PANI modified paper electrodes, and reproducibility, selectivity, stability, and real sample studies of the fabricated paper sensor.

The Electricity Journal 29 (2016) 22–27

Contents lists available at ScienceDirect

The Electricity Journal

journal homepage: www.elsevier.com/locate/electr

Power system restructuring models in the Indian context

Madan Mohan Tripathi[a,*], Anil Kumar Pandey[b], Dinesh Chandra[c]

[a] Delhi Technological University, New Delhi, India
[b] Uttar Pradesh Power Corporation Limited, Lucknow, India
[c] Motilal Nehru National Institute of Technology (MNNIT), Allahabad, India

ARTICLE INFO

Article history:
Available online xxx

Keywords:
Power system
Restructuring
Power pool
Retailer
Whole sale competition
Scheduling coordinator
Power exchange
Power purchase agreement

ABSTRACT

A range of new models is available for power system restructuring in India to meet the requirements of state and central government policies as well as the social and market needs of the state. Uttar Pradesh Power Corporation Limited provides a useful case study of these possibilities.

1. Introduction

The Electricity Act of 2003 ("the Act") came into effect on June 10, 2003, to replace earlier laws governing the Indian power sector, namely, the Indian Electricity Act 1910, the Electricity (Supply) Act of 1948 and the Electricity Regulatory Commissions Act of 1998.[1] The Act sought to create a liberal framework for the development of the power industry, promoting competition, protecting the interests of consumers and the supply of electricity to all areas, rationalization of the electricity tariff and ensuring transparent policies and the promotion of efficiency, among others. The Act came out with the National Electricity policy, mandatory creation of state electricity regulatory commissions (SERCs), emphasis on rural electrification, open access in transmission distribution, and some other provisions. It mandated that the regulatory commissions regulate tariffs and issues of license. It focused on laws relating to generation, transmission, distribution, trading and the uses of electricity. The objectives of the 2003 act are as follows:

- To consolidate the laws relating to generation, transmission, distribution, trading and the use of electricity.
- Promote competition.
- Protect the interest of consumers.
- Insure the supply of electricity to all areas.
- Rationalize electricity tariffs.
- Ensure transparent policies regarding subsidies.
- Promote efficient and environmentally benign policies.
- Guide the constitution of the Central Electricity Authority (CEA) and regulatory commissions.
- Establish an Appellate Tribunal.

The Act was amended on May 28, 2007, with stronger power and clarity and with greater emphasis on assessments, fines and the legal framework to check commercial losses due to theft and unauthorized use of electricity.[2]

With the enactment of the Electricity Act of 2003 and the implementation of open access, the market structure in the power sector changed from a single-buyer structure to a multi-buyer model. The generator could sell power to any buyer using the open access provision in transmission and users were given a choice of supplier: Since the Act was introduced, there has been increased competition among generators and suppliers, thereby improving the sector's performance. Currently many states, which have unbundled the state electricity boards (SEBs), have reported improvements in their operational efficiency and are able to ensure a reliable power supply to consumers.

Reforms in the power sector in India are underway to create more generation to foster greater competition among producers

* Corresponding author.
E-mail address: mmmtripathi@gmail.com (M.M. Tripathi).

[1] http://www.cea.nic.in/reports/electricity_act2003.pdf.

[2] http://www.mserc.gov.in/acts/no5_electricity_act_2007.pdf.

http://dx.doi.org/10.1016/j.tej.2016.05.002
1040-6190/

and greater choice for customers. The power sector in India was established as a vertically integrated/regulated monopoly organization and the generation, transmission and distribution facilities were owned and controlled by the central and state governments. (Both the central government and state governments were involved in generation and transmission, whereas distribution was handled by state governments only.) Different generating companies (independent power producers, or IPPs) and distribution companies (Discos) have been getting involved at the generation and distribution levels, respectively.

This restructuring has been accompanied by a variety of new problems, which have given rise to controversy among governmental organizations and private companies. The changing nature of the electricity utility industry has brought many new practices to power system operation.[3] The philosophy and techniques of planning and operation that had been well established over past decades have begun to change, and India needs to recognize and meet these challenges. To create competition in the power market, there may be different ways of restructuring the power industry. With a view to the organizational setup, financial condition, control structure and their coordination, several different types of reforms are being proposed in this article.

The rest of this article is organized as follows. Section II presents the various components of India's restructured power system. Various proposed restructuring models for the Uttar Pradesh Power Corporation Limited (UPPCL) are discussed in Section III. Section IV outlines the conclusions.

2. Components of restructured power system in India

The individual components of the restructured power system in India are discussed in detail below.

2.1. Central electricity regulatory commission

Under a new system of mixed entities comprising private and public firms, regulatory bodies at the central and state levels should provide a level playing field to all generating firms, reduce system costs, and protect consumer interests. In July 1998, a Central Electricity Regulatory Commission (CERC) was created to set tariffs and regulate interstate power exchange, licensing, planning, and other functions for all central generation and transmission utilities. The role of CERC in the states is largely advisory. It cannot overrule the state electricity regulatory commission (SERC). All appeals against a SERC decision can only be handled by the state's high court. We believe CERC should be empowered to fix the tariff for generation and transmission, enforce rules and regulations, and finalize the matter regarding interstate power exchange.[4]

2.2. Independent system operator

At the national level, an independent system operator (ISO) named the Power System Operation Corporation Ltd. (POSCO) – a wholly owned subsidiary of Power Grid Corporation of India Ltd (PLCIL)[5] – has been set up to serve as the supreme entity in control of the transmission system. We believe the ISO should be disassociated from all market participants, and abstain from any financial interest in the generation and distribution businesses. However, there is no such requirement, in the context of open access, to separate transmission ownership and operation. The ISO is not involved in energy markets and its role in generation (or transmission) scheduling will be limited to ensuring that submitted schedules are feasible. The ISO does not perform real-time control of power system facilities, which is performed instead by the regional load dispatch centre (RLDC), state load dispatch centre (SLDC) and area load dispatch centre (ALDC) that are hierarchically dependent on it. However, it monitors system operation to ensure the adequacy of available reserves and auxiliary services.[6] It coordinates measures to alleviate transmission congestion and performs contingency analysis to ensure system security against credible contingencies.

2.3. Transmission utilities

PGCIL started functioning as transmission unit (TU) in August 1991 with the mission of establishing and operating the regional and national power grids to facilitate the transfer of power within and across the region with reliability, security, and economy on sound commercial principles. As of Feb. 28, 2015, PGCIL owned and operated more than 1,13,841Ckt. kms network of transmission lines with 2,20,894 MVA transformation capacity and 189 nos. substations that constitutes most of India's interstate and inter-regional electric power transmission system and carries electric power across India. The total inter-regional power transfer capacity of PGCIL is 45,850 MW. PGCIL transmits mostly at 400 kV, together with 220 kV and some 132 kV AC transmission system crisscrossing the entire length and breadth of the country. HVDC back-to-back stations at Vindhyachal and Chandrapur and an HVDC bipole link (830 km) between Rihand and Dadri are also in operation. PGCIL is maintaining transmission system availability of over 99% and earned the unique distribution of being ranked among the best transmission utilities in the world. PGCIL also maintains 29,641 km of telecom network and it has a presence in 370 locations throughout the country with an intracity network of 68 cities across India.[7]

2.4. Central generation utilities

The National Thermal Power Corporation (NTPC), the National Hydro Power Corporation (NHPC), and the Nuclear Power Corporation (NPC) are central generating utilities which generate and supply power in bulk to the state utilities.[8]

2.5. Power pool controller

The power pool is controlled by a power pool controller (PPC) at the state level, with the price of electricity supplied through the pool determined every hour during peak hours and every three hours during other period, depending on system demand, bid prices, and the availability of generation and transmission. Wholesale sellers, retailers, or contestable customers buy electricity from the pool. The power pool thus provides a trading mechanism linking generators, wholesalers, and retail authorities and customers.[9] A separate unit can be created in the state's generation corporation to work as power pool controller. The PPC should have following responsibilities:

[3] http://www.cea.nic.in/reports/powersystems/nep2012/generation_12.pdf.
[4] http://www.cercind.gov.in/.
[5] http://posoco.in/.
[6] Khaparde, A S. A. Power sector reforms and restructuring in India, http://dspace.library.iitb.ac.in/jspui/bitstream/10054/260/3/30010.pdf.
[7] http://www.powergridindia.com/.
[8] http://powermin.nic.in/.
[9] Wadhera, Shym and Mazumdar, Robin, Evolution of regional power pools in India—current status and trends, Energy Conversion Engineering Conference, 1996. IECEC 96., Proceedings of the 31st Intersociety (Vol. 3), doi: 10.1109/IECEC.1996.553337.

- Accept bids from market participants; bids can be invited/accepted from market participants from other states, too.
- Calculate the pool price for every hourly trading interval for peak load periods and for every three or four hours during other periods.
- Calculate the amount payable by participants.
- Disclose the market at activities like the current pool price, successful bidders, etc.
- Prepare the economic power dispatch schedules.

2.6. State electricity regulatory commission

The state electricity regulatory commission (SERC) works at the apex of the state structure to finalize policy matters regarded the electric power market. SERCs have been established in all states and are statutorily responsible for efficient and economic development of the power sector in their respective states or union territories. SERCs are authorized to fix the distribution tariff, which could be inclusive of the market forces to be determined at an appropriate time in the future through government directions.[10]

2.7. State utilities

The SEBs, created under the ES act, have the monopoly right to generate and distribute power in their respective states. The constitution and composition of SEBs, their power, operation, staff, financial accounts, and audit procedures are comprehensively covered under the ES act. The ES act empowers state government to give directions on policy matters, if necessary, to guide the functioning of the boards. The issue of what constitutes policy has been left open to interpretation. In practice, directions from the state government are not just limited to matters of policy but extend to operations.[11]

2.8. Regional load dispatch center

A system operator at regional level has been established which comprises several states in its region. Hierarchically it is dependent on the NLDC and hence must follow the instructions issued by the NLDC. It is responsible for monitoring and controlling the scheduling/dispatch of power among states in the region. It establishes better coordination in the states for efficient and economic use of interstate tie lines. RLDC may direct the SLDC, interstate generating stations to increase/decrease their draw/generation in case of contingencies such as overloading of lines/transformers, abnormal voltages, and threats to system security. Such directions must immediately be acted upon. For all outages of the generation and transmission system, RLDC must plan carefully to achieve the best optimization. It coordinates in bilateral agreements to identify the state's share of interstate generating station projects. RLDC ensures the concept of frequency linked load dispatch and pricing of deviations from schedule i.e. unscheduled interchanges.[12]

3. State load dispatch center

An independent system operator at state level should be established to look after system operation and performance control.[13] This can be performed by the state transmission utilities or a separate arm can be established. The state load dispatch center (SLDC) should have the following responsibilities:

- Issue dispatch instructions.
- Monitor the economic power dispatch schedules.
- Ensures the reliability of the system, transmission line maintenance, and proper pricing.
- Ensure proper system planning.

The SLDCs have the following objectives:

- Protection of consumers from the exercise of monopoly power.
- Reduction of congestion and reflection of line losses.
- Enhancement of interstate power transfer facilities.
- Creation of an even-handed regulating structure for all generators and consumers.

3.1. Power exchange

The power exchange (PX) handles the power pool, which provides a forum to match electric energy supply and demand based on bidding. The time horizon of the pool market may range from half an hour to a week or longer.[14,15] The day-ahead market is used in many electricity markets where energy trading is done one day before each operating day. An hour-ahead market is also used to take care of any shortfall in energy on a shorter time scale.

3.2. Scheduling coordinator

Scheduling coordinators (SCs) would be involved in aggregating the market participants in energy trades and these participants may enter a market being operated by an SC with its own rules, which may be different from the pool rule, thereby leading to different market strategies. Scheduling coordinators may also directly bid or self-schedule resources, as well as handle the settlement process.[16]

3.3. State transmission utilities

State transmission utilities (STUs) operate and maintain the whole transmission network spread over the whole state. They keep upgrading and extending the transmission network to provide transmission services with better efficiency and security.

3.4. State distribution utilities

The distribution network of the state (state distribution utility, or SDU) would work for power distribution in that state and be owned and operated by the utility itself. At some future date the distribution network's ownership and operation and control can be separated, and retailers allowed to use this distribution network.

4. Proposed models for Uttar Pradesh Power Corporation restructuring

The Indian power industry has varying degrees of monopoly, competition, and choices available. They correspond broadly to r-

[10] http://www.uperc.org/Default2.aspx.
[11] http://planningcommission.nic.in/reports/genrep/arep_seb11_12.pdf.
[12] http://www.nrldc.in.
[13] http://www.delhisldc.org/.
[14] http://www.cercind.gov.in/2014/MMC/AR1314.pdf.
[15] http://www.powerexindia.com.
[16] https://www.caiso.com/participate/Pages/SchedulingCoordinator/Default.aspx.

tric power systems in India. Many models are already implemented or have been proposed for the restructuring of the Indian power system and may vary in their actual arrangements at the time of implementation.[17] In these models the states would have full operational autonomy. The states would have their power pool and the regional grids would be operated as loose power pools. State utilities would have the responsibility for the following:

i. Scheduling/dispatching their own generation (including the generation of their captive licenses).
ii. Regulating the demand of their customers.
iii. Scheduling their draw according to their share from the interstate generating stations.
iv. Arranging bilateral interchanges.
v. Regulating their net draw for the regional grids following central and state guidelines.

The reforms in the electricity sector in the state of Uttar Pradesh have already begun and new models are proposed which would be implemented in gradual manner in the state.[18,19] Complete open access at transmission as well as at the distribution level may not be implemented in the immediate future but over time it may become a reality. A gradual approach has been suggested in this section to implement a new deregulated structure in Uttar Pradesh. Many models have been proposed for restructuring the Uttar Pradesh Power Corporation Limited that can be adopted by any other state in India or at the national level with suitable modifications. The various proposed models are discussed below.

4.1. Model A—State pool with retailer fixed-purchase model

In this model, along with the CGU and SGU, new power producers called independent generators or independent power producers (IPPs) are also permitted to supply and compete. All generating stations would sell their power to a power pool which acts as the purchasing agency. The pool in turn sells the power to state distribution utilities, distribution companies, or retailers in the service area. SDUs, Discos, and retailers have no choice but to purchase the power from the pool, as shown in Fig. 1. Power purchase agreements would be negotiated through the power pool only. These agreements may be designed to cover fixed costs, the cost of energy, and variable costs of generation. The customer would have no choice in this model and its power supplier would be fixed.

The new thing in this model is that retailers can directly purchase the power from the pool and can sell to the customer. The sale from the pool to retailer takes place at a price which follows the marginal cost system. An interstate tie line would be used to maintain a loose regional power pool. Regional or state transmission utilities may own and operate the transmission network, whereas the distribution network may be operated by state distribution utilities. Likewise, the retailer would own and operate the distribution system of its area. The social obligation of the government can be accommodated in this model only where state distribution utilities would supply the power.

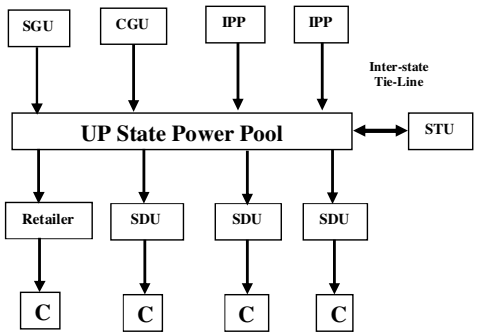

Fig. 1. State Pool with retailer fixed-purchase model.

4.2. Model B—State pool with retailer flexible model

This model has most of the things common with the state pool with retailer fixed-purchase model. However in this model, the consumer would have the option of purchasing power either from the state distribution utilities or from private retailers. SDUs and retailers would own their own network of wires and services in their respective areas. Both of them would take power from the state power pool only (Fig. 2).

4.3. Model C—State pool with bulk consumer flexible purchase model

In this model, the CGU, SGU and IPPs are competing to supply the power. All generating stations would sell their power to the state power pool, which is the purchasing agency. State distribution utilities, distribution companies, or retailers purchase their power from the pool. A new entity, the "bulk consumer," has been introduced in this model, as indicated in Fig. 3. The bulk consumer may take supply from the generation units directly by erecting its own transmission lines.

As a standby arrangement and to cope with peak hour demand, the bulk consumer may take power from state distribution utilities, too. Regional or state transmission utilities would have no link with the lines used between the generating station and bulk consumer; however, they may own and operate the transmission network for other small consumers. Bulk consumers may own, operate, and maintain their own transmission lines.

4.4. Model D—Wholesale competition with retailer pool model

This model requires "open access" to the transmission network, and the development of a spot market. There is a choice of suppliers, with the SDU, Discos and retailers among competing generators. The pool concept has come to the distribution level rather than at the transmission level, where customer can directly purchase the power from the pool, and SDUs, Discos, and retailers

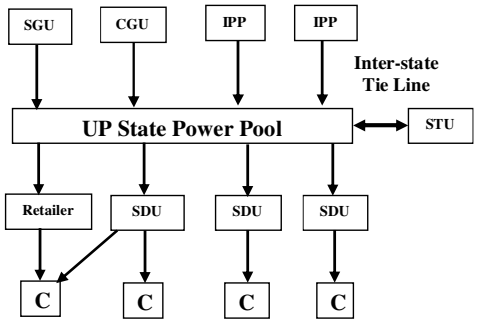

Fig. 2. State pool with retailer flexible purchase model.

[17] Upadhyay, K.G. "Design of electricity utility restructuring model for Indian power system", Ph.D. Thesis, U.P. Technical University, Lucknow, India, October 2001.
[18] http://saiindia.gov.in/english/home/our_products/audit_report/Government_-Wise/state_audit/recent_reports/Uttar_Pradesh/rep_2004/com_chapter2.4.pdf.
[19] http://www.uppcl.org/reforms.html.

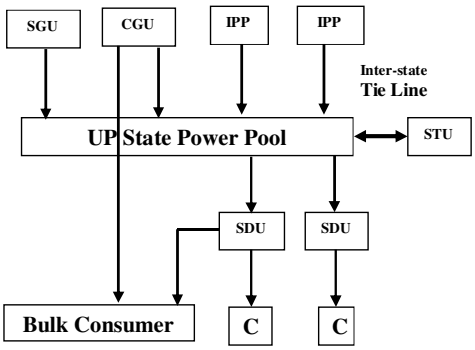

Fig. 3. State Pool with bulk consumer flexible purchase model.

would sell the power to the customer through the power pool acting as the purchasing agency. It is a multi-buyer model where generating companies may sell power directly to any distribution company but open access to distribution wires is not allowed. With this model the "obligation to supply" will move to the SDUs, which still have monopoly over customers, since they own, operate, and maintain the distribution wires. The transmission network would be owned and maintained by the STU, PGCIL and private transmission companies. NLDC, RLDC, and SLDC would have operational control. This model only requires transmission prices for the transmission wires. These prices must provide the right economic incentives for plant location and dispatch, and sufficient revenue for the transmission owners (Figs. 4–6).

4.5. Model E—Wholesale plus retail competition pool model

In this model all customers have access to competing generation units either directly or through their choice of SDU, Discos, retailers or franchises. There would be a complete separation of generation and retailing from the transport business at both the high-voltage and low-voltage levels, leading to open access at both levels.

There would be free entry for retailers as well as franchises. Franchise is a function in this model, which does not require ownership of the distribution wires, although the owner of the wires can also compete as a retailer. In this his model the power pool would work as an auctioneer, neither owning the power nor taking the market risk. It would behave like a single transporter, moving power to facilitate multilateral trading. There would be provision for bidding into a spot market to facilitate merit order dispatch. The pool will match supply and demand and determine the spot price for each hour of the day. It collects money from purchasers and distributes it to producers. All the trading of power would be done through an integrated network of wires where the operator of wires would measure and account for the power trade.

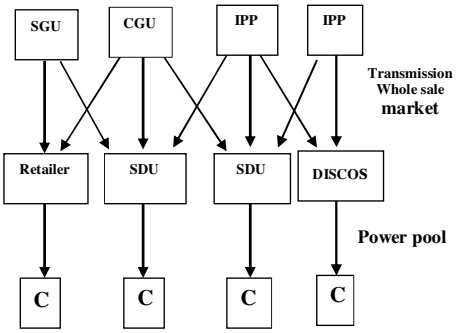

Fig. 4. Wholesale Competition with Retailer Pool Model.

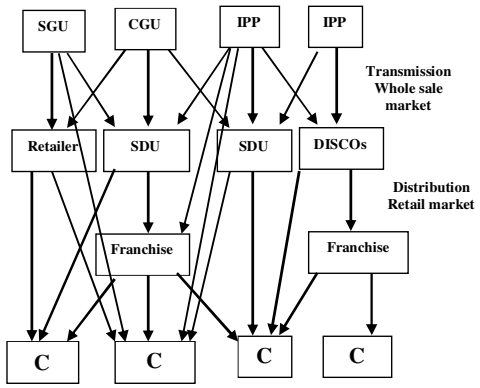

Fig. 5. Whole sale plus Retail Competition Pool Model.

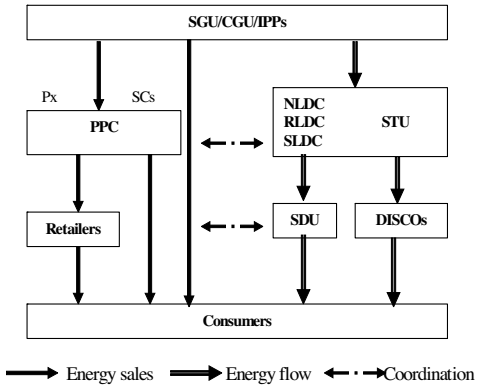

Fig. 6. Pool with bilateral and multilateral Trade.

4.6. Model F—State pool with multilateral trade model

In this model two different purchase models (1) power pool model and (2) multilateral/bilateral purchase model would work simultaneously.

In the pool model, all the power from all generating companies would be sold to power pool and all distribution utilities or companies would be required to purchase the power from the power pool only. In the later model, sellers and buyers can enter into transactions under bilateral or multilateral contracts where the quantities traded and the trade prices are at the discretion of these parties and not the concern of the RLDC/SLDC.

Consumers would be able to make power purchase agreements directly with generation companies or retailers or may purchase from the power pool as needed. In multilateral trade, a scheduling coordinator (SC) or power broker would be required to form and manage a group of energy producers and buyers to insure balanced transactions. This model may put lot of constraints related to security of the power system as a whole.

5. Conclusion and discussion

The Indian Electricity Act of 2003 aims to create a liberal framework for the development of the power industry, promoting competition, protecting the interests of consumers and the supply of electricity to all areas, the rationalization of the electricity tariff and to ensure transparent policies and promote efficiency in the Indian power system. The Act focused on laws relating to generation, transmission, distribution, trading, and uses of electricity. With the enactment of the Act and implementation

of open access, the market structure in the Indian power sector started changing from the old single-buyer structure to a multi-buyer market model. In recent days, many states, which have unbundled the SEBs, have reported improvements in their operational efficiency and are able to ensure reliable power supply to consumers. The Indian power sector is now in the process of a restructuring towards a free-market-based system.

At the same time restructuring has been accompanied by a variety of new problems as the changing nature of the electricity utility industry has brought many new practices, and technical and operational challenges, to power system operation. The success of the new deregulated power system completely depends upon creation of competition in power market. To achieve this there may be different ways of restructuring the power industry but, considering the organizational setup, financial condition, control structure and their coordination, many models are in place or proposed for implementing it gradually as the system matures in India.

As reforms in the state of Uttar Pradesh have already begun, some new models have been proposed especially for that system, which may be implemented in a gradual manner that leads ultimately to completely open access at both the transmission and distribution levels, providing full choice to consumers to choose their supplier.

Model A suggests a small step forward from the existing monopolistic system to a deregulated system where a power pool can be created for the exchange of power between generators and distributors and power can be purchased by the customer from a SDU, Disco or retailer but there is no choice of supplier at the distribution level. Model B moves further towards deregulation at the distribution level by allowing the consumer to choose its supplier at the low-voltage level. Model C provides complete freedom to bulk users to purchase power directly from generation companies, to own and maintain their private transmission lines, and at the same time, gives them the option to take power from distribution companies.

A wholesale transmission market has been proposed in Model D with the power pool moving down to the distribution level. In this model the distribution companies/retailers can purchase power directly from any generator but can sell it only to the power pool and consumers can purchase power only from the pool. Model E proposes a full-fledged electricity market where competition is expected at the transmission level as well as the distribution level. Transmission wires may be operated and maintained by any utility. The distributor has a choice to buy power from any generator and to sell to any customer, while at the same time customers can buy power directly from the generator, distributor, or retailer. Model F shows a hybrid but practical model where the power pool and bilateral/multilateral contracts both are supported.

These proposed models may be adopted by states based on the policies of the state and the central government, as well as social and market needs of the state for a more efficient, secure, and reliable power system. A better restructured power system with a high degree of competition would provide cheaper and good-quality electricity to the consumer while increasing the profit of all market entities.

Madan Mohan Tripathi received his B. Tech. from Madan Mohan Malaviya Engineering College, Gorakhpur, India, and his Ph.D. from G. B. Technical University, Lucknow, India, in 1994 and 2010, respectively. He has worked as an Engineer-SC with the Institute for Plasma Research, Gandhinagar, India, and the National Institute of Electronics & Information Technology, New Delhi. Presently he is Associate Professor at Delhi Technological University, New Delhi. His research interests include sustainable energy, power system restructuring, ANN application to power system problems and the application of IT in power system control and monitoring.

Anil Kumar Pandey received his B. E. from M. M. M. Engineering College, Gorakhpur, India, and his M. Tech. from Allahabad University, Allahabad, India, in 1985 and 1988, respectively. Presently he is working with Uttar Pradesh Power Corporation Limited, Lucknow, India. His research interests include power system restructuring and ANN application to power system problems.

Dinesh Chandra received his B. E. from M. M. M. Engineering College, Gorakhpur, India, and his M.E. and Ph.D. degrees from Motilal Nehru National Institute of Technology (MNNIT), Allahabad, India, in 1973, 1979, and 2000, respectively. Presently Dr. Chandra is Professor at MNNIT. His research interests include control systems, model reduction techniques, optimization theory and fuzzy systems.

Accepted Manuscript

Recent developments in affective recommender systems

Rahul Katarya, Om Prakash Verma

PII: S0378-4371(16)30231-X
DOI: http://dx.doi.org/10.1016/j.physa.2016.05.046
Reference: PHYSA 17170

To appear in: *Physica A*

Received date: 8 March 2016
Revised date: 14 April 2016

Please cite this article as: R. Katarya, O.P. Verma, Recent developments in affective recommender systems, *Physica A* (2016), http://dx.doi.org/10.1016/j.physa.2016.05.046

Recent developments in affective recommender systems

Rahul Katarya, Om Prakash Verma
Department of Computer Science & Engineering
Delhi Technological University, Delhi, India
rahulkatarya@dtu.ac.in

Abstract

Recommender systems (RSs) are playing a significant role since 1990's as they provide relevant, personalized information to the users over the internet. Lots of work have been done in information filtering, utilization, and application related to RS. However, an important area recently draws our attention is affective. Affective recommender system (ARS) is latest trending area of research, as publication in this domain are few and recently published. ARS are associated with human behaviour, human factors, mood, senses, emotions, facial expressions, body gesture and physiological with human-computer interaction (HCI). Due to this assortment and various interests, more explanation is required, as it is in premature phase and growing as compared to other fields. So we have done literature review (LR) in the affective recommender systems by doing classification, incorporate reputed articles published from the year 2003 to February 2016. We include articles which highlight, analyse, and performed a study on affective recommender systems. This article categorizes, synthesize, and discussed the research and development in ARS. We have classified and managed ARS papers according to different perspectives: research gaps, nature, algorithm or method adopted, data sets, the platform on executed, types of information and evaluation techniques applied. The researchers and professionals will positively support this survey article for understanding the current position, research in affective recommender systems and will guide future trends, opportunity and research focus in ARS.

Keywords: Recommender Systems, Affective, Human factors, Review, Emotions

1. Introduction

Recommender systems are information prediction-delivery systems, in which user will receive the relevant information according to user choices over the Internet[1–6]. Affective recommender systems recently adopted by the humans and trending, so more exploration is required for analysis and recognition. Rosalind W. Picard [7] highlighted and explained the term affective computing and its challenges by including numerous criticisms of affective computing with human-computer interaction. Human factors, emotions, and feeling play the important role in our daily life decisions and activities. Buder et al. [8] highlighted the abilities of recommender systems for knowledge from a psychological point of view in which recommender systems possible adaptations are discussed with concerning learners as receivers of data and learners as creators of data. In today's world human cannot survive alone, he needs society or group of people to share his feelings and knowledge. Yu Chen [9] consider these approaches as by doing a survey of the group and social recommender systems. Zeng et al. [10] highlighted human emotion sensitivity from a psychological viewpoint and shortlisted scientific and engineering challenges to improve human sensing knowledge. Santos et al. [11] highlighted the advantages of affective approach in educational recommender systems and explained the semantic educational recommender systems (SERS) which are influenced by e-learning facilities. This article performed literature survey and offered the papers according to different perspective and goal in affective recommender systems. The major question of this article is: *What is new and interesting in the affective recommender systems?*

As this article is based upon the affective recommender systems, so we consider those papers in which authors adopted this attitude, so that relevant and significant answers to the above-given question may be delivered. This article is organised as follows: Section 2 highlights the research methodology, in this peer, reviewed articles publish during 2003 to February 2016

are discussed. Section 3 discuss the Table 1 in a systematic order and explained according to questions classifications. Section 4 is concerned with this literature review results, and finally, conclusion and future work are discussed in section 5.

Table 1. Investigation & analysis questions (IAs) for affective recommender systems.

IA1:	"What was the nature & approach of affective recommender systems?"
IA2:	"Which algorithms and methods for various recommender systems used for delivering efficient results for affective recommender systems?"
IA3:	"Which datasets were taken into consideration for the analysis of affective recommender systems?"
IA4:	"On which platforms affective recommender systems were analysed?"
IA5:	"Which evaluation techniques and information were used to measure the affective recommender systems performance?"

2. Research methodology

The aim of this review is to recognize the development of ARS research by investigating the published research papers and help the experts and researchers with vision and future direction of affective recommender systems. The beginning step of the review was searched process of peer reviewed articles from authenticating and well know resources. In this article, we have collected journals and conferences papers from well know libraries: ACM, IEEE, ScienceDirect, Springerlink, Google scholar. We used these resources and strictly searched and followed our investigation & analysis questions (IAs) for retrieving the articles till February 2016.

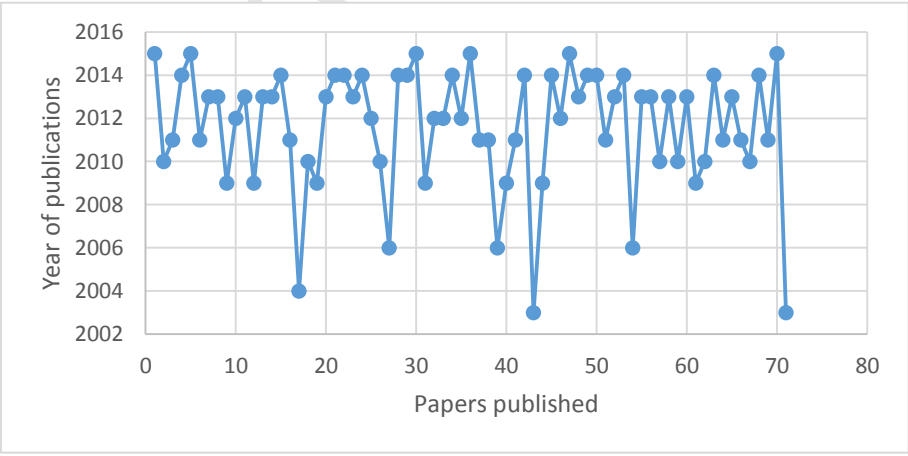

Figure 1. Pattern of affective recommender systems papers

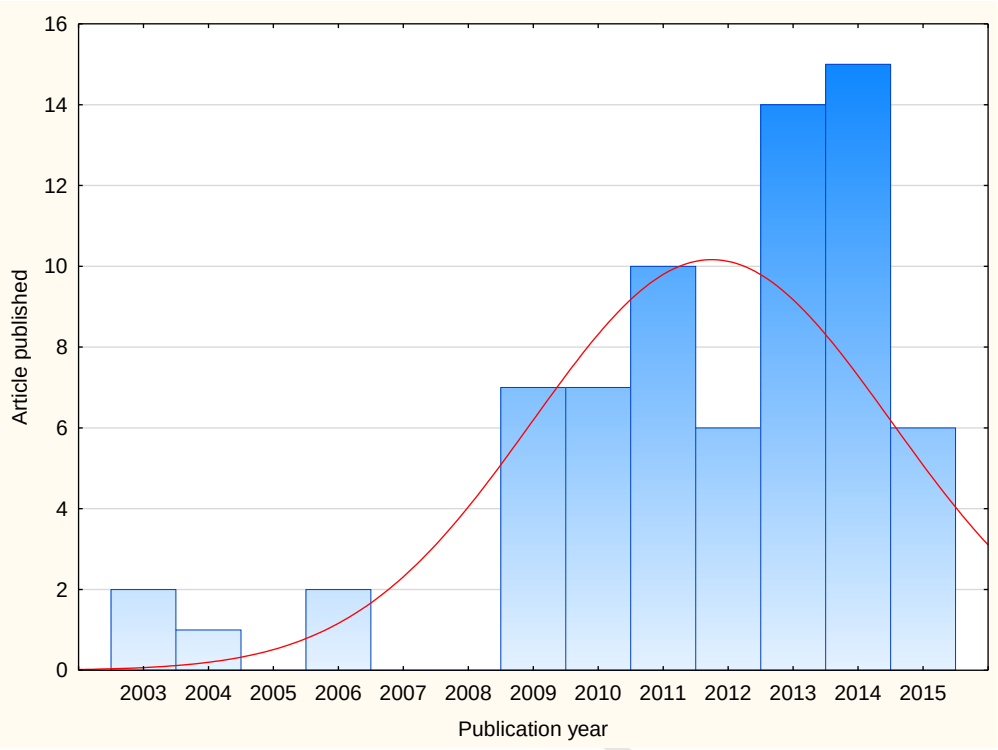

Figure 2. Distribution of affective recommender systems articles

As from figures 1 and 2, we concluded that between, 2011 to 2014, numbers of publications tremendously increased. Also figure 1 shows that during the period, 2002-2008 negligible research was done. Most of the publications were done in the year during 2012-14.

3. Investigation & Analysis questions with classification

In this section, we will highlight the questions that were included in Table 1. We categorize and prepared this segment agreeing to the questions with well clarifications and justifications. In the subsections recommender systems, papers are classified according to Table 1.

3.1 Affective recommendation nature & approach

Recommender systems are important filtering systems for users in which information is suggested according to user's interest [12–14]. In Table 1, first question IA1 is:

"What was the nature & approach of affective recommender systems?"

Affective recommender systems articles involved in various natures and flavours as given in figure 3. Majority of ARS research were towards: frameworks[15–28], approaches [29–40], systems[41–47], studies [47–55], methods [57–61], models [62–68], applications [69–74], review [9,75,76], and tools [77–80].

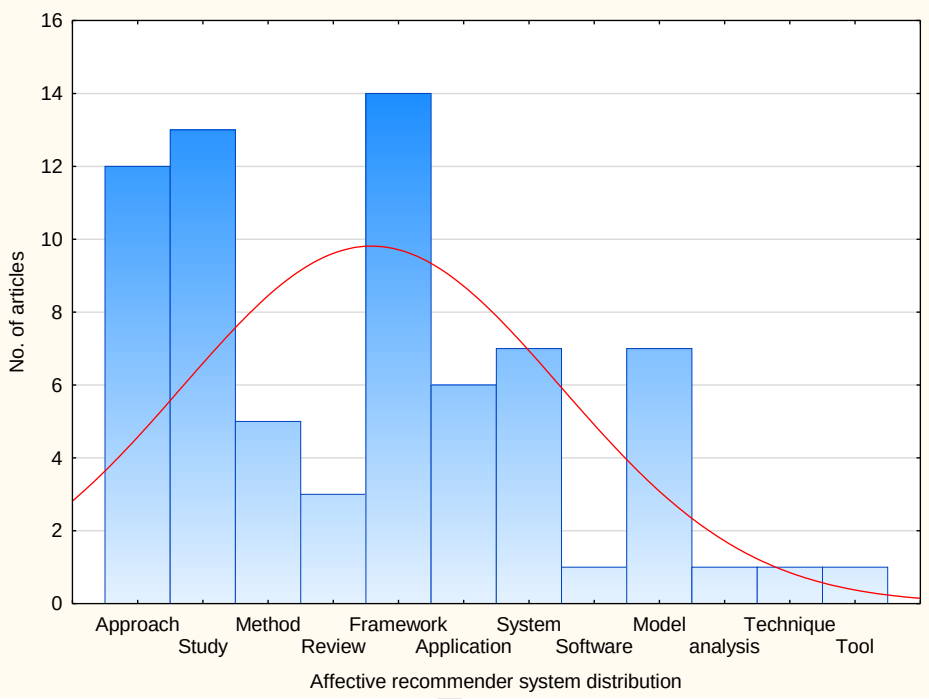

Figure 3. Affective recommender systems articles distribution by nature

Majorly papers were related to human factors in which different aspects were taken into account as shown.

3.2 Affective recommendation algorithms and methods

This subsection classified and organized the affective recommender systems papers according to algorithms and methods they used for implementation, as this subsection is based upon the question number 2 of Table 1 (IA2):

"Which algorithms and methods for various recommender systems used for delivering efficient results for affective recommender systems?"

1. *Data mining & information fusion:* Information fusion is an approach to delivering new information by combining heterogeneous data, some authors worked on it [66, 75, 80]. Researchers have also adopted data mining algorithms and methods in the

affective recommender system for suggesting relevant recommendation to humans[42, 64, 69, 81]. Athena Vakali [22] proposed a framework for applications design and development in social data reality.

2. *Content- based filtering:* This method works when recommender systems recommend the similar items which user have liked in past. Authors also used this method in affective recommender systems [67, 70, 82]. Oliveira et al. [69] explored the contrasting of movie content properties using emotional influence on the users and also included historical, emotional information for evaluation of users' emotional reactions to movies.
3. *Collaborative filtering:* This kind of recommender system carry the recommendations, in which public has same tastes. Affective recommender systems also demonstrated by utilizing such type of filtering approach [80, 83–86]. Cumbreras et al. [72] applied collaborative filtering algorithms and calculated user's score on a particular movie without having any remark, in which calculated a distance among the user and item when there is no relation at all. Winoto et al. [73] changed the existing collaborative-filtering based recommendation method by injecting user temper and projected a mood-aware collaborative filtering method. Lim et al. [44] proposed an affective model and n-gram model which were a combination of semantic knowledge with collaborative & content filtering approaches.
4. *Context based filtering:* Context based recommender systems work on the contextual information such as day-night time, weather forecasting, rain prediction. Most of the affective recommender systems are now applying this context approach for efficient utilization of information [81, 86–88]. Rodriguez et al. [36] suggested a methodology that automatically fetch out affective context from person comments related films existing in YouTube. Likamwa et al. [37] included acceleration, light, and other

physical properties in their affective recommender system which dealings the psychological status of the person and delivers mood for participation in context-aware computing. Arapakis et al. [21] suggested a multimodal recommender approach which contains communication data, contextual data, and users' affective reactions and delivered significant recommendations of unnoticed videos.

5. *Semantic-based:* This type of recommender system employed the web in the form of ontologies. Affective recommender systems showed their behaviour towards semantic approaches [89, 90]. Fong et al. [33] presented a semantic web usage mining method for determining periodic web access configurations from interpreted web usage logs by utilising fuzzy temporal and web usage ontology. Kannan et al. [47] proposed a movie consolidate system which generates semantically significant personalized movie summary by considering users' conduct, personality, data coverage, and range.
6. *Group filtering:* In this type of recommendations, recommender systems act on the recommendation, projected by the group of people of similar concentration or likes. Affective recommender systems also delivered recommendations to their users in the particular group for saving time and infrastructure[91–94]. Bauer et al. [61] demonstrated a method which dynamically produce contextually suitable music playlists for groups of persons, and they can listen to music according to their present mood instead of handling playlists. Masthoff et al. [64] highlighted the individual's satisfaction in a particular group by modelling emotional impact with different relationship types and also discovers the problem of privacy such as feeling safe in the group.
7. *Tagged Filtering:* Tagged based recommendation system is grounded upon the action connected to keyword or expression connected to photo, video, or article. In the affective recommender systems, this approach is also effective for the users to provide

recommendations [91, 95, 96]. Vig et al. [38] focused on tagging appearance in which preference elicitation shared the tagging and rating systems.

8. *Sentiment Analysis:* Sentiment analysis approaches used the human factors for analysing the recommender system. Affective recommender system also utilized this analysis [74]. Cumbreras et al. [72] applied sentiment analysis in recommender systems by classifying users by average polarity of remarks. Rodriguez et al. [26] explored tourist travel destinations contents and opinions by using sentiment analysis techniques in which sentiment score is found and studied by seeing numerous traveller characteristics opinions.
9. *Others methods:* Affective recommender systems articles also used these methods to provide effective recommendations to the users: Latent Dirichlet allocation [29,32,65], Fuzzy [91, 97], Support vector machine [69, 84, 94], feature selection [68, 95], Gaussian process [70, 87, 96], Naïve Bayes [19, 58, 94].

3.3 Affective recommendation datasets

In this subsection we will debate on the data used by the affective recommendation which is based on the question number 3 of Table 1 (IA3):

"Which datasets were taken into consideration for the analysis of affective recommender systems?"

In this way, we classified and managed the data and its constituents for affective recommendations to the users.

1. *Movie data:* Most of the authors used movies and its related data such as Internet Movie Database (IMDb) in the affective recommender system for their results.[18, 72, 94].
2. *Music data:* Authors also predicted the behaviour by using human factors in the music application [8, 87, 88, 93].

3. *Participants data:* Maximum of the authors conducted the survey, demos, and experiments by presenting questions, by utilising people related to universities, e-commerce [14, 87, 98].
4. *Miscellaneous data:* Apart from above-given data usage, authors also adopted different data to show affective recommender system performance such as news articles [65], blog posts [24, 25, 83], metadata [20, 23,58], etc.

3.4 Affective recommendation platforms

Here in this subsection, we will see the platforms or base on which affective recommender system was analysed their performance as this is the question number 4 of Table 1 (IA4):

"On which platforms affective recommender systems were analysed?"

We have classified the platform on which the affective recommender system was executed.

1. *Single platform:* In the initial phase affective recommender systems performance is evaluated on the stand-alone platforms. Some authors utilized this platform for better recommendations [77–79].
2. *Client-server:* In this platform various authors analysed affective recommender systems performance [8, 15, 20, 22].
3. *Web-based:* affective recommender systems were also analysed on the web platform. [14, 19, 21, 24]
4. *Mobile based:* in this environment mobile behavioural patterns were analysed for affective recommender systems [86–88].

3.5 Affective recommendation evaluation techniques and information

This is a mandatory approach to evaluating the affective recommender systems so that performance of the particular system is checked. In this subsection we will highlight the evaluation approach which is the part of question number 5 of Table 1 (IA5):

"Which evaluation techniques and information were used to measure the affective recommender systems performance?"

Here we have categorized evaluation techniques adopted by affective recommender systems:

1. *Qualitative:* The importance of this approach is to reduce the error. Affective recommender systems also utilized this such as accuracy calculation [8, 9, 89, 98].
2. *Probabilistic:* In this approach motive is to deliver higher or lower range of probability [7, 94, 97, 99].
3. *Ranking:* To judge the item from first to second, that how much first is better than second will use ranking approach, most of the papers adopted this [15, 18, 24, 39].
4. *Software & Tools:* Some authors also designed software and tools for demonstrating the performance of affective recommender systems [23, 79, 81, 87, 95]. Here also we are discussing the information used by affective recommender systems:

1. *Context based:* Most of the papers of affective recommender systems were based on context based information[9, 75, 81, 95, 97].
2. *Content-based:* This type of information is also utilized by affective recommender systems [66–69, 81].
3. *Implicit based:* This type of information was also adopted by affective recommender systems [21, 22, 24].

4. Literature review results: a comprehensive analysis, findings, lessons learned.

This section discusses the results of the articles which supported affective recommender systems. Data collected from every major paper according to five investigation & analysis questions (IAs) are summarised in Appendix A. All these issues perspective and results are discussed in the next subsections. This review contains the articles till February 2016.

4.1 Affective recommendation nature & approach

In section 3.1, we discussed the nature and approaches accepted by the affective recommender systems. We concluded that most of the work in affective recommender system were done in the proposing frameworks, studies and suggesting approaches that are given in figure 3. More attention is required to design software and tools for affective recommender system who can analyse the human emotion and sentiments automatically. In the same section, we have categorized the approach adopted by affective recommender systems. We also reach to the point that majority of papers we reviewed were based on the human factors such as opinion mining, facial expressions, emotions, sentiments, moods, body gesture psychological factors. However, there some more areas in which affective recommender system should focus such as health systems, privacy, trust, educational and social networks.

4.2 Affective recommendation algorithms and methods

This section 3.2 widely explained the papers related to algorithms and methods in a systematic manner such as: data mining & information fusion, content-based filtering, collaborative filtering, context-based filtering, semantic based, group filtering, tagged filtering, sentiment analysis, and others methods. Various articles used different types of methods such as: ML algorithm, SVM, hybrid filtering methods, Power Method algorithm, sentiment mining algorithm, time based IRF techniques, Fuzzy Logic, Titanic algorithm, data mining, implicit affective labelling method, CBR Method, Self-Assessment Manikin (SAM) Method, confidence rule, Smart Prediction Assistant (SPA), user-similarity measure (USM), unimodal and multimodal methods, hierarchical Bayesian, Latent Dirichlet Allocation (LDA), Russell's circumplex model of affection, term-based matching technique, non-intrusive and low cost methods, TORMES methodology, dimension reduction methods, LambdaMART method, OCCF methods, Gaussian mixture models (GMMs), Ripple effect,

content-based recommender algorithms, feature selection methods, ANN, principal components analysis (PCA), Collaborative Filtering algorithms, Morphological analyzing and Parsing.

4.3 Affective recommendation datasets

In section 3.3, we discussed various data sets used in affective recommender systems. We classified the affective recommender system's data set into the movie data, music data, participant's data, and miscellaneous data. We studied that most of the articles used participant's data because of analysing human factors and response. Some authors also used these data sets: Hiroshima sightseeing data, Game Players, LDOS-PerAff-1, TED, YouTube's API, multi-domain, psychological data, Cohn-Kanade dataset, social data, etc.

4.4 Affective recommendation platforms

In the section, we highlighted the various modes of the platform on which affective recommender systems perform their actions. So we classified and organized these platforms as a single platform, client-server, web-based, mobile based. We analyzed that cloud-based mobile affective recommender systems were more demanding and delivered efficient results.

4.5 Affective recommendation evaluation techniques and information

In section 3.5, we explained the evaluation techniques and information adopted by affective recommender systems. We classified the evaluation techniques as Qualitative, Probabilistic, Ranking, Software & tools which are used in the articles. Most of the papers used evaluation approaches as: ANOVA, mean, standard deviation, scalability, reliability, confusion matrix (CM), Precision, recall, F1, Correlations, Hausdorff distance, intra-class correlation coefficient (ICC), Self-Assessment Manikin (SAM), SVR, sparse Bayesian regression (SBR), tenfold cross-validation, mean average precision (MAP), mean reciprocal rank (MRR) , Pearson correlation, similarity index, accuracy, Earth mover's distance, Kendall's

tau metric, Mann-Whitney Test, Minkowski distance, Euclidean distance, Normalization, Novelty, effectiveness, root mean square error (RMSE) and mean absolute error (MAE).

5. Conclusion and future work

This article achieved a well-ordered literature review and classified, synthesize, and also presented the articles according to the various perception of affective recommender systems. We found and collected the papers from 2003 to February 2016. We initially categorized the papers according to five questions are given in Table 1 and then also performed classification according to their necessity in that class. Papers were organized according to affective recommendation systems: nature & approaches, algorithms and methods, datasets used, platform and information, evaluation techniques.

Results of this paper are highlighted with valuable suggestions and future work:

- By published articles so far, affective recommendation publications are still growing and trending research area.
- There is a need for affective recommender systems in which: use of emotions as the context in the entry stage and modelling affective content profiles should be maintained.
- Some algorithms or models should be designed to predicate users' current emotional states or mood that can help in critical areas such as clinical application to each patient, fire stations, road safety, and traffic analysis.
- Further attention is required on affective computing with the human decision-making process.
- Security and privacy are still the major issues in the affective recommender systems.
- The foremost focus should be on optimized approaches: Managing affective data quality, spatial crowdsourcing, semantic, for efficient affective recommender systems.

- Participation of big data & social networking lacks in the affective recommender systems.
- Affective recommender systems are majorly designed for the particular user, but more focus is required to the group of users such as group sentiments, group anxious, group privacy.
- Hybrid methods and models with context-based algorithms are demanding for affective recommender systems with human-computer interaction.
- Most of the users are mobile friendly so such affective recommender system should be formed so that it may be free from platform and language.
- Performance and computational abilities of affective recommender system should be improved by the high-performance intelligent environment with considering cross domains and multi-lingual provision.
- There is a need to design such affective recommender algorithms that utilize expression tag data, the point of interest, check in behaviour in context social networking domain.

References

[1] H. Wang, S. Shao, X. Zhou, C. Wan, A. Bouguettaya, Preference Recommendation for Personalized Search, Knowledge-Based Syst. (2016).

[2] X. Hu, A. Zeng, M.-S. Shang, Recommendation in evolving online networks, Eur. Phys. J. B. 89 (2016) 46.

[3] P.N. Bennett, D. Kelly, R.W. White, Y. Zhang, Overview of the Special Issue on Contextual Search and Recommendation, ACM Trans. Inf. Syst. 33 (2015) 1e.

[4] J. Bao, Y. Zheng, D. Wilkie, M. Mokbel, Recommendations in location-based social networks: a survey, Geoinformatica. (2015) 525–565.

[5] L. Chen, G. Chen, F. Wang, Recommender systems based on user reviews: the state of the art, User Model. User-Adapt. Interact. (2015) 99–154.

[6] R. Katarya, O.P. Verma, A collaborative recommender system enhanced with particle swarm optimization technique, Multimed. Tools Appl. (2016) 1–15.

[7] R.W. Picard, Affective computing: challenges, Int. J. Hum. Comput. Stud. 59 (2003) 55–64.

[8] J. Buder, C. Schwind, Learning with personalized recommender systems: A psychological view, Comput. Human Behav. 28 (2012) 207–216.

[9] Y. Chen, Interface and interaction design for group and social recommender systems, Proc. Fifth ACM Conf. Recomm. Syst. RecSys 11. (2011) 363.

[10] Z. Zeng, M. Pantic, G.I. Roisman, T.S. Huang, A survey of affect recognition methods: Audio, visual, and spontaneous expressions, IEEE Trans. Pattern Anal. Mach. Intell. 31 (2009) 39–58.

[11] O.C. Santos, J.G. Boticario, Affective issues in semantic educational recommender systems, CEUR

[12] D. Véras, T. Prota, A. Bispo, R. Prudêncio, C. Ferraz, A literature review of recommender systems in the television domain, Expert Syst. Appl. 000 (2015) 1–31.

[13] F.O. Isinkaye, Y.O. Folajimi, B. a. Ojokoh, Recommendation systems: Principles, methods and evaluation, Egypt. Informatics J. (2015).

[14] J. Bobadilla, F. Ortega, a. Hernando, a. Gutiérrez, Recommender systems survey, Knowledge-Based Syst. 46 (2013) 109–132.

[15] P. Pu, L. Chen, R. Hu, A user-centric evaluation framework for recommender systems, Proc. Fifth ACM Conf. Recomm. Syst. - RecSys '11. (2011) 157.

[16] L. Canini, S. Benini, R. Leonardi, Affective recommendation of movies based on selected connotative features, IEEE Trans. Circuits Syst. Video Technol. 23 (2013) 636–647.

[17] M. Tkalčič, A. Košir, J. Tasič, M. Kunaver, Affective recommender systems : the role of emotions in recommender systems, Proc. RecSys 2011 Work. Hum. Decis. Mak. Recomm. Syst. (2011) 9–13. http://ceur-ws.org/Vol-740/UMMS2011_paper6.pdf.

[18] K.-I. Benta, A. Hoszu, V. Lucia, O. Cret, Agent Based Smart House Platform with Affective Control, Proc. 2009 Euro Am. Conf. Telemat. Inf. Syst. New Oppor. to Increase Digit. Citizsh. (2009) 1–7.

[19] F. Chaosheng, Connotative Features Based Affective Movie Recommendation System, (2012).

[20] S. Poria, A. Gelbukh, E. Cambria, A. Hussain, G. Bin Huang, EmoSenticSpace: A novel framework for affective common-sense reasoning, Knowledge-Based Syst. 69 (2014) 108–123.

[21] I. Arapakis, Y. Moshfeghi, H. Joho, R. Ren, D. Hannah, J. Jose, Enriching user profiling with affective features for the improvement of a multimodal recommender system, (2009).

[22] A. Vakali, Evolving social data mining and affective analysis methodologies, framework and applications, Proc. 16th Int. Database Eng. Appl. Sysmposium - IDEAS '12. (2012) 1–7.

[23] M. Tkalčič, A. Odić, A. Košir, J. Tasič, Exploiting implicit affective labeling for image recommendations, Conf. Proc. - IEEE Int. Conf. Syst. Man Cybern. (2012) 3321–3326.

[24] J.M.J. Ioannis Arapakis, Yashar Moshfeghi, Hideo Joho, Reede Ren, David Hannah, integrating facial expressions into user profiling for the improvement of a multimodal recommender system Ioannis Arapakis , Yashar Moshfeghi , Hideo Joho , Reede Ren , David Hannah , Joemon M . Jose Department of Computing Science University of Glasgow L, (2009) 1440–1443.

[25] J. Sun, G. Wang, X. Cheng, Y. Fu, Mining affective text to improve social media item recommendation, Inf. Process. Manag. 51 (2014) 444–457.

[26] C. Computing, Monitoring travel-related information on Social Media through sentiment analysis, (2014).

[27] J. Wache, The Secret Language of Our Body - Affect and Personality Recognition Using Physiological Signals, (2014) 389–393.

[28] S.E. Shepstone, Z. Tan, S. Member, Using Audio-Derived Affective Offset to Enhance TV Recommendation, 16 (2014) 1999–2010.

[29] F. Colace, M. De Santo, L. Greco, V. Moscato, A. Picariello, A collaborative user-centered framework for recommending items in Online Social Networks, Comput. Human Behav. 51 (2015) 694–704.

[30] O.C. Santos, M. Saneiro, S. Salmeron-Majadas, J.G. Boticario, A Methodological Approach to Eliciting Affective Educational Recommendations, 2014 IEEE 14th Int. Conf. Adv. Learn. Technol. (2014) 529–533.

[31] S. Salmeron-Majadas, O.C. Santos, J.G. Boticario, An evaluation of mouse and keyboard interaction indicators towards non-intrusive and low cost affective modeling in an educational context, 18th Int. Conf. Knowl. Based Intell. Inf. Eng. Syst. - KES2014. 35 (2014) 691–700.

[32] W. Liang, H. Wang, Y. Chu, C. Wu, Emoticon Recommendation in Microblog using Affective Trajectory Model, (2014).

[33] a. C.M. Fong, B. Zhou, S. Hui, J. Tang, G. Hong, Generation of personalized ontology based on consumer emotion and behavior analysis, IEEE Trans. Affect. Comput. 3 (2012) 152–164.

[34] K. Bakhtiyari, M. Taghavi, H. Husain, Hybrid affective computing—keyboard, mouse and touch screen: from review to experiment, Neural Comput. Appl. (2014) 1277–1296.

[35] T. Liu, L. Researcher, Learning to Rank for Joy, (2014) 569–570.

[36] C. Orellana-rodriguez, E. Diaz-aviles, W. Nejdl, Mining Affective Context in Short Films for Emotion-Aware Recommendation, (2015) 185–194.

[37] R. LiKamWa, Y. Liu, N.D. Lane, L. Zhong, MoodScope: Building a Mood Sensor from Smartphone Usage Patterns, Proceeding 11th Annu. Int. Conf. Mob. Syst. Appl. Serv. - MobiSys '13. (2013) 389.

[38] J. Vig, M. Soukup, S. Sen, J. Riedl, Tag Expression: Tagging with Feeling, 23nd Annu. ACM Symp. (2010) 323–332.

[39] M. Tkalčič, A. Košir, J. Tasič, The LDOS-PerAff-1 corpus of facial-expression video clips with affective, personality and user-interaction metadata, J. Multimodal User Interfaces. 7 (2013) 143–155.

[40] X. Li, T. Murata, Toward affective recommendation: A contextual association approach for eliciting user preference, Int. Conf. Inf. Soc. (i-Society 2011). (2011) 47–54.

[41] S. Sasaki, T. Hirai, H. Ohya, S. Morishima, Affective music recommendation system reflecting the mood of input image, Proc. - 2013 Int. Conf. Cult. Comput. Cult. Comput. 2013. (2013) 153–154.

[42] G. González, J.L. De La Rosa, M. Montaner, S. Delfin, Embedding emotional context in recommender systems, Proc. - Int. Conf. Data Eng. (2007) 845–852.

[43] E. Mavridou, D.D. Kehagias, D. Tzovaras, G. Hassapis, Mining affective needs of automotive industry customers for building a mass-customization recommender system, J. Intell. Manuf. 24 (2013) 251–265.

[44] G.H. Lim, S.W. Hong, I. Lee, I.H. Suh, M. Beetz, Robot recommender system using affection-based episode ontology for personalization, Proc. - IEEE Int. Work. Robot Hum. Interact. Commun. (2013) 155–160.

[45] C.Y. Chi, Y.S. Wu, W.R. Chu, D.C. Wu, J.Y.J. Hsu, R.T.H. Tsai, The power of words: Enhancing music mood estimation with textual input of lyrics, Proc. - 2009 3rd Int. Conf. Affect. Comput. Intell. Interact. Work. ACII 2009. (2009).

[46] a. Kaklauskas, E.K. Zavadskas, M. Seniut, G. Dzemyda, V. Stankevic, C. Simkevičius, et al., Web-based Biometric Computer Mouse Advisory System to Analyze a Users Emotions and Work Productivity, Eng. Appl. Artif. Intell. 24 (2011) 928–945.

[47] R. Kannan, G. Ghinea, S. Swaminathan, What do you wish to see? A summarization system for movies based on user preferences, Inf. Process. Manag. 51 (2015) 286–305.

[48] I. Arapakis, K. Athanasakos, J. Jose, A comparison of general vs personalised affective models for the prediction of topical relevance, (2010) 371–378.

[49] Y. Moshfeghi, Affective adaptive retrieval: Study of emotion in adaptive retrieval, Sigir '09. (2009) 2009.

[50] C. Reynolds, R. Picard, Affective sensors, privacy, and ethical contracts, Ext. Abstr. 2004 Conf. Hum. Factors Comput. Syst. - CHI '04. (2004) 1103–1106.

[51] C. Cool, I. Xie, Affective utterances as contextual feedback in interactive information retrieval, Proceeding Third Symp. Inf. Interact. Context - IIiX '10. (2010) 277.

[52] Y. Moshfeghi, J.M. Jose, An effective implicit relevance feedback technique using affective, physiological and behavioural features, Proc. 36th Int. ACM SIGIR Conf. Res. Dev. Inf. Retr. - SIGIR '13. (2013) 133–142.

[53] Z. Lin, An empirical investigation of user and system recommendations in e-commerce, Decis. Support Syst. 68 (2014) 111–124.

[54] A. Pommeranz, J. Broekens, P. Wiggers, W.P. Brinkman, C.M. Jonker, Designing interfaces for explicit preference elicitation: A user-centered investigation of preference representation and elicitation process, User Model. User-Adapted Interact. 22 (2012) 357–397.

[55] S.M. Lui, W. Hui, Effects of smiling and gender on trust toward a recommendation agent, Proc. - 2010 Int. Conf. Cyberworlds, CW 2010. (2010) 398–405.

[56] E.H. Trainer, B. Al-ani, D.F. Redmiles, Impact of Collaborative Traces on Trustworthiness, Organization. 17 (2011) 40–47.

[57] S. Benini, L. Canini, R. Leonardi, A connotative space for supporting movie affective recommendation, IEEE Trans. Multimed. 13 (2011) 1356–1370.

[58] J. Broekens, W.P. Brinkman, AffectButton: A method for reliable and valid affective self-report, Int. J. Hum. Comput. Stud. 71 (2013) 641–667.

[59] M. Tkalčič, A. Odić, A. KoTkalšičir, J. Tasič, Affective labeling in a content-based recommender system for images, IEEE Trans. Multimed. 15 (2013) 391–400.

[60] A. Mourão, J. Magalhães, Q. Torre, Competitive Affective Gaming : Winning with a smile, ACM Int. Conf. Multimed. (2013) 83–92.

[61] J.S. Bauer, A. Jansen, J. Cirimele, MoodMusic: A Method for Cooperative, Generative Music Playlist Creation, Proc. 24th Annu. ACM Symp. Adjun. User Interface Softw. Technol. - UIST '11 Adjun. (2011) 85.

[62] J.J. Deng, C.H.C. Leung, A. Milani, L.I. Chen, Emotional States Associated with Music : Classification , Prediction of Changes , and Consideration in Recommendation, 5 (2015).

[63] K. Bakhtiyari, H. Husain, Fuzzy model of dominance emotions in affective computing, Neural Comput. Appl. (2014) 1467–1477.

[64] J. Masthoff, A. Gatt, In pursuit of satisfaction and the prevention of embarrassment : affective state in group recommender systems, (2006) 281–319.

[65] S. Bao, S. Xu, L. Zhang, R. Yan, Z. Su, D. Han, et al., Joint emotion-topic modeling for social affective text mining, Proc. - IEEE Int. Conf. Data Mining, ICDM. (2009) 699–704.

[66] B. Wu, E. Zhong, A. Horner, Q. Yang, Music Emotion Recognition by Multi-label Multi-layer Multi-instance Multi-view Learning Categories and Subject Descriptors, (2014) 117–126.

[67] A. Karran, S. Fairclough, K. Gilleade, Towards an adaptive cultural heritage experience using physiological computing, CHI '13 Ext. Abstr. Hum. Factors Comput. Syst. (2013) 1683–1688.

[68] M. Tkalčič, U. Burnik, A. Košir, Using affective parameters in a content-based recommender system for images, User Model. User-Adapted Interact. 20 (2010) 279–311.

[69] E. Oliveira, P. Martins, T. Chambel, Accessing movies based on emotional impact, Multimed. Syst. 19 (2013) 559–576.

[70] E. Oliveira, P. Martins, T. Chambel, iFelt: Accessing Movies Through Our Emotions, Proceddings 9th Int. Interact. Conf. Interact. Telev. - EuroITV '11. (2011) 105.

[71] D. Cosley, S.K. Lam, I. Albert, J. a. Konstan, J. Riedl, Is seeing believing?, Proc. Conf. Hum. Factors Comput. Syst. - CHI '03. (2003) 585.

[72] M.Á. García-Cumbreras, A. Montejo-Ráez, M.C. Díaz-Galiano, Pessimists and optimists: Improving collaborative filtering through sentiment analysis, Expert Syst. Appl. 40 (2013) 6758–6765.

[73] P. Winoto, T.Y. Tang, The role of user mood in movie recommendations, Expert Syst. Appl. 37 (2010) 6086–6092.

[74] A.A.O. Kane, Trusting Experience Oriented Design, Methodology. (2011) 923–928.

[75] K. Ravi, V. Ravi, A survey on opinion mining and sentiment analysis: Tasks, approaches and applications, Knowledge-Based Syst. (2015).

[76] A. Vlachostergiou, G. Caridakis, S. Kollias, Investigating Context Awareness of Affective Computing Systems: A Critical Approach, Procedia Comput. Sci. 39 (2014) 91–98.

[77] T. Ichimura, Affective Recommendation System for Tourists by Using Emotion Generating Calculations, (2014) 9–14.

[78] B.P. Bailey, J. a. Konstan, On the need for attention-aware systems: Measuring effects of interruption on task performance, error rate, and affective state, Comput. Human Behav. 22 (2006) 685–708.

[79] F. Silveira, B. Eriksson, A. Sheth, A. Sheppard, Predicting audience responses to movie content from electro-dermal activity signals, Proc. 2013 ACM Int. Jt. Conf. Pervasive Ubiquitous Comput. - UbiComp '13. (2013) 707.

[80] J. Broekens, A. Pronker, M. Neuteboom, Real time labeling of affect in music using the affectbutton, Proc. 3rd Int. Work. Affect. Interact. Nat. Environ. - Affin. '10. (2010) 21.

[81] T. Yuan, J. Cheng, X. Zhang, Q. Liu, H. Lu, How friends affect user behaviors? An exploration of social relation analysis for recommendation, Knowledge-Based Syst. (2015).

[82] U. Panniello, A. Tuzhilin, M. Gorgoglione, Comparing context-aware recommender systems in terms of accuracy and diversity, User Model. User-Adapt. Interact. 24 (2014) 35–65.

[83] T. Takehara, S. Miki, N. Nitta, N. Babaguchi, Extracting Context Information from Microblog Based on Analysis of Online Reviews, 2012 IEEE Int. Conf. Multimed. Expo Work. (2012) 248–253.

[84] C.-L. Huang, P.-H. Yeh, C.-W. Lin, D.-C. Wu, Utilizing user tag-based interests in recommender systems for social resource sharing websites, Knowledge-Based Syst. 56 (2014) 86–96.

[85] X. Han, L. Wang, N. Crespi, S. Park, Á. Cuevas, Alike people , alike interests ? Inferring interest similarity in online social networks, Decis. Support Syst. 69 (2015) 92–106.

[86] W. Chen, Z. Niu, X. Zhao, Y. Li, A hybrid recommendation algorithm adapted in e-learning environments, World Wide Web. 17 (2014) 271–284.

[87] M.F. Alhamid, M. Rawashdeh, H. Al Osman, M.S. Hossain, A. El Saddik, Towards context-sensitive collaborative media recommender system, Multimed. Tools Appl. (2014).

[88] J.M. Mayer, Q. Jones, S.R. Hiltz, Identifying Opportunities for Valuable Encounters: Toward Context-Aware Social Matching Systems, ACM Trans. Inf. Syst. 34 (2015) 1–32.

[89] M. Braunhofer, M. Kaminskas, F. Ricci, Location-aware music recommendation, Int. J. Multimed. Inf. Retr. 2 (2013) 31–44.

[90] E. Ben Ahmed, W. Tebourski, W. Ben Abdessalem Karaa, F. Gargouri, SMART: Semantic multidimensional group recommendations, Multimed. Tools Appl. (2014).

[91] H.A. and Y.T. Taiga Yoshida, Go [rie, Towards Semantic And Affective Content-Based Video Recommendation, (2012).

[92] J. a. Recio-García, L. Quijano, B. Díaz-Agudo, Including social factors in an argumentative model for Group Decision Support Systems, Decis. Support Syst. 56 (2013) 48–55.

[93] J. Masthoff, The Pursuit of Satisfaction : Affective State in Group Recommender Systems, (2005) 297–306.

[94] L. Quijano-sanchez, J.A. Recio-garcia, B. Diaz-agudo, Social Factors in Group Recommender Systems, 4 (2013) 1–30.

[95] M.S. Pera, Y.-K. Ng, A group recommender for movies based on content similarity and popularity, Inf. Process. Manag. 49 (2013) 673–687.

[96] L. Baltrunas, F. Ricci, Experimental evaluation of context-dependent collaborative filtering using item splitting, User Model. User-Adapt. Interact. 24 (2013) 7–34.

[97] J. Hu, B. Wang, Y. Liu, D.-Y. Li, Personalized Tag Recommendation Using Social Influence, J. Comput. Sci. Technol. 27 (2012) 527–540.

[98] S. Yan, X. Zheng, Y. Wang, W.W. Song, W. Zhang, A graph-based comprehensive reputation model : Exploiting the social context of opinions to enhance trust in social commerce, Inf. Sci. (Ny). (2014).

[99] A. Pommeranz, J. Broekens, W. Visser, W.-P. Brinkman, P. Wiggers, C.M. Jonker, Multi-angle view on preference elicitation for negotiation support systems, Proc. First Int. Work. Conf. Hum. Factors Comput. Model. Negot. (2008) 19{\textendash}26.

[100] V. Evers, N. Menezes, L. Merino, D. Gavrila, F. Nabais, M. Pantic, et al., The Development and Real-World Deployment of FROG , the Fun Robotic Outdoor Guide, HRI '14 Proc. 9th ACM/IEEE Int. Conf. Human-Robot Interact. 1 (2014) 100.

Research Article Vol. 55, No. 15 / May 20 2016 / Applied Optics 4095

Rectangular-core large-mode-area photonic crystal fiber for high power applications: design and analysis

Reena,[1] Than Singh Saini,[1] Ajeet Kumar,[2,*] Yogita Kalra,[1] and Ravindra Kumar Sinha[1,2]

[1]Department of Applied Physics, Delhi Technological University, Delhi, India
[2]CSIR-Central Scientific Instruments Organization (CSIO), Chandigarh, India
*Corresponding author: ajeetdph@gmail.com

Received 1 February 2016; revised 5 April 2016; accepted 27 April 2016; posted 28 April 2016 (Doc. ID 258618); published 16 May 2016

A rectangular-core large-mode-area photonic crystal fiber structure has been designed based on the principle of higher order mode filtering by introducing fluorine-doped material rods in the cladding region. The proposed structure has an effective-mode area of fundamental mode (FM) as large as 2147 μm² at 1.064 μm with nominal loss of 1.36×10^{-2} dB/m and 9.34 dB/m at first higher order mode (FHOM), which confirms effective single-mode operation after ~2.14 m propagation length. The same structure offers effective-mode area of 5688 μm² at $\lambda = 1.55$ μm with confinement loss of $\sim 6.3 \times 10^{-2}$ dB/m for FM and ~20.23 dB/m for FHOM. The loss of FHOM is above 8 dB/m from $\lambda = 1$ μm to $\lambda = 1.6$ μm with very small loss in FM, which offers extended single-mode operation within a broad spectral range.

OCIS codes: (060.5295) Photonic crystal fibers; (060.2430) Fibers, single-mode; (060.4005) Microstructured fibers.

http://dx.doi.org/10.1364/AO.55.004095

1. INTRODUCTION

In the last few years, photonic crystal fibers (PCFs) have become an exciting research topic due to their distinctive attributes such as dispersion tailoring [1,2], large-mode area with single-mode operation [3,4], high birefringence [5–7], and super continuum generation [8–10]. PCF is the kind of optical fiber with a periodic array of air holes in its cladding region running along its length. Such fibers guide light due to a center defect created at a design stage. Among all the attributes of PCFs, having a large-mode area (LMA) is the most important because it supports high transmission in fiber lasers and amplifiers [11,12]. In high power devices, the main limitation in its performance consists of nonlinear effects such as self-phase modulation (SPM), four-wave mixing (FWM), stimulated Raman scattering (SRS), and stimulated Brillouin scattering (SBS) [13,14]. Due to SPM, in high-bit-rate transmission systems, there is a change in the dispersive behavior. SRS and SBS increase the noise to signal ratio. FWM and SRS increase the crosstalk between different WDM systems. These limitations due to nonlinear effects may be overcome by using LMA fibers. LMA fibers have potential applications in different fields such as high power delivery, multiwavelength guidance, short pulse delivery, broadband interferometry, and laser pig tailing. LMA fiber facilitates high power levels to be transmitted through the optical fiber without the effects produced by the nonlinear properties of the fiber.

Due to the increase of numerical aperture (NA), fiber with LMA is limited by the fact that fiber becomes multimode, which causes modal dispersion. Therefore, there is a trade-off between LMA with single-mode operation. The LMA and single-mode operation can also be obtained by scaling down the NA of the conventional step index fiber [15] and by using special cladding geometries or index profiles to discriminate higher order modes [16–32]. A graded index cladding design with a radial increase of refractive index profile has been proposed for optical fiber for LMA single-mode operation in [16]. A LMA optical fiber design consisting of a cladding formed by alternative high and low index regions has been proposed in [17]. This LMA fiber specially designed for confinement loss characteristics (fiber design with large confinement loss for higher order modes and nominal confinement loss for fundamental mode). LMA with single-mode operation optical fiber design with coaxial dual cores and leaky cladding has been proposed in [18]. Dussardier *et al.* [19] fabricated a LMA with single-mode operation based on leaky-mode filtering by a modified chemical vapor deposition (MCVD) technique. This fiber structure has a leaky cladding that discriminates the fundamental mode from higher order modes. However, there are some disadvantages of these LMA step-index fibers. The extended single-mode operation is impossible in conventional LMA fiber; a few higher order modes are always supported in this type of LMA fiber. However, the PCF

structure has many interesting properties compared to the conventional fibers.

Earlier, different design approaches of air holes in the cladding region had been considered for achieving LMA PCFs with single-mode operation [20–23]. Limpert *et al.* demonstrated a high power air-clad microstructure ytterbium-doped PCF laser with a 350 μm^2 mode field area of the propagating mode[20]. Tsuchida *et al.* proposed a novel LMA PCF with single-mode operation and low bending loss for high power delivery applications [22]. Using the fact that silica PCF with a doped center core enables the reduction of confinement and bending losses, a novel technique has been applied to improve these properties in LMA PCF by employing a different level of doping concentration around the core region [23]. Napierala *et al.* demonstrated experimentally an asymmetric design having a set of small air holes on one side of the fiber and larger air holes on the opposite sides [24]. In this PCF design, for increasing the loss of higher order modes at the bending of the PCF, two additional missing air holes are inserted in the cladding region. Recently, Ademgil and Haxha proposed endlessly single-mode PCF with improved effective-mode area based on introducing higher index material in the cladding region [25]. The effective-mode area of the proposed PCF reported is smaller than 200 μm^2 at 1.064 μm wavelength. Novel LMA PCF structures have been designed based on selective material-filled technology [26,27]. More recently, photonic bandgap fiber with single-mode operation and multiple cladding regions has been designed with a very large mode area of ∼2650 μm^2 [32]. However, single-mode operation has only been achieved at a single wavelength.

In this paper, we have designed a rectangular-core (RC) LMA PCF structure that offers extended single-mode operation by suppressing all higher order modes. The PCF is designed in such a way that initially it supports several leaky modes, out of which only the fundamental mode survives after a finite propagation length. A 20 dB confinement loss to the first higher order modes ensures effective single-mode operation. Simulated results show that the confinement loss of the first higher order mode at $\lambda = 1.064$ μm is 9.34 dB/m. Therefore, the proposed PCF structure supports effective single-mode operation only after 2.14 m of the fiber with effective-mode area as large as 2147 μm^2, which can mitigate nonlinear effects effectively.

2. RC LMA PCF DESIGN

The transverse cross-sectional view of a proposed RC LMA PCF design is shown in Fig. 1. The design is characterized by the rectangular array of air holes drawn in the fused silica along the length of the fiber.

One air hole has been removed from the center to make a core. As illustrated in Fig. 1, there are four rectangular rings of air holes around the central core. The second ring of the structure has been modified by replacing the air holes with down-doped fused silica rods. The rods in the second ring have diameter d_1 ($= 2 \times r_1$, where, r_1 is the radius of the larger rods in the second ring). The diameter of the air holes in the first, third, and fourth rings is taken as d_2 ($= 2 \times r_2$, where r_2 is the radius of the air holes in the third and fourth rings). Distance between the centers of two adjoining air holes, i.e., pitch, has been taken as a constant value Λ.

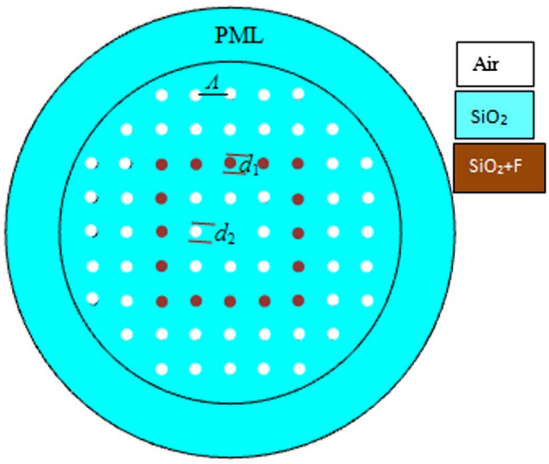

Fig. 1. Proposed RC LMA PCF structure.

3. FORMULATION

The effective indices and the confinement losses of the modes are calculated using commercially available COMSOL Multiphysics software based on a full vectorial finite element method. A circular perfectly matched layer has been implemented around the cladding of the fiber to avoid the unnecessary reflections. The propagation constant of the PCF structure is complex. The real part of the propagation constant corresponds to the effective index of the mode, and the imaginary part corresponds to the confinement loss of the propagating mode. The confinement loss can be calculated using the imaginary part of the modes by the following relation [28]:

$$L\left[\frac{dB}{m}\right] = \frac{40\pi}{\ln(10)\lambda}\,\mathrm{Im}(n_{\mathrm{eff}}) = 8.686 k_0\,\mathrm{Im}(n_{\mathrm{eff}}), \quad (1)$$

where $\mathrm{Im}(n_{\mathrm{eff}})$ is the imaginary part of the effective-mode index of that mode and λ is the operating wavelength of light in meters.

The effective-mode area of the mode of the proposed LMA PCF has been calculated using the following equation [23,31]:

$$A_{\mathrm{eff}} = \frac{\left(\iint E^2 \mathrm{d}_x \mathrm{d}_y\right)^2}{\int E^4 \mathrm{d}_x \mathrm{d}_y}, \quad (2)$$

where E is the amplitude of the transverse electric field propagating through the fiber.

4. NUMERICAL RESULTS

In the proposed structure, we have investigated the effective-mode index, confinement loss and effective-mode area using the full vectorial finite element method. The refractive index of fused silica has been taken as 1.45 at 1.064 μm. For this structure, the confinement losses of the modes increase on increasing mode order. To confirm this in our study, we have investigated the first three modes, i.e., fundamental mode (FM), the first higher order mode (FHOM), and the second higher order mode (SHOM).

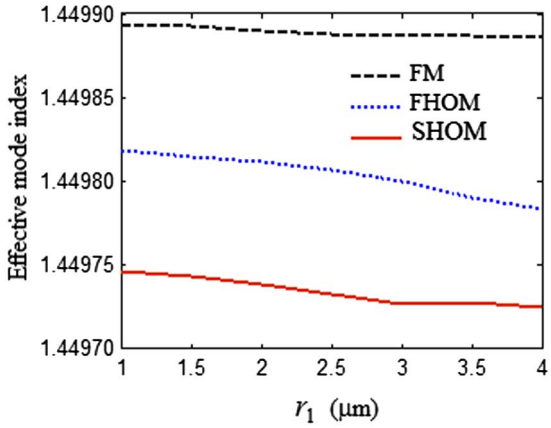

Fig. 2. Variation of the effective-mode indices of FM, FHOM, and SHOM with r_1 while keeping other parameters fixed as $n_f = 1.435$, $r_2 = 2$ μm, $\Lambda = 19$ μm, and $\lambda = 1.064$ μm.

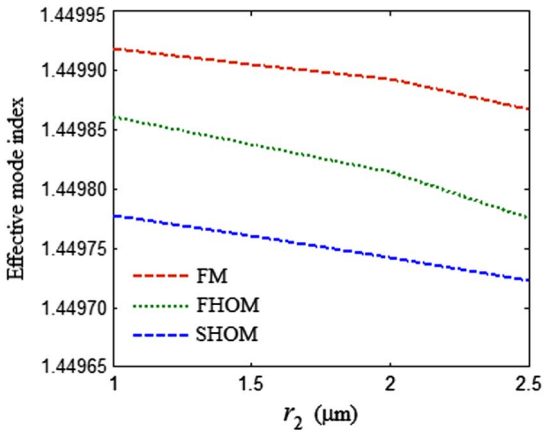

Fig. 4. Variation of effective-mode indices of FM, FHOM, and SHOM with r_2 while keeping other parameters fixed as $n_f = 1.435$, $r_1 = 1.5$ μm, $\Lambda = 19$ μm, and $\lambda = 1.064$ μm.

Initially, we have chosen the structural parameters as: $r_2 = 2$ μm, $\Lambda = 19$ μm, and $n_f = 1.435$, and then we observed the effect of r_1.

As illustrated in Fig. 2, the effective-mode indices of FM, FHOM, and SHOM decrease with r_1. This is due to the increase in the air filling fraction of the structure on increasing r_1. It is also clear from the figure that the effective index of FM is always larger than that of FHOM and SHOM.

Figure 3 shows the variation of confinement loss and effective-mode area of FM, FHOM, and SHOM modes of the proposed PCF structure. Initially, the confinement loss of FHOM increases up to $r_1 = 2$ μm and then starts to decrease. This is due to the resonance effect of FHOM to the cladding in this range of r_1. Due to the resonance effect of FHOM at $r_1 = 2$ μm, the design introduces the confinement loss of ~10.18 dB/m; however, FM offer very small confinement loss at this value of r_1 with an effective-mode area of 1269 μm^2. The confinement loss of the SHOM is always larger than that of FHOM. The effective-mode area of FM decreased on increasing r_1, which is quite obvious. The index contrast between core and cladding increases on increasing r_1. Therefore, there is more and more enhancement in the guidance of FM, leading to the reduction in effective-mode area. In order to achieve the maximum allowed mode area for FM with the maximum possible confinement loss to FHOM, we have chosen $r_1 = 1.5$ μm. At this value of r_1, the confinement losses of FM and FHOM are 1.36×10^{-2} dB/m and 9.34 dB/m, respectively. Thus, the design can work as a single-mode PCF with a very large mode area of ~2147 μm^2.

Figure 4 illustrates the effect of r_2 on the effective-mode indices of FM, FHOM, and SHOM. The effective-mode indices of the modes decrease slowly with r_2. The variation of confinement losses of FM, FHOM, and SHOM modes and the effective-mode area of FM mode with r_2 are revealed in Fig. 5. The confinement loss of FHOM is in between 8 to 10 dB/m for 1 μm $< r_2 <$ 2.5 μm. A further increase in r_2 leaks out of the modes more quickly at the cost of the mode area well below 2000 μm^2. Thus, the suitable choice of r_2 is

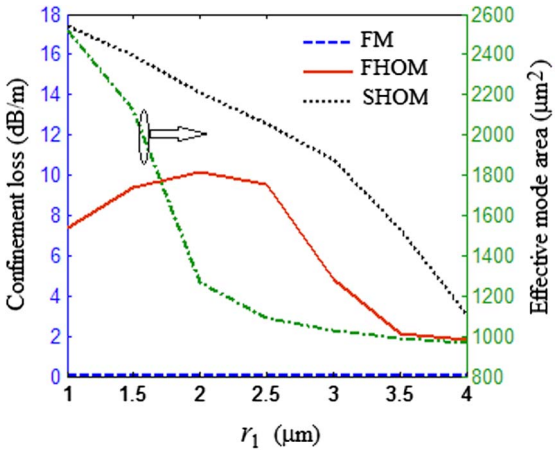

Fig. 3. Variation of the effective-mode area of FM and the confinement losses of FM, FHOM, and SHOM modes with r_1 while keeping other parameters fixed as $n_f = 1.435$, $r_2 = 2$ μm, $\Lambda = 19$ μm, and $\lambda = 1.064$ μm.

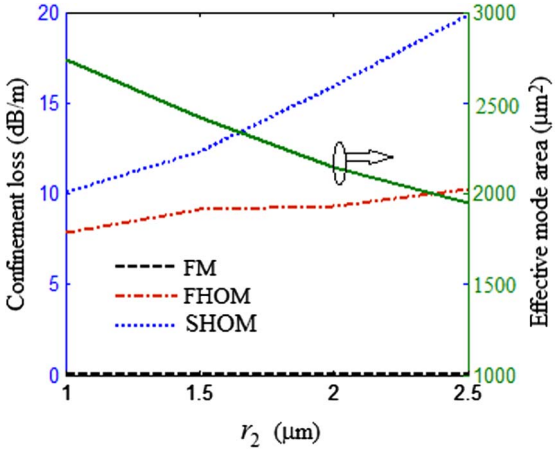

Fig. 5. Variation of effective-mode area of FM and the confinement losses of FM, FHOM, and SHOM modes with r_2 while keeping other parameters fixed as $n_f = 1.435$, $r_1 = 1.5$ μm, $\Lambda = 19$ μm, and $\lambda = 1.064$ μm.

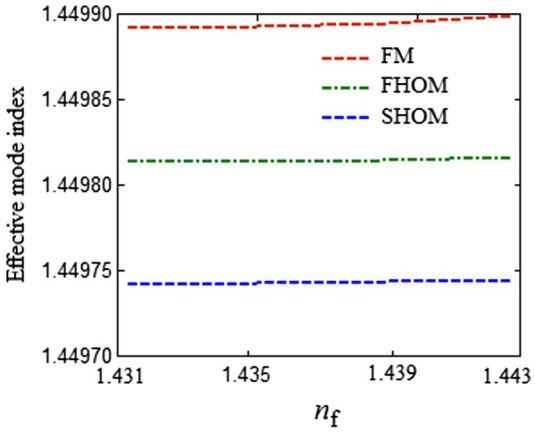

Fig. 6. Variation of effective-mode indices of FM, FHOM, and SHOM modes with the refractive index of fluorine-doped rods while keeping other parameters fixed as $r_1 = 1.5$ μm, $r_2 = 2$ μm, $\Lambda = 19$ μm, and $\lambda = 1.064$ μm.

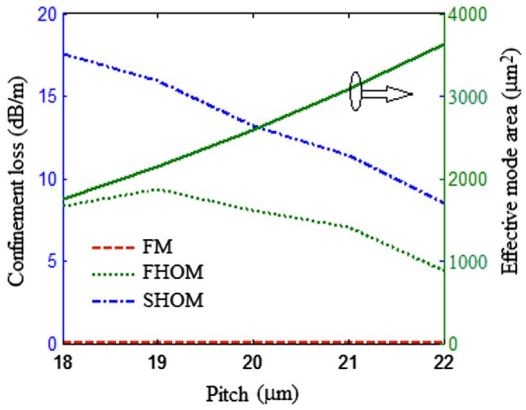

Fig. 8. Variation of effective-mode area of FM and the confinement loss of FM, FHOM, and SHOM with wavelength while keeping other parameters fixed as $n_f = 1.435$, $r_1 = 1.5$ μm, $r_2 = 2$ μm, $\lambda = 1.064$ μm.

1 μm $< r_2 <$ 2.5 μm for high-power applications. The confinement loss of FHOM is ∼9.34 dB/m around $r_2 = 2$ μm and the effective-mode area of FM is 2147 μm^2, which makes the fiber suitable for high power applications.

We can observe from Fig. 6 that the effective-mode index of FHOM and SHOM is almost independent of the increase in the refractive index of the fluorine-doped rods in the second ring. A small increase in the effective-mode index of FM can be observed on increasing n_f.

Figure 7 depicts the dependence of confinement losses of FM, FHOM, and SHOM and effective-mode area of FM with n_f. The confinement loss of FM is always very small, while the loss of FHOM decreases slowly on increasing n_f. Although the effective-mode area of FM is larger at larger values of n_f, the confinement loss of FHOM becomes $< \sim 8$ dB/m, which can lead to propagation of higher order modes. Therefore, for single-mode operation, the value of n_f should be less than 1.44. The confinement of the SHOM is always very large.

Figure 8 illustrates the variation of confinement losses of FM, FHOM, and SHOM modes and the effective-mode area of FM with the pitch of the structure. On increasing the value of the pitch, the effective-mode area of FM mode increases, but at higher value of pitch, the losses of all the modes decrease, which leads to the confinement of the higher order modes within the PCF structure. At a pitch of 19 μm, the PCF structure offers an effective-mode area as large as 2147 μm^2 with very low confinement loss of 1.36×10^{-2} dB/m. The confinement loss of FHOM is 9.34 dB/m at a pitch of 19 μm. Therefore, fiber will offer effective single-mode operation after the 2.14 m propagation length of the PCF.

Figure 9 illustrates the variation of confinement losses of FM, FHOM, and SHOM modes and the effective-mode area of FM with wavelength ranging from 0.9 to 1.6 μm. The confinement losses of all three modes and the effective-mode area of FM increase with an increase in wavelength due to the spreading of the field in the leaky cladding region at higher wavelengths. At $\lambda = 1.064$ μm, the confinement loss of FM is as low as $\sim 1.36 \times 10^{-2}$ dB/m with an effective-mode area as large as 2147 μm^2, and the confinement loss of FHOM

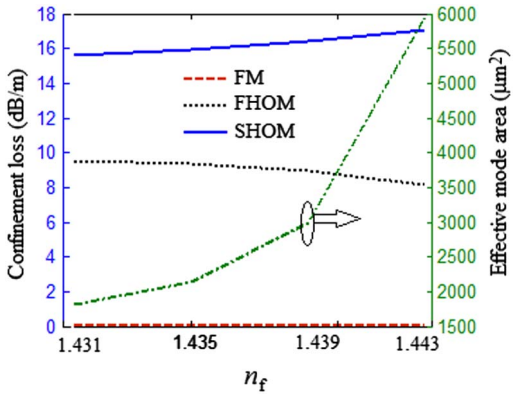

Fig. 7. Variation of effective-mode area of FM and the confinement loss of FM, FHOM, and SHOM modes with the refractive index of fluorine-doped rods while keeping other parameters fixed as $r_1 = 1.5$ μm, $r_2 = 2$ μm, $\Lambda = 19$ μm, and $\lambda = 1.064$ μm.

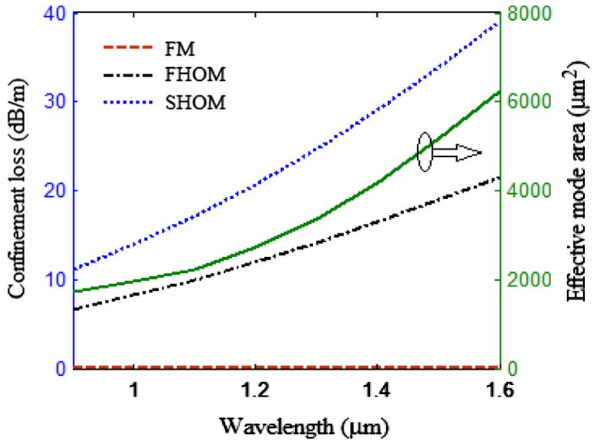

Fig. 9. Variation of effective-mode area of FM and the confinement loss of FM, FHOM, and SHOM with wavelength while keeping other parameters fixed as $n_f = 1.435$, $r_1 = 1.5$ μm, $r_2 = 2$ μm, and $\Lambda = 19$ μm.

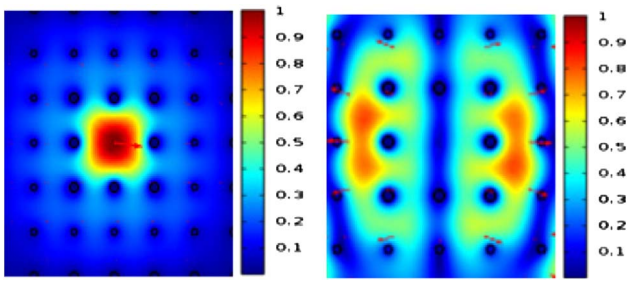

Fig. 10. Contour plot of the normalized electric field intensity of FM and FHOM modes at optimized parameters as $n_f = 1.435$, $r_1 = 1.5$ μm, $r_2 = 2$ μm, $\Lambda = 19$ μm, and $\lambda = 1.064$ μm.

is as high as ∼9.34 dB/m. On the other hand, at $\lambda = 1.55$ μm, the confinement loss of FM is as low as ∼0.6 dB/m with the effective-mode area of FM as large as ∼5688 μm^2, and the confinement loss of FHOM is as high as 20.23 dB/m.

The maximum confinement loss of FM is ∼0.7 dB/m at 1.6 μm. The minimum confinement loss of FHOM is ∼8 dB/m at 1 μm. Therefore, a ∼2.5-m-long PCF is suitable to offer extended effective single-mode operation in the spectral range of 1.0–1.6 μm.

Finally, the contour plots of FHOM and FM are shown in Fig. 10 for $\lambda = 1.064$ μm, $r_1 = 1.5$ μm, $r_2 = 2$ μm, $\Lambda = 19$ μm, and $n_f = 1.435$. It can be observed that FHOM is leaking toward the cladding region while FM is well confined within the core of the PCF structure.

5. CONCLUSION

In conclusion, we can articulate that by choosing the proper structure and refractive index of the material rods, one can tune the confinement losses of FM and FHOM modes of the proposed RC PCF structure. The proposed PCF structure possesses effective-mode area as large as 2147 μm^2 at $\lambda = 1.064$ μm with confinement losses of $\sim 1.36 \times 10^{-2}$ dB/m and ∼9.34 dB/m for FM and FHOM, respectively. Therefore, after a 2.14 m propagating length, the loss of FHOM exceeds 20 dB, and FM mode is only a propagating mode at 1.064 μm. At 1.55 μm, the structure possesses the effective-mode area of FM mode as large as 5688 μm^2 with confinement losses of 0.6 dB/m and ∼20.23 dB/m for FM and FHOM, respectively. After travelling approximately 1 m distance through the PCF, FHOM suffers a more than 20 dB loss while FM offers only a 0.6 dB loss. Therefore, only a 1-m-long PCF is sufficient to obtain effective single-mode operation at 1.55 μm. Our proposed RC-PCF design offers an effective-mode area larger than that of the design recently reported in other triangular core and hexagonal geometries [3,27]. Such a large-mode-area PCF structure is able to eliminate all the unwanted nonlinear effects. Based on these mentioned numerical results and analysis, the proposed PCF structure can be used for high power applications such as high power fiber lasers, amplifiers, and sensors.

Funding. Science and Engineering Research Board (SERB)

Acknowledgment. This work has been partially supported by the DST Fast Track Project on "Specialty large-mode-area rectangular waveguides and fibers for high power applications."

REFERENCES

1. W. H. Reeves, D. V. Skryabin, F. Biancalana, J. C. Knight, P. St. J. Russell, F. G. Omenetto, A. Efimov, and A. J. Taylor, "Transformation and control of ultra-short pulses in dispersion-engineered photonic crystal fibers," Nature **424**, 511–515 (2003).
2. F. Beltrán-Mejía, C. M. B. Cordeiro, P. André, and E. Silvestre, "Broadband dispersion compensation using inner cladding modes in photonic crystal fibers," Opt. Express **20**, 3467–3472 (2012).
3. T. S. Saini, A. Kumar, and R. K. Sinha, "Triangular-core large-mode-area photonic crystal fiber with low bending loss for high power applications," Appl. Opt. **53**, 7246–7251 (2014).
4. K. Kishor, R. K. Sinha, and A. D. Varshney, "Experimental verification of improved effective index method for endlessly single mode photonic crystal fiber," Opt. Lasers Eng. **50**, 182–186 (2012).
5. G. Jiang, Y. Fu, and Y. Huang, "High birefringence rectangular-hole photonic crystal fiber," Opt. Fiber Technol. **26**, 163–171 (2015).
6. J. Liao and J. Sun, "High birefringent rectangular lattice photonic crystal fibers with low confinement loss employing different sizes of elliptical air holes in the cladding and the core," Opt. Fiber Technol. **18**, 457–461 (2012).
7. I. Abdelaziz, H. Ademgil, F. Abdelmalek, S. Haxha, T. Gorman, and H. Bourchiha, "Design of a large effective mode area photonic crystal fiber with modified rings," Opt. Commun. **283**, 5218–5223 (2010).
8. T. S. Saini, A. Kumar, and R. K. Sinha, "Broadband mid-IR supercontinuum generation in As_2Se_3 based chalcogenide photonic crystal fiber: a new design and analysis," Opt. Commun. **347**, 13–19 (2015).
9. T. S. Saini, A. Kumar, and R. K. Sinha, "Broadband mid-infrared supercontinuum spectra spanning 2–15 μm using As_2Se_3 chalcogenide glass triangular-core graded-index photonic crystal fiber," J. Lightwave Technol. **33**, 3914–3920 (2015).
10. L. E. Hooper, P. J. Mosley, A. C. Muir, W. J. Wadsworth, and J. C. Knight, "Coherent supercontinuum generation in photonic crystal fiber with all-normal group velocity dispersion," Opt. Express **19**, 4902–4907 (2011).
11. S. K. Varshney, K. Saitoh, M. Koshiba, B. P. Pal, and R. K. Sinha, "Design of S-band erbium doped concentric dual core photonic crystal fiber amplifiers with ASE suppression," J. Lightwave Technol. **27**, 1725–1733 (2009).
12. K. Wen, H. Peng, J. Wang, R. Wang, and J. H. Li, "Finite element analysis of a novel weak pressure sensor based on fiber Bragg grating in photonic crystal fibers," Opt. Eng. **48**, 034402 (2009).
13. J. Limpert, F. Röser, D. N. Schimpf, E. Seise, T. Eidam, S. Hädrich, J. Rothhardt, C. Jauregui, and A. Tünnermann, "High repetition rate gigawatt peak power fiber laser systems: challenges, design and experiment," IEEE J. Sel. Top. Quantum Electron. **15**, 159–169 (2009).
14. M. F. S. Ferreira, "Nonlinear effects in optical fibers: limitations and benefits," Proc. SPIE **6793**, 679302 (2008).
15. N. G. R. Broderick, H. L. Offerhause, D. J. Richardson, R. A. Sammut, J. E. Caplen, and L. Dong, "Large mode area fibers for high power applications," Opt. Fiber Technol. **5**, 185–196 (1999).
16. V. Rastogi and K. S. Chiang, "Leaky optical fiber for large mode area single mode operation," Electron. Lett. **39**, 1110–1112 (2003).
17. A. Kumar and V. Rastogi, "Design and analysis of a multilayer cladding large-mode-area optical fiber," J. Opt. A **10**, 015303 (2008).
18. A. Kumar, V. Rastogi, C. Kakkar, and B. Dussardier, "Co-axial dual-core resonant leaky fibre for optical amplifiers," J. Opt. A **10**, 115306 (2008).
19. B. Dussardier, V. Rastogi, A. Kumar, and G. Monnom, "Large-mode-area leaky optical fiber fabricated by MCVD," Appl. Opt. **50**, 3118–3122 (2011).
20. J. Limpert, T. Schreiber, S. Nolte, H. Zellmer, A. Tünnermann, R. Iliew, F. Lederer, J. Broeng, G. Vienn, A. Petersson, and C. Jakobsen, "High-power air-clad large-mode-area photonic crystal fiber laser," Opt. Express **11**, 818–823 (2003).

21. S. Yang, Y. Zhang, X. Peng, Y. Lu, S. Xie, and J. Li, "Theoretical study and experimental fabrication of high negative dispersion photonic crystal fiber with large area mode field," Opt. Express **14**, 3015–3023 (2006).
22. Y. Tsuchida, K. Saitoh, and M. Koshiba, "Design of single-mode holey fibers with large-mode-area and low bending losses: the significance of the ring-core region," Opt. Express **15**, 1794–1802 (2007).
23. H. Ademgil and S. Haxha, "Bending insensitive large mode area photonic crystal fiber," Optik **122**, 1950–1956 (2011).
24. M. Napierala, E. B. Pawlik, T. Nasilowski, P. Mergo, F. Berghmans, and H. Thienpont, "Photonic crystal fiber with large mode area and characteristic bending properties," IEEE Photon. Technol. Lett. **24**, 1409–1411 (2012).
25. H. Ademgil and S. Haxha, "Endlessly single mode photonic crystal fiber with improved effective mode area," Opt. Commun. **285**, 1514–1518 (2012).
26. T. S. Saini, A. Kumar, V. Rastogi, and R. K. Sinha, "Selectively filled large-mode-area photonic crystal fiber for high power applications," Proc. SPIE **8847**, 88471Q (2013).
27. J. Li, J. Wang, Y. Cheng, R. Wang, B. Zhang, and H. Wang, "Novel large mode area photonic crystal fibers material-filled structure," Opt. Laser Technol. **48**, 375–380 (2013).
28. S. Haxha and H. Ademgil, "Novel design of photonic crystal fibres with low confinement losses, nearly zero ultra-flatted chromatic dispersion, negative chromatic dispersion and improved effective mode area," Opt. Commun. **281**, 278–286 (2008).
29. T. Martynkien, J. Olszewski, F. Berghmans, and H. Thienlont, "Experimental investigation of bending loss oscillations in large mode area photonic crystal fibers," Opt. Express **15**, 13547–13556 (2007).
30. N. H. Vu, I. K. Hwang, and Y. H. Lee, "Bending loss analyses of photonic crystal fibers based on the finite difference time domain method," Opt. Lett. **33**, 119–121 (2008).
31. A. Dutt, S. Mahapatra, and S. K. Varshney, "Capillary optical fiber: design and application for attaining a large effective mode area," J. Opt. Soc. Am. **28**, 1431–1438 (2011).
32. G. Gu, F. Kong, T. W. Hawkins, M. Jones, and L. Dong, "Extending mode areas of single-mode all-solid photonic bandgap fibers," Opt. Express **23**, 9147–9156 (2015).

Nuclear Instruments and Methods in Physics Research B xxx (2016) xxx–xxx

Contents lists available at ScienceDirect

Nuclear Instruments and Methods in Physics Research B

journal homepage: www.elsevier.com/locate/nimb

Refractive index dispersion of swift heavy ion irradiated BFO thin films using Surface Plasmon Resonance technique

Ayushi Paliwal [a], Savita Sharma [b], Monika Tomar [c], Fouran Singh [d], Vinay Gupta [a,*]

[a] Department of Physics and Astrophysics, University of Delhi, Delhi 110007, India
[b] Department of Applied Physics, Delhi Technological University, Delhi, India
[c] Physics Department, Miranda House, University of Delhi, Delhi 110007, India
[d] Inter University Accelerator Centre, Aruna Asaf Ali Marg, New Delhi 110075, India

ARTICLE INFO

Article history:
Received 4 November 2015
Received in revised form 12 April 2016
Accepted 23 April 2016
Available online xxxx

Keywords:
Irradiation
Fluence
Dielectric constant
Refractive index
Dispersion

ABSTRACT

Swift heavy ion irradiation (SHI) is an effective technique to induce defects for possible modifications in the material properties. There is growing interest in studying the optical properties of multiferroic $BiFeO_3$ (BFO) thin films for optoelectronic applications. In the present work, BFO thin films were prepared by sol–gel spin coating technique and were irradiated using the 15 UD Pelletron accelerator with 100 MeV Au^{9+} ions at a fluence of 1×10^{12} ions cm^{-2}. The as-grown films became rough and porous on ion irradiation. Surface Plasmon Resonance (SPR) technique has been identified as a highly sensitive and powerful technique for studying the optical properties of a dielectric material. Optical properties of BFO thin films, before and after irradiation were studied using SPR technique in Otto configuration. Refractive index is found to be decreasing from 2.27 to 2.14 on ion irradiation at a wavelength of 633 nm. Refractive index dispersion of BFO thin film (from 405 nm to 633 nm) before and after ion radiation was examined.

1. Introduction

Swift heavy ion (SHI) irradiation has been realized as an effective method for material modifications from the past research studies [1–3]. The material response to the incident SHI irradiation has a crucial dependence upon the characteristics of the ions, the fabrication parameters, stoichiometry and the type of the material [4]. The bombardment of these ions can create disorder in the form of point defects, cluster defects or a perturbed atomic distribution along its path as they pass through the material [4]. There is continuing research going on in studying the interaction of ion beam irradiation with low-dimensional structures [5,6]. The impact of ion beam irradiation on the bulk materials has been extensively studied. Huang et al. have investigated the light- and heavy-ion radiation damage in single-crystal $LiNbO_3$ in terms of defect clusters, elastic strain, surface deformation, as well as change in elemental composition [7]. Olivares et al. have exploited heavy mass ions like Kr and Xe, having energies in the ~10 MeV/amu range to produce thick planar optical waveguides at the surface of lithium niobate ($LiNbO_3$) [8]. The impact of these heavy ions leads to partial amorphization and refractive index change at the surface [8]. Amorphization and disordering has been observed in single crystalline Al_2O_3 by swift heavy ions [9]. Recently, Park et al. have observed an increase in the amorphous fraction as a function of fluence for polycrystalline $La_2Ti_2O_7$ powders [10]. The concept of ion beam irradiation effect on nanostructures has become a captivating field of research. This aroused interest in the use of ion beams to synthesize and modify physical and chemical properties of the nanostructures for various applications [11–13]. The mass of the incident ion, irradiation energy and fluence greatly affect the induced modifications due to irradiation [14].

Interest has been growing in bismuth ferrite (BFO) due to its room temperature multiferroic properties. Both magnetic and ferroelectric properties have been simultaneously observed with high ferroelectric Curie temperature (T_C = 1100 K) and antiferromagnetic temperature (T_N = 643 K) [15,16]. BFO has several potential applications in data storage, spin valves, spintronics and sensors [17–19]. There is growing interest in the study of its optical properties making it useful for the development of optoelectronic devices. Recently, several research groups have studied the optical properties of BFO thin films including its optical band gap, photoconductivity, and linear and nonlinear optical properties [20–22]. There is recent paper on theoretical investigation of optical properties of BFO using first principle calculations [23]. The relation between SHI created structural defects and ferroelectric ordering in BFO thin films has been of considerable interest underlying their optical, multiferroic, magneto-dielectric, and magnetoelectric

* Corresponding author.
E-mail address: drguptavinay@gmail.com (V. Gupta).

http://dx.doi.org/10.1016/j.nimb.2016.04.051
0168-583X/

properties [24–26]. However, the effect of swift heavy ion irradiation on the optical properties of BFO thin films has not been reported previously. Surface Plasmon Resonance (SPR) is the most relevant technique to examine the optical properties of dielectric materials and could be easily modified for optical measurements under different ambient conditions. The interface between two media with dielectric constants of opposite signs, such as a metal and a dielectric supports surface plasmon wave (SPW) excited by an incident electromagnetic light wave. Otto configuration is one of the method to excite the SP by attenuated total reflection (ATR) utilizing prism coupling technique [27]. In the Otto configuration, a laser beam is reflected off the base of a prism and adjacent to the base is a gap of low refractive index material (or dielectric) with a thickness of the order of the employed laser wavelength. On the other side of the gap is a metal layer of optimized thickness. When the total internal reflection condition is satisfied, the evanescent wave propagates at the interface of prism and dielectric spacer layer exciting SP modes on the dielectric/metal interface.

In the present work, the optical properties of BFO thin films have been studied after irradiating it with swift heavy ion (Au^{8+}) beam of radiations. The films have been prepared by sol–gel chemical route technique on Pt/Si substrate. Structural, morphological and optical properties of thin films were examined using XRD, AFM studies and UV–Visible spectrophotometer respectively. An Otto prism coupler arrangement is designed to excite the surface plasmons for probing the optical properties of BFO thin films. Refractive index dispersion of BFO thin film, before and after ion radiation was examined by varying the incident wavelength of the laser from 405 nm to 633 nm.

2. Experimental details

The BFO thin films were prepared on Pt(111)/Ti/SiO_2/Si substrates by a sol–gel spin coating technique. The starting materials were bismuth nitrate (($Bi(NO_3)_3{\cdot}5H_2O$), iron nitrate (($Fe(NO_3)_3{\cdot}9H_2O$), acetic acid and 2-methoxyethanol as solvents with acetylacetone being chelating agent. The BFO precursor solution was prepared by dissolving bismuth nitrate and iron nitrate in 2-methoxyethanol and 1 ml acetic acid was added dropwise. The solutions were stirred to get the homogenous transparent solutions and then aged for 24 hours. The BFO solutions thus obtained were spin coated over the Pt/Ti/SiO_2/Si substrates maintaining the thickness of BFO thin film at 220 nm. The as-deposited BFO thin film was annealed at 550 °C for two hours in air ambient. The as grown BFO thin film was irradiated using the 15 UD Pelletron accelerator at Inter University Accelerator Centre (IUAC), New Delhi with 100 MeV Au^{8+} ions at a fluence of 1×10^{12} ions cm^{-2}. The beam current was maintained to be 1 pnA (particle nanoampere) to avoid heating effects of the samples during irradiation. The ion beam incident normal to the surface of BFO thin film was made to scan over an area of 10 mm × 10 mm to achieve dose uniformity across the sample area. Structural characterization of prepared samples was carried out using X-ray diffraction (XRD) analysis (Bruker D8). Optical properties in reflectance mode were studied using UV–Visible spectrophotometer (Perkin Elmer Lambda 35). Surface morphology was studied by Atomic force microscopy (AFM) technique using Bruker Dimension Icon.

The details of the experimental setup used for studying the optical properties of BFO thin films using SPR technique have been explained elsewhere [28]. The SPR reflectance curves were obtained for prism/air-gap/Au/Pt/Ti/SiO_2/Si, prism/air-gap/Au/BFO (as grown)/Pt/Ti/SiO_2/Si and prism/air-gap/Au/BFO(after irradiation)/ Pt/Ti/SiO_2/Si by varying the incident angle of laser beam (λ = 633 nm). The SPR measurements were carried out after depositing 40 nm thin Au layer on BFO thin films using thermal evaporation technique. The SPR reflectance curves were also obtained for the prism/air-gap/Au/BFO(as grown)/Pt/Ti/SiO_2/Si and prism/air-gap/Au/BFO(after radiation)/Pt/Ti/SiO_2/Si by varying the wavelength of laser beam from 405 nm to 633 nm in order to obtain the refractive index dispersion.

3. Results and discussion

The XRD patterns of the as-grown and irradiated BFO thin film with 100 MeV Au^{8+} ions are presented in Fig. 1. In the XRD spectra of pristine BFO thin film, peaks are observed at 2θ = 33.1°, 46.3°, 55.2° corresponds to (104) and (110), (024) and (300) planes respectively of BFO thin films. All XRD peaks corresponding to distorted rhombohedral structure of BFO [29,30] having space group R3c were indexed and found to be matching well with International Centre of Diffraction Data (ICDD Card No. 00-020-0169). The XRD peak for (006) plane corresponds to the presence of secondary Fe-rich phase or Bi deficient compositions such as Fe_2O_3. The characteristic peaks i.e. (104) and (110), (300) diminished in the XRD spectra of BFO thin film after irradiation with 100 MeV Au^{8+} ions (Fig. 1) confirming that the irradiation results in the degradation in the crystallinity of BFO thin films due to defects and dislocations [24].

Fig. 2 shows the AFM images of the surface of as grown and irradiated BFO thin films respectively (2 μm × 2 μm area scan). The surface morphology of as grown BFO thin films was found to be fine having uniformly distributed grains (Fig. 2). The grain size of the film was found to be reduced and diminished their boundaries after ion irradiation [31]. The observed value of root-mean-square (RMS) surface roughness for pristine sample is about 5 nm which increased to 21 nm for the irradiated film. The increased value of surface roughness on ion irradiation is in accordance with earlier reports [24].

Fig. 3 represents the UV–Visible reflectance spectra of both the pristine and irradiated BFO thin films. The reflectance of BFO thin film increased significantly in the lower wavelength region (<400 nm) and fringes were also observed after irradiation with 100 MeV Au^{+8} ions at 1×10^{12} ions cm^{-2} fluence. The increased reflectance clearly indicates increased losses on ion irradiation. The increased surface roughness as seen from the AFM analysis supports the higher losses in the irradiated films.

The SPR reflectance curves obtained for prism/air-gap/Au/Pt/Ti/SiO_2/Si and prism/air-gap/Au/BFO/Pt/Ti/SiO_2/Si (with as grown BFO film) systems at an incident light laser wavelength of 633 nm

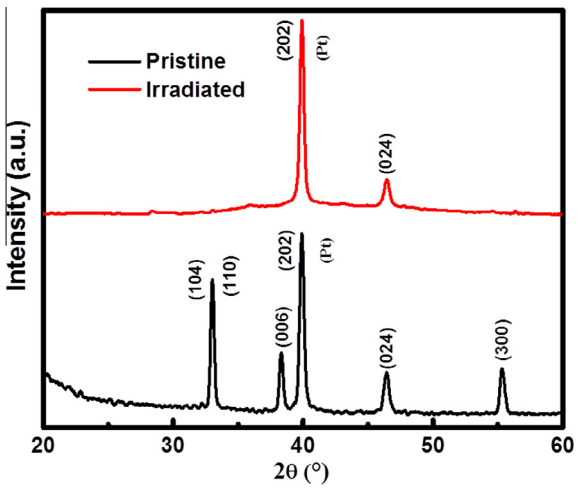

Fig. 1. XRD patterns observed for $BiFeO_3$ thin films (as grown and after irradiation) deposited on Pt/Ti/SiO_2/Si substrate.

Please cite this article in press as: A. Paliwal et al., Refractive index dispersion of swift heavy ion irradiated BFO thin films using Surface Plasmon Resonance technique, Nucl. Instr. Meth. B (2016), http://dx.doi.org/10.1016/j.nimb.2016.04.051

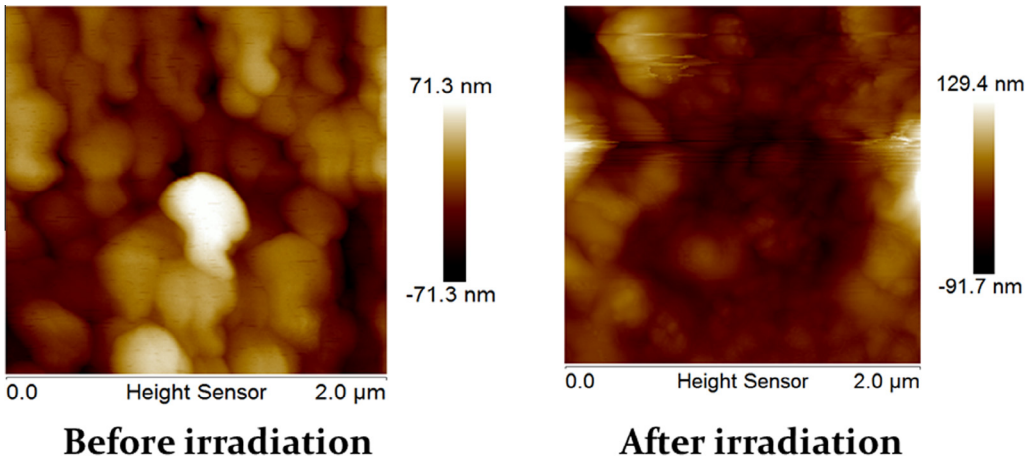

Fig. 2. AFM images of as-grown and irradiated BFO thin films at 1×10^{12} ions cm^{-2}.

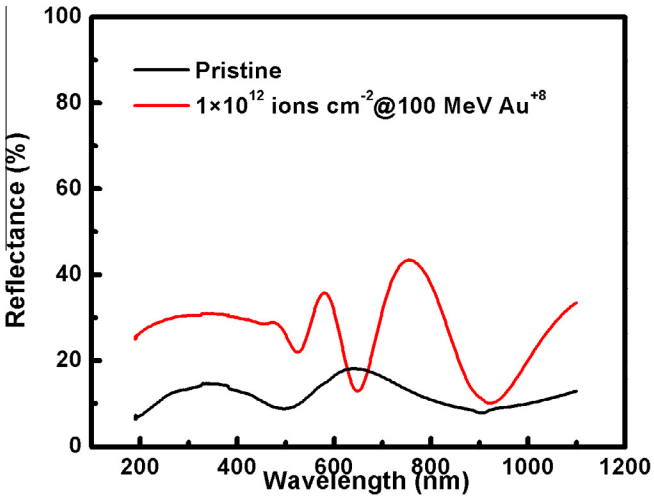

Fig. 3. UV–Visible reflectance spectra of as-grown and irradiated BFO thin film with 100 MeV Au^{+8} ions at a fluence of 1×10^{12} ions cm^{-2}.

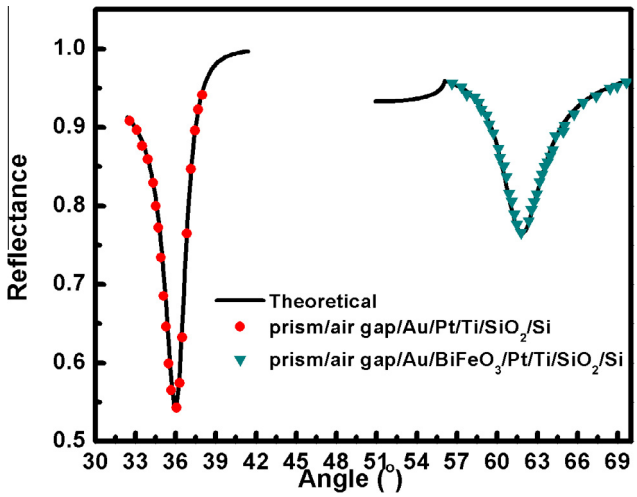

Fig. 4. SPR reflectance curves obtained for prism/air-gap/Au/Pt/Ti/SiO_2/Si and prism/air-gap/Au/$BiFeO_3$/Pt/Ti/SiO_2/Si systems.

under Otto configuration are shown in Fig. 4. The SPR resonance angle (θ_{SPR}) for prism/air-gap/Au/Pt/Ti/SiO_2/Si system is observed at about 36.1° which shifts towards higher resonance angle of 61.9° after integration of as grown BFO thin film with Pt/Ti/SiO_2/Si substrate (Fig. 4). The full width at half maxima i.e. (FWHM) of the SPR reflectance curves corresponds to the absorption losses which increase for prism/air gap/Au/BFO/Pt/Ti/SiO_2/Si system in comparison to that of the prism/air-gap/Au/Pt/Ti/SiO_2/Si system. The symbols in Fig. 4 represent the experimental SPR data points and continuous line corresponds to the theoretically fitted curve. Fresnel's equations were utilized along with the experimental SPR data in order to evaluate the complex dielectric constant and refractive index of the BFO thin films [32]. The estimated values of complex dielectric constant (5.27 + i0.09) and refractive index (2.29 + i0.019) match very well to the reported value at $\lambda = 633$ nm [33]. Fig. 5 shows the SPR reflectance curves for prism/air-gap/Au/BFO/Pt/Ti/SiO_2/Si systems for as grown and irradiated BFO thin films. The θ_{SPR} obtained for the prism/air-gap/Au/BFO/Pt/Ti/SiO_2/Si system having as grown and irradiated BFO thin films respectively are about 61.9° and 50.9°. The observed shift in SPR curve towards lower angle is related to the change in dielectric media from as grown BFO film to the irradiated BFO thin film and the decrease in the refractive index. The absorption losses in the BFO thin film increase on exposure to swift heavy ion radiation

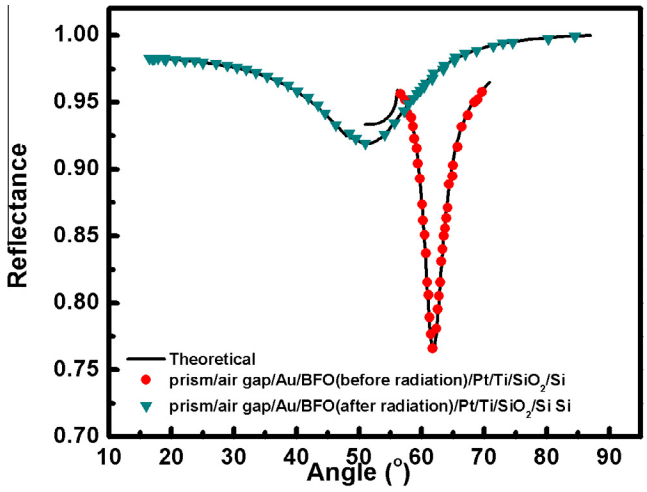

Fig. 5. SPR reflectance curves for prism/air-gap/Au/BFO/Pt/Ti/SiO_2/Si system having both as grown and irradiated BFO thin films.

(Fig. 5). The complex dielectric constant and refractive index of BFO thin film after radiation were found to be about 4.58 + i0.1 and 2.14 + i0.01 respectively at $\lambda = 633$ nm. The value of refractive

Please cite this article in press as: A. Paliwal et al., Refractive index dispersion of swift heavy ion irradiated BFO thin films using Surface Plasmon Resonance technique, Nucl. Instr. Meth. B (2016), http://dx.doi.org/10.1016/j.nimb.2016.04.051

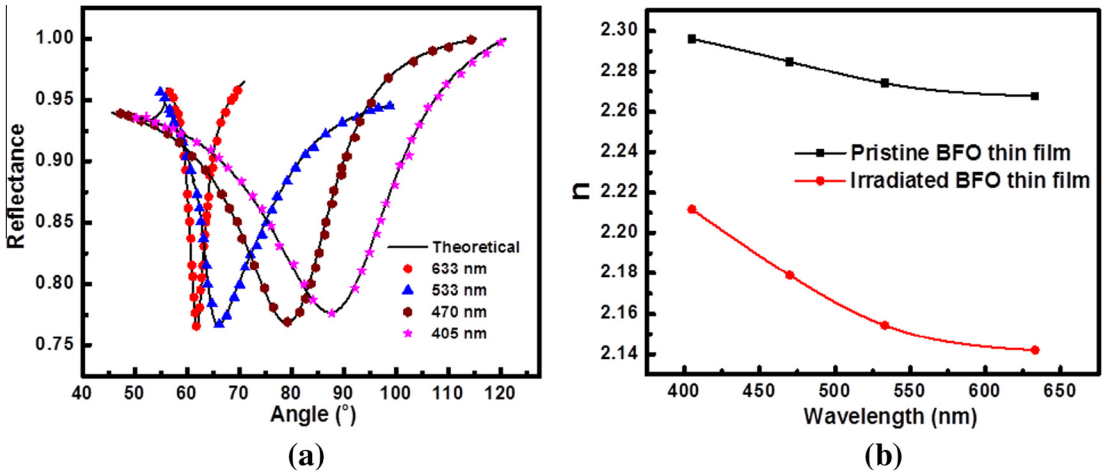

Fig. 6. (a) Variation in SPR reflectance curve for prism/air-gap/Au/pristine BFO/Pt/Ti/SiO_2/Si system at different wavelength of incident laser in visible region, (b) Refractive index dispersion (i.e. variation of refractive index with wavelength) for both pristine and irradiated BFO thin films.

index decreases after irradiation for BFO thin film which may be related to the defects and voids created in the BFO thin film after irradiation [34].

3.1. Refractive index dispersion

The refractive index dispersion of BFO thin film before and after Au^{8+} ion irradiation at optical frequencies has also been studied using SPR technique. The SPR reflectance curves of the prepared prism/air-gap/Au/BFO/Pt/Ti/SiO_2/Si system having as grown BFO thin films obtained by varying the wavelength of incident laser from 405 nm to 633 nm are shown in Fig. 6(a). It may be noted from Fig. 6(a) that the SPR curve along with resonance angle (θ_{SPR}) shift continuously towards higher angle whereas magnitude of minimum reflectance (R_{min}) and FWHM of SPR reflectance curve increase with decrease in the wavelength of incident laser from 633 nm to 405 nm. The SPR curves obtained at different wavelengths of incident light were fitted to Fresnel's equations in order to obtain the refractive index dispersion of BFO thin films as a function of the incident wavelength. The theoretically best fitted SPR curves are shown by solid lines in Fig. 6(a). The refractive index shows a strong dispersion with wavelength of incident light and is found to decrease from 2.29 to 2.27 with increase in wavelength from 405 nm to 633 nm for pristine BFO thin film. Similar measurements were repeated for the prism/air-gap/Au/BFO/Pt/Ti/SiO_2/Si system having irradiated BFO thin film and refractive index was found to decrease from 2.21 to 2.14 with wavelength. Similar dispersion in the refractive index has been observed by several workers for various metal oxide thin films and reported to follow the well known Sellmeier behavior [35]. It is important to note that the refractive index showed more dispersion for the irradiated BFO as compared to pristine BFO thin film.

4. Conclusion

The impact of swift heavy ions (SHI) on the crystallographic structure, surface morphology and optical properties of bismuth ferrite thin film has been investigated after irradiation with 100 MeV Au^{+8} ions at ion fluence of 1×10^{12} ions cm^{-2}. The as-grown BFO thin film corresponds to the rhombohedrally distorted perovskite crystalline structure with space group R3c. Irradiation induced roughness in the as-deposited BFO thin film. The optical properties of both the as grown BFO and irradiated BFO thin films have been studied using SPR technique under Otto configuration. The complex dielectric constant and refractive index of BFO thin film were found to be 5.27 + i0.09 and 2.29 + i0.019 respectively at a wavelength of 633 nm which changed to 4.58 + i0.1 and 2.14 + i0.01 respectively on ion irradiation. A decrease in the refractive index was observed for irradiated BFO thin film. A strong dispersion in refractive index with wavelength of incident light is obtained for both pristine and irradiated BFO thin film and has the well known Sellmeier behavior.

Acknowledgements

The authors are thankful to the Pelletron group of IUAC, New Delhi for providing good quality scanned beam during irradiation and to Nanoscale Research Facility (NRF) for providing AFM facility at Indian Institute of Technology (IIT), New Delhi. Authors are also thankful to Department of Science and Technology (DST) and University of Delhi for the financial support.

References

[1] W.M. Arnoldbik, P.A. Emmichoven, V. Zeijlmans, F.H.P.M. Habraken, Phys. Rev. Lett. 94 (2005) 245504.
[2] G. Rizza, E.A. Dawi, A.M. Vredenberg, I. Monner, Appl. Phys. Lett. 95 (2009) 043105.
[3] W. Wesch, C.S. Schnohr, P. Kluth, Z.S. Hussain, L.L. Araujo, R. Giulian, D.J. Sprouster, A.P. Byrne, M.C. Ridgway, J. Phys. D Appl. Phys. 42 (2009) 115402.
[4] N. Tripathi, S. Rath, ECS J. Solid State Sci. Technol. 3 (3) (2014) P21.
[5] S. Kuriakose, D.K. Avasthi, S. Mohapotra, Beilstein J. Nanotechnol. 6 (2015) 928–937.
[6] J. Li, B. Zhang, L. Li, H. Ma, M. Yu, J. Li, Radiat. Phys. Chem. 94 (2014) 80.
[7] H.-C. Huang, L. Zhang, G. Malladi, J.I. Dadap, S. Manandhar, K. Kisslinger, R.S.R. Vemuri, V. Shutthanandan, H. Bakhru, R.M. Osgood Jr., Opt. Mater. Express 5 (5) (2015) 1071.
[8] J. Olivares, M.L. Crespillo, O. Caballero-Calero, M.D. Ynsa, A. García-Cabañes, M. Toulemonde, C. Trautmann, F. Agulló-López, Opt. Express 17 (26) (2009) 24175.
[9] N. Okubo, N. Ishikawa, M. Sataka, S. Jitsukawa, Nucl. Instr. Meth. Phys. Res. B 314 (2013) 208.
[10] S. Park, M. Lang, C.L. Tracy, J. Zhang, F. Zhang, C. Trautmann, P. Kluth, M.D. Rodriguez, R.C. Ewing, Nucl. Instr. Meth. Phys. Res. B 326 (2014) 145.
[11] A. Abedini, F. Larki, E. Saion, A. Zakaria, M.Z. Hussein, Radiat. Phys. Chem. 81 (2012) 1653.
[12] V. Gokulakrishnan, S. Parthiban, E. Elangovan, K. Jeganathan, D. Kanjilal, K. Asokan, R. Martins, E. Fortunato, K. Ramamurthi, Radiat. Phys. Chem. 81 (2012) 589.
[13] S.P. Patel, J.C. Pivin, R. Chandra, D. Kanjilal, Lokendra. Kumar, Vacuum 111 (2015) 150.
[14] P. Prabukanthan, K. Asokan, D. Kanjilal, R. Dhanasekaran, I.O.P. Publishing, Semicond. Sci. Technol. 23 (2008) 125042.
[15] P. Fischer, M. Polomska, I. Sosnowska, M. Szymanski, J. Phys. C: Solid State Phys. 13 (1980) 1931.
[16] F. Kubel, H. Schmid, Acta Crystallogr. C 46 (1990) 698.

[17] J. Wang, J.B. Neaton, H. Zheng, V. Nagarajan, S.B. Ogale, B. Liu, D. Viehland, V. Vaithyanathan, D.G. Schlom, U.V. Waghmare, N.A. Spaldin, K.M. Rabe, M. Wuttig, R. Ramesh, Science 299 (2003) 1719.
[18] J.B. Neaton, C. Ederer, U.V. Waghmare, N.A. Spaldin, K.M. Rabe, Phys. Rev. B 71 (014113) (2005) 1220.
[19] T. Zhao, A. Scholl, F. Zavaliche, K. Lee, M. Barry, A. Doran, M.P. Cruz, Y.H. Chu, C. Ederer, N.A. Spaldin, R.R. Das, D.M. Kim, S.H. Baek, C.B. Eom, R. Ramesh, Nat. Mater. 5 (2006) 823.
[20] A. Kumar, R.C. Rai, N.J. Podraza, S. Denev, M. Ramirez, Y.-H. Chu, L.W. Martin, J. Ihlefeld, T. Heeg, J. Schubert, D.G. Schlom, J. Orenstein, R. Ramesh, R.W. Collins, J.L. Musfeldt, V. Gopalan, Appl. Phys. Lett. 92 (2008) 121915.
[21] J.F. Ihlefeld, N.J. Podraza, Z.K. Liu, R.C. Rai, X. Xu, T. Heeg, Y.B. Chen, J. Li, R.W. Collins, J.L. Musfeldt, X.Q. Pan, J. Schubert, R. Ramesh, D.G. Schlom, Appl. Phys. Lett. 92 (2008) 142908.
[22] S.R. Basu, L.W. Martin, Y.H. Chu, M. Gajek, R. Ramesh, R.C. Rai, X. Xu, J.L. Musfeldt, Appl. Phys. Lett. 92 (2008) 091905.
[23] H. Wang, Y. Zheng, M.-Q. Cai, H. Huang, H.L. Chan, Solid State Commun. 149 (2009) 641.
[24] B.N. Dash, P. Mallick, P. Dash, R. Biswal, J. Prakash, A. Tripathi, D. Kanjilal, N.C. Mishra, Bull. Mater. Sci. 36 (2013) 813.
[25] B.N. Dash, P. Dash, H. Rath, P. Mallick, R. Biswal, P.K. Kulriya, N.C. Mishra, Indian J. Phys. 84 (10) (2010) 1315.
[26] Z. Wen, D. Wu, J. Zhu, A. Li, J. Phys. D Appl. Phys. 47 (2014) 045310.
[27] A. Otto, Z. Physik 216 (1968) 398.
[28] A. Paliwal, A. Sharma, M. Tomar, V. Gupta, J. Appl. Phys. 115 (2014) 043104.
[29] S.K. Singh, K. Maruyama, H. Ishiwara, Appl. Phys. Lett. 91 (2007) 112913.
[30] G. Catalan, J.F. Scott, Adv. Mater. 21 (2009) 2463.
[31] M. Kumar, F. Singh, S.A. Khan, V. Baranwal, S. Kumar, D.C. Agarwal, A.M. Siddiqui, A. Tripathi, A. Gupta, D.K. Avasthi, A.C. Pandey, J. Phys. D Appl. Phys. 38 (2005) 637.
[32] T.S. Gonul, J. Lightwave Technol. 21 (2003) 805.
[33] A. Paliwal, A. Sharma, M. Tomar, V. Gupta, Physica B 448 (2014) 120.
[34] S. Sharma, A. Paliwal, M. Tomar, F. Singh, N.K. Puri, V. Gupta, J. Mater. Sci. (2016), http://dx.doi.org/10.1007/s10853-016-9725-x.
[35] V. Gupta, A. Mansingh, J. Appl. Phys. 80 (1996) 1063.

Please cite this article in press as: A. Paliwal et al., Refractive index dispersion of swift heavy ion irradiated BFO thin films using Surface Plasmon Resonance technique, Nucl. Instr. Meth. B (2016), http://dx.doi.org/10.1016/j.nimb.2016.04.051

Slow light generation in single-mode rectangular core photonic crystal fiber

Sandeep Yadav, Than Singh Saini, and Ajeet Kumar

Citation: AIP Conference Proceedings **1728**, 020389 (2016); doi: 10.1063/1.4946440
View online: http://dx.doi.org/10.1063/1.4946440
View Table of Contents: http://scitation.aip.org/content/aip/proceeding/aipcp/1728?ver=pdfcov
Published by the AIP Publishing

Slow Light Generation in Single-Mode Rectangular Core Photonic Crystal Fiber

Sandeep Yadav[1], Than Singh Saini[1], Ajeet Kumar[1, a)]

[1]*Department of Applied Physics, Delhi Technological University (Formerly Delhi College of Engineering), Delhi-110 042, INDIA*

[a)] Corresponding author: ajeetdph@gmail.com

Abstract. In this paper, we have designed and analyzed a rectangular core photonic crystal fiber (PCF) in Tellurite material. For the designed photonics crystal fiber, we have calculated the values of confinement loss and effective mode area for different values of air filling fraction (*d/Λ*). For single mode operation of the designed photonic crystal fiber, we have taken *d/Λ*= 0.4 for the further calculation of stimulated Brillouin scattering based time delay. A maximum time delay of 158 ns has been achieved for input pump power of 39 mW. We feel the detailed theoretical investigations and simulations carried out in the study have the potential impact on the design and development of slow light-based photonic devices.

INTRODUCTION

The group velocity of the pulse is defined as the speed with which the light waves travel in any media. In normal condition, due to the ultrahigh speed of the light wave, it becomes hard to control these waves in time domain; hence we need to slow down the speed of the light to make efficient controlling of the light wave [1].

There is a wide range of applications of slow light such as delay and processing of microwave photonic waveforms, the enhancement of nonlinear interactions, and many others [2-5]. A large number of researches have been done using the slow light employing standard fiber at room temperature that showed good results in their potential incorporation in optical communication and microwave photonic systems [6-7]. When light interact with the resonant medium, its speed and other propagation characteristics can be controlled [8-9]. Recently, *Saini et al*. [8] reported a time delay of 88 ns using 1 meter long Tellurite (PCF) with hexagonal core pumped with 140 mW pump power.

In this paper, we have designed a rectangular core PCF structure for tuneable slow light application based on stimulated Brillouin scattering (SBS). The photonic crystal fiber structure has been simulated using commercially available software 'COMSOL Multiphysics'. The values of confinement loss and effective mode area *(Aeff)* for different values of the air filling fraction (*i.e*. *d/Λ*) have been calculated.

THEORY OF SBS

Let A_p and ω_p be the amplitude of the amplitude and frequency of the pump wave and A_s and ω_s be the amplitude and frequency of counter-propagating signal wave respectively. So the differential equation for pump wave and signal wave can be given as Eq. (1 & 2) [8]

$$\frac{dA_P}{dz} = -g(\omega_s)A_p^2A_s^2 - \alpha_p I_p \qquad (1)$$

$$-\frac{dA_s}{dz} = -g(\omega_s)A_p^2A_s^2 - \alpha_s I_s \qquad (2)$$

Let the pump wave is undepleted and hence $\alpha_p \approx \alpha_s = \alpha$. So the solution for the above non-linear differential equations is given by

$$A_S(0) = A_S(L)\exp\left(g(\omega_s)L_{eff} - \alpha L\right) \qquad (3)$$

International Conference on Condensed Matter and Applied Physics (ICC 2015)
AIP Conf. Proc. 1728, 020389-1–020389-4; doi: 10.1063/1.4946440
Published by AIP Publishing. 978-0-7354-1375-7/$30.00

Here L and L_{eff} are the real and effective length of the fiber respectively.

The maximum allowable pump power P_{max} is defined as the maximum pump power below which the output pulse is undistorted is given by [11]

$$P_{max} = 21\frac{A_{eff}}{Kg_BL_{eff}} \quad (4)$$

Here A_{eff} is the effective mode area of the designed PCF, L_{eff} is the effective length of the fiber, K is the polarization factor, and g_B is the Brillouin gain coefficient of the PCF for Tellurite material taken from *Saini et al*.

Similarly, P_{min} is defined as the minimum pump power below which SBS effect can't occur given by [10]

$$P_{min} = \frac{\alpha A_{eff}L}{Kg_BL_{eff}} \quad (5)$$

The value of SBS-induced time delay can be calculated using the following expression [10]

$$\frac{\Delta t_d}{L_{eff}} = \frac{P_P g_0 K}{\Gamma_B} \quad (6)$$

Here P_p is the input pump power, g_0 is inherent material gain coefficient given by $g_0 = g_B/Aeff$, K is the polarization factor taken from *Saini et al.* K=0.667 and Γ_B is the SBS linewidth.

DESIGN OF PROPOSED PCF

The transverse cross-sectional view of the proposed PCF design has been shown in Fig. 1. The core of the PCF has been designed in a rectangular shape with all the air holes having same radius (*i.e.* r = 0.5 μm) and the distance between the holes (*i.e.* Λ) is kept constant to 2.5 μm.

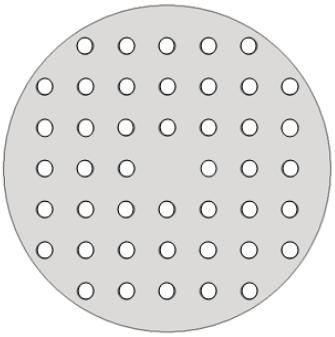

FIGURE 1 Cross-sectional view of designed PCF

RESULT AND DISCUSSION

In this paper, we have controlled the effective mode area of the designed PCF by tuning the air filing fraction of the structure. By keeping the pitch constant and varying the diameter of the air holes, we have varied the air filling fraction of the PCF. The variation of the effective mode area with respect to air filling fraction has been illustrated in Fig. 2.

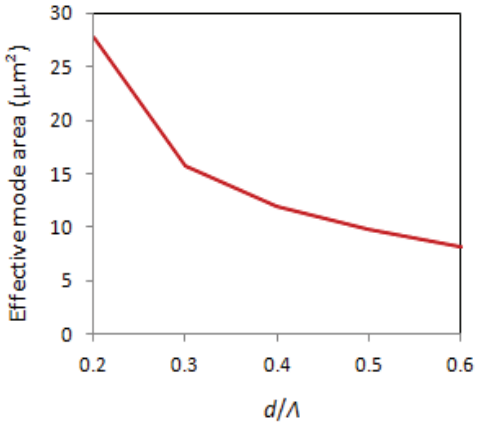

FIGURE 2 Variation of Effective Mode Area with respect to d/Λ

Another effective parameter that we have calculated is confinement loss. The variation of the confinement loss with respect to air filling fraction has been shown in Fig. 3. Initially, the value of confinement loss is very high *i.e*. 15.15 dB/m for $d/\Lambda = 0.2$. But as the d/Λ value increases, the value of confinement loss keeps on decreasing. For single mode operation of the designed photonic crystal fiber structure, the value of d/Λ has been taken as 0.4 [6] and for $d/\Lambda = 0.4$, the confinement loss is found to be 0.0607 dB/m and it keeps on decreasing as the value of d/Λ increases.

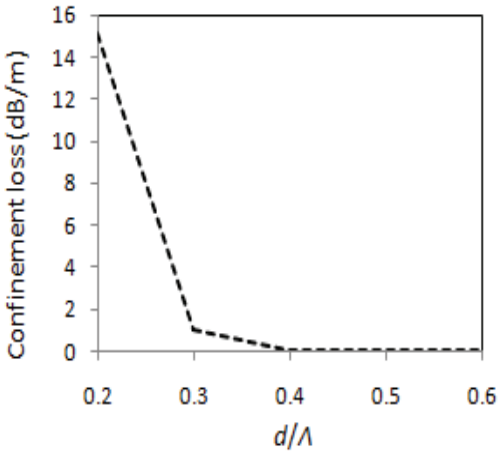

FIGURE 3 Variation of Confinement Loss with respect to d/Λ

For single mode operation, we have calculated the maximum and the minimum allowable power for SBS operation and found to be P_{max} =39.18 mW and P_{min} = 2.39 mW. For these values, we had calculated the variation of time delay for input pump power ranging between P_p = 3 mW to P_p = 39 mW. A maximum time delay of 158 ns has been achieved on input pump power of 39 mW and the minimum time delay found was 12.19 ns for input pump power of 3 mW. The variation of the time delay has been shown in Fig. 4.

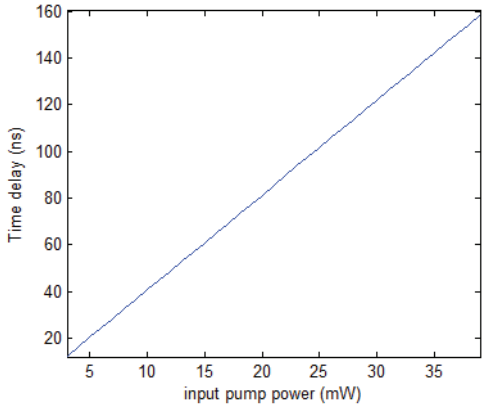

FIGURE 4 SBS induced time delay with varying input pump power

CONCLUSION

A rectangular core Tellurite material PCF has been designed and analyzed for tuneable slow light generation based on stimulated Brillouin scattering. The effective mode area and confinement loss has been calculated for different values of air filling fraction. A maximum time delay of 158 ns has been achieved for a 100 m long designed PCF. Due to this time delay, the designed photonic crystal fiber is expected to have potential applications in the realization of compact slow light devices.

ACKNOWLEDGEMENT

The authors gratefully acknowledge the TUN-IND bilateral research project, Department of Science and Technology, Govt. of India.

REFERENCES

1. T. Baba, Nature Photon., **2**, 465-473, (2008)
2. L. T. Mok and B. J. Eggleton, Nature (News & Views), **433**, 811–812, (2005).
3. S. Rawal, R. K. Sinha, and R. M. De La Rue, J. Nanophoton., **6**, 063504-1–063504-12 (2012).
4. M. Santagiustina, G. Eisenstein, L. Thevenaz, J. Capmany, J. Mork, J. P. Reithmaier, A. D. Rossi, S. Sales, K. Yvind, S. Combrie, and J. Bourderionnet. IEEE Photon. Soc. Newsletter, **26**, 5–12 (2012).
5. R. K. Sinha, A. Kumar, and T. S. Saini, IEEE J. Sel. Topics Quant. Electron., (Online) ISSN: 1077-260X, Doi: 10.1109/JSTQE.2015.2477781, (2015).
6. L. Thevenaz, Nat. Photon., **2**, 471-481, (2008).
7. G. M. Gehring, R.W. Boyed, A. L. Gaeta, D. J. Gauthier, and A. E. Willner, J. Lightwave Technol., **26**, 3752-3762, (2008).
8. T. S. Saini, A. Kumar, and R. K. Sinha, Proc. Photonics, 12th International Conference on Fiber Optics and Photonics @ OSA, IIT Kharagpur, WB, India, Dec 13-16, 2014, T3A.28, (2014)
9. S. Yang, H. Chen, C. Qiu, M. Chen, S. Xie, J. Li, and W. Chen. Optt. Lett., **33**, 95-97, (2008).
10. T. S. Saini, A. Kumar, and R. K. Sinha. Journal of Modern Optics, **7**, 508-513, (2015).

Trans Indian Inst Met
DOI 10.1007/s12666-016-0905-9

TECHNICAL PAPER

Wear Characteristics of Al5083 Surface Hybrid Nano-composites by Friction Stir Processing

N. Yuvaraj[1] · S. Aravindan[2] · Vipin[1]

Received: 28 December 2015 / Accepted: 13 May 2016

Abstract Friction stir processing (FSP) is used to produce surface composites with the retainment of bulk properties. In the present study, FSP was utilized to incorporate nano particles of Boron carbide (B_4C) and Titanium carbide (TiC) into the matrix of Al5083 alloy individually and in combined form in order to produce mono and hybrid surface composite layer. The FSPed regions were analyzed through scanning electron microscope (SEM) and XRD studies. Mechanical properties of the FSPed surface composites were evaluated through micro hardness and tensile tests. Wear characteristics of the composites were evaluated through pin on disc dry sliding wear test at sliding speed of 1 m/s and under the normal load ranging from 20 to 100 N in steps of 20 N. The mechanical and wear resistance properties of the composite were higher than the base alloy. Among the processed composites, Al–B_4C composites have exhibited the highest hardness and tensile strength. However the hybrid composites (Al–B_4C–TiC) have exhibited significant increase in wear resistance. Worn out surfaces and wear debris were analyzed through SEM studies.

Keywords Friction stir processing · Boron carbide (B_4C) · Titanium carbide (TiC) · Wear

✉ S. Aravindan
aravindan@mech.iitd.ac.in

[1] Department of Mechanical Engineering, Delhi Technological University, Delhi 110 042, India

[2] Department of Mechanical Engineering, Indian Institute of Technology, Delhi 110 016, India

1 Introduction

Aluminum based metal matrix composites are widely used in aerospace, automobile and marine areas due to their precise balances of mechanical and physical properties and wear resistance. In most of engineering applications, surface plays a predominant role in dictating the service life of the component. Instead of making bulk composites, the surface layer on the substrate improves the mechanical and wear resistance [1]. For the fabrication of such surface composite layer, the new modification technique, friction stir processing (FSP) is used. FSP technique is used to produce defect-free surface composite with a good bonding and uniform distribution of reinforcement particles within an aluminum matrix. The reinforcement particles are preplaced in the grooves/holes on the surface of the metallic substrate plate and then processed with the FSP tool to form the surface composite layer. The FSP process has been explained in detail elsewhere [2]. FSP process is used for enhancing the properties of cast aluminum alloys, uniform dispersion of hard reinforcement material in matrix, microstructure refinement of composites, homogenization of nano phase and to produce fine and ultra fine grained structure in aluminum alloys [3–5]. Literature is available on the fabrication of aluminum based surface composite layer (SCL) through FSP process with various nano reinforcement particulates such as SiC [6], Al_2O_3 [7], ZrO_2 [8], Si_3N_4 [9], TiO_2 [10], B_4C [11] and CNT [12]. Some studies on hybrid surface composite layer fabricated by FSP also have been reported in the literature. Hosseini et al. [13] reported that FSPed hybrid composite containing Al5083/CNTs/CeO_2 in the volume ratio of 75–25 % exhibit 42 % higher value of ultimate tensile strength and 118 % of hardness when compared to the base alloy. Asl and Khandani [14] observed a significant effect of the

Published online: 26 May 2016

hybrid ratio on mechanical and wear properties of the Al5083/Al_2O_3/Graphite fabricated by FSP. Hybrid ratio of 50 % composite specimen results in highest tensile strength with reduced wear rate. The mechanical and tribological properties of Al5083/SiC/MoS_2 surface composite have been improved by FSP. The MoS_2 particles induce lubricating effect and lowers the friction coefficient and hard SiC particles lead to increase in hardness and tensile properties [15]. Similar results have been reported by Alidokht et al. [16] for FSPed A356/SiC/MoS_2 composites. The presence of MoS_2 assists in the formation and retention of solid lubricant film to prevent metal-to-metal contact and it reduces the wear and lowers the friction coefficient. The wear resistance and ballistic resistance of FSPed Al7075/B_4C/MoS_2 composite is enhanced. The B_4C particle increases the hardness and wear resistance. The addition of MoS_2 particles act as a solid lubricant which improves the wear resistance which in turn decreases the depth of penetration of projectile in Ballistic testing. It even leads to complete stopping of projectile in the specimen [17]. Mahmoud et al. [18] indicated that hybrid ratio in the hybrid composite of Al1050 reinforced with SiC and Al_2O_3 particulates has a strong influence on the hardness and wear resistance. 80 % SiC + 20 % Al_2O_3 FSPed composite exhibit higher hardness and superior wear resistance than other hybrid reinforcement ratios. The hardness and wear resistance is improved in the Al6061/SiC/Gr FSPed composite layer due to presence and pinning effect of hard reinforcement particles and mechanically mixed layer between the surface composite and steel disc surfaces. The SiC particles serve as a load bearing element and the Gr particles acts as solid lubricant [19]. Rejil et al. [20] fabricated AA6360 (B_4C + TiC) hybrid SCL using FSP and analyzed the wear behavior. Their study reveals that AA6360(50 % B_4C + 50 % TiC) hybrid composite layer exhibits higher wear resistance compared to AA6360/100 % B_4C or AA6360/100 % TiC surface composite layer. TiC particles act as solid lubricant, and pulled out TiC particles from wear test specimen forms a thin oxide film during sliding and act as solid lubricant and improves the wear resistance by reducing the frictional coefficient.

In this work, aluminum alloy (5083) surface composites by FSP with the reinforcement of B_4C and TiC nano particles are fabricated. The effects of mechanical properties and wear behavior of different sliding loads (20–100 N) are investigated and compared with base alloy and without particle FSPed specimens. An effect of these nano reinforcing particles in combined form has not been reported so far. Boron carbide (B_4C) has the mechanical properties such as high hardness (Knoop hardness = 2800 kg/mm^2), low density (2.52 g/cm^3), high impact resistance, wear resistance and good thermal and chemical stability [21], Titanium carbide (TiC) is another potential reinforcement which has high elastic modulus, good wettability, low chemical reactivity and it induces grain refining effect [22].

Table 1 Chemical composition of base material

Elements	Mg	Cr	Mn	Fe	Zn	Si	Ti	Cu	Ni	Al
wt%	4.162	0.064	0.554	0.191	0.029	0.230	0.049	0.051	0.023	Bal

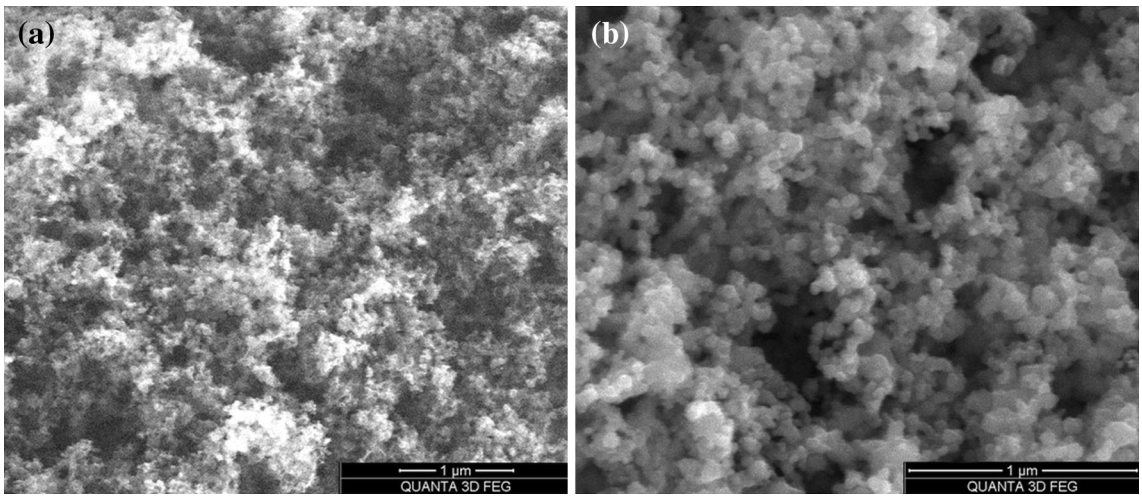

Fig. 1 SEM micrographs of **a** B_4C nano particles, **b** TiC nano particles

2 Materials and Methods

Aluminium alloy of 5083-O rolled plate of 8 mm thickness was used. The chemical composition is presented in Table 1. The nano sized B_4C particles of 99.5 % purity with the particle size of 30–60 nm and nano sized TiC particles of 99.5 % purity with the particle size of 30–60 nm were used as reinforcement materials. The SEM micrographs of the particles are shown in Fig. 1. These micrographs revealed the size & morphology of particles.

The tool was made of H-13 hot working tool steel with a shoulder of 18 mm diameter with cylindrical threaded pin diameter of 6 mm and pin length of 5 mm was used for FSP. A longitudinal groove with 3 mm depth and 1 mm width was made on the surface of the Aluminum plates and the groove was then filled with various (by vol%) of reinforcements. Plates were prepared with various combinations of particles such as base material, without particle, 100 % B_4C, 100 % TiC and 50 % B_4C + 50 % TiC. B_4C and TiC particles were thoroughly blended before packing. A probeless tool was initially used to prevent the escape of the particles from the FSP zone. Then the samples were subjected to four passes for uniform powder distribution. FSW machine at the capacity of 11 kW, 40 kN with hydraulic fixture was used to fabricate the surface composite layer. The optimum rotational speed and transverse speed were fixed at 1000 rpm and 40 mm/min respectively after carrying number of preliminary trials. The advancing and retreating sides of the metal plates were changed after each FSP pass. For every pass, the specimen was allowed to be cooled to the room temperature and all the experiments were carried out at room temperature. Figure 2a, b shows the FSP experimental setup and schematic of FSP experiment, respectively. After FSP, the samples were cut in the transverse direction and polished with different grades of emery sheets and alumina powder and the samples were analyzed through optical microscope. A modified poulton's reagent [23] (30 ml HCl, 40 ml HNO_3, 2.5 ml HF, 12 g Cr_2O_3, and 42.5 ml H_2O) was used to etch the polished surface to study microstructure of the base metal and the stir zone of the composite layer. Scanning Electron Microscope (SEM) (Hitachi S3700 and Quanta 3D FEG) was used to examine the distribution of the reinforcement particles. XRD (Bruker D8 Advance) was used to identify the presence of phases in the Stir zone of SCL.

The Vickers micro hardness (Leica VM HT Auto) values of the FSPed regions(cross section) was measured in the middle of the stir zone using a load of 100 g with dwell

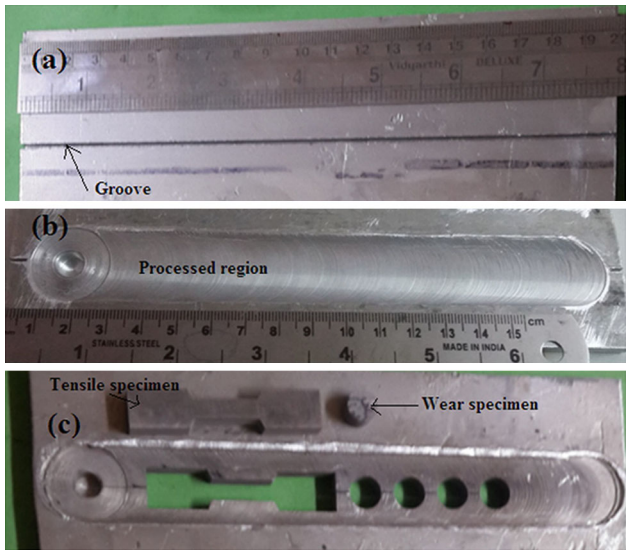

Fig. 3 **a** The groove for filling of the reinforcement particles, **b** FSPed composite layer, **c** macrograph of tensile and wear test specimens extracted from the processed region

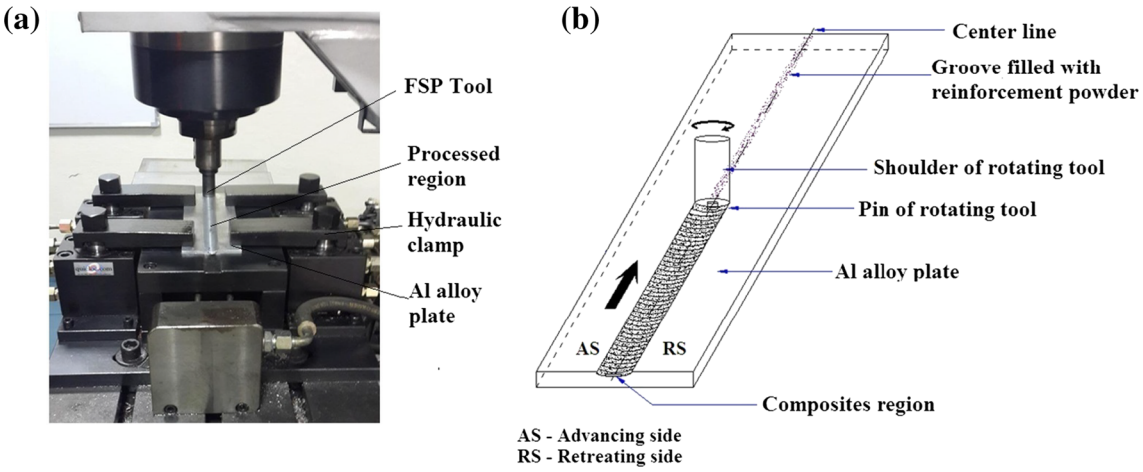

Fig. 2 **a** FSP experimental setup, **b** schematic of FSP experiment

time of 10 s. The tensile properties of the FSPed specimens were examined using computer controlled universal testing machine (Tinius Olsen H50KS) at a constant cross head speed of 1 mm/min in room temperature. The longitudinal tensile specimens were prepared on the middle of the FSP stir zone by wire EDM as per ASTM: E8/E8M-011 standard. The wear behavior of the SCL was studied through pin on disc tribometer (make DUCOM) in room temperature condition. Wear test specimens of 10 mm diameter were cut from the middle of stirred zone of FSPed surface by wire EDM. Tribo tests were conducted as per ASTM G99-04 standard. The counterpart discs were made of EN-24 steel hardened to 55–58 HRC and the surface roughness (Ra) of 0.2 µm. A constant track diameter, 100 mm was used in all the tests. Before the test, the surface of each pin was polished with 1600 grit emery paper. The tribological tests were carried out in the range of applied normal loads of 20–100 N in step of 20 N and at constant sliding distance of 3000 m. The samples were cleaned with acetone and weighed to an accuracy of 0.01 mg by electronic weighing balance. To understand the wear mechanisms, the wear samples were examined using SEM with EDS. Wear debris was also analyzed using SEM with EDS. Figure 3 shows the macrograph of tensile and wear test specimens extracted from the processed region.

3 Results and Discussion

3.1 Particle Distribution

In FSP, metals never reach their melt temperature and processed region occurs due to rotational tool and the forging force exerted by rotating tool is responsible for

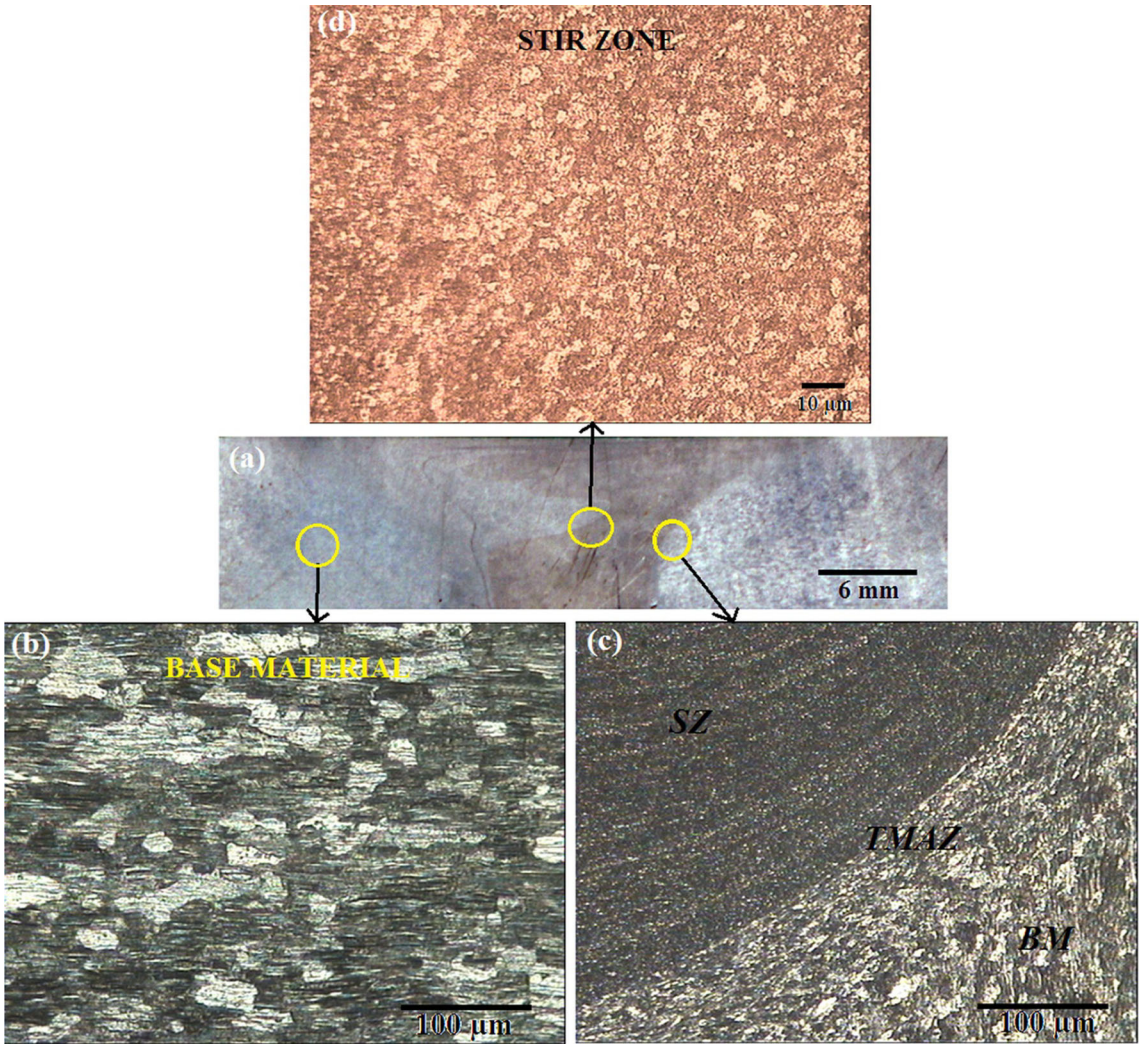

Fig. 4 Micrograph showing the different zones of composite specimen fabricated by FSP **a** cross sectional macrostructure of the specimen, **b** base material (BM), **c** interface between stir zone and thermo mechanically affected region (TMAZ) and **d** stir zone (SZ)

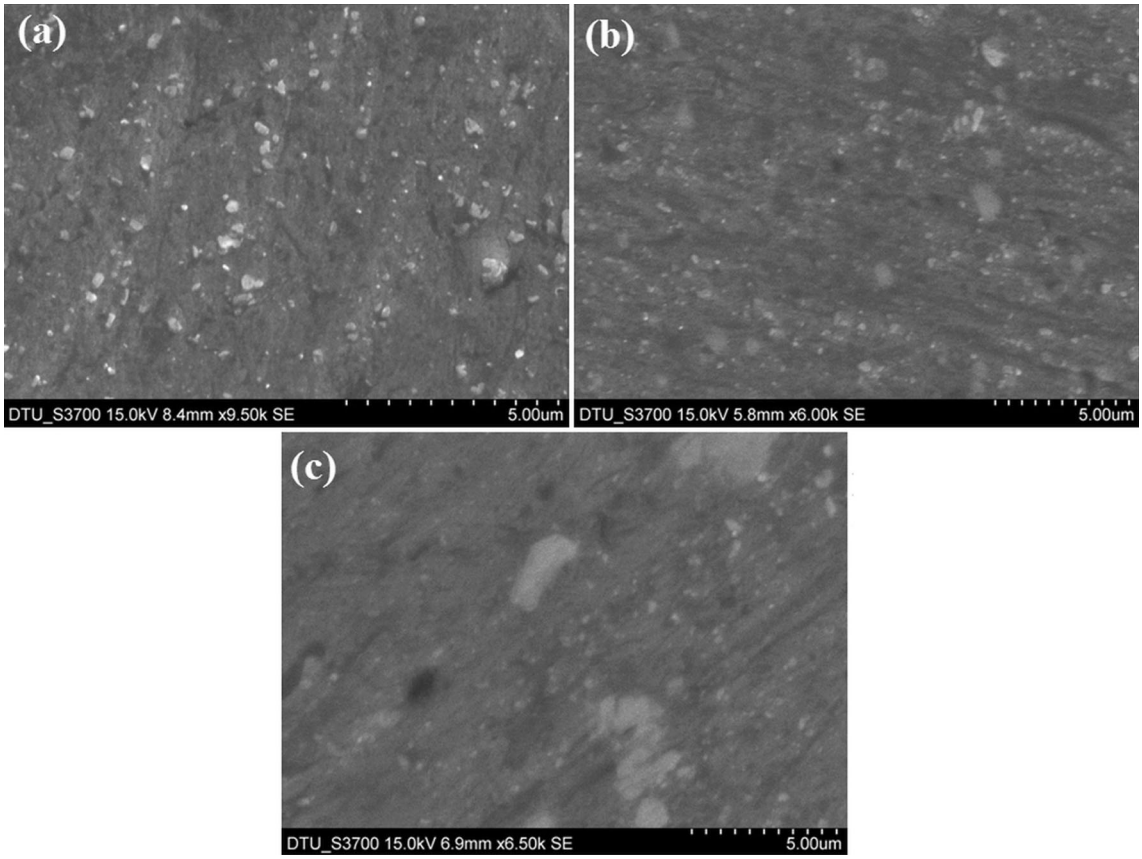

Fig. 5 SEM shows the distribution of reinforcements in the matrix **a** Al–B_4C composite, **b** Al–TiC composite, **c** hybrid composite

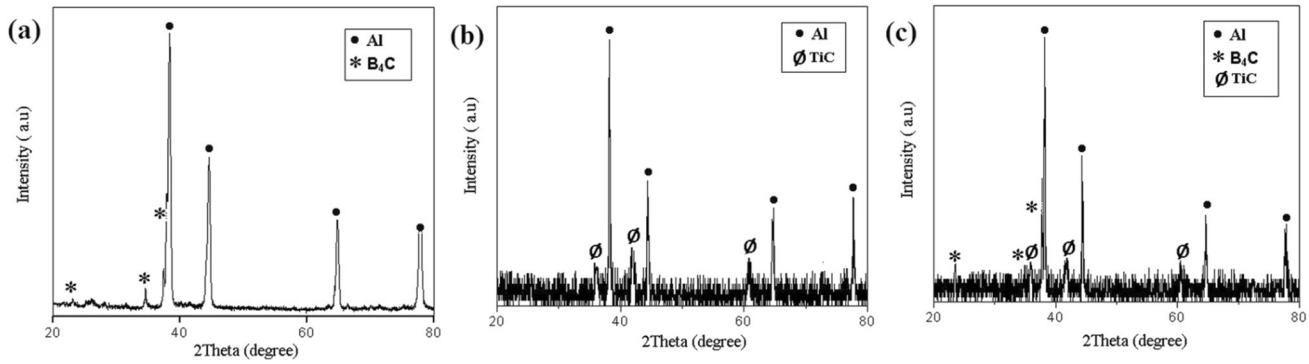

Fig. 6 XRD patterns for **a** Al–B_4C composite, **b** Al–TiC composite, **c** hybrid composite

generation of heat and plastic deformation in the FSP region. The processing parameters such as tool traverse speed, rotational speed, tool pin profile and shoulder diameter to pin diameter ratio are mainly responsible for the behavior of the material flow. Various researchers have shown that hot working tool steels (for example, H13 hardened at 55–58 HRC) with D/d (Shoulder diameter; D and Pin diameter; d) ratio of 3 are suitable for processing of aluminum alloys [3, 4, 7]. In the FSP process, the frictional heat softens the matrix alloy and the hard ceramic particles are uniformly distributed within the matrix by the stirring action of the rotating tool. Increase in the number of FSP passes enhances the grain refinement of the matrix material and improves the uniformity in dispersion of nano particles in the matrix. Excessive number of passes will generate large amount of heat during FSP, which may cause adverse effect on the properties on the processed material [24]. So the maximum number of passes has been limited to four in

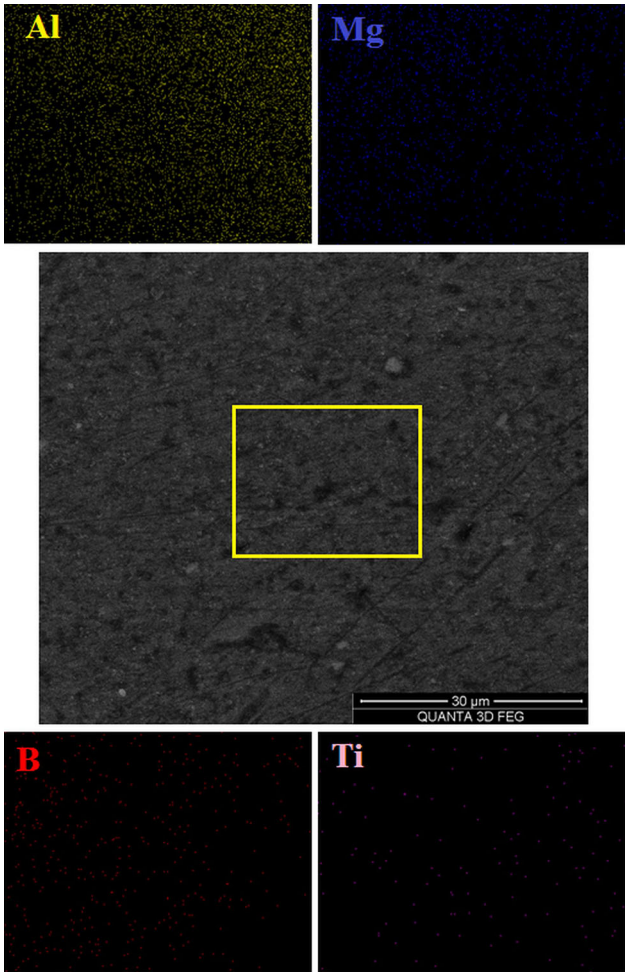

Fig. 7 Elemental composition mapping of the hybrid composite

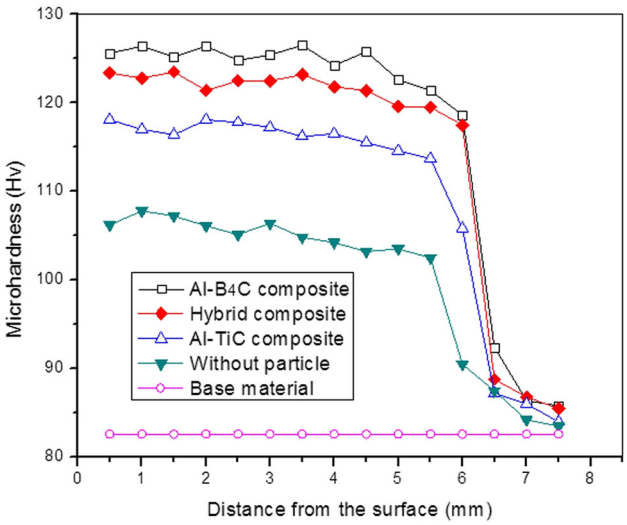

Fig. 8 Micro hardness profiles of the cross section region of FSPed specimens (as a function of depth)

this study. During FSP, the accumulation of particles is induced and material flow occurs on the advancing side. For balancing the material flow at the advancing side and retreating side, the second and fourth FSP passes are carried out in opposite directions.

Figure 4 shows the different zones of composite specimen fabricated by FSP, (a) cross sectional macrostructure of the specimen (b) base material zone (c) interface between Stir zone and Thermo mechanically affected zone and (d) stir zone. The average grain size of the base material is 49.5 µm. After FSP, the grain size is reduced to 14.5 µm and for the friction stir processed composite sample the grain size is reduced to about 3 µm. The reduction in the grain size of the processed sample without particle is due to dynamic recrystallization and grain refinement.

During FSP, materials are heavily deformed nearest to the pin tool, and a larger strain rate occurs due to high temperature. The refinement of grain size of the Aluminium alloys in the Stir Zone (SZ) of FSP is due to various mechanisms such as dynamic recovery (DRV), continuous dynamic recrystallization (CDRX), discontinuous dynamic recrystallization (DDRX), geometric, dynamic recrystallization (GDRX) and particle stimulated nucleation (PSN) [2, 3]. The distribution of reinforcement particles is spread over the entire surface composite layer in a homogeneous manner. The rotating threaded tool provides a stirring action and plasticizing the matrix with the ceramic particles in a homogeneous manner. The grain size of the composite specimen is further reduced due to the addition of hard nano reinforcement particles which act as a nuclei, and their pinning effect and preventing the grain growth of the matrix material after dynamic recrystallization. In the FSP region, the temperature reaches the range of 450–500 °C for Al Alloys and this temperature is measured by using Thermal imaging camera. The temperature is only (0.17–0.20)T_m of the reinforcement. So the temperature is insufficient to melt the ceramic particles and cause any reaction with the Al alloy since no intermetallics are formed in the composite. Besides the particles are not deformed, dislocations may occur during processing. The presence of reinforcement particles interrupts the movement of dislocations in the matrix due to the large difference between the coefficient of thermal expansion between the matrix and ceramics (dislocation strengthening) [23]. Our previous studies have reported that the increase in the number of FSP passes and changing the direction of tool rotation in second pass leads to (1) homogeneous distribution of reinforcements in the matrix (Orowan strengthening

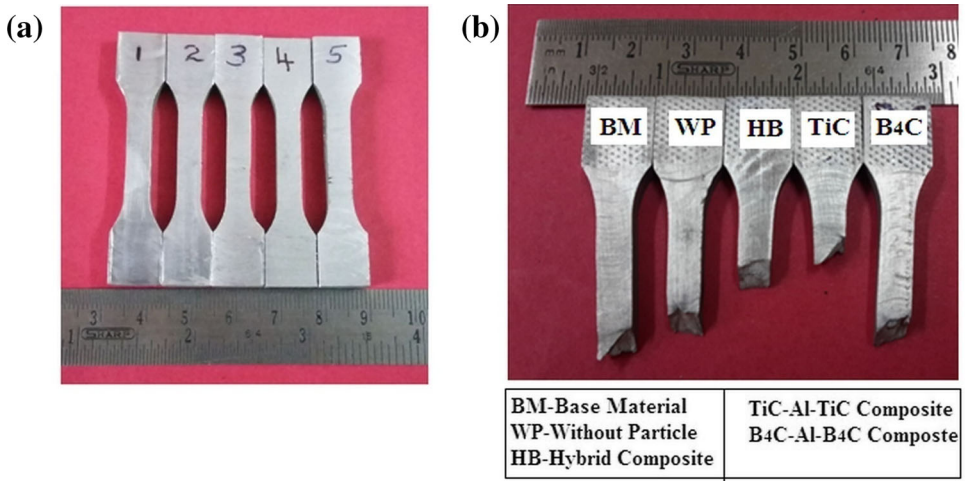

Fig. 9 Tensile test specimen **a** before test and **b** after test

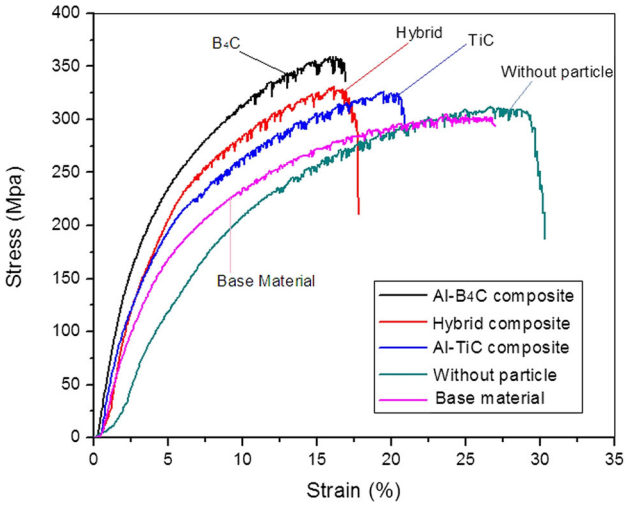

Fig. 10 Typical stress–strain curves of the tensile tested composite specimens

mechanism) [11] and (2) more strain is imposed by the stir zone to attain grain refinement [16]. The SEM micrographs of the prepared composites are shown in Fig. 5. Typical XRD patterns for the Aluminum FSPed surface composites are presented in Fig. 6a–c. The clear peaks of aluminum and marginal peaks of B_4C and TiC are observed in the figure. Figure 7 shows the elemental composition of hybrid composite cross section.

3.2 Microhardness

The base material used in the present study has a hardness value of 83 ± 1 Hv. For experimental purpose the average of three hardness value have been taken for all the samples. Figure 8 shows the variation in hardness across the FSP zone. i.e. from the surface to bulk. The hardness variation is observed for base metal, FSPed without particle, Aluminum reinforced with TiC, base metal with B_4C, base material with blend of B_4C and TiC. An increase in hardness is clearly observed. The variation in hardness data in depth direction is almost uniform. This again confirms the potentiality of friction stir process to induce uniformity in reinforcement distribution. Compared to the hardness of base material without any reinforcement, others exhibit an increased hardness of 107 ± 5 Hv. This is attributed to the refinement of grains. TiC reinforcement in Aluminum alloy improves the hardness further. Not much difference can be observed in hardness of B_4C and TiC and B_4C blend of reinforcements. However B_4C reinforcement exhibit the highest hardness, among the fabricated composites. According to Hall–petch relationship, finer the grain size, higher the hardness of the matrix. In addition, good bonding strength between matrix and reinforcement is an important factor for the composite to operate effectively. The nano sized particulates have high cohesive energy

Table 2 Mechanical properties of FSPed Al composites

	Grain size (μm)	Hardness (Hv)	Tensile strength (Mpa)	Total elongation (%)
Base material	49.85	83 ± 1	300	27.1
FSP without particle	14.5	107 ± 5	312	30.2
Al–B_4C composite	3	127 ± 2	364	16.5
Al–TiC composite	4.5	118 ± 1	325	20.6
Hybrid composite	4.2	124 ± 2	330	17.4

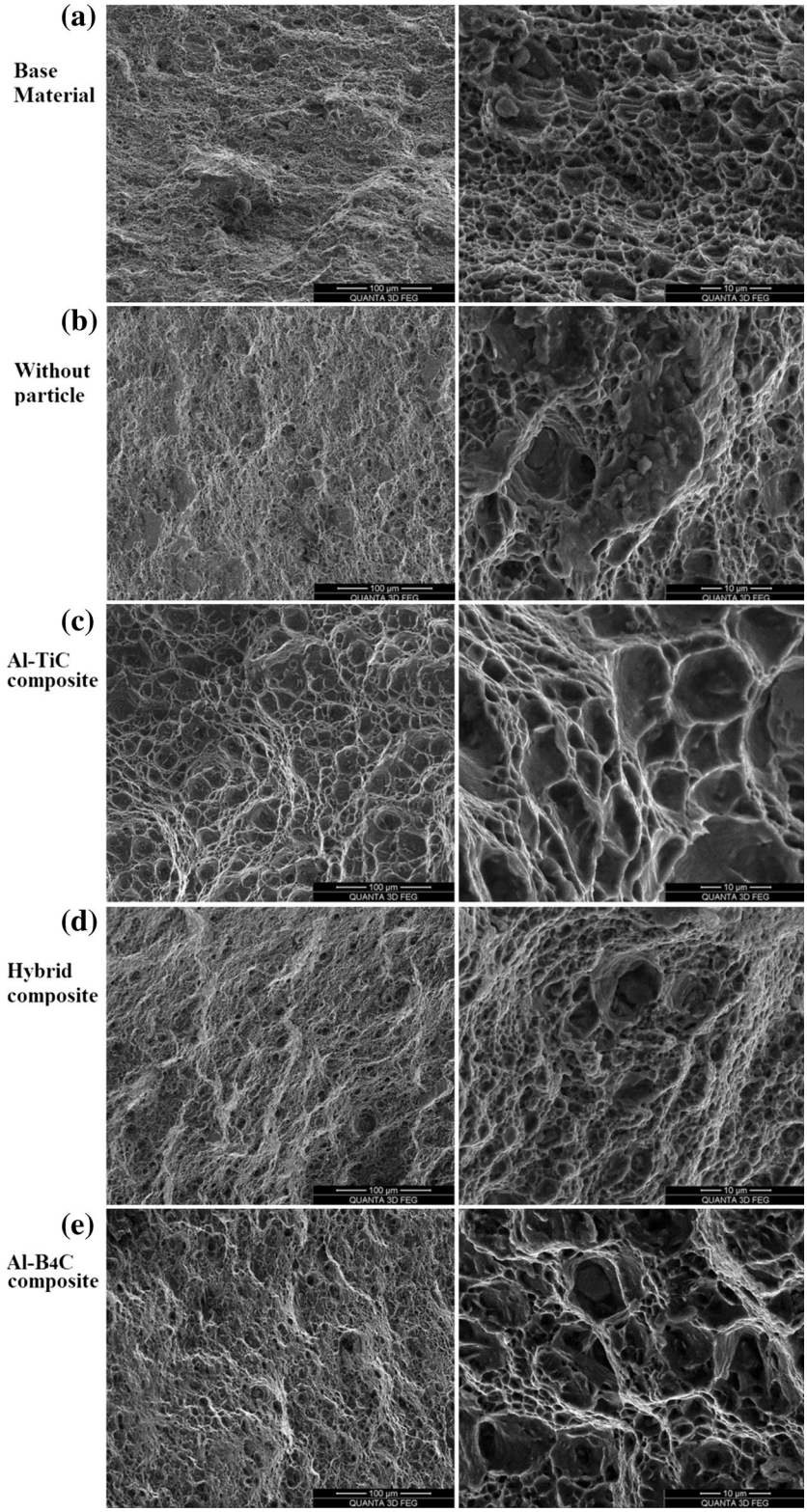

Fig. 11 SEM fractographs of tensile fractured surfaces **a** base material, **b** FSPed Al alloy without particle, **c** Al–TiC composite, **d** hybrid composite, **e** Al–B_4C composite (*right column micrographs* are higher magnification micrographs of respective *left column*)

which can minimize the pull out of hard ceramic reinforcement particles from the matrix and maximize the strength of the material because the load is transferred from weaker matrix to hard reinforcements. In addition, nano particle improves the flexural strength of the composite and the particles prevent the quick expansion of cracks and limit the deformation of the composite [13, 23].

3.3 Tensile Test

Figure 9a, b shows the tensile specimens before and after testing. The typical stress–strain curves of the nano composites are shown in Fig. 10. Table 2 shows the hardness and tensile results of FSPed Al composites. The tensile strength of the FSPed composites is higher than the base alloy. The frictional heat softens the matrix alloy and the hard ceramic particles are uniformly distributed within the matrix by stirring action of the rotating tool. FSP with the ceramic reinforcements increases the hardness and tensile properties of the substrates by the promotion of the uniform grain refinement due to the pinning effect of the reinforcements and it's extremely high hardness. Al–B_4C FSPed nano composite has the highest tensile strength and least elongation when compared to Al–TiC and Al–B_4C/TiC composites. Various mechanisms discussed in the previous section are also responsible for enhancing the tensile strength of the composite. The tensile fractured surface of the base alloy and FSPed base alloy (without particle) and FSPed composite are shown in Fig. 11. The fractured surface of the FSPed base alloy (without particle) has large number of small dimples. The specimen undergoes a significant elongation

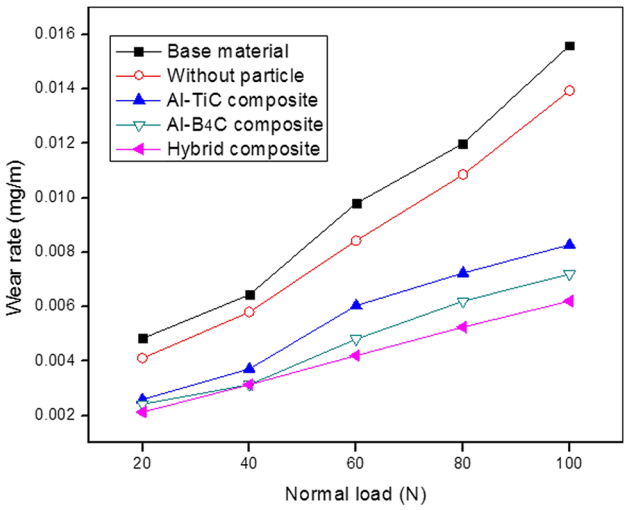

Fig. 12 Effect of applied load on wear rate of Al 5083 alloy under different conditions

prior to failure. Yadav and Bauri [25] reported that the decrease in grain size of FSPed Al alloy is due to higher percentage of high angle grain boundaries. Similarly the FSPed specimen exhibit fine grained microstructure and may also contains the high fraction of high angle grain boundaries. In the FSPed nano composite, the fractured surface shows very fine dimples that are associated with the matrix material and in between, shallower dimples indicate the presence of reinforcement particles. In the fractured surface of the composites, the pullout reinforcement particles from matrix are visible which indicates that FSPed composites have good interfacial bonding with the matrix material and reinforcement particles. In addition, the second phase particles are seen in the composite fractured surface. It shows that the dimples are created by the nucleation, growth and micro voids between the second phase particles and reinforcements. Al–B_4C composite exhibits higher strength and slightly lower elongation when compared to Al–TiC composite.

3.4 Wear Properties

The wear rates of the base material and the friction stir processed surface composites are shown in Fig. 12. This reveals that the wear resistance is significantly improved with addition of the reinforcement particles in all sliding loads. The wear rate is observed to be increased at higher applied loads for all samples. However, the difference in wear rate of the wear samples is more pronounced at higher loads. The uniform dispersion of hard nano reinforcement particles in the SCL and fine grain size of matrix are major contributions for increase in wear resistance. The various strengthening mechanisms discussed in the previous section are also responsible for enhancement of wear resistance of the FSPed composite samples when compared to the base material.

3.4.1 Wear Behavior of the Base Al Alloy and FSPed Base Al Alloy

At lower loads of 20 N, the type of wear observed is due to oxidization and plastic deformation. The SEM image Fig. 13a shows the damaged pits formed along the sliding direction and some areas of wear surface are charged with bright contrast, which can be clearly seen in the higher magnification micrograph. The EDS analysis confirms the considerable amount of oxygen on the wear surface (Fig. 15a). At 40 and 60 N loads, the large and deeper surface pits are observed and plastic deformation occurs during the wear test. The overall

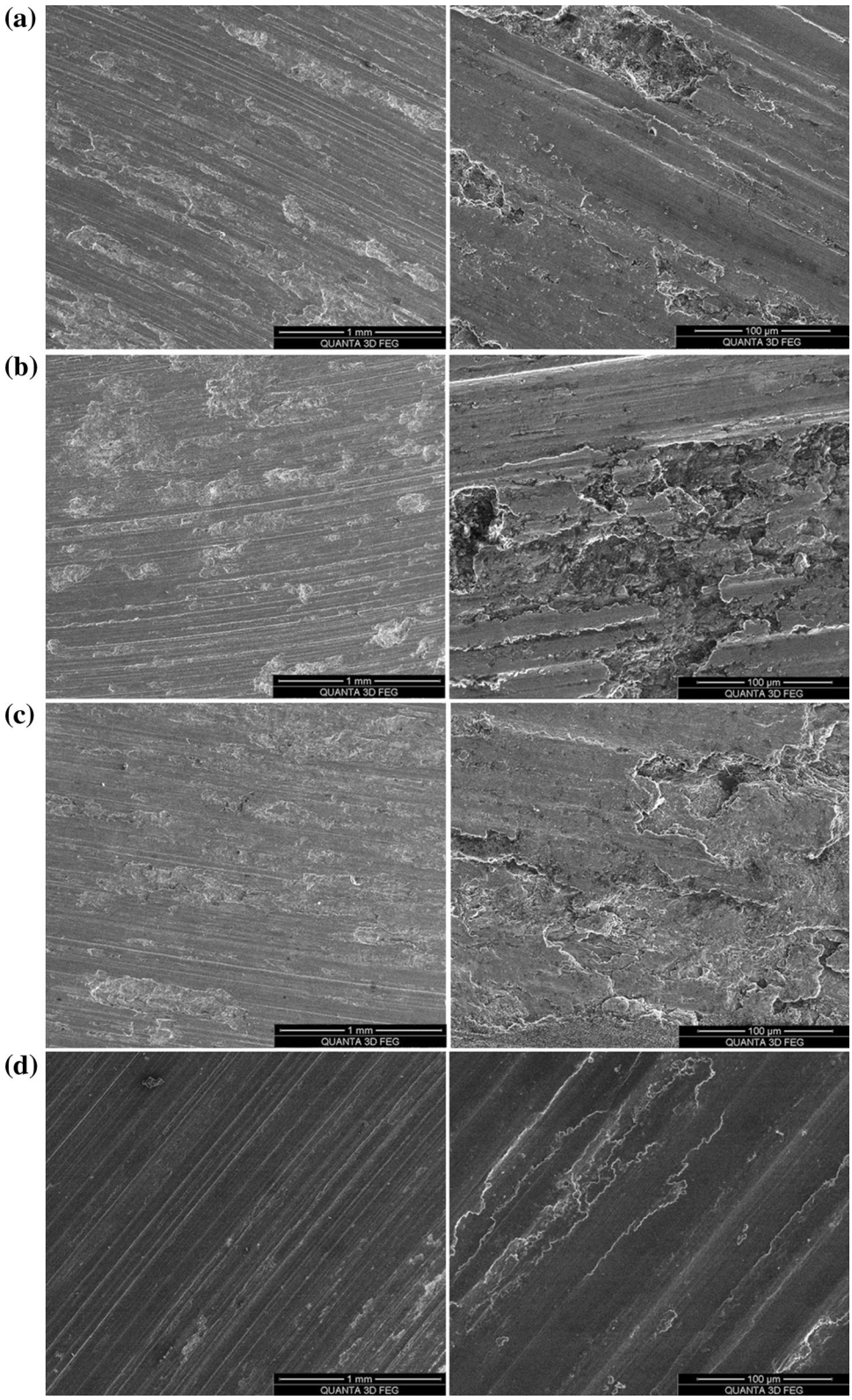

Fig. 13 SEM micrographs of worn surface of Al 5083 base alloy at **a** 20 N, **b** 60 N, **c** 80 N, **d** 100 N (*right column micrographs* are higher magnification micrographs of respective *left column*)

appearance of the worn surface in the lower magnification shows the abrasion marks and deeper pits, and traces of oxide film also are clearly seen in Fig. 13b. At higher magnification, surface pits and cracks are visible. The plastic flow lines clearly visible in the Fig. 14a confirms the occurrence of the excessive plastic deformation at 60 N load of FSPed Al alloy (without particle specimen). In case of higher loads 100 N, higher wear rate is observed. Higher temperature is generated between the sliding surfaces and reduces the shear strength of the specimen. Excessive amount of material is removed from the matrix and the same is transferred to the steel disc. In addition, wear debris are entrapped in pits during the wear test. The type of wear changes from severe to very severe wear and delamination wear. The SEM micrographs (Figs. 13d, 14b) are the evidence of the delamination and severe wear.

3.4.2 Wear Behavior of the Fsped Al–B_4C, Al–TiC and Al–B_4C/TiC composites

The property of Al-based metal matrix composite depends upon the shape, size and distribution of the reinforcement material in the matrix material. In the mono composite wear sample, the presence of hard nano reinforcement particles whose hardness is greater than base alloy, act as a load bearing elements for enhancement of the wear resistance. The hard nano particle resists the micro cutting action of the wear specimen and lowers the removal of material from the specimen. Composite containing TiC particles exhibits higher wear rate when compared to composites containing B_4C particles because the B_4C nano reinforcement particle is relatively harder than TiC nano reinforcement particle. Figure 16 shows the effect of reinforcement particles on the microhardness and wear

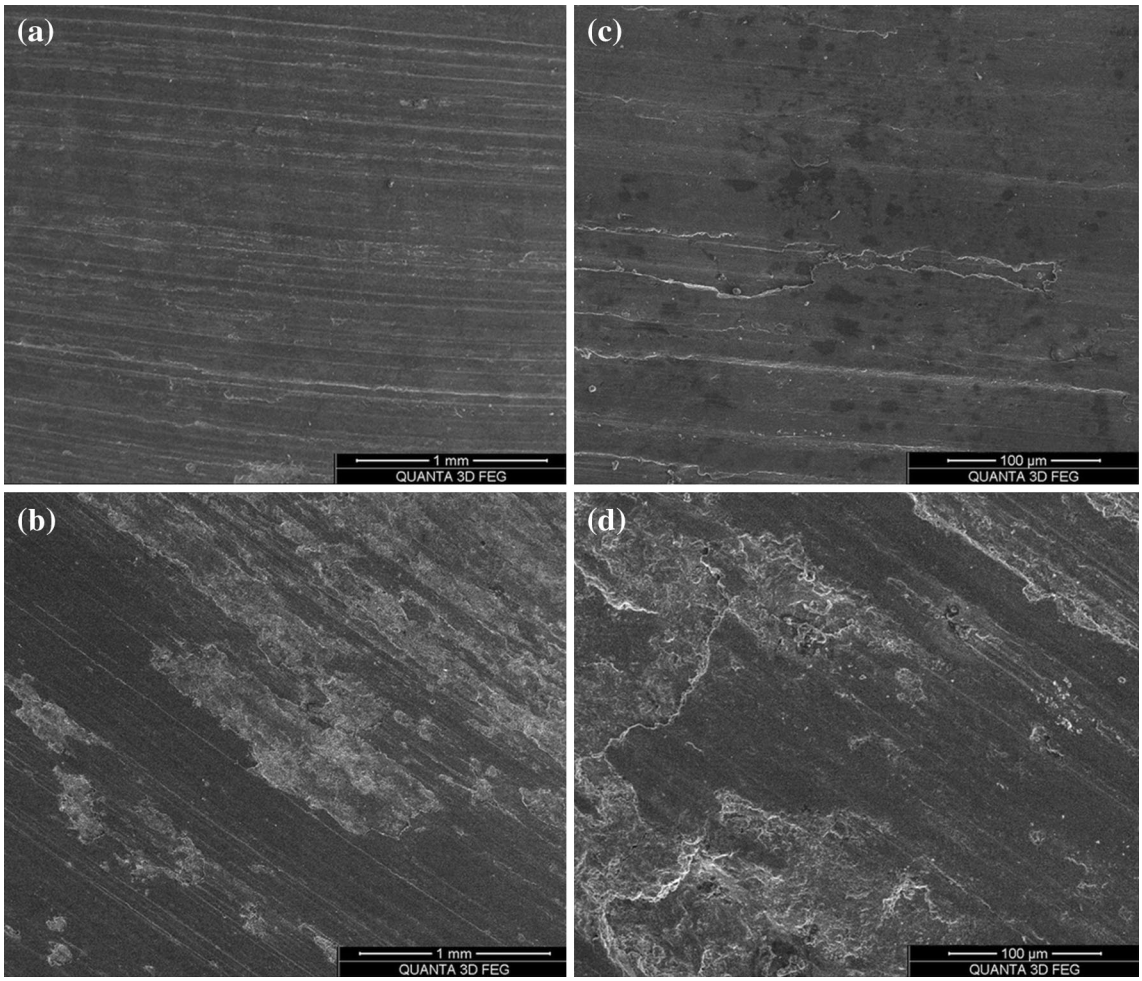

Fig. 14 SEM micrographs of worn surface of FSPed without particle base alloy at **a** 60 N, **b** 100 N, **c**, **d** are high magnification view of **a** and **b**

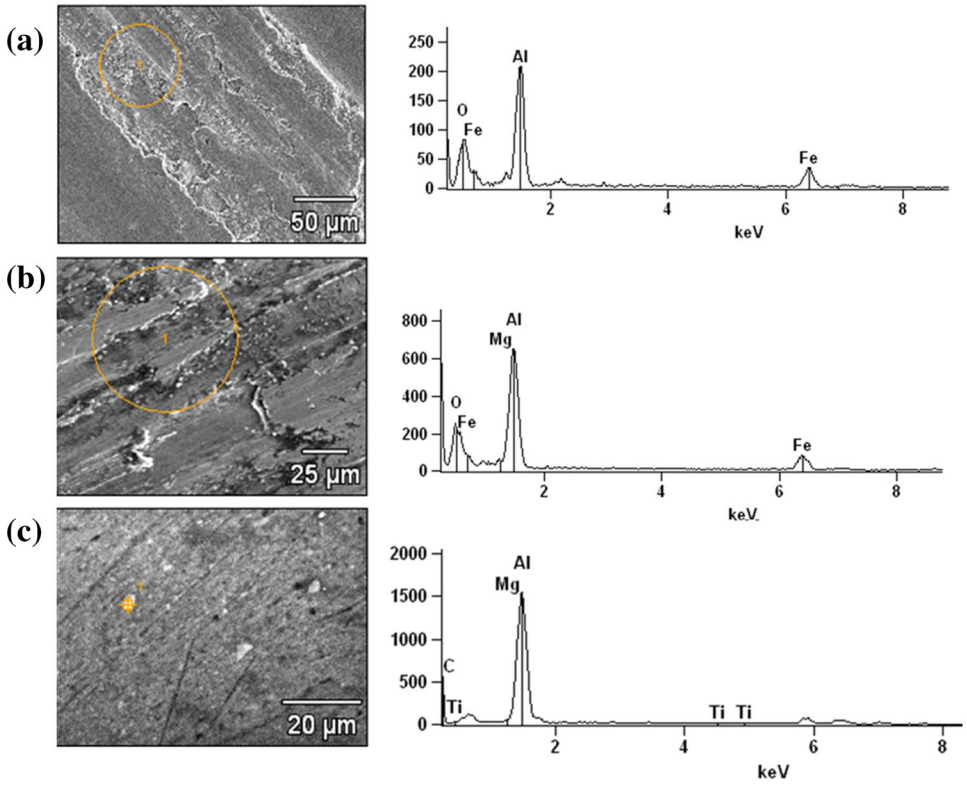

Fig. 15 SEM image and EDS analysis of selective worn surface of specimen tested at 20 N and 1 m/s **a** base material, **b** Al–B_4C nano composite specimen, **c** hybrid composite specimen

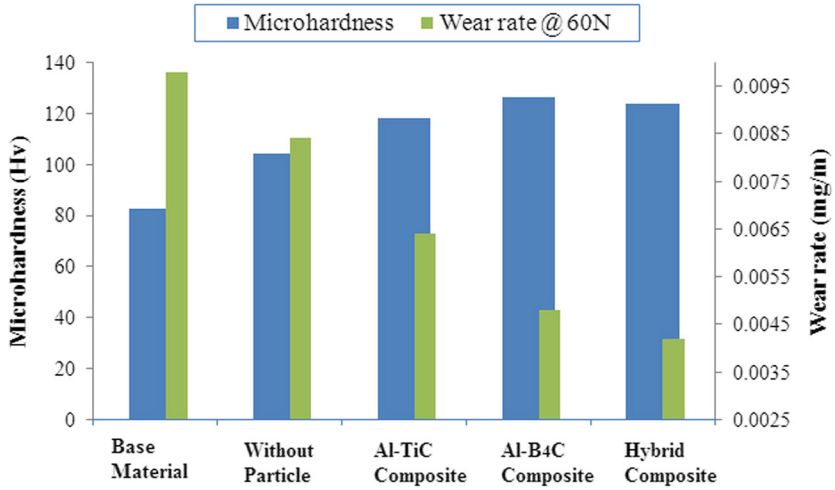

Fig. 16 The effect of reinforcement particles on the microhardness and wear rate at a sliding load of 60 N

rate (sliding load 60 N) of the composite specimens. Al–B_4C composite provides maximum hardness when compared to Al–TiC and Al–B_4C/TiC composite. Despite the lower hardness of the hybrid composite when compared to Al–B_4C composite, it has enhanced wear resistance. The pullout of TiC particles act as an effective solid lubricant and the particles form oxide film on the surface for the enhancement of the wear resistance. Figure 15c shows EDS analysis of the selective worn surface of the hybrid composite specimen tested at 20 N. It confirms the worn surface having TiC particles which act as solid lubricant during wear test. Similar type of results have been reported by Rejil et al. [20] for FSPed Al/B_4C/TiC composite. The presence of the B_4C ceramic particles in the matrix material increases hardness, strength and thermal stability of the base alloy and improves the wear resistance of the nano composite and tribological layer stability [20, 26].

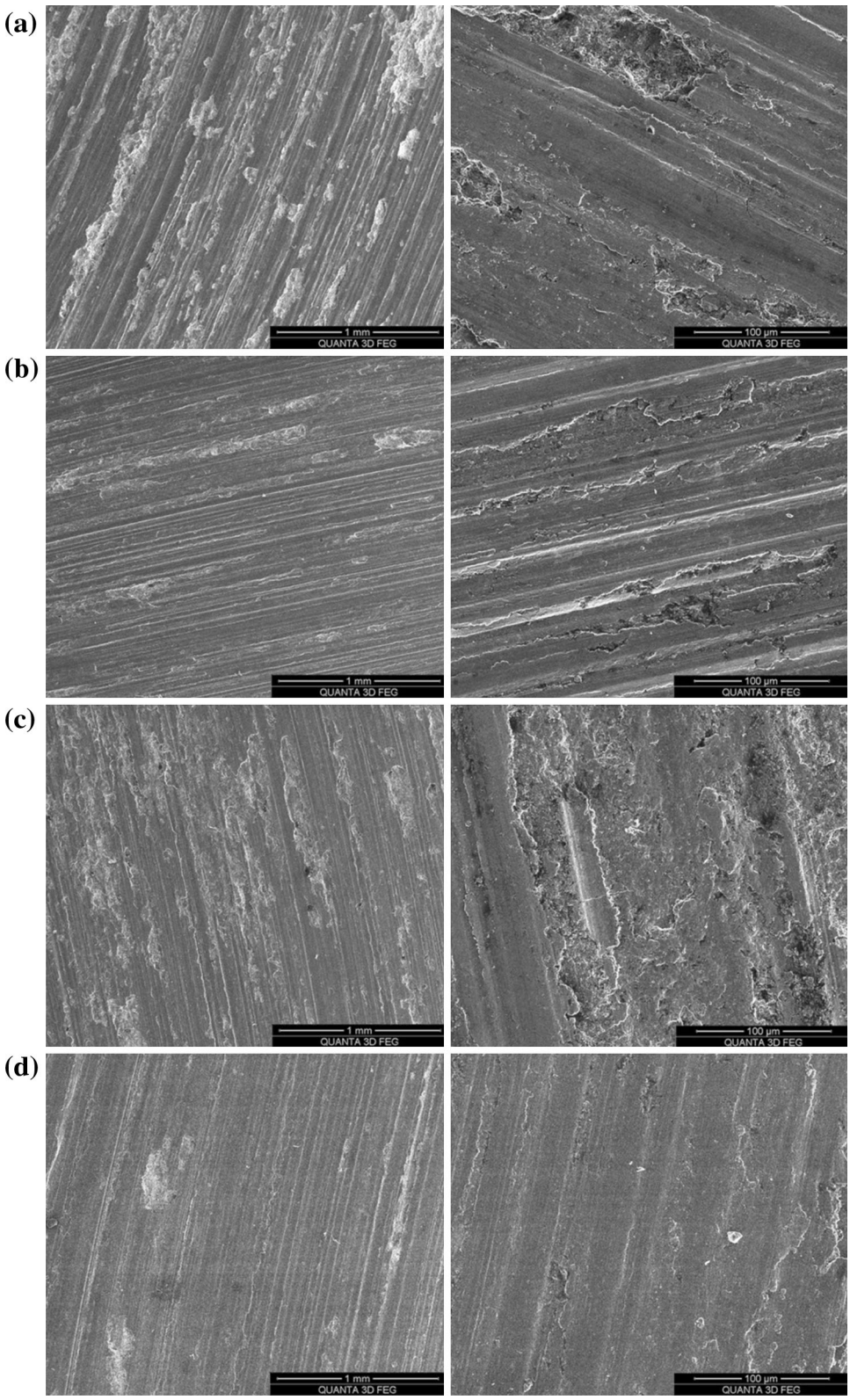

Fig. 17 SEM micrographs of worn surface of FSPed Al–B_4C nano composite at **a** 20 N, **b** 60 N, **c** 80 N and **d** 100 N (*right column micrographs* are higher magnification micrographs of respective *left column*)

Figures 17, 18 and 19 show the SEM images of worn surfaces of composite specimens at different sliding loads. During the wear test of Al-TiC composite, large amount of plastic flow of the specimen occurs at the surface of the pin. Heat is developed between the pin and the disc during the sliding wear test which plasticizes the wear specimen. The TiC particles resist the movement of the matrix and reduce, the contact between the pin and disc. At lower load

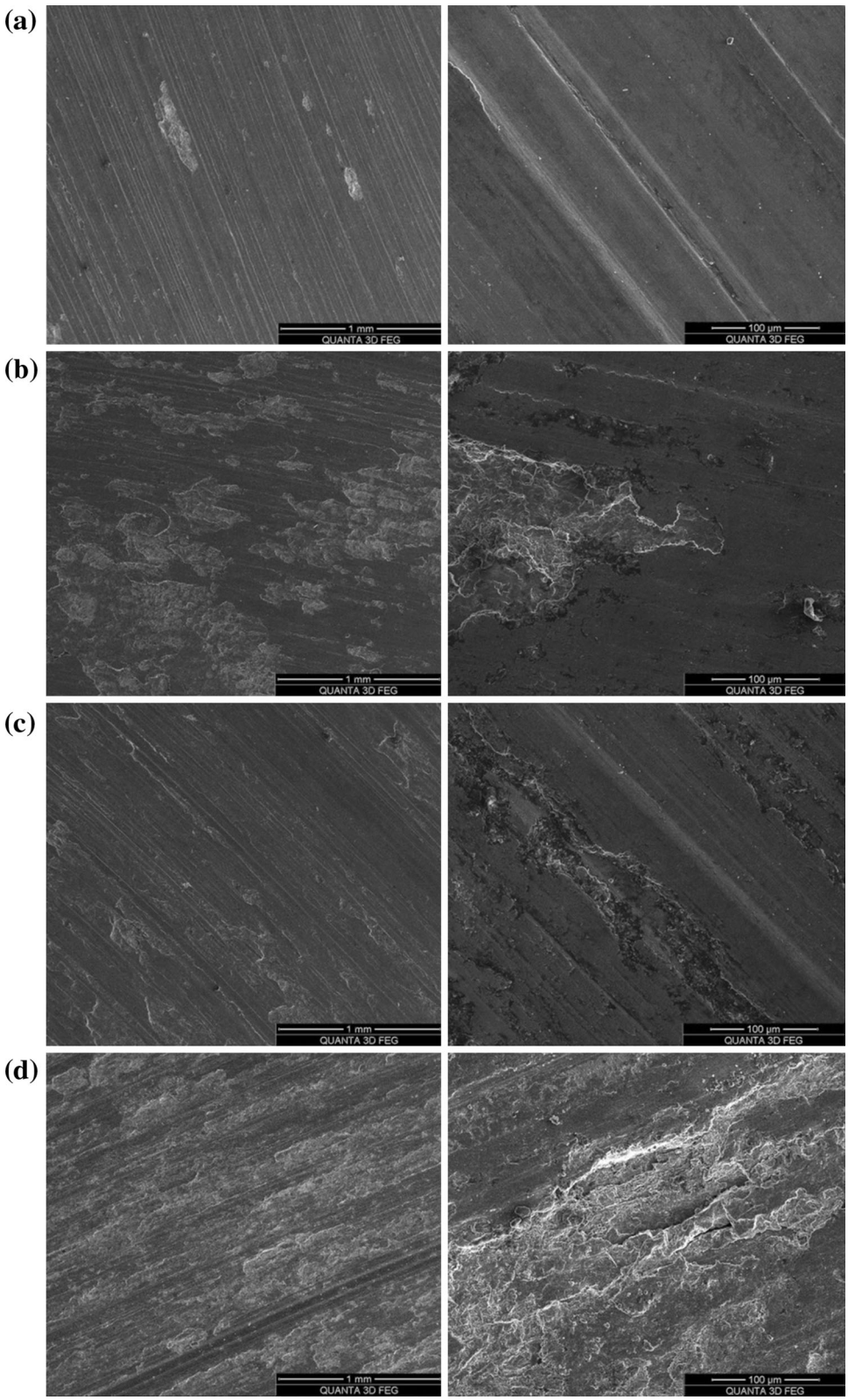

Fig. 18 SEM micrographs of worn surface of FSPed Al–TiC nano composite at **a** 40 N, **b** 60 N, **c** 80 N and **d** 100 N (*right column micrographs* are higher magnification micrographs of respective *left column*)

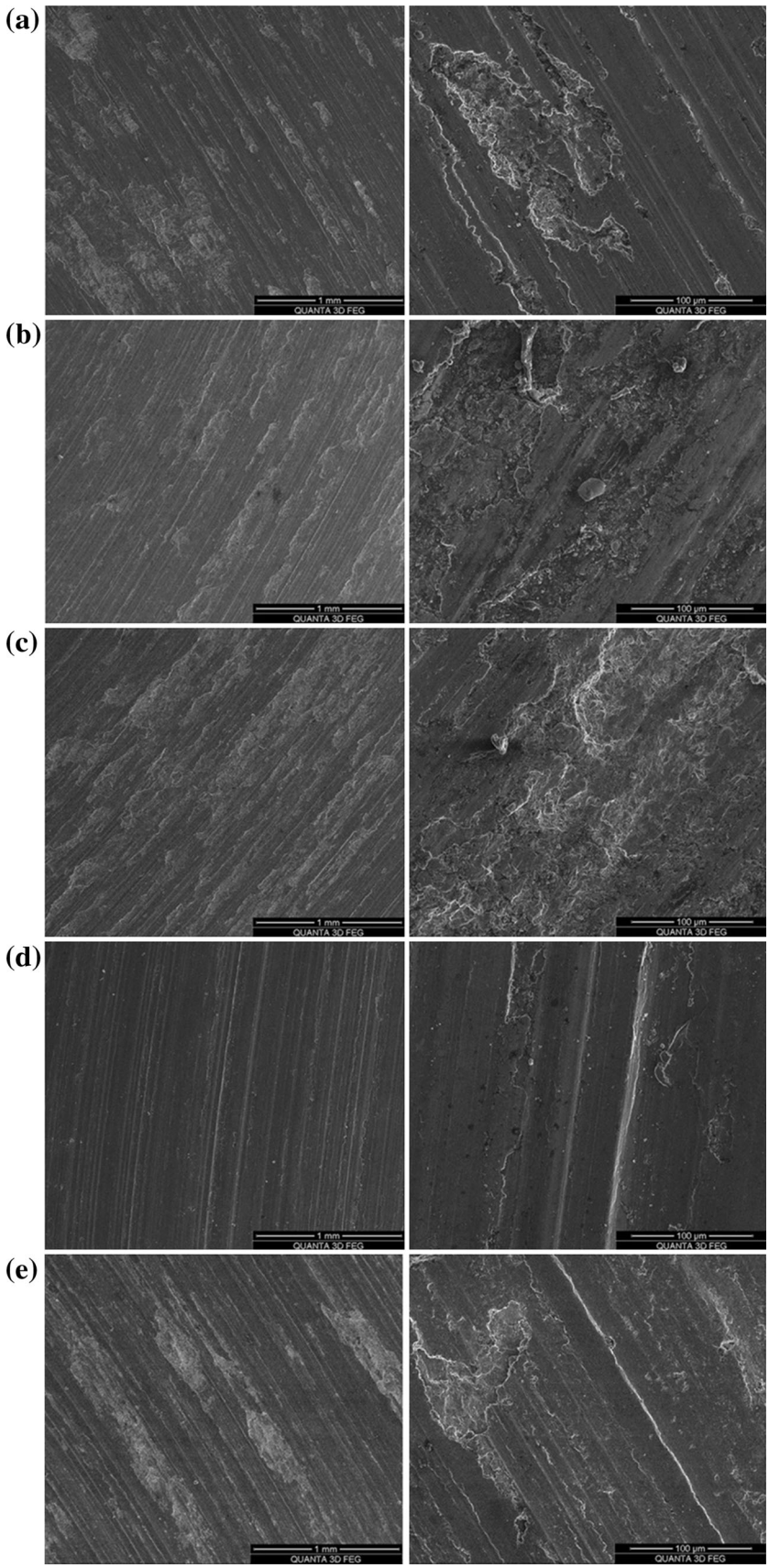

Fig. 19 SEM micrographs of worn surface of of FSPed Al–B_4C/TiC nano composite at **a** 20 N, **b** 40 N, **c** 60 N, **d** 80 N, **e** 100 N (*right column micrographs* are higher magnification micrographs of respective *left column*)

(20 N) the wear rate of mono and hybrid composite are almost similar. The main wear mechanisms are observed as oxidation and abrasion. The worn surface images of hybrid composite subjected to 20 N load is shown in Fig. 19a. The worn surface exhibits oxide layer marks and abrasion marks are visible in low magnification and at higher magnification the bright surface indicates the oxidation and abrasion grooves. The EDS analysis indicates that the oxidation wear mechanism is the major mechanism for composite specimen at lower loads (Fig. 15b). At 40 N load, the wear mechanism changes from mild wear to severe wear. Wear mechanisms such as oxidation, abrasive and delamination are observed with increased load. The SEM images (Fig. 19b) show the presence of subsurface cracks and abrasion marks on the wear surface. Presence of mild traces of oxides are observed, which indicates the degree of oxidation.

At 60 N load the type of wear changes from mild to severe wear. Irregular plastic flow lines are observed on the wear specimen and indicate the excessive plastic deformation wear observed on the surface. The shear strain is induced during the wear process and is transmitted to the matrix alloy. The composites wear at a faster rate after load exceeds 60 N. The change of wear mechanism occurs at certain load, and this critical load value is an important factor for designing the material for anti wear applications [18]. At 80 N loads, abrasive and severe wear are clearly visible in the Fig. 19d. In addition, pull out of reinforcement particles entrapped in between the wear specimen and counter disc, converts the wear mode from two-body to three body causing the excessive abrasive marks on the softer wear specimen [7]. The delamination and severe wear are observed on the surface of 100 N wear specimen (Fig. 19e). During wear process, large hydrostatic pressure exists on the wear specimen and deformation continues as a result of cracks and extensive pits formed on the surface. Further loading on the cracks during the sliding test causes deformation on the cracks to extend and propagate, and thus joining with neighboring cracks, resulting in even deeper and wider subsurface cracks [27, 28].

3.4.3 *Coefficient of Friction*

Figure 20a shows the variation of friction coefficient of 5083 aluminum alloy under different conditions. The similar pattern of coefficient of friction observed in the hybrid composites and mono composites at lower loads of 20 and 40 N. The Typical variations of coefficient of friction with sliding distance of 60 N wear samples are displayed in Fig. 20b. The coefficients of friction of the composite specimens are lower than those of the base alloy

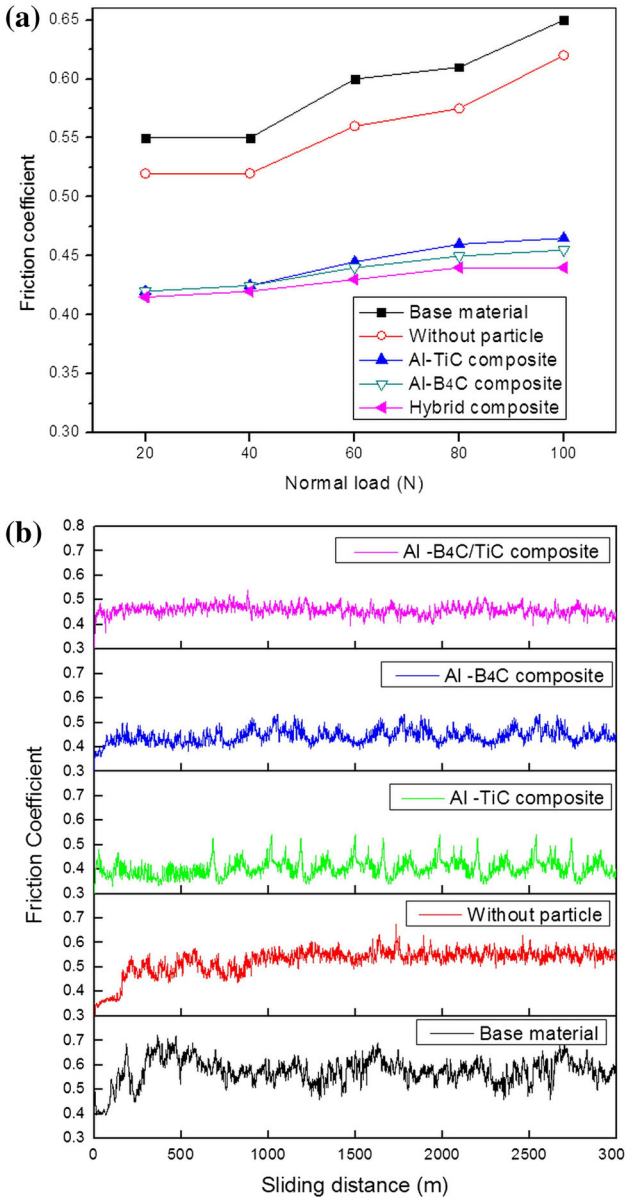

Fig. 20 **a** Variation of friction coefficient of 5083 aluminum alloy under different conditions. **b** Typical coefficient of friction graph of FSPed composite at 60 N and 1 m/s sliding velocity

FSPed base alloy (without particle). The low coefficient of friction in composites indicates that the mechanism of wear is predominantly abrasive in nature, due to the harder steel disc surface scratching over the softer wear specimen. The coefficient of friction of the Al-B_4C/TiC composite specimen shows the low flucations at entire sliding distance. In the hybrid composites, the presence of the TiC particles forms tribolayer on the surface and B_4C particles act as load bearing element as a result of improved friction stability and slightly lower coefficient of friction is observed when compared to mono composite specimens.

3.4.4 Wear Debris

Figure 21 shows the wear debris morphology of the base alloy and composite specimen. The EDS analysis confirms that the percentage of the iron content in the wear debris is highest for the Al–B_4C composite and second highest for Al–B_4C/TiC composite followed by Al–TiC composite, without FSPed particle and finally base material specimens (Fig. 22). The results are attributed to the higher hardness of the sample. The higher hardness leads to lower wear rate and the detachment of iron particles from the steel surface is higher in the composite samples. The composite specimen consists of hard nano reinforcement particles which are pulled out from the wear specimen and forms oxide

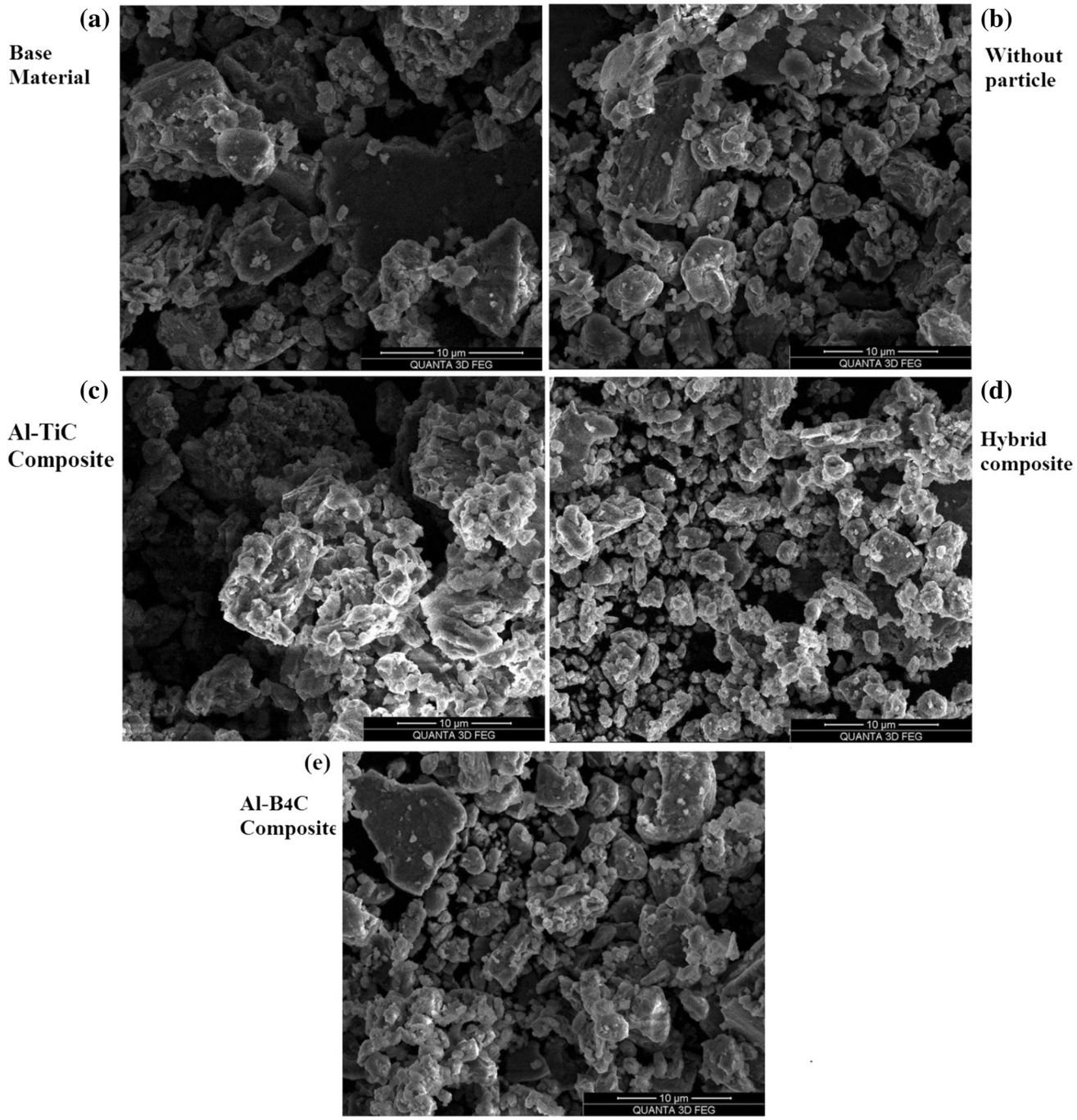

Fig. 21 Typical SEM micrographs showing the wear debris of 100 N Normal load wear test specimens **a** base material, **b** FSPed Al alloy without particle, **c** FSPed Al–TiC composite, **d** FSPed Al–B_4C/TiC composite, **e** FSPed Al–B_4C composite

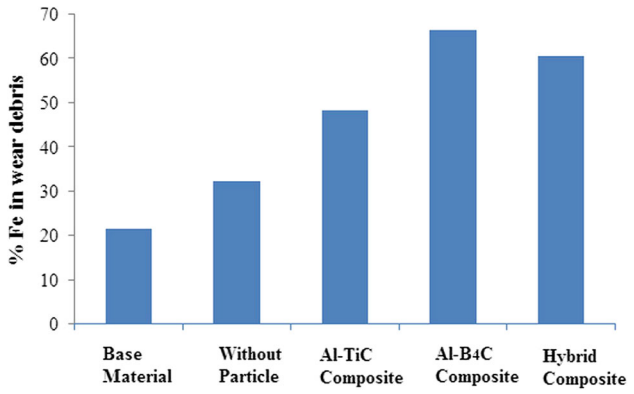

Fig. 22 % of iron content in the wear debris of the wear tested samples

layer on the contact surface which act as a solid lubricant for wear resistance. In the hybrid composite samples, the TiC particles provides a tribolayer formation which protects the material from the subsurface damage. Rejil et al. [20] reported that in the Al-B_4C/TiC composite, the pulled out TiC particles act as a solid lubricant which forms tribofilm during wear test. In addition, during the wear test, the pulled out Aluminum oxides from the wear specimen together with the iron particles from the counterface, form a mechanically mixed layer (MML). The MML forms thin tribofilm on the surface which increases the wear resistance in the composite [28]. The base alloy and the FSPed base alloy exhibit larger coefficient of friction which can be is attributed to localized welding of the wear debris to the wear sample.

4 Conclusions

FSP process is suitable for fabrication of surface composites in solid state condition. It is also suitable for selective surfacing applications. In the present investigation, the Al 5083/B_4C, Al 5083/TiC and Al5083/B_4C/TiC surface nano composites were successfully fabricated by the FSP. The mechanical properties and tribological characterization of the composite layer produced by four passes was studied.

The obtained results can be summarized as follows.

1. FSPed composite specimens (mono and hybrid) exhibited uniform dispersion of reinforcement particles in the matrix and higher hardness and strength than the FSPed Al alloy (without particles) and base alloy.
2. Al–B_4C nano reinforced composite exhibited the highest hardness and tensile strength. However it had lower ductility observed when compared to Al–TiC and Al–B_4C/TiC nano reinforced composites. The microhardness value for Al–TiC, Al–B_4C/TiC and Al–B_4C surface composites were about 118 ± 1 Hv, 124 ± 2 Hv and 127 ± 2 Hv respectively while that for sample FSPed without particle and base material where about 107 ± 5 Hv and 83 ± 1 Hv respectively.
3. The wear rates of the composite specimens were found to be lower than the base alloy and FSPed base alloy at all applied loads (20–100 N). The Al–B_4C/TiC composite wear specimen was found to have higher wear resistance, despite lower hardness than Al–B_4C composite. TiC particles acted as a solid lubricant and B_4C particles acted as a load bearing element in the hybrid composite.
4. Mild wear was observed in the composites at lower loads (20 N) and the mechanism of the wear was mainly due to oxidization. At 40 and 60 N loads, the type of wear was observed to change from mild to severe wear and mechanism of the wear was observed to be an abrasive, and severe plastic deformation. At higher loads of 80 and 100 N, the type of wear changed from severe to very severe wear and the mechanism was observed as abrasive, and delamination wear.
5. Improved wear resistance of the nano surface layer might be attributed to a lower coefficient of friction when compared to the base alloy and FSPed base alloy.

References

1. Miracle D B, *Comp Sci Tech* **65** (2005) 2526.
2. Sharma V, Prakash U, and Kumar B V M, *J Mater Process Technol* **224** (2015) 117.
3. Mishra R S, and Ma Z Y, *Mater Sci Eng R* **50** (2005) 1.
4. Arora H S, Singh H, and Dhindaw B K, *Int J Adv Manuf Technol* **61** (2012) 1043.
5. Cam G, and Mistikoglu S, *J Mater Eng Perform* **23** (2014) 1936.
6. Saadatmand M, and Mohandesi J A, *Trans Indian Inst Met* **68** (2015) 319.
7. Zarghani A S, Bozorg S F K, and Hanzaki A Z, *Wear* **270** (2011) 403.
8. Shahraki S, Khorasani S, Behnagh R A, Fotouhi Y, and Bisadi H, *Metall Mater Trans B* **44** (2013) 1546.
9. Moghaddas M A, and Bozorg S F K, *Mater Sci Eng A* **559** (2013) 187.
10. Khodabakhshi F, Simchi S, Kokabi A H, Nosko M, Simancik F, and Svec P, *Mater Sci Eng A* **605** (2014) 108.
11. Yuvaraj N, Aravindan S, and Vipin, *J Mater Res Tech* **4** (4) (2015) 398.
12. Liu Q, Ke L, Liu F, Huang C, and Xing L, *Mater Des* **45** (2013) 343.
13. Hosseini S A, Ranjbar K, Dehmolaei R, and Amirani A R, *J Alloys Compd* **622** (2015) 725.
14. Asl A M, and Khandani S T, *Mater Sci Eng A* **559** (2013) 549.
15. Soleymani S, Zadeh AA, and Alidokht S A, *Wear* **278–279** (2012) 41.
16. Alidokht, S A, Zadeh A A, Soleymani S, and Assadi H, *Mater Des* **32** (2011) 2727.

17. Sudhakar I, Madhu V, Reddy G M, and Rao K S, *Def Tech* **11** (2015) 10.
18. Mahmoud E R I, Takahashi M, Shibayanagi T, and Keuchi K, *Wear* **268** (2010) 1111.
19. Devaraju A, Kumar A, and Kotiveerachari B, *Mater Des* **45** (2013) 576.
20. Rejil C M, Dinaharan I, Vijay S J, and Murugan N, *Mater Sci Eng A* **552** (2012) 336.
21. Topan F, Kerti I, and Rocha L A, *Wear* **290–291** (2012) 74.
22. Thangarasu A, Murugan N, Dinaharan I and Vijay S J, *Arch Civil Mech Eng* **15** (2015) 324.
23. Amra M, Ranjbar K, and Dehmolaei R, *J Mater Eng Perform* **24** (2015) 3169.
24. Hashemi R, and Hussain G, *Wear* **324-325** (2015) 45.
25. Yadav D, and Bauri R, *Mater Sci Eng A* **539** (2012) 85.
26. Bradeswaran A, and Perumal A E, *Compos: Part B* **54** (2013) 146.
27. Deuis R L, Subramanian C, and Yellup J M, *Comp Sci Tech* **57** (1997) 415.
28. Abdollahi A, Alizadeh A and Baharvandi H R, *Mater Des* **55** (2014) 471.